

Final Technical Progress Report
Engineering Support for an Ultraviolet Imager for the ISTP Mission

Contract NAS8-37586

George C. Marshall Space Flight Center
Space Sciences Laboratory -
National Aeronautics and Space Administration
Marshall Space Flight Center, Alabama 35812

by

Dr. Douglas G. Torr
Principal Investigator
The University of Alabama in Huntsville
Center for Space Plasma and Aeronomic Research and Physics Department
Huntsville, Alabama 35899

February 1991

(NASA-CR-104138) ENGINEERING SUPPORT FOR AN
ULTRAVIOLET IMAGER FOR THE ISTP MISSION
(Alabama Univ.) 343 p CSCL 228

N91-22364

Unclass

68/19 0007597

Final Report on NAS8-37586

Under this contract UAH was involved in a collaborative program with MSFC to carry out design and development activities for the Ultraviolet Imager to be flown on the Polar Spacecraft of the International Solar Terrestrial Physics (ISTP) Mission. In addition several other related tasks were carried out as per statement of work. These are described below.

The following tasks were performed:

1. Design and Fabrication of Prototype/Engineering Model of the UVI Imager

Following completion of the conceptual design and table top testing at UAH, modifications were identified in accordance with the test results and, a subcontract was awarded to Perkin Elmer Corporation to optimize the UAH design and to develop and fabricate an engineering model of the optical bench.

The program was initiated with a statement of work to Perkin Elmer on 2/15/89. This was followed by a meeting on March 31, 1989. Work commenced with UAH issuing a letter of intent on 4/17/89. However, to provide the funding required to support the overall effort at Perkin Elmer, additional funding had to be provided through a second contract supporting ISTP activities at UAH, namely NAS8-36955, an umbrella contract with MSFC that was used to provide the balance in the short turn-around needed to get the Perkin Elmer effort going on schedule. The funding was provided under Delivery Order Number 59.

The work was divided into 2 phases. During phase 1 the following tasks were accomplished.

- The system and subsystem level requirements were defined
- The UAH optical design was optimized
- A sensitivity analysis of the final optical design was performed
- A straylight analysis was performed and the conceptual layout of the baffles was done with a rework done under D.O. 59
- The conceptual layout of the optical bench was generated, with final fine-tuning done under D.O. 59
- The design and layout of the optical elements was finalized and alignment tolerances and mounting interfaces defined

During Phase II an engineering model of the optical bench was fabricated and detailed engineering drawings developed. Copies of the drawings which were preliminary are attached.

The unit incorporated appropriate interfaces for the detector assemblies, filter wheel and other system interfaces. Critical components were lightweighted. A coarse NASTRAN model of the optical bench was produced and the delta temperature limits were

analyzed. A weight analysis was performed. System alignment tests were performed and an alignment procedure generated.

The deliverable of a mid-term, final report and Engineering unit Ultraviolet Imager with associated engineering drawings were delivered to MSFC on June 11, 1990.

Note: During the design development UAH identified the need for a second system of reflective filter components in the optical train which were needed to provide additional filtering to meet the UVI science spectral purity requirements. To incorporate this filter requirement Perkin Elmer was requested to insert a 45° reflective surface at the entrance aperture to the system and to fold the optical beam through 90°. This effort was carried out under subcontract NAS8-36955 - Delivery Order Number 59 and will be reported on separately. This was the main task carried out on D.O. 59.

Attached as Appendix A to this report are the Mid-Term and Final Reports received from Perkin Elmer (now Hughes Danbury). Note: Hughes Danbury did not separate out the two tasks in their reports and their final design reflects the above-mentioned changes. The reports give details on the list of tasks discussed above including the performance evaluation of the design.

It is noteworthy that the UAH design which was fine-tuned by Perkin Elmer constitutes a technological breakthrough in far ultraviolet imaging in that it represented the first high speed ($f/\# = 2.8$) imaging camera with high spatial resolution developed to date for this wavelength regime. The sensitivity improvement of the instrument over existing systems exceeded a factor of 10, placing UAH at the forefront of this technology.

2. Preliminary Design Review

UAH supported the UVI PDR at MSFC on October 17, 1989 in the following areas:

- Presentation of the optical system (not included in the attached report on PDR)
- Presentation of the data analysis software
- Report on the status of the filter design

Note: The data analysis software flowchart shown in the PDR report was generated by Science and Engineering Associates. However, UAH provided the science algorithms needed to evaluate the dependence of intensity ratios on the characteristic energy of precipitating particles. UAH presented the UVI scientific goals and described the model development that has been used to support the UVI requirements definition.

Relevant sections of the UAH contributions to PDR can be found in the copies of the PDR presentation included as Appendix B and in the Perkin Elmer reports (Appendix A). Because Perkin Elmer could not attend PDR, the optics review was conducted with the GSFC review team optics specialist in a splinter session telecon with Mr. Andreas Nonnenmacher of Perkin Elmer. Dr. D. G. Torr convened this session.

3. Vacuum Ultraviolet Filter Design

Narrowband filters with the spectral performance specified for the UVI had never been fabricated before. In order to meet the spectral requirements of the filters, a novel design strategy was developed. First, it was discovered that suitable materials

for use in the VUV had never been identified, and second, the effects of absorption which occurs in the VUV had not yet been incorporated into thin film design theory. Third, accurate measurement techniques for determining the transmission and reflectance of thin films (needed for the determination of optical constants) had not yet been developed.

All these shortcomings were addressed as follows:

- A technique was developed for the experimental determination of the reflectance and transmission of thin films and substrates in the VUV
- A mathematical algorithm was developed for the retrieval of optical constants of thin films and substrates from measurements of their reflectance and transmittance.
- Thin film multilayer theory was modified to include the effects of absorption. This essentially involved starting from scratch with Maxwell's equations.

A detailed report of the above work was published in two papers entitled "Vacuum Ultraviolet Thin Films 1: Optical Constants of BaF₂, CaF₂, LaF₂, MgF₂, Al₂O₃, HfO₂ and SiO₂ Thin Films" and "Vacuum Ultraviolet Thin Films 2: Vacuum Ultraviolet All-dielectric Narrowband Filters" attached as Appendix C.

Reprints of both papers are attached. However, it must be noted that the work reported in these two papers covers the overall development of the filter program during the course of the ISTP program under contracts NAG8-086, NAG8-639, NAS8-37576, and D.O. 59. The final reports on the above four contracts describe the early phase of the work including establishing a VUV coating facility at UAH, debugging it, and developing the state-of-the-art filter technology in existence at UAH today. The fabrication of the engineering model filters being done under this contract.

This work will have very broad applications in NASA and will open up the VUV to high resolution interferometry, photometry and high powered VUV lasers with the future development of Fabry-Perot etalons, beam splitters and high reflectance mirrors.

At the time of PDR two prototype filters had been developed and their spectral characteristics are given in the PDR report attached as Appendix B. Also shown in the PDR report are the characteristics of commercially available VUV filters. A comparison of these with the UVI filters demonstrates that we have achieved an order of magnitude improvement in performance. The filter at 135.6 nm is a narrowband filter, and the filter labeled LBH_{LONG} is a specially designed broadband filter with a rectangular bandpass which meets the specific requirements of the ISTP science.

Fabrication of the flight filters was carried out under the prime contract NAS8-38145 and is described separately in the reports on that contract.

4. Auroral Energy Deposition Code

UAH was also responsible for the development of a computer code to calculate the auroral energy deposition rate from the images to be taken by the UVI instrument. This code is needed for two purposes:

1. To determine what wavelengths and filter characteristics are needed for the UVI.
2. To provide the auroral source function to a global ionospheric model which will be used by the ISTP community in the interpretation of the measurements taken.

This task was a major undertaking and under NAS8-37586 the code was developed to a point where the filter design requirements could be finalized. Results achieved to date were published in the Journal of Geophysical Research under the title, "Auroral Modeling of the 3371 Å Emission Rate: Dependence on Characteristic Electron Energy." In addition the application of this code to interpretation of the UVI images was published in the same journal under the title, "The Dependence of Model OI 1356 Å and N₂ LBH Auroral Emissions on the Neutral Atmosphere". Other relevant associated papers partially supported under this contract are also attached as Appendix D.

5. Model of LBH Vehicle Glow

This component of the work was carried out to study the effects of optical contamination due to interactions of the spacecraft with the natural environment. Previous observations of Vacuum Ultraviolet glow had been observed on Spacelab 1 and on the DoD satellite S3-4. A preliminary model of a mechanism that could generate the glow was developed under NAS8-057 "Assessment of Vehicle Contamination In Spacelab 1 Spectroscopic Data." The model invoked surface production (and desorption) of metastable N₂(A) via surface recombination of atomic nitrogen. The N₂(A) is then collisionally excited to the a¹Πg state which radiates in the LBH bands. However, no adequate mechanism for the production of surface N could be found. In addition the mathematical development of the mechanism to account for the altitude dependence of the LBH glow was incorrect. Nevertheless, the basic concept of surface production of N₂(A) leading to a¹Πg was a major conceptual step forward. The calculations also utilized the concept of a gas build-up on vehicle surfaces which D. Torr had previously developed in conjunction with R. Rantanen of Science and Engineering Associates, Inc. This approach also proved to be crucial in the development of the understanding of the glow.

Under the current contract the following new developments occurred:

1. A source for surface N was found. It was argued that ambient N₂ impacting the vehicle surface would acquire vibrational excitation which could provide the exothermicity needed for the reaction



to proceed, thereby providing an abundant source of surface N.

2. The surface chemistry was updated to take account of the production and loss mechanisms for N₂(X) $\nu \geq 13$, O, N and N₂(A).
3. The effects of radial outflow on the N₂(A) gas cloud distribution was included.
4. An analytical formulation of the model was generated in which the scale height dependence of both the N₂(A) and N₂(a¹Πg) could be easily predicted. Previous calculations of Rantanen and Gordon of the re-emitted gas cloud around a 1m disk were

scaled to provide an estimation of the contaminant cloud concentrations. The model correctly predicted both N₂ LBH and Vegard Kaplan (VK) emission intensities for the glow observed on Spacelab 1 and S3-4 as well as the height dependence observed on the S3-4 satellite. A paper reporting these results was submitted for publication to the Journal of Geophysical Research, and a copy of this version of the paper is attached as Appendix E. However, one reviewer argued that VK emissions were not observed on S3-4, and thus questioned the validity of the model. This was the status of the paper at the conclusion of the work under this contract. Since that time, the work has been continued by Science and Engineering Associates under DoD funding and it appears that the conflict with the S3-4 data will be resolved.

6. Laboratory Measurement Program of Collision Cross-Sections

Dr. C. Keffer was supported for the period June 1 through September 30, 1989 on this contract. During this period the following tasks were accomplished:

- Completed drawings for using the new large vacuum chamber as an EUV calibration facility.
- Implemented the EUV calibration facility and conducted tests on a CCD detector system.
- The cross-section chamber was assembled which was delivered mid July, 1989. This task involved numerous minor time consuming activities. For example, the rotary platform did not turn freely when installed, because the mating flanges were not flat. All parts had to be cleaned before use of the 5 eV O beam. Assembly was completed by mid September.
- The system appeared to be working satisfactorily upon pump-down.
- Development of the system software was continued.
- Alignment tests commenced mid September, but it was found that the chamber goes out of alignment while under vacuum. Additional hardware was ordered to repair the problem.

This effort represented all the work done on the establishment of the cross-section facility at MSFC under this contract. Continued work on this project was funded under other contracts.

7. Support of ISTP Meetings

UAH personnel attended and participated in the ISTP design review meetings at GSFC and GE, Science Working Group meetings and meetings held with the NASA Headquarters Program Office personnel to resolve the issue of merging the UVI and Visible Imager teams of Iowa and Johns Hopkins Universities.

APPENDIX A



The University
Of Alabama
In Huntsville

Huntsville, Alabama 35899
(205) 895-6000
Telefax: (205) 895-6677

Research Administration

M E M O R A N D U M

TO: Dr. D. G. Torr
Physics

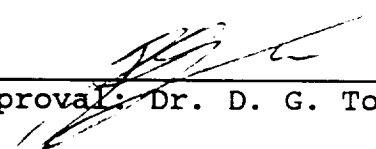
FROM: Kathy Niemi *nk*
Contract Assistant

SUBJECT: Final Report for SUB89-117 amd SUB90-064

DATE: August 6, 1990

I have enclosed a copy of the final report on the above referenced subcontracts. If this report satisfactorily meets the reporting requirements of these subcontracts and all deliverables have been received and accepted, please sign the concurrence line below signifying such and return this memorandum to me.

If you have any questions, I can be reached at the above number. Thank-you.


Approval: _____
Dr. D. G. Torr



Danbury Optical Systems, Inc.

100 Webster Heights Road
Danbury, CT 06810-1569

RECEIVED JUL 18 1990

CD-JMC-1611
July 16, 1990

University of Alabama
Research Administration
Huntsville, AL 35899

Attention: R. McKinley

Subject: Ultra-Violet Imager Final Report

Reference: Subcontracts SUB89-117 and SUB90-064

Dear Ms. McKinley:

Enclosed is a Final Report for the Ultra-Violet Imager Optical System. This document is submitted in accordance with final report requirements and completes our contractual obligations under the referenced subcontracts.

Very truly yours,

HUGHES DANBURY OPTICAL SYSTEMS

Jean M. Cassavechia
Principal Contract Administrator

JMC/cac
Enclosure

ULTRA-VIOLET IMAGER OPTICAL SYSTEM

- **UVI Optical Design**
- **Error Budget**
- **Straylight Requirements and Analysis**
- **Engineering Model Hardware and Analysis**

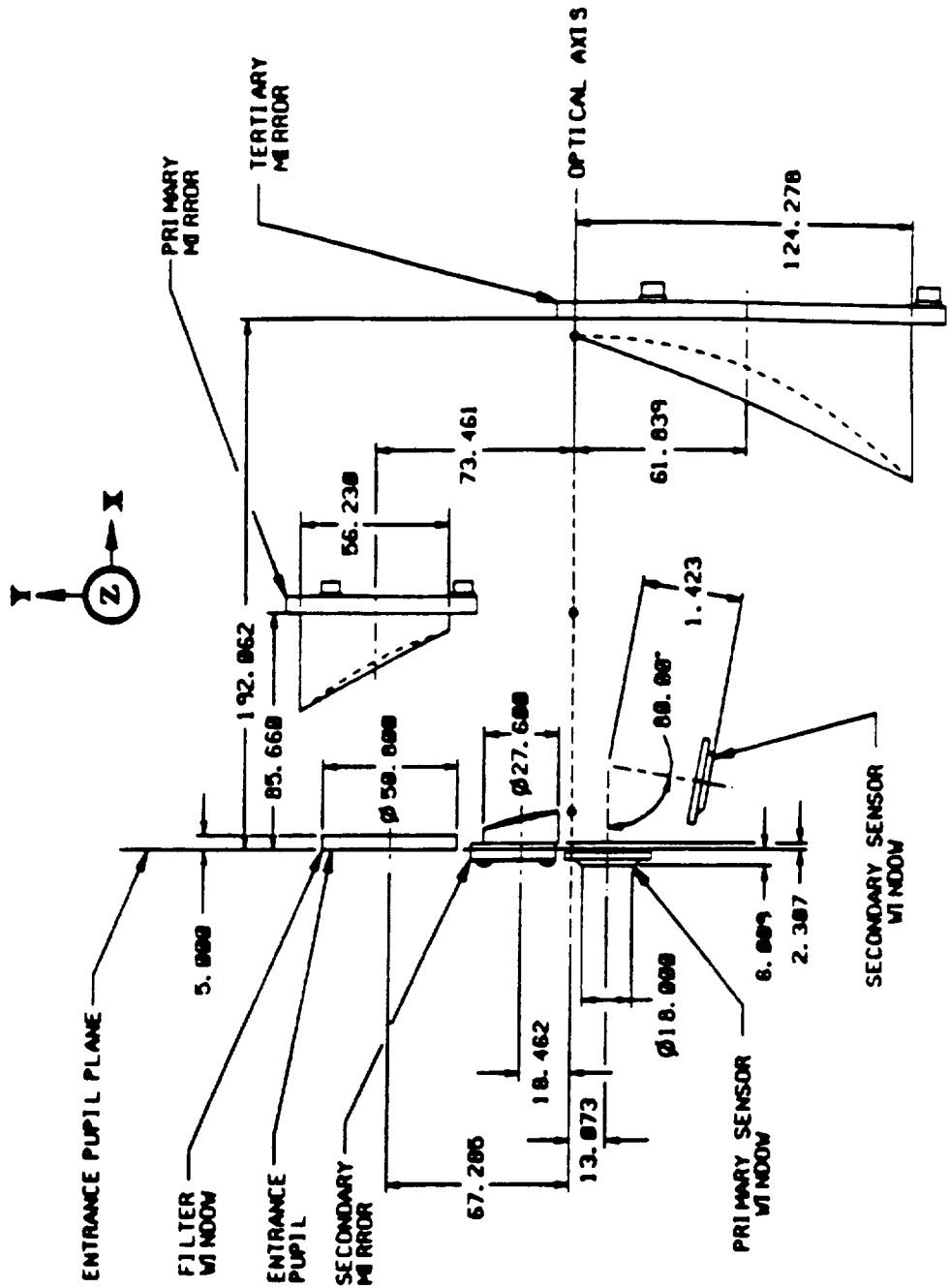
UVI Optical Design

- **UVI is a reflective, three element, eccentric, generalized aspheric telescope.**
- **Telescope performance has been optimized to minimize encircled energy variations across the FOV.**
- **This configuration affords a small, compact telescope with imaging properties commensurate with the UVI focal plane.**

Ultra-Violet Telescope Parameters

Telescope EFL: 123.968614 mm
Entrance Pupil Ø: 42.976800 mm (offset 67.2846 mm from optical axis)
System f/#: 2.884547
Full Field of View: 8° (circular)
Field Bias: -6.0°
Plate Scale: 2.1637 mm/degree
Detector Pixel Size: 54 µm x 32 µm (apparent)

UVI Optical Layout



UVI OPTICAL LAYOUT

ALL DIMENSIONS IN MM

ORIGINAL PAGE IS
OF POOR QUALITY

1.3,0,-1
WAVELENGTH

0.213860 0.213860 0.213860

PHI 0.000000E+00

[TOLKHO]

NO.	SURFACE TYPE	TILT TYPE	DIFFRACT TYPE	RADIUS	THICKNESS	ND-INDEX	NI-INDEX	LO-INDEX	ABBE NO.	GLASS NAME	CLEAR APERT	OUTER BOUND
0	ENTRANCE PUPIL				85.5975	-1.000000	-1.000000	-1.000000				
1	SPHERE			INFINITE	-50.0000	-1.000000	-1.000000	-1.000000	0.00	AIR	54.95	0.00
2	SPHERE	RESTORE		INFINITE	0.0000	1.000000	1.000000	1.000000	0.00	AIR	65.41	0.00
3	SPHERE	NORMAL		INFINITE	35.5975	1.000000	1.000000	1.000000	0.00	AIR	47.96	0.00
4	SPHERE	NORMAL		INFINITE	0.0000	1.000000	1.000000	1.000000	0.00	AIR	43.53	0.00
5	SPHERE			INFINITE	5.0000	1.415660	1.415660	1.415660	0.00	AIR	43.53	0.00
6	SPHERE			INFINITE	0.0000	1.000000	1.000000	1.000000	0.00	AIR	44.77	0.00
7	SPHERE	NORMAL		INFINITE	80.7123	1.000000	1.000000	1.000000	0.00	AIR	179.34	0.00
8	ASPHERE			-162.3568	-72.0000	-1.000000	-1.000000	-1.000000	0.00	AIR	196.80	0.00
9	ASPHERE			-83.4644	172.0000	1.000000	1.000000	1.000000	0.00	AIR	58.19	0.00
10	ASPHERE			-174.2186	-186.8951	-1.000000	-1.000000	-1.000000	0.00	AIR	241.47	0.00
11	SPHERE			INFINITE	-4.8260	-1.415660	-1.415660	-1.415660	0.00	AIR	45.46	0.00
12	SPHERE			INFINITE	0.0000	-1.000000	-1.000000	-1.000000	0.00	AIR	44.03	0.00
13	SPHERE			INFINITE	0.0000	-1.000000	-1.000000	-1.000000	0.00	AIR	44.03	0.00

TABLE OF DECENTRATIONS, TILTS AND ROTATIONS

NO.	TYPE	X-DEC.	Y-DEC.	Z-DEC.	(Y-TILT) THETA Z	(Z-TILT) THETA Y	THETA X
2	3		0.000000E+00	0.000000E+00	-4.500000E+01	0.000000E+00	0.000000E+00
3	1		0.000000E+00	0.000000E+00	-9.000000E+01	0.000000E+00	0.000000E+00
4	1		0.000000E+00	0.000000E+00	-6.000000E+00	0.000000E+00	0.000000E+00
7	1		-6.728460E+01	0.000000E+00	0.000000E+00	0.000000E+00	0.000000E+00

SURFACE TYPE 2 ASPHERIC COEFFICIENTS

NO.	Epsilon (CC+1.0)	C'	D'	E'	F'
8	6.115486E-01	0.000000E+00	9.347959E-13	-4.898472E-17	1.190927E-21
9	-3.159321E+00	0.000000E+00	1.849998E-09	-2.136067E-12	8.004905E-15

ORIGINAL PAGE IS
OF POOR QUALITY

OBJECT DISTNCE	ENTR.PUP.DIST	FRST.PPAL.PNT	EFF.FCL.LNGTH	SCND.PPAL.PNT	EXT.PUP.DSTNC	IMAGE DISTNCE
INF	-85.597500	385.838109	123.968614	-124.542469	43.653432	-0.573855
OBJECT HEIGHT	ENTR.PUP.DIAM	OBJT.SPCE.FNO	INF.OBJCT.FNO	INSE.SPCE.FNO	EXT.PUPL.DIAM	IMAGE HEIGHT
INF	42.976800	INF	2.884547	2.884547	-15.333181	17.422653
MAGNIFICATION	SEMIANG.FIELD	BACK VTX.DIST	BARREL LENGTH	FRMT.VTX.DIST	SEMIANG.FIELD	MAGNIFICATION
0.000000	8.000000	- INF	-20.411292	-20.411292	-22.422901	INF
APT.STOP DIAM	APT.STOP DIST	FROM SRFCE.NO	XXXXXXXXXXXX	FLD.STOP DIAM	FLD.STOP DIST	FROM SRFCE.NO
42.976800	-85.597500	0		14.845305	-0.573855	12

CASE FNO/SIZE	AFOCAL CODE	TARGET OBJ DIST	TARGET F.L.	OBJ.CURV	BASE COLOR	Y-YEAR	OBJ/IMG
1 1	0	0.00000+00	2.54000+01	0.00000+00	3	0	-9

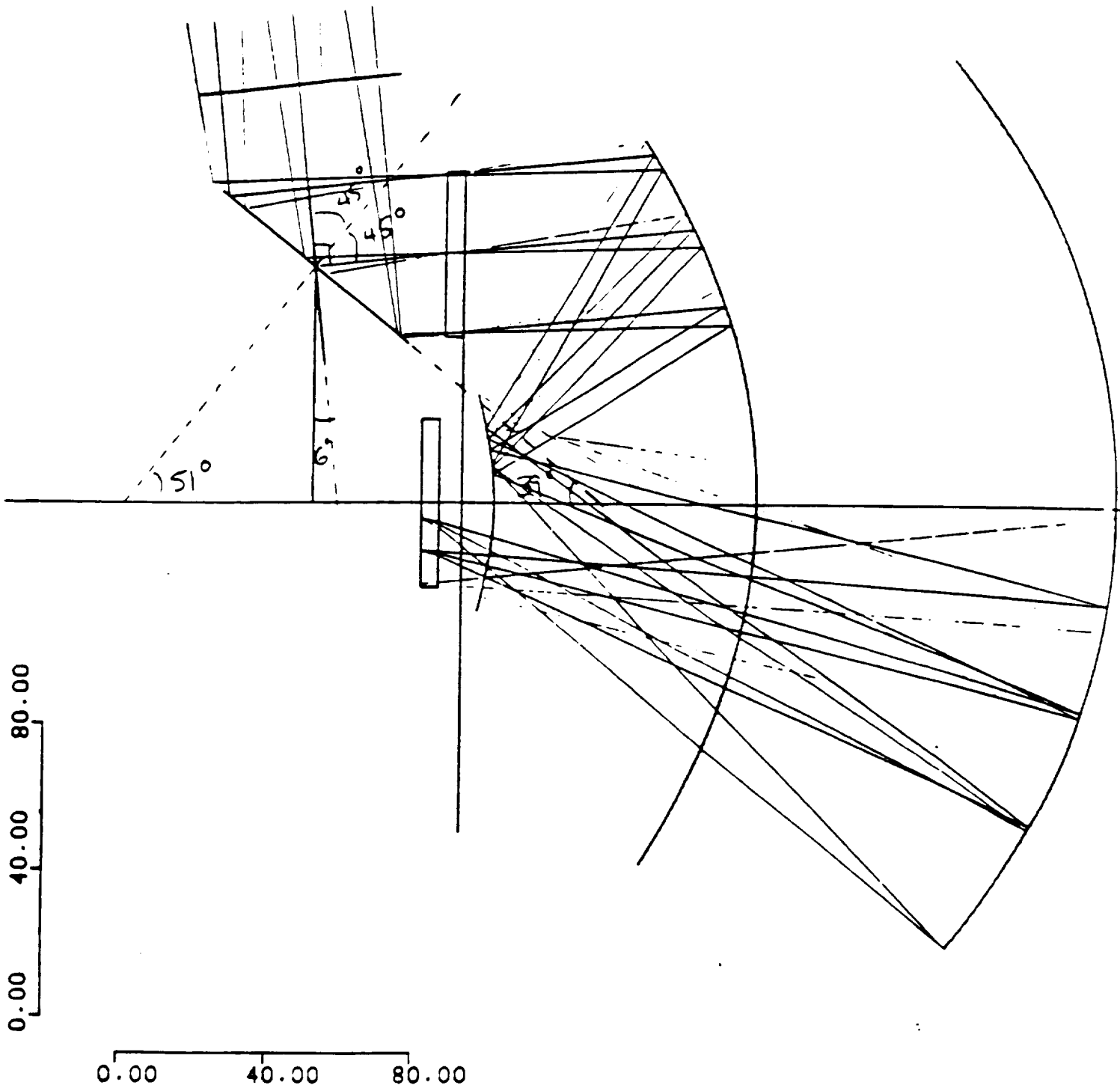
REAL ENTR. PUPIL CODES : 0 0

C

ORIGINAL PAGE IS
OF POOR QUALITY

TORR'S TELESCOPE

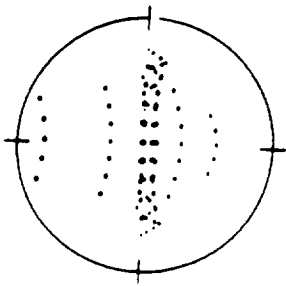
09:38:40----- 1/ 5/90





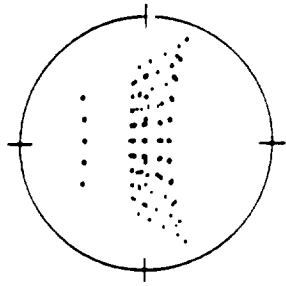
Danbury Optical Systems, Inc.

Spot Diagrams



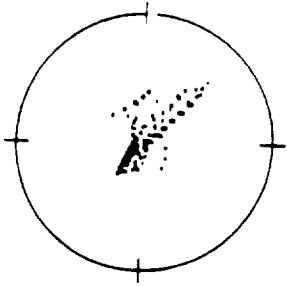
RMS RADIUS 2.26084 $\cdot 10^{-02}$

(0,0)



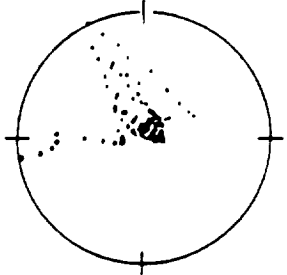
RMS RADIUS 2.12793 $\cdot 10^{-02}$

(4,0)



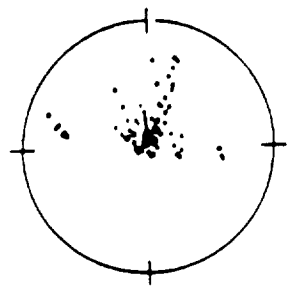
RMS RADIUS 1.28592 $\cdot 10^{-02}$

(4,45)



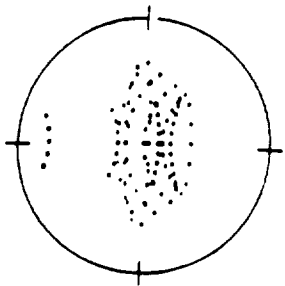
RMS RADIUS 1.79178 $\cdot 10^{-02}$

(4,90)



RMS RADIUS 2.43953 $\cdot 10^{-02}$

(4,135)

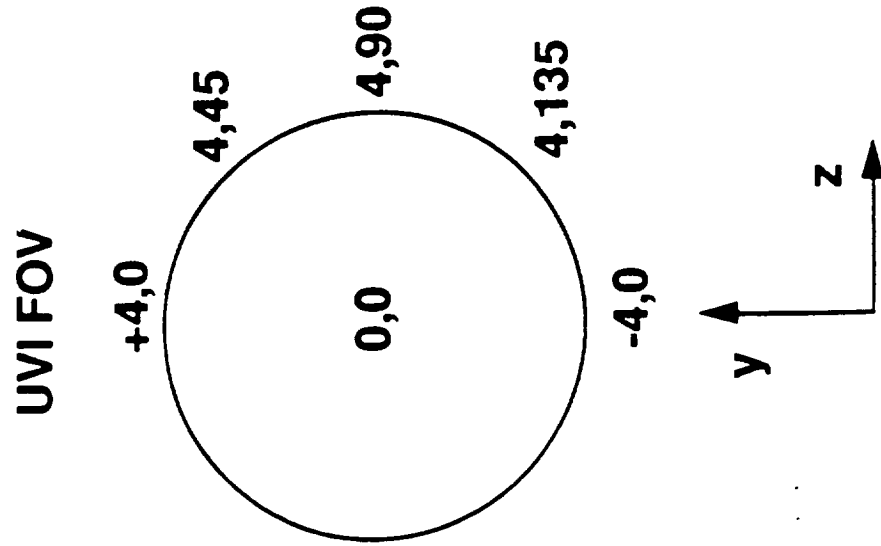


RMS RADIUS 1.93407 $\cdot 10^{-02}$

(-4,0)

ORIGINAL PAGE IS OF POOR QUALITY

UVI Nominal Optical Performance



Field Location (degrees)	Spot Size (μm rms)	Encircled Energy (% in 27 μm radius)
(0,0)	22.808	71.134
(+4,0)	21.279	77.320
(-4,0)	19.361	86.598
(4,90)	17.918	85.567

These numbers are based on nominal design values with no environmental or manufacturing errors corrupting performance

Local optical design coordinate system

UVI Error Budget

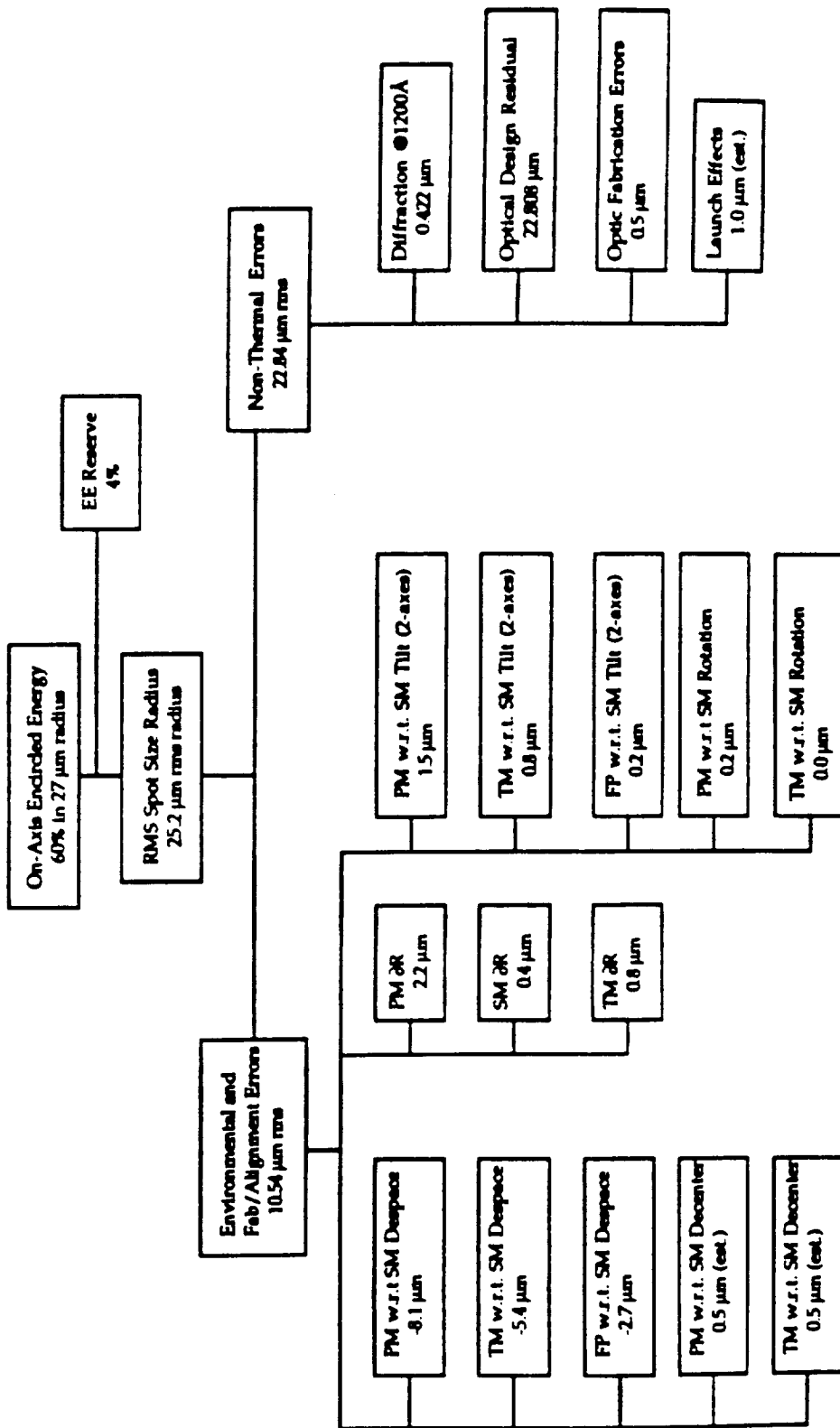
- Error budgeting effort driven by requirement of $\geq 60\%$ encircled energy in a $27 \mu\text{m}$ radius spot.
- Error budget done in terms of on-axis rms spot size, which can be directly related back to encircled energy.
- Error budget takes into account initially provided thermal and mechanical environments as well as mirror fabrication errors, and alignment errors.
- Mirror figure requirements ($\lambda/2$ rms @ 6328\AA) arrived at via iterative raytrace/encircled energy evaluation.

Error Budget Assumptions

- Error budget based on the following thermal environmental data:
 - Bulk Ground-to-orbit ΔT : $-20\text{ }^{\circ}\text{C}$ ($-36\text{ }^{\circ}\text{F}$)
 - Orbit-to-orbit ΔT : $\pm 5.5\text{ }^{\circ}\text{C}$ ($\pm 10\text{ }^{\circ}\text{F}$)
 - On-orbit gradient: $\pm 0.1\text{ }^{\circ}\text{C/cm}$ ($\pm 0.5\text{ }^{\circ}\text{F/in}$)
- Launch environment taken from ICD

UVI Error Budget Tree

Ultra-Violet Imager Error Budget
(On-Axis with -6° bias)



Primary Mirror w.r.t. Secondary Mirror Despace Contributors

$$\Delta l(\text{in.}) = \alpha(\text{in./in./}^\circ\text{F}) l(\text{in.}) \Delta T(^\circ\text{F})$$

Bulk Temperature Change - Ground to Orbit $\Delta T = -36^\circ\text{F} (-20^\circ\text{C})$

	Length	Material	CTE(in/in/°F)	Δ (in.)
SM Body to Flange	0.449	Al 6061-T651	1.36E-05	2.20E-04
Flang to Housing Shim	0.05	AISI 410	5.50E-06	-9.90E-06
Housing	3.182	Al 6061-T651	1.36E-05	-1.56E-03
PM Flang to Housing Shim	0.05	AISI 410	5.50E-06	-9.90E-06
PM Body to Flange	0.25	Al 6061-T651	1.36E-05	1.22E-04

$$\Delta l = -0.00124 \text{ in.}$$

$$(-0.032 \text{ mm})$$

Bulk Temperature Change - Orbit to Orbit $\Delta T = \pm 10^\circ\text{F} (\pm 5.5^\circ\text{C})$

	Length	Material	CTE(in/in/°F)	$\pm \Delta$ (in.)
SM Body to Flange	0.4488	Al 6061-T651	1.36E-05	6.10E-05
Flang to Housing Shim	0.0500	AISI 410	5.50E-06	-2.75E-06
Housing	3.1804	Al 6061-T651	1.36E-05	-4.33E-04
PM Flang to Housing Shim	0.0500	AISI 410	5.50E-06	-2.75E-06
PM Body to Flange	0.2499	Al 6061-T651	1.36E-05	3.40E-05

$$\Delta l = \pm 0.00034 \text{ in.}$$

$$(\pm 0.009 \text{ mm})$$

Manufacturing and Assembly Errors

Measurement of Optical Surfaces to Reference Surfaces : $\pm 0.00014 \text{ in.}$ (includes both PM and SM)

Measurement of Spacing between Optics: $\pm 0.0005 \text{ in.}$

Total Errors: $\pm 0.00052 \text{ in.}$ ($\pm 0.0132 \text{ mm}$)

A conservative total Primary Mirror w.r.t Secondary Mirror Despace Error is given by the rss of these values:

$$\epsilon = \pm 0.0014 \text{ in.} (\pm 0.035 \text{ mm})$$

Total Allowable: $\epsilon_t = \pm 0.002 \text{ in.}$ ($\pm 0.050 \text{ mm}$)

Margin: $\epsilon_m = \pm 0.0014 \text{ in.}$ ($\pm 0.035 \text{ mm}$)

Error Budget Summary

- **Margin has been built into the numbers used in the sensitivity studies, which in turn were flowed into error budget.**
- **The current error budget with large Δ temperatures can meet the 60 % encircled energy requirement.**
- **With further refinement of thermal environment, error budget will be revised.**
- **The 3 element telescope system is flexible enough to allow for re-optimization of the focal plane location to compensate for fabrication and/or alignment errors.**

UVI Straylight Analysis

Objective:

To maintain the straylight level of the system at least 1 order of magnitude lower than the naturally occurring day/night glow in the scene being imaged.

Key contributors:

Direct and diffuse light from the sun and earth limb reflected thru the system

Design variables:

Baffle geometry and surface finish

Optical bench internal surface finishes

Mirror smoothness

Design Considerations

- **Baffle**
 - Envelope constraints and number of internal vanes**
 - Manufacturability of baffle subassembly**
 - Baffle surface finish**
- **Optics**
 - How much energy is scattered out of the image as a function of μ -roughness?**
 - How smooth can one polish electroless-nickel plated, diamond turned optics?**
- **Internal surfaces**
 - Are internal vanes required?**
 - What surface finishes provide adequate absorption and are compatible with the manufacturing process?**

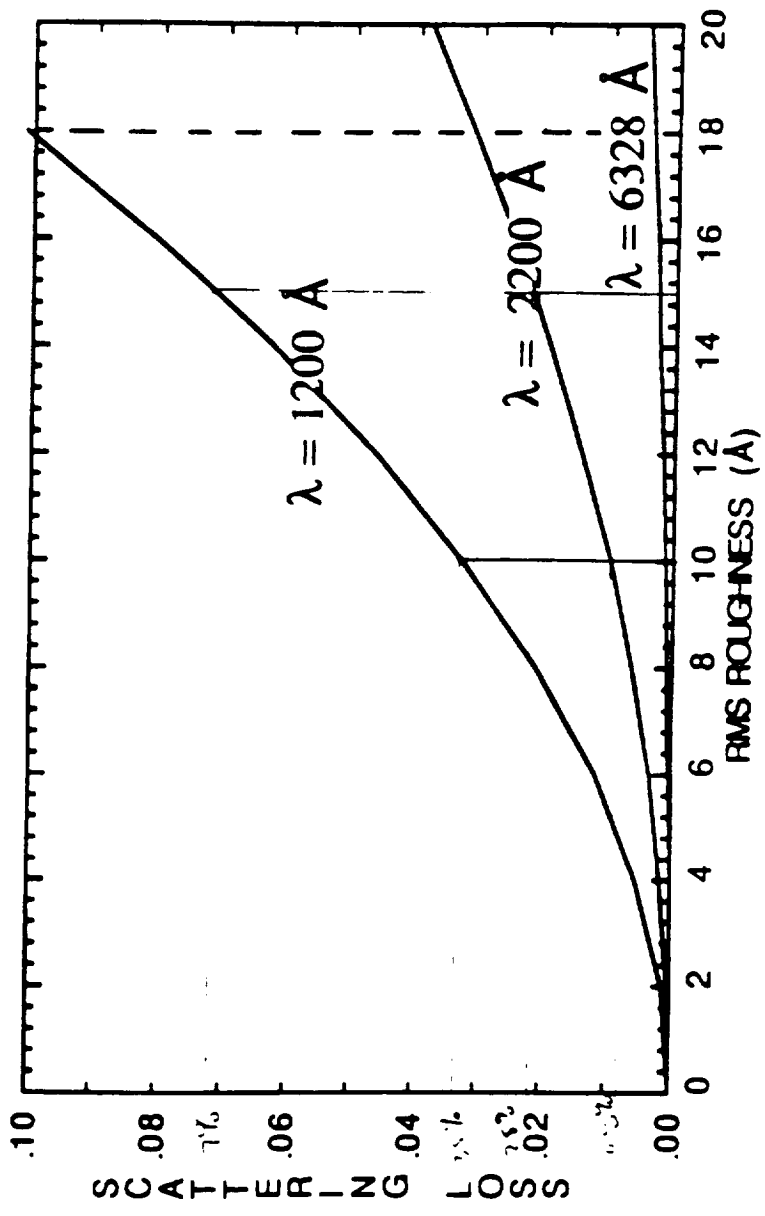
Straylight Analysis

- **Performed Total Integrated Scatter (TIS) analysis to determine required mirror μ -roughness specification**
- **Detailed APART model of UVI was developed and baffle design and internal configuration were optimized**
- **APART model run using Chemglaze (Z306) and ITTRI MH21-1C paints for baffle coating and Chemglaze for internal surfaces and 15A rms μ -roughness for each mirror**



Danbury Optical Systems, Inc.

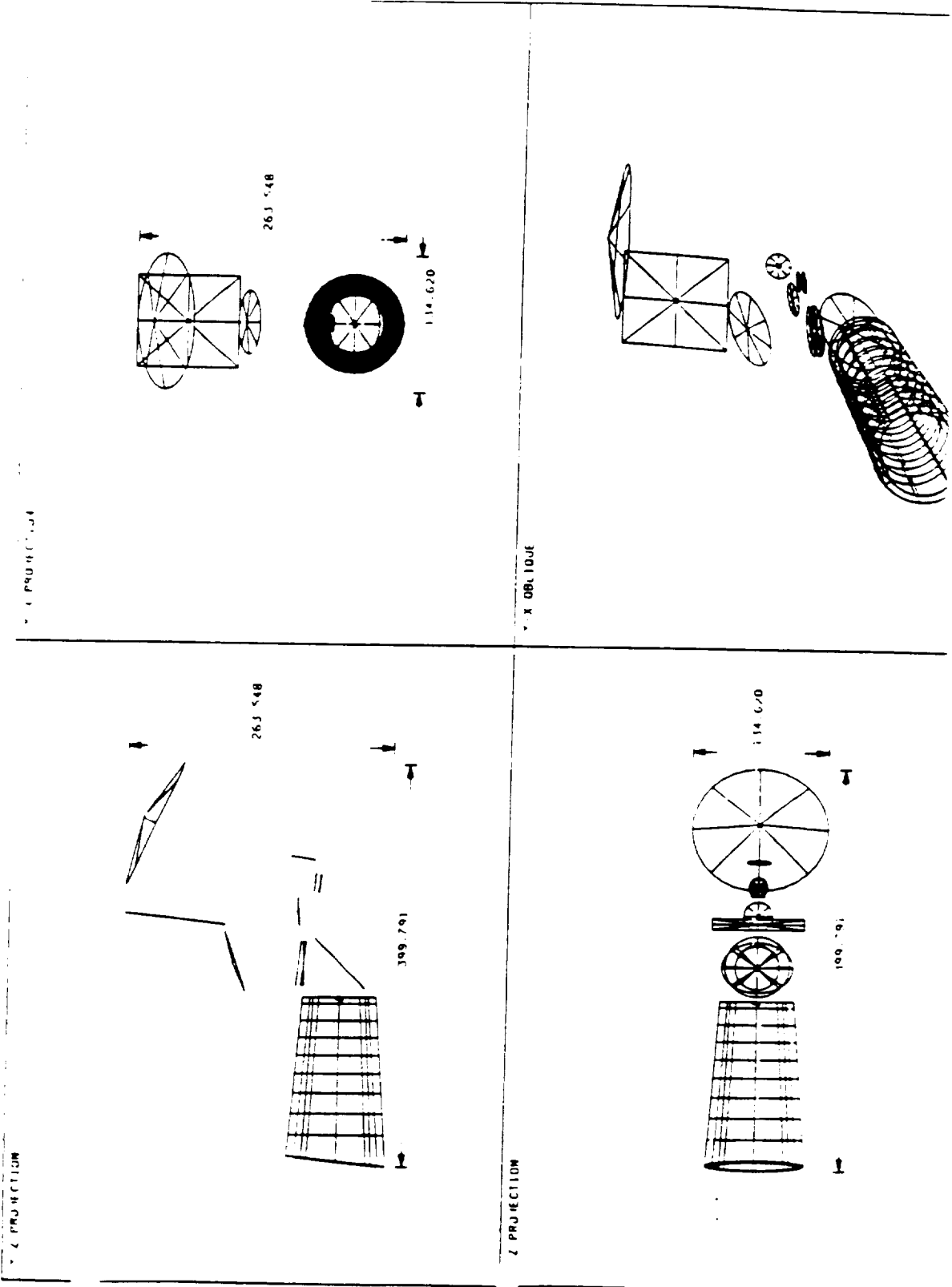
Total Integrated Scatter Curve



HUGHES

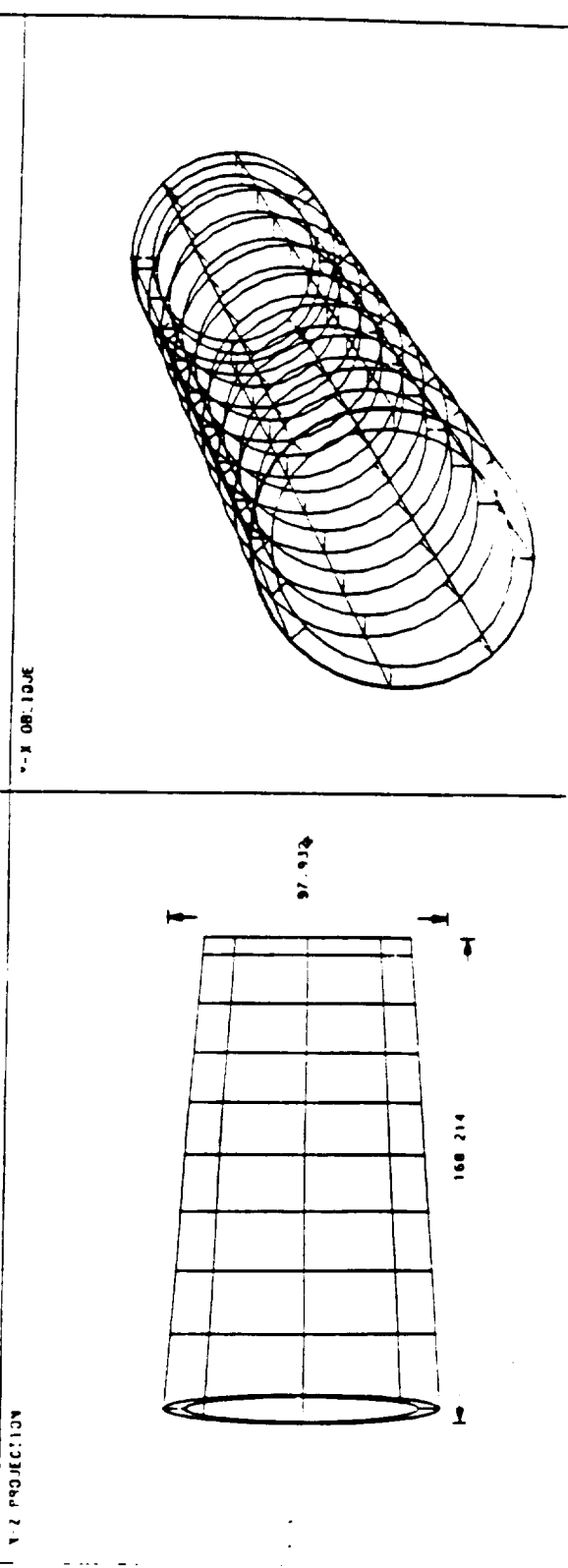
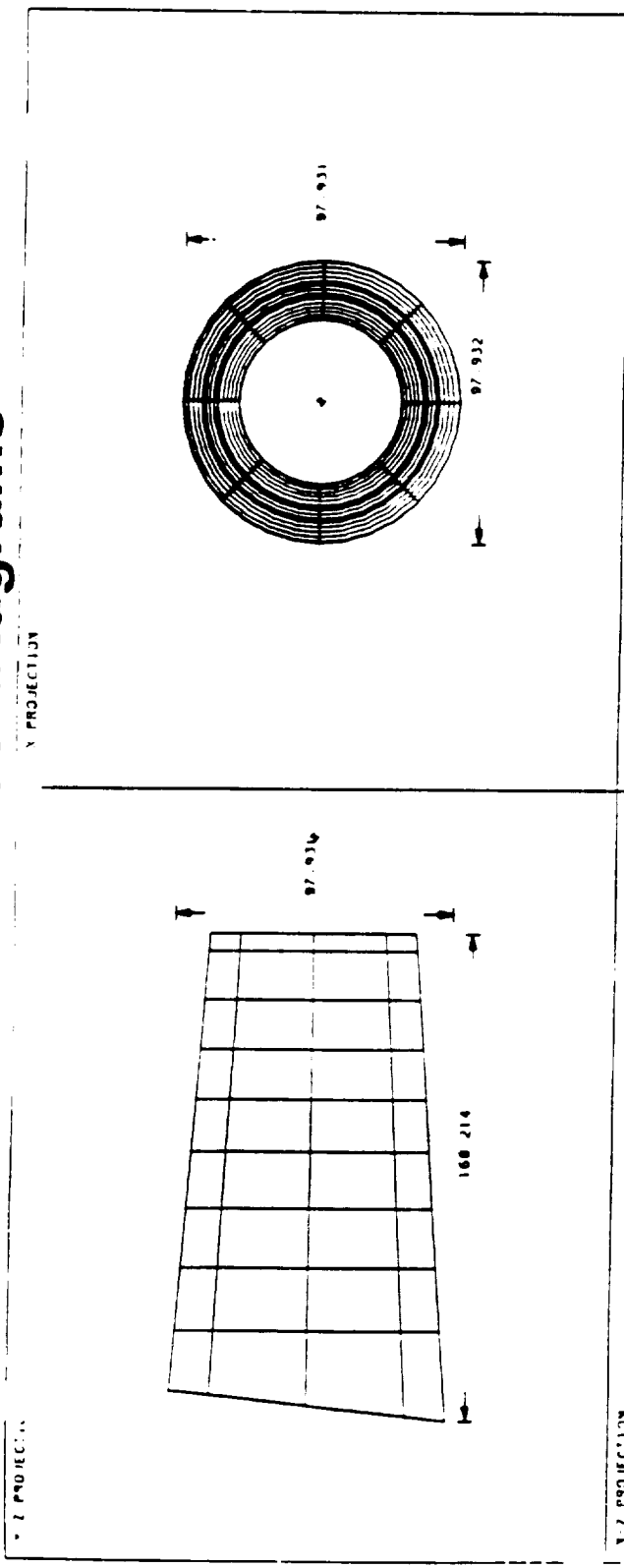
Denbury Optical Systems, Inc.

APART Model Diagrams



ORIGINAL PAGE IS
OF POOR QUALITY

APART Model Diagrams



ORIGINAL PAGE IS
OF POOR QUALITY

Straylight Analysis Results

Wavelengths A	Mean Background (W/cm ²)	Straylight Throughput - In-Band Altitude = 2 Earth Radii (W/cm ²)			Straylight Throughput - In-Band Altitude = 9 Earth Radii (W/cm ²)		
		0 deg.	90 deg.	135 deg.	0 deg.	90 degrees	135 degrees
1191 - 1241	7.351E-08	0E+00	0E+00	2.79E-14	0E+00	0E+00	2.79E-14
1279 - 1304	4.570E-08	0E+00	0E+00	7.59E-14	0E+00	0E+00	7.59E-14
1331 - 1381	4.395E-09	0E+00	0E+00	1.28E-13	0 E+00	0E+00	1.28E-13
1400 - 1700	1.127E-09	0E+00	0E+00	4.21E-12	0E+00	0E+00	4.21E-12
1468 - 1518	1.331E-10	0E+00	0E+00	4.10E-13	0E+00	0E+00	4.10E-13
1700 - 2000	9.465E-10	7.67E-14	3.59E-15	2.06E-11	5.04E-14	1.00E-14	2.06E-11
2125 - 2175	7.392E-09	3.88E-14	1.82E-15	9.69E-12	2.54E-14	5.08E-15	9.69E-12

UVI Straylight Summary

- E-Model baffle is presently coated with Chemglaze.
- Current baffle configuration and surface finish selection meet straylight requirements with margin.

UVI Engineering Model

- **All 3 optics are SPDT electroless nickel plated, Al optics. machined from 6061-T651 aluminum stress relieved and aged followed by electroless nickel coating each mirror assembly single point diamond turned to $\leq \lambda/2$ super-polished to $\leq 12 \text{ \AA}$ rms**
- **Optical bench assembled at HDOS and optics integrated and aligned to opto-mechanical tolerances.**
- **Assembled and aligned taking into account eventual thermal shrinkage.**
- **Post build optical analysis was performed using as-built numbers and focal plane location optimized for in-air testing at MSFC.**

ULTRA-VIOLET IMAGER OPTICAL BENCH & BASEPLATE

- Description of Hardware Configuration
- E-Model Hardware

Optical Bench & Baseplate

- **Optical Bench and Baseplate design are driven by weight, dynamics and manufacturing requirements and desires.**
- **Optical Bench mounted off of Baseplate using 3 flexures to minimize dynamic/thermal induced motion of bench.**
- **Mirrors are coaligned, pinned and bolted to Optical Bench structure.**
- **Baseplate is fabricated from single boule of material, lightweighted and stress-relieved.**

UVI Assembly & Alignment

Assembly Flow Overview:

- Optical Bench & Flexures assembled and aligned**
- Primary Mirror & Secondary Mirror aligned and pinned in PM/SM Housing**
- PM & SM Ass'y aligned to reference surfaces on optical bench**
- Tertiary Mirror aligned to PM/SM Ass'y and Optical Bench**
- PM/SM Ass'y pinned to Optical Bench**
- Tertiary Mirror pinned to Optical Bench**
- Baffle integrated into Optical Bench Ass'B**
- Optical bench Ass'y aligned and pinned to Baseplate**
- Remaining optical elements integrated into Optical Bench Ass'y**

HUGHES

Danbury Optical Systems, Inc.

100 Wooster Heights Road
Danbury CT 06810-7589

CD-JMC-1507
February 2, 1990

University of Alabama
Research Administration
Huntsville, AL 35899

Attention: D. Torr

Subject: Optical Performance Error Budget Report for the
ISTP Ultra-Violet Imager - UVI-100

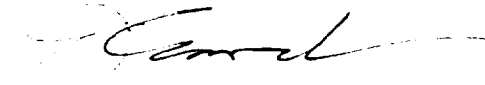
Reference: UAH Subcontract SUB89-117 and SUB90-064

Dear Dr. Torr:

Enclosed for your information is a copy of the subject document.

Very truly yours,

HUGHES DANBURY OPTICAL SYSTEMS


Jean M. Cassavechia
Sr. Contract Administrator

JMC/cac

Enclosure

cc: Dr. M. Torr - w/encl.
M. Miller - ltr only

Hughes Danbury Optical Systems, Inc.
(Formerly the Electro-Optics Technology
Division of the Perkin-Elmer Corporation)

**ORIGINAL PAGE IS
OF POOR QUALITY**

UVI-100
January 29, 1990

**Optical Performance Error Budget Report
for the
ISTP Ultra-Violet Imager**

Prepared by:

Andreas L. Nonnenmacher
Space Science Programs

Hughes Danbury Optical Systems, Inc.
100 Wooster Heights Road
Danbury, CT 06810

Table of Contents

	Page
1. Introduction	1
2. Ultra-Violet Imager Mission Summary	2
3. Ultra-Violet Imager Telescope Description	3
4. Development of the UVI Error Budget Tree	22
5. UVI Telescope Error Budget	25
6. Conclusions	28
7. References	29
Appendix A - Error Budget Calculation Details	A-1

List of Tables

		Page
Table 3.1	UVI System Parameters	3

List of Figures

Figure 3.1	UVI Optical Layout	4
Figure 3.2	UVI - Original Prescription	6
Figure 3.3	UVI - Optimized Prescription	9
Figure 3.4	Spot Diagrams for Optimized System	12
Figure 3.5	Optimized Prescription with Filter Mirror	18
Figure 4.1	Image Quality Descriptors	23
Figure 5.1	UVI Error Budget Tree	27

1. Introduction

This report summarizes the approach taken and analyses performed in deriving the optical performance error budget for the International Solar-Terrestrial Physics Ultra-Violet Imager (UVI).

Presently under contract to the University of Alabama/Huntsville for the UVI engineering model (Subcontracts SUB89-117 and SUB90-064), Hughes DOS responsibilities formally encompass only the UVI telescope, i.e. the three off-axis aspheric mirrors and the structure required to maintain alignment between these optics, telescope baffling, interfaces to the spacecraft and MSFC hardware, as well as the associated systems engineering, and optical (encircled energy and straylight performance) and structural dynamics analyses.

Additional analyses, primarily a detailed thermal analysis of the instrument to determine ground-to-orbit and on-orbit environments, are being performed by MSFC. As results from these analyses are released, appropriate revisions to the error budget will be made.

2. Ultra-Violet Imager Mission Description

The Ultra-Violet Imager mission objective is to spatially and temporally map the aurora oval in the vacuum ultra-violet region of the spectrum, thereby providing a description of the Earth's magnetic field boundaries. This in turn offers one insight into the behavior of the energetic particles associated with the solar wind. In particular, total particle energy in-flux, particle acceleration processes, and characteristic energies of incoming particles can be determined. A major mission objective is the ability to image both the sunlit and nightside aurora, therefore requiring an instrument with extremely good straylight rejection and out-of-band rejection capabilities.

UVI is to be mounted on the single-axis despun platform of the POLAR spacecraft which will orbit the earth in a highly elliptical polar orbit, providing viewing of the entire northern and southern hemispheres. Since observation of the entire aurora oval is desired at orbit apogee (approximately 9 earth radii), the UVI telescope has been designed with an 8° circular full field-of-view.

3. UVI Telescope Description

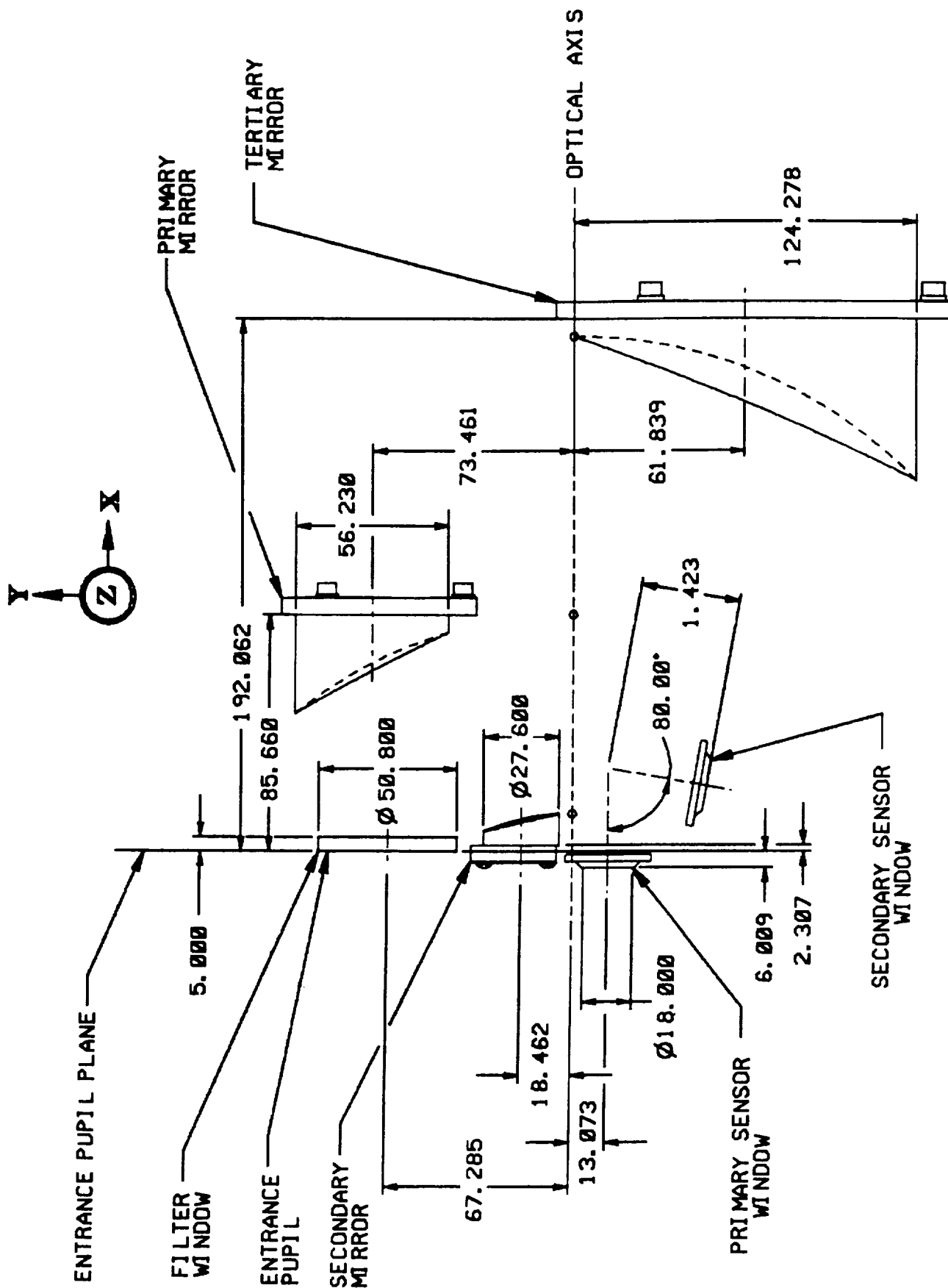
The Ultra-Violet Imager telescope being fabricated is a three mirror design with an effective focal length (EFL) of 123.97 mm and an entrance pupil diameter of 42.98 mm implying a telescope speed of $f/2.88$. However, since the aperture of the system is 67.28 mm eccentric to the optical axis, the system is, from an optical design point of view, effectively an $f/0.7$ system, making it an extremely fast telescope.

Figure 3.1 shows a functional plan view of the final optical layout. Depicted are optical element bodies (without mounting flange details), mirror body diameters, and nominal dimensions between optics showing axial locations and how far off-axis each element is located. Note that the filter mirror (refer to Figure 3.5) is not depicted here. Table 3.1 provides some nominal system parameters.

Table 3.1 UVI System Parameters

Telescope EFL:	123.968614 mm
Entrance Pupil \varnothing :	42.976800 mm (off-set 67.2846 mm from optical axis)
System $f/\#$:	2.884547
Full Field of View:	8° (circular)
Field Bias:	-6°
Plate Scale:	2.1637 mm/degree
Detector Pixel Size:	54 μm x 32 μm (apparent)

The original candidate three mirror optical system with a -6.25° field bias (Figure 3.2) was provided to Hughes DOS by MSFC. Using MEXP, a HDOS proprietary



UVI OPTICAL LAYOUT

ALL DIMENSIONS IN MM

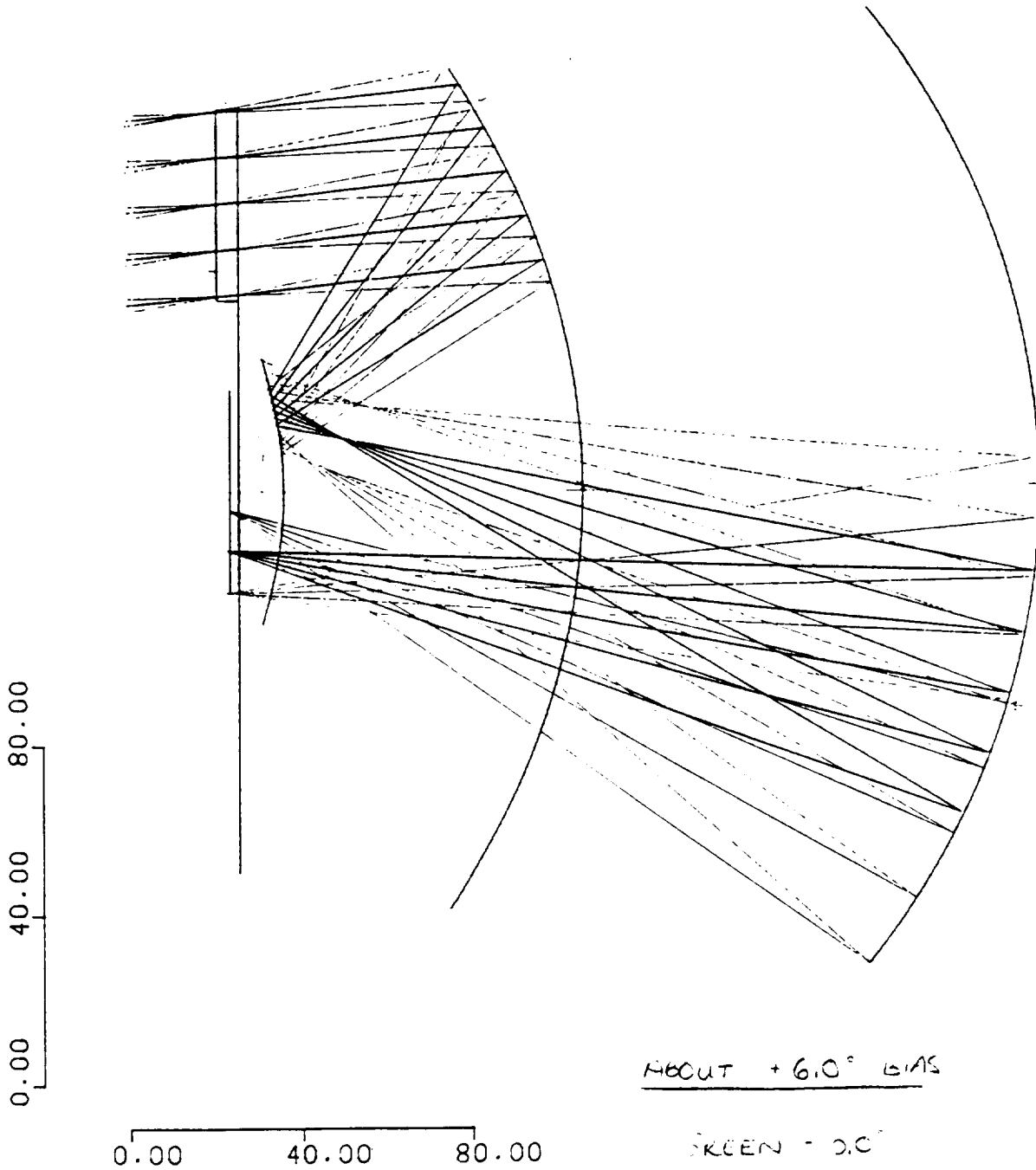
optical analysis code, preliminary analyses showed that the system had relatively poor on-axis encircled energy (EE) performance (48% in a 27 μm radius) which varied greatly across the total FOV from a minimum of 31% (at $-4^\circ, 0^\circ$) to 87% (at $+4^\circ, 0^\circ$) in the 27 μm radius.

The three mirror system was subsequently optimized adjusting the spacings between the optics, changing the field bias to -6.0° , and altering the aspheric terms of the three mirrors (Figure 3.3), resulting in improved on-axis performance as well as minimizing variations across the field. The on-axis EE performance was improved to 71% in a 27 μm radius, and the EE variation across the FOV ranged from 71% (at $0^\circ, 0^\circ$) to 86% (at $-4^\circ, 0^\circ$) in the 27 μm radius. Figure 3.4 show spot diagrams for this system. Figure 3.5 show the final instrument configuration with the reflective filter mirror in front of the transmissive filters. This change was made because of filter fabrication constraints and provides for improved performance in terms of straylight rejection.

Figure 3.2
UVI - Original Optical Prescription

TORR'S TELESCOPE

14:42:41----- 4/18/89



ABOUT +6.0° BIAS

SCREEN - 0.0°

BLUE - +4.0°

RED - -4.0°

ORIGINAL PAGE IS
OF POOR QUALITY

TORR'S POLAR UV IMAGER

4/19/89

1.30e-1
WAVELENGTH

$\lambda = 0.213860 \quad 0.213860 \quad 0.213860$

PHI 7.627119E-05

[TORR2]

NO.	SURFACE TYPE	TILT TYPE	DIFFRACT TYPE	RADIUS	THICKNESS	ND-INDEX	HI-INDEX	LO-INDEX	ABBE NO.	GLASS NAME	CLEAR APERT	OUTER BOUND
0	ENTRANCE PUPIL				0.0000	1.000000	1.000000	1.000000				
1	SPHERE	NORMAL		INFINITE	0.0000	1.000000	1.000000	1.000000	0.00	AIR	43.53	0.00
2	SPHERE			INFINITE	5.0000	1.415660	1.415660	1.415660	0.00	HGF2	43.53	0.00
3	SPHERE	WINDOW		INFINITE	0.0000	1.000000	1.000000	1.000000	0.00	AIR	44.77	0.00
4	SPHERE	NORMAL		INFINITE	80.7123	1.000000	1.000000	1.000000	0.00	AIR	179.34	0.00
5	ASPHERE	PRIMARY		-162.3568	-70.1294	-1.000000	-1.000000	-1.000000	0.00	-AIR	196.83	0.00
6	ASPHERE	SECONDARY		-83.4644	176.6570	1.000000	1.000000	1.000000	0.00	AIR	62.18	0.00
7	ASPHERE	TERTIARY		-174.2185	-188.9348	-1.000000	-1.000000	-1.000000	0.00	-AIR	223.94	0.00
8	SPHERE	FOCUS		INFINITE	-0.4200	-1.000000	-1.000000	-1.000000	0.00	-AIR	47.53	0.00

TABLE OF DECENTRATIONS, TILTS AND ROTATIONS

NO.	TYPE	X-DEC.	Y-DEC.	Z-DEC.	(Y-TILT) THETA Z	(Z-TILT) THETA Y	THETA X
1	1		0.000000E+00	0.000000E+00	-6.000000E+00	0.000000E+00	0.000000E+00
4	1		-6.728460E+01	0.000000E+00	0.000000E+00	0.000000E+00	0.000000E+00

SURFACE TYPE 2 ASPHERIC COEFFICIENTS

NO.	Epsilon (CC+1.0)	C'	D'	E'	F'
5	5.057000E-01	0.000000E+00	4.471127E-13	-2.596465E-17	8.101326E-22
6	-5.224000E-01	0.000000E+00	1.793339E-09	-1.955779E-12	7.437767E-16
7	8.750000E-01	0.000000E+00	-6.075323E-14	2.268059E-18	-1.505506E-22

ORIGINAL PAGE IS OF POOR QUALITY

FIRST ORDER PARAMETERS ON Y-MERIDIONAL PLANE

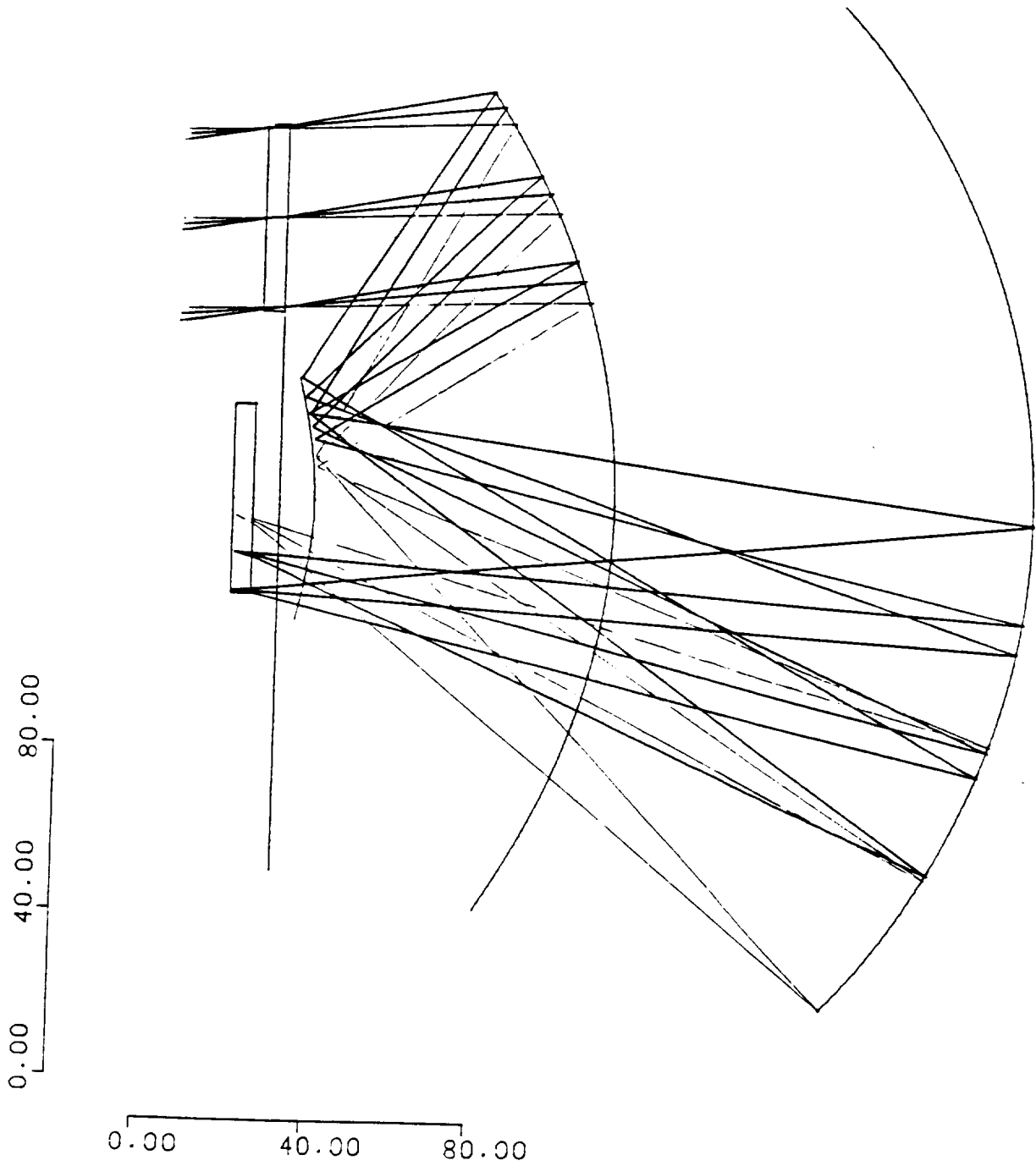
MEASURED FROM FIRST SURFACE				MEASURED FROM LAST SURFACE			
OBJECT DISTNCE	ENTR.PUP.DIST	FRST.FPAL.PNT	EFF.FCL.LNGTH	SCMD.FPAL.PNT	EXT.PUP.DSTNC	IMAGE DISTNCE	
INF	0.000000	-504.358174	129.043374	-317.998144	-144.550051	-189.354770	
OBJECT HEIGHT	ENTR.PUP.DIAM	OBJT.SPCE.FNO	INF.OBJCT.FNO	IMGE.SPCE.FNO	EXT.PUPL.DIAM	IMAGE HEIGHT	
INF	42.976800	INF	3.003094	3.003094	-14.779463	18.138674	
MAGNIFICATION	SEMIANG.FIELD	BACK.VTX.DIST	BARREL LENGTH	FRNT.VTX.DIST	SEMIANG.FIELD	DEMAGNIFICATION	
0.000000	8.000000	INF	192.239700	2.885130	23.262668	INF	
APT.STOP DIAM	APT.STOP DIST	FROM SFCE.NO	*****	FLD.STOP DIAM	FLD.STOP DIST	FROM SFCE.NO	
42.976800	0.000000	0		36.277449	-189.354770	0	

MCASE	FNO/SIZE	AFOCAL CODE	TARGET OBJ DIST	TARGET F.L.	OBJ.CHEM	BASE COLOR	Y-YEAR	OBJ.DIM
1	1	0	0.000000E+00	0.000000E+01	0.00000000	0	0	0

Figure 3.3
UVI - Optimized Optical Prescription

TORR'S TELESCOPE

11:20:15----- 5/15/89



TORR UV IMAGER w/ MgF
WINDOWS

MAY 15, 198

1.3,0,-1
WAVELENGTH
(TORR4)

0.213860 0.213860 0.213860 PHI 3.247676E-04

NO.	SURFACE TYPE	TILT TYPE	DIFFRACT TYPE	RADIUS	THICKNESS	MD-INDEX	HI-INDEX	LO-INDEX	ABBE NO.	GLASS NAME	CLEAR APERT	OUTER BOUND
0	ENTRANCE PUPIL				0.0000	1.000000	1.000000	1.000000				
1	SPHERE	NORMAL		INFINITE	0.0000	1.000000	1.000000	1.000000	0.00	AIR	43.53	0.00
2	SPHERE			INFINITE	5.0000	1.415660	1.415660	1.415660	0.00	AIR MgF	43.53	0.00
3	SPHERE			INFINITE	0.0000	1.000000	1.000000	1.000000	0.00	AIR	44.77	0.00
4	SPHERE	NORMAL		INFINITE	80.7123	1.000000	1.000000	1.000000	0.00	AIR	179.34	0.00
5	ASPHERE			-162.3568	-72.0000	-1.000000	-1.000000	-1.000000	0.00	AIR	196.80	0.00
6	ASPHERE			-83.4644	172.0000	1.000000	1.000000	1.000000	0.00	AIR	58.19	0.00
7	ASPHERE			-174.2186	-186.8951	-1.000000	-1.000000	-1.000000	0.00	AIR	241.47	0.00
8	SPHERE			INFINITE	-4.8260	-1.415660	-1.415660	-1.415660	0.00	AIR MgF	45.46	0.00
9	SPHERE			INFINITE	0.0000	-1.000000	-1.000000	-1.000000	0.00	AIR	44.03	0.00
10	SPHERE			INFINITE	0.0000	-1.000000	-1.000000	-1.000000	0.00	AIR	44.03	0.00

TABLE OF DECENTRATIONS, TILTS AND ROTATIONS

NO.	TYPE	X-DEC.	Y-DEC.	Z-DEC.	(Y-TILT) THETA Z	(Z-TILT) THETA Y	THETA X
1	1		0.000000E+00	0.000000E+00	-6.000000E+00	0.000000E+00	0.000000E+00
4	1		-6.728460E+01	0.000000E+00	0.000000E+00	0.000000E+00	0.000000E+00

SURFACE TYPE 2 ASPHERIC COEFFICIENTS

NO.	Epsilon (CC+1.0)	C'	D'	E'	F'
5	6.115486E-01	0.000000E+00	9.347959E-13	-4.898472E-17	1.180927E-21
6	-3.159321E+00	0.000000E+00	1.869898E-09	-2.136067E-12	8.004905E-16
7	9.210447E-01	0.000000E+00	2.303461E-14	-1.941800E-18	8.919179E-24

* REOPTIMIZED COEFFICIENTS
REFER TO MAY 5, 1989
SYSTEM FOR PERFORMANCE

FIRST ORDER PARAMETERS ON Y-MERIDIONAL PLANE

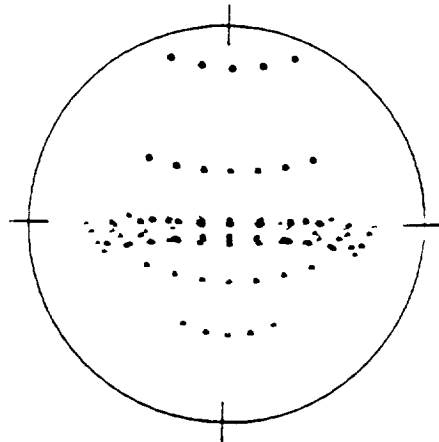
MEASURED FROM FIRST SURFACE				MEASURED FROM LAST SURFACE			
OBJECT DISTNCE	ENTR.PUP.DIST	FRST.PPAL.PNT	EFF.FCL.LNGTH	SCND.PPAL.PNT	EXT.PUP.DSTNCE	IMAGE DISTNCE	
INF	0.000000	-471.435609	123.968614	-124.542469	43.655432	-0.573855	
OBJECT HEIGHT	ENTR.PUP.DIAM	OBJT.SPCE.FNO	INF.OBJCT.FNO	IMGE.SPCE.FNO	EXT.PUPL.DIAM	IMAGE HEIGHT	
INF	42.976800	INF	2.884547	2.884547	-15.333181	17.422653	
MAGNIFICATION	SEMIANG.FIELD	BACK VTX.DIST	BARREL LENGTH	FRNT.VTX.DIST	SEMIANG.FIELD	DEMAGNIFICATION	
0.000000	8.000000	INF	-6.008792	-6.008792	22.422901	INF	
APT.STOP DIAM	APT.STOP DIST	FROM SRFCE.NO	*****	FLD.STOP DIAM	FLD.STOP DIST	FROM SRFCE.NO	
42.976800	0.000000	0		34.945705	-0.573855	0	

Figure 3.4
Spot Diagrams for Optimized System

FIELD COORDINATES

(DEG)

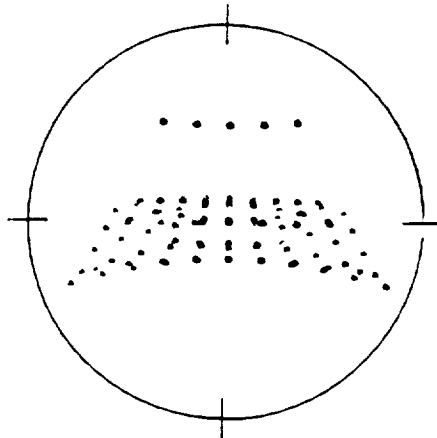
Y Z
0.000 0.000



COLOR 1

RMS RADIUS $2.28084 \cdot 10^{-02}$

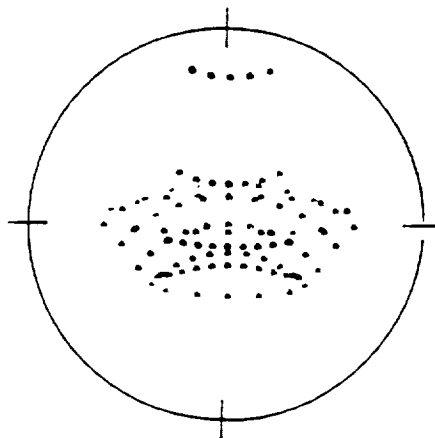
Y Z
4.000 0.000



COLOR 1

RMS RADIUS $2.12793 \cdot 10^{-02}$

Y Z
-4.000 0.000



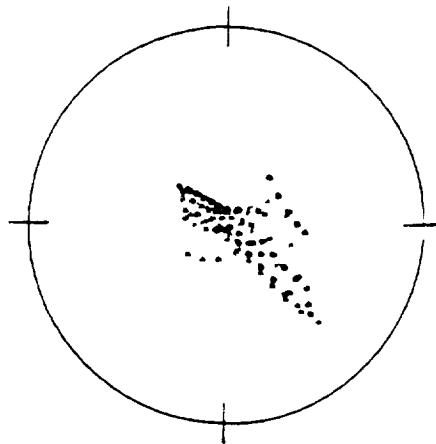
COLOR 1

RMS RADIUS $1.93607 \cdot 10^{-02}$

CIRCLE DIAMETER = 100 MICRON

FIELD COORDINATES
(DEG)

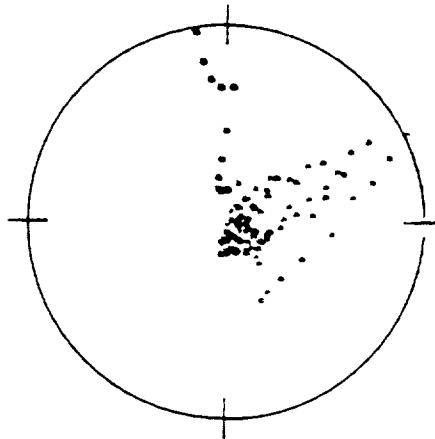
Y Z
4.000 45.000



COLOR 1

RMS RADIUS $1.28582 \cdot 10^{-02}$

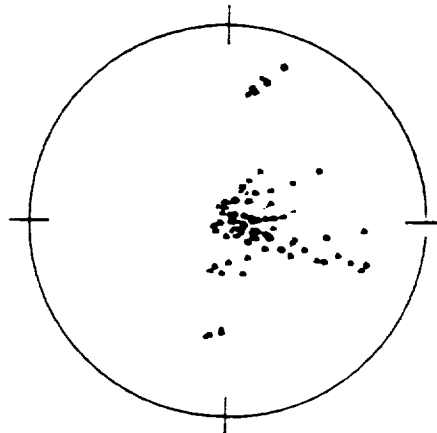
Y Z
4.000 90.000



COLOR 1

RMS RADIUS $1.79178 \cdot 10^{-02}$

Y Z
4.000 135.000



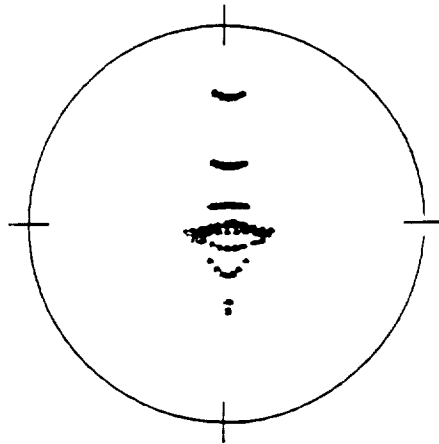
COLOR 1

RMS RADIUS $2.43853 \cdot 10^{-02}$

CIRCLE DIAMETER = 100 MICRON

FIELD COORDINATES
(DEG)

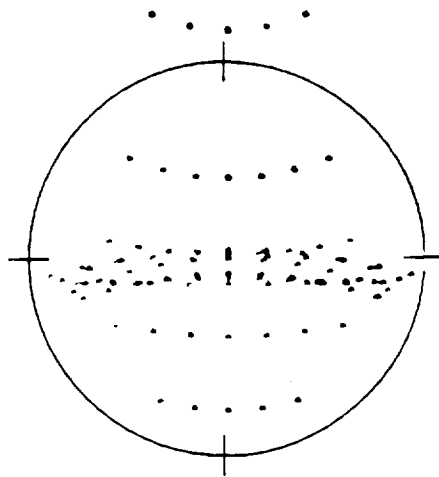
Y Z
2.000 0.000



COLOR 1

RMS RADIUS $1.14744 \cdot 10^{-02}$

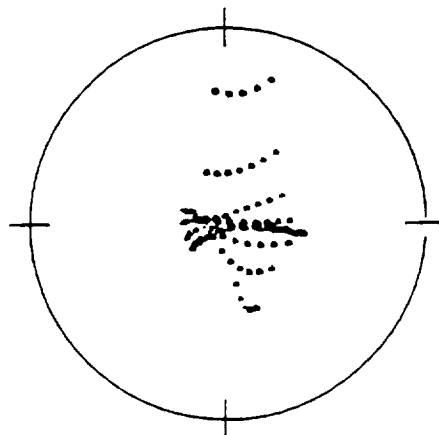
Y Z
-2.000 0.000



COLOR 1

RMS RADIUS $2.98356 \cdot 10^{-02}$

Y Z
2.000 45.000



COLOR 1

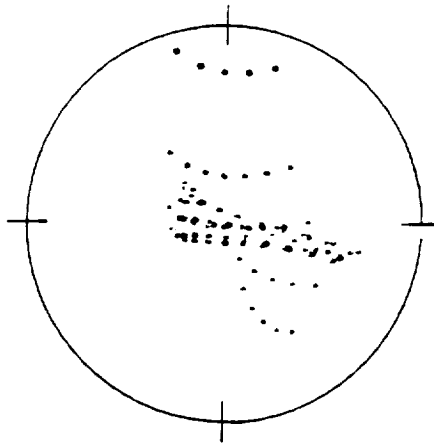
RMS RADIUS $1.33593 \cdot 10^{-02}$

CIRCLE DIAMETER = 100 MICRON

FIELD COORDINATES

(DEG)

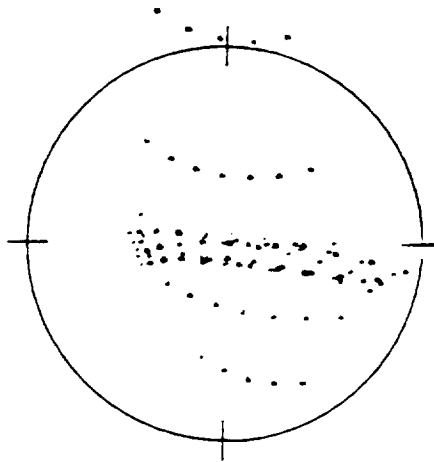
Y	Z
2.000	90.000



COLOR 1

RMS RADIUS $1.81158 \cdot 10^{-02}$

Y	Z
2.000	135.000



COLOR 1

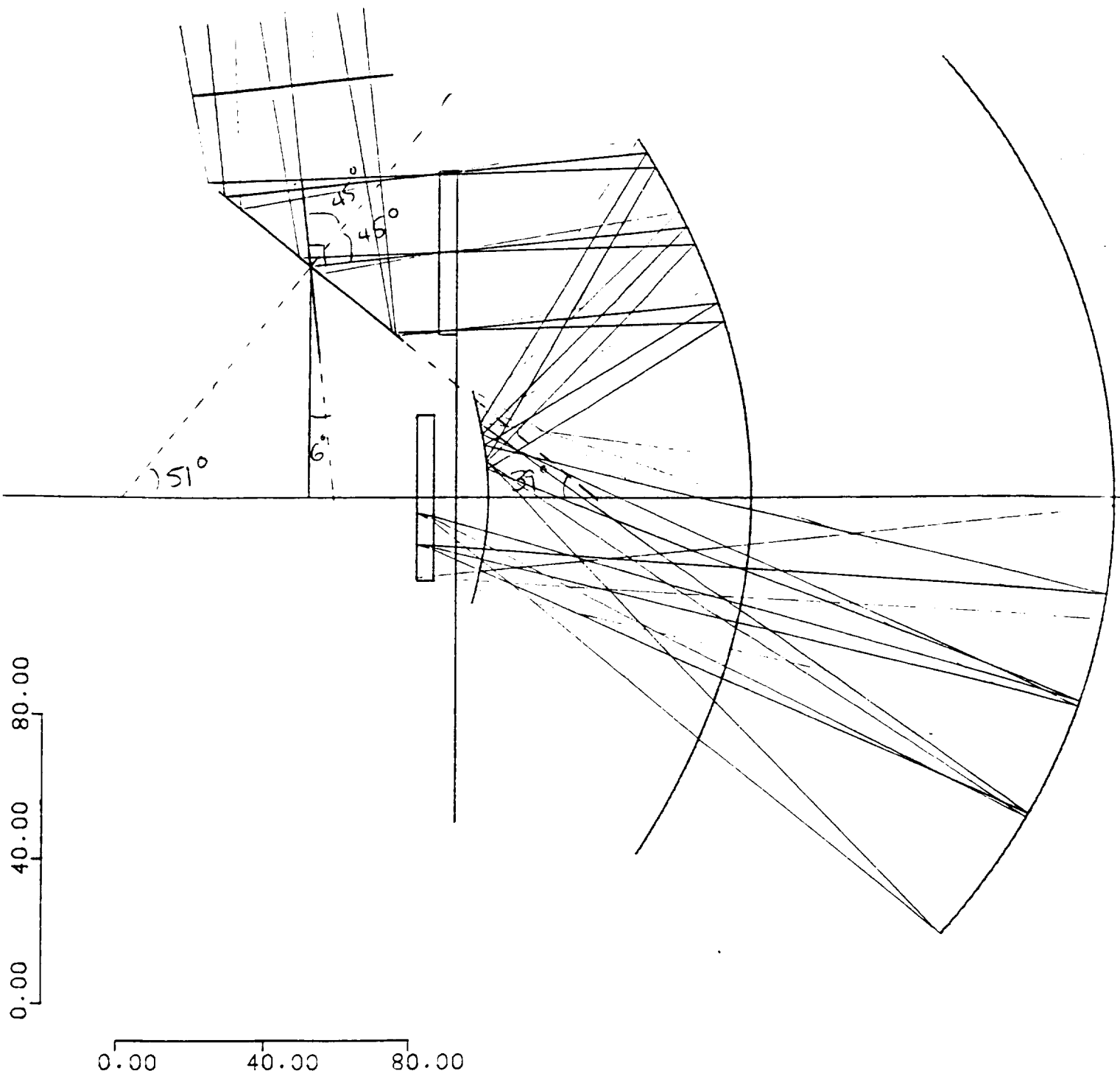
RMS RADIUS $2.50139 \cdot 10^{-02}$

CIRCLE DIAMETER = 100 MICRON

Figure 3.5
Optimized Prescription with Filter Mirror

TORR'S TELESCOPE

09:38:40----- 1/ 5/90



1/4/90
87

TORR TELESCOPE 45° FOLD

1.3,0,-1
WAVELENGTH

0.213860 0.213860 0.213860 PHI 0.000000E+00

[TORR40]

NO.	SURFACE TYPE	TILT TYPE	DIFFRACT TYPE	RADIUS	THICKNESS	ND-INDEX	HI-INDEX	LO-INDEX	ABBE NO.	GLASS NAME	CLEAR APERT	OUTER BOUND
0	ENTRANCE PUPIL				85.5975	-1.000000	-1.000000	-1.000000				
1	SPHERE			INFINITE	-50.0000	-1.000000	-1.000000	-1.000000	0.00	AIR	54.95	0.00
2	SPHERE	RESTORE		INFINITE	0.0000	1.000000	1.000000	1.000000	0.00	AIR	65.41	0.00
3	SPHERE	NORMAL		INFINITE	35.5975	1.000000	1.000000	1.000000	0.00	AIR	47.96	0.00
4	SPHERE	NORMAL		INFINITE	0.0000	1.000000	1.000000	1.000000	0.00	AIR	43.53	0.00
5	SPHERE			INFINITE	5.0000	1.415660	1.415660	1.415660	0.00	AIR	43.53	0.00
6	SPHERE			INFINITE	0.0000	1.000000	1.000000	1.000000	0.00	AIR	44.77	0.00
7	SPHERE	NORMAL		INFINITE	80.7123	1.000000	1.000000	1.000000	0.00	AIR	179.34	0.00
8	ASPHERE			-162.3568	-72.0000	-1.000000	-1.000000	-1.000000	0.00	AIR	196.80	0.00
9	ASPHERE			-83.4644	172.0000	1.000000	1.000000	1.000000	0.00	AIR	58.19	0.00
10	ASPHERE			-174.2186	-186.8951	-1.000000	-1.000000	-1.000000	0.00	AIR	241.47	0.00
11	SPHERE			INFINITE	-4.8260	-1.415660	-1.415660	-1.415660	0.00	AIR	45.46	0.00
12	SPHERE			INFINITE	0.0000	-1.000000	-1.000000	-1.000000	0.00	AIR	44.03	0.00
13	SPHERE			INFINITE	0.0000	-1.000000	-1.000000	-1.000000	0.00	AIR	44.03	0.00

TABLE OF DECENTRATIONS, TILTS AND ROTATIONS

NO.	TYPE	X-DEC.	Y-DEC.	Z-DEC.	(Y-TILT) THETA Z	(Z-TILT) THETA Y	THETA X
2	3		0.000000E+00	0.000000E+00	-4.500000E+01	0.000000E+00	0.000000E+00
3	1		0.000000E+00	0.000000E+00	-9.000000E+01	0.000000E+00	0.000000E+00
4	1		0.000000E+00	0.000000E+00	-6.000000E+00	0.000000E+00	0.000000E+00
7	1		-6.728460E+01	0.000000E+00	0.000000E+00	0.000000E+00	0.000000E+00

SURFACE TYPE 2 ASPHERIC COEFFICIENTS

NO.	Epsilon (CC+1.0)	C'	D'	E'	F'
8	6.115486E-01	0.000000E+00	9.347959E-13	-4.898472E-17	1.190927E-21
9	-3.159321E+00	0.000000E+00	1.349899E-09	-2.134047E-12	8.004805E-16

ORIGINAL PAGE IS OF POOR QUALITY

FIRST ORDER PARAMETERS ON Y-MERIDIONAL PLANE

MEASURED FROM FIRST SURFACE				MEASURED FROM LAST SURFACE			
OBJECT DISTNCE	ENTR.PUP.DIST	FRST.PPAL.PNT	EFF.FCL.LNGTH	SCND.PPAL.PNT	EXT.PUP.DSTNC	IMAGE DISTNCE	
INF	-85.597500	385.838109	123.968614	-124.542469	43.655432	-0.573855	
OBJECT HEIGHT	ENTR.PUP.DIAM	OBJT.SPCE.FNO	INF.OBJCT.FNO	IMGE.SPCE.FNO	EXT.PUPL.DIAM	IMAGE HEIGHT	
INF	42.976800	INF	2.884547	2.884547	-15.333181	17.422653	
MAGNIFICATION	SEMIANG.FIELD	BACK VTX.DIST	BARREL LENGTH	FRNT.VTX.DIST	SEMIANG.FIELD	MEMAGNIFICATION	
0.000000	8.000000	INF	-20.411292	-20.411292	-22.422901	INF	
APT.STOP DIAM	APT.STOP DIST	FROM SRFCE.NO	*****	FLD.STOP DIAM	FLD.STOP DIST	FROM SRFCE.NO	
42.976800	-85.597500	0		44.845305	-0.573855	12	

MCASE	FNO/SIZE	AFOCAL CODE	TARGET OBJ DIST	TARGET F.L.	OBJ.CURV	BASE COLOR	Y-YBAR	OBJ/IMG
1	1	0	0.0000D+00	2.5400D+01	0.0000D+00	3	0	-9

REAL ENTR. PUPIL CODES : 0 0

C

ORIGINAL PAGE IS
OF POOR QUALITY.

4. Development of the Error Budget

The proper criterion for evaluating optical performance depends on a number of different factors: the nature of the source to be imaged, limitations of the optical system, the type of detector, and the goal of the application. Figure 4.1 shows the relationships between various commonly used image quality criteria.

Since this telescope is dominated by geometric aberration as shown in the spot diagrams (the on-axis rms spot radius is ≈ 54 times larger than the diffraction-limited performance of an $f/2.88$ system at 1200 \AA), error budgeting in terms of wavefront error would not provide a practical figure of merit. Because spatial and temporal intensity variations in the scene are of primary interest to the instrument scientists, encircled energy and rms spot size, which are calculated from the point spread function, were chosen to provide a convenient means of assessing telescope performance.

An optical transfer function (OTF) budget (or equivalent) might well be considered appropriate for this system given the desire to spatially resolve aurora features. OTF, however, can in turn be translated via a Fourier transform into a point spread function from which the original image quality criteria were calculated.

Since no specific optical performance requirements were handed down to Hughes DOS by MSFC or the University of Alabama, the approach of "best effort" was taken giving the constraints of manufacturing and assembly tolerances, environmental contributors, and budget and schedule. Traditionally, a degradation of 15%-20% in the optical performance of a telescope due to environmental influences, and fabrication and assembly errors has been tolerated. With this in mind, a target of 60% encircled energy in a 27 \mu m radius circle, corresponding to the half-

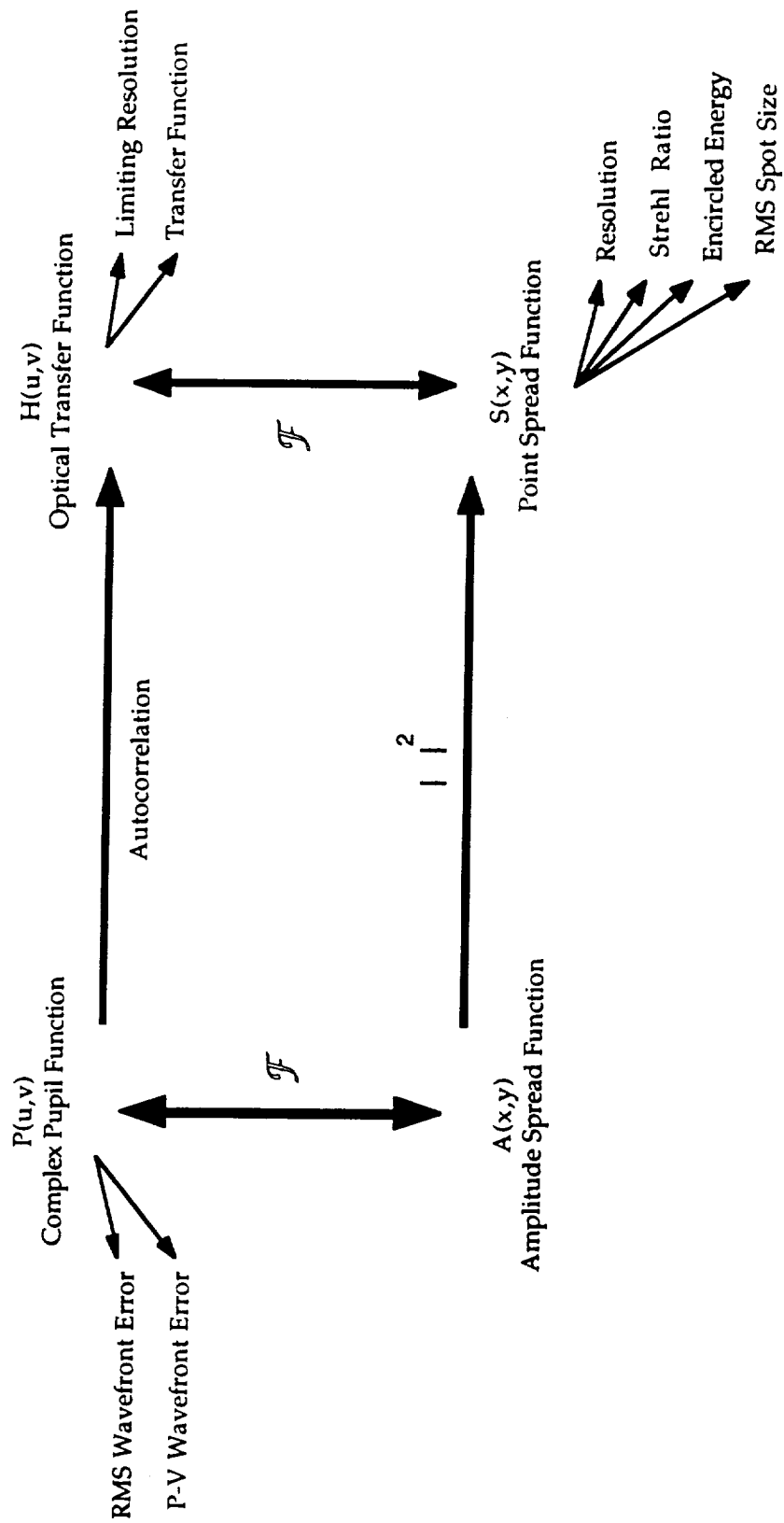


Figure 4.1 Some frequently used image quality criteria are properties of the complex pupil function. Others are obtained from the PSF or OTF. This figure shows the relationship between some of the different image quality criteria.

width of the long side of UVI's CCD pixels, was established. This requirement is contingent on a reasonable set of manufacturing and assembly tolerances for both the optics and the assembly of the telescope, i.e. the use of ultra-high precision (sub-micron) alignment techniques would not be used.

5. UVI Error Budget

Since cost is a major program consideration and given the speed of the parent optics, it was decided that the optics should be diamond-turned using nickel-coated aluminum substrates and subsequently post-polished. This provides one with very smooth (typically 10-12 Å rms) surfaces and allows one to put high-order aspheric surfaces on the substrate. Based on input from the optical designers, it was determined that the optical surface should be ≤ 0.5 waves rms ($\lambda = 6328$ Å) for each optic. This amount of surface figure error would not noticeably affect encircled energy or rms spot size (i.e. $< 1\%$) and is comfortably achieved with current diamond-turning practices.

The principle contributor to optical performance degradation for this optical system is the large bulk temperature change associated with the transition from ground to orbit. Based on MSFC's initial estimate of the on-orbit thermal environment, the nominal on-orbit bulk environment was specified to be 0 °C (32 °F) with allowable orbit-to-orbit bulk temperature variations of ± 5.5 °C (± 10 °F) while the instrument was operating. Bulk temperature changes contribute to relative despace and decenter misalignments, as well as changes to the radius of curvatures of the three mirrors. Temperature gradients through the optical bench in each of the axes were estimated to be ± 0.1 °C/cm (± 0.5 °F/in.). These gradients were assumed to be superimposed over the bulk average, thereby contributing only to changes in the mirror radius of curvatures and relative tilts between the optics.

Because UVI is compromised in terms of on-axis performance so that performance variations across the large FOV could be minimized, a simple error sensitivity analysis could not be performed. As a result, once error allocations were determined, each misalignment case had to be run through MEXP separately to determine its impact on performance.

Appendix A details the calculations made to determine misalignment errors due to the various contributors. Calculated values are based on the current design dimensions as shown in detail piece part and assembly level drawings. Total misalignment (shown as total allowable error) due to environment and manufacturing errors plus margin were run and the impact on on-axis encircled energy and rms spot size were calculated. These values are illustrated in the following error budget (Figure 5.1) and the top level number is the rss of the contributors. This in turn is related back to encircled energy to determine margin.

Note that misalignment terms were calculated with respect to the secondary mirror rather than the focal plane. This results from the physical location of the SM in the telescope and the approach taken in assembling and aligning the optics. During assembly and alignment both the primary and tertiary mirrors are to be aligned to the secondary mirror.

Ultra-Violet Imager Error Budget
(On-Axis with -6° bias)

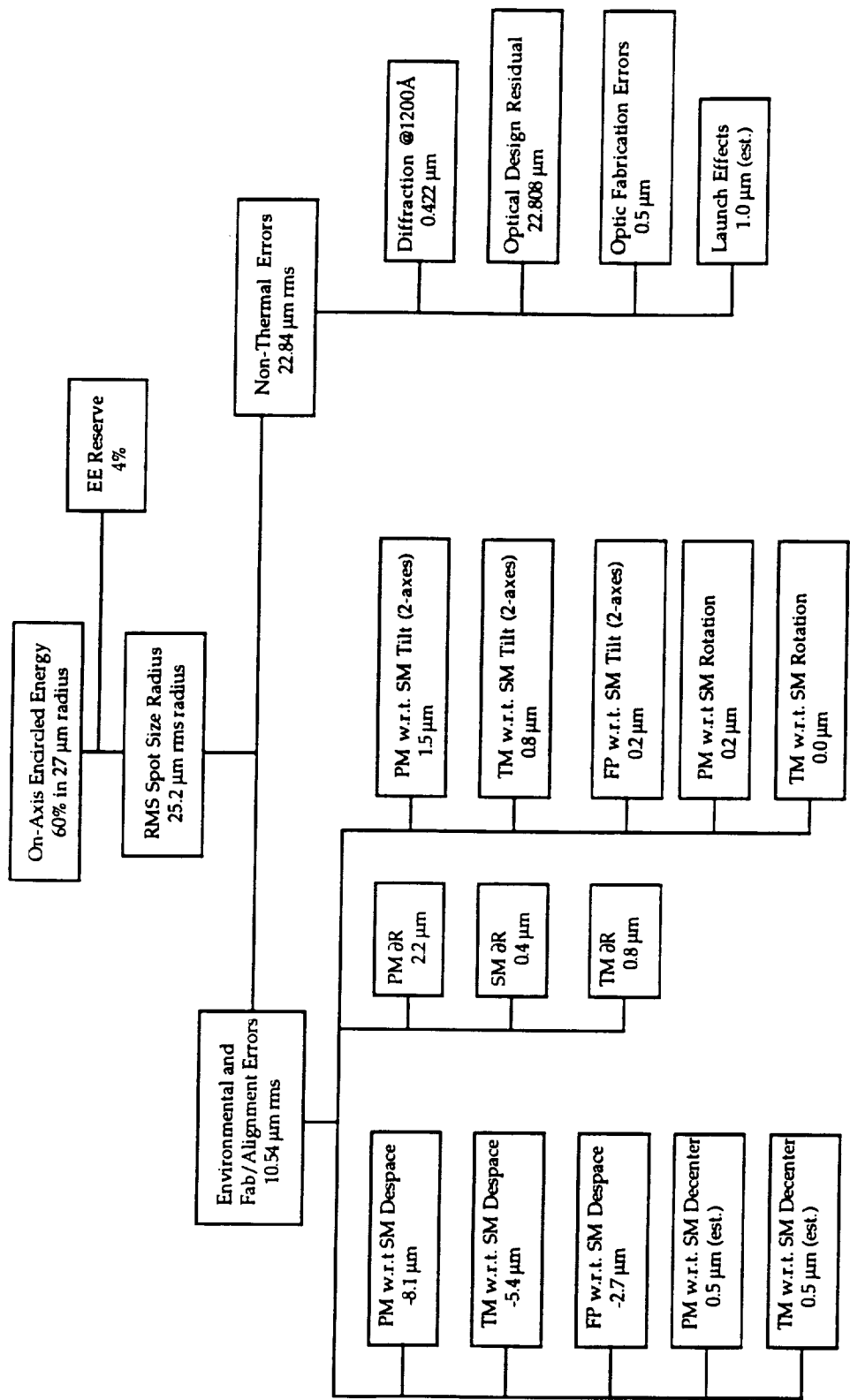


Figure 5.1 UVI Error Budget Tree showing image degradation contributors in terms of rms spot size radius. Based on initial MSFC thermal environment with preliminary margin allocations (see Appendix A).

6. Conclusions

As is seen in the error budget, the target of 60% encircled energy in a 27 μm radius is met with some margin. This 4% margin, together with the margin initially allocated to each error contributor, helps ensure that any subsequent changes in the thermal environment or drastic changes in assembly philosophy or procedures will not require a relaxation of the target budget requirement.

During recent conversations with MSFC, preliminary indications were provided that the thermal environment would be significantly less severe in terms of ground-to-orbit bulk temperature changes. This information will be folded back into the error budget when available.

7. References

Documents:

Johnson, R. B., "Wide field of view three-mirror telescopes having a common optical axis", Optical Engineering Vol. 27, No. 12, Dec. 1988, p. 1046-1050

MSFC Document provided by Dr. M. Torr, Section A - Investigation Description, June 1988.

Tausanovitch, J., "Review of 3 Mirror Telescope from M. Torr", PE Memo to M. Krim, January 19, 1989

Harvey, James, "Optical Surface Scattering Effects on the UV Imager", PE Memo to A. Nonnenmacher, March 9, 1989.

Drawings:

C13-10000-001 Primary Mirror
C13-10001-001 Secondary Mirror
C13-10002-001 Tertiary Mirror
C13-10003-002 UVI Optical Layout
C13-10016-001 Primary and Secondary Housing Assembly
C13-10017-001 Sensor and Tertiary Housing Assembly
C13-10020-001 UVI Assembly

Metering structure part drawings were also used in developing the details of the error budget.

APPENDIX A
UVI Error Budget Calculation Details

Primary Mirror w.r.t. Secondary Mirror Despace Contributors

$$\Delta l(\text{in.}) = \alpha(\text{in./in./}^\circ\text{F}) l(\text{in.}) \Delta T(^\circ\text{F})$$

Bulk Temperature Change - Ground to Orbit $\Delta T = -36^\circ\text{F} (-20^\circ\text{C})$

	Length	Material	CTE(in/in/°F)	Δ (in.)
SM Body to Flange	0.449	Al 6061-T651	1.36E-05	2.20E-04
Flang to Housing Shim	0.05	AISI 410	5.50E-06	-9.90E-06
Housing	3.182	Al 6061-T651	1.36E-05	-1.56E-03
PM Flang to Housing Shim	0.05	AISI 410	5.50E-06	-9.90E-06
PM Body to Flange	0.25	Al 6061-T651	1.36E-05	1.22E-04

$$\Delta l = -0.00124 \text{ in.}$$

$$(-0.032 \text{ mm})$$

Bulk Temperature Change - Orbit to Orbit $\Delta T = \pm 10^\circ\text{F} (\pm 5.5^\circ\text{C})$

	Length	Material	CTE(in/in/°F)	$\pm\Delta$ (in.)
SM Body to Flange	0.4488	Al 6061-T651	1.36E-05	6.10E-05
Flang to Housing Shim	0.0500	AISI 410	5.50E-06	-2.75E-06
Housing	3.1804	Al 6061-T651	1.36E-05	-4.33E-04
PM Flang to Housing Shim	0.0500	AISI 410	5.50E-06	-2.75E-06
PM Body to Flange	0.2499	Al 6061-T651	1.36E-05	3.40E-05

$$\Delta l = \pm 0.00034 \text{ in.}$$

$$(\pm 0.009 \text{ mm})$$

Manufacturing and Assembly Errors

Measurement of Optical Surfaces to Reference Surfaces : $\pm 0.00014 \text{ in.}$ (includes both PM and SM)

Measurement of Spacing between Optics: $\pm 0.0005 \text{ in.}$

Total Errors: $\pm 0.00052 \text{ in.}$ ($\pm 0.0132 \text{ mm}$)

A conservative total Primary Mirror w.r.t Secondary Mirror Despace Error is given by the rss of these values:

$$\epsilon = \pm 0.0014 \text{ in.} (\pm 0.035 \text{ mm})$$

Total Allowable: $\epsilon_t = \pm 0.002 \text{ in.}$ ($\pm 0.050 \text{ mm}$)

Margin: $\epsilon_m = \pm 0.0014 \text{ in.}$ ($\pm 0.035 \text{ mm}$)

Tertiary Mirror w.r.t. Secondary Mirror Despace Contributors

$$\Delta l(\text{in.}) = \alpha(\text{in./in./}^\circ\text{F}) l(\text{in.}) \Delta T(^\circ\text{F})$$

Bulk Temperature Change - Ground to Orbit $\Delta T = -36^\circ\text{F} (-20^\circ\text{C})$

	Length	Material	CTE(in/in/°F)	Δ (in.)
SM Body to Flange	0.449	Al 6061-T651	1.36E-05	2.20E-04
Flang to Housing Shim	0.05	AISI 410	5.50E-06	-9.90E-06
Housing	7.521	Al 6061-T651	1.36E-05	-3.68E-03
TM Flang to Housing Shim	0.05	AISI 410	5.50E-06	-9.90E-06
TM Body to Flange	0.25	Al 6061-T651	1.36E-05	1.22E-04

$$\Delta l = -0.0034 \text{ in.}$$

$$(-0.085 \text{ mm})$$

Bulk Temperature Change - Orbit to Orbit $\Delta T = \pm 10^\circ\text{F} (\pm 5.5^\circ\text{C})$

	Length	Material	CTE(in/in/°F)	$\pm\Delta$ (in.)
SM Body to Flange	0.4488	Al 6061-T651	1.36E-05	6.10E-05
Flang to Housing Shim	0.0500	AISI 410	5.50E-06	-2.75E-06
Housing	7.5173	Al 6061-T651	1.36E-05	-1.02E-03
TM Flang to Housing Shim	0.0500	AISI 410	5.50E-06	-2.75E-06
TM Body to Flange	0.2499	Al 6061-T651	1.36E-05	3.40E-05

$$\Delta l = \pm 0.00093 \text{ in.}$$

$$(\pm 0.024 \text{ mm})$$

Manufacturing and Assembly Errors

Measurement of Optical Surfaces to Reference Surfaces :	$\pm 0.00014 \text{ in.}$ (includes both PM and SM)
Measurement of Spacing between Optics:	$\pm 0.0005 \text{ in.}$
Total Errors:	$\pm 0.00052 \text{ in.}$ ($\pm 0.0132 \text{ mm}$)

A conservative total Tertiary Mirror w.r.t Secondary Mirror Despace Error is given by the rss of these values:

$$\epsilon = \pm 0.0035 \text{ in.} (\pm 0.091 \text{ mm})$$

$$\text{Total Allowable: } \epsilon_t = \pm 0.0047 \text{ in.} (\pm 0.120 \text{ mm})$$

$$\text{Margin: } \epsilon_m = \pm 0.0029 \text{ in.} (\pm 0.073 \text{ mm})$$

Focal Plane w.r.t. Secondary Mirror Despace Contributors

$$\Delta l(\text{in.}) = \alpha(\text{in./in./}^\circ\text{F}) l(\text{in.}) \Delta T(^\circ\text{F})$$

Bulk Temperature Change - Ground to Orbit $\Delta T = -36^\circ\text{F} (-20^\circ\text{C})$

	Length	Material	CTE(in/in/°F)	Δ (in.)
SM Body to Flange	0.449	Al 6061-T651	1.36E-05	2.20E-04
Flang to Housing Shim	0.05	AISI 410	5.50E-06	-9.90E-06
Housing (to pin)	0.165	Al 6061-T651	1.36E-05	-8.08E-05
Top Plate to Det. Plate	1.28	Al 6061-T651	1.36E-05	-6.27E-04
Pin C/L to Det. Pad	0.97	Al 6061-T651	1.36E-05	-4.75E-04
Det. Shim	0.1	AISI 410	5.50E-06	-1.98E-05
Det. Foot to FP	1.31	Al 6061-T651	1.36E-05	6.41E-04

$$\Delta l = \pm 0.0004 \text{ in.} \\ (\pm 0.010 \text{ mm})$$

Bulk Temperature Change - Orbit to Orbit $\Delta T = \pm 10^\circ\text{F} (\pm 5.5^\circ\text{C})$

	Lengths	Material	CTE(in/in/°F)	$\pm\Delta$ (in.)
SM Body to Flange	0.4488	Al 6061-T651	1.36E-05	1.22E-05
Flang to Housing Shim	0.0500	AISI 410	5.50E-06	5.50E-07
Housing (to pin)	0.1649	Al 6061-T651	1.36E-05	4.49E-06
Top Plate to Det. Plate	1.2794	Al 6061-T651	1.36E-05	3.48E-05
Pin C/L to Det. Pad	0.9695	Al 6061-T651	1.36E-05	2.64E-05
Det. Shim	0.1000	AISI 410	5.50E-06	1.10E-06
Det. Foot to FP	1.3094	Al 6061-T651	1.36E-05	3.56E-05

$$\Delta l = \pm 0.0001 \text{ in.} \\ (\pm 0.0025 \text{ mm})$$

Manufacturing and Assembly Errors (estimated)

Assembly of Detector Assembly: $\pm 0.001 \text{ in.}$

Total Errors: $\pm 0.001 \text{ in.} (\pm 0.0254 \text{ mm})$

A conservative total Focal Plane w.r.t Secondary Mirror Despace Error is given by the rss of these values:

$$\epsilon = \pm 0.0011 \text{ in.} (\pm 0.028 \text{ mm})$$

Total Allowable: $\epsilon_t = \pm 0.0012 \text{ in.} (\pm 0.031 \text{ mm})$

Margin: $\epsilon_m = \pm 0.0005 \text{ in.} (\pm 0.013 \text{ mm})$

This is only an estimate, since it will be dictated by MSFC tolerances and assembly procedures.

Primary Mirror w.r.t Secondary Mirror Decenter Contributors

$$\Delta l(\text{in.}) = \alpha(\text{in./in./}^\circ\text{F}) l(\text{in.}) \Delta T(^\circ\text{F})$$

Bulk Temperature Change - Ground to Orbit $\Delta T = -36^\circ\text{F} (-20^\circ\text{C})$

	Length	Material	CTE(in/in/°F)	Δ (in.)
SM to PM Decenter(Y-axis)	2.165	Al 6061-T651	1.36E-05	-1.06E-03
SM to PM Decenter (Z-axis)				0.0

Bulk Temperature Change - Orbit to Orbit $\Delta T = \pm 10^\circ\text{F} (\pm 5.5^\circ\text{C})$

	Length	Material	CTE(in/in/°F)	± Δ (in.)
SM to PM Decenter (Y-axis)	2.1639	Al 6061-T651	1.36E-05	5.89E-05
SM to PM Decenter (Z-axis)				0.0

Manufacturing and Assembly Errors

- Measurement of Vertex to Reference Surfaces (Y-Axis): ± 0.00014 in. (includes both PM and SM)
- Measurement of Vertex to Reference Surfaces (Z-Axis): ± 0.00014 in. (includes both PM and SM)
- Measurement of Spacing between Optics (Y-Axis): ± 0.0005 in.
- Measurement of Spacing between Optics (Z-Axis): ± 0.0005 in.
- Total Errors: ± 0.0007 in. (± 0.0132 mm)

A conservative estimate of the total Primary Mirror w.r.t. Secondary Mirror Decenter error is given by the rss of the above values:

$$\epsilon = \pm 0.0013 \text{ (in.) } (\pm 0.032 \text{ mm})$$

Total Allowable: $\epsilon_t = \pm 0.0015$ in. (± 0.038 mm)

Margin: $\epsilon_m = \pm 0.0007$ in. (± 0.019 mm)

Tertiary Mirror w.r.t Secondary Mirror Decenter Contributors

$$\Delta l(\text{in.}) = \alpha(\text{in./in./}^\circ\text{F}) l(\text{in.}) \Delta T(^\circ\text{F})$$

Bulk Temperature Change - Ground to Orbit $\Delta T = -36^\circ\text{F}$ (-20°C)

	Length	Material	CTE(in/in/ $^\circ\text{F}$)	Δ (in.)
SM to TM Decenter (Y-Axis)	3.161	Al 6061-T651	1.36E-05	-1.55E-03
SM to TM Decenter (Z-Axis)				0.0

Bulk Temperature Change - Orbit to Orbit $\Delta T = \pm 10^\circ\text{F}$ ($\pm 5.5^\circ\text{C}$)

	Length	Material	CTE(in/in/ $^\circ\text{F}$)	$\pm\Delta$ (in.)
SM to TM Decenter(Y-Axis)	3.1595	Al 6061-T651	1.36E-05	8.59E-05
SM to TM Decenter (Z-Axis)				0.0

Manufacturing and Assembly Errors

Measurement of Vertex to Reference Surfaces (Y-Axis): ± 0.00014 in. (includes both PM and SM)

Measurement of Vertex to Reference Surfaces (Z-Axis): ± 0.00014 in. (includes both PM and SM)

Measurement of Spacing between Optics (Y-Axis): ± 0.0005 in.

Measurement of Spacing between Optics (Z-Axis) ± 0.0005 in.

Total Errors: ± 0.0007 in. (± 0.0132 mm)

A conservative estimate of the total Tertiary Mirror w.r.t. Secondary Mirror Decenter error for all axes is given by the rss of the above values:

$$\epsilon = \pm 0.0017 \text{ (in.) } (\pm 0.043 \text{ mm})$$

Total Allowable: $\epsilon_t = \pm 0.002$ in. (± 0.038 mm)

Margin: $\epsilon_m = \pm 0.001$ in. (± 0.026 mm)

Mirror Δ Radius of Curvature Contributors

$$\Delta R \text{ (in.)} = \alpha \text{ (in./in./}^\circ\text{F)} R \text{ (in.) } \Delta T_{\text{bulk}} \text{ (}^\circ\text{F)}$$

$$\Delta R \text{ (in.)} = \alpha \text{ (in./in./}^\circ\text{F)} R^2 \text{ (in.}^2\text{)} (T_{\text{front}} - T_{\text{back}}) \text{ (}^\circ\text{F)} / \text{Thickness (in.)}$$

Bulk Temperature Change - Ground to Orbit $\Delta T = -36^\circ\text{F}$ (-20°C)

	R (in.)	Material	CTE(in/in/ $^\circ\text{F}$)	ΔR (in.)
Primary Mirror Radius	6.39200	Al 6061-T651	1.36E-05	-3.13E-03
Secondary Mirror Radius	3.28600	Al 6061-T651	1.36E-05	-1.61E-03
Tertiary Mirror Radius	6.85900	Al 6061-T651	1.36E-05	-3.36E-03

Bulk Temperature Change - Orbit to Orbit $\Delta T = \pm 10^\circ\text{F}$ ($\pm 5.5^\circ\text{C}$)

	R (in.)	Material	CTE(in/in/ $^\circ\text{F}$)	$\pm \Delta R$ (in.)
Primary Mirror Radius	6.3889	Al 6061-T651	1.36E-05	$\pm 1.74\text{E-}04$
Secondary Mirror Radius	3.2844	Al 6061-T651	1.36E-05	$\pm 8.93\text{E-}05$
Tertiary Mirror Radius	6.8556	Al 6061-T651	1.36E-05	$\pm 1.86\text{E-}04$

Axial Temperature Gradient (along optical axis) - On-Orbit $\Delta T/\text{in.} = \pm 0.5^\circ\text{F}/\text{in.}$ ($\pm 0.1^\circ\text{C}/\text{cm}$)

	R (in.)	Ave. Thick. (in.)	CTE(in/in/ $^\circ\text{F}$)	$\pm \Delta R$ (in.)
Primary Mirror Radius	6.3889	0.8250	1.36E-05	$\pm 2.78\text{E-}04$
Secondary Mirror Radius	3.2844	0.3745	1.36E-05	$\pm 7.34\text{E-}05$
Tertiary Mirror Radius	6.8556	1.2650	1.36E-05	$\pm 3.20\text{E-}04$

Radial Temperature Gradients effects are too small to account for.

A conservative total delta radius of curvature for each mirror is given by the rss of these values:

	$\pm \Delta R$ (in.)	$\pm \Delta R$ (mm)	Total Allow. (mm)
Primary Mirror Radius	± 0.0031	± 0.079	± 0.81
Secondary Mirror Radius	± 0.0016	± 0.041	± 0.42
Tertiary Mirror Radius	± 0.0034	± 0.086	± 0.88

Primary Mirror w.r.t Secondary Mirror Tilt Contributors

Thermal gradients in the Y and Z axes will contribute to a relative tilt as well as alignment errors. a gradient along the optical axis will not contribute. It is assumed that a 0.5 °F/in through the optical bench in each of these axes is present. Note that the numbers attributed to thermal misalignment is very conservative given the hardware configuration.

PM to SM Tilt (Y-axis): 3 arc-sec

PM to SM Tilt (Z-axis): 2 arc-sec

rss Total: 3.5 arc-sec

Manufacturing and Assembly Errors

Measurement of relative tilt in 2-axes: 30 arc-sec

Total: 30.2 arc-sec

Total Allowable: 108 arc-sec (1.8 arc-min)

This conservative total allowable was allocated prior to details of assembly and hardware.

Tertiary Mirror w.r.t. Secondary Mirror Tilt Contributors

Thermal gradients in the Y and Z axes will contribute to a relative tilt as well as alignment errors. a gradient along the optical axis will not contribute. It is assumed that a 0.5 °F/in through the optical bench in each of these axes is present. Note that the numbers attributed to thermal misalignment is very conservative given the hardware configuration.

TM to SM Tilt (Y-axis): 12 arc-sec

TM to SM Tilt (Z-axis): 15 arc-sec

rss Total: 20 arc-sec

Manufacturing and Assembly Errors

Measurement of relative tilt in 2-axes: 20 arc-sec

Total: 28 arc-sec

Total Allowable: 60 arc-sec (1 arc-min)

This conservative total allowable was allocated prior to details of assembly and hardware.

Focal Plane w.r.t. Secondary Mirror Tilt Contributors

This contributor again is driven by MSFC assembly procedures. It is estimated that alignment can be done as well as the mirrors.

Primary Mirror w.r.t. Secondary Mirror Rotation Contributors

This error contributor is driven by how well one can measure height variations of the precision alignment surface on the flanges of each surface and subsequently determining the angular tilt of the alignment surface.

PM Alignment Surface Length: ≈ 1.4 in. (35.56 mm)

Height Measurement Sensitivity: 0.0002 in. (0.0025 mm)

Angular Resolution: 30 arc-sec

Total Allowable: 2 arc-min

Tertiary Mirror w.r.t. Secondary Mirror Rotation Contributors

This error contributor is driven by how well one can measure height variations of the precision alignment surface on the flanges of each surface and subsequently determining the angular tilt of the alignment surface.

TM Alignment Surface Length: ≈ 2.3 in. (58.4 mm)

Height Measurement Sensitivity: 0.0002 in. (0.0025 mm)

Angular Resolution: 18 arc-sec

Total Allowable: 2 arc-min

APPENDIX B

ULTRAVIOLET IMAGER

POLAR/GGS

PRELIMINARY DESIGN REVIEW

OCTOBER 17, 1989

PDR TITLE

ULTRAVIOLET IMAGER INVESTIGATION/POLAR

PRELIMINARY DESIGN REVIEW
MSFC Building 4481/Room 369

OCTOBER 17, 1989

PRELIMINARY AGENDA

8:30am	INTRODUCTION introductions agenda/objectives instrument overview	M. TORR
9:30am	MECHANICAL DESIGN optical bench, mechanisms, housing, s/c interface, radiator, electronics stack housing (45 min)	L. WALKER
	mass/c.g. status	L. WALKER
	ICD summary (10min)	J. SPANN
10:25am	BREAK	
10:40am	THERMAL DESIGN camera, radiator, electronics stack, reduced thermal model (30 min)	L. WALKER
	ICD summary (20 min)	J. SPANN
11:30am	MISC. ICD SECTIONS magnetic interface electrostatic cleanliness environmental interface (30min)	J. SPANN
12:00noon	LUNCH	

1:15pm	ELECTRONICS DESIGN system, processor, memory, detector, detector interface, s/c interface, TLM format, housekeeping, mechanism control,power supplies,health and safety data (60min)	L. SAVAGE
	power status	L.SAVAGE
	NSPARS	L. SAVAGE
	ICD summary (30min)	J. SPANN
2:45pm	DEVELOPMENT STATUS AND SCHEDULES (15min)	M. TORR
3:00pm	BREAK	
3:15pm	SOFTWARE/DATA MANAGEMENT flight software (15min)	L. SAVAGE
	GSE software (15min)	L.SAVAGE
	Data Management Plan (15 min)	G. GERMANY
	data analysis software (30min)	D. TORR
4:30pm	ISSUES, CONCERNS ACTION ITEMS	
5:00pm	AJOURN	

ULTRAVIOLET IMAGER
POLAR/GGS

INVESTIGATION OVERVIEW

PRELIMINARY DESIGN REVIEW

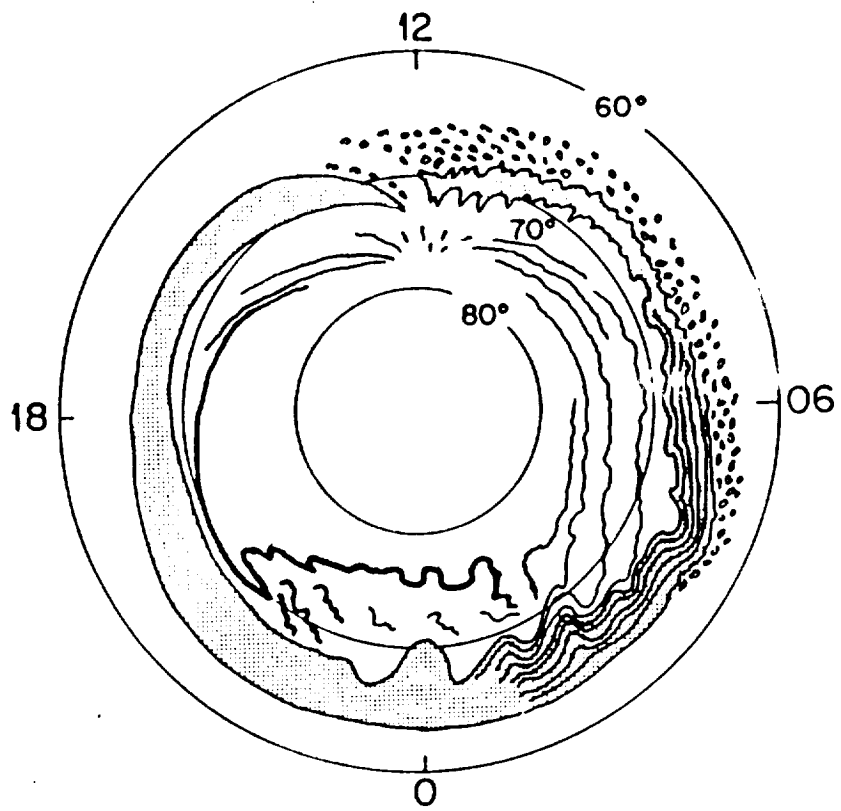
PDR TITLE/001

ULTRAVIOLET IMAGER

SCIENTIFIC OBJECTIVES

To provide global coherent information on

- * the total particle energy influx into the atmosphere
- * the spatial and temporal morphology of the aurora
- * an estimate of the characteristic energy of the precipitating particles
- * correlation of auroral/polar cap regimes with other ISTP elements in related parts of the magnetosphere



4 ELEMENTS CRITICAL TO INSTRUMENT CONCEPT

1)2-D FOCAL PLANE DETECTOR:-

LARGE DYNAMIC RANGE/HIGH SENSITIVITY

2)OPTICS:- LOW SCATTER/ GOOD IMAGING

3)FILTERS:- ABILITY TO SEPARATE KEY WAVELENGTH

FEATURES/ CALIBRATION

4)ON-BOARD CONTROLLER:- DATA COMPRESSION

PDR/KEY FEATURES

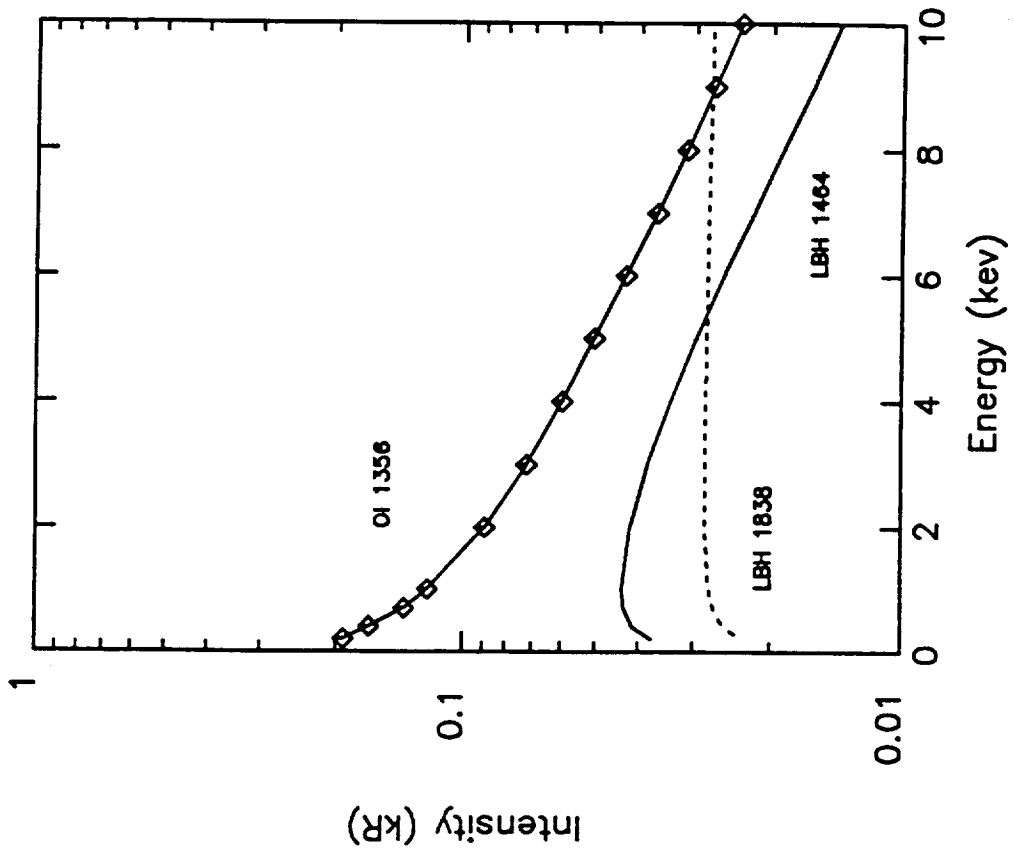


Figure 2

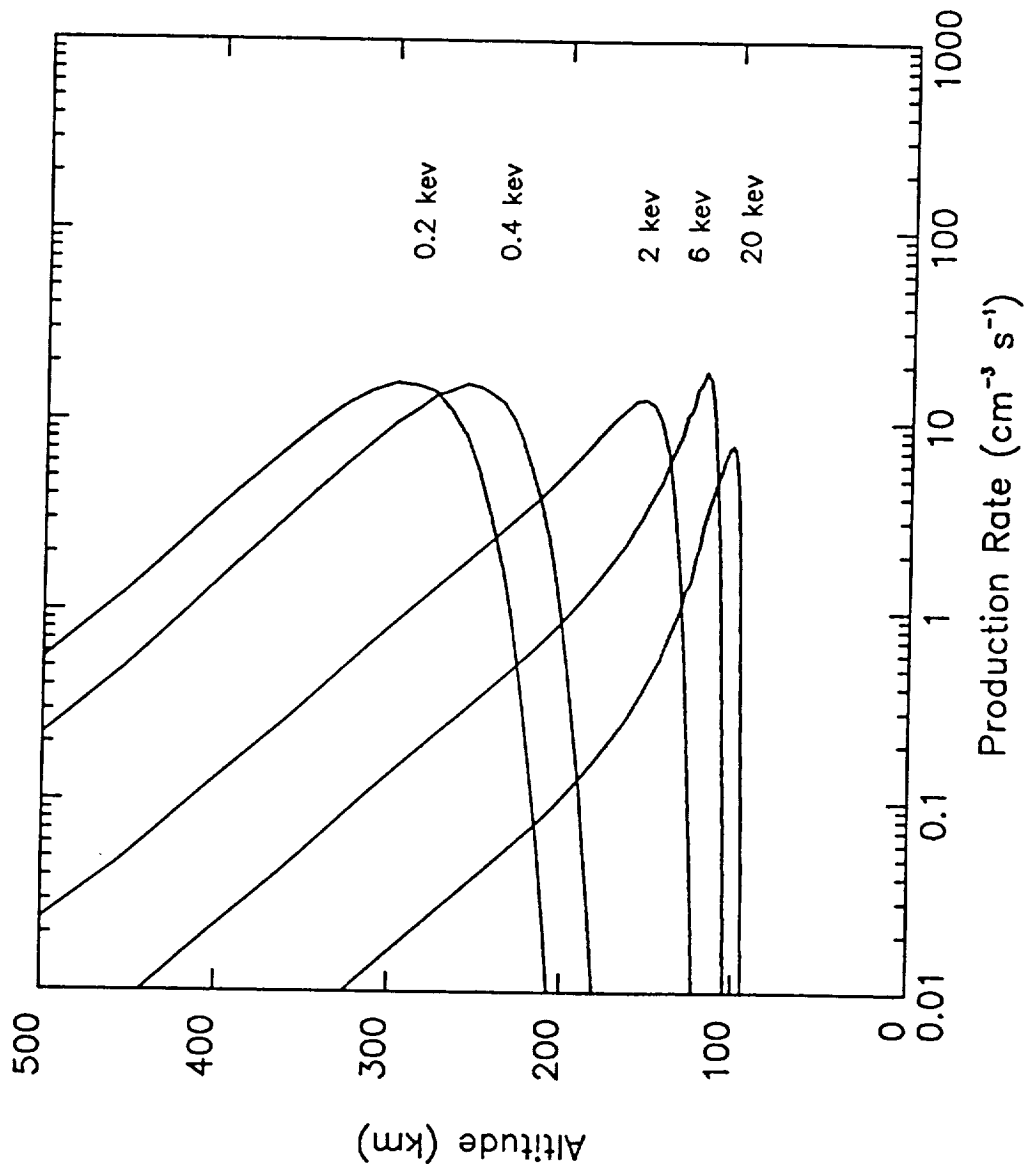
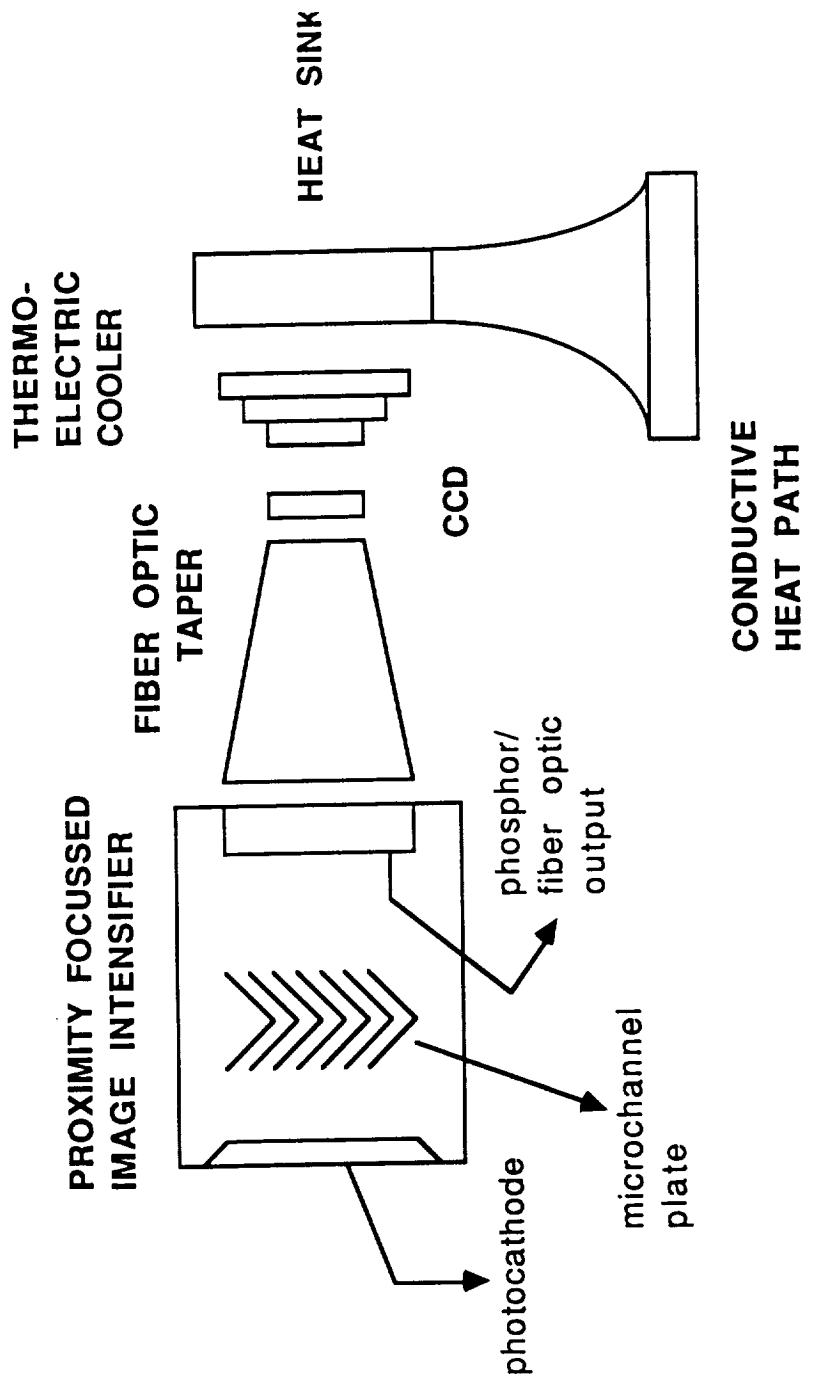


Figure 3



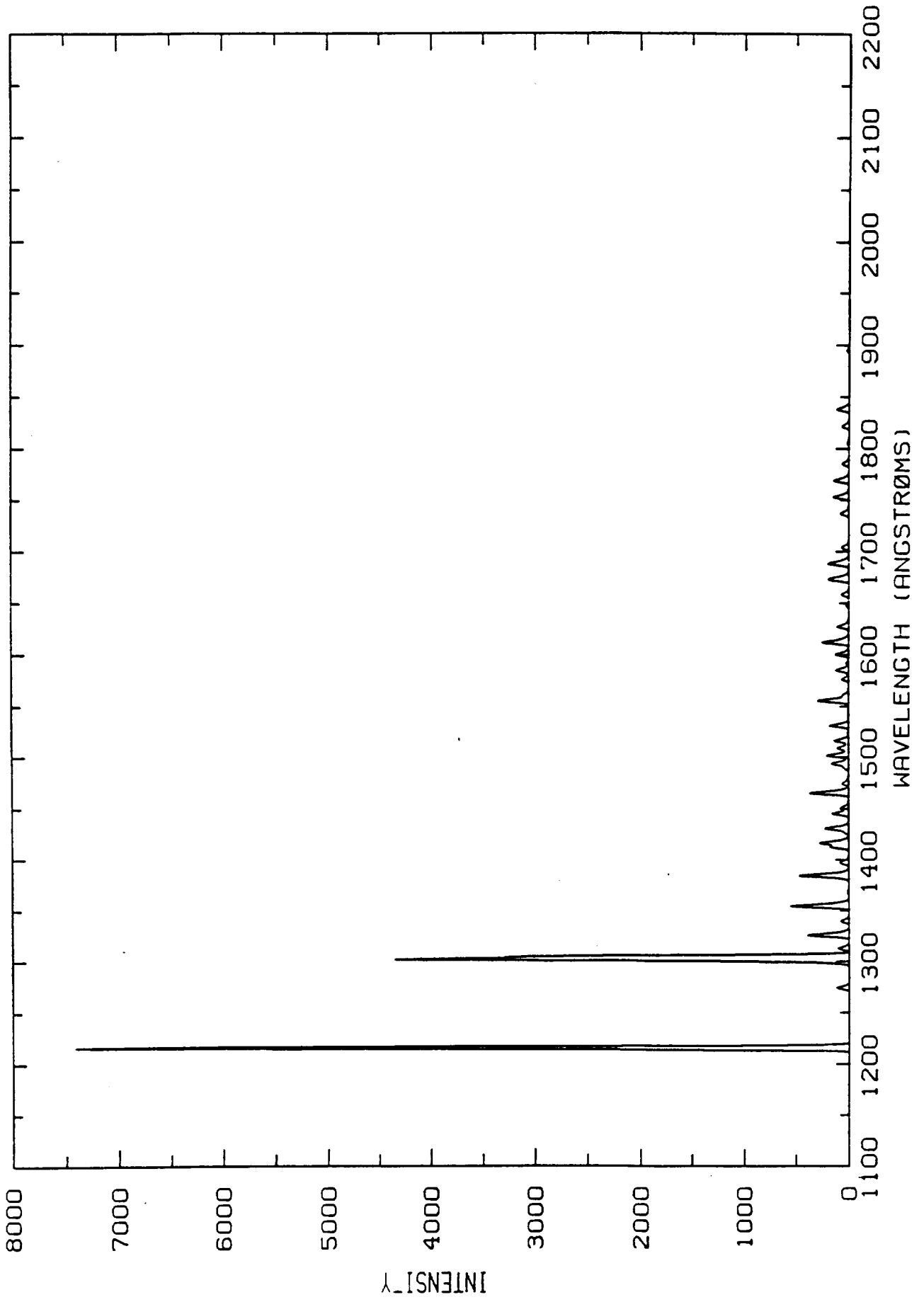
PRINCIPAL ELEMENTS OF DETECTOR

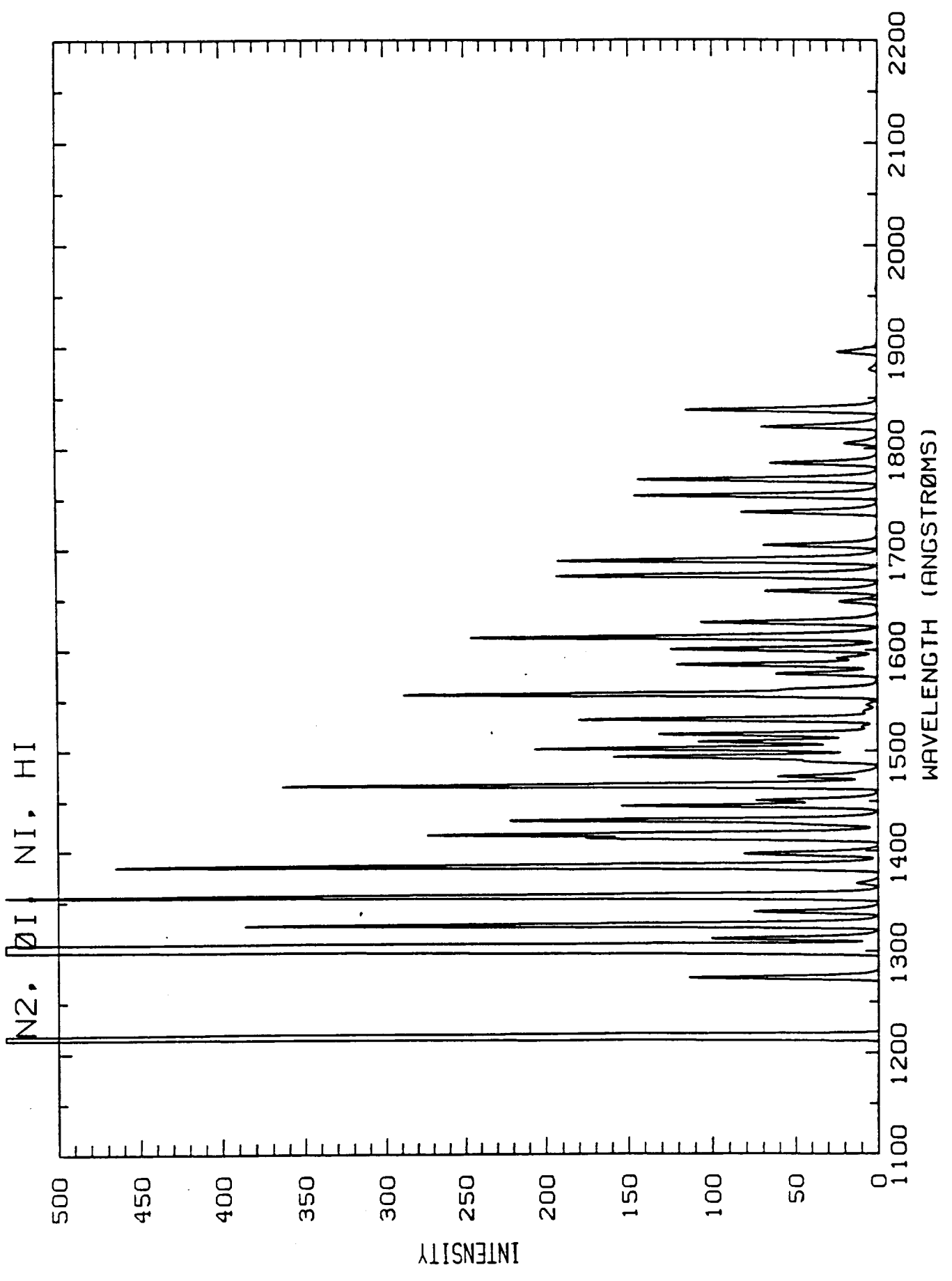
ULTRAVIOLET IMAGER

GLOBAL COVERAGE AND SPATIAL RESOLUTION

ORBIT HEIGHT (R_E)	GLOBAL COVERAGE (LATITUDE CENTERED ON POLE)	SPATIAL RESOLUTION PER PIXEL (km)
10	49.8° x 60.5°	27 x 15
8	60.1 x 67.5	21 x 12
6	69.2 x 74.2	16 x 9
4	77.8 x 80.6	11 x 6
2	86.0 x 86.9	5 x 3
1	89.6 x 89.7	3 x 2

N2, OI, NI, HI





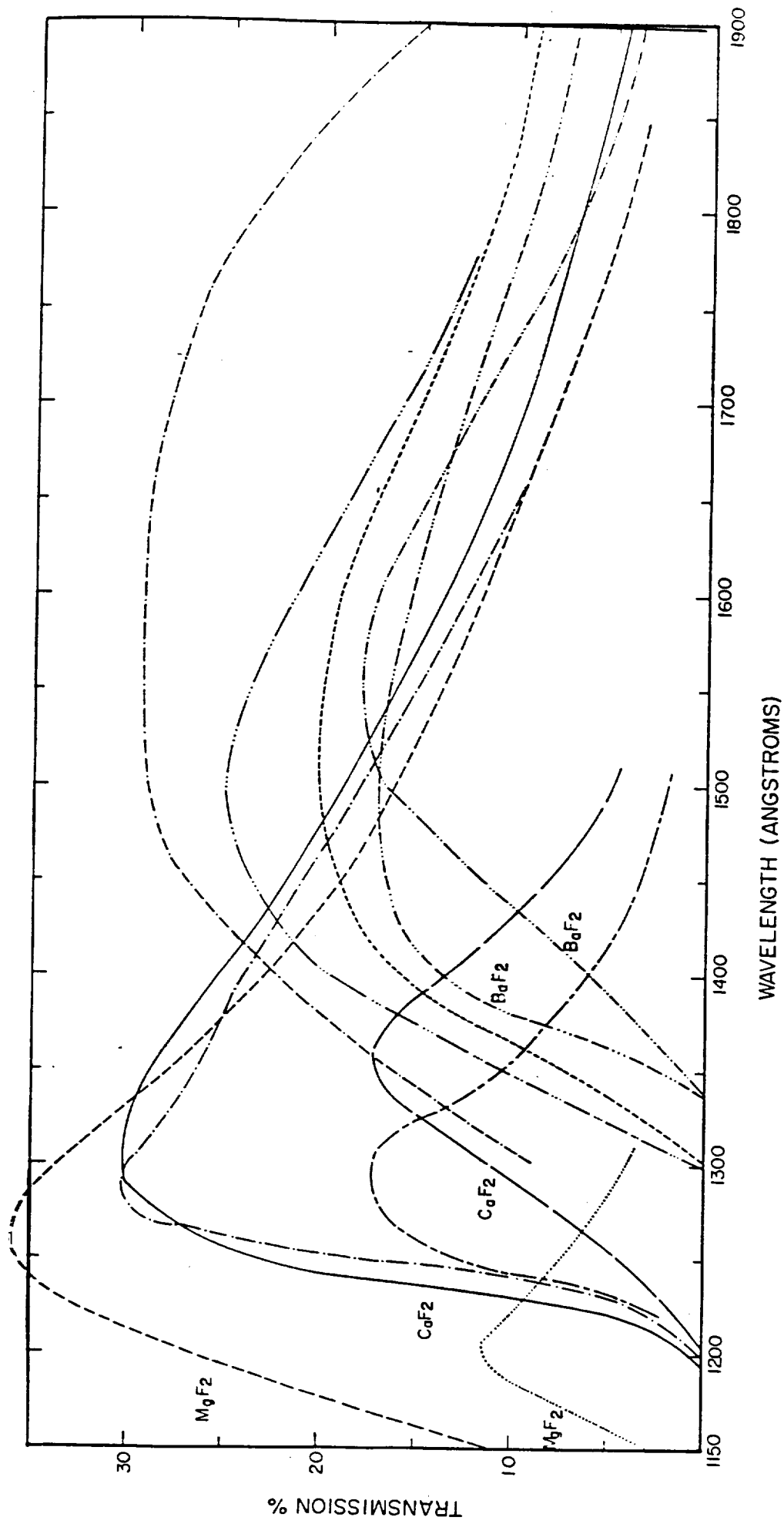
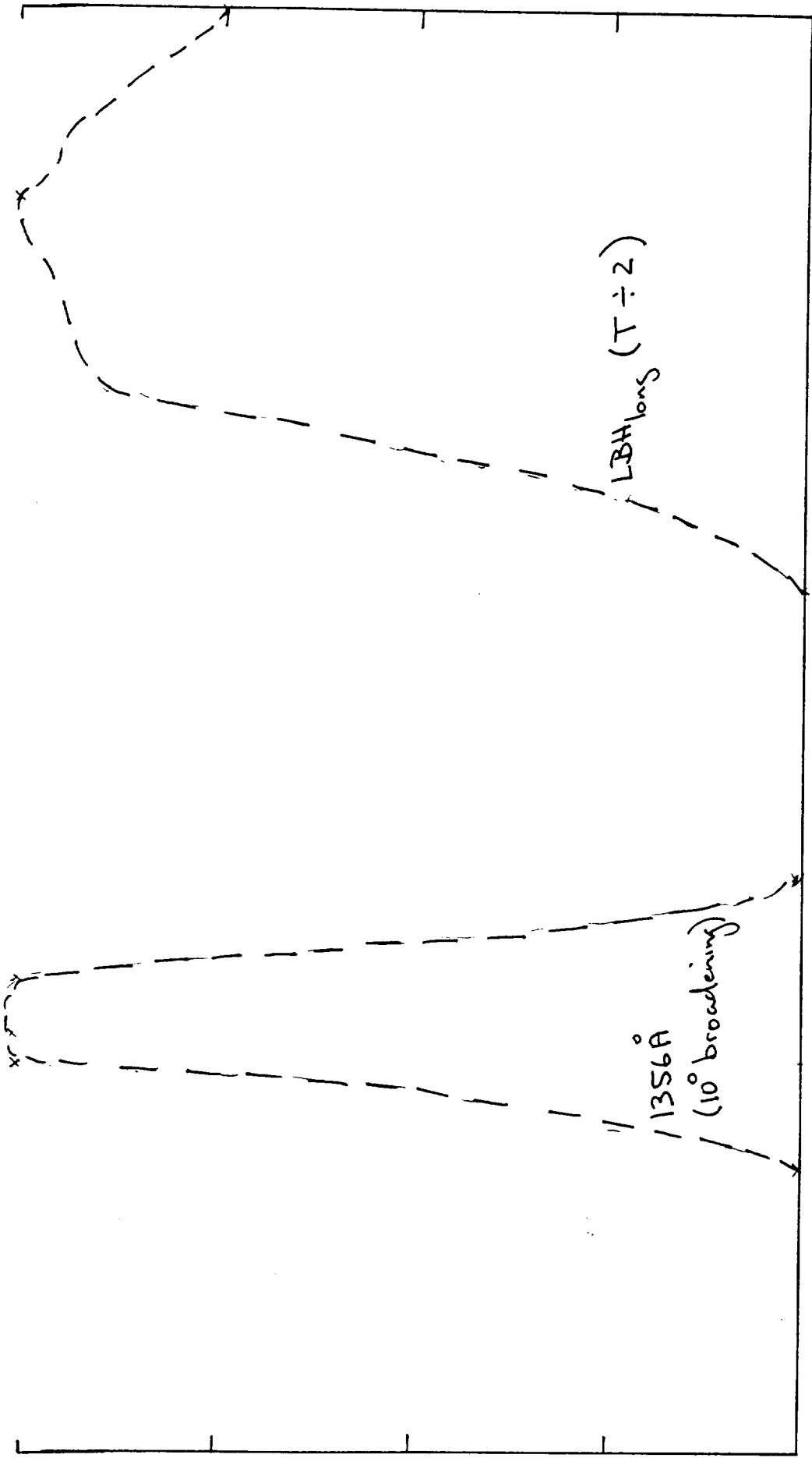


Figure 2.1.2.3



ULTRAVIOLET IMAGER

FILTERS

1. 1216A - TO REMOVE CONTAMINATION
2. 1384A - TO REMOVE CONTAMINATION/ATOMIC OXYGEN
3. 1356A - CHARACTERISTIC ENERGY
4. ±1500A - LBHS, TOTAL ENERGY/ O₂
5. 1493A - N/CONTAMINATION
6. ±1800A - LBH_L, TOTAL ENERGY
7. 2150A - NO (COUPLING OF ENERGY INTO ATMOSPHERIC COMPOSITION)

AGREED TO RESOURCES SUMMARY

MASS	19.5 KGMS
POWER	20 WATTS
DATARATE	12 KBPS

PDR/RESOURCES

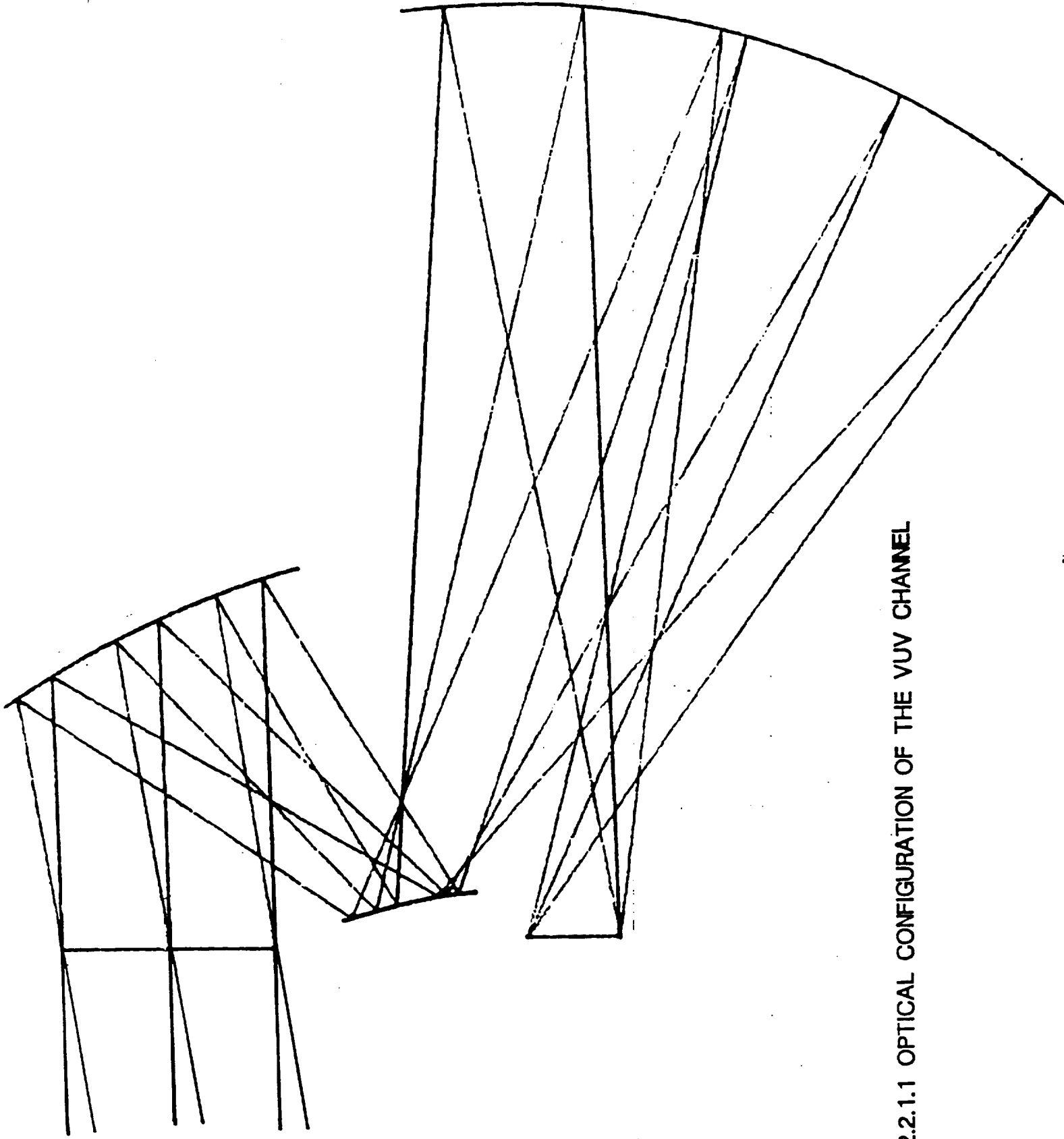


FIGURE 2.2.1.1 OPTICAL CONFIGURATION OF THE VUV CHANNEL

UV IMAGER SCATTERING LOSS

PERKIN ELMER
Electro-Optical Technology Division

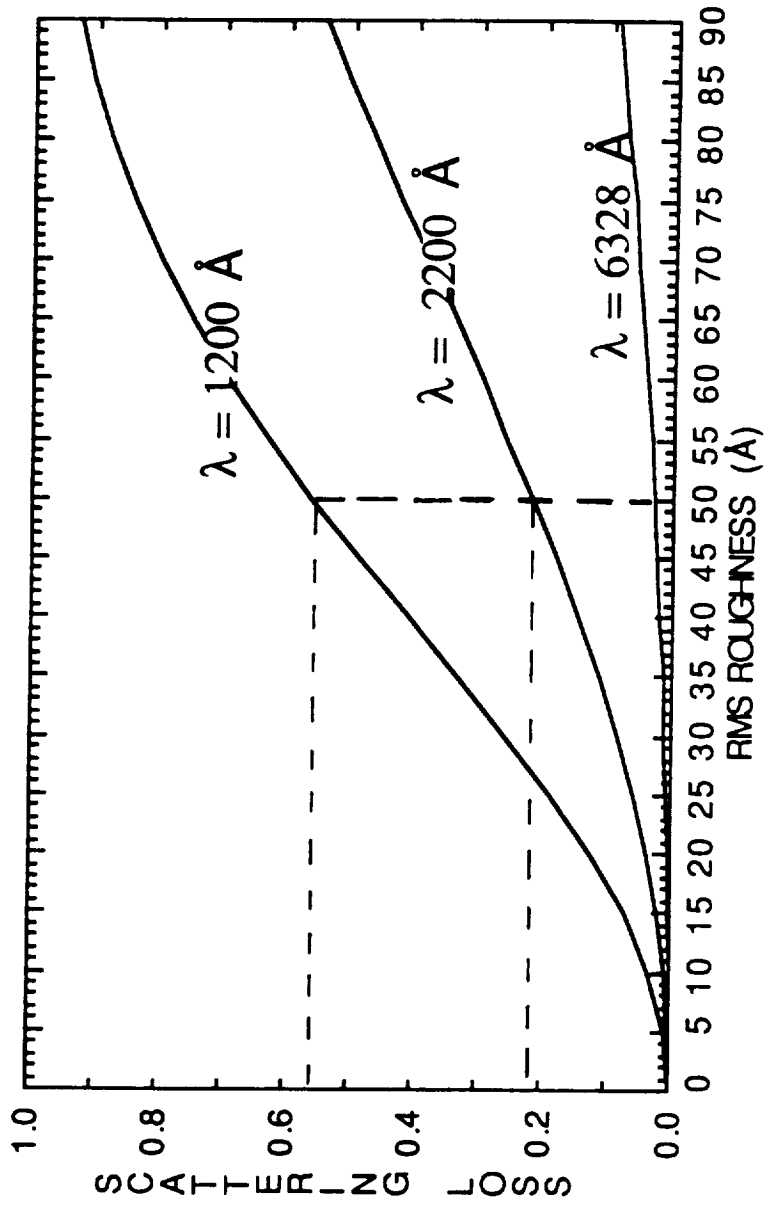


Figure 1

UV IMAGER SCATTERING LOSS

PERKIN ELMER
Electro-Optical Technology Division

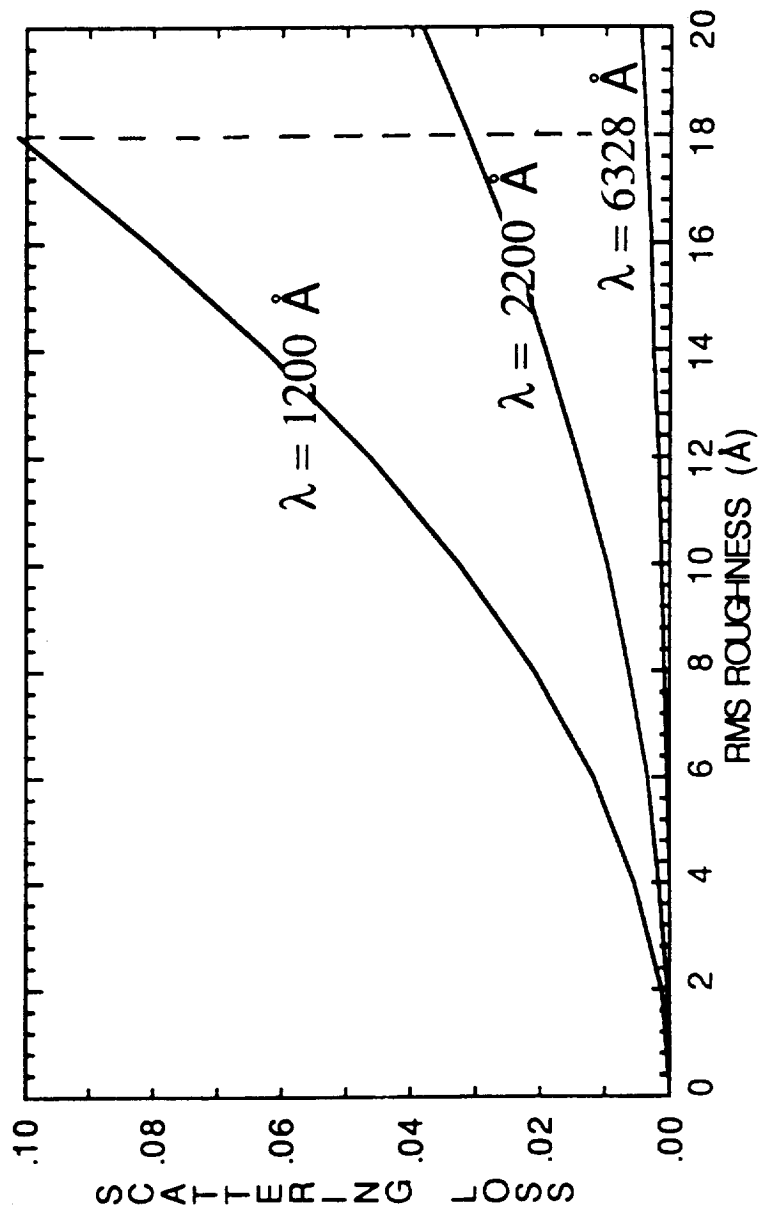
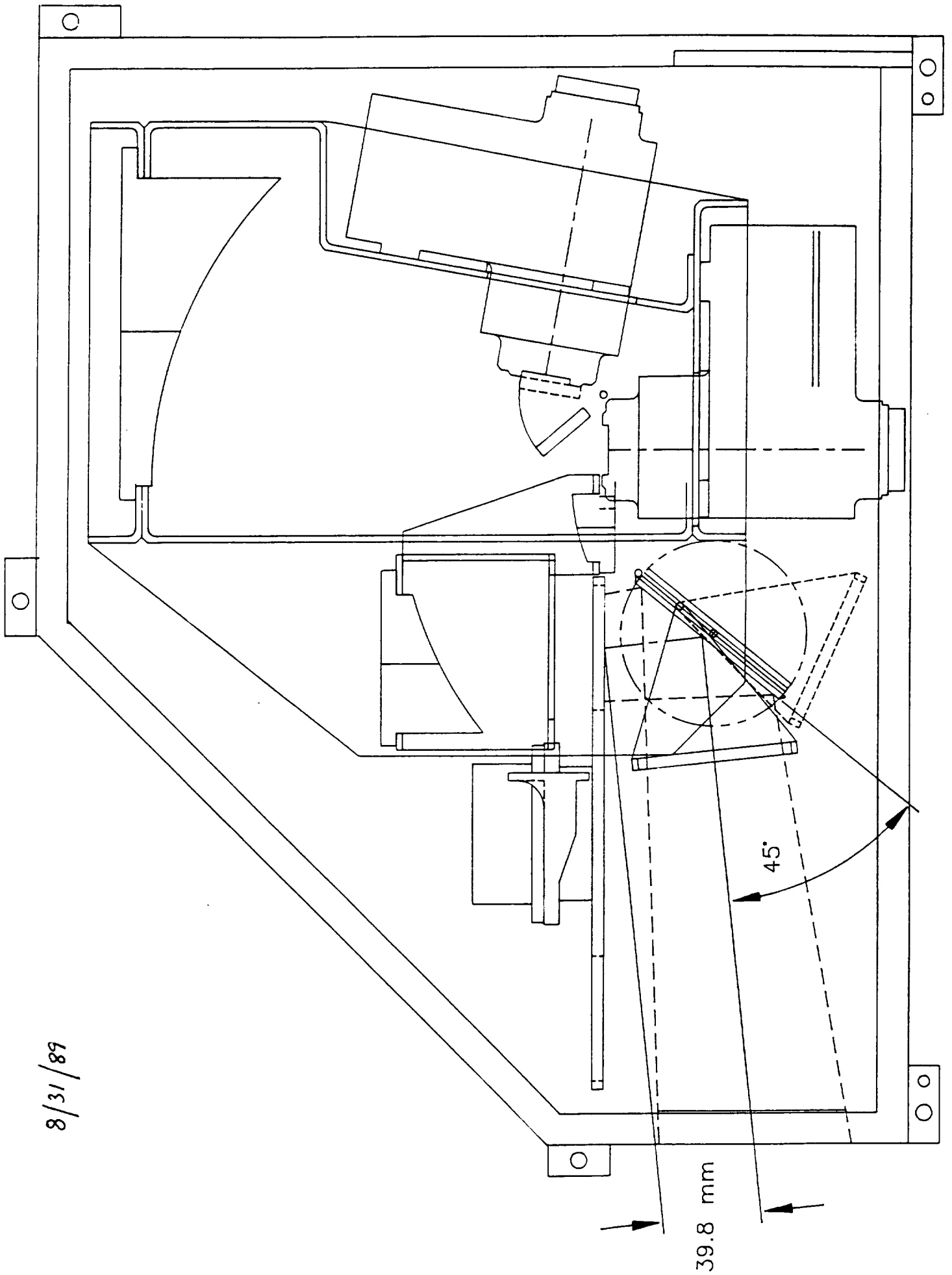
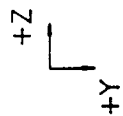


Figure 2



ULTRAVIOLET IMAGER
 ISTP-POLAR
 ALL DIMENSIONS IN MM



MASS PROPERTIES*	
CAMERA MASS	12.00 KG.
INERTIAL PROPERTIES (KG-M ²)	
I _{xx}	TBD
I _{yy}	TBD
I _{zz}	TBD
*MASS PROPERTIES DO NOT INCLUDE THE MASS OF THE COLDPLATE OR THE MU	

INSTRUMENT COORDINATES
 X = 60
 Y = 22
 Z = 0

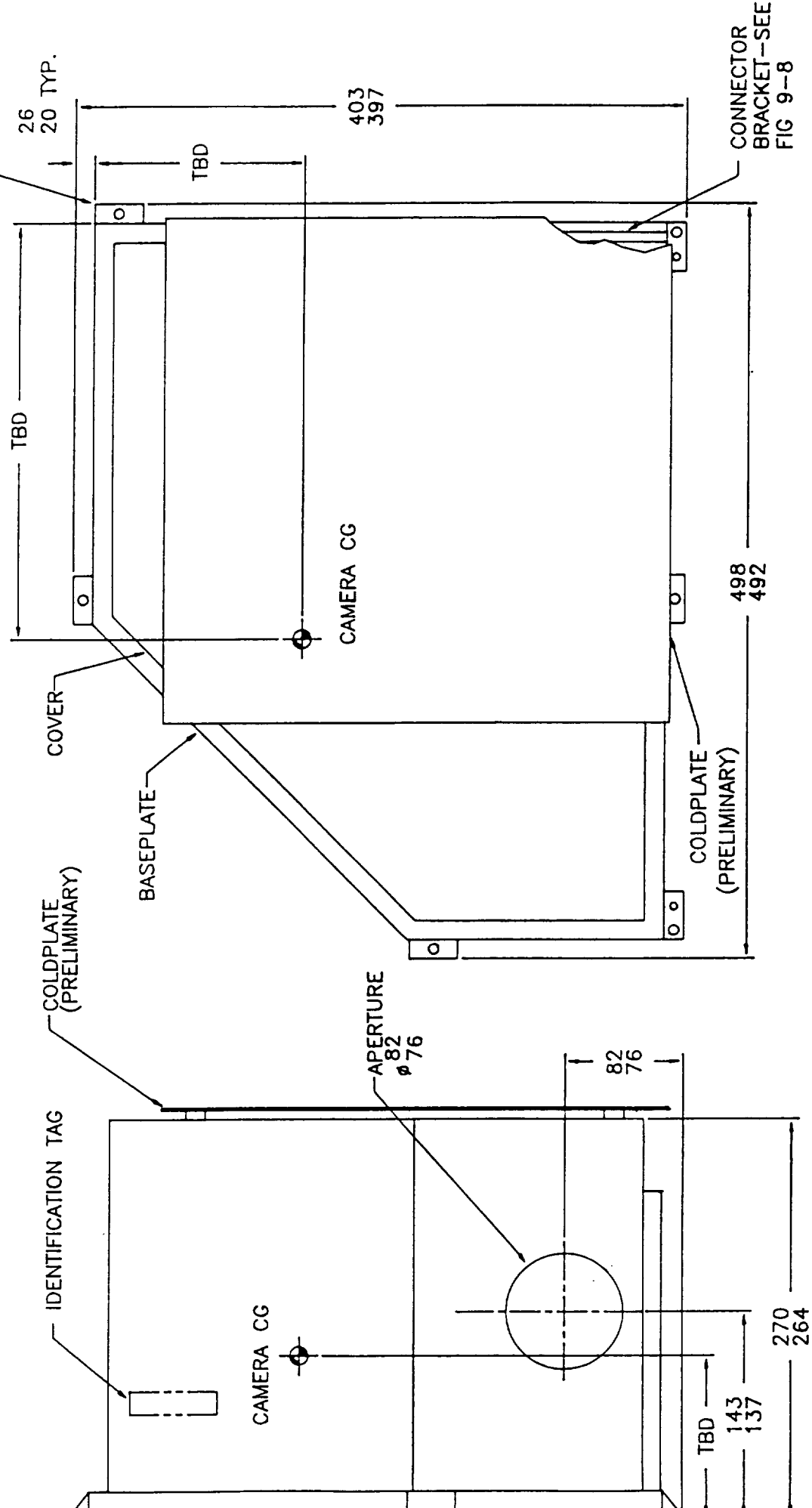
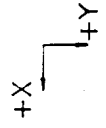
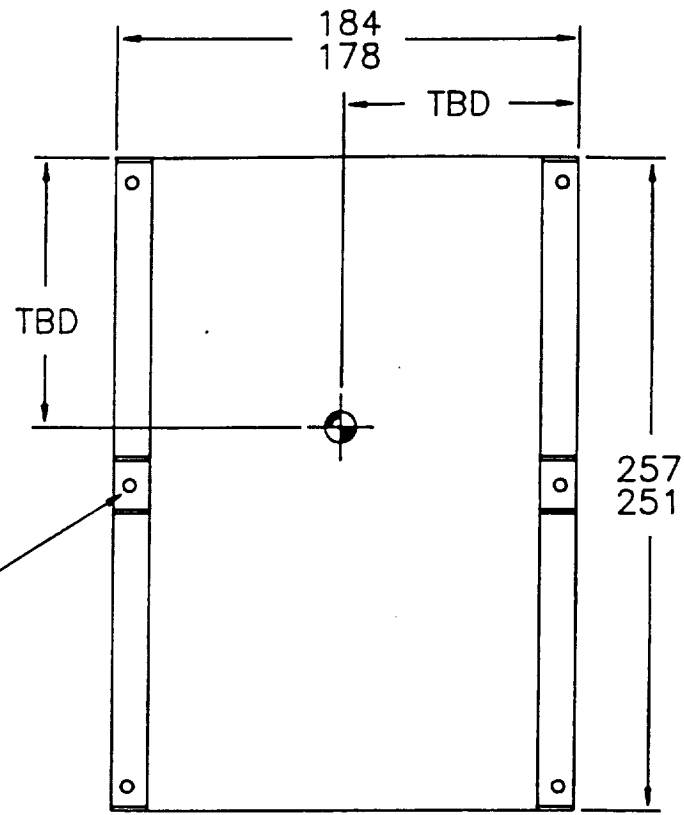


FIGURE 9-3 - DETAIL "A" - CAMERA

ULTRAVIOLET IMAGER
 ISTEP-POLAR
 ALL DIMENSIONS IN MM



SEE FIG. 9-6
 FOR HOLE PATTERN

IDENTIFICATION TAG

GROUNDING STRAP
 SCREW (6-32)

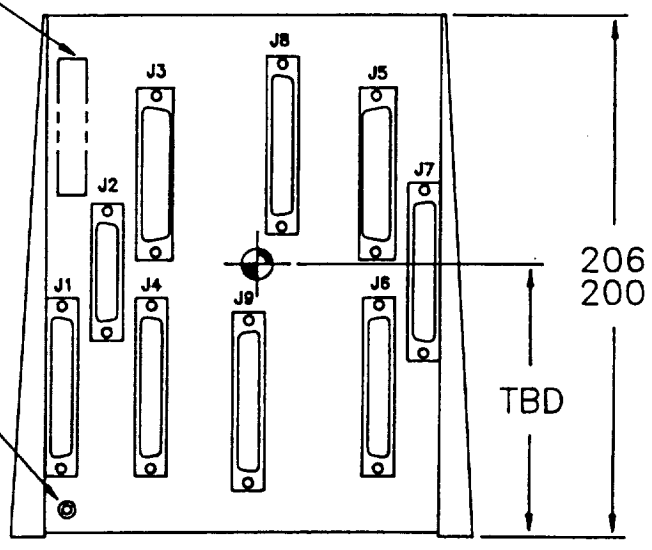


FIGURE 9-4 - DETAIL "B" - ELECTRONICS STACK

ULTRAVIOLET IMAGER

SUMMARY OF PARAMETERS

wavelength range	1200A - 2150A
f#	3.0
aperture, cm ²	14.5
solid angle, sr	15×10^{-2}
field of view	8°
number of spatial elements	244 x 550
size of spatial elements	54 x 32 microns
sensitivity of spatial elements	0.005
angular resolution per spatial element	$0.024^\circ \times 0.014^\circ$

HIGHLIGHTS OF THE ULTRAVIOLET IMAGER INVESTIGATION

OPTICS

fast ($f/3$) system with wide field of view (8 degrees) and excellent image quality (< 1 pixel over most of image), state-of-the-art low scatter design

DETECTORS

proven intensified-CCD system that provides compact 2-D sensor with low noise and large dynamic range (4000 instantaneous selectable over a range of six to seven orders of magnitude)

DATA SYSTEM

on-board microprocessor (80C86) controller and data formatter allows programmable operations and substantial real-time data compression that is further enhanced by data compression algorithms

FILTERS

narrow bandpass filters with excellent out of band rejection for key emissions (e.g. 1304Å, 1356Å) allows the first truly quantitative auroral imaging

CALIBRATION FACILITIES

existing vacuum ultraviolet calibration facilities allowing absolute calibration of imager at all wavelengths

ATMOSPHERIC/AURORAL MODELS

models of the upper atmosphere and energetic particle impact on the atmosphere developed by our group over the last 20 years are essential to the interpretation of the auroral information content

UVI8186

ULTRAVIOLET IMAGER

WHAT UVI WILL DO

- * 2-D imaging
- * VUV wavelength range allows imaging of sunlit and dark sides of the Earth
- * low scatter design allows bright and weak signals to be imaged simultaneously
- * filter design and atmospheric auroral models allow first quantitative interpretation of information
- * dynamic range of instrument allows first simultaneous imaging of weak detail (e. g. in polar cap) and bright auroral features

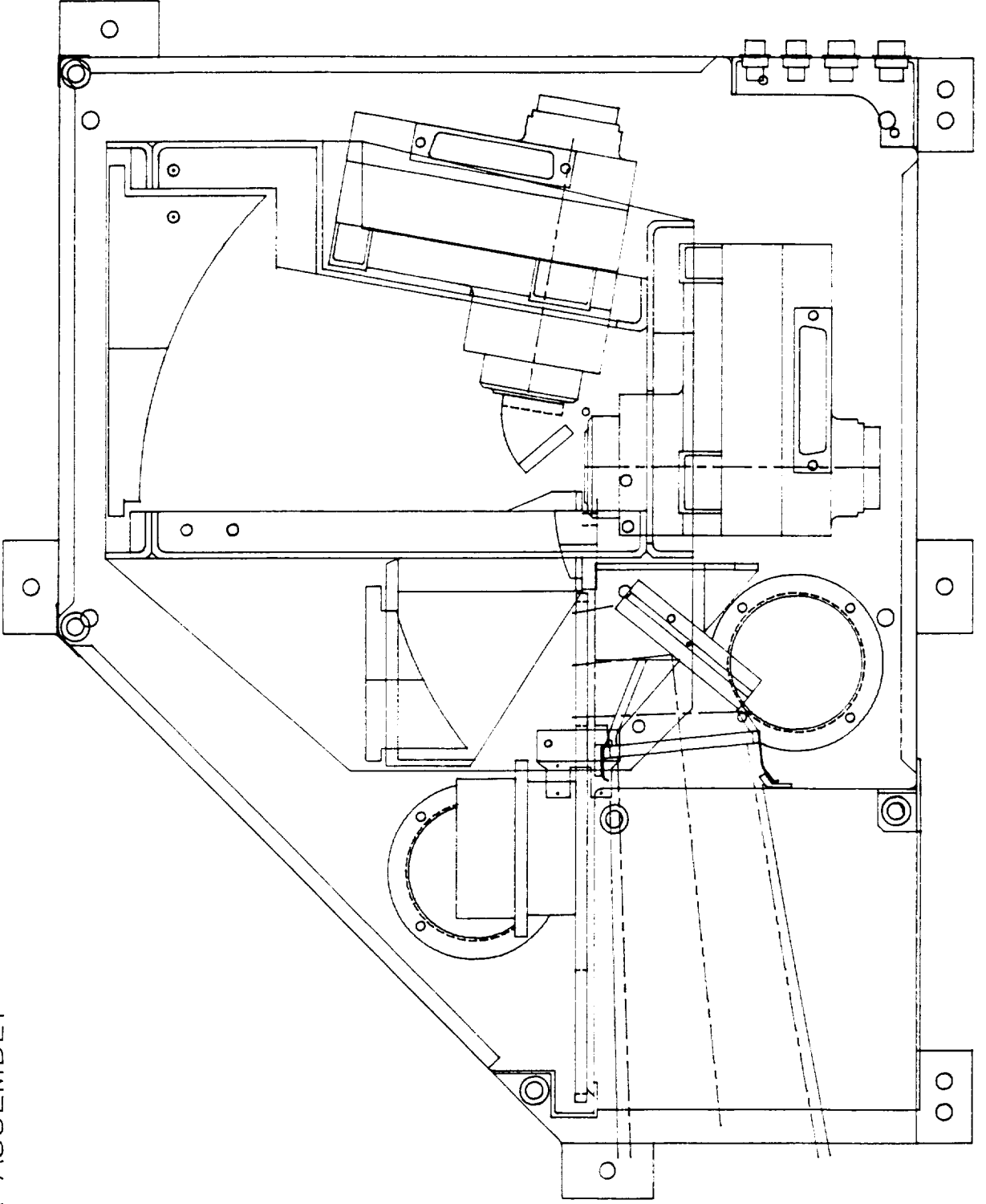
ULTRAVIOLET IMAGER
POLAR/GGS

MECHANICAL DESIGN

PRELIMINARY DESIGN REVIEW

PDR TITLE/002

ISTP-UVI
CAMERA ASSEMBLY



ISTP-UVI
CAMERA ASSEMBLY

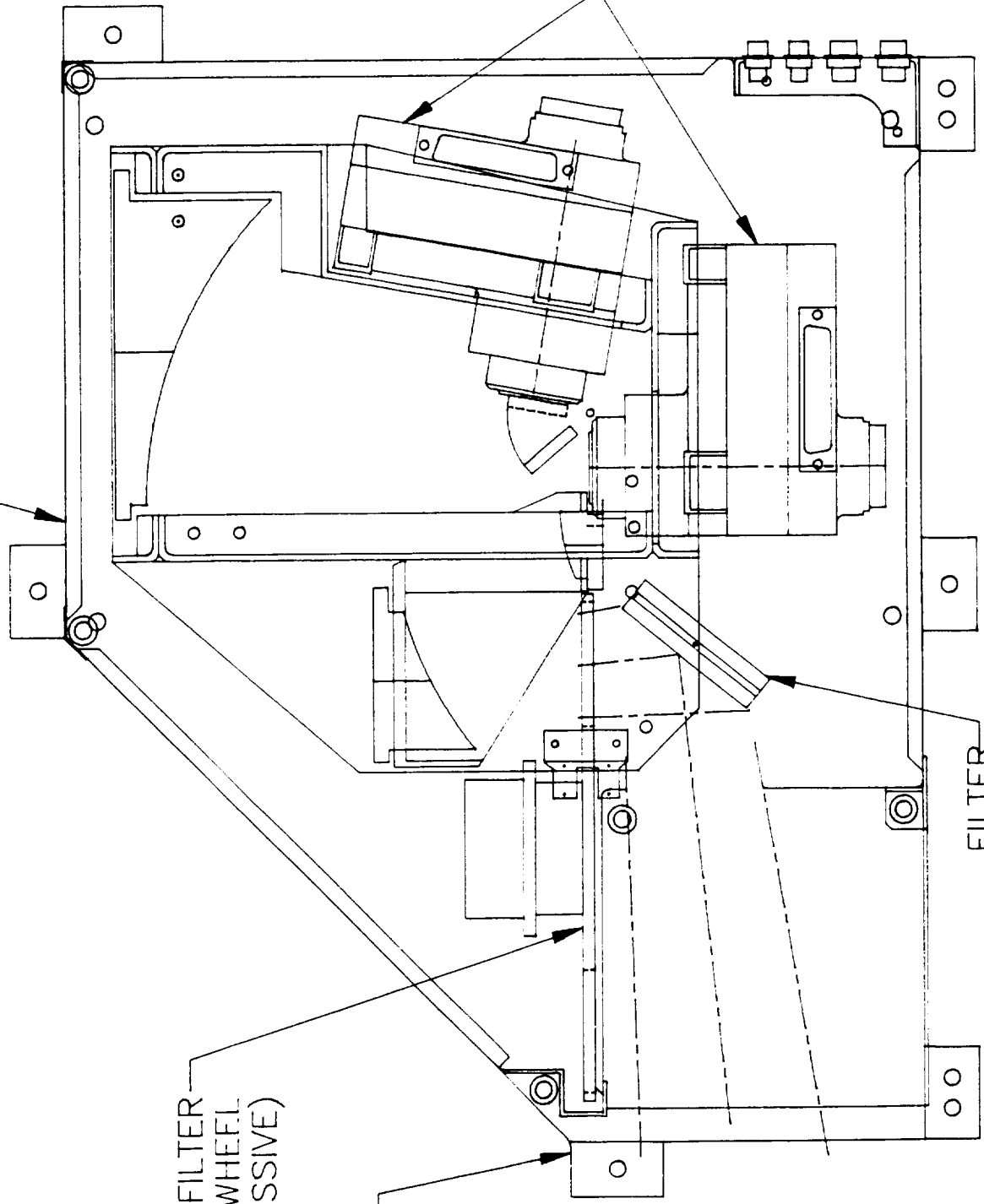
FILTER
WHEEL
(TRANSMISSIVE)

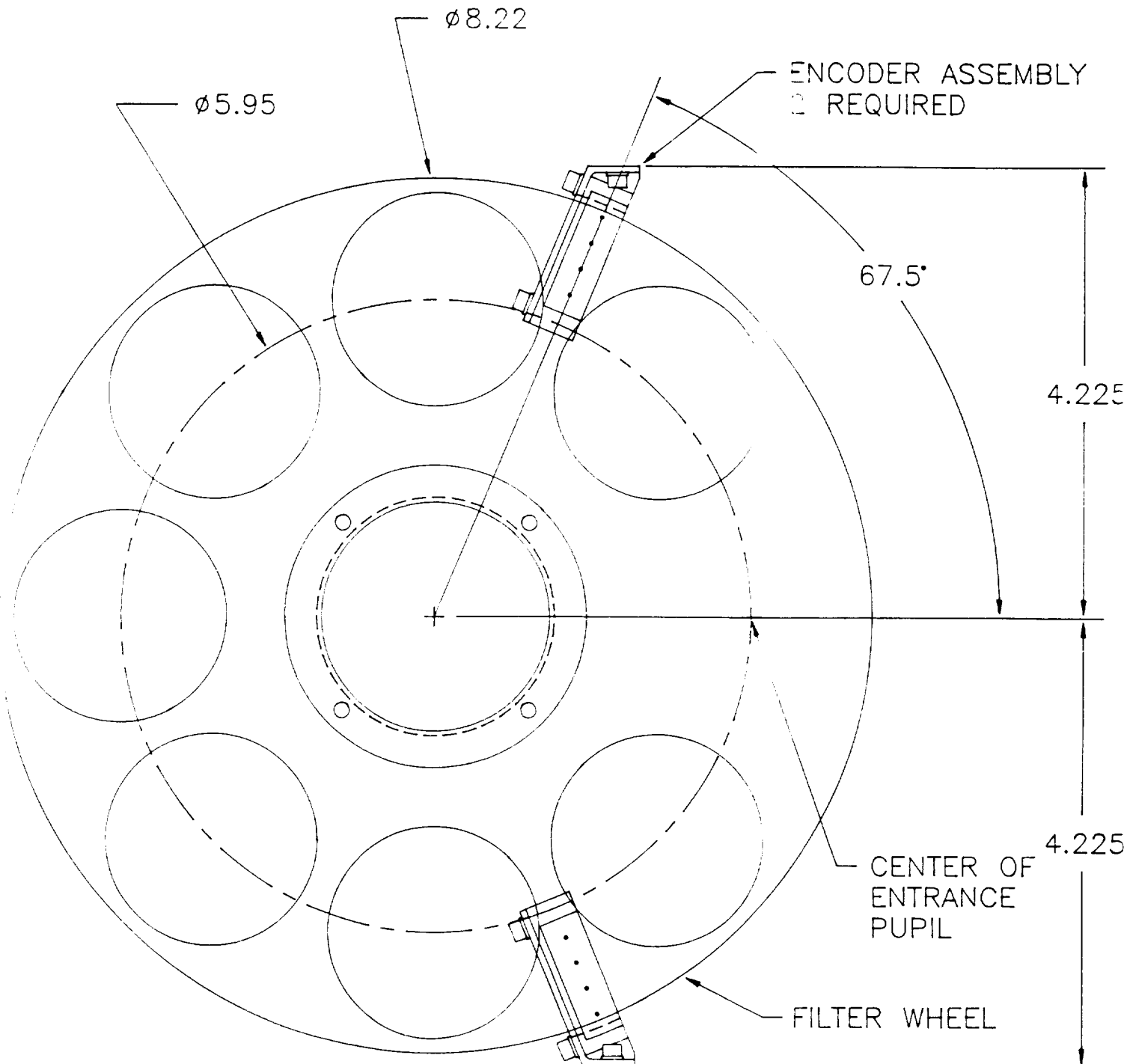
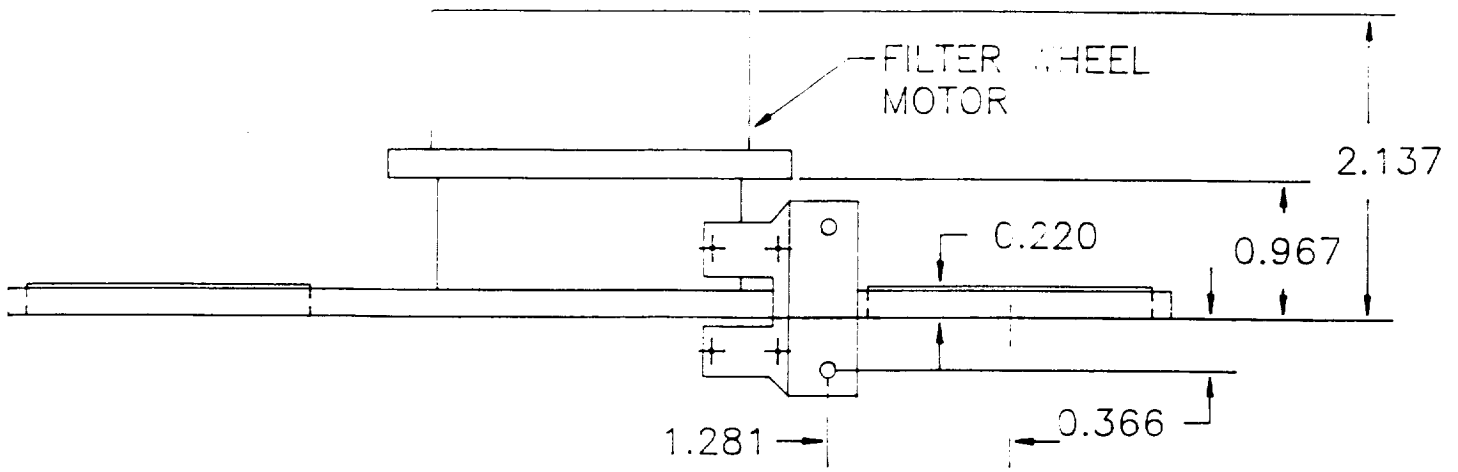
OPTICAL BENCH ASSEMBLY

SPACECRAFT
INTERFACE
STRUCTURE

PRIMARY &
SECONDARY
DETECTORS

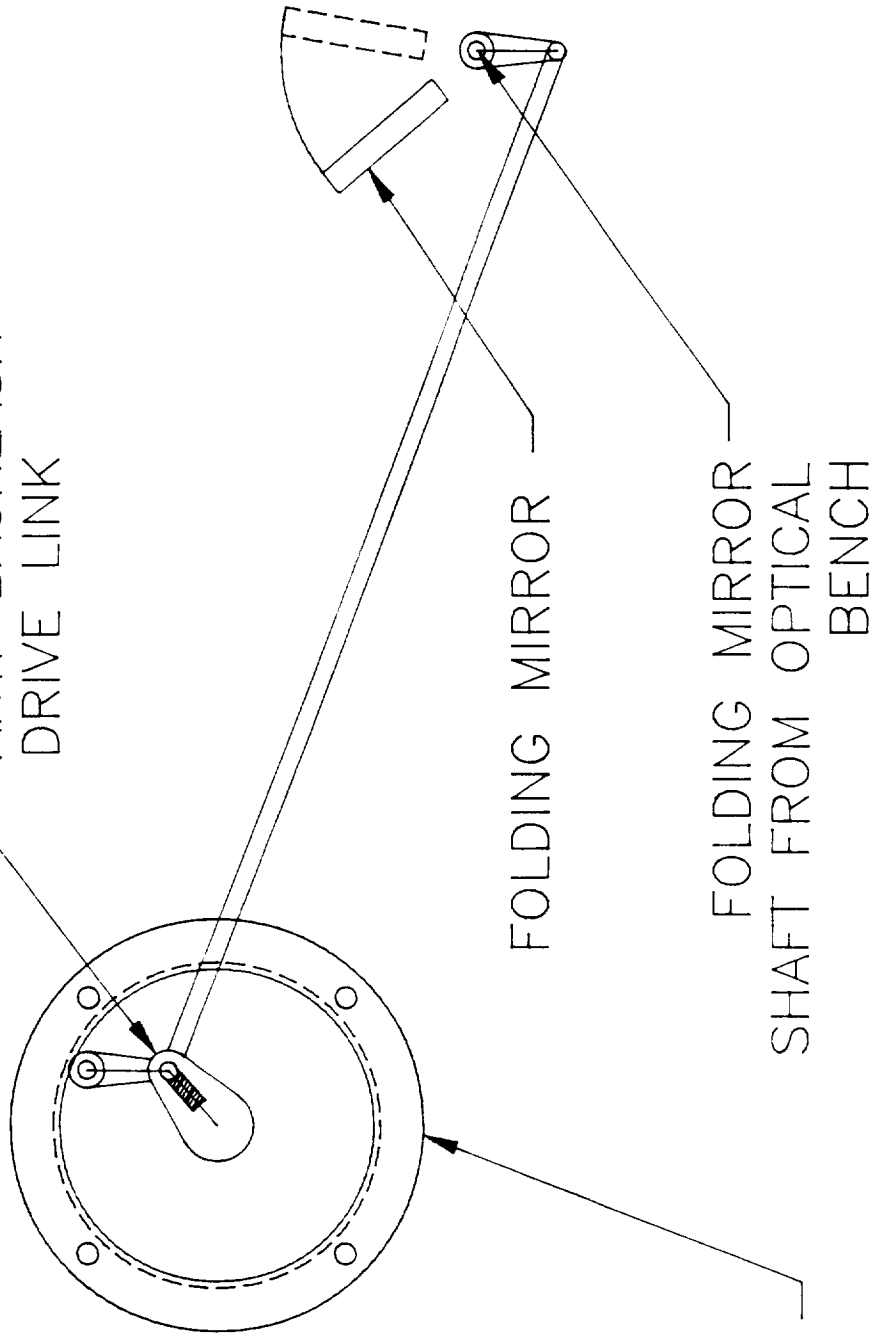
FILTER
MIRROR
(REFLECTIVE)





ISTP-UVI
CAMERA
MECHANISMS

ANTI-BACKLASH
DRIVE LINK



DRIVE MOTOR
(Ø 2.85)

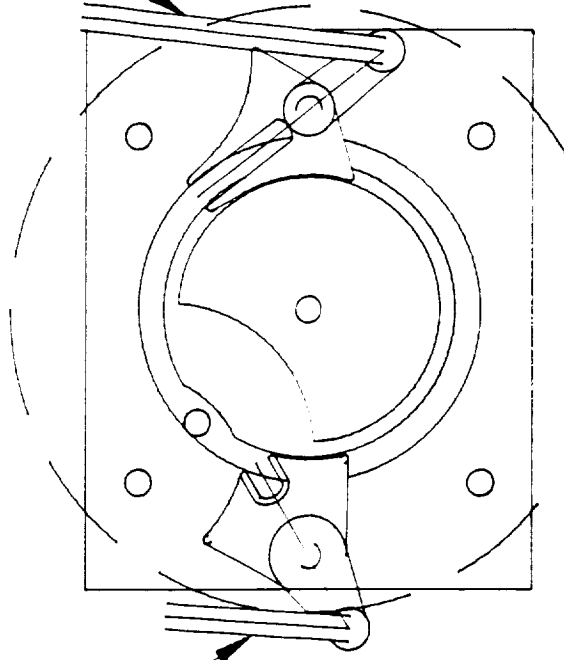
FOLDING MIRROR

FOLDING MIRROR
SHAFT FROM OPTICAL
BENCH

ISTP - UVI
CAMERA
MECHANISMS

LINK TO
REFLECTIVE
FILTER

LINK TO
APERTURE
DOOR



OUTLINE OF
DRIVE MOTOR
FLANGE
($\phi 2.85$)

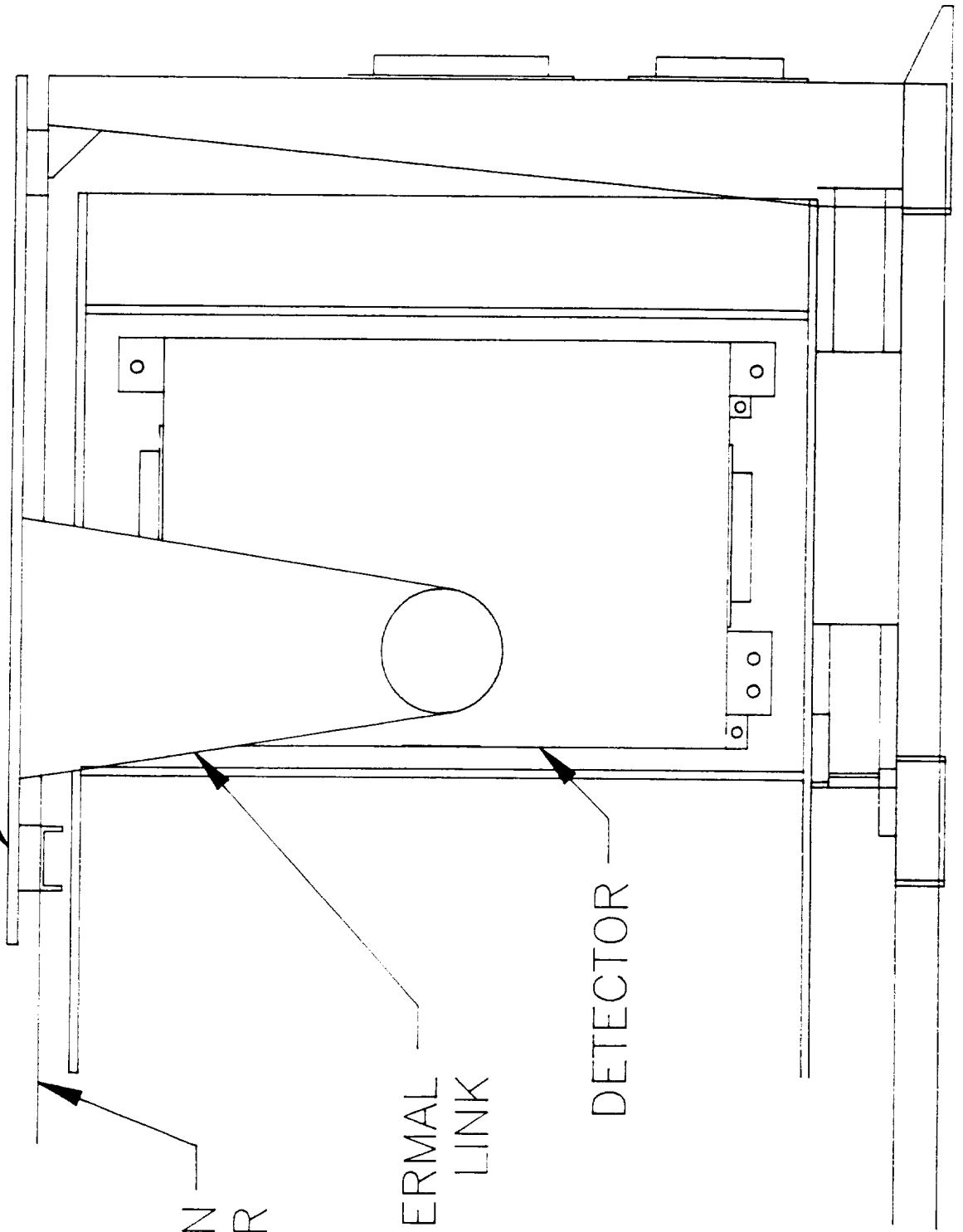
ISTP-UVI
CAMERA ASSEMBLY

RADIATOR

CONTAMINATION
COVER

THERMAL
LINK

DETECTOR

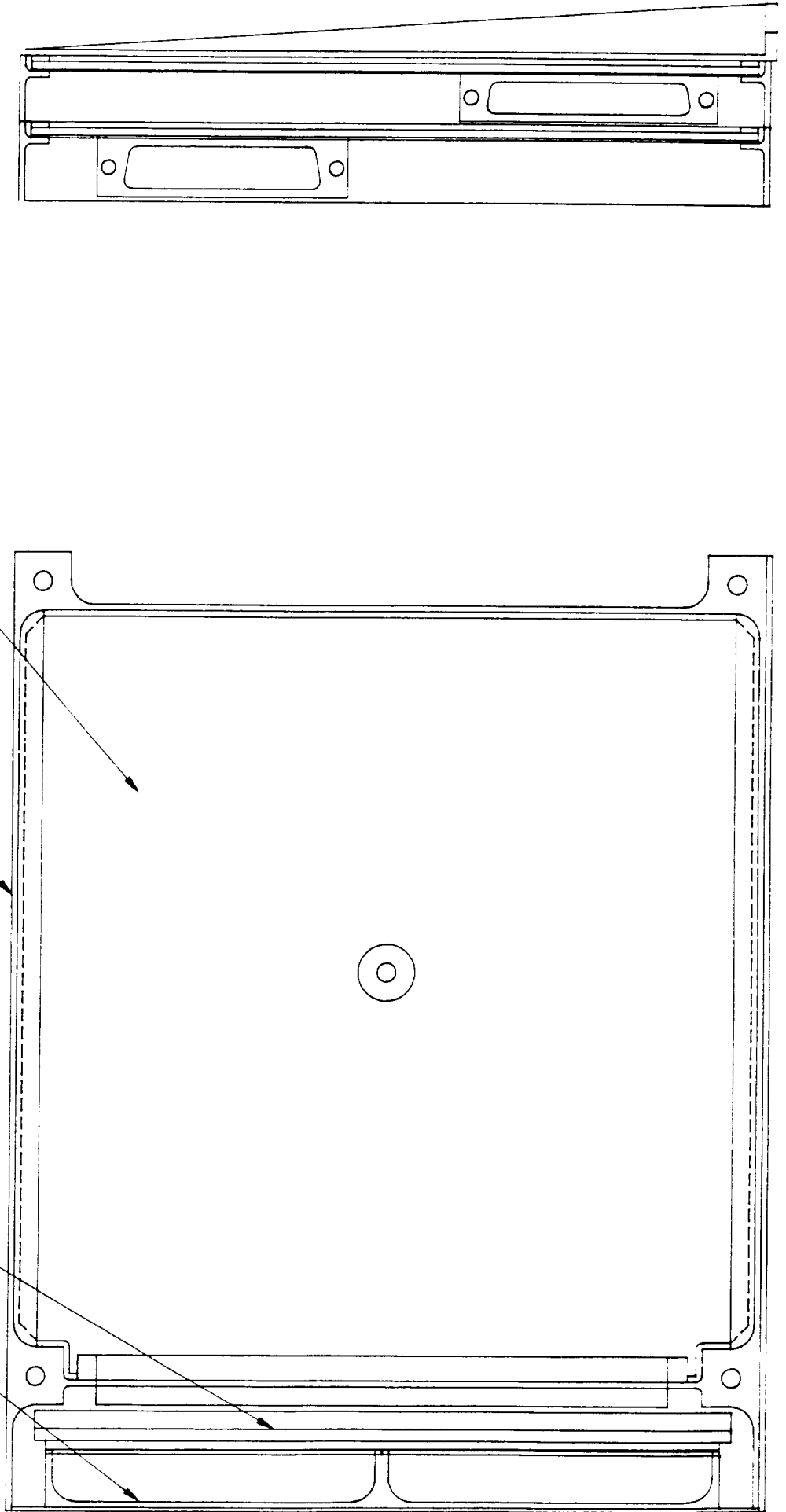


POWER SUPPLY

MOTHERBOARD

CRATE

CIRCUIT BOARD



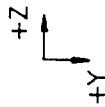
ISTP-UVI CAMERA MASS AND CG
 08:02 PM 16-Oct-89

ITEM NAME	MASS (KG)	XCG (MM)	YCG (MM)	ZCG (MM)
PRIMARY DETECTOR	1.111	167.64	284.48	144.78
SECONDARY DETECTOR	1.111	114.3	215.9	144.78
MIRROR MECH. ASSY	0.572	287.02	223.52	76.2
CABLE HARNESSSES	1.706	101.6	317.5	101.6
FILTER WHEEL ASSY	1.075	325.12	228.6	144.78
BAFFLE DOOR ASSY	0.610	266.7	279.4	127
BASEPLATE ASSY	1.797	266.7	228.6	7.62
CAMERA COVER ASSY	0.642	266.7	228.6	152.4
OPTICAL BENCH ASSY	4.950	213.36	243.84	144.73
THERMAL LINKS	0.200	127	241.3	195.58
COLDPLATE ASSY	1.030	139.7	190.5	232.1
INSTRUMENT TOTAL	14.803	205.26	246.60	131.04

ISTP-UVI CAMERA MASS AND CG

ITEM NAME	MASS (LB)	XCG (IN)	YCG (IN)	ZCG (IN)
PRIMARY DETECTOR	2.450	6.6	11.2	5.7
SECONDARY DETECTOR	2.450	4.5	8.5	5.7
MIRROR MECH. ASSY.	1.260	11.3	8.8	3
CABLE HARNESSSES	3.760	4	12.5	4
FILTER WHEEL ASSY	2.370	12.3	9	5.7
RFILTER/APER ASSY	1.345	10.5	11	5
BASEPLATE ASSY	3.960	10.5	9	0.3
CAMERA COVER ASSY	1.415	10.5	9	6
OPTICAL BENCH ASSY	10.910	8.4	9.6	5.7
THERMAL LINKS	0.44	5	9.5	7.7
COLDPLATE ASSY	2.270	5.5	7.5	11.5
INSTRUMENT TOTAL	32.630	8.0814	9.7086	5.1591

ULTRAVIOLET IMAGER
 ISTEP-POLAR
 ALL DIMENSIONS IN MM



MASS PROPERTIES*	
CAMERA MASS	13.50 KG.
INERTIAL PROPERTIES (KG-M ²)	
I _{xx}	TBD
I _{yy}	TBD
I _{zz}	TBD
*MASS PROPERTIES DO NOT INCLUDE THE MASS OF THE MU	

INSTRUMENT COORDINATES
 X= 60
 Y= 22
 Z= 0

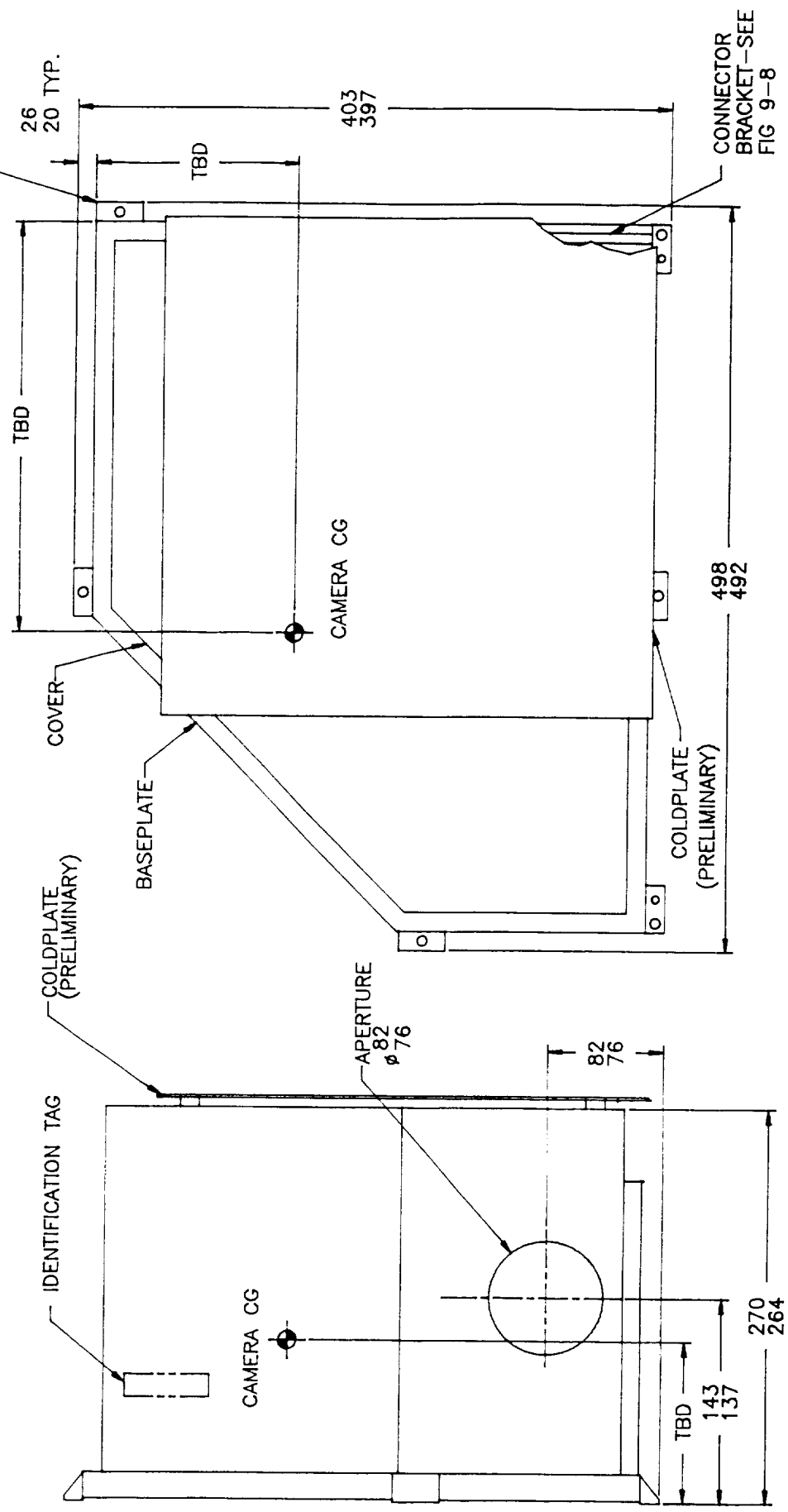
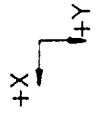


FIGURE 9-3 -- DETAIL "A" -- CAMERA

ISTP-UVI ELECTRONICS MASS AND CG
 08:13 PM 16-Oct-89

ITEM NAME	MASS (KG)	XCG (MM)	YCG (MM)	ZCG (MM)
CPU/SCIF A&B	0.422	139.7	88.9	101.6
MEMORIES A&B	0.462	133.35	88.9	101.6
DETECTOR I/F A&B	0.422	142.24	88.9	101.6
HOUSEKEEPING BOARD	0.185	139.7	21.59	101.6
TEU CONTROL BOARD	0.185	139.7	147.32	101.6
DUAL MOTOR CONTROLLE	0.256	142.24	170.18	101.6
MOTHERBOARD ASSY	0.198	41.275	88.9	101.6
POWER SUPPLIES A&B	0.556	12.7	88.9	101.6
CRATE STACK	1.234	121.92	88.9	101.6
STACK ENDPLATES	0.596	127	88.9	101.6
TENSION RODS	0.149	127	88.9	101.6
FASTENER ALLOWANCE	0.054	127	88.9	101.6
INSTRUMENT TOTAL	4.718	113.5604	92.95792	101.6

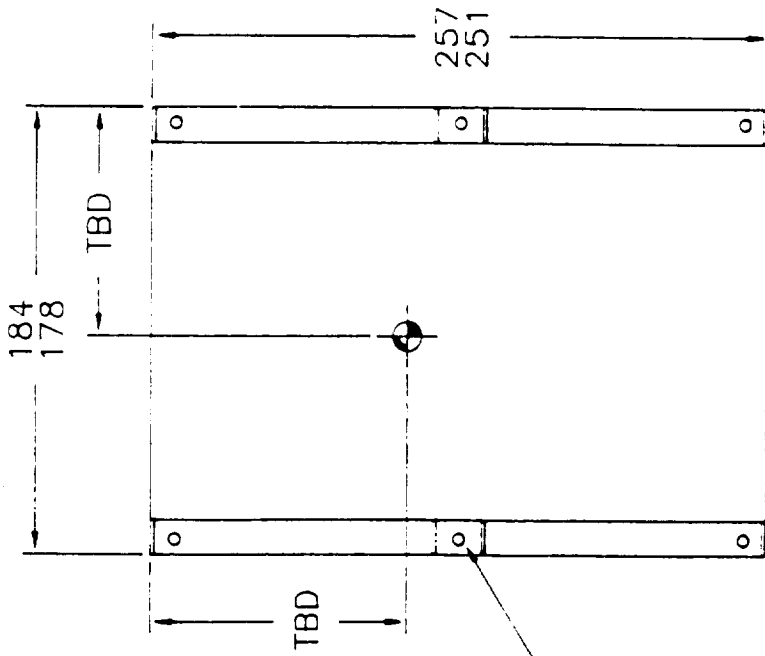
ISTP-UVI ELECTRONICS MASS AND CG

ITEM NAME	MASS (LB)	XCG (IN)	YCG (IN)	ZCG (IN)
CPU/SCIF A&B	0.930	5.5	3.5	4
MEMORIES A&B	1.018	5.25	3.5	4
DETECTOR I/F A&B	0.930	5.6	3.5	4
HOUSEKEEPING BOARD	0.407	5.5	0.85	4
TEU CONTROL BOARD	0.407	5.5	5.8	4
DUAL MOTOR CONTROLLE	0.564	5.6	6.7	4
MOTHERBOARD ASSY	0.436	1.625	3.5	4
POWER SUPPLIES A&B	1.225	0.5	3.5	4
CRATE STACK	2.720	4.3	3.5	4
STACK ENDPLATES	1.314	5	3.5	4
TENSION RODS	0.329	5	3.5	4
FASTENER ALLOWANCE	0.120	5	3.5	4
INSTRUMENT TOTAL	10.401	4.470883	3.859760	4

ORIGINAL PAGE IS
 OF POOR QUALITY

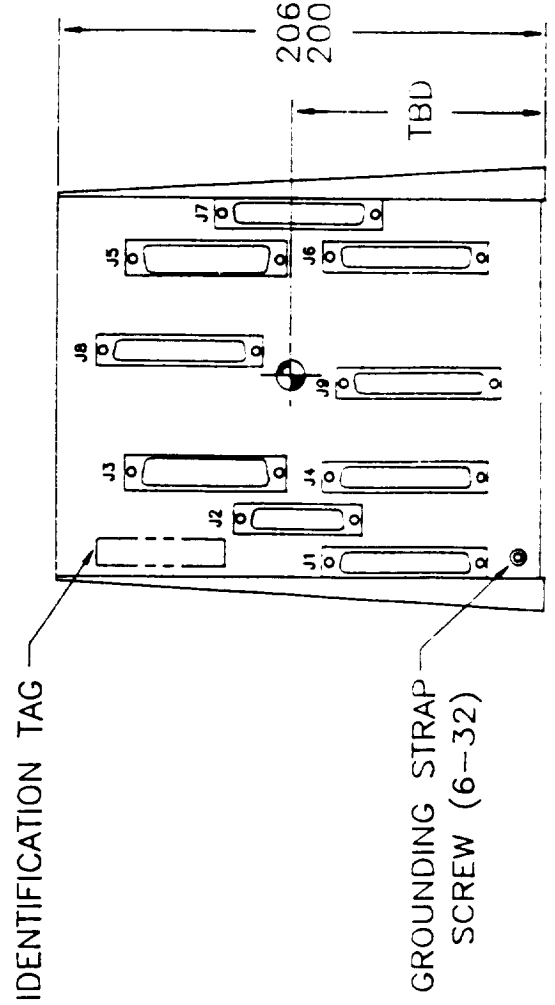
ULTRAVIOLET IMAGER
ISTP-POLAR

ALL DIMENSIONS IN MM



SEE FIG. 9-6
 FOR HOLE PATTERN

MASS PROPERTIES *		
ELECTRONICS MASS 6.0 KG.		
INERTIAL PROPERTIES (KG-M ²)		
I _{xx}	TBD	I _{xy} TBD
I _{yy}	TBD	I _{xz} TBD
I _{zz}	TBD	I _{yz} TBD
*MASS PROPERTIES DO NOT INCLUDE MILI		



IDENTIFICATION TAG

GROUNDING STRAP
 SCREW (6-32)

CONNECTOR TABLE			
CONN.	TYPE	REF DES*	REMARKS
J1	DSUB	TBD	CAMERA MECHANISM MOTOR INTERFACE
J2	DSUB	TBD	CAMERA TE COOLER CONTROL INTERFACE
J3	DSUB	TBD	CAMERA DIGITAL INTERFACE
J4	DSUB	TBD	CAMERA DIGITAL INTERFACE
J5	DSUB	TBD	CAMERA DIGITAL INTERFACE
J6	DSUB	TBD	CAMERA DIGITAL INTERFACE
J7	DSUB	TBD	CAMERA ANALOG & POWER INTERFACE
J8	DSUB	TBD	SPACECRAFT INTERFACE
J9	DSUB	TBD	SPACECRAFT INTERFACE

* REFERENCE DESIGNATIONS ARE PER "TBD-ULTRAVIOLET IMAGER AVIONICS INTERFACE CONTROL DOCUMENT"

FIGURE 9-4 --- DETAIL "B" --- ELECTRONICS STACK

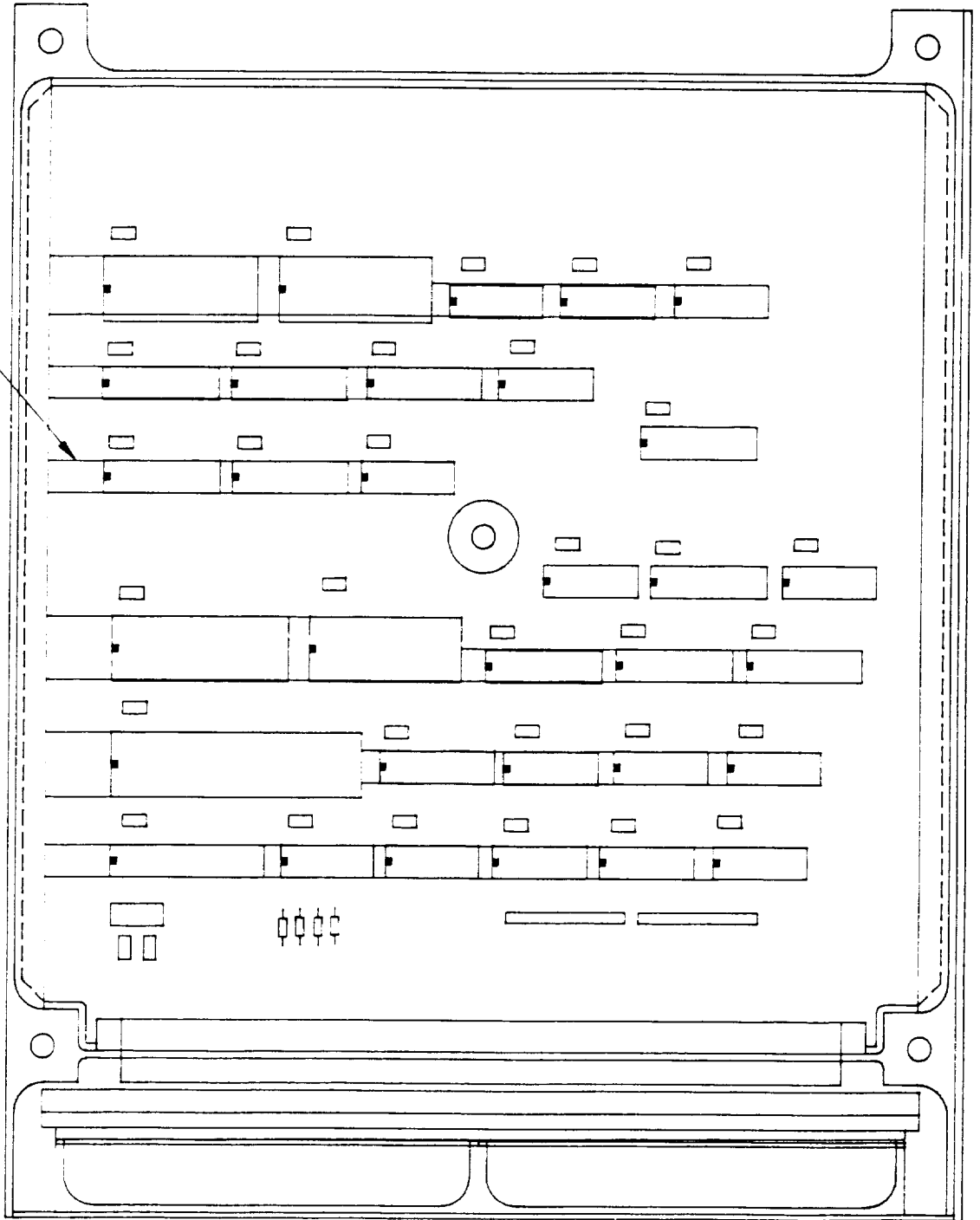
ULTRAVIOLET IMAGER
POLAR/GGS

THERMAL DESIGN

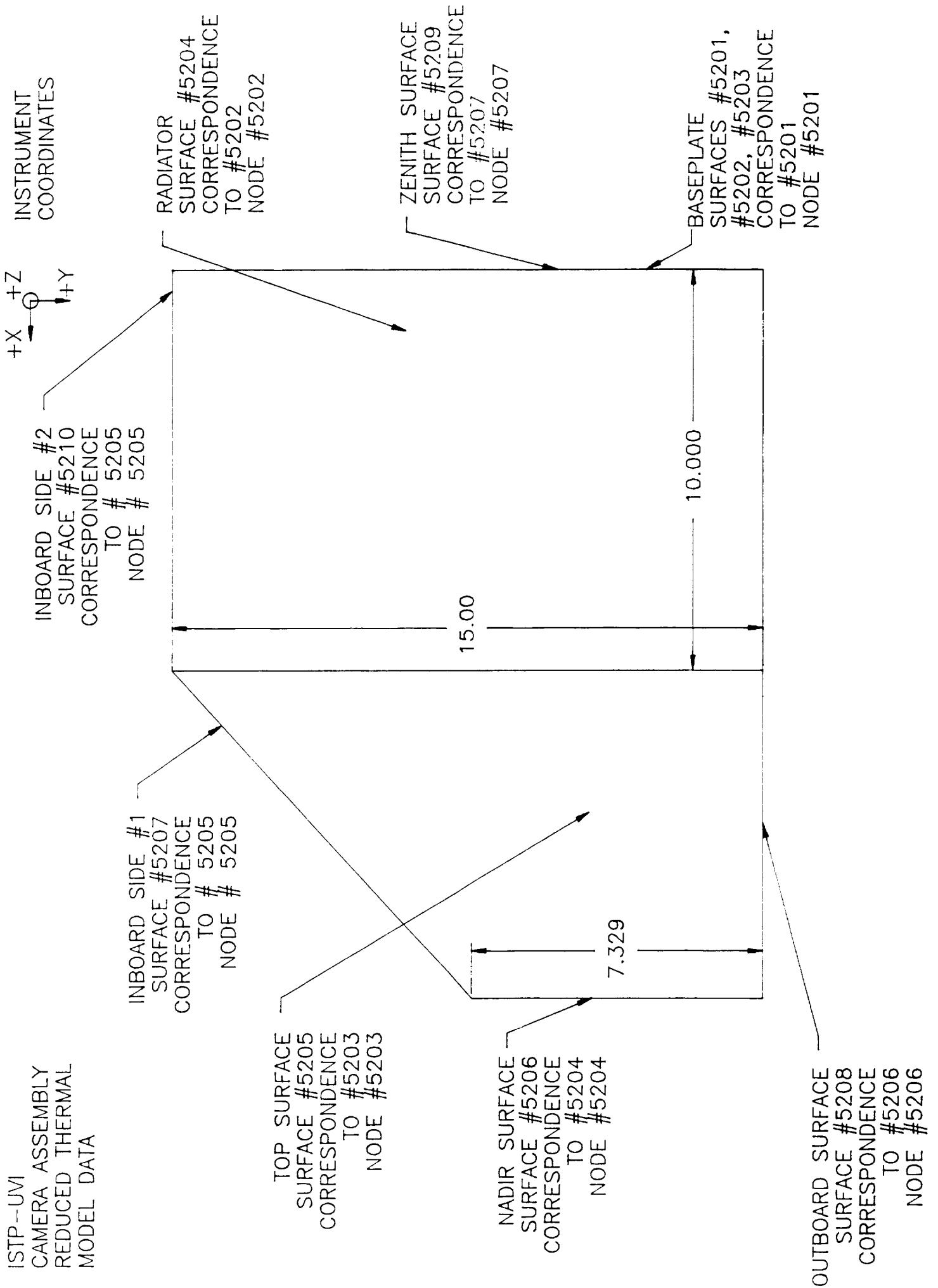
PRELIMINARY DESIGN REVIEW

PDR TITLE/008

THERMAL OVERLAY

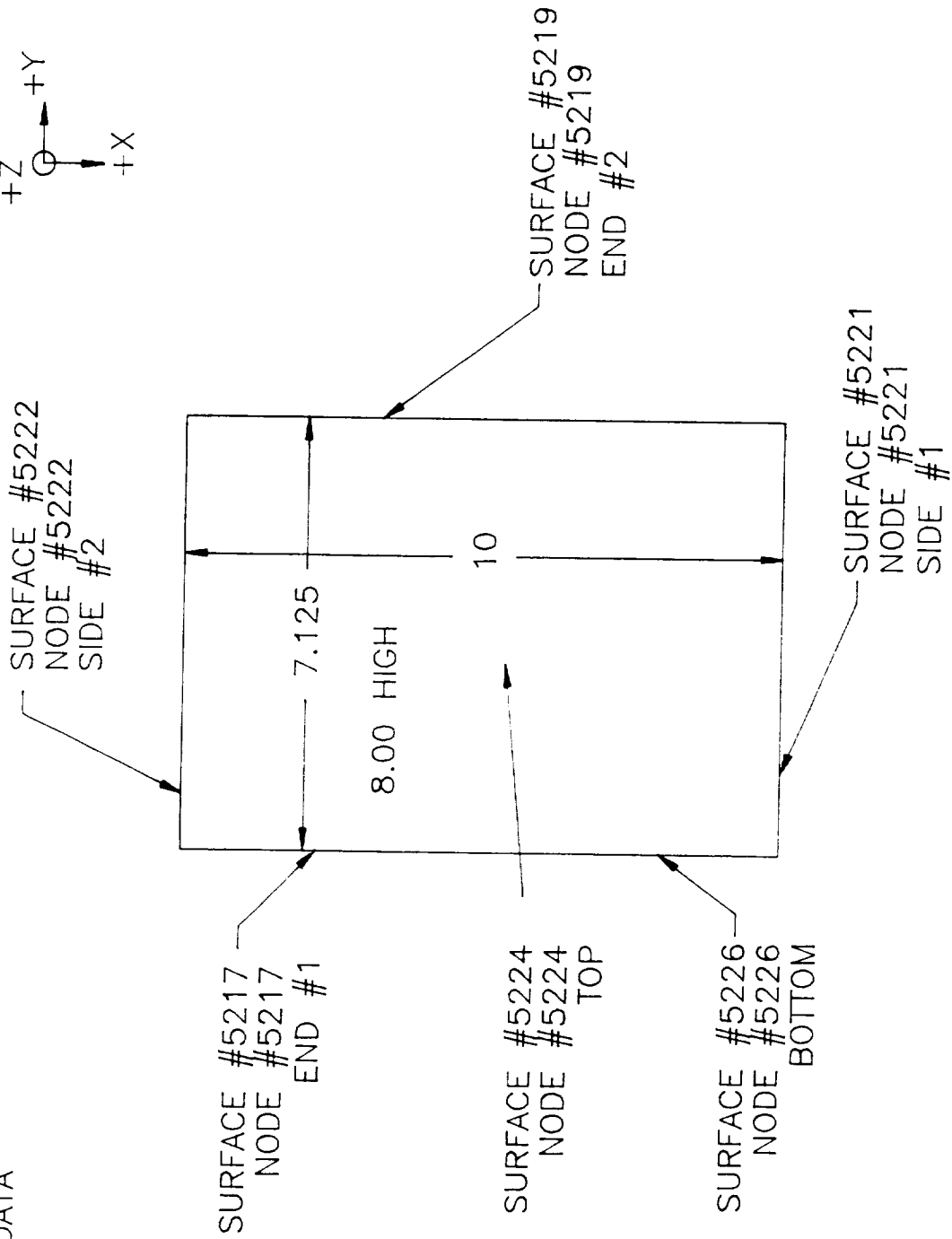
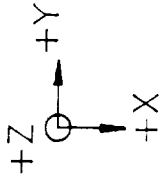


ISTP-UVI
CAMERA ASSEMBLY
REDUCED THERMAL
MODEL DATA



ISTP-UVI
ELECTRONICS STACK
REDUCED THERMAL
MODEL DATA

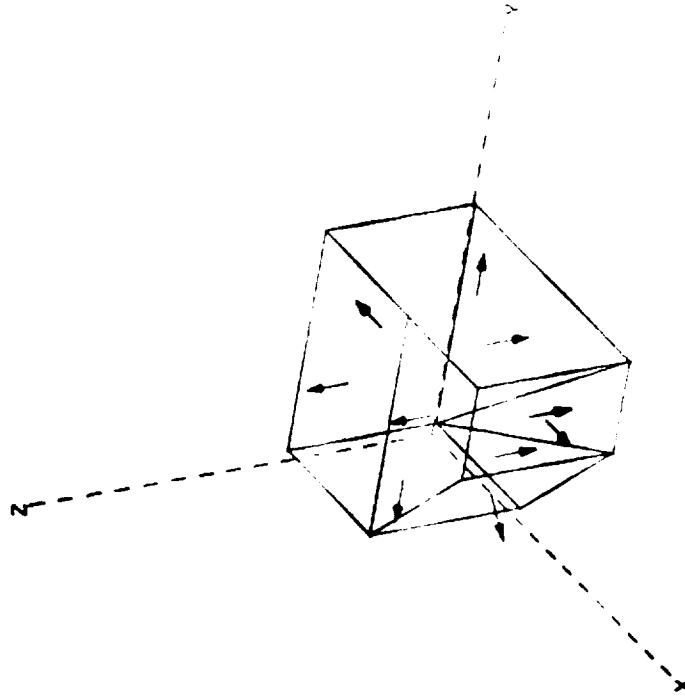
INSTRUMENT
COORDINATES



TYPE 'C'-CONTINUE, 'R'-REDRAW, 'E'-ENLARGE

Plot number: 1

UJI CAMERA SURFACE FITTH MODEL, PRELIMINARY



VIEW - 3-D
SCALE - 1.2325
VIEW NUMBER - 1

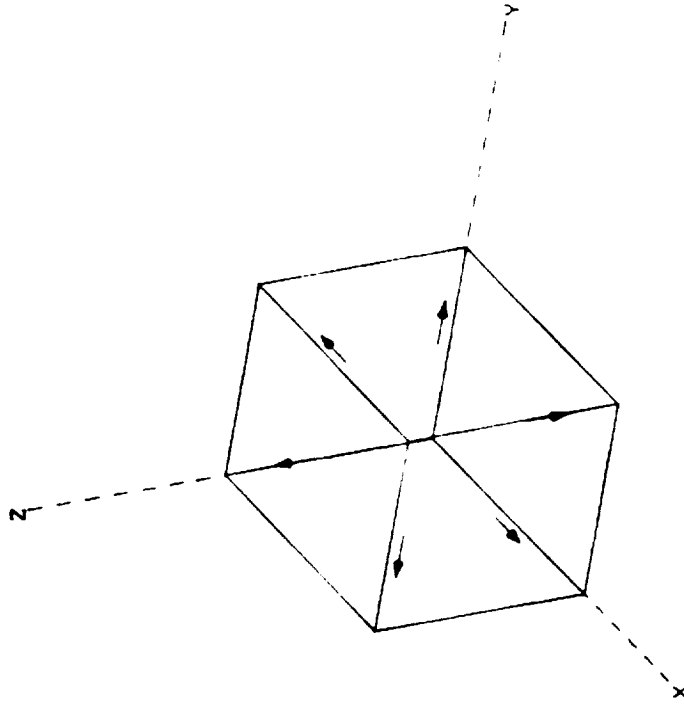
ORIGINAL PAGE IS
OF POOR QUALITY

3

TYPE 'C'-CONTINUE. 'R'-REDRAW. 'E'-ENLARGE

Plot number: 1

UJI ELECTRONICS STACK SURFACE MATH MODEL, PRELIMINARY



VIEW = 3-D
SCALE = 2.2339
VIEW NUMBER = 1

ORIGINAL PAGE IS
OF POOR QUALITY

UVI ICD MECHANICAL SECTION

STATUS:

Signed by GE and UVI

COMMENTS:

Instrument Mass

Total mass does not include
MLI blankets and intra-
instrument harness

Instrument Frequency

Primary resonance
frequency for both boxes
expected to be >100 Hz

Values for CG are available

UVI ICD THERMAL SECTION

STATUS:

Inputs provided to GE

COMMENTS:

GE providing MLI blankets

CONCERNS:

Camera Operating Temperature

ICD does not reflect current
IIRD temperature ranges

Thermal Backload Analysis

Values of heat load on
instrument surfaces are
preliminary

Heat Flow Limits

Values for heat flow limits
based on current operating
temperatures and mounting
surface contact area are not
provided

3.3 Thermal Interface Requirements

3.3.1 General. The interface conditions specified in this section are intended to maintain each UVI item within the temperature range shown in Table 3.3-1 when its internal heat dissipation is within the range indicated. The Camera and electronics stack are isolated from the despun platform and the space environment with thermal isolators and thermal blankets except portions of the +Z facing surfaces are covered with selected coatings to radiate internal dissipation to space.

Table 3.3-1 UVI Thermal Characteristics

<u>Item</u>	<u>Operating</u>		<u>Non-Operate</u>	
	<u>Tmin/Tmax,C</u>	<u>Qmin/Qmax,w</u>	<u>Tmin/Tmax,C</u>	<u>Qmin/Qmax,w</u>
Camera	-20/+20	0/0	-20/+40	0/0
Camera (Radiator)	-20/0	10.0/10.0	-20/+40	0/0
Digital Elect Box	-20/+40	0/0	-20/+40	0/0
Digital Elect (Radiator)	-20/0	10.0/10.0	-20/+40	0/0

NOTE:

- 1) Cold plate temperature should be +/- 1°C when operating, load dissipated by radiator is a function of temperature. See Figure 10.
- 2) Camera box dissipation is assumed to be dissipated entirely through radiator.
- 3) Electronics box dissipation is assumed to be dissipated entirely through radiator.

Unless otherwise noted, all interface conditions specified in this section are to be interpreted as orbit-average and spatial-average values.

Thermal interfaces are specified in terms of parameters depicted schematically in Appendix 1. These parameters define temperature, heat flow, and coupling limits which should result in adequate thermal balance for all instrument units. Appendix 1 explains the derivation and use of the thermal backload parameter for external surfaces.

3.3.2 Laboratory Exterior.

3.3.2.1 Externally Mounted Instruments. The UVI instrument is mounted on the despun platform of the POLAR laboratory and is classified as an externally mounted instrument. The following paragraphs specify the thermal interface for this unit.

3.3.2.2 Instrument Exterior Thermal Environment. Radiation couplings and thermal backloads for the exterior surfaces of UVI sensor are specified in Table 3.3-2. These values are based on the surface finishes defined in paragraph 3.3.2.3.

3.3.2.3 Instrument Thermal Surface Finishes. Finishes and thermal properties of the exterior surfaces of the UVI sensor are specified in Table 3.3-3.

3.3.2.4 Conductive Coupling. The UVI Camera is mounted to but is thermally isolated from the despun platform. The UVI Electronics box is mounted to but is thermally isolated from the despun platform with GE-Astro supplied thermal isolators. Physical constraints on this interface shall apply as written in paragraph 3.3.3.4.2 of the GIIS. Table 3.3-4a specifies the nominal mounting area, conductance, and limits of despun platform temperature at this interface. Limits of heat flow by conductive interchange across this interface are specified in Table 3.3-4b.

Size	Code Ident No.	IS-3282161
A	49671	
		Sheet 35

Table 3.3-3 UVI Exterior Surface Definition (TBR)

<u>Item</u>	<u>Surface</u>	<u>Area sq.in.</u>	<u>Type</u>	<u>IR Emis</u>	<u>UV BOM</u>	<u>Alpha EOM</u>
Camera	Sides	TBD	(Black body)	TBD	TBD	TBD
	+Z face (top)	TBD	(Black body)	TBD	TBD	TBD
	-Z face	TBD	(Black body)	TBD	TBD	TBD
E-Box	Sides	TBD	(Black body)	TBD	TBD	TBD
	+Z face (top)	TBD	(Black body)	TBD	TBD	TBD
	-Z face	TBD	(Black body)	TBD	TBD	TBD

Table 3.3-4a UVI Exterior Mounting Thermal Interface, Tif (TBR)

<u>Unit</u>	<u>Filler</u>	<u>Contact Area.sq.in</u>	<u>Conduct- ance.w/C</u>	<u>Temperature (Min/Max),C</u>	
				<u>Operating</u>	<u>Non-Operate</u>
Camera	Isolators	5 x 0.75	0.36	-20/30	-30/40
E Box	Isolators	6 x 0.25	0.12	-20/30	-30/40

Notes:

- 1) Temperatures shown are on the spacecraft side of the interface.

Table 3.3-4b UVI Exterior Mounting Conductive Limits (TBR)

<u>Unit</u>	<u>Item</u>	<u>Heat Flow Limits, Qif (Note 2), w</u>			
		<u>Operating</u>		<u>Non-operate</u>	
		<u>Cold</u>	<u>Hot</u>	<u>Cold</u>	<u>Hot</u>
Camera	Isolated mount	-3/+3	-3/+3	-4/+4	-4/+4
Digital Box	Isolated mount	-2/+2	-2/+2	-3/+3	-3/+3

Notes:

- 1) Heat flow is defined as positive INTO the instrument.
- 2) Cold and hot refer to laboratory conditions defined in Table 3.3-4a.

The range shown for each case assumes the instrument unit at its coldest/hottest allowable temperature.

3.3.3 Laboratory Interior N/A

Table 3.3-2 UVI Exterior Surface Thermal Environment (TBR)
PRELIMINARY

Thermal Backload, Qbl (Min/Max),w

<u>Item</u>	<u>Surface</u>	<u>Rad Coup,</u> <u>sq.in.</u>	<u>Sun Ang</u> <u>5 deg</u>	<u>Sun Ang</u> <u>90 deg</u>	<u>Sun Ang</u> <u>160 deg</u>
Camera	Sides	36.0	4.0/ 4.9	9.5/11.5	3.2/ 4.0
	+Z face (top)	36.0	27.0/35.8	0.0/ 2.0	0.0/ 1.0
	-Z face	N/A	N/A	N/A	N/A
E-box	Sides	36.0	4.0/ 4.9	9.5/11.5	3.2/ 4.0
	+Z face (top)	36.0	27.0/35.8	0.0/ 2.0	0.0/ 1.0
	-Z face	N/A	N/A	N/A	N/A

Notes:

- 1) Radiation couplings are defined as surface area times surface emissivity times a view factor of unity. When used with thermal backload, these values should couple the surface to a 0 deg K heat sink and no other external couplings should be used.
- 2) Thermal backload is the total heat absorbed by the surface from its external environment. It includes solar, albedo, and earth flux contributions, as well as IR input from nearby surfaces.
- 3) The instrument will be operating at sun angles between 90 and 160 deg. It will, however, be exposed to sun angles between 25 and 160 deg in a non-operate mode.
- 4) Coupling has been normalized for a 36 sq. in. surface, actual load is dependant on box surface area and scales directly with area.
- 5) Initial values based on e and alpha values of 1.00 (blackbody).

Size	Code Ident No.	IS-3282161
A	49671	

ULTRAVIOLET IMAGER
POLAR/GGS

MISCELLANEOUS ICD SECTIONS

PRELIMINARY DESIGN REVIEW

UVI ICD EMC/EMI/ESC SECTIONS

STATUS:

First inputs to GE

COMMENTS:

Aperture Window

Dielectric MgF_2
window inside baffle is
non-conducting

Baffle Surface

Interior baffle surface will
be conducting

CONCERNS:

Degaussing

Degaussing of instrument must
not affect operation of
permanent magnet stepper
motors

Surface Coatings

Value for minimum
conductivity is not specified

UVI ICD ENVIRONMENTAL SECTION

STATUS:

First inputs to GE

CONCERNS:

Instrument Purge

Nitrogen should be 99.999%
pure with hydrocarbon content
< 2 ppm (boil-off purity)

Transportation and Storage

Temperature limits should be
+10/+30 °C
Hydrocarbon content of
surrounding atmosphere
should be < 10 ppm

Vibration, Shock and Acceleration Tests

Design is based on a *time*
consistant environment

3.4 Magnetic Interface

3.4.1 Spacecraft Generated Magnetic Fields. The maximum spacecraft induced magnetic flux the instrument will experience on the spacecraft will be TBS gauss.

3.4.2 Instrument Generated Magnetic Fields. Instrument magnetic field characteristics shall be documented here. (TBS by instrument)

3.4.3 Instrument Degaussing. The instrument, unless noted here, will be degaussed prior to mounting on the spacecraft. The maximum field strength used during degaussing will be TBS gauss. The degaussing frequency will be TBS Hz.

3.5 Electromagnetic Interference (EMI)

3.5.1 General. Instruments with electrical devices inherently susceptible to low level EMI shall indicate special procedures and requirements here.

3.6 Electrostatic Cleanliness (ESC)

3.6.1 General. Bonding and insulation requirements of the instrument(s): TBD

3.6.2 Conductivity and Grounding of Conductive Finishes.

List of instrument coatings: TBS
resistivity:TBS (ohms/meter.)

3.6.3 Bonding of Case Parts. Physical discontinuities (non-conductive) in the instrument case must be identified here.

3.6.4 Instrument Aperture ESC Design. See Instrument aperture drawing TBD.

3.6.5 ESC of Hinged Mechanisms. Hinged mechanisms must be identified here.

3.6.6 Exposed Connectors and Harnessing. Applies as written the GIIS.

3.7 Environmental Interface.

3.7.1 General Environment. Applies as written the GIIS unless specified here.

3.7.2 Storage, Transportation, and Handling Environment. Applies as written the GIIS unless specified here.

3.7.2.1 Instrument Environment Before Mounting on Spacecraft. Applies as written the GIIS unless specified here.

3.7.2.2 Instrument Stored Mounted on Spacecraft. Applies as written the GIIS unless specified here.

Size	Code Ident No.
A	49671

IS-3282161

Sheet 40

3.7.2.3 Instrument Transportation while Mounted on Spacecraft. Applies as written the GIIS unless specified here.

3.7.2.4 Instrument Purging.

Purging requirements:TBD

Connector type: TBD

Purge Interface: See Mechanical Drawing for location.

The instrument team will be notified of interruptions longer than TBD.

3.7.3 Flight Environment. The instrument, while integrated on the satellite, shall withstand the flight-induced environment detailed in the following paragraphs.

3.7.3.1 Temperature. The instrument shall specify nonoperating survival temperature range and expected operating temperature ranges here.

NOTE: To ensure that the Qualification Temperature limits are not exceeded during emergency conditions during spacecraft thermal-vacuum testing, a "Safety Heater" and a monitoring thermocouple will be attached to the instrument unless directed otherwise here.

The "Safety Heater" will be approved for thermal-vacuum chamber operation and will be powered form a +28V supply not connected to the spacecraft power. The capacity shall be sufficient to maintain the instrument at +10degC when the chamber walls are at LN2 temperature. Astro will mount the heater to the instrument when it is put onto the spacecraft. Heater location TBD. See figure TBD.

3.7.3.2 Thermal-Vacuum. The instrument shall operate within specification over the temperature range specified here while subjected to a nominal pressure of one (1) atmosphere or to a vacuum pressure of $.75 \times 10^{-5}$ Torr or lower.

Min (1 Atm): TBD

Max (1Atm): TBD

Min (Vac): TBD

Max (Vac): TBD

3.7.3.3 Vibration, Shock, and Acceleration. Applies as written the GIIS.

3.7.3.3.1 Sinusoidal Vibration. Expected test levels: TBD

3.7.3.3.2 Shock. Applies as written the GIIS unless specified here.

3.7.3.3.3 Acceleration. Applies as written the GIIS unless specified here.

3.7.3.4 Acoustic/Random Vibration. Applies as written the GIIS unless specified here.

Size	Code Ident No	IS-3282161
A	49671	
		Sheet 11 5

3.6.4 Instrument Aperture ESC Design. A continuous conductive surface shall exist between the solar array substrate, which will be conductively bonded to the primary structure, and instrument sensors which protrude through solar array apertures (see Paragraph 3.2.6.3). The instrument surface required to interface with the gasket will be developed jointly by Astro and the Instrumenter.

3.6.5 ESC of Hinged Mechanisms. Hinged mechanisms which do not rotate through 360° shall utilize a conductive strap connected across the hinge connected to spacecraft ground to preclude charge buildup on the mechanism.

3.6.6 Exposed Connectors and Harnessing. All external, exposed electric terminals shall be rounded and coated with insulating material and, finally, overcoated with a conductive material. Such encapsulation shall not preclude the removal, interchange, additions, and/or repair of any wire/pin connection. All external instrument connectors shall have connector covers with a conducting outer surface. All harnessing external to the laboratory surface will be shielded in accordance with the GGS Electromagnetic and Magnetic Compatibility Plan, (Astro TBD) with the outer surface of the shielding coated with conductive finish per paragraph 3.6.2.

3.7 Environmental Interface

All instruments will be exposed to the environmental conditions specified in the following paragraphs. These environments represent conditions which will arise during the transportation, storage, handling, test, launch and orbital operation of the instrument when on the spacecraft.

3.7.1 General Environment. At the spacecraft contractor's facility, controlled environments will be provided when necessary as specified in the Instrument-Unique ICD to bring the temperature, humidity, shock and vibration to levels less severe than those pertaining to launch, ascent, and orbital operations.

3.7.2 Storage, Transportation, and Handling Environment

3.7.2.1 Instrument Environment Before Mounting on Spacecraft. The environments experienced by the instrument during fabrication, storage, and all modes of handling and transportation should be controlled so as to be significantly less severe than worst-case flight conditions. Storage will be in vendor's shipping container in a normal factory environment unless the Instrument-Unique ICD specifies other requirements.

3.7.2.2 Instrument Stored Mounted on Spacecraft

- (1) Storage of the instrument when mounted on the spacecraft will be at Class 100,000 or better, as defined in FED-STD-209.

During transportation and handling, the laboratory may temporarily be in areas not meeting class 100,000. During these periods, the spacecraft will be in a protective tent. When this tent cannot be used, the instrument

PRECEDING PAGE BLANK NOT FILMED

Size	Code Ident No.	3282065
A	49671	
		Sheet 81

PRECEDING PAGE BLANK NOT FILMED

will be bagged to prevent its being contaminated.

- (2) Humidity Limits of Storage Area: Maximum Humidity 50%. Laboratory may be stored in a tent purged with LN2 boiloff.
- (3) Temperature Limits: -10 to +40°C

3.7.2.3 Instrument Transportation while Mounted on Spacecraft. The environments experienced during spacecraft transportation and handling will be controlled to be significantly less severe than worst-case flight conditions.

3.7.2.4 Instrument Purging. If required, the instrument will be provided a nearly continuous dry filtered nitrogen gas purge system, distributed through teflon tubes. The nitrogen will have a greater than 99.998% purity and less than 1 ppm of hydrocarbons. The purge gas flow will be available throughout integration at Astro and during launch site integration. Purge will be interrupted during thermal-vac testing and during some ground handling procedures. Instrument teams will be notified of interruptions longer than specified in the instrument-unique ICD. Purging requirements of the instruments shall be specified in the Instrument-Unique ICD.

3.7.3 Flight Environment. All instruments integrated on the satellite shall be designed to withstand the flight-induced environment detailed in the following paragraphs.

3.7.3.1 Temperature. All instruments installed on the spacecraft shall specify nonoperating survival temperature range and expected operating temperature ranges in their respective Instrument-Unique ICD.

NOTE: To ensure that the Qualification Temperature limits are not exceeded during emergency conditions during spacecraft thermal-vacuum testing, a "Safety Heater" and a monitoring thermocouple will be attached to the instrument unless directed otherwise in the Instrument Unique ICD.

The "Safety Heater" will be approved for thermal-vacuum chamber operation and will be powered from a +28V supply not connected to the spacecraft power. The capacity shall be sufficient to maintain the instrument at +10°C when the chamber walls are at LN2 temperature. Astro will mount the heater to the instrument when it is put onto the spacecraft.

The thermocouple shall be copper-constantan, mounted close to the location of the instrument's analog temperature telemetry sensor. The leads of this TC shall be independent of the S/C-instrument harness. Sensor leads inside the instrument case shall be properly secured so that only the flying leads need to be clipped during preflight preparations.

3.7.3.2 Thermal-Vacuum. The instrument shall operate within specification over the temperature range specified in the Instrument Unique ICD while subjected to a

Size	Code Ident No.	3282065
A	49671	
		Sheet 82



nominal pressure of one (1) atmosphere or to a vacuum pressure of $.75 \times 10^{-5}$ Torr or lower. In addition, the instrument shall be capable of operating after a rate of pressure change of 1.27 psia/sec. The full pressure rate of change is shown in Table 7.

Temp Constant

3.7.3.3 Vibration, Shock, and Acceleration. All instruments shall be designed to withstand the vibration, shock, and acceleration environments experienced during test, launch and orbital operation and shall operate in accordance with the instrument performance specification requirements for those environments.

3.7.3.3.1 Sinusoidal Vibration. The sinusoidal vibration qualification levels experienced by the protoflight spacecraft in each of three orthogonal axes are listed in Table 8. The levels experienced by each instrument during these tests shall be specified in each Instrument-Unique ICD.

3.7.3.3.2 Shock. The spacecraft will experience a shock impulse when the separation band is released during test as well as during separation in orbit. A test of this event will be performed on the integrated spacecraft. The maximum expected flight shock levels are shown in Figure 31.

3.7.3.3.3 Acceleration. The instruments will experience worst case expected steady-state accelerations during launch as delineated in Table 9 for platform and body mounted WIND and POLAR instruments.

3.7.3.4 Acoustic/Random Vibration. The instrument, while mounted on the spacecraft, shall be capable of withstanding and shall operate within specification after a single exposure of a 1.0 min. duration to the acoustic excitation levels defined in Figure 32. An acoustic test may also be required if evaluation indicates sensitivity to direct acoustic energy. The instrument shall survive and operate within specification after exposure to the random vibration levels specified in Table 10.

3.7.4 Radiation Environment. Preliminary radiation levels for the orbital environments of the WIND and POLAR laboratories are shown in Figure 33 and Figure 34. Instruments located within the laboratory will experience protective shielding provided by the laboratory outer shell, as indicated by the effective shielding values in Figure 33 and Figure 34. Instruments, or portions of instruments adjacent to openings in the laboratory shell, or otherwise exposed to the external environment, will receive radiation dosages dependent upon the degree of exposure and the equivalent thickness of protection provided by the instrument housing.

Size	Code Ident No.	3282065
A	49671	
		Sheet 83



TABLE 8. SINUSOIDAL VIBRATION CRITERIA PROTOFLIGHT LEVELS

	FREQUENCY (Hz)	ACCELERATION (g's zero-to-peak)
Thrust Axis	5 to 6.8	0.5 in. double amplitude
	6.8 to 30	1.2
	30 to 40	1.5
	40 to 100	1.0
Lateral Axis	5 to 6.2	0.5 in. double amplitude
	6.2 to 100	1.0

Sweep Rate = 4 oct./min.

PRECEDING PAGE BLANK NOT FILMED

Size	Code Ident No.	3282065
A	49671	
		Sheet 85

TABLE 9: INSTRUMENT DESIGN LOADS (g's)^{1,2}

Instrument Mounting Location	X	Y	Z
Despun Platform ³ (or +Z Exterior Sensors)	15.2	14.7	13.
Body Mounted on Equipment Decks	5.9	5.9	13.0

1. Referenced to S/C Coordinate System (See Figure 20).
2. Preliminary results based on Delta II Inputs and S/C Structure Coupling Effects.
3. Applies to: POLAR - UVI, VIS, PIXIE, SEPS, DRT
WIND - TGRS, KONUS, 3-D PLASMA

PRECEDING PAGE BLANK NOT FILMED

Size	Code Ident No.	3282065
A	49671	
		Sheet 87

PRECEDING PAGE BLANK NOT FILMED

UVI ICD GSE SECTION

STATUS:

First inputs to GE

CONCERNS:

S/C Interface Emulator

Verification of S/C
interface emulator hardware
and software

Synchronization Signals

Data rate signal lacking

Environment

Temperature limits should be
20°C to 30°C

Relative humidity limits
should be 40% to 55%

4.0 INSTRUMENT GROUND SUPPORT EQUIPMENT (GSE).

Instrument GSE designed and fabricated primarily for use in tests performed at Astro facilities or a test site shall be capable of:

- a) Verifying that the instrument has survived shipment; and
- b) Demonstrating successful completion of spacecraft systems test requirements.

All Instrument GSE required to electrically interface with the GGS spacecraft checkout station (SCS) shall be provided the interfaces specified in Section 4.1.

4.1 Instrument GSE Interfaces

The Instrument GSE test sets shall interface with the laboratory GSE as illustrated in Figure 35, and described in the sections that follow. In general, the Instrument GSE shall monitor instrument performance via laboratory science data supplied in real time, or as played back from a laboratory GSE tape recorder. Instrument GSE processing of this data shall not require on-line support from any laboratory GSE computer. All Instrument GSE interface requirements shall be documented in the Instrument-Unique ICD.

4.1.1 Power. The instrument GSE test set shall operate on single phase 120 +12/-6 volt ac power supplied at 57 to 63 Hz and shall draw a maximum of 20 amperes current.

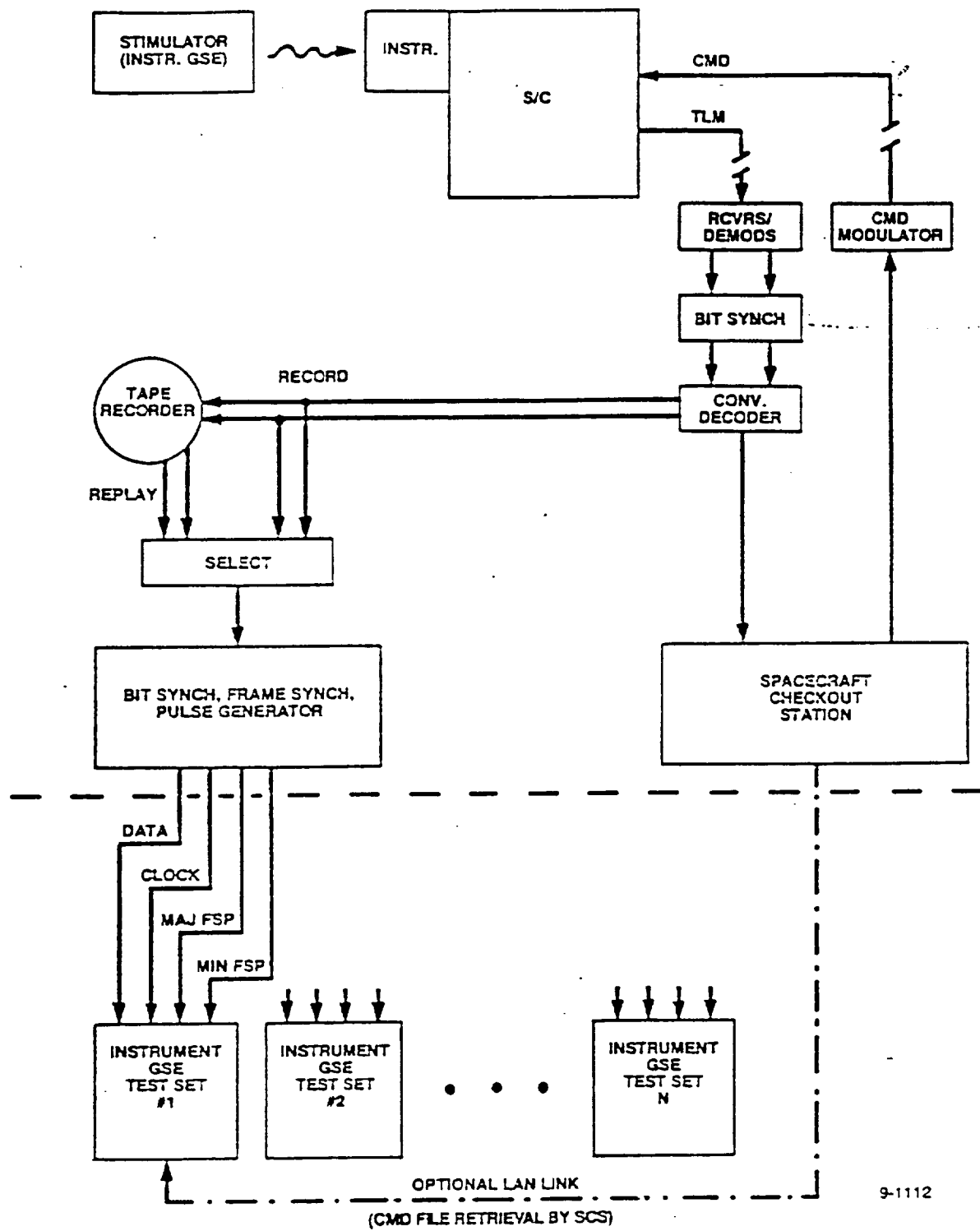
4.1.2 Instrument Data. The instrument GSE will be provided both low-rate engineering and science laboratory downlink telemetry and high-rate instrument playback downlink telemetry. The telemetry will be decoded biphas-L or NRZ-L PCM serial data, at bit rates equivalent to laboratory downlink rates. The data shall be received by the instrument GSE on a differential line driver/receiver interface per Figure 36.

local pulse?
4.1.3 Synchronization Signals. The instrument GSE shall be provided major and minor frame sync pulses and a data bit sync clock for processing the engineering and science data of Section 4.1.2. Low-rate data shall be clocked at a bit rate equal to the real time rate for each laboratory. High-rate instrument playback data shall be synchronized with a 500 kbps clock. All clock and frame sync signals shall be received on a differential line driver/receiver interface per Figure 36.

4.1.4 Local Area Network Interface (Optional). At the option of the instrument contractor, a local area network interface, e.g. Ethernet, also will be provided to instrument GSE test sets to allow the SCS to update its command load database from the instrument GSE. The protocol for this command file retrieval function will be established at System Requirements Review.

PRECEDING PAGE BLANK NOT FILMED

Size	Code Ident No.	3282065
A	49671	
		Sheet 92



9-1112

Figure 35. Instrument GSE Interfaces at Astro

Size	Code Ident No.	3282065
A	49671	
		Sheet 93

4.2 Instrument GSE Safety Requirements

Safety engineering principles should be applied in accordance with MIL-S-38130. Particular attention shall be paid to fail-safe provisions in the equipment design to avoid damage to other laboratory GSE components in the event of catastrophic failure.

4.3 Instrument GSE Environmental Requirements

The Instrument GSE shall be capable of operation over a temperature range of 55° to 95°F and a relative humidity range of 20 to 70%.

4.4 Instrument GSE Complement

The instrument contractor shall supply Astro with a detailed list of the Instrument GSE to be used at Astro at the Instrument PDR. The list shall include:

- (a) Type of Instrument GSE
- (b) Function of Instrument GSE
- (c) Power requirements
- (d) Approximate size and weight of racks, targets, etc.

5.0 NOTES

5.1 Acronyms

In addition to common acronyms, the special acronyms listed below are used throughout this document.

A/D	Analog to Digital
ATM2	Ampere-Turn Meter Squared
C&DH	Command and Data Handling
CDR	Critical Design Review
CEI	Contract End Item
CDU	Control Distribution Unit
COS/MOS	Complementary Symmetry/Metal Oxide Semiconductor
D/A	Digital to Analog
EMI	Electromagnetic Interference
FAT	Flight Acceptance Test
FCC	Flat Conductor Cable
FSP	Frame Sync Pulse
GFE	Government Furnished Equipment Instrument
GSE	Ground Support Equipment
GSFC	Goddard Space Flight Center
GTM	GGG Telemetry Module
PC	Power Converter
PDR	Preliminary Design Review
RFEM	Reduced Finite Element Model
R&QAE	Reliability and Quality Assurance Engineering

PRECEDING PAGE BLANK NOT FILMED

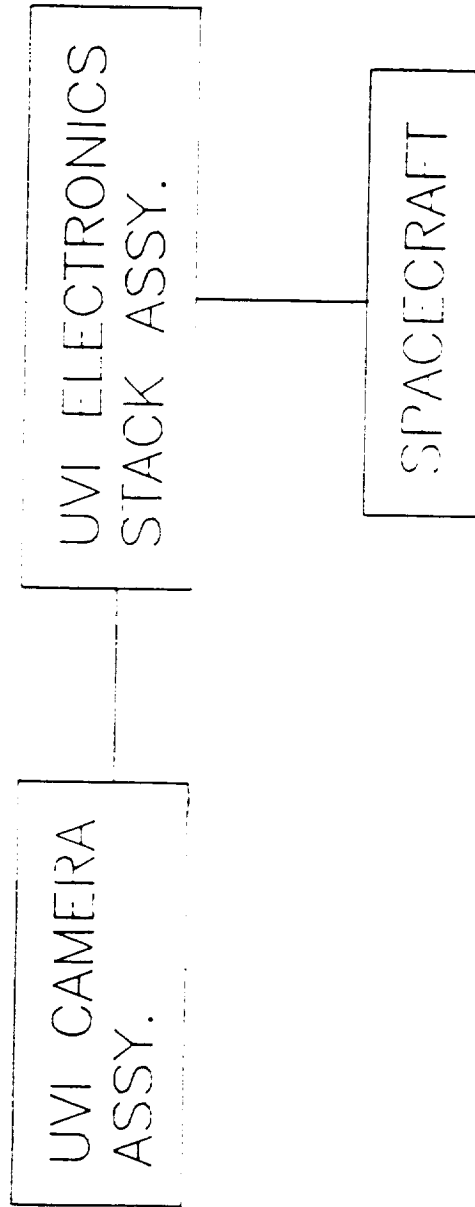
Size	Code Ident No.	3282065
A	49671	
		Sheet 95

ULTRAVIOLET IMAGER
POLAR/GGS

ELECTRONICS DESIGN

PRELIMINARY DESIGN REVIEW

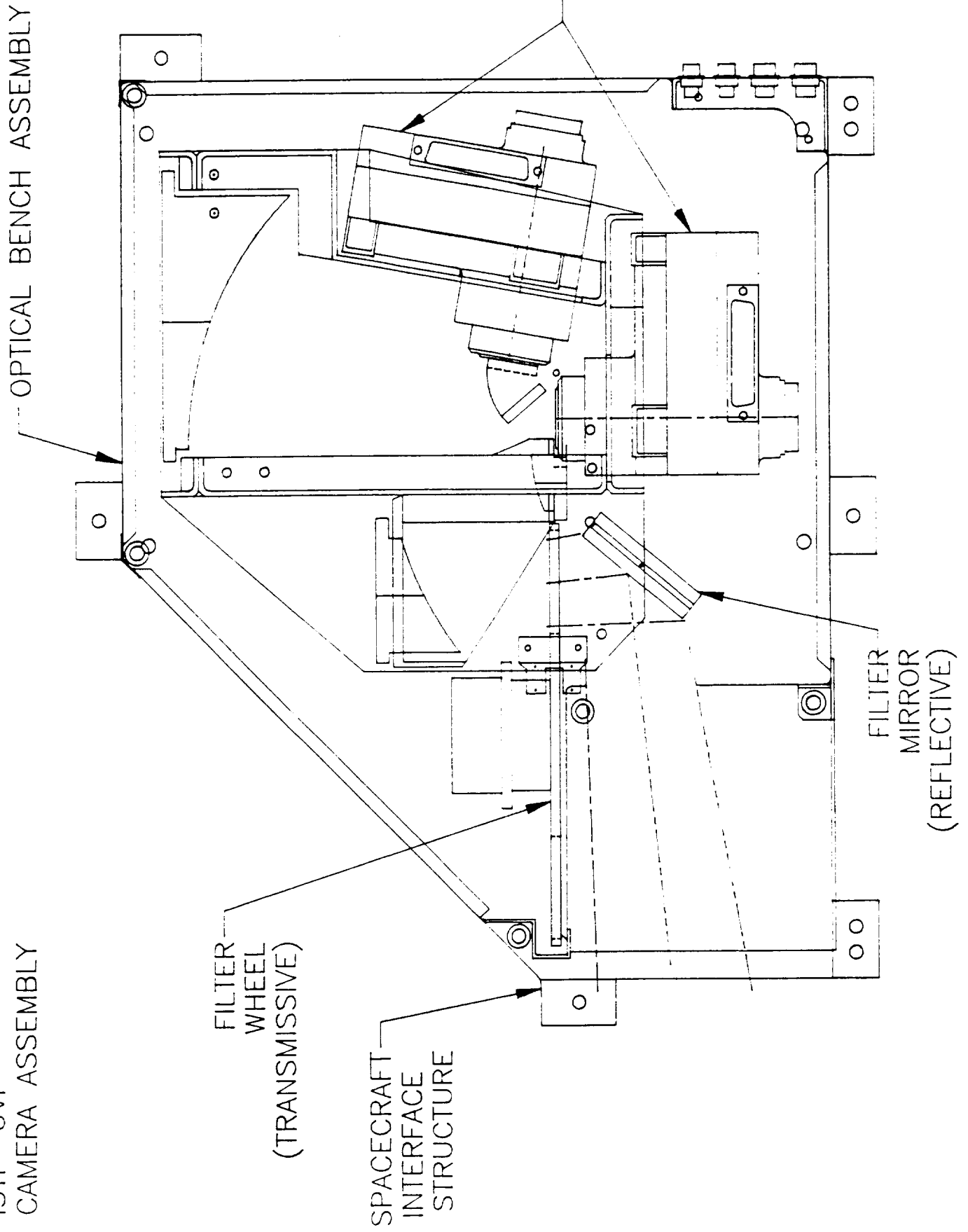
PDR TITLE/003

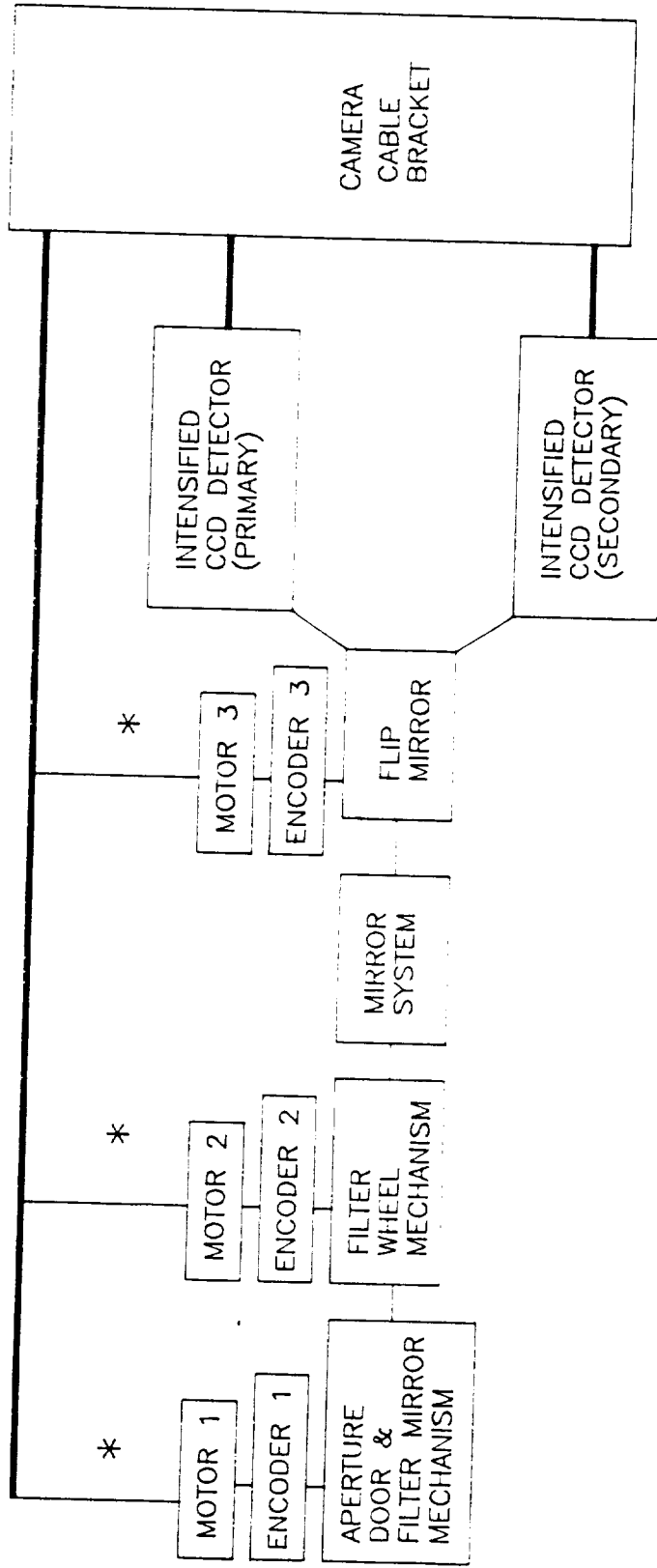


ORIGINAL PAGE IS
OF POOR QUALITY

DIAGRAM
1.1

ISTP--UVI
CAMERA ASSEMBLY





UV

* MOTORS HAVE REDUNDANT WINDINGS. ENCODERS HAVE REDUNDANCY ALSO.

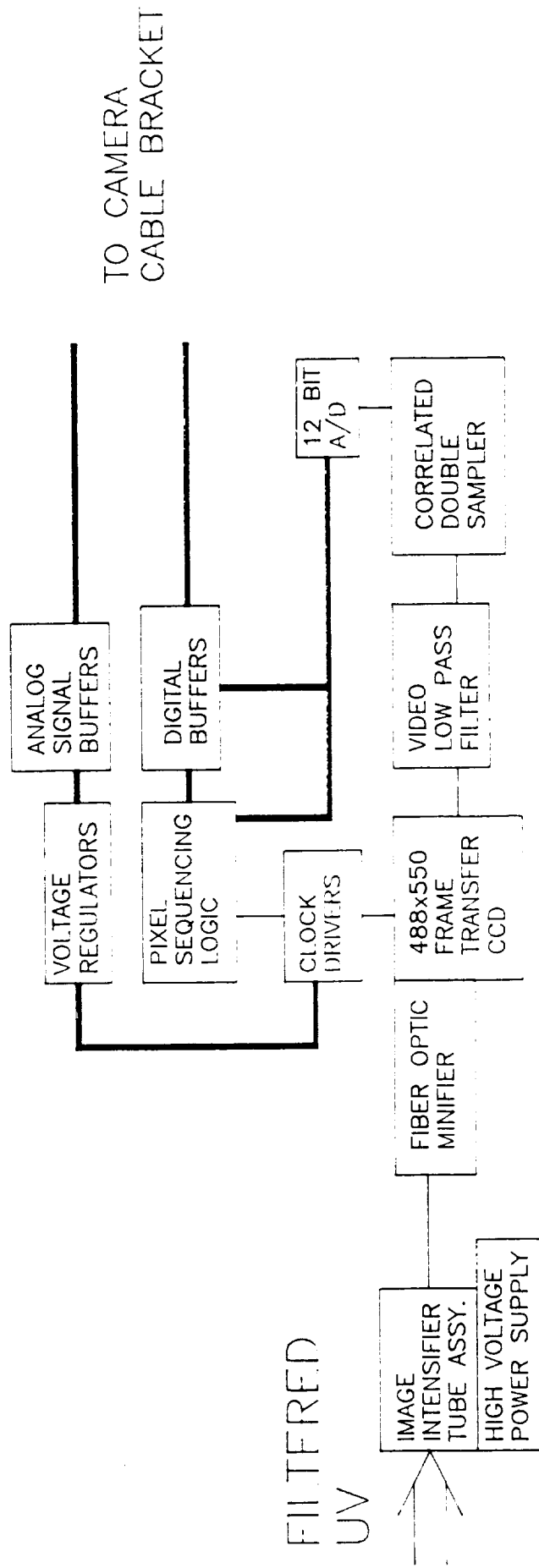
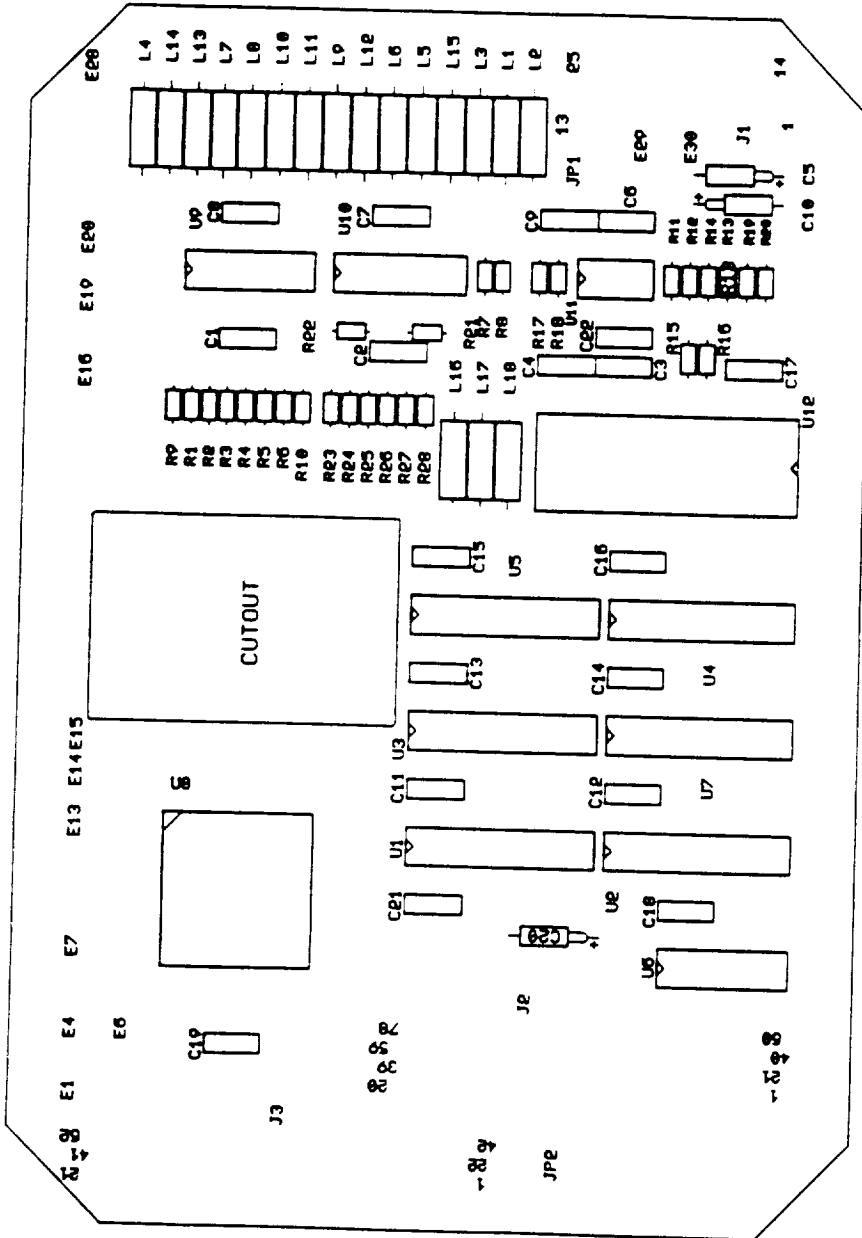


DIAGRAM 2.2

ISTP UV1 DETECTOR BOARD 2 # 52308 SILK SCREEN COMPONENT SIDE



GGs/UVI ELECTRONIC STACK SUBSYSTEM DIAGRAM 3

MOTHERBOARD
BACKPLANE

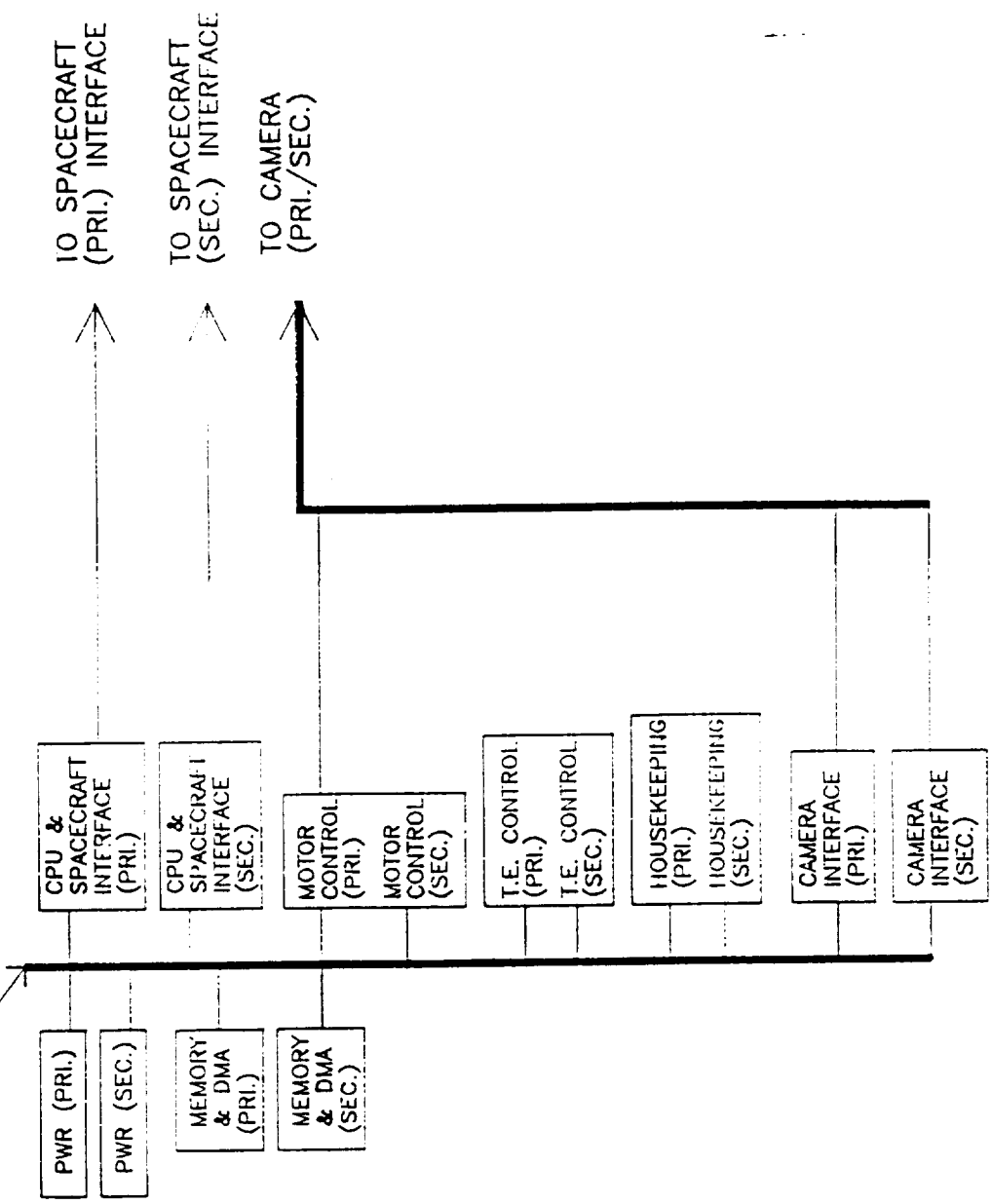


DIAGRAM
3.1

THERMAL OVERLAY

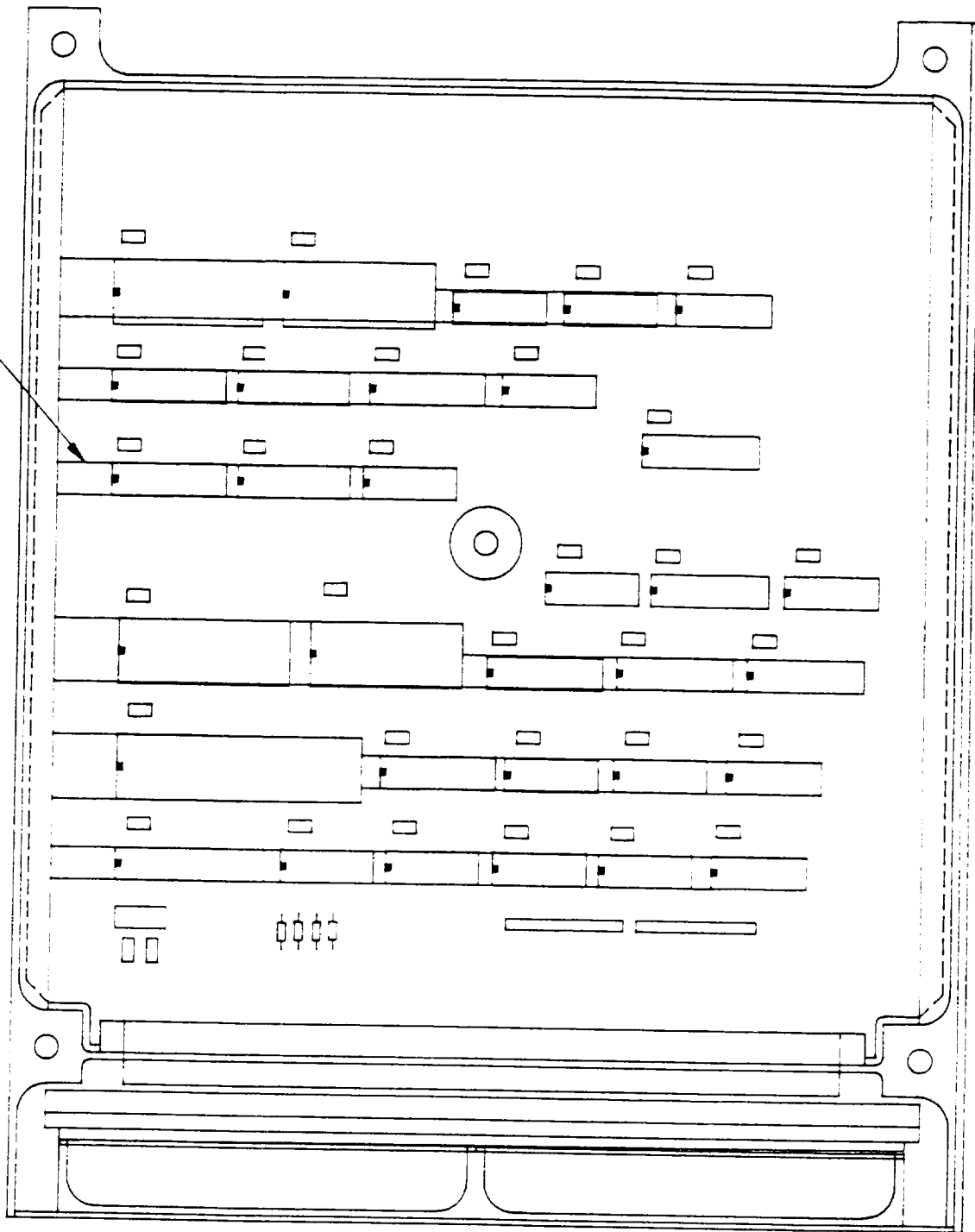
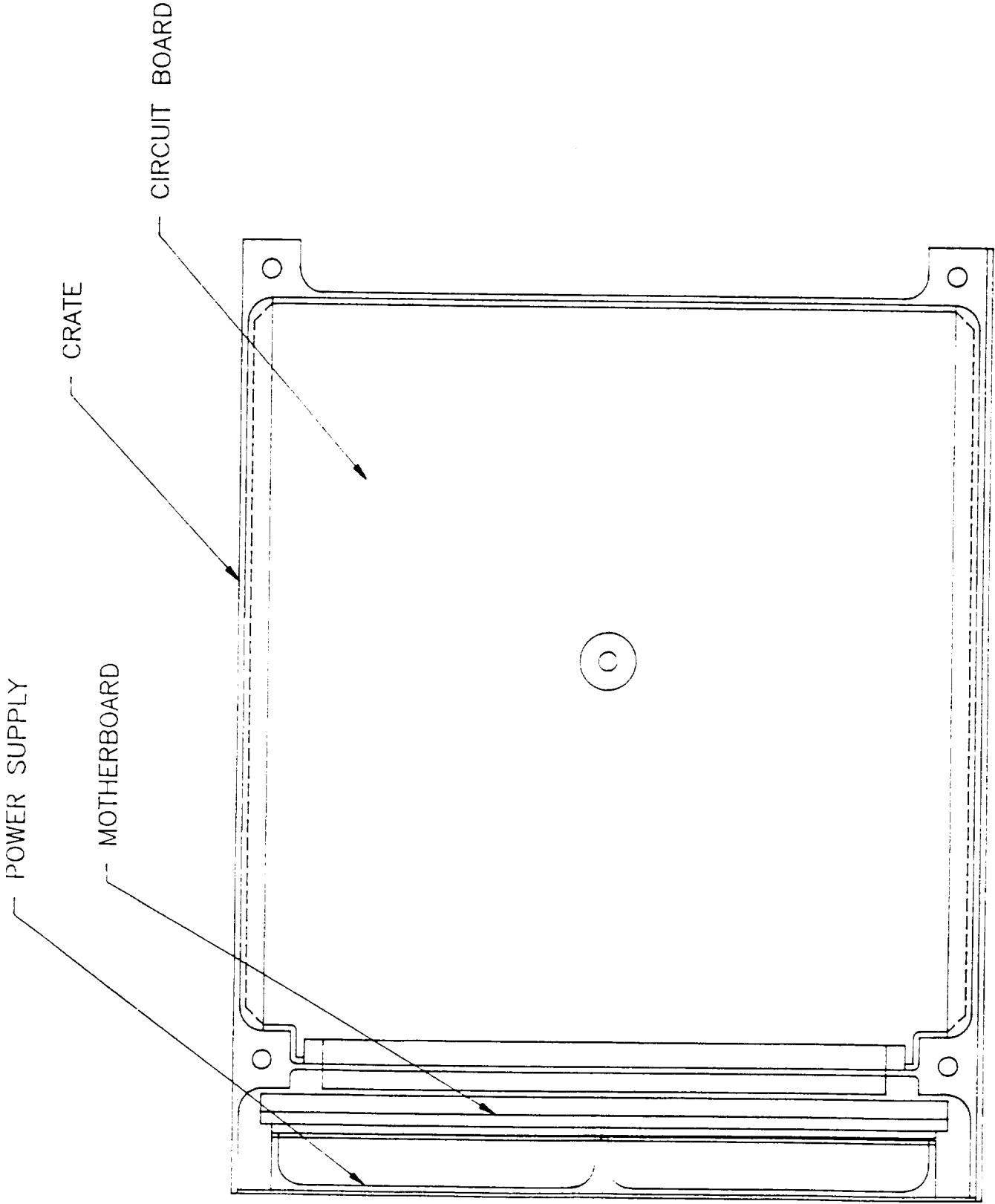
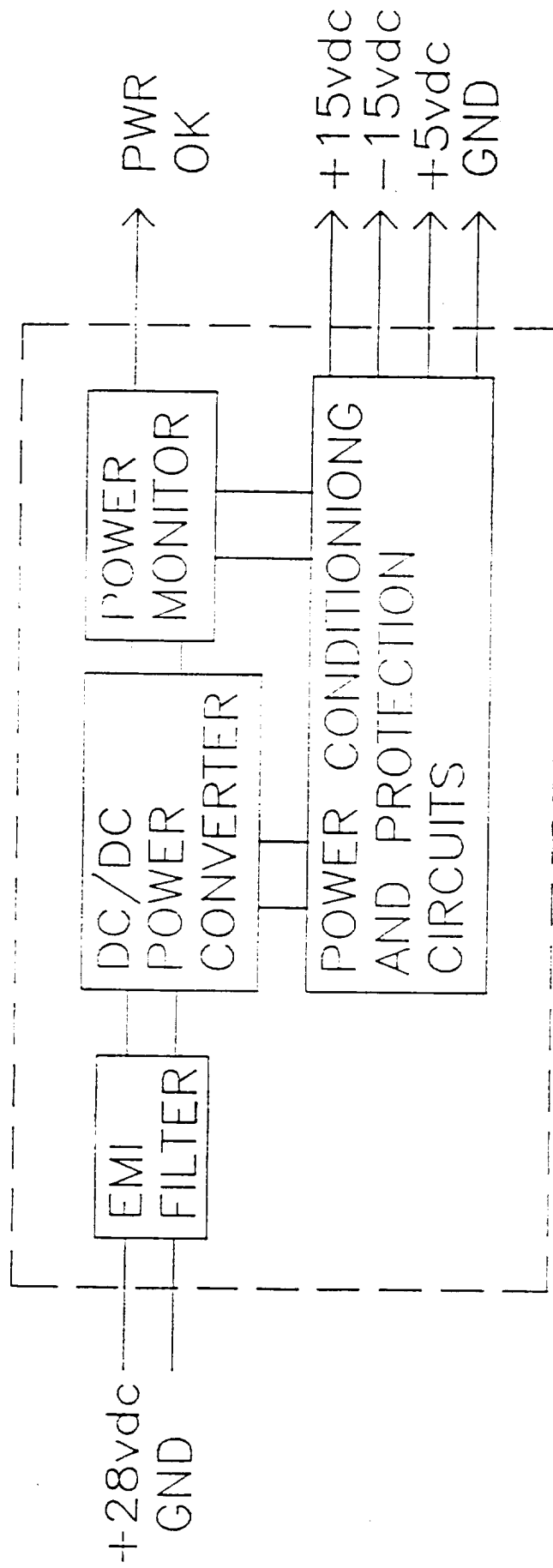


DIAGRAM
3.2



HPS 3015 POWER MODULE



RADIATION HARDENED DC-DC CONVERTER

MODEL HPS-3015



RADIATION HARDNESS FEATURES

Hardened to Survive High Radiation Levels

Operates through a Gamma Dose Rate Environment

100% Tested Certified Operate-Through Performance and Latchup Free Operation

GENERAL FEATURES

30 Watts Regulated $\pm 5V$ $\pm 15V$ Outputs

28VDC Input meets MIL-STD-704

EMI Filter meets CEO1 and CEO3 of MIL-STD-461

Soft Start, Short Circuit and Overvoltage Protection

Electrical and Environmental Screening referencing MIL-STD-883 Test Methods

IRT's HPS-3015 Radiation Hardened DC-DC Converter survives exposure to the radiation environments associated with a nuclear blast and continues to supply DC power to critical electronic components throughout the event.

The HPS-3015 survives high radiation levels in three critical environments: gamma dose rate [10^5 rad(Si) sec], gamma total dose [10^6 rad(Si)] and neutron fluence [10^{11} n/cm²]. In addition, the $\pm 5V$ output operates within $\pm 20\%$ of nominal voltage throughout a gamma dose rate environment of up to 5×10^5 rad(Si) sec. Operate-through performance and latchup free operation are 100% tested at a facility that simulates the gamma dose rate environment. A certificate is supplied with each serially numbered converter reporting its radiation test results.

This 11 pin hybrid DC-DC converter supplies 15W from the regulated $\pm 5V$ output and 7.5W from each of the $\pm 15V$ outputs with 70% full load efficiency. The converter maintains regulation over steady-state input voltages of 18 to 32 VDC and transient voltages up to 50V for less than 50ms. Ground isolation between the primary and secondary is maintained with transformer coupling.

Other features include an EMI filter and a soft start circuit. Internal current limiting protects the primary power switching elements and provides short circuit protection.

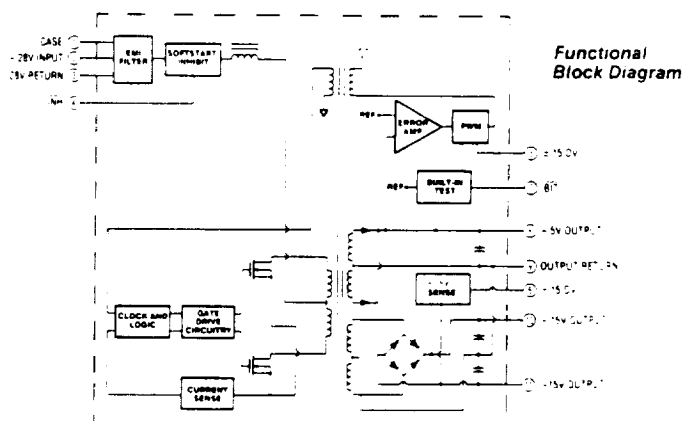
An active low inhibit input (INH) allows on-off control of the converter from an open collector logic signal and provides an efficient means of system power cycling.

The Built-In-Test (BIT) output is an active low digital signal which indicates when the $\pm 5V$ output is within the operating range of 4.5V to 5.5V. The $\pm 5V$ output has inherent

overvoltage protection. Additional overvoltage protection on the $\pm 15V$ output is available by shorting pin 5 to pin 6 and is used when the minimum load requirements on the $\pm 15V$ outputs are not met.

The all metal, hermetically sealed hybrid package features a base plate with flanges to facilitate heat dissipation. The HPS-3015 is ideal for pc board mounting with a compact size of 3.6x3.0x0.6 inches.

The electrical and environmental test methods reference MIL-STD-883 to ensure quality and reliability.



RADIATION HARDENED DC-DC CONVERTER DIAGRAM C

HPS-3015 SPECIFICATIONS

PARAMETER	CONDITIONS	LIMITS AT T _{case} =					UNITS
		-55°C, +85°C		+25°C			
		Min	Max	Min	Typ	Max	
ELECTRICAL CHARACTERISTICS							
Input Voltage		18	32	18	28	32	V
Continuous			50			50	V
< 50 ms							
Inhibit Input (INH):							
V _{IL}	V _{IL} = 0V, V _{in} = +32V					9.0	V
I _{IL}	V _{IL} = 0V, V _{in} = +50V					-8.5	mA
						-13.5	mA
Standby Input Current:	V _{in} = +9V				115		mA
Output Voltage							
+5V	Min to Max load	4.50	5.50	4.50	5.0	5.50	V
±15V	V _{in} = +18V to 32V	12.0	17.0	12.0	15.0	17.0	V
Output Power	V _{in} = +18V to 32V						
+5V		1.5	15.0	1.5		15.0	W
±15V		0.75	7.5	0.75		7.5	W
Built-in-Test Output (BIT):							
V _{OL}	I _{OL} = 1.5mA					1.5	V
I _{OH}	V _{OH} = 2.5V					-400	μA
Output Voltage Ripple							
+5V	Bandwidth = 1 MHz			80		125	mV
±15V	V _{in} = +28V Max load			150			mV
-5V Step Load Response:	Half to Max Load on 5V			100			mV
	±15V Max load, V _{in} = +28V						
-5V Dose Rate Perturbation							
	1 x 10 ⁻³ rad(Si)/sec		0.25			0.25	
	5 x 10 ⁻³ rad(Si)/sec		1.0			1.0	
Start-Up Time	V _{in} = +28V, Max load,			5			ms
	BIT = Logic 1						
Inhibit Time	V _{in} = +28V, Max load			8			ms
	BIT Output = +1V						
Efficiency	V _{in} = +28V, Max load			70			%
Input/Output Isolation	V _{in} = +500V	100		100			MΩ
GENERAL CHARACTERISTICS							
Switching Frequency	125 kHz						
Operating Temperature	-55°C to +85°C						
Storage Temperature	-55°C to +125°C						
MTBF-Airborne Inhabited Fighter	141,000 hours @ 50°C						
Weight	200 grams nominal						

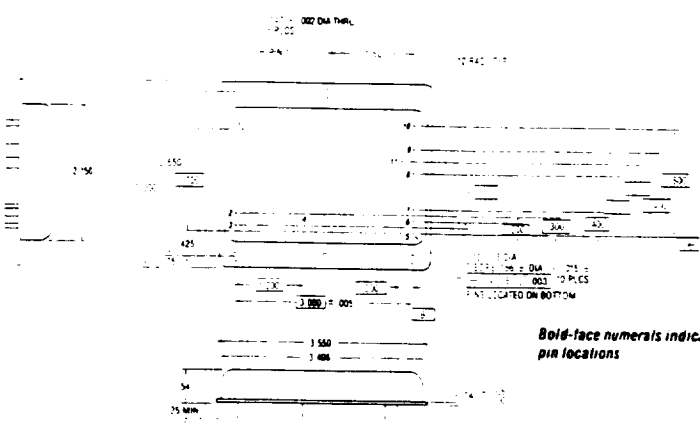
ENVIRONMENTAL SCREENING

- Pre-shipment: visual inspection per method 2017
- Stabilization Bake: 24 hrs @ +25°C per method 1008
- Temperature Cycle: 10 times per method 1010 condition B
- Constant Acceleration: 500 g @ 1 axis per method 2001
- Gross Leak: per method 1014 condition C
- Fine Leak: per method 1014 condition A
- Burn-in: 160 hrs @ maximum case temperature
- Final Electrical Testing: +55°C, +25°C, -55°C
- Final External Visual Inspection: per method 2009

RADIATION HARDNESS LEVELS

Dose Rate (operating through)	5x10 ⁻³	rad(Si)/sec
Dose Rate (survival)	1x10 ⁻²	rad(Si)/sec
Total Dose	1x10 ⁴	rad(Si)
Neutron Fluence	1x10 ¹⁷	1/cm ²

MECHANICAL DIMENSIONS



PIN CONNECTIONS

PIN #	FUNCTION
1	GND
2	+28V Input
3	28V Return
4	Inhibit
5	+15V Output
6	+15V Output
7	Built-in-Test
8	+5V Output
9	Output Return
10	+15V Output
11	+15V Output

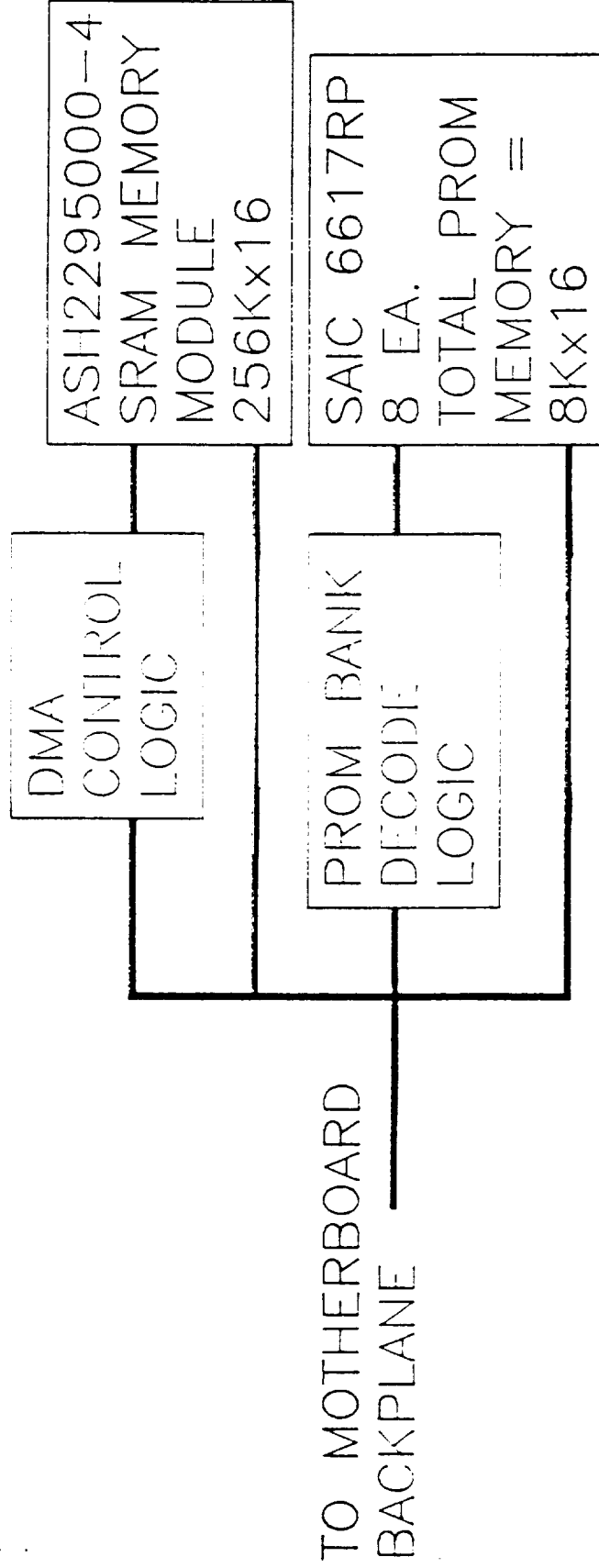
ORIGINAL PAGE IS OF POOR QUALITY

IRT

ENG. LARS, LONDON

GGS/UVI

STACK MEMORY/DMA DIAGRAM 7



ISTP DATA SYSTEM

9-26-89

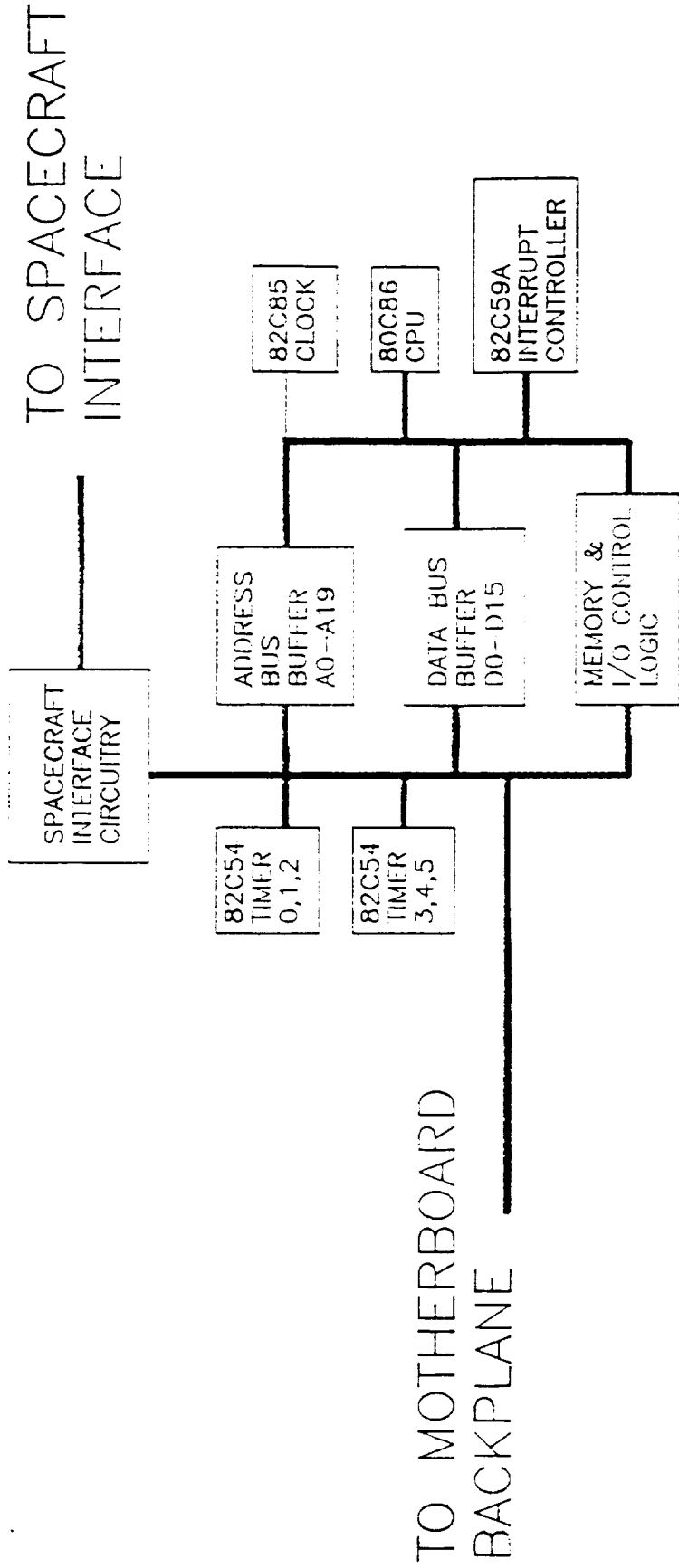
MEMORY MAP

Larry L. Savage

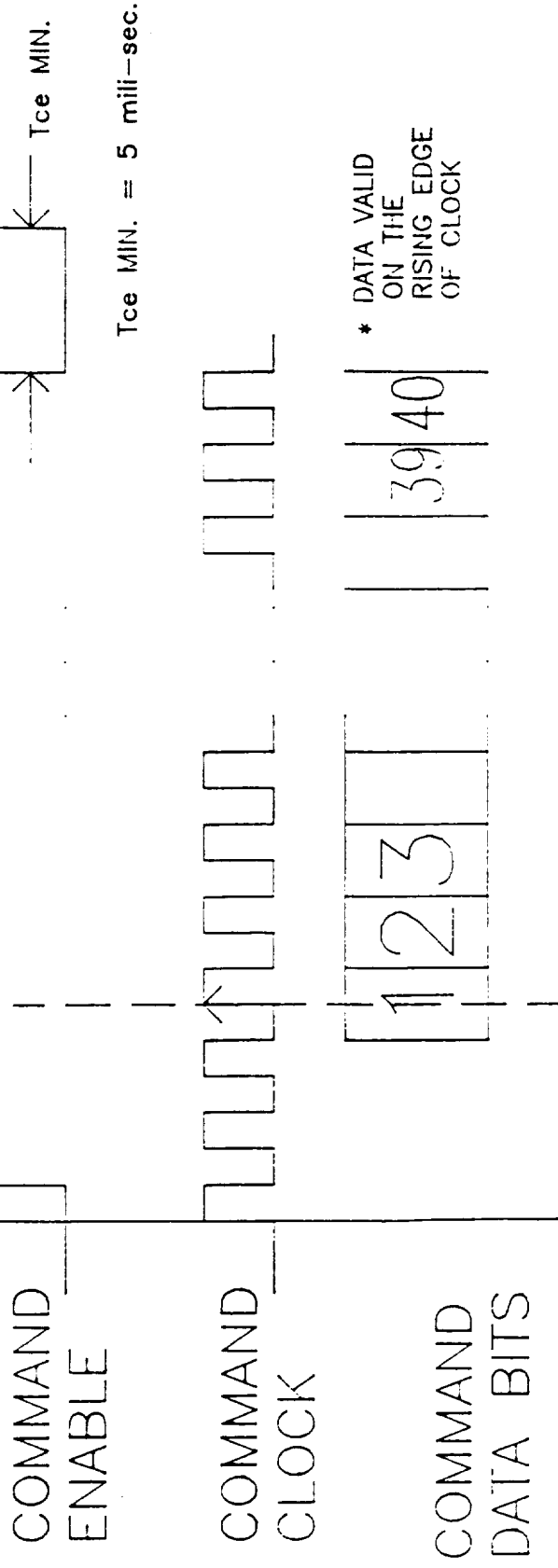
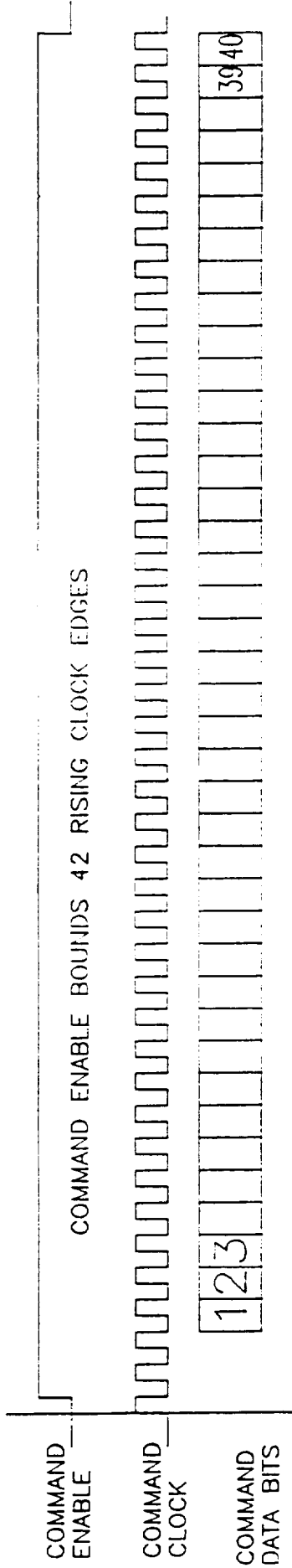
1. CPU MEMORY MAP

ASSUMPTIONS: TELEDYNE 256K RAM MODULE
 HARRIS 2Kx8 PROM
 TOTAL ROM MEMORY = 8Kx16
 TOTAL HARD RAM = 256Kx16

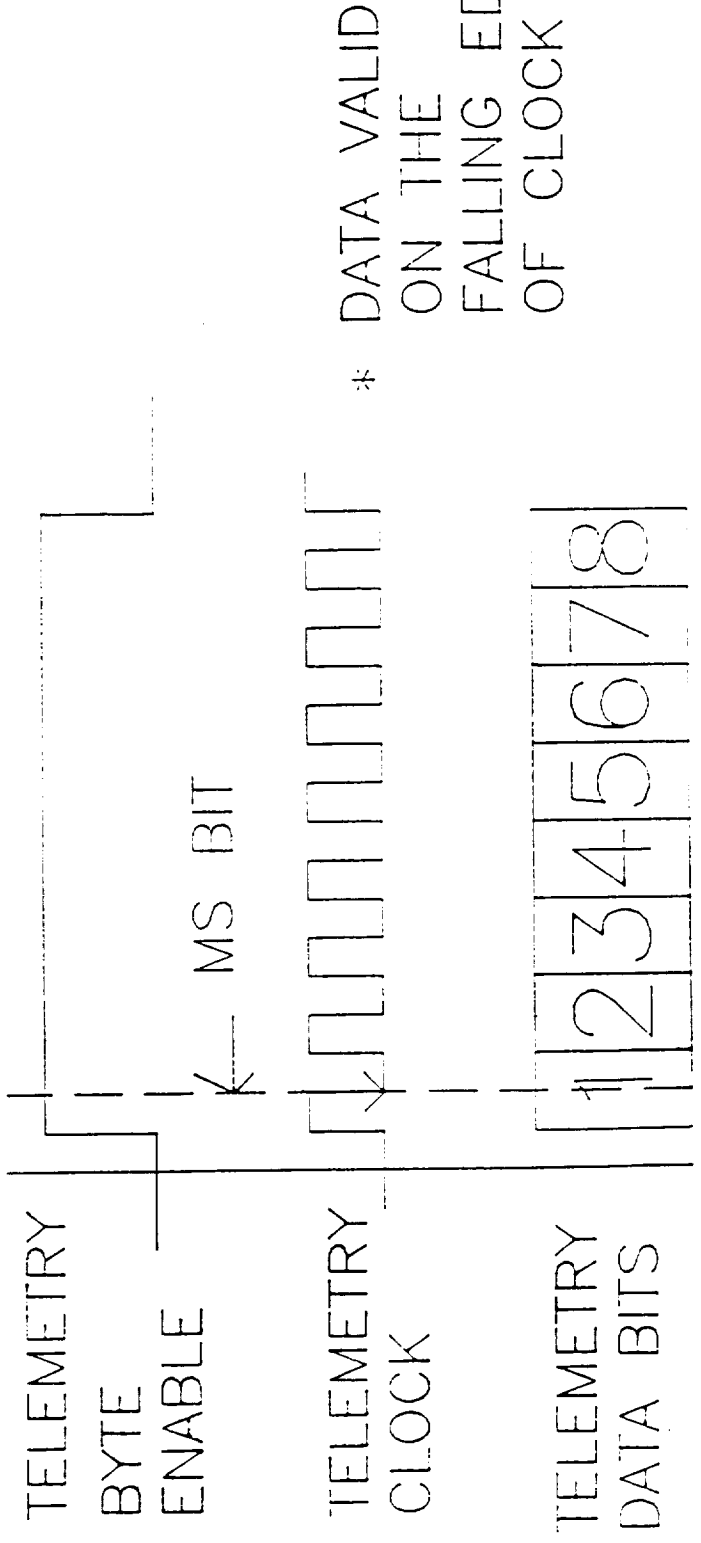
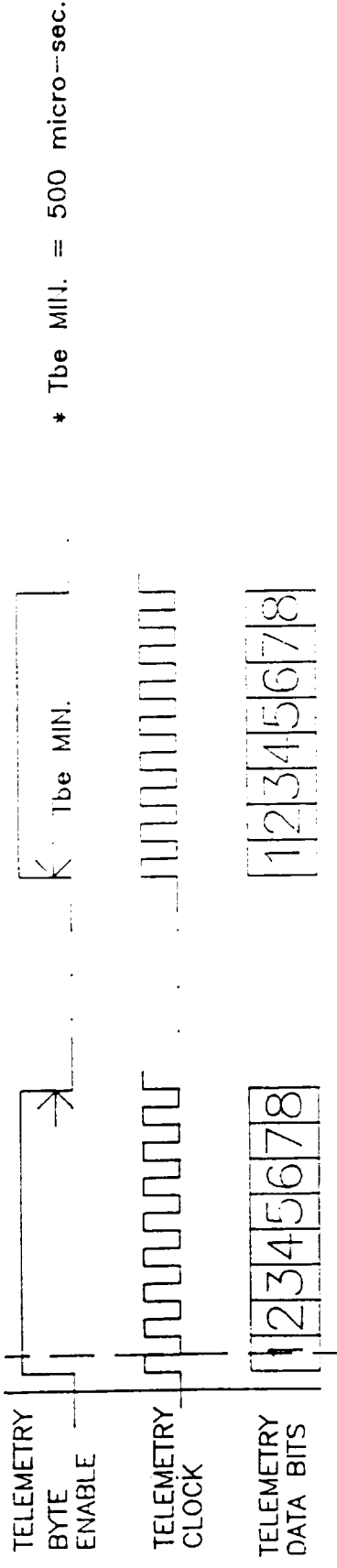
ADDRESS (HEX)	MEMORY TYPE	COMMENT'S (END OF 8086 ADDRESS SPACE)
FFFF	BANK4 END	RESET VECTOR
FFFE	PWR ON RESET JMP	BANK4 START
FF80	BANK4 ROM	BANK3 END
FF7F	BANK3 ROM	BANK3 START
FF00	BANK3 ROM	BANK2 END
FEFF	BANK2 ROM	BANK2 START
FE80	BANK2 ROM	BANK1 END
FE7F	BANK1 ROM	PROGRAM ROM START
FE00	BANK1 ROM	
	ADDRESS SPACE NOT USED	
3FFF	RAM	BANK8 END
3800	RAM	BANK8 START
37FF	RAM	BANK7 END
3000	RAM	BANK7 START
2FFF	RAM	BANK6 END
2800	RAM	BANK6 START
27FF	RAM	BANK5 END
2000	RAM	BANK5 START
1FFF	RAM	BANK4 END (32K PER BANK)
1800	RAM	BANK4 START
17FF	RAM	BANK3 END
1000	RAM	BANK3 START
0FFF	RAM	BANK2 END
0800	RAM	BANK2 START
07FF	RAM	BANK1 END
0000	RAM	BANK1 START

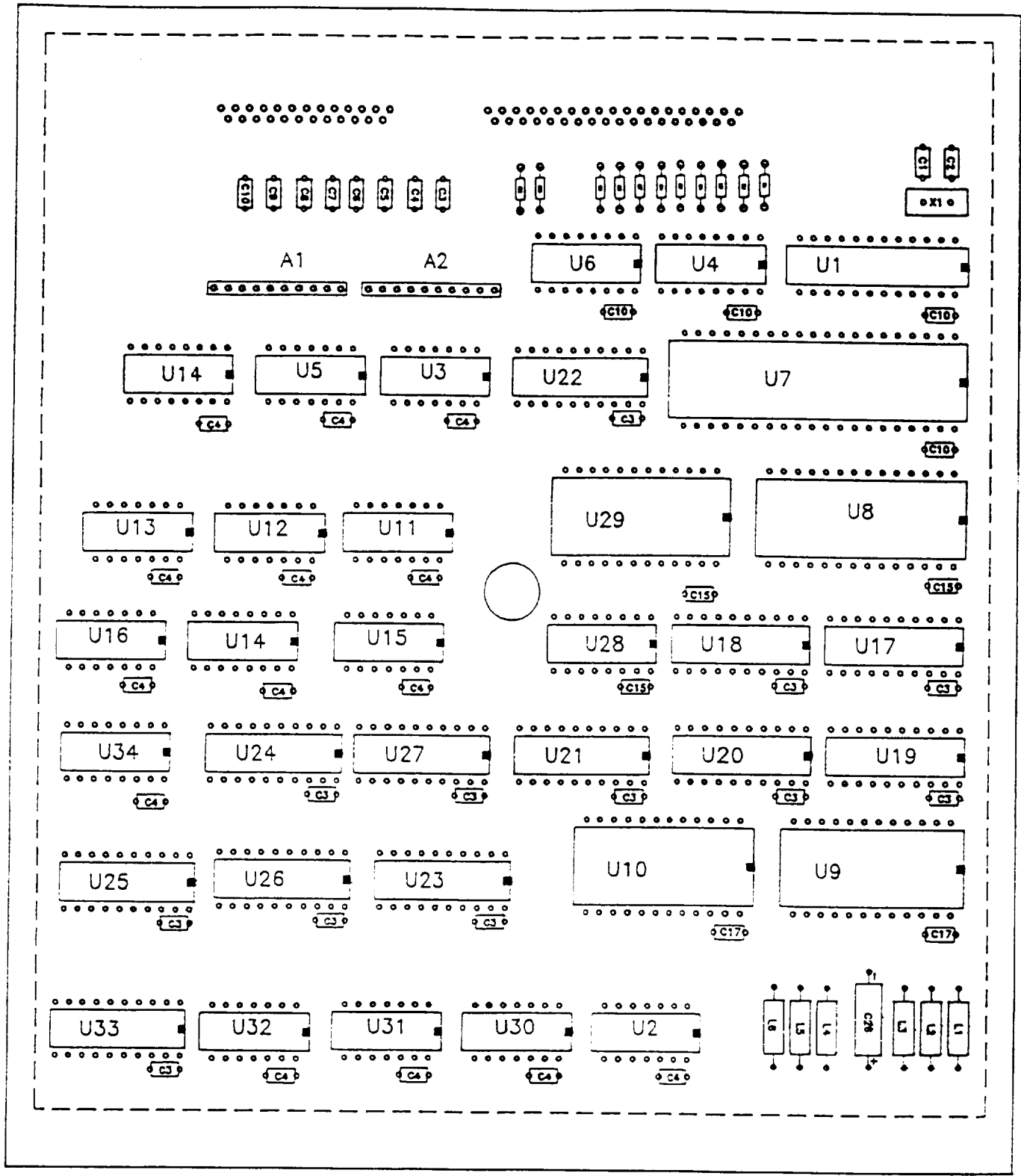


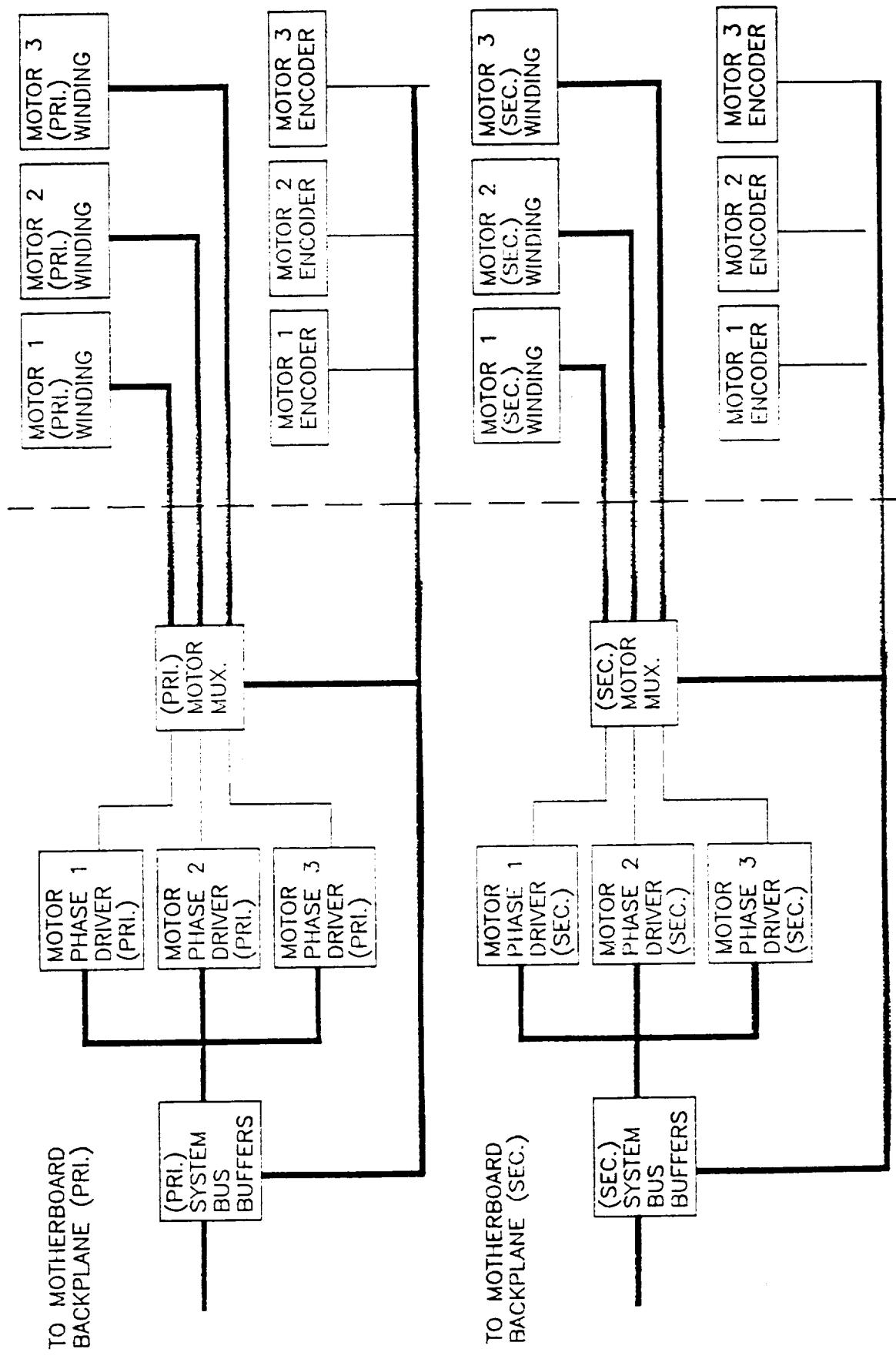
GG5/UVI COMMAND INTERFACE TIMING DIAGRAM 10



GGS/UVI TELEMETRY INTERFACE TIMING DIAGRAM 11

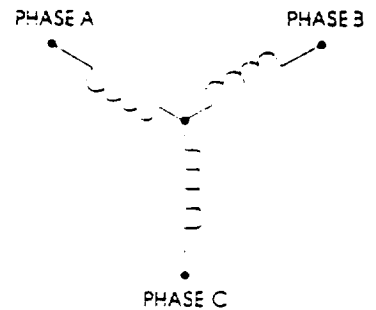






Specifically developed for high reliability space flight applications: Schaeffer Magnetics Rotary incremental Actuators employ a small angle permanent magnet stepper motor to directly drive an integral harmonic drive speed reducer.

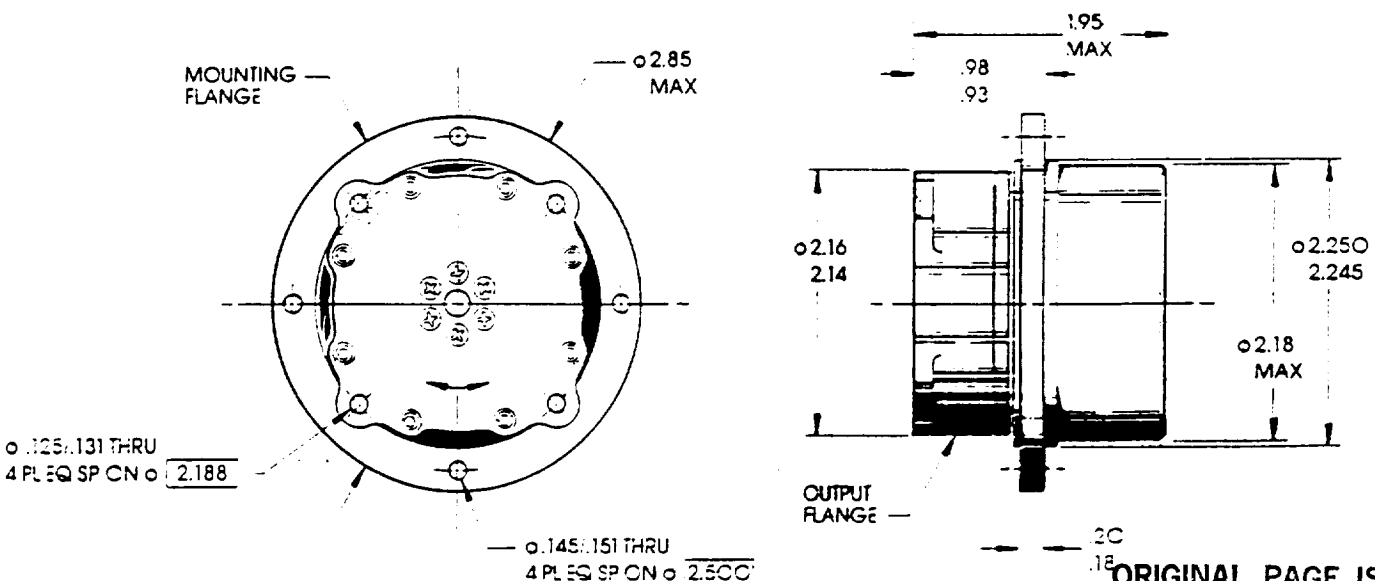
- OUTPUT STEP ANGLE: .0625°
- STEPS / REVOLUTION: 5,760
- HARMONIC DRIVE RATIO: 60:1
- DRIVE MOTOR: 3.75° PERMANENT MAGNET TYPE
- STEP RATE: 0 TO 500 STEPS / SEC (31.25° / SEC)
- POWER: 5.0 WATTS PEAK (NOMINAL)
- OUTPUT CAPABILITY:
INERTIAL: 1 SLUG-FT²
FRICTIONAL: 13.0 IN-LBS
- HOLDING TORQUE: (a)
POWERED: 13.0 IN-LBS
UNPOWERED: 6.0 IN-LBS
- TORSIONAL STIFFNESS: 3,000 IN-LBS/RADIAN
- SHAFT LOAD CAPABILITY: (a)
AXIAL: 1100 LBS
TRANSVERSE: 1100 LBS
MOMENT: 45 FT-LBS
- TOTAL ASSEMBLY WEIGHT: 11 LBS
- OPTIONAL FEATURES:
REDUNDANT MOTORS
BRUSHLESS D.C. MOTOR
INTEGRAL SHAFT POSITION INDICATION
- TYPICAL APPLICATIONS:
SOLAR ARRAY DRIVE
ANTENNA DRIVE
DEPLOYMENT MECHANISM
- CONTROLLER:
SCHAEFFER ELECTRONIC CONTROL UNITS
ARE AVAILABLE



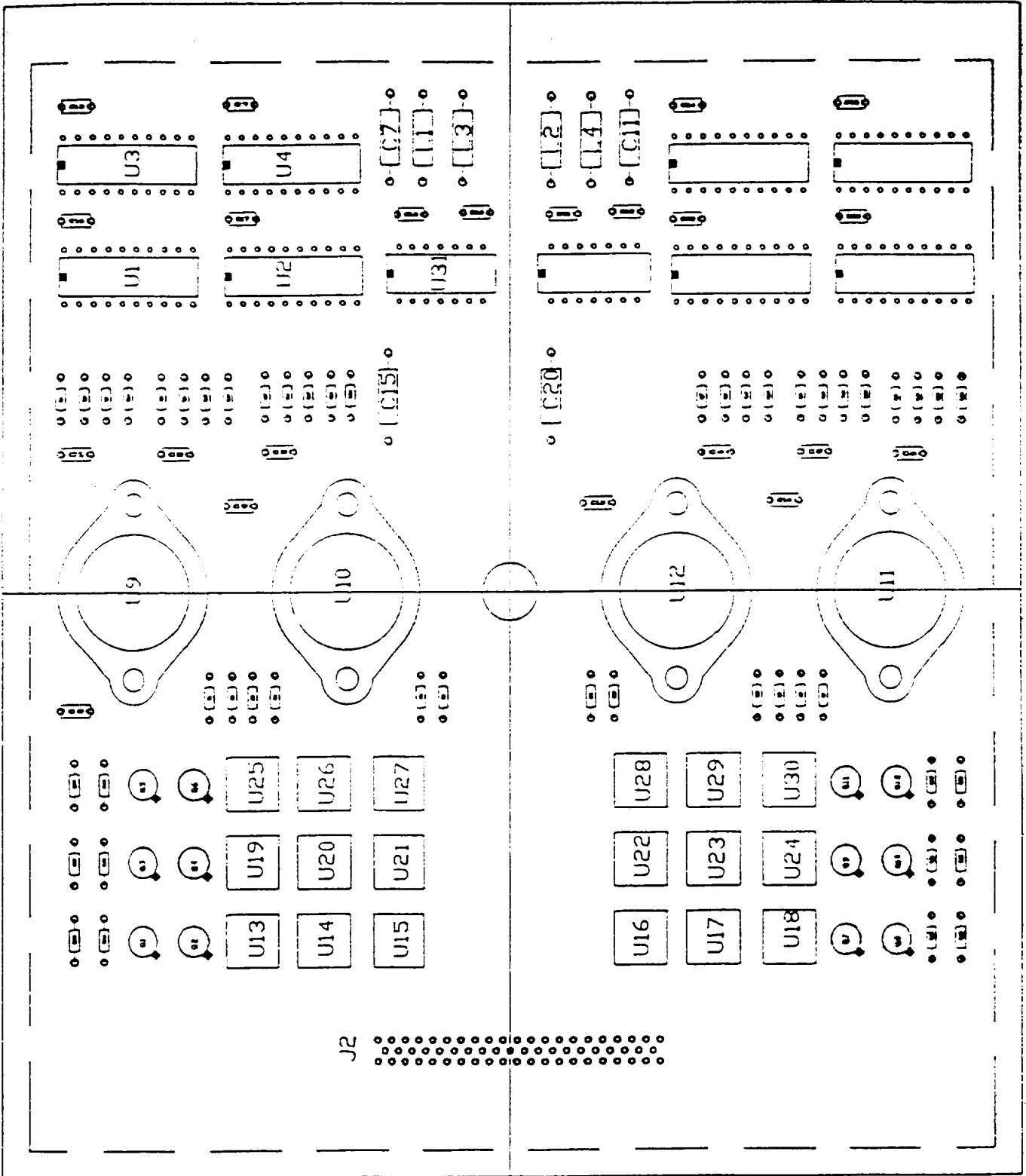
CONNECTION DIAGRAM

STATE	PHASE		
	A	B	C
1	+	+	-
2	-	-	-
3	+	-	+
4	-	-	+
5	-	+	+
6	-	+	-

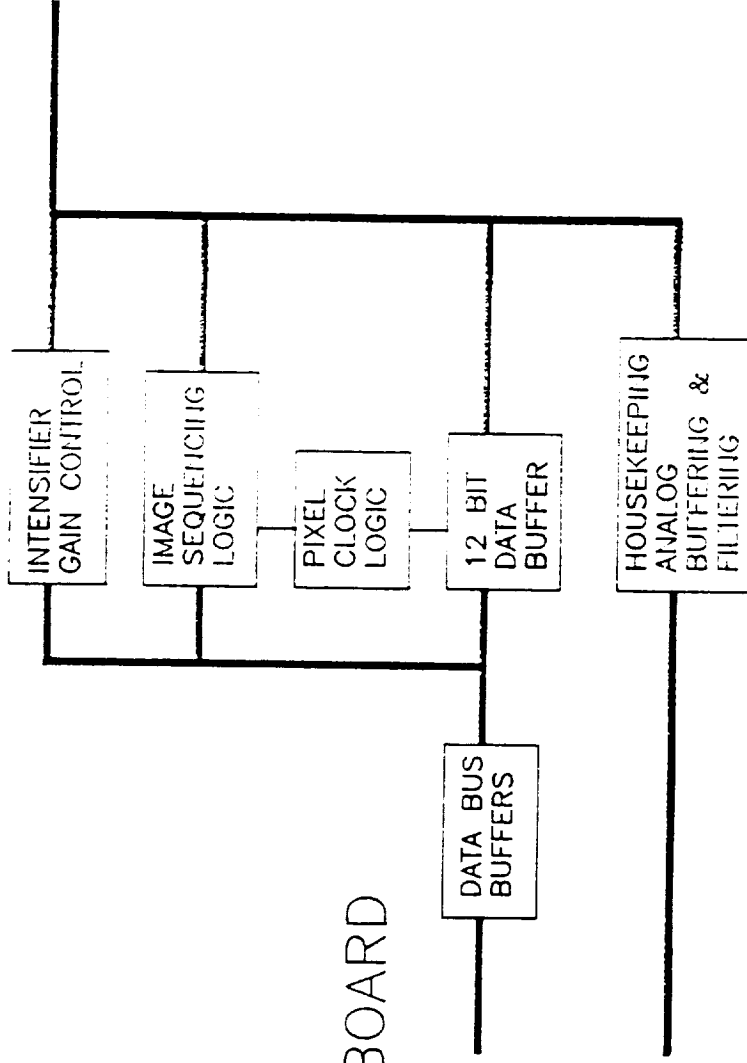
(a) TORQUE CAPABILITY LIMITED BY SPEED AND TEMPERATURE.
 (b) TORQUE CAPABILITY LIMITED BY SPEED AND TEMPERATURE.
 (c) TORQUE CAPABILITY LIMITED BY SPEED AND TEMPERATURE.
 (d) TORQUE CAPABILITY LIMITED BY SPEED AND TEMPERATURE.



ORIGINAL PAGE IS OF POOR QUALITY



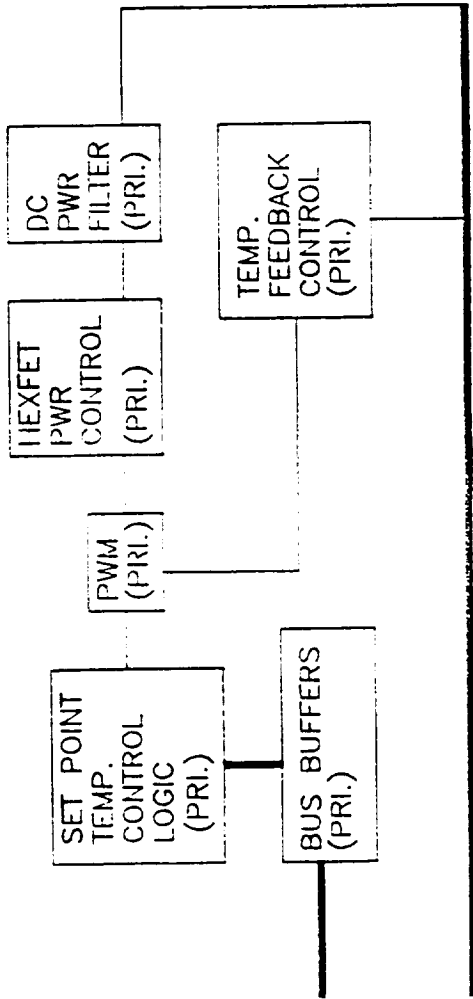
TO CAMERA
INTERFACE



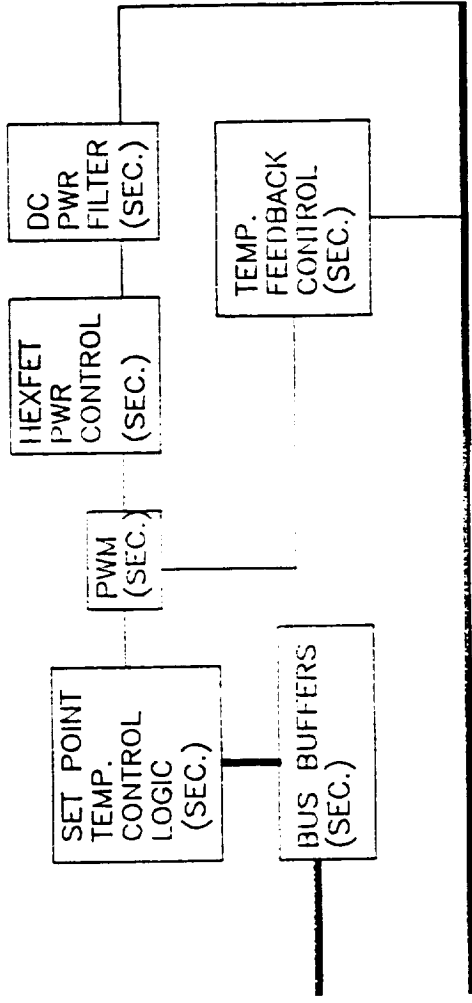
TO MOTHERBOARD
BACKPLANE

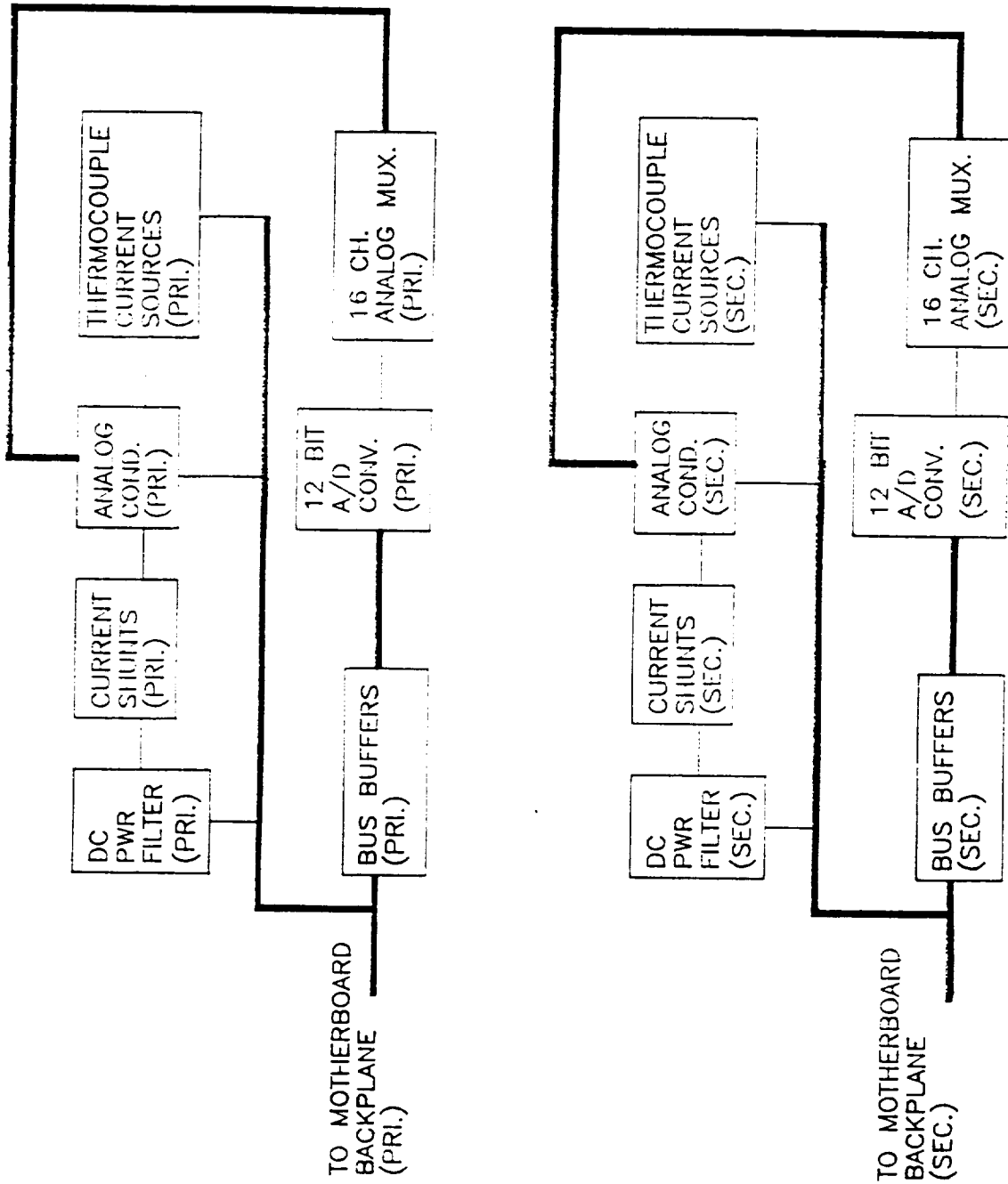
GGS/UVI STACK THERMOELE. CONTROL DIAGRAM 17

TO MOTHERBOARD
BACKPLANE
(PRI.)



TO MOTHERBOARD
BACKPLANE
(SEC.)





UVI ICD ELECTRICAL SECTION

STATUS:

First inputs to GE

COMMENTS:

Cable Shielding

Clarification of shielding
in Electronics Stack for
Camera S/C interface signals

Command Timming

On which edge of clock is
command clocked in?

Major Frame Telemetry Format

Clarification of S/C
housekeeping and instrument
housekeeping formats

Power Supply Frequency

125 KHz

Time Code in Command Data

Required every 10 min

UVI ICD ELECTRICAL SECTION

CONCERNS:

Major Frame Telemetry Format
Contiguous word enable in
instrument houskeeping
telemetry

UVI S/C INTERFACE

S/C

UVI

```
----- +28 Volt (regulated) ----->
----- +28 Volt (pulse) ----->

----- Command Enable ----->
----- Command Clock ----->
----- Command Data ----->
----- Telemetry Clock ----->
----- Telemetry Enable ----->
----- Major Frame Sync ----->
----- Minor Frame Sync ----->
<----- Telemetry Data ----->
----- Platform Status ----->

<---- Camera Radiator Temp ----->
<-- Elec Stack Radiator Temp --->
<----- 0° Aperture Temp ----->
<----- 90° Aperture Temp ----->
<----- 180° Aperture Temp ----->
<----- 270° Aperture Temp ----->
<---- Aperture Door Status ----->
<-- Filter Wheel Home Status --->
```

Note: Interface is redundant

All of the above grounds will be returned as twisted pairs with their power lines through separate leads (in the spacecraft harness) to a single ground tie-point herein after referred to as "laboratory" or "star" ground. All command, data, and telemetry voltage levels shall be referenced to "laboratory" ground. For command and data signals, the ground level offset from instrument to spacecraft "star" ground shall be assumed to be 0.1 volt maximum (0.04 V typical). See Figure 6 for the GGS grounding philosophy. The telemetry ground return length will be no longer than 20 feet of AWG 24 stranded wire, (28.1 ohms per thousand feet).

3.1.1.2 +28 Volt Main Power Ground. The +28 Volt Main Power ground shall be used as the return for all current drawn from the spacecraft +28 volt main regulated bus.

Current in the power ground shall be limited to 500 mA per #22 conductor or 1 Amp per allocated connector pin (see paragraph 3.1.2.3.2) excluding transient current drawn during instrument turn on in order to minimize the effects of harness drops.

Feedthrough filters must be grounded to chasses to maintain box shielding effectiveness and must have a capacitance value less than 0.1 μ fd to limit AC currents flowing to structure from the power bus.

3.1.1.3 +28 Volt Pulse Load Ground. The Pulse Load ground shall be used as the power return line for all pulse loads (steppers, heaters, etc.) which do not comply with the main bus ripple specification (see paragraph 3.1.3.2.6). Current in this power ground shall be limited to 500 mA per #22 conductor or 1A per allocated connector pin.

Feedthrough filters must be grounded to chasses to maintain box shielding effectiveness and must have a capacitance value less than 0.1 μ fd to limit AC currents flowing to structure from the pulse power bus.

3.1.1.4 +5V Keep-Alive Power Ground. The +5 volt memory keep-alive power shall be returned over the signal ground pin.

3.1.1.5 Signal Ground. Signal ground shall be the power return line for the secondary side of the instrument dc/dc converters. Current in the signal ground output of the experiment shall not be more than 75 mA per connector pin.

The signal ground may be connected to chassis by audio frequency/radio frequency (AF/RF) bypass capacitors (less than 0.5 μ fd total) with short leads to minimize the effects of impedance of the signal ground lead at high frequencies.

3.1.1.6 Shield Grounding. For each preassigned shielded cable that carries a signal into the instrument, a connector pin shall be dedicated to that cable's shield. The connector pins so dedicated shall not be connected, but held in reserve. No other signal returns or grounds shall be connected to the shield ground pins. Shield ground shall not be used with triax cables. Except for coaxial cable, cable shields shall not be used as a return path.

PRECEDING PAGE BLANK NOT FILMED

Size	Code Ident No.	3282065
A	49671	
		Sheet 12

PRECEDING PAGE BLANK NOT FILMED

For non-RF signal cables, the shield shall be grounded at the signal source end only. The shield will be terminated at the connector backshell (chassis) and also carried through a pin into the instrument. Each signal connector must provide at least one chassis grounded pin. The chassis ground pin must be bonded internally to the equipment chassis

3.1.1.7 Chassis Ground. Chassis (case) ground shall be provided on the same connector (see Section 3.1.2.3.6) used to interface the spacecraft power input with the instrument. Chassis ground shall be dc connected to the case (including outside wrapper and mounting surface) of the instrument. Bond straps (jumpers) must be used across all hinges and connections that would not otherwise meet the bonding requirement.

The chassis ground connection to the spacecraft will be made through the mounting surfaces and mounting hardware of the instrument. The instrument mount shall be designed to provide a total contact resistance of less than 0.0025 ohm from the chassis to the spacecraft. Provisions shall be made for the installation of a ground strap if required.

The shells of all connectors interfacing with the spacecraft harness shall be grounded to the chassis of the instrument. Conductive harness overwrap will be connected to the connector shell on the harness side.

3.1.1.8 Pyrotechnic Return. A separate pyrotechnic return will be supplied for each pyrotechnic device. It shall be separated from all other grounds within the unit.

3.1.1.9 Passive Analog Telemetry Ground. Passive analog telemetry points (thermistors and multi-turn potentiometers) shall have a common return line to the GTM.

3.1.2 Wiring and Connectors

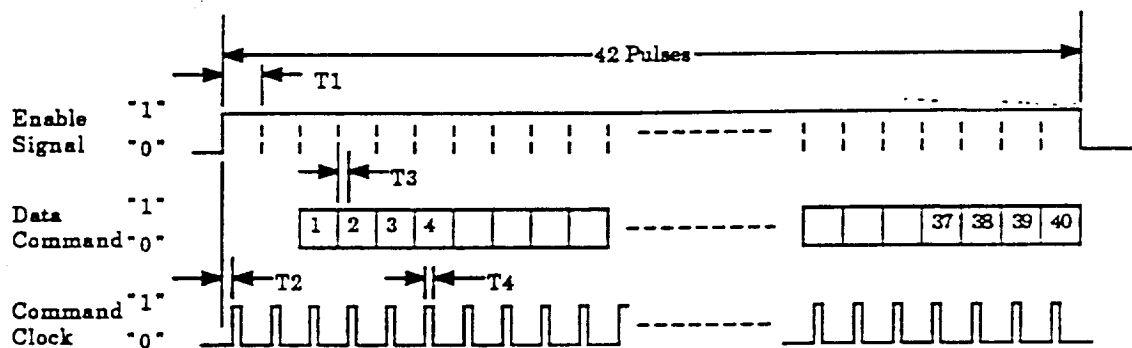
3.1.2.1 Harness Design Philosophy. The laboratory harness will be designed in accordance with the following guidelines:

- (a) Harness runs will be selected to minimize overall length and weight.
- (b) Power returns will be routed in the same bundle as the associated power lines and returned to the source in order to minimize current loops.
- (c) Telemetry (GTM) signals will be bundled together and in a separate bundle from power and digital command lines in order to minimize crosstalk.
- (d) Signal returns will be routed in the same bundle as the associated signal lines in order to minimize electromagnetic emission and susceptibility.

PREVIOUS PAGE BLANK NOT FILMED

Size	Code Ident No.	3282065
A	49671	
		Sheet 14

PREVIOUS PAGE BLANK NOT FILMED



Bit Rate bps	T1 ms	T2 ms	T3 ms	T4 ms
1000 ±2%	1.0 ±2%	0.50 ±2%	0.25 ±2%	0.25 ±2%

Figure 17. Serial Command Phasing Relationship

PRECEDING PAGE BLANK NOT FILMED

Size A	Code Ident No. 49671	3282065
		Sheet 44

ULTRAVIOLET IMAGER

POLAR/GGS

**SCHEDULES AND
DEVELOPMENT STATUS**

PRELIMINARY DESIGN REVIEW

PDR TITLE/005

MARSHALL SPACE FLIGHT CENTER		ISTP ULTRAVIOLET IMAGER												ORIG. APPUL. / /											
APPROVAL ACCOMP. M. R. TORR		SUMMARY												LAST CHANGE / /											
MILESTONES		Page 1 of 3 STATUS AS OF 10/16/89																							
		89												91											
		F	M	A	M	J	J	A	S	O	N	D	J	F	M	A	M	J	J	A	S	O	N	D	J
01	"KICK OFF" MEETING (GSFC)	▼																							
02	MEETING GSFC/GE		▼																						
03	DEVELOP ENG. MODEL																								
04	INTERFACE DEF. (IIRD/ICD)																								
05																									
06	PDR																								
07																									
08	TEST ENG. MODEL (RADIATION)																								
09	(SHAKE)																								
10	RELEASE DRAWINGS																								
11																									
12	CDR																								
13																									
14	FLIGHT PROCUREMENT																								
15	DEL. STRUC. ANAL. MODEL																								
16	DEL. THERMAL ANAL. MODEL																								
17	DEL. DRILL TEMPLATES																								
18	KEY PARAMETER S/W																								
19	ORDAF PLANNING/REVIEW																								
20	ORDAF PROCUREMENT																								

Note:

MARSHALL SPACE FLIGHT CENTER APPROVAL ACCOMP. M. R. TORR		ISTP ULTRAVIOLET IMAGER SUMMARY Page 3 of 3		ORIG. APPUL. / / LAST CHANGE / / STATUS AS OF 10/16/89																																		
MILESTONES		92	93	94																																		
		J	F	M	A	M	J	J	A	S	O	N	D	J	F	M	A	M	J	J	A	S	O	N	D	J	F	M	A	M	J	J	A	S	O	N	D	
01	LAB. INTEGRATION AND TEST																																					
02																																						
03	LAB. ENVIRONMENTAL TESTING																																					
04																																						
05	FINAL CAL/REWORK																																					
06																																						
07	LAUNCH																																					
08																																						
09	ON-ORBIT CHECKOUT																																					
10																																						
11	MISSION SUPPORT																																					
12																																						
13	SCIENCE ALGORITHM DEVELOPMENT																																					
14																																						
15	RDAF MAINTENANCE																																					
16																																						
17																																						
18																																						
19																																						
20																																						
Note:																																						

UVI PDR/ PROCUREMENTS STATUS

FILTER MATERIALS: 50% ON ORDER
REMAINDER BY END OF DECEMBER, 89

ELECTRONICS: ENGINEERING PARTS: 90% ON HAND
FLIGHT: ALL ORDERS TO BE PLACED
BY DECEMBER 15, 1989

MECHANICAL: ALL FLIGHT FASTENER PROCUREMENTS
TO BE PLACED BY 3/20/90

DETECTORS: ENGINEERING MODEL: ALL COMPONENTS
ON ORDER
FLIGHT: ALL PROCUREMENTS TO BE PLACED
BY 3/15./90

PDR/PROCUREMENTS

UVI PDR/ DOCUMENT STATUS

SIGNED: 1)ICD - mechanical section
 2)MOU

SUBMITTED IN PRELIMINARY FORM:

1)FMECA	9/20/89
2)MATERIALS LIST	9/20/89
3)SAFETY PLAN	9/20/89
4)ESD PLAN	9/20/89
5)DATA MANAGEMENT PLAN	10/17/89
6)THERMAL MODEL	10/17/89

PDR/DOCUMENTS

UVI PDR/ DESIGN STATUS

SUBSYSTEM	ELEMENT	DESIGN COMPLETE	ENG MOD FABRICATION	FLIGHT FAB
OPTICS	MIRRORS	100%	AWAITING MACHINING	7/1/90
	FILTERS	70%	IN PROCESS	9/1/90
MACHINING	DETECTORS	COMPLETE	IN PROCESS	10/30/90
	FILTER WHEEL	50%	1 / 5	10/30/90
	FOLDING MIRROR	10%	3 / 5	10/30/90
	MIRROR/DOOR	10%	2 / 1	10/30/90
	BAFFLES	80%	2 / 1	10/30/90
	OPTICAL BENCH	90%	2 / 1	10/30/90
	BASE PLATE	70%	2 / 1	10/30/90
	ELECTRONICS BOX	30%	5 / 10	10/30/90
	PASSIVE RADIATOR	15%	4 / 5	10/30/90
ELECTRONICS	DETECTOR A	95%	10/30	10/30/89
	DETECTOR B	95%	10/30	10/30/90
	DETECTOR INTERFACE	40%	1/5/90	10/30/90
	S/C INTERFACE	50%	12/15/89	10/30/90
	TEC	50%	1/5/90	10/30/90
	HOUSEKEEPING	50%	2/1/90	10/30/90
	CPU	70%	12/1/89	10/30/90
	MEMORY	70%	1/5/89	10/30/90
	MOTOR DRIVERS	70%	12/15/89	10/30/90
	POWER SUPPLIES	80%	11/1/89	10/30/89
	BACK PLANE	50%	12/15/89	10/30/90
	ENCODER BOARDS	10%	1/15/90	10/30/90
	SOFTWARE	FLIGHT	10%	2/1/90
GSE		10%	2/1/90	1/1/91
KEY PARAM/TLM		0%	7/1/90	7/1/91
ALGORITHMS		10%	-----	10/1/91

ULTRAVIOLET IMAGER

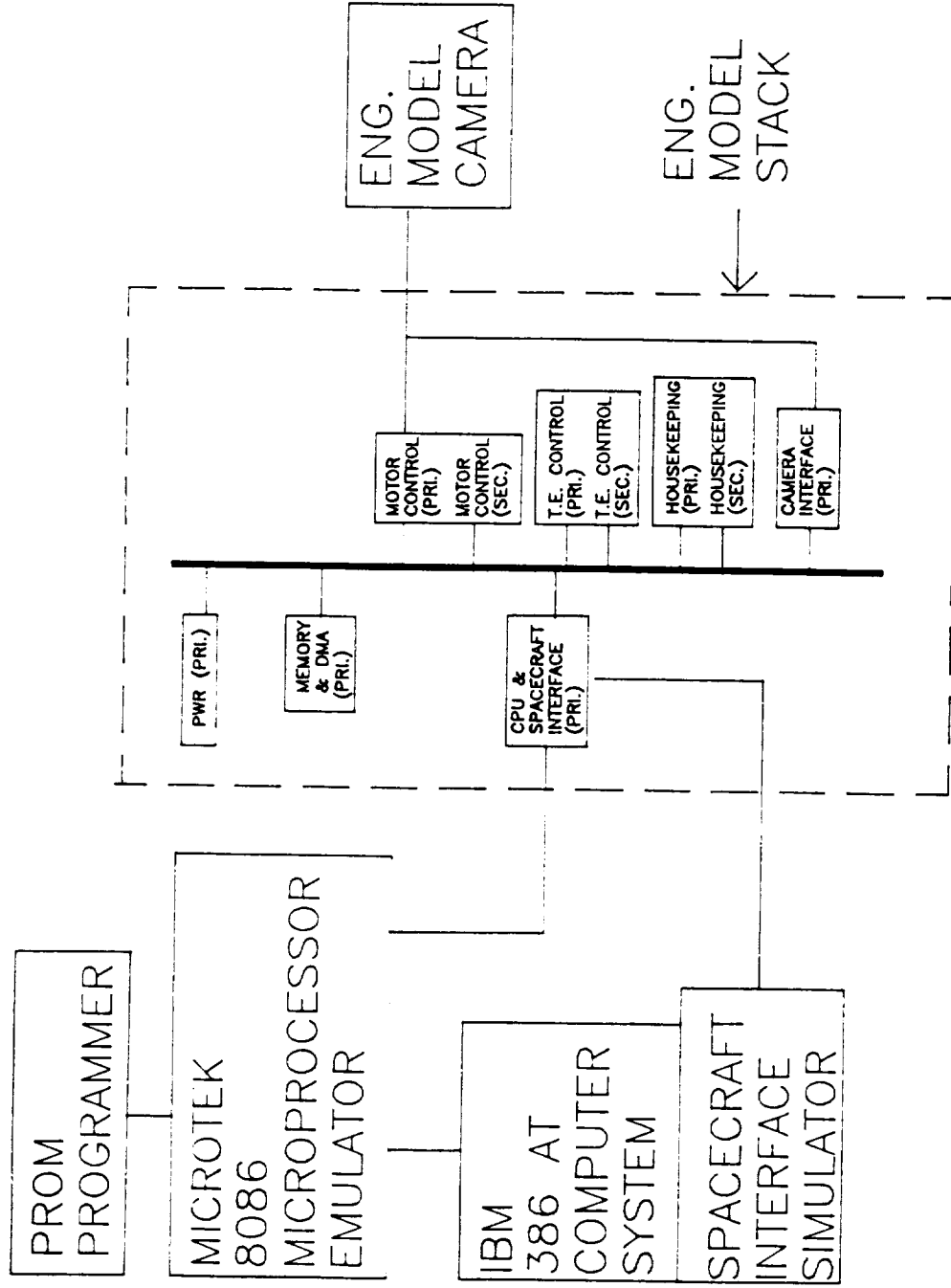
POLAR/GGS

**SOFTWARE/DATA
MANAGEMENT**

PRELIMINARY DESIGN REVIEW

PDR TITLE/006

FLIGHT SOFTWARE DEVELOPMENT CONFIGURATION



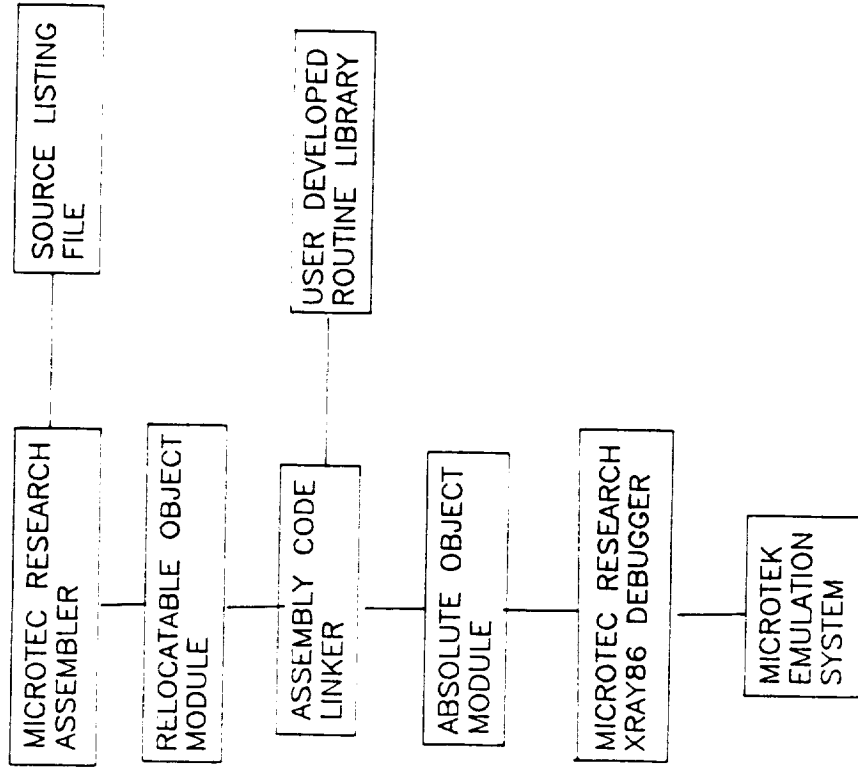
GGG/UVI FLIGHT SOFTWARE REQUIREMENTS

DIAGRAM 2

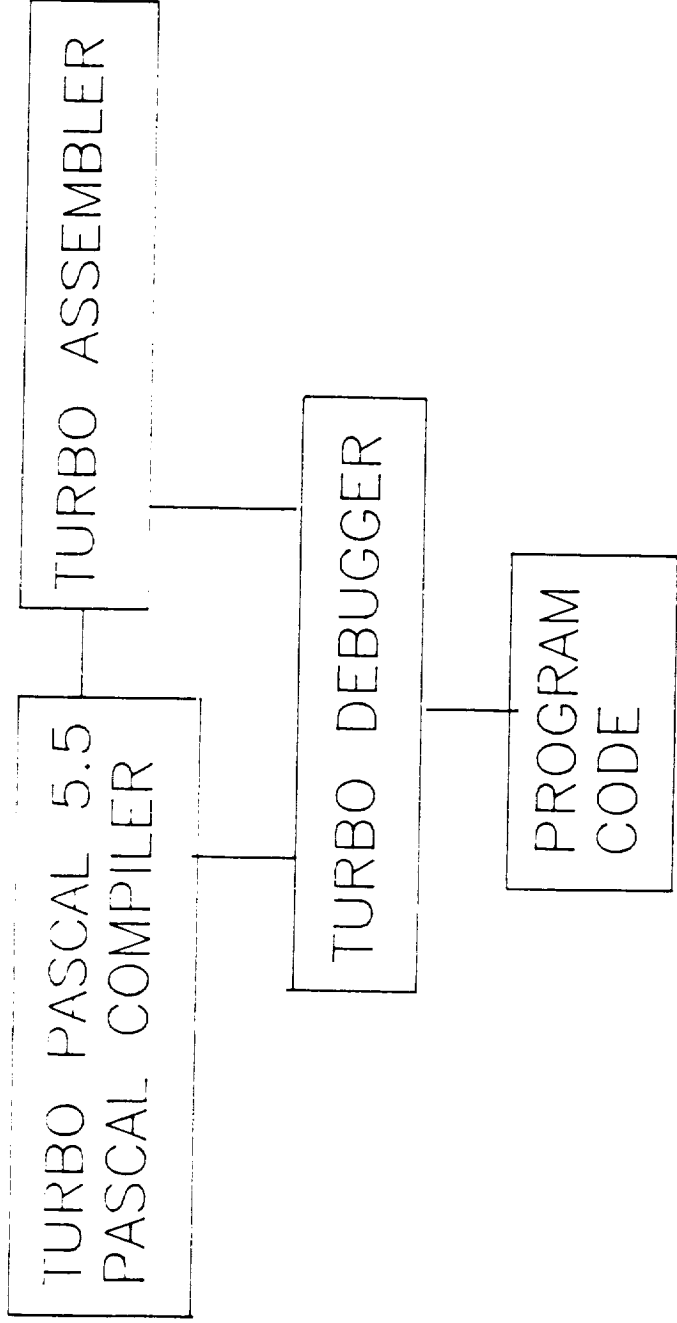
1. Program code shall not utilize more than 8k words of PROM space.
2. Program code shall not utilize more than 256k of RAM memory.
3. A means shall be provided by the flight program for uploading program "patches" in the event of a software or hardware malfunction or failure. This implies that the program code shall allow portions of the main flight program to reside in RAM memory.
4. The code shall be structured in such a manner as to circumvent and report minor faults where possible.
5. The flight program shall implement a power on self test (POST).
The POST routine shall verify instrument functionality.
6. The software program architecture shall be a table driven state machine. This software structure optimizes code size and process execution time.

* CODE IS DEVELOPED AND DEBUGGED ON AN IBM 386 PC AT COMPATIBLE COMPUTER

* CODING LANGUAGE IS 8086 ASSEMBLY



- * GSE CODE IS DEVELOPED ON AN IBM 386 PC AT COMPATIBLE COMPUTER
- * ALL GSE CODING IS DONE IN A COMBINATION OF 8086 ASSEMBLY CODE AND PASCAL. EXECUTION TIME CRITICAL ROUTINES ARE WRITTEN IN 8086 ASSEMBLY CODE.



uv imager

DATA MANAGEMENT PLAN

Preliminary Design Review

17 October 1989

UV imager

Images

Key Parameters

Definitive Orbit
/Attitude

Command History

TYPES of UVI DATA

Housekeeping

Communications

UV imager

DAILY DATA VOLUME

- Nominal sequence: 20 frames
10 minutes
- Each frame: 244 x 275 x 12 bits
- Each day: 144 sequences
2880 frames
 2.3×10^9 bits

uv imager

KEY PARAMETERS	WORDS	FORMAT
1. Total global energy influx	1	32-bit float
2. Total energy influx to polar cap	1	"
3. Total energy influx to auroral oval	1	"
4. Size of polar cap	1	"
5. Equatorward boundary of auroral oval	1	"
6. Event flag	1	"
7. Selected auroral images	6.7×10^4	12-bit integer

uv imager

DATA MANAGEMENT

TASKS

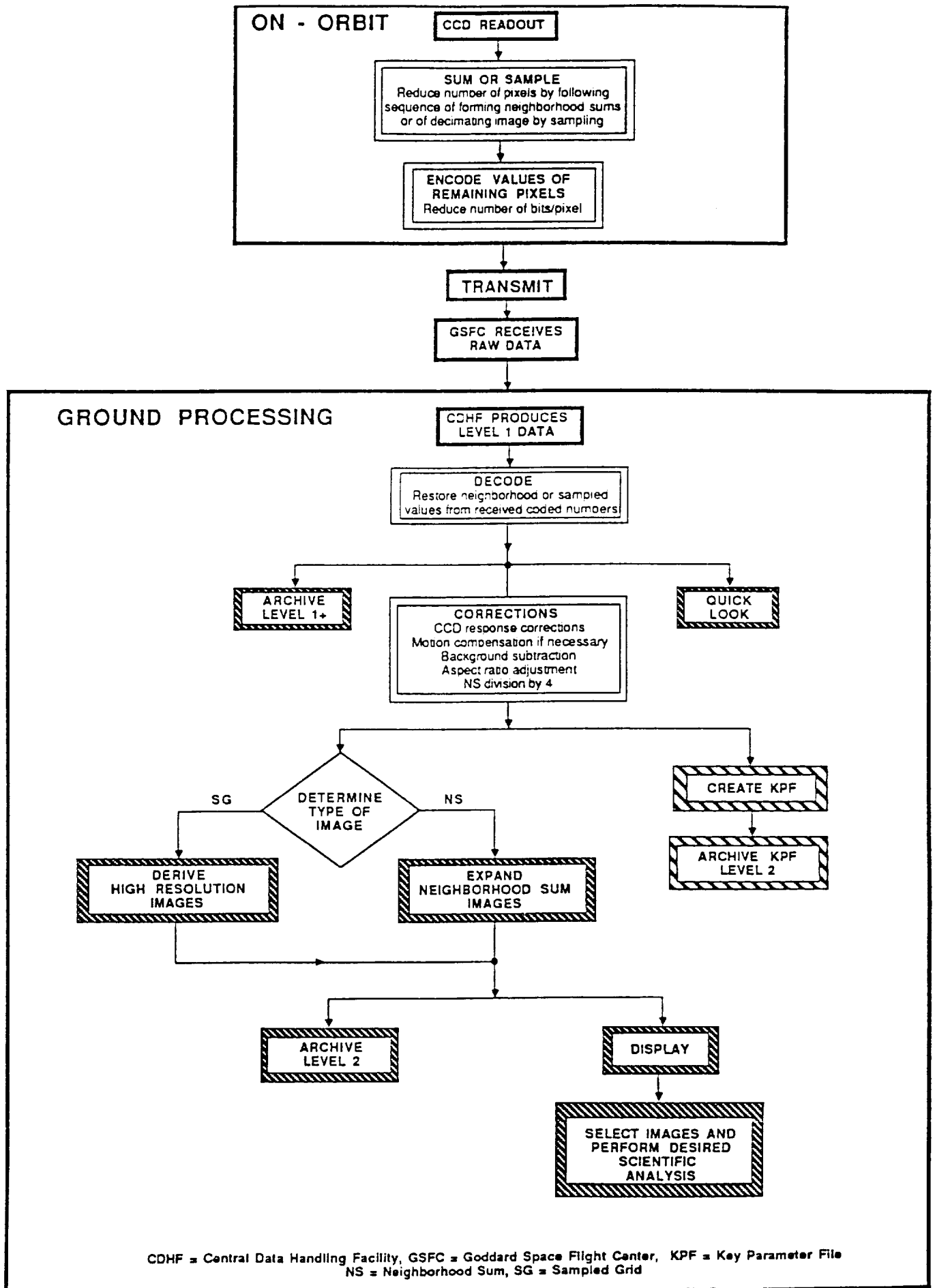
Image
Reconstruction

KP Generation
/ Update

Science
Analysis

Distribution

Archival



OVERVIEW OF DATAFLOW FROM ULTRAVIOLET IMAGER IN NOMINAL OBSERVING SEQUENCE

uv imager

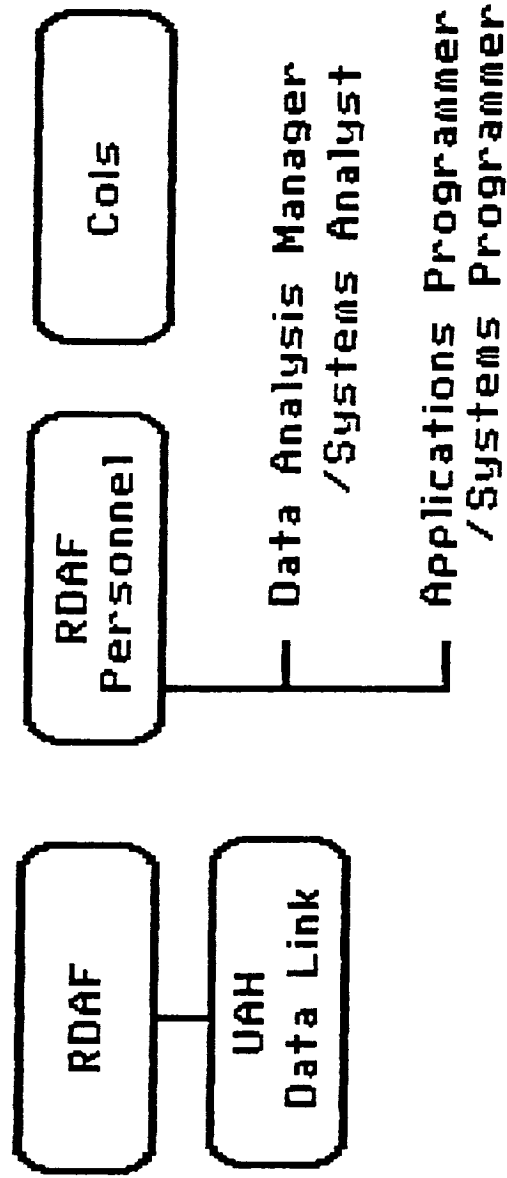
COMPUTATIONAL ESTIMATES

Reconstruct images	391	Mflops/sequence
Display images	20	Mflops/sequence
Storage	20	Mflops/sequence
Characteristic energy determination	431	Mflops/sequence
<hr/>		
	862	Mflops/sequence
x 144	1.2×10^5	Mflops/day

(Scientific Modeling Activities Not Included)

uv imager

DATA MANAGEMENT RESOURCES

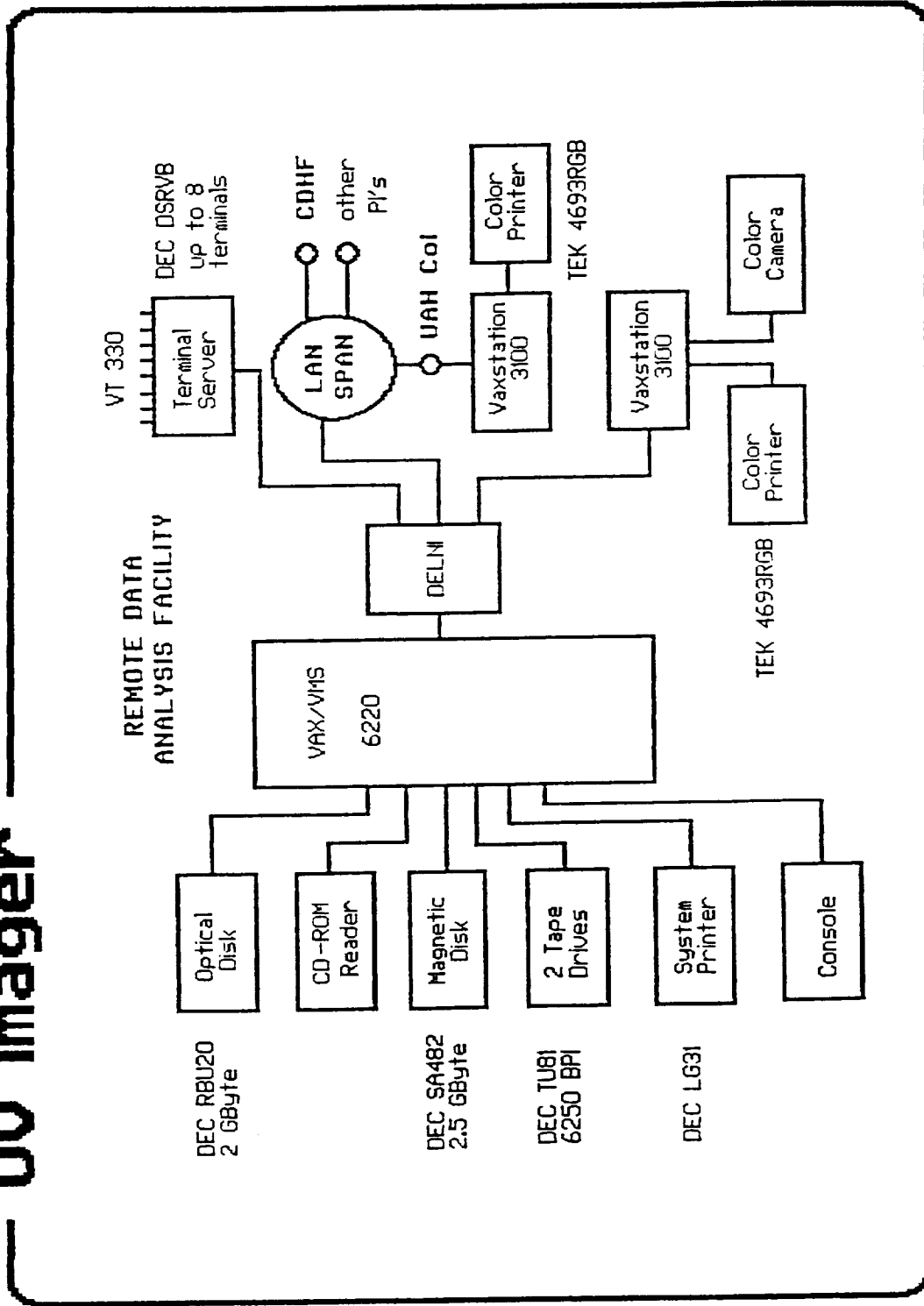


uv imager

PROCESSOR PERFORMANCE

PROCESSOR	RELATIVE PERFORMANCE	MFLOPS/SEC	DAILY CPU HOURS
11/780	1	0.5	67
8350	2.3	1.2	28
6220	5.5	2.8	12
8550	6.0	3.0	11

uv imager

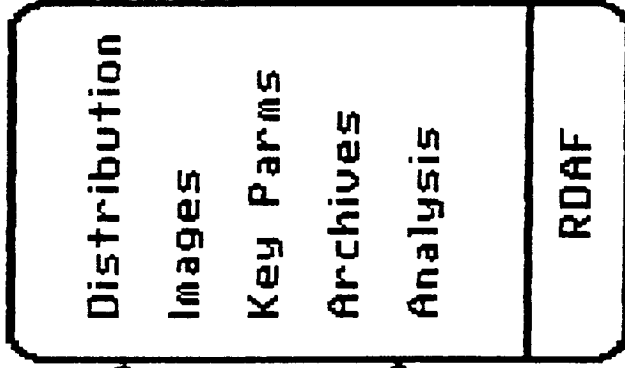


UV imager

DATA MANAGEMENT PLAN

Level 0
Key Parm
Def Orbit
/Attitude
Command History

DDF



Cols / PIS
Data Requests

CDHF
Commands
KP Update

CDHF
Communications
SPOF

CDHF

Online Data

DATA ANALYSIS SOFTWARE

THREE MAIN CATEGORIES:

1. KEY PARAMETERS

THIS PROVIDES SUMMARY DATA USEFUL TO THE
ENTIRE ISTEP COMMUNITY

2. FULL SCALE DATA REDUCTION

REDUCTION OF SPECTRAL IMAGES TO GEOPHYSICAL
QUANTITIES

3. SCIENTIFIC MODELING OF OBSERVATIONS

INTERPRETATION OF MEASUREMENTS BY GLOBAL
MODELING OF EMISSIONS

INPUT CALIBRATED RECONSTRUCTED SPECTRAL IMAGES
BRIGHTNESS GIVEN IN RAYLEIGHS

KEY PARAMETERS

1. TOTAL GLOBAL POWER INPUT AND AVERAGE ENERGY FLUX
2. SIZE AND SHAPE OF THE POLAR CAP
3. SIZE AND SHAPE OF THE AURORAL OVAL
4. TOTAL POWER INPUT AND AVERAGE ENERGY FLUX TO THE POLAR CAP
5. TOTAL POWER INFLUX AND AVERAGE ENERGY FLUX TO THE AURORAL OVAL
6. ACTIVITY INDICES
7. CHARACTERISTIC ENERGY ESTIMATE AT SELECT LOCATIONS
8. SELECTED AURORAL IMAGES

INVESTIGATIVE METHOD

THE UVI IMAGER WILL OBTAIN GLOBAL IMAGES OF THE EARTH AT SEVERAL ULTRAVIOLET WAVELENGTHS. THESE WAVELENGTHS WERE SELECTED SPECIFICALLY TO PROVIDE THE INFORMATION NEEDED TO EXTRACT THE KEY PARAMETERS

THE WAVELENGTHS SELECTED DEFINE EMISSIONS THAT ARE GENERATED:

- BY DIFFERENT ATMOSPHERIC CONSTITUENTS
- AT DIFFERENT ALTITUDES
- WITH DIFFERENT LEVELS OF ABSORPTION



TASK: OBTAIN INTENSITY AT THE
REQUIRED WAVELENGTHS



SPECTRAL DECONVOLUTION SOFTWARE

UVI FILTER WAVELENGTHS AND FUNCTION

λ (nm)	SOURCE SPECIES	FUNCTION
121.6	H L _α	PROTONS & GEOCORONA
130.4	O	O ABUNDANCE
135.6	O	ELECTRON ENERGY SPECTRUM
150 (BROAD)	N ₂ (LBH SHORT)	ELECTRON ENERGY SPECTRUM
150 (NARROW)	N/N ₂	SPECTRAL DECONVOLUTION
165 (BROAD)	N ₂ (LBH MID)	SPECTRAL DECONVOLUTION ELECTRON ENERGY SPECTRUM
185 (BROAD)	N ₂ (LBH LONG)	TOTAL ENERGY INPUT ELECTRON ENERGY SPECTRUM
215	NO	NITRIC OXIDE ABUNDANCE

IMAGE RECOGNITION PACKAGE

IRP

THIS SOFTWARE PACKAGE IS DESIGNED TO RECOGNIZE THE INNER AND OUTER BOUNDARIES OF THE AURORAL OVAL.

TECHNIQUE INTENSITY THRESHOLD/GRADIENT DETECTION

RMS FITTING OF BOUNDARIES WITH SNAKE FUNCTIONS OR SIMILAR TECHNIQUES

THE IRP PACKAGE WILL PROVIDE THE KEY PARAMETERS:

- SIZE (AND SHAPE) OF THE AURORAL OVAL
- SIZE (AND SHAPE) OF THE POLAR CAP

FROM THE SIZE AND SHAPE, THE TOTAL ENERGY INFLUX PACKAGE (TEP) WILL GENERATE THE KEY PARAMETERS:

- TOTAL ENERGY INFLUX TO THE AURORAL OVAL
- TOTAL ENERGY INFLUX TO THE POLAR CAP

TOTAL ENERGY PACKAGE

TEP

THE TEP PACKAGE USES OUTPUT FROM IRP (IMAGE RECOGNITION PACKAGE) TO OBTAIN A MAP OF THOSE PIXELS COMPRISING THE AURORAL OVAL AND THE POLAR CAP.

TEP THEN CALLS EFF (ELECTRON FLUX FUNCTION) TO OBTAIN THE ENERGY FLUX AT EACH PIXEL.

TEP SUMS THE ENERGY FLUX PER PIXEL WITHIN THE DEFINED PIXEL MAP.

FROM THE FOLLOWING MAPS TEP WILL PROVIDE

GLOBAL MAP: TOTAL GLOBAL POWER INPUT DUE TO ELECTRONS

AURORAL OVAL MAP: TOTAL AURORAL POWER INPUT DUE TO
ELECTRONS

POLAR CAP MAP: TOTAL POLAR CAP POWER INPUT DUE TO ELECTRONS

ENERGY FLUX FUNCTION [EFF]

THE EFF ALGORITHM WILL COMPUTE THE ENERGY FLUX GIVEN THE MEASURED LBH-LONG INTENSITY

SPECTRAL DECONVOLUTION PACKAGE

SPECDEC

UNDER THE UVI PROGRAM AN ENTIRE NEW TECHNOLOGY WAS DEVELOPED TO BUILD FILTERS WITH SUFFICIENTLY NARROW BANDPASS AS TO BE ABLE TO ISOLATE KEY SPECTRAL LINES. BECAUSE OF THE PROXIMITY OF SOME OF THE SPECTRAL FEATURES SOME DECONVOLUTION IS REQUIRED. THIS PROCESS UTILIZES THE SPECTRAL INFORMATION FROM SEVERAL FILTERS TO ISOLATE INDIVIDUAL LINES

GRIP POINTS ROUTINE

GP

THIS ROUTINE IS USED TO DEFINE THE LOCATIONS AT WHICH THE CHARACTERISTIC ENERGIES OF THE PRECIPITATING ELECTRONS ARE TO BE COMPUTED. THE DEFAULT GRID WILL BE AXES CENTERED ON THE DAWN-DUSK AND NOON-MIDNIGHT GEOMAGNETIC MERIDIANS.

THE GRID SPACING WILL BE 1 ° TO 5 ° IN LATITUDE WITH SPECIFIED HIGH-LOW BOUNDARIES

CHARACTERISTIC ELECTRON ENERGY

CHEE

THE CHEE PACKAGE WILL COMPUTE THE CHARACTERISTIC ENERGY OF
PRECIPITATING ELECTRONS AT A SPECIFIED SET OF GRID POINTS.
DEFINED BY THE GP ROUTINE

THE DEFAULT GRID WILL BE ALONG AXES SAMPLING FOUR
SECTORS COVERING THE DAWN-DUSK AND NOON-MIDNIGHT MERIDIANS
AT 1 TO 5 ° IN LATITUDE

THIS ROUTINE WILL COMPUTE THE RATIOS:

$I_{1356}/LBH-LONG$ $LBH-SHORT/LBH-LONG$

IT WILL USE LOOK UP TABLES ILLUSTRATED IN FIGURES 1
AND 2 TO ESTIMATE THE CHARACTERISTIC ENERGY AT THE
PRESCRIBED GRID POINTS

Intensity Ratio (OI 1356/LBH 1838)

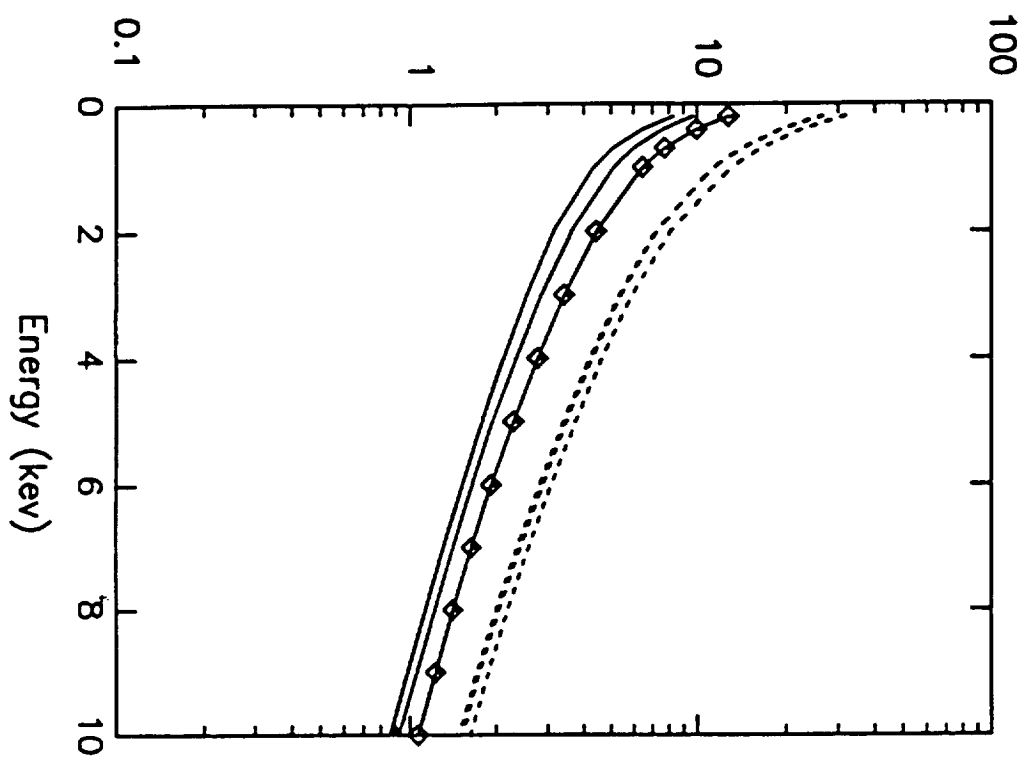


Figure 1

Ratio (LBH 1838/LBH 1464)

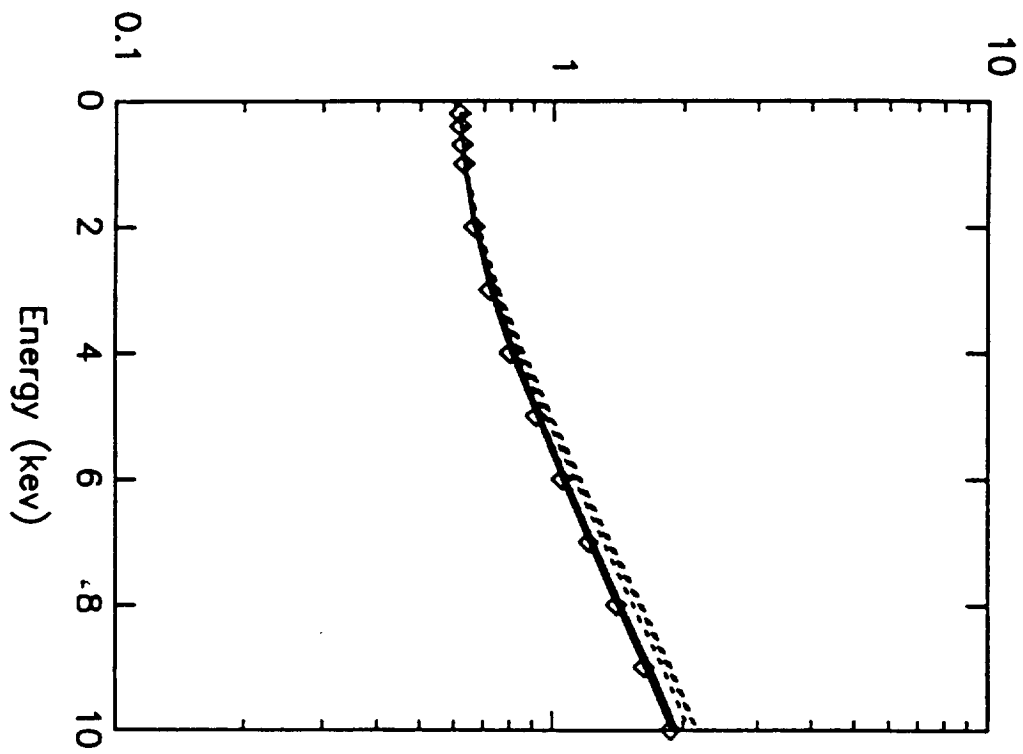


Figure 2

SELECTED AURORAL IMAGE PACKAGE

SAI

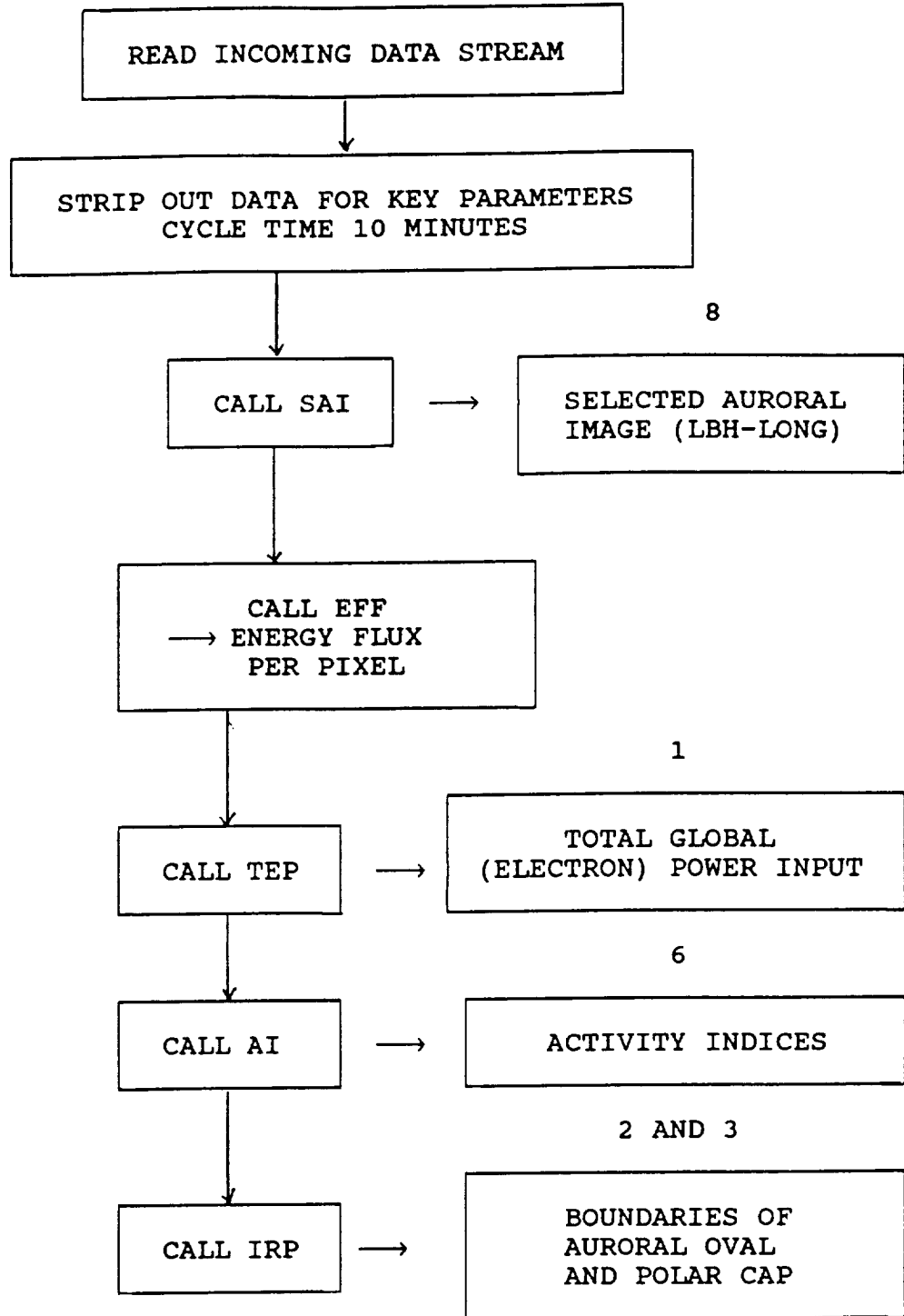
THE SAI PACKAGE WILL GENERATE A FULL INTENSITY COLOR PLOT OF THE LBH-LONG EMISSION (\propto TOTAL ENERGY FLUX) APPROXIMATELY ONCE EVERY 10 MINUTES.

ACTIVITY INDICES

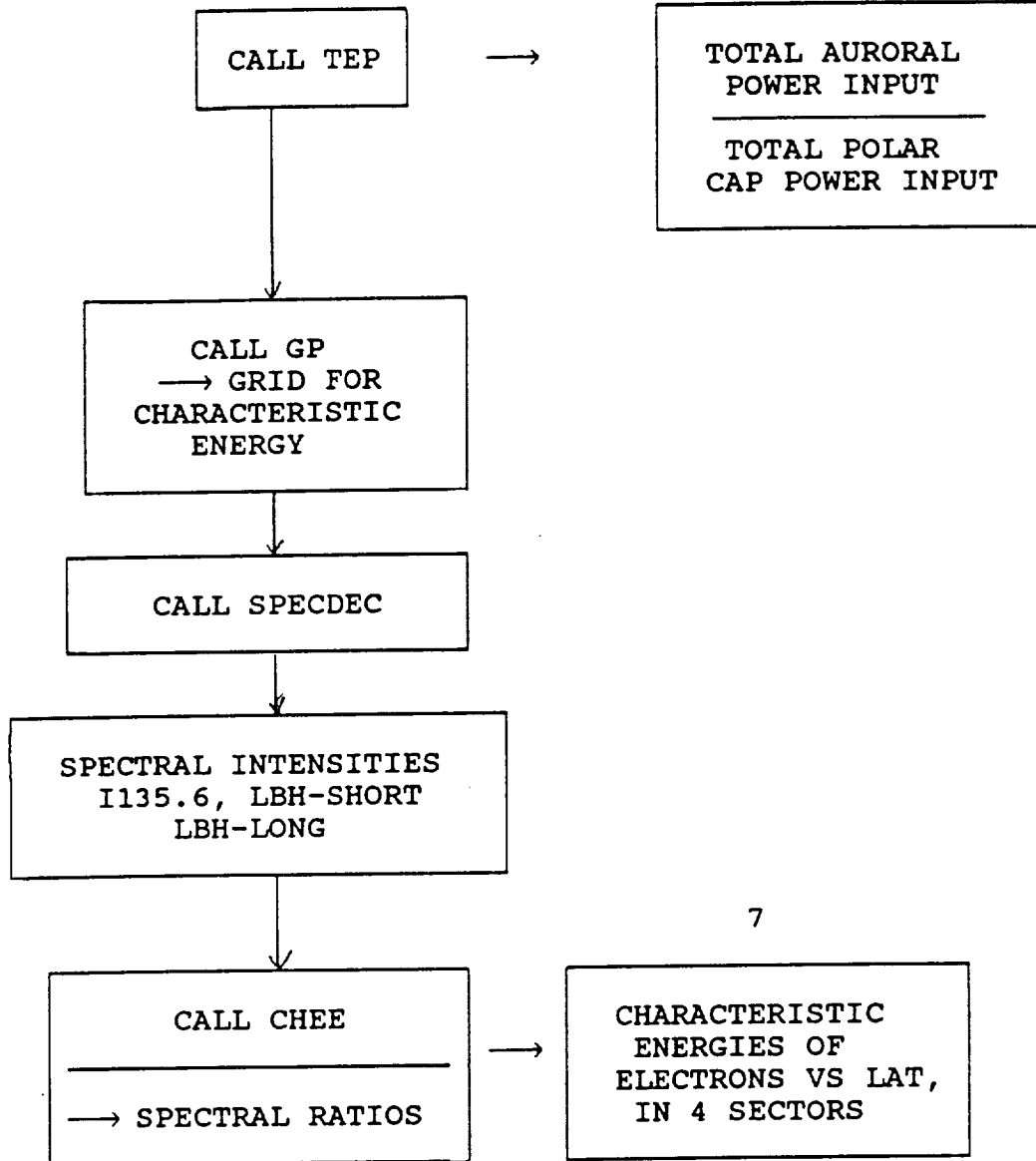
AI

THE AI PACKAGE WILL SCAN THE LBH-LONG IMAGE AT INTERVALS OF 10 MINUTES AND COMPUTE THE PERCENTAGE AREA IN FOUR SECTORS FOR WHICH THE IMAGE BRIGHTNESS EXCEEDS GIVEN THRESHOLDS, E.G. 1KR, 10KR, 100 KR.

KEY PARAMETER FLOW CHART



4 AND 5



FULL-SCALE DATA REDUCTION

THE UVI WILL PRODUCE ONE IMAGE EVERY ~30 SECONDS.

THE NOMINAL OPERATIONAL MODE WILL BE TO CYCLE THROUGH THE FILTERS.

THUS THE MAXIMUM TEMPORAL RESOLUTION POSSIBLE IN THIS MODE IS ~4 MINUTES FOR 8 FILTERS.

THE FULL-SCALE DATA REDUCTION WILL INVOLVE THE FOLLOWING STEPS:

1. GENERATE GLOBAL GRID OF THE ENERGY FLUX USING LBH-LONG.
2. DECONVOLUTE THE SPECTRAL FEATURES.
3. COMPUTE SPECTRAL RATIOS NEEDED FOR CHARACTERISTIC ENERGIES.
4. COMPUTE THE GLOBAL GRID OF CHARACTERISTIC ENERGIES.
 1. USING I135.6/LBH-LONG (SEE FIG. 1)
 2. USING LBH-SHORT/LBH-LONG (SEE FIG. 2)
5. COMPUTE THE GLOBAL NO COLUMN ABUNDANCE RUN I215.
6. COMPUTE THE GEOCORONAL BRIGHTNESS FROM H Ly α .
7. COMPUTE THE GLOBAL COLUMN O ABUNDANCE FROM I130.4

SCIENTIFIC MODELING

THE IMAGES TO BE TAKEN BY THE VISIBLE AND ULTRAVIOLET IMAGERS ON THE ISTP MISSION REPRESENT THE END PRODUCT OF MULTIFARIOUS PROCESSES WHICH RESULT IN THE TRANSPORT OF ENERGETIC PARTICLES FROM THE SUN TO THE EARTH. THE IMAGES THEREFORE CAN BE MAPPED BACK INTO VARIOUS DISTANT REGIONS OF THE SOLAR TERRESTRIAL ENVIRONMENT. THUS MEMBERS OF THE ISTP IIWG WILL HAVE THEIR OWN PARTICULAR INTEREST IN VARIOUS ASPECTS OF THE IMAGING DATABASE.

WE CONCENTRATE HERE ON THE SPECIFIC INTERESTS OF THE UVI TEAM.

UVI SCIENTIFIC GOALS:

PRIMARY GOAL: GLOBAL MODELING OF THE TERRESTRIAL IONOSPHERE,
AIRGLOW AND AURORA.

MODEL: FIELD LINE INTERHEMISPHERIC PLASMA MODEL (FLIP) (TO BE
UPGRADED FOR ISTEP) → GLOBAL EMISSIONS MODEL

MAJOR PREVIOUS LIMITATION: GLOBAL CORPUSCULAR IONIZATION AND
EXCITATION SOURCES WERE UNKNOWN.

NOTE: NO IMAGING SYSTEM OF THE PAST HAS PROVIDED
SUFFICIENT INFORMATION TO GENERATE GLOBAL IONIZATION
AND EXCITATION RATES.

THE UVI WILL DO THIS.

NEEDED DATA: ENERGY FLUX AND CHARACTERISTIC ENERGY PER PIXEL.

FLIP → GLOBAL ALTITUDE PROFILES OF
IONIZATION AND EXTRACTION RATES.

→ GLOBAL MODELING

MID AND LOW LATITUDE MODEL OF THERMOSPHERIC EMISSIONS:

1. $O^+(^2P)$ 7320 Å AND $N_2(^2P)$ 3371 Å

Marsha R. Torr
Space Sciences Laboratory
NASA Marshall Space Flight Center
Huntsville, AL 35812

D. G. Torr and P. G. Richards
University of Alabama in Huntsville
Huntsville, AL 35899

S. P. Yung
Boeing Corporation
Huntsville, AL 35899

Submitted to J. Geophys. Res.

September 1989

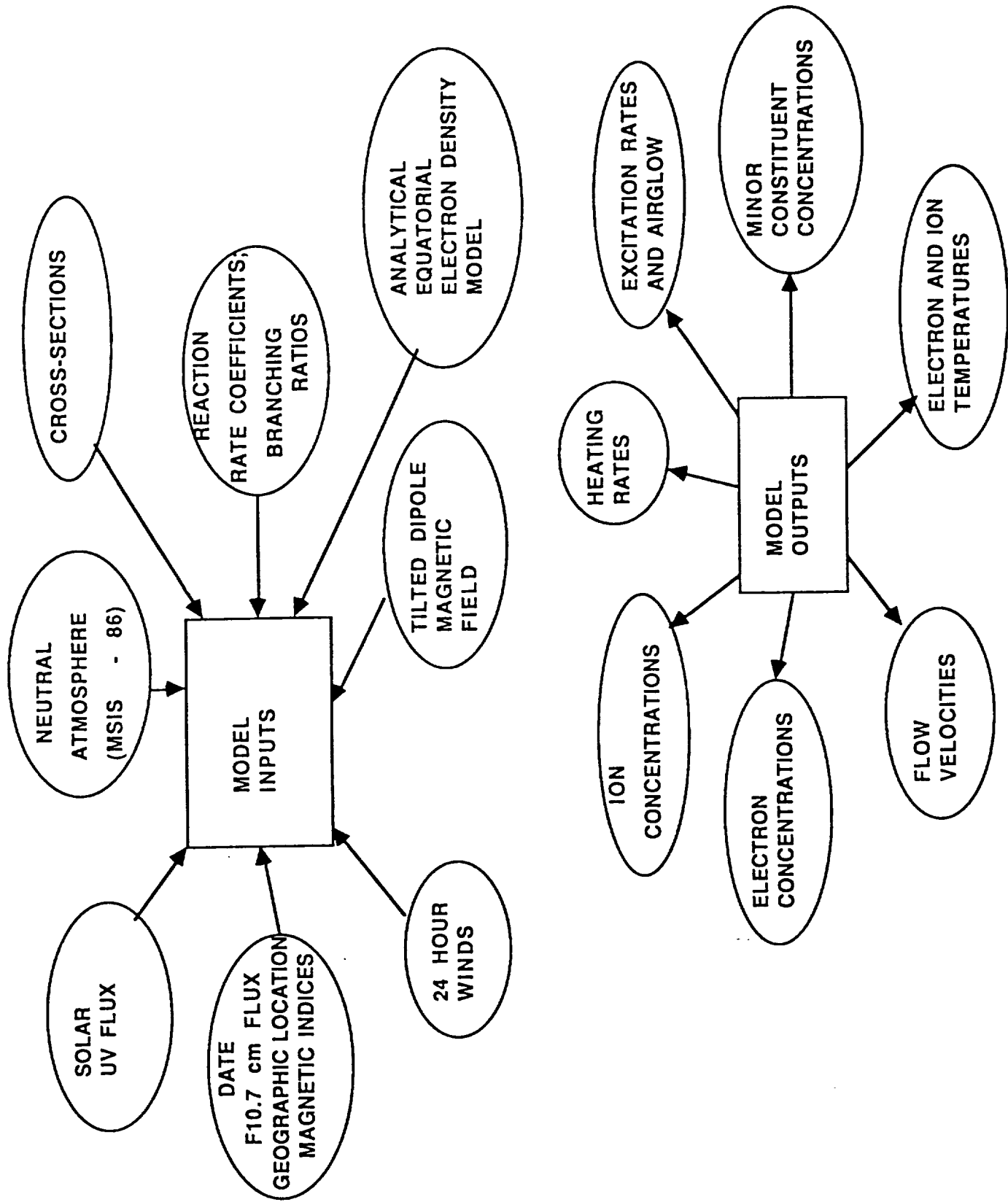


FIGURE 3b

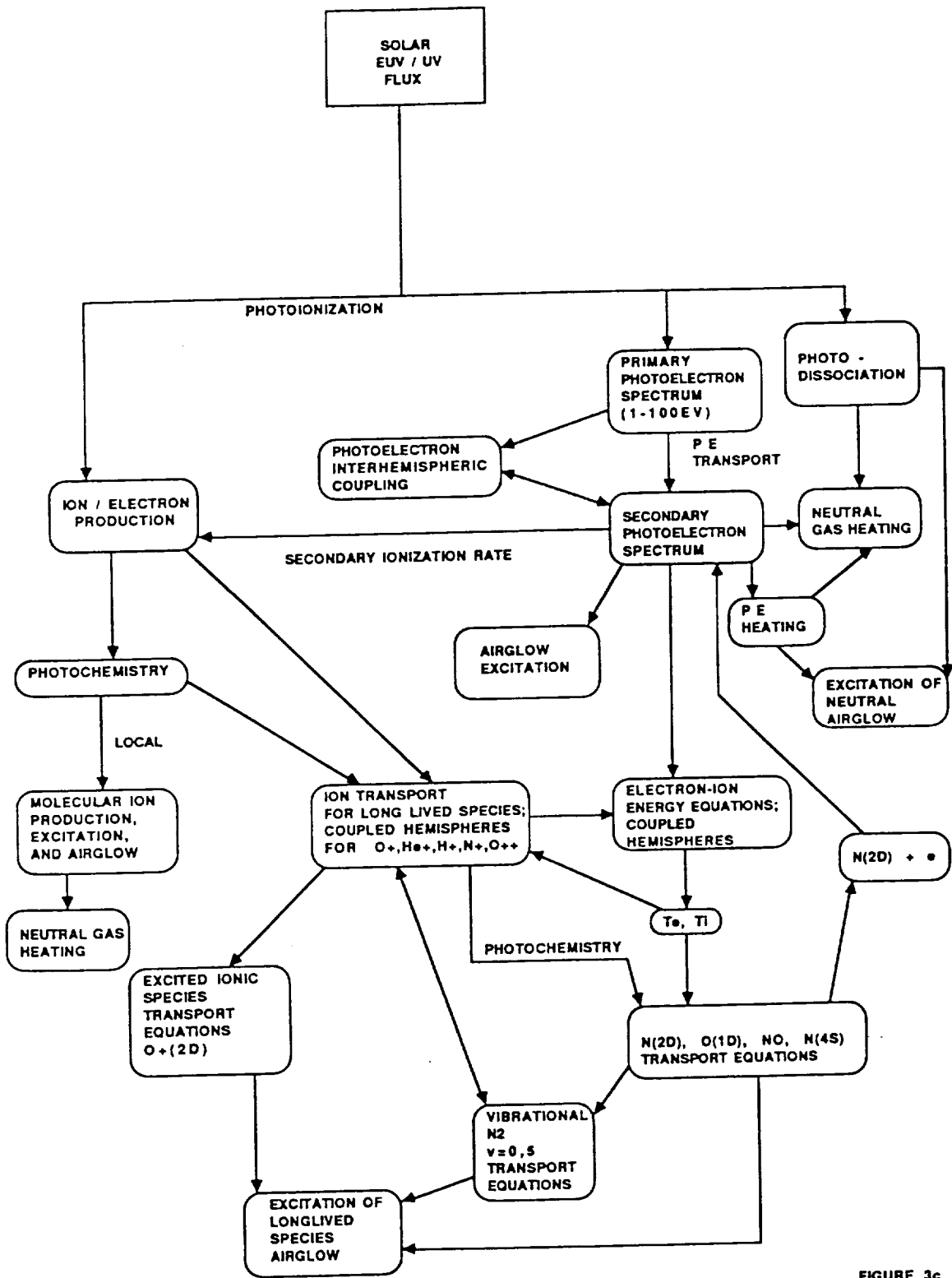


FIGURE 3c

Auroral Modelling of the 3371 Å Emission Rate: Dependence on Characteristic Electron Energy

P. G. RICHARDS

*Computer Science Department and Center for Space Plasma and
Aeronomic Research, University of Alabama in Huntsville*

D. G. TORR

*Physics Department and Center for Space Plasma and Aeronomic
Research, University of Alabama in Huntsville*

We have developed an efficient two-stream auroral electron model to study the deposition of auroral energy and the dependence of auroral emission rates on characteristic energy. This model incorporates the concept of average energy loss to reduce the computation time. Our simple two-stream model produces integrated emission rates that are in excellent agreement with the much more complex multistream model of *Strickland et al.* [1983] but disagrees with a recent study by *Rees and Lummerzheim* [1989] that indicates that the N₂ second positive emission rate is a strongly decreasing function of the characteristic energy of the precipitating flux. Our calculations reveal that a 10 keV electron will undergo approximately 160 ionizing collisions with an average energy loss per collision of 62 eV before thermalizing. The secondary electrons are created with an average energy of 42 eV. When all processes including the backscattered escape fluxes are taken into account, the average energy loss per electron-ion pair is 35 eV in good agreement with laboratory results.

Short title

RICHARDS AND TORR: AURORAL 3371 Å EMISSION RATE

RICHARDS AND TORR: AURORAL 3371 Å EMISSION RATE

The Dependence of Modeled OI 1356 and N₂ LBH
Auroral Emissions on the Neutral Atmosphere

G. A. Germany¹ and M. R. Torr

Space Sciences Laboratory, NASA Marshall
Space Flight Center, Huntsville, Al 35812

P. G. Richards and D. G. Torr

University of Alabama in Huntsville,
Huntsville, Al 35899

¹ This work was done while the author held a National
Research Council-NASA Research Associateship.

Submitted to Journal of Geophysical Research,
September 1989

A Midlatitude Interhemispheric Model of the $O^+(^2P)$
Airglow Emission at 7320 Å

by

Marsha R. Torr
Space Science Laboratory
Marshall Space Flight Center
Huntsville, Alabama 35812

D. G. Torr and P. G. Richards
The University of Alabama in Huntsville
Huntsville, Alabama 35899

Submitted to Geophysical Research Letters

June 1989
Revised: August 1989

ULTRAVIOLET IMAGER
POLAR/GGS

**ISSUES, CONCERNS,
ACTION ITEMS**

PRELIMINARY DESIGN REVIEW

PDR TITLE/007

APPENDIX C

Vacuum ultraviolet thin films.

1: Optical constants of BaF₂,

CaF₂, LaF₃, MgF₂, Al₂O₃, HfO₂,

and SiO₂ thin films

Muamer Zukic, Douglas G. Torr, James F. Spann,
and Marsha R. Torr

a reprint from Applied Optics

Vacuum ultraviolet thin films. 1: Optical constants of BaF_2 , CaF_2 , LaF_3 , MgF_2 , Al_2O_3 , HfO_2 , and SiO_2 thin films

Muamer Zukic, Douglas G. Torr, James F. Spann, and Marsha R. Torr

The optical constants of MgF_2 (bulk) and BaF_2 , CaF_2 , LaF_3 , MgF_2 , Al_2O_3 , HfO_2 , and SiO_2 films deposited on MgF_2 substrates are determined from photometric measurements through an iteration process of matching calculated and measured values of the reflectance and transmittance in the 120–230-nm vacuum ultraviolet wavelength region. The potential use of the listed fluorides and oxides as vacuum ultraviolet coating materials is discussed in part 2 of this paper.

1. Introduction

The optical constants of materials in the vacuum ultraviolet (VUV) region of the spectrum are of interest to several areas of technology. Most applications such as high reflectivity mirrors and bandpass and narrow bandpass interference filters involve thin films. The design of optical instrumentation for space astronomy, space aeronomy, spectroscopy, and the development of electrooptic devices are critically dependent on experimental data for optical constants of thin films.

We report measurements of optical constants of BaF_2 , CaF_2 , LaF_3 , MgF_2 , Al_2O_3 , HfO_2 , and SiO_2 thin films, and MgF_2 bulk material over the 120–230 nm VUV spectral range. The optical properties of MgF_2 film and bulk materials in the vacuum ultraviolet spectral range have been reported in a number of papers,^{1–9} while optical constants of other fluoride and oxide films presented in this paper are reported we believe for the first time for the 120–230 nm wavelength range. It is found that BaF_2 and LaF_3 may be used as high refractive index film materials for constructing a high-low index pair with MgF_2 being the most useful low index material in the VUV.

Optical properties of lanthanide trifluoride films and their potential use as high refractive index film materials in the vacuum ultraviolet were investigated by Lingg *et al.*¹⁰ Although optical constants of lantha-

nide trifluorides for the VUV range are not presented in the paper, plots of the measured transmittance suggest that some of these trifluorides may be useful coating materials for wavelengths as low as 140 nm. Measured transmittances of films obtained by the ion-assisted and conventional depositions are compared and discussed within the paper.

Optical constants of an isotropic material—refractive index n and extinction coefficient k —can be inferred from photometric or polarimetric measurements. Since compensators or transmission polarizers are not generally available in the VUV from 120 to 230 nm, photometric methods are almost exclusively used for obtaining n and k . A number of methods exist for extracting optical constants from reflectance (R) and transmittance (T) measurements at both normal and oblique angles of incidence. Because R and T are very complicated functions of optical constants^{11,12} it is generally impossible to express optical constants as explicit functions of R and T . Most approaches to solving this complicated dependence involve either graphic or numerical techniques.^{13–20} The expressions are nonlinear so the problem may be considered as a numerical exercise in which n and k are found through an iteration process of matching calculated and measured values of reflectance and transmittance. The retrieval of optical constants from measurements of R and T is a well-established approach, but it has not been fully exploited for the VUV regime. The numerical method employed by us is based on the use of a damped least-squares fit approach which is incorporated into a thin film design computer program. The damped least-squares fit technique provides a rapid and reliable retrieval mechanism for n and k in matching measured and calculated quantities. It is surprising that to our knowledge the method has not been fully utilized previously. This fitting method is described in Sec. II.

James Spann and M. R. Torr are with NASA George C. Marshall Space Flight Center, Huntsville, Alabama 35812; the other authors are with University of Alabama in Huntsville, Physics Department, Huntsville, Alabama 35899.

Received 28 September 1989.

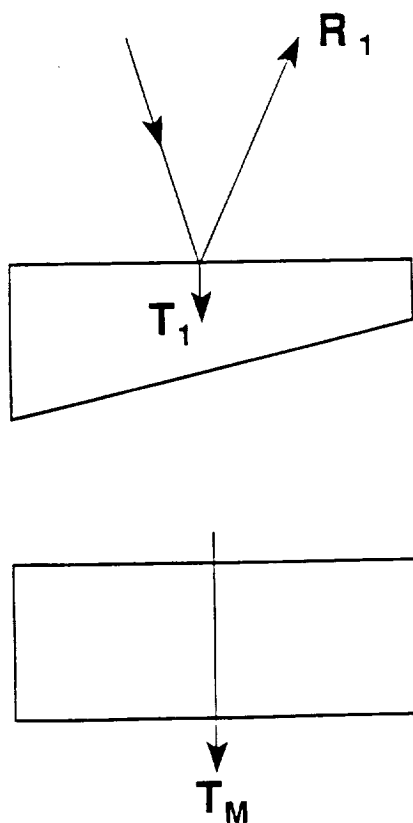


Fig. 1. Measurement of reflectance R_1 from the wedged substrate to avoid contribution from the back side reflectance. Transmittance T_M was measured on a 2-mm thick parallel substrate.

In Sec. III the experimental techniques are presented, including sample preparation and handling, reflectance and transmittance measurements, and deposition of thin films. The optical constants of MgF_2 (bulk) and BaF_2 , CaF_2 , LaF_3 , MgF_2 , Al_2O_3 , HfO_2 , and SiO_2 thin films (deposited on MgF_2 substrates) are given in Sec. IV. Conclusions and a summary are given in Sec. V.

II. Determination of Optical Constants

Beam diagrams for the measurement and calculation of the optical constants of the substrate and substrate with a single thin film are shown in Figs. 1-4. Reflectance R_1 from the semi-infinite media is measured by means of a wedged substrate, and transmittance T_M is measured using a plane-parallel substrate as shown in Fig. 1. From the beam diagram for theoretical derivation of transmittance of the nonabsorbing slab T_0 , shown in Fig. 2, it follows that

$$T_0 = T_1(1 - R_1) + T_1R_1^2(1 - R_1) + T_1R_1^4(1 - R_1) + T_1R_1^6(1 - R_1) + \dots \quad (1)$$

and after multiplying we get

$$T_0 = T_1(1 - R_1 + R_1^2 - R_1^3 + R_1^4 - R_1^5 + R_1^6 + \dots) \quad (2)$$

Using the binomial expression, the transmittance of a thick nonabsorbing slab can be written as

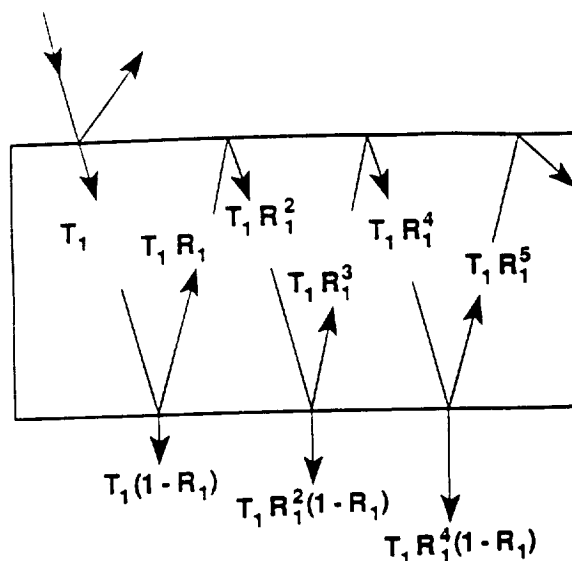


Fig. 2. Beam diagram for theoretical derivation of the transmittance of the nonabsorbing thick slab.

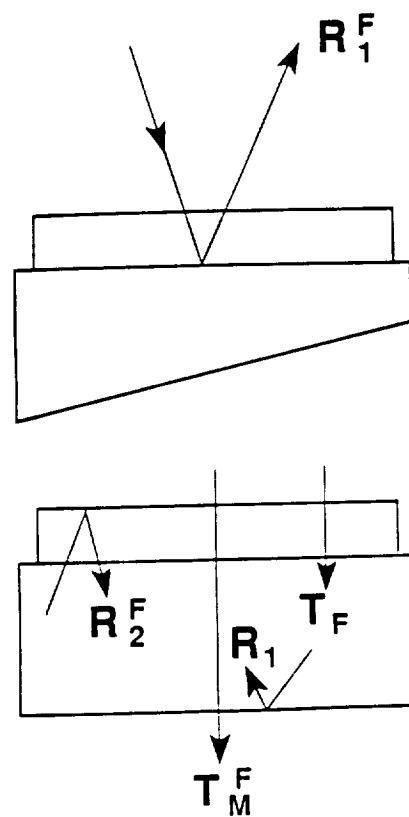


Fig. 3. Measurement of reflectance R_1^F of the single film deposited on the wedged substrate. R_1^F is the calculated reflectance of the single film with the substrate as an incident medium and air as an emerging medium. T_F is the calculated transmittance of the single film sandwiched between two semi-infinite media—air and substrate.

$$T_0 = \frac{T_1}{1 + R_1} = \frac{1 - R_1}{1 + R_1} \quad (3)$$

where R_1 is the measured reflectance from the single side of the substrate. If absorption is present in the

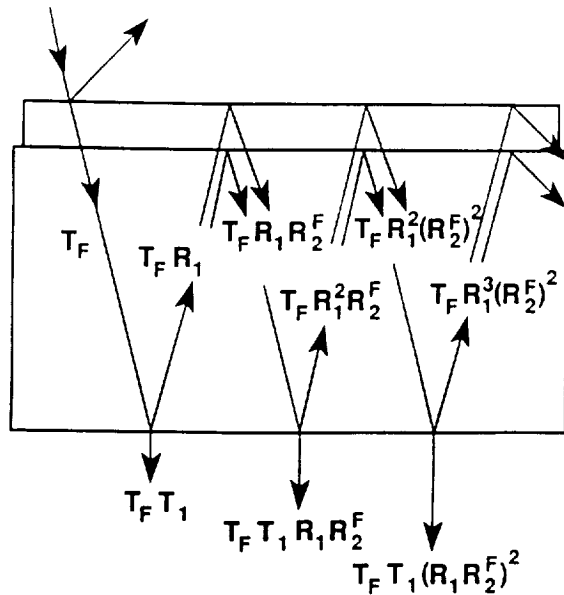


Fig. 4. Beam diagram for theoretical derivation of transmittance T_0^f of the single film deposited on the nonabsorbing substrate.

slab, the measured transmittance is smaller than that calculated theoretically using Eq. (3). If the measured transmittance is denoted as T_M , the total loss due to the substrate absorption is given by

$$A = 1 - \frac{T_M}{T_0} \quad (4)$$

and the correction factor for any other transmittance measurement on this substrate at the particular wavelength by

$$C = \frac{T_M}{T_0} \quad (5)$$

Since the imaginary part of the refractive index of the MgF_2 substrate is very low (of the order of 10^{-7}), it does not affect significantly the measured reflectance R_1 on the wedged substrate. Thus, R_1 can be used in the calculation of refractive index n of the substrate, i.e.,

$$R_1 = \frac{(n-1)^2}{(n+1)^2} \quad (6)$$

$$n = \frac{1 + \sqrt{R_1}}{1 - \sqrt{R_1}} \quad (7)$$

The correction factor given in Eq. (5) can be considered as the intrinsic transmission of the substrate material. Using the known relation for light propagating through the absorbing media

$$I(z) = I(0) \exp(-\alpha z), \quad (8)$$

where the coefficient of absorption α is given by

$$\alpha = \frac{4\pi}{\lambda} k, \quad (9)$$

we get

$$k = -\frac{\lambda}{4\pi z} \ln \left[\frac{I(z)}{I(0)} \right] \quad (10)$$

The ratio $I(z)/I(0)$ is the so-called intrinsic transmission of the medium (no reflection occurs). Using our correction factor C defined in Eq. (6) we have

$$k = -\frac{\lambda}{4\pi D} \ln \left(\frac{T_M}{T_0} \right), \quad (11)$$

where D is the thickness of the substrate. Thus, from measured values R_1 and T_M using Eqs. (7) and (11), optical constants of the weakly absorbing substrate (MgF_2 in our measurements) can be obtained. As an example, consider measurements done at $\lambda = 135$ nm on the MgF_2 substrate with thickness $D = 2$ mm. The measured reflectance of the wedged substrate was $R_1 = 5.5\%$ and the measured transmittance $T_M = 77.4\%$ giving $n = 1.61$ and $k = 6.2 \times 10^{-7}$ which agrees perfectly with known values for bulk MgF_2 in the VUV.⁷

From the beam diagrams for reflectance and transmittance measurements given in Figs. 3 and 4 it follows that T_0^f is

$$T_0^f = T_F T_1 [1 + R_1 R_2^f + (R_1 R_2^f)^2 + (R_1 R_2^f)^3 + (R_1 R_2^f)^4 + \dots], \quad (12)$$

and again using the binomial expansion we obtain

$$T_0^f = \frac{T_F T_1}{1 - R_1 R_2^f} = \frac{T_F (1 - R_1)}{1 - R_1 R_2^f}, \quad (13)$$

where R_2^f is the calculated reflectance of a single film with a substrate as an incident medium and air as an emerging medium (substrate), and T_F is the calculated transmittance of a single film sandwiched between the incident medium and semi-infinite substrate.

Equation (13) gives the transmittance of the single absorbing film on the nonabsorbing substrate. Using the correction factor defined in Eq. (5) we express the transmittance of the substrate with a single film

$$T_C^f = C \frac{T_F (1 - R_1)}{1 - R_1 R_2^f} \quad (14)$$

Using Eq. (14) and calculating R_C^f from the initial values of n and k , we form the merit function F defined as

$$F = W_1 (R_1^f - R_C^f)^2 + W_2 (T_M^f - T_C^f)^2, \quad (15)$$

where R_1^f and R_C^f are the measured and calculated reflectances of the film on the wedged (semi-infinite) substrate; T_M^f and T_C^f are measured and calculated values of transmittance through the plane-parallel substrate with a single film; W_1 and W_2 are the weighting factors chosen according to the relative accuracy of the R and T measurements for each wavelength.

Merit function F is then minimized using a damped least-squares approach. This is implemented as a subroutine in a computer program for thin film design.²¹ Reflectances R_1^f and R_C^f and transmittance T_C^f are calculated using values of n and k at the particular wavelength. Merit function

$$F = F[R_1^f, R_C^f, T_M^f, T_C^f, (R_2^f)] \quad (16)$$

depends on five variables of which three are dependent on n and k of the film. Thus, the minimum value of F has a high probability of providing accurate values for the optical constants of the thin film.

To minimize uncertainties in the optical constant determination, several single films of the same material but with different thicknesses are deposited on separate substrates. The total merit function F_T is then given by

$$F_T = \sum_{n=1}^L F_n \quad (17)$$

where F_n is the merit function of the n th film defined in Eq. (15) and L is the total number of single films with different thicknesses deposited either on the same type of substrate material or on several different types of substrate material.

III. Experimental Techniques

A. Sample Preparation and Handling

All depositions are made on 12.7-mm diam by 2-mm thick magnesium fluoride substrates with root mean square roughness (usually referred as rms²³) <2.5 nm. To eliminate the contribution of the back side reflection to the reflectance measurements, some of the substrates have a 3° bias. The substrates were cleaned by the supplier (Acton Research Corp., Acton, MA) using the following procedure: optical soap wash, water rinse, ethanol soak then ultrasonic bath, fresh ethanol rinse, and finally a Freon rinse.

The substrates were shipped in Delrin holders wrapped with lens paper and were only removed immediately prior to deposition. After deposition, the substrates were allowed to cool to 40°C, and the vacuum chamber was vented with dry nitrogen. The substrates were kept in the flow of dry nitrogen and placed in a stainless steel container to prevent contamination due to exposure. All depositions were made at the University of Alabama in Huntsville Optical Astronomy Laboratory and the transmittance and reflectance measurements were made at Atomic Physics Branch of the Marshall Space Flight Center.

B. Deposition of Thin Films

The vacuum system consists of a cryo pump and a sorption pump giving an oil-free environment for all depositions and therefore providing a very low probability for hydrocarbon contamination of the films.

The film materials BaF₂, CaF₂, and LaF₃ were prepared for vacuum deposition by CERAC with a typical purity of 99.9%. Al₂O₃ (99.5%), SiO₂ (99.98%), and MgF₂ (99.95%) are standard Balzers coating materials while HfO₂ with a purity of 99.5% was prepared by EM Chemicals.

The fluoride films were deposited with low deposition rates on heated substrates. To reoxidize dissociated molecules of the oxides Al₂O₃, HfO₂, and SiO₂, the films were deposited at a low deposition rate on heated substrates in an oxygen residual atmosphere. The temperature of the substrate was monitored with a Chromel-Alumel thermocouple attached to the aluminum substrate ring holder. The substrate and its ring holder were placed in a 6-mm thick stainless steel plate

Table I. Deposition Conditions

Material	P_n (Torr)	P (Torr)	D_R (nm/s)	d (nm)
BaF ₂	9.5×10^{-7}	1.5×10^{-6}	0.16	53.0
CaF ₂	8.5×10^{-7}	2.5×10^{-6}	0.20	99.0
LaF ₃	8.5×10^{-7}	2.0×10^{-6}	0.14	51.0
MgF ₂	8.5×10^{-7}	2.5×10^{-6}	0.23	68.0
Al ₂ O ₃ ^a	8.5×10^{-7}	1.0×10^{-4}	0.10	112.0
HfO ₂	8.5×10^{-7}	1.5×10^{-4}	0.10	30.0
SiO ₂	9.5×10^{-7}	1.2×10^{-4}	0.10	51.0

^a Oxygen leaked into the chamber during deposition of the oxides.

with 40-cm diameter. Further details about the conditions of depositions are given in Table I.

The depositions were made with an electron gun. The gun had a fixed voltage of 10 kV and low power depositions were maintained by supplying low current to the gun. The source-to-substrate distance is 50 cm and the source-to-thickness monitor distance was 35 cm. The thickness control and rate measurements during film depositions were done with the Kronos Digital Film Thickness Monitor QM-300 series and the Kronos Deposition Rate/Thickness Output Accessory RI-100/RO-200 series with FFT-300 transducer.

The vacuum chamber geometry provided excellent calibration constants C_c for all film materials. The calibration constant C_c is defined as the ratio of the film thickness expressed in transducer counts (hertz) and the measured thickness in nanometers, i.e., the number of counts (hertz) needed to obtain a 1-nm thick film. The values of C_c varied from 44.09 Hz/nm for MgF₂ up to 72.23 Hz/nm for LaF₃. The physical thickness measurements of the films were made with a Talystep stylus profilometer. The stylus radius is 2 μm and the stylus loading is 1 mg.

The physical thicknesses for each material are chosen according to the following criteria:

- nonzero transmittance measurements over most of the considered spectrum;
- no overlap of maxima and minima for R and T measurements; and
- at least one measurement must be close to the possible physical thickness in the design of either a multilayer interference filter or an absorbing single layer coating.

C. Photometric Measurements

Transmittance and reflectance measurements were performed in a hydrocarbon-free vacuum system at pressures below 10⁻⁵ Torr. A sealed deuterium lamp with a MgF₂ window was used in tandem with a 0.2-m monochromator producing a beam with 1-nm FWHM spectral resolution. Folding and collimating optics were used to produce a 1- × 0.75-cm reference beam which is incident on an eight-position filter wheel containing the substrates. Different detectors were used for transmittance and reflectance measurements. Each detector consists of a sodium salicylate-coated Pyrex window placed in front of a bialkali photometer. A schematic diagram of the system optics is shown in Fig. 5.

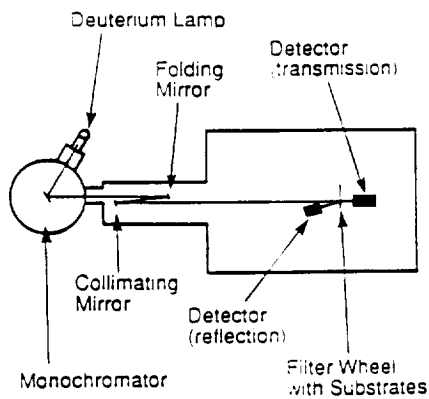


Fig. 5. Schematic diagram of the single beam VUV spectrophotometer.

Absolute transmittance and reflectance were measured by determining the ratio of the transmitted or reflected beam intensity and the unattenuated incident beam intensity. For reflectance measurements, the unattenuated beam intensity was determined by the measured reflectance of a calibrated VUV-enhanced aluminum mirror located in one of the filter wheel positions. The reflectance measurements were made at a 6° angle of incidence.

The aluminum mirror was calibrated by Acton using the ACE-type²³ self-calibrating VUV photometer. The estimated error of this instrument for reflectance measurements is $<2\%$. The uncertainties associated with the thin film thickness, reflectance, and transmittance measurements resulted in the total uncertainty for optical constants determination of the order of $\pm 5\%$. This uncertainty is derived from discrepancies between the theoretically and experimentally obtained spectral performance of deposited VUV multilayer filters. In the theoretical calculation, films are assumed to be homogeneous, isotropic, and bounded by two infinite ideal planes. Thus, the discrepancy between theory and experiment is caused by both physical effects (such as film inhomogeneity, surface and volume scattering, diffusion, and possible contamination) neglected in the theoretical calculation and the uncertainty in the optical constant determination. Taking all this into account we might say that the maximum uncertainty for optical constant determination is $<5\%$.

IV. Optical Constants

A. MgF_2 Substrate

The reflectance and transmittance measurements shown in Fig. 6 were made on wedged and 2-mm thick parallel substrates, respectively. Optical constants n and k shown in Fig. 7 were determined using Eqs. (8) and (12).

B. Fluoride Films

The temperature of the MgF_2 substrate during deposition of the fluoride films is 250°C . The pressure before (P_0) and during deposition (P) as well as the

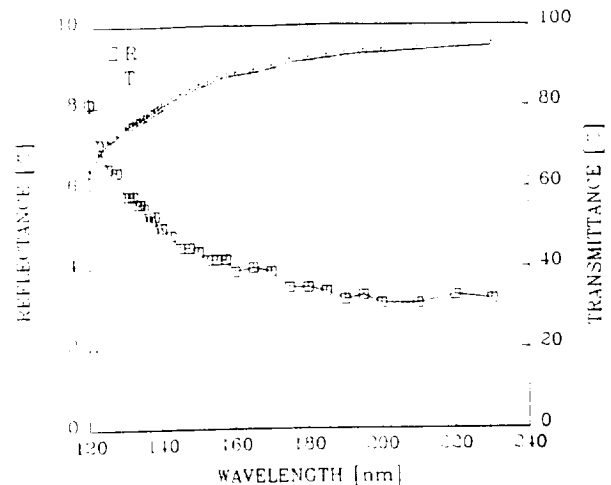


Fig. 6. Reflectance R and transmittance T_M measurements on the MgF_2 wedged and a 2-mm thick parallel substrate, respectively.

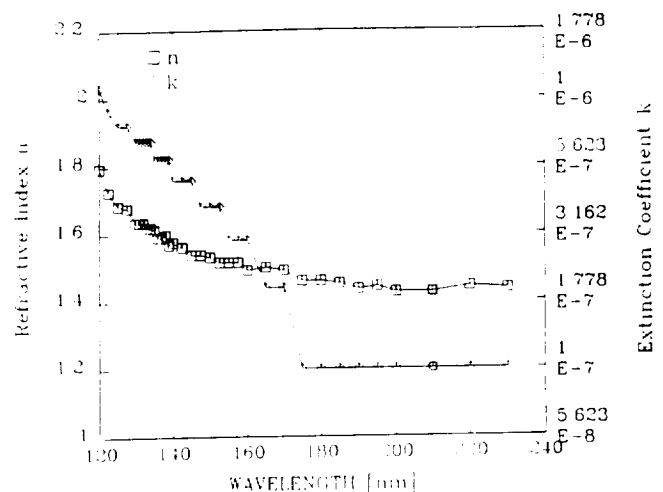


Fig. 7. Optical constants of the MgF_2 substrate determined using Eqs. (8) and (12).

deposition rates (D_R) and physical thicknesses of the films (d) are listed in Table I. Single sets of the R and T measurements of BaF_2 , CaF_2 , LaF_3 , and MgF_2 films deposited on MgF_2 substrates are given in Figs. 8, 10, 12, and 14, respectively. The corresponding optical constants determined from at least two independent R and T measurements [Eq. (19)] are given in Figs. 9, 11, 13, and 15.

From the reflectance and transmittance curves of a 53-nm single film of BaF_2 , it follows that this coating material can be used for wavelengths longer than 135 nm. Even a single film of BaF_2 could be used as a cut-on filter if wavelengths shorter than 130 nm are not desired. Refractive index n has values between 1.87 and 2 for wavelengths from 125 to 135 nm and it is higher than 1.7 throughout the region from 140 to 210 nm, increasing up to 1.98 at 230 nm. Extinction coefficient k has values of the order of 10^{-2} for wavelengths from 140 to 230 nm.

The measured reflectance and transmittance of a 99-

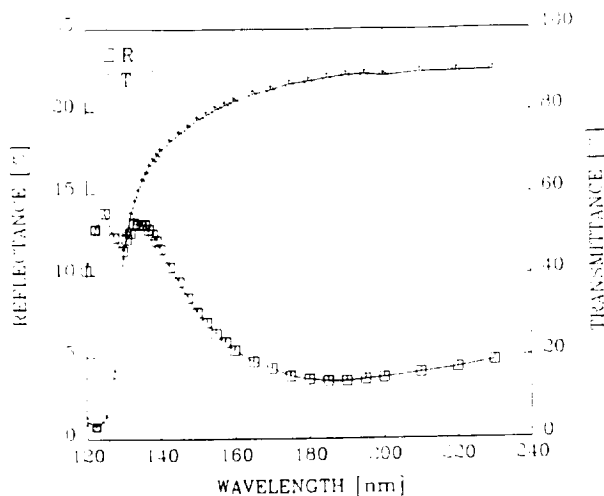


Fig. 8. Reflectance R_f^f and transmittance T_M^f of a 53-nm thick BaF_2 film deposited on the MgF_2 substrate.

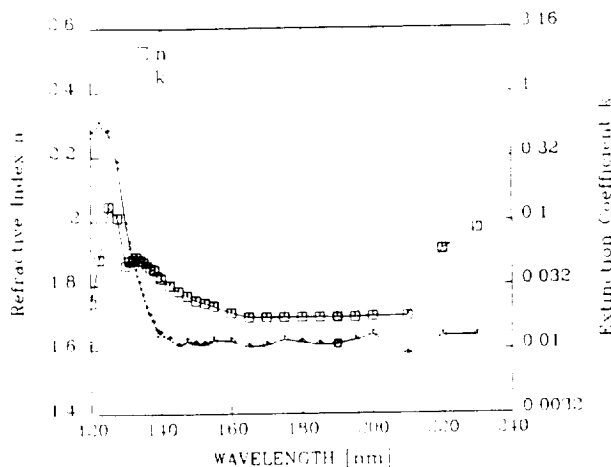


Fig. 9. Optical constants of BaF_2 determined from R and T measurements of 53-, 45-, and 94.5-nm thick films deposited on the MgF_2 substrate.

nm thick CaF_2 film indicate low values of refractive index n and a relatively small extinction coefficient k for wavelengths longer than 135 nm. The values of refractive index n of CaF_2 are lower than 1.3 for $\lambda \geq 180$ nm, and the k values are of the order of 10^{-2} for the same wavelength region. Low values of the refractive index make CaF_2 suitable for use as the alternative low index material for the longer wavelengths of the VUV.

The material with the highest values of refractive index among all the fluorides $n \geq 1.85$ within the 135–230 nm range of the VUV wavelengths is LaF_3 . The extinction coefficient has values lower than 2.2×10^{-2} for $\lambda \geq 145$ nm. Compared with other fluoride and oxide coating materials LaF_3 seems to be the best choice for the high index material in the considered spectral region.

Magnesium fluoride films have extinction coefficient values lower than 10^{-4} throughout the entire 140–230-nm wavelength region. This makes MgF_2 the

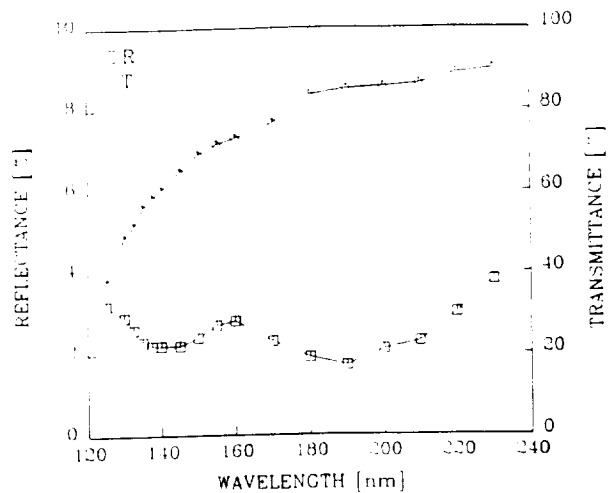


Fig. 10. Reflectance R_f^f and transmittance T_M^f of a 99-nm thick CaF_2 film deposited on the MgF_2 substrate.

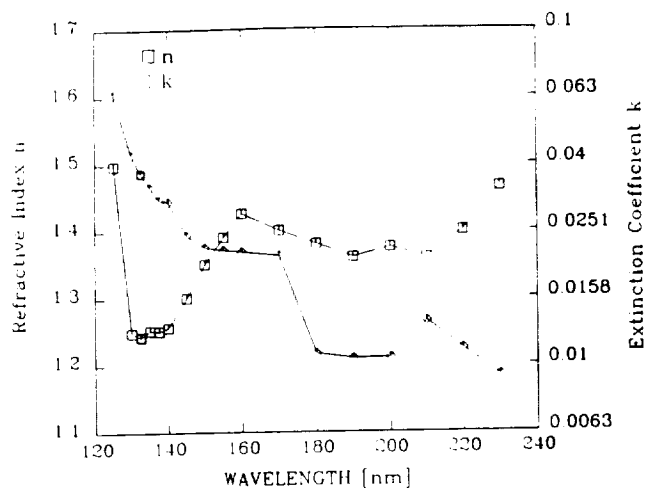


Fig. 11. Optical constants of CaF_2 determined from R and T measurements of 99- and 54.5-nm thick films deposited on the MgF_2 substrate.

most attractive low index material for the VUV. The n and k values of MgF_2 film deposited on the substrate heated up to 250°C reported by Wood *et al.*⁷ at 121.6 nm are $n = 1.7 \pm 0.1$ and k close to 0.01 are in good agreement with values reported here. Unfortunately, we are unable to compare these n and k values of MgF_2 with the values obtained by some other authors because either the MgF_2 films were prepared in different conditions or insufficient experimental data were provided by the other workers.^{1–10}

C. Oxide Films

The temperature of the MgF_2 substrate during deposition of oxide films was 300°C . The deposition conditions P_0 , P , and D_R , as well as the physical thicknesses of films d , are listed in Table I. The measured spectral curves of R and T for Al_2O_3 , HfO_2 , and SiO_2 films deposited on MgF_2 substrates are shown in Figs. 16, 18, and 20 while the corresponding optical con-

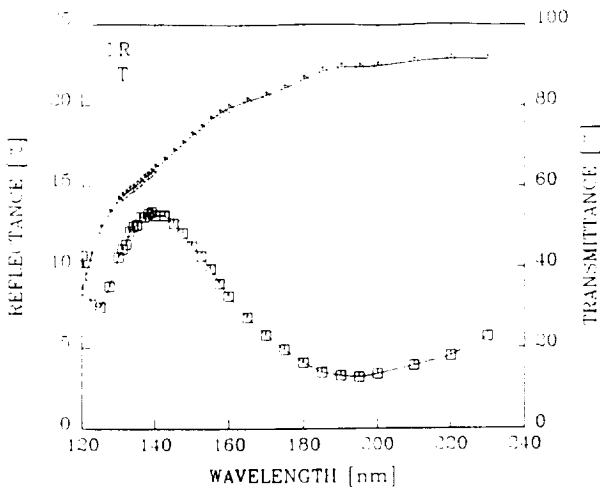


Fig. 12. Reflectance R_f^F and transmittance T_M^F of a 51-nm thick LaF_3 film deposited on the MgF_2 substrate.

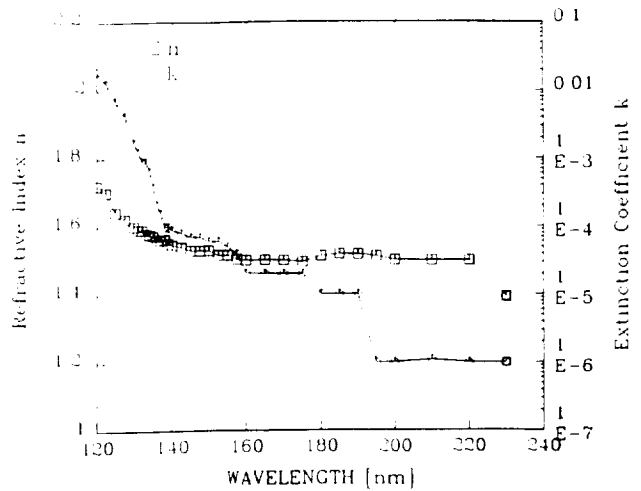


Fig. 15. Optical constants of MgF_2 determined from R and T measurements of 68- and 109-nm thick films deposited on the MgF_2 substrate.

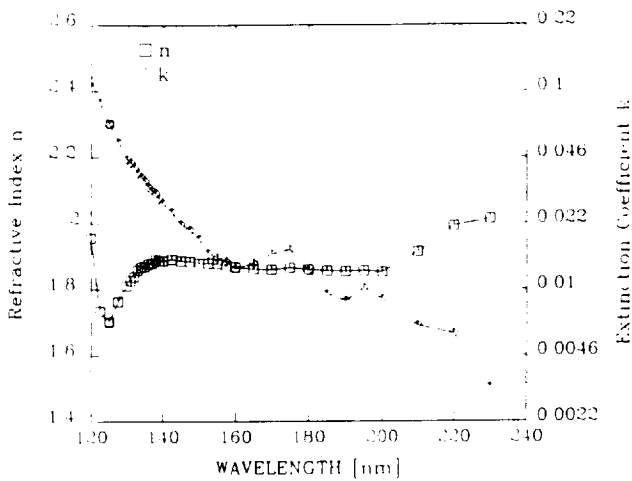


Fig. 13. Optical constants of LaF_3 determined from R and T measurements of 51-, 68-, and 83-nm thick films deposited on the MgF_2 substrate.

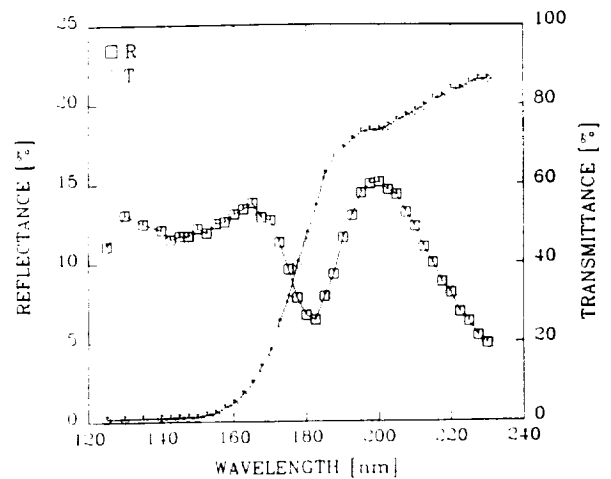


Fig. 16. Reflectance R_f^F and transmittance T_M^F of a 112-nm thick Al_2O_3 film deposited on the MgF_2 substrate.

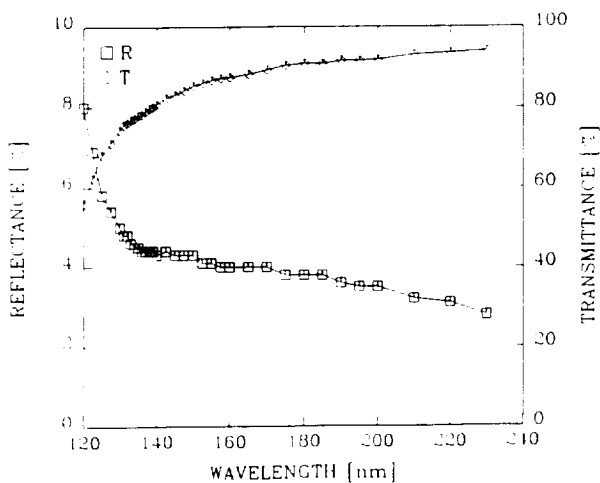


Fig. 14. Reflectance R_f^F and transmittance T_M^F of a 68-nm thick MgF_2 film deposited on the MgF_2 substrate.

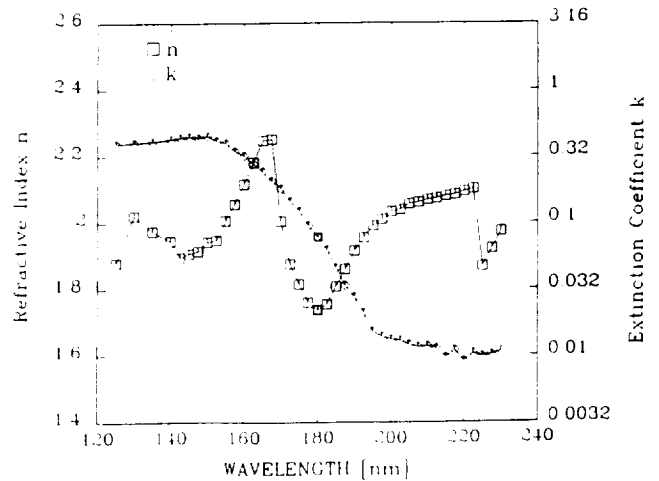


Fig. 17. Optical constants of Al_2O_3 determined from R and T measurements of 112-, 152-, and 99-nm thick films deposited on the MgF_2 substrate.

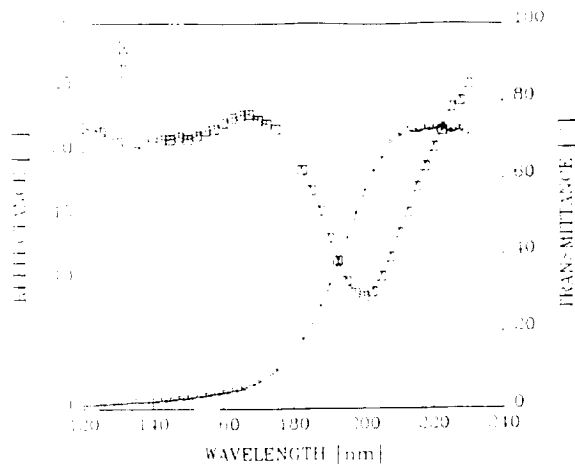


Fig. 18. Reflectance R_f^f and transmittance T_M^f of a 30-nm thick HfO_2 film deposited on the MgF_2 substrate.

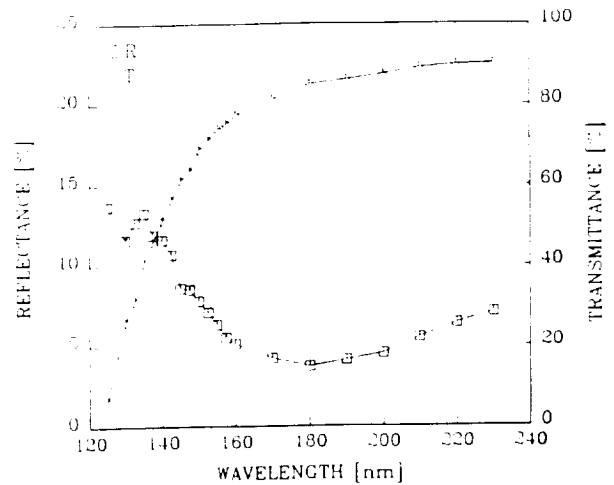


Fig. 20. Reflectance R_f^f and transmittance T_M^f of a 51-nm thick SiO_2 film deposited on the MgF_2 substrate.

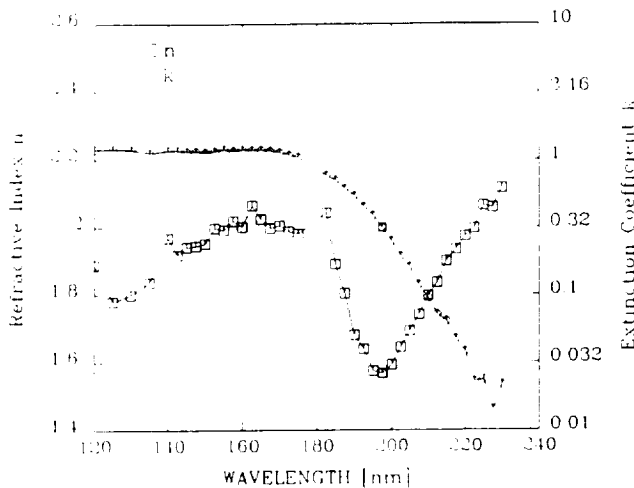


Fig. 19. Optical constants of HfO_2 determined from R and T measurements of 30- and 48.5-nm thick films deposited on the MgF_2 substrate.

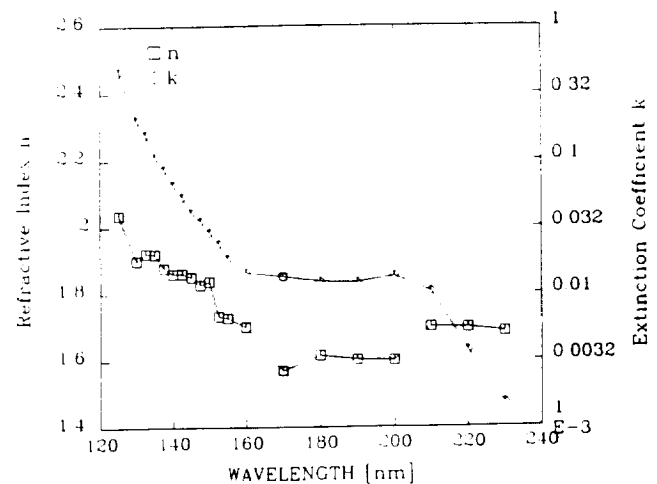


Fig. 21. Optical constants of SiO_2 determined from R and T measurements of 131-, 121-, and 51-nm thick films deposited on the MgF_2 substrate.

stants are given in Figs. 17, 19, and 21, respectively.

The transmittance curve of a 112-nm thick Al_2O_3 single film suggests that this material could possibly be used for the design of absorption edge filters with cut-on wavelengths between 160 and 180 nm depending on the thickness of the Al_2O_3 film. The values of refractive index n are higher than 1.85 for almost the entire region from 120 to 230 nm while the k values are higher than 10^{-1} for $120 \text{ nm} \leq \lambda \leq 175 \text{ nm}$.

The HfO_2 film has the highest extinction coefficient (shown in Fig. 19) and it does not seem that this material could be useful for the vacuum ultraviolet wavelength region, particularly for wavelengths below 200 nm.

The values of refractive index n of SiO_2 films are very close to the values of bulk SiO_2 , while the k values are an order of magnitude higher.²⁴ The refractive index $n \geq 1.8$ for $125 \text{ nm} \leq \lambda \leq 150 \text{ nm}$ and decreases gradually to 1.6 at 200 nm. Extinction coefficient k is

of the order of 10^{-1} for $120 \text{ nm} \geq \lambda \geq 135 \text{ nm}$ which makes SiO_2 a useful material for the design of a single layer absorption edge filter with cut-on wavelengths within the interval from 125 to 135 nm depending on the relative thickness of SiO_2 film.

V. Summary

We demonstrated that iterative mathematical modeling of transmittances and reflectances measurements provides a reliable way for determining the optical constants of thin films deposited on the weakly absorbing substrates. In part 2, proof of the validity of the approach is demonstrated by design and fabrication of multilayer coatings. The model is used for the VUV wavelength region but its application extends over the whole visible and IR spectrum whenever a substrate has a low value of extinction coefficient k such that its effects on the substrate reflectance are negligible.

The fluoride film materials have generally lower extinction coefficients than the oxides. High values of refractive index n make LaF_3 and BaF_2 useful materials for the VUV, particularly for constructing a high-low index pair with MgF_2 being the most useful low index material. The designs of the VUV coatings such as narrowband pass, and narrowband reflection filters are possible with these materials.

SiO_2 coating material, among other oxides measured in the VUV, seems to be the most applicable for design of multilayer stacks such as the narrowband reflection filters. Al_2O_3 coating material may be used for the design of absorption edge filters for $\lambda \geq 160$ nm, while HfO_2 becomes a useful high index material for wavelengths longer than 230 nm.

We are indebted to Lennart Petterson for his assistance in measuring the reflectance and transmittance of the single films and filters and to Kathy Waites for editing and proofreading the manuscript. The first author would like to thank the Physics Department of the University of Alabama in Huntsville (UAH) for the graduate student assistantship received during this study, and the ZRAK Optics Co. in Sarajevo, Yugoslavia, for additional financial support.

This work was supported by NASA contracts NAS8-37586 and NAS8-37576, and NASA grants NAG8-639 and NAG8-086.

References

1. E. T. Hutcheson, G. Hass, and J. T. Cox, "Effect of Deposition Rate and Substrate Temperature on the Vacuum Ultraviolet Reflectance of MgF_2 - and LiF -Overcoated Aluminum Mirrors," *Appl. Opt.* **11**, 2245-2248 (1972).
2. T. T. Cole and F. Oppenheimer, "Polarization by Reflection and Some Optical Constants in the Extreme Ultraviolet," *Appl. Opt.* **1**, 709-710 (1962).
3. G. Stephan, Y. Le Calvez, J. C. Lemonier, et Mme S. Robin, "Propriétés optiques et spectre électronique du MgF_2 et du CaF_2 de 10 à 48 eV," *J. Phys. Chem. Solids* **30**, 601-608 (1969).
4. A. S. Barriere and A. Lachter, "Optical Transitions in Disordered Thin Films of the Ionic Compounds MgF_2 and AlF_3 as a Function of Their Conditions of Preparation," *Appl. Opt.* **16**, 2865-2871 (1977).
5. B. Vodar, "Absorption Spectra of Gases and Absorption and Reflection Spectra of Solids," (A review of work at Bellevue), *J. Quant. Spectrosc. Radiat. Transfer* **2**, 393-412 (1962).
6. M. W. Williams, R. A. MacRae, and E. T. Arakawa, "Optical Properties of Magnesium Fluoride in the Vacuum Ultraviolet," *J. Appl. Phys.* **38**, 1701-1705 (1967).
7. O. R. Wood II, H. G. Craighead, J. E. Sweeney, and P. J. Maloney, "Vacuum Ultraviolet Loss in Magnesium Fluoride Films," *Appl. Opt.* **23**, 3644-3649 (1984).
8. A. Bideau-Mehu, Y. Guern, and R. Abjean, "Influence of the Optical Constants on Fabry-Perot Coatings Characteristics in the Vacuum Ultraviolet Wavelength Range," in *American Institute of Physics Handbook*, D. E. Gray, Ed. (McGraw-Hill, New York, 1984), pp. 265-267.
9. E. Spiller, "Interference Filters for the Ultraviolet and the Surface Plasmon of Aluminum," *Appl. Opt.* **13**, 1209-1225 (1974).
10. L. J. Lingg, J. D. Targove, J. P. Lehan, and H. A. Macleod, "Ion-Assisted Deposition of Lanthanide Trifluorides for VUV Applications," *Proc. Soc. Photo-Opt. Instrum. Eng.* **818**, 86-92 (1987).
11. O. S. Heavens, "Measurement of Optical Constants of Thin Films," *Phys. Thin Films* **2**, 193-238 (1964).
12. M. Born and E. Wolf, *Principles of Optics* (Pergamon, New York, 1980), p. 611.
13. D. P. Arndt *et al.*, "Multiple Determination of the Optical Constants of Thin-Film Coating Materials," *Appl. Opt.* **23**, 3571-3596 (1984).
14. J. M. Bennett and M. J. Booty, "Computational Method for Determining n and k for a Thin Film from the Measured Reflectance, Transmittance, and Film Thickness," *Appl. Opt.* **5**, 41-43 (1966).
15. J. M. Bennett and M. J. Booty, "Computer Program for Determining Optical Constants of a Film on an Opaque Substrate," *Appl. Opt.* **8**, 2366-2368 (1969).
16. W. N. Hansen, "Optical Characterization of Thin Films: Theory," *J. Opt. Soc. Am.* **63**, 793-801 (1973).
17. L. Ward, "A Survey of the Accuracies of Some Methods for the Determination of the Optical Constants of Thin Films," *Opt. Acta* **32**, 155-167 (1985).
18. M. C. Gupta, "Optical Constant Determination of Thin Films," *Appl. Opt.* **27**, 954-956 (1988).
19. F. Abeles, "Methods for Determining Optical Parameters of Thin Films," *Prog. Opt.* **2**, 249-288 (1963).
20. P. O. Nilsson, "Determination of Optical Constants from Intensity Measurements at Normal Incidence," *Appl. Opt.* **7**, 435-442 (1968).
21. M. Zukic, "Damped Least Squares Technique for the Design of Optical Multilayer Filters," M.S. Thesis, Imperial College, London (1984).
22. J. M. Bennett, "Scattering and Surface Evaluation Techniques for the Optics of the Future," *Opt. News* **7**, 17-27 (1985).
23. J. M. Zwiner, "Space Station Induced Environment Monitoring," NASA Conference Publication 3021.
24. H. R. Philipp, "Silicon Dioxide (SiO_2) (Glass)," in *Handbook of Optical Constants of Solids*, E. D. Palik, Ed. (Academic, Orlando, FL, 1985), p. 749.

Vacuum ultraviolet thin films.

**2: Vacuum ultraviolet all-dielectric
narrowband filters**

Muamer Zukic, Douglas G. Torr, James F. Spann,
and Marsha R. Torr

a reprint from Applied Optics

Vacuum ultraviolet thin films. 2: Vacuum ultraviolet all-dielectric narrowband filters

Muamer Zukic, Douglas G. Torr, James F. Spann, and Marsha R. Torr

We report the design and performance of narrowband transmission filters employing the rapidly changing extinction coefficient that is characteristic of BaF_2 and SiO_2 films within certain wavelength intervals in the vacuum ultraviolet. We demonstrate the design concept for two filters centered at 135 nm for BaF_2 and at 141 nm for SiO_2 . It is found that these filters provide excellent narrowband spectral performance when combined with narrowband reflection filters. The filter centered at 135 nm has a peak transmittance of 24% and a bandwidth of 4 nm at full width at half-maximum for collimated incident light. The transmittance for $\lambda_0 \leq 130$ nm is $<0.1\%$ and for $138 \leq \lambda_0 \leq 230$ nm the average transmittance is $<3\%$. Another filter centered at 141 nm has a peak transmittance of 25% and a bandwidth of 3.5 nm.

I. Introduction

The design of all-dielectric multilayer interference filters for the vacuum ultraviolet (VUV) wavelength region from 120 to 230 nm is limited by the lack of film materials with suitable optical constants. Film materials such as MgF_2 and LiF have low values of refractive index n (the real part of the optical constant) and relatively low values of extinction coefficient k (the imaginary part of the optical constant) within the VUV wavelength region. The low resistance to high energy radiation damage in a space environment¹ makes LiF not very useful as a material for interference optical filters intended for many space applications, reducing the choice of low index film materials to just MgF_2 .

For their values of the extinction coefficient, both BaF_2 and LaF_3 may be used as the high index materials² to form a high-low (HL) index pair together with MgF_2 . A HL pair, made either with BaF_2 - MgF_2 or LaF_3 - MgF_2 , can provide the basic sequence of a multilayer design which can be used for wavelengths as low as 130 nm. A brief review of the basic theory for such multilayers is given in Sec. II, while theoretical calculations of so-called tuned multilayer interference filters with absorbing film materials are given in Sec. III.

All-dielectric Fabry-Perot type filters employing

BaF_2 and MgF_2 are considered in Sec. IV along with an alternative design for narrowband transmission filters. Designs of narrowband reflection filters are also given in that section. Spectral performance is compared to transmission filters. It is found that, for a small cone of light ($\pm 5^\circ$) centered about some incident angle, reflection filters when combined with transmission filters can provide excellent spectral performance in the VUV. A summary and conclusions are given in Sec. V.

II. Basic Theory

A. VUV Absorption of Dielectrics

Absorption of dielectrics in the VUV can be treated with classical or quantum mechanical theory. Because of the present accuracy of the reflectance and transmittance measurements there is no advantage to using the quantum mechanical approach; thus the classical model is used for the calculation of optical constants. In this model, bound electrons in a dielectric illumination with electromagnetic radiation are treated as damped harmonic oscillators.³

To determine the optical constants of metals, the classical theory uses the free electron gas model.⁴ Absorption of incident electromagnetic radiation in dielectrics and in metals are two different physical phenomena (bound electrons in dielectrics and free electrons in metals), but the final result is the same, i.e., loss of incident intensity.

Both phenomena can be described in terms of a complex optical constant. However, the transition from the real optical constant of a lossless medium (dielectrics in the visible part of the spectrum) to the complex one of an absorbing medium requires a redefinition of phase velocity v and wavenumber k_λ such that

James Spann and M. R. Torr are with NASA George C. Marshall Space Flight Center, Huntsville, Alabama 35812; the other authors are with University of Alabama in Huntsville, Physics Department, Huntsville, Alabama 35899.

Received 9 November 1989.

$$r = \frac{r}{N} \quad (1)$$

$$k_i = \frac{r}{c} N \quad (2)$$

(where N is the complex optical constant) are now the complex quantities. In addition, the angles between the direction of the light propagation and the normal to the film plane are also the complex quantities and they no longer represent just the refraction of the propagating light.

B. Multilayers with Absorbing Film Materials

The VUV coatings presented in this paper consist of an HL pair with BaF_2 , LaF_3 , or SiO_2 as the high index materials and MgF_2 as the low index material. Since extinction coefficient k of the MgF_2 films is $<10^{-3}$ for wavelengths longer than 130 nm, it is neglected in the theoretical discussion concerning the angles of light propagation through the absorbing multilayers. However, the extinction coefficient of MgF_2 films is taken into account in the exact calculation of multilayers.

The amplitude reflection and transmission coefficients for the plane electromagnetic wave incident on a multilayer are³

$$r = \frac{(M_{11} + M_{12}\eta_s)\eta_0 - (M_{21} + M_{22}\eta_s)}{(M_{11} + M_{12}\eta_s)\eta_0 + (M_{21} + M_{22}\eta_s)} \quad (3)$$

$$t = \frac{2\eta_0}{(M_{11} + M_{12}\eta_s)\eta_0 + (M_{21} + M_{22}\eta_s)} \quad (4)$$

where η_0 and η_s are the effective optical constants of the incident medium and the substrate, respectively. They are defined as

$$\eta_0 = n_0 \cos\theta_0 \quad (5)$$

$$\eta_s = \eta_s \cos\theta_s \quad (6)$$

for s-polarization; and for p-polarization

$$\eta_0 = \frac{\cos\theta_0}{n_0} \quad (7)$$

$$\eta_s = \frac{\cos\theta_s}{n_s} \quad (8)$$

where n_0 and n_s are the refractive indices of the incident medium and the substrate, respectively. It is assumed that both the substrate and incident medium have negligible extinction coefficients and, therefore, real optical constants. The terms M_{ij} , $i, j = 1, 2$ are the elements of the multilayer characteristic matrix \mathbf{M} which is defined as the product of the matrices of the individual layers \mathbf{M}_l ($l = 1, 2, \dots, P$),

$$\mathbf{M} = \mathbf{M}_1 \mathbf{M}_2 \dots \mathbf{M}_P \quad (9)$$

where P is the total number of layers. Matrices \mathbf{M}_l are given by

$$\mathbf{M}_l = \begin{pmatrix} \cos\delta_l & \frac{i}{\eta_l} \sin\delta_l \\ i\eta_l \sin\delta_l & \cos\delta_l \end{pmatrix} \quad (10)$$

The phase terms δ_l , which are usually referred to as the phase thicknesses of the films, are defined by

$$\delta_l = \frac{2\pi}{\lambda_0} N_l d_l \cos\theta_l \quad (11)$$

where λ_0 is the vacuum wavelength of the incident light, N_l is the optical constant of the l th layer defined as

$$N_l = n_l(1 + i\kappa_l) = n_l + in_l\kappa_l = n_l + ik_l \quad (12)$$

with $\kappa_l = k_l/n_l$, and where n_l is the refractive index, k_l is the extinction coefficient, d_l is the physical thickness, and θ_l is the complex angle of light within the l th film.

If the complex angle θ_l is written as

$$\sin\theta_l = q_l \exp(i\gamma_l) \quad (13)$$

the generalized Snell's law applied at the interface between the nonabsorbing $(l-1)$ th medium and absorbing l th medium is given by

$$N_l \sin\theta_l = (n_l + ik_l)q_l \exp(i\gamma_l) = n_{l-1} \sin\theta_{l-1} \quad (14)$$

The right-hand side of Eq. (14) is real, thus

$$n_l q_l \cos\gamma_l - k_l q_l \sin\gamma_l = n_{l-1} \sin\theta_{l-1} \quad (15)$$

$$n_l q_l \sin\gamma_l + k_l q_l \cos\gamma_l = 0 \quad (16)$$

From Eqs. (15) and (16) it follows that q_l and γ_l are given by

$$q_l = \frac{n_{l-1} \sin\theta_{l-1}}{\sqrt{n_l^2 + k_l^2}} \quad (17)$$

$$\gamma_l = \cos^{-1} \left(\frac{n_l}{\sqrt{n_l^2 + k_l^2}} \right) \quad (18)$$

If $k_l = 0$, then

$$q_l = \frac{n_{l-1} \sin\theta_{l-1}}{n_l} \quad (19)$$

$$\gamma_l = 0 \quad (20)$$

and the generalized Snell's law [Eq. (14)] should reduce to the well-known law of refraction.

The reflection and transmission coefficients are complex numbers of the form

$$r = |r| \exp(i\phi_r) \quad (21)$$

$$t = |t| \exp(i\phi_t) \quad (22)$$

where ϕ_r and ϕ_t represent the phase changes on reflection and transmission, respectively. The phase change of reflected light ϕ_r is referred to the plane boundary between the semi-infinite incident medium and the front surface of the multilayer, while the phase change of transmitted light ϕ_t is referred to the plane boundary between the multilayer and the semi-infinite medium of the substrate. Reflectance R , transmittance T , and absorptance A of the multilayers are given by

$$R = rr^* \quad (23)$$

$$T = \frac{\eta_0}{\eta_s} t t^* \quad (24)$$

$$A = 1 - (R + T) \quad (25)$$

III. Tuned Multilayers

Multilayers formed by high and low index materials alternating throughout the stack are, by analogy with electrical networks, called tuned filters or tuned multilayers. Because of their importance in the design of VUV coatings presented in this paper, we investigate the properties of tuned multilayers with absorbing film materials in more detail here.

Consider the multilayer (HL)^p with a total number of films $P = 2p$. Let the angle of incidence be zero, i.e., $\theta_0 = 0$. By denoting the angle within the low index material as θ_L and the angle within the high index material as θ_H we may write

$$\theta_H = \theta_L = 0. \quad (26)$$

Thus, phase thickness δ_H and δ_L are now given by

$$\delta_H = \frac{2\pi}{\lambda_0} (n_H + ik_H)d_H \quad (27)$$

for the high index material, and for the low index material

$$\delta_L = \frac{2\pi}{\lambda_0} (n_L + ik_L)d_L \quad (28)$$

If the optical thicknesses of both the H and L materials are quarterwave relative to the same reference wavelength λ_r , then

$$n_L d_L = \frac{\lambda_r}{4} \quad (29)$$

$$n_H d_H = \frac{\lambda_r}{4} \quad (30)$$

Phase thicknesses δ_H and δ_L are given by

$$\delta_H = \frac{\pi}{2} \frac{\lambda_r}{\lambda_0} \left(1 + i \frac{k_H}{n_H} \right) \quad (31)$$

$$\delta_L = \frac{\pi}{2} \frac{\lambda_r}{\lambda_0} \left(1 + i \frac{k_L}{n_L} \right) \quad (32)$$

Further, with

$$\kappa_H = \frac{k_H}{n_H} \quad (33)$$

$$\kappa_L = \frac{k_L}{n_L} \quad (34)$$

Eqs. (31) and (32) can be written as

$$\delta_H = \frac{\pi}{2} \frac{\lambda_r}{\lambda_0} (1 + i\kappa_H) \quad (35)$$

$$\delta_L = \frac{\pi}{2} \frac{\lambda_r}{\lambda_0} (1 + i\kappa_L) \quad (36)$$

The matrices of such quarterwave films at $\lambda_r = \lambda_0$ become

$$\mathbf{M}_H = \begin{pmatrix} -i \sinh \alpha_H & \frac{i}{N_H} \cosh \alpha_H \\ i N_H \cosh \alpha_H & -i \sinh \alpha_H \end{pmatrix} \quad (37)$$

$$\mathbf{M}_L = \begin{pmatrix} -i \sinh \alpha_L & \frac{i}{N_L} \cosh \alpha_L \\ i N_L \cosh \alpha_L & -i \sinh \alpha_L \end{pmatrix} \quad (38)$$

where

$$\alpha_H = \frac{\pi}{2} \frac{k_H}{n_H} = \frac{\pi}{2} \kappa_H \quad (39)$$

$$\alpha_L = \frac{\pi}{2} \frac{k_L}{n_L} = \frac{\pi}{2} \kappa_L \quad (40)$$

At this point, we shall assume (just for theoretical consideration of the tuned multilayers with absorbing films and not for exact calculation) that the hyperbolic functions in Eqs. (37) and (38) may be approximated by their values at the origin, i.e., $\sinh x \rightarrow 0$ and $\cosh x \rightarrow 1$ for $x \rightarrow 0$. Matrices \mathbf{M}_H and \mathbf{M}_L within this approximation and for $\lambda_0 = \lambda_r$ can be written as

$$\mathbf{M}_H = \begin{pmatrix} 0 & \frac{i}{N_H} \\ i N_H & 0 \end{pmatrix} \quad (41)$$

$$\mathbf{M}_L = \begin{pmatrix} 0 & \frac{i}{N_L} \\ i N_L & 0 \end{pmatrix} \quad (42)$$

giving matrix \mathbf{M}_1 of the basic sequence (HL):

$$\mathbf{M}_1 = \mathbf{M}_H \mathbf{M}_L = \begin{pmatrix} \frac{-N_L}{N_H} & 0 \\ 0 & \frac{-N_H}{N_L} \end{pmatrix} \quad (43)$$

The characteristic matrix of multilayer (HL)^p is then given by

$$\mathbf{M}_P = (\mathbf{M}_H \mathbf{M}_L)^P = \begin{bmatrix} \left(\frac{-N_L}{N_H} \right)^P & 0 \\ 0 & \left(\frac{-N_H}{N_L} \right)^P \end{bmatrix} \quad (44)$$

From Eq. (3) the amplitude reflection coefficient follows as

$$r = \frac{1 - \frac{n_s}{n_0} \left(\frac{N_H}{N_L} \right)^{2p}}{1 + \frac{n_s}{n_0} \left(\frac{N_H}{N_L} \right)^{2p}} \quad (45)$$

The ratio of optical constants N_H and N_L can be written as

$$\frac{N_H}{N_L} = \frac{n_H (1 + i\kappa_H)}{n_L (1 + i\kappa_L)} = \frac{n_H}{n_L} (a^2 + b^2)^{1/2} \exp(i\beta) \quad (46)$$

where

$$a = \frac{1 + \kappa_H \kappa_L}{1 + \kappa_L^2} \quad (47)$$

$$b = \frac{\kappa_H - \kappa_L}{1 + \kappa_L^2} \quad (48)$$

$$\beta = \tan^{-1} \left(\frac{b}{a} \right). \quad (49)$$

Thus, $(N_H/N_L)^p$ can be written as

$$\left(\frac{N_H}{N_L} \right)^p = F(p) \exp[i\psi(p)]. \quad (50)$$

where

$$F(p) = \left(\frac{n_H}{n_L} \right)^p (a^2 + b^2)^{p/2}. \quad (51)$$

$$\psi(p) = p\beta. \quad (52)$$

Now, Eq. (45) for r becomes

$$r(p) = \frac{1 - \left(\frac{n_s}{n_0} \right) F(2p) \exp[i\psi(2p)]}{1 + \left(\frac{n_s}{n_0} \right) F(2p) \exp[i\psi(2p)]}. \quad (53)$$

giving for reflectance $R(p)$ of the (HL)^p multilayer tuned at wavelength $\lambda_0 = \lambda_r$:

$$R(p) = \frac{1 + \left(\frac{n_s}{n_0} \right)^2 F^2(2p) - 2 \left(\frac{n_s}{n_0} \right) F(2p) \cos\psi(2p)}{1 + \left(\frac{n_s}{n_0} \right)^2 F^2(2p) + 2 \left(\frac{n_s}{n_0} \right) F(2p) \cos\psi(2p)}. \quad (54)$$

If $p = 0$, i.e., if no films are present on the substrate, Eq. (54) reduces to the well-known Fresnel formula for reflectance at the boundary between two semi-infinite media with indices n_0 and n_s :

$$R(0) = \frac{\left(1 - \frac{n_s}{n_0} \right)^2}{\left(1 + \frac{n_s}{n_0} \right)^2}. \quad (55)$$

From Eq. (54) it follows that the reflectance of the (HL)^p stack will have maximum values if, for $l = 0, 1, 2, \dots$

$$\psi(2p) = (l + \frac{1}{2})\pi. \quad (56)$$

Thus, for $l = 0$ from Eqs. (47)–(49), (51), (52), and (56) it follows that the maximum reflectance is achieved if

$$p = p_0 = \frac{\pi}{4} \left[\tan^{-1} \left(\frac{\kappa_H - \kappa_L}{1 + \kappa_H \kappa_L} \right) \right]^{-1}. \quad (57)$$

Equation (54) indicates that $R(p_0) = 1$ if p satisfies Eq. (57). This is caused by the high level of approximation at the beginning of our derivation. Equation (57) is the final goal of this theoretical consideration for determining the maximum useful number of layers for achieving the highest possible reflectance with absorbing materials.

From a certain number of (HL) pairs p_0 , both the reflectance and absorptance of the stack will remain practically constant, adding to unity, and no significant improvement of the stack's reflectance can be achieved by adding new (HL) pairs, i.e., for $p \geq p_0$:

$$R(p) + A(p) \rightarrow 1. \quad (58)$$

The transmittance of the stack will be equal to zero for all practical purposes.

The results of exact calculation of how reflectance $R(p)$ and absorptance $A(p)$ depend on the number of (HL) pairs p of multilayers formed with BaF₂, LaF₃, and SiO₂ as the high index materials and MgF₂ as the low index material are shown in Figs. 1, 2, and 3, respectively. The optical film thicknesses of all the films are quarterwave relative to wavelength $\lambda_0 = \lambda_r = 135$ nm. At this wavelength the ratio κ for the SiO₂ film is $\kappa_H = 0.05759$, and for the MgF₂ $\kappa_L = 0.00025$, giving $p_0 = 13.7$, i.e., $p_0 \rightarrow 14$, which agrees with the exact calculation shown in Fig. 1. Since the extinction coefficients of BaF₂ and LaF₃ are an order of magnitude lower than the extinction coefficient of SiO₂, p_0 attains higher values if these fluorides are used as the high index material.

From the reflectance $R(p)$ and absorptance $A(p)$ curves shown in Figs. 1–3, it follows that BaF₂ has the highest potential as the high index material for wavelengths close to 135 nm. At longer wavelengths, $\lambda_0 \geq 150$ nm, the extinction coefficients of LaF₃ and BaF₂ become similar while the refractive index of LaF₃ remains higher.²

The $R(p)$ and $A(p)$ curves shown in Figs. 4–6 are calculated again for multilayers with BaF₂, LaF₃, and SiO₂ as the high index materials but with optical thicknesses of

$$n_H d_H = \frac{\lambda_r}{6}, \quad (59)$$

$$n_L d_L = \frac{\lambda_r}{3}, \quad (60)$$

where n_L is the refractive index of MgF₂, and $\lambda_0 = \lambda_r = 135$ nm. This type of tuned multilayer stack is sometimes referred to as the third wave (TW) design, by analogy with quarterwave (QW) stacks. The thickness of the (absorbing) high index material is larger in the QW than in the TW multilayers, thus one may expect that the TW designs will have lower absorptance and therefore higher reflectance. That this expectation is justified follows from comparison of the $R(p)$ and $A(p)$ curves for the QW multilayers shown in Figs. 1–3 and $R(p)$ and $A(p)$ curves for TW multilayers shown in Figs. 4–6.

The maximum reflectance of the QW stack with BaF₂ is $R = 85.4\%$ (Fig. 1), while the TW multilayer with the same high index material has a maximum reflectance of $R = 87.6\%$ (Fig. 4). The largest relative difference between the maximum reflectances of the TW and QW stacks is for a multilayer with SiO₂ as the high index material. The maximum reflectance of the QW stack is $R = 60.9\%$ (Fig. 3), while for the TW stack $R = 66.3\%$ (Fig. 6).

The number p_0 found for the quarterwave multilayers using Eq. (57) seems to be useful even for the third wave stacks. It again represents the minimum number of (HL) pairs p_0 needed to obtain the maximum value of reflectance or zero transmittance.

A more rigorous treatment of absorbing multilayers with the so-called potential transmittance and absorptance is given by Knittl⁵ and the original references listed therein.

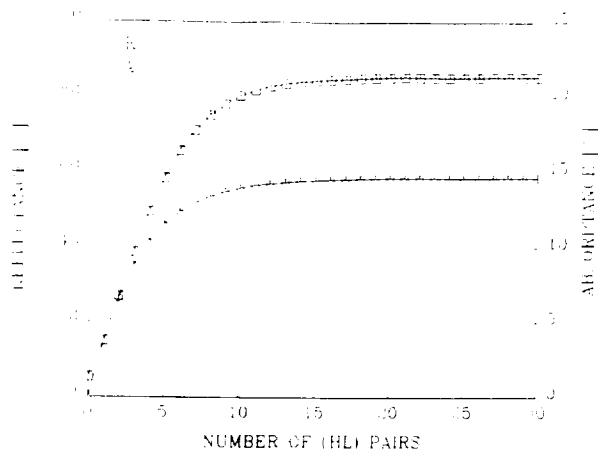


Fig. 1. Reflectance and absorbance of the QW stack as functions of the number of (HL) pairs: H = barium fluoride and L = magnesium fluoride.

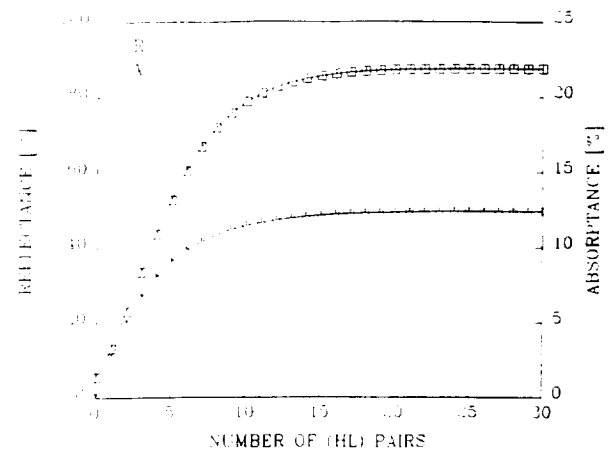


Fig. 4. Reflectance and absorbance of the TW stack as functions of the number of (HL) pairs: H = barium fluoride and L = magnesium fluoride.

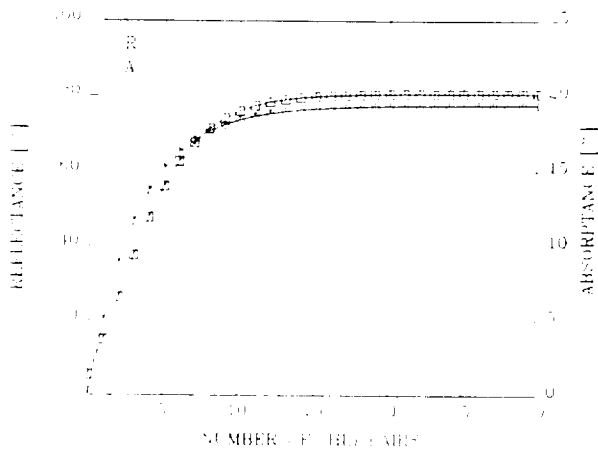


Fig. 2. Reflectance and absorbance of the QW stack as functions of the number of (HL) pairs: H = lanthanum fluoride and L = magnesium fluoride.

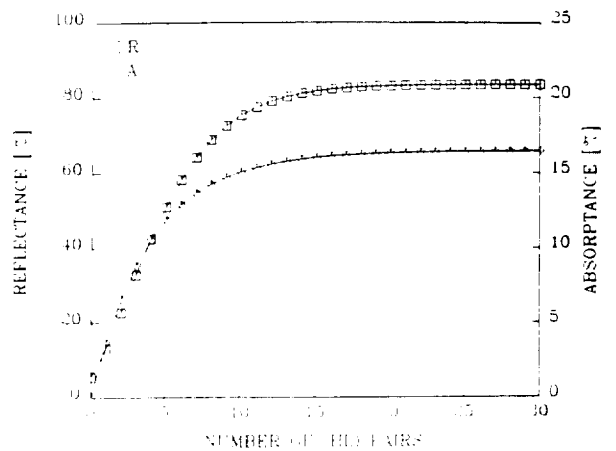


Fig. 5. Reflectance and absorbance of the TW stack as functions of the number of (HL) pairs: H = lanthanum fluoride and L = magnesium fluoride.

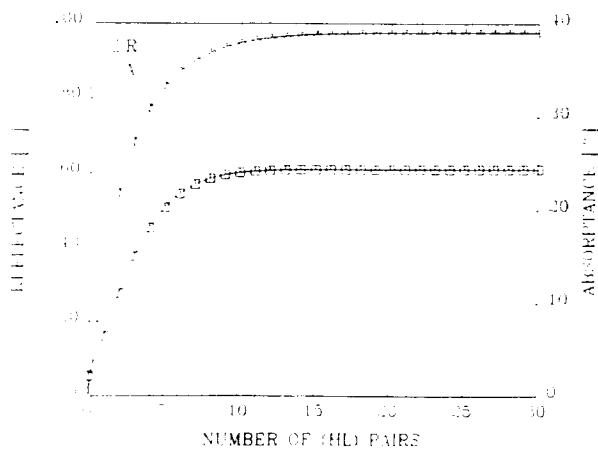


Fig. 3. Reflectance and absorbance of the QW stack as functions of the number of (HL) pairs: H = silicon dioxide and L = magnesium fluoride.

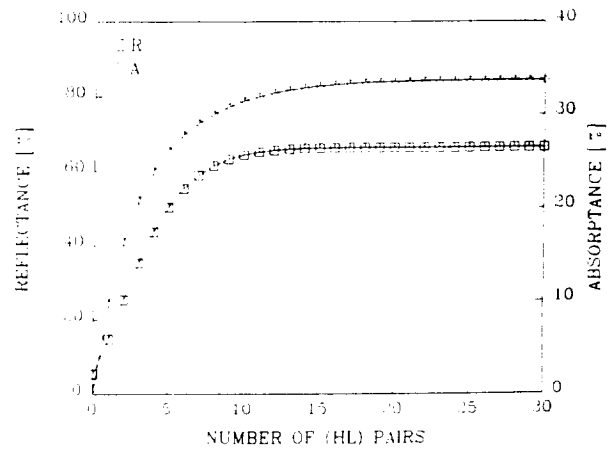


Fig. 6. Reflectance and absorbance of the TW stack as functions of the number of (HL) pairs: H = silicon dioxide and L = magnesium fluoride.

IV. Narrowband Filters

A. Transmission Filters

1. Fabry-Perot Filters

Transmission or bandpass filters are frequently designed using the basic structure of the Fabry-Perot (F.P.) interferometer—the multilayer in which one of the layers (spacing layer or spacer) is bounded by two partial reflectors. The transmittance of such an interference filter is given by^{6,7}

$$T = \frac{T_{\max}}{1 + F \sin^2 \Psi} \quad (61)$$

where

$$T_{\max} = \frac{T_1 T_2}{(1 - \sqrt{R_1 R_2})^2} \quad (62)$$

$$F = \frac{4\sqrt{R_1 R_2}}{(1 - \sqrt{R_1 R_2})^2} \quad (63)$$

$$\Psi = \delta - \frac{\phi_1 + \phi_2}{2} \quad (64)$$

R_1 and R_2 are the reflectances and T_1 and T_2 are the transmittances of the partial reflectors bounding the spacing layer, calculated with the spacer taken as the incident medium (seen from inside the spacer). The emerging medium for reflector R_1 is air and for partial reflector R_2 it is the substrate. δ is the phase thickness of the spacing layer defined in Eq. (11), ϕ_1 and ϕ_2 are the phase changes [Eq. (17)] associated with reflections on partial reflectors R_1 and R_2 . The maxima of transmission according to Eq. (61) are given by

$$\Psi = \delta - \phi = m\pi \quad (65)$$

where

$$\phi = \frac{\phi_1 + \phi_2}{2} \quad (66)$$

and the bandwidth $(\Delta\lambda)_h$ full width at half-maximum (FWHM) is given by⁷

$$(\Delta\lambda)_h = 2\lambda_0^{m+1} \left[\pi \sqrt{F} \left| m - \frac{1}{\pi} \left(\frac{d}{d\lambda_0} (\lambda_0 \phi) \right)_{\lambda_0 = \lambda_0^{m+1}} \right| \right]^{-1} \quad (67)$$

of the m th order filter ($m = 1, 2, \dots$).

For BaF_2 , LaF_3 , and SiO_2 the values of the extinction coefficients are too high in the VUV² to be used as film materials for the spacing layer. Thus, in all our designs MgF_2 was used as the film material of the spacer. The possible designs of F.P. type interference filters are then given by

$$\text{air}[\text{H}(\text{LH})^p \text{L}(\text{HL})^p \text{H}] \text{substrate}, \quad (68)$$

or

$$\text{air}[(\text{LH})^p \text{L}(\text{HL})^p] \text{substrate}, \quad (69)$$

where L denotes the quarterwave optical thickness of the MgF_2 , H is the quarterwave optical thickness of one of the high index materials (BaF_2 , LaF_3 , or SiO_2), and the substrate is bulk MgF_2 . The optical thick-

nesses are quarterwave relative to the central pass wavelength of the F.P. filter.

Reflectances R and R_2 and transmittances T_1 and T_2 appearing in the above basic equations for the F.P. filter are seen from inside the spacing layer. The R_1 and T_1 are calculated for the boundary between the spacing layer and one side of the F.P. filter including the incident medium (air), while R_2 and T_2 are calculated for the boundary between the spacing layer and the other side of the F.P. filter including the substrate. The partial reflectors in both designs [(68) and (69)] are $(\text{HL})^p$ QW tuned multilayers with an additional outer H layer in design (69).

The dependences of reflectances R_1 and R_2 on the number of (HL) pairs p for BaF_2 , LaF_3 , and SiO_2 are shown in Figs. 7, 8, and 9, respectively. The maximum values of transmittance T_{\max} calculated using Eq. (62) and the corresponding bandwidths $(\Delta\lambda)_h$ calculated according to Eq. (67) for the first-order filter ($m = 1$) are plotted vs p in Figs. 10–12 (for the high index materials listed above). The differentiation of the function

$$\Phi(\lambda_0) = \lambda_0 \phi(\lambda_0) \quad (70)$$

in Eq. (67) was done numerically according to

$$\left[\frac{d}{d\lambda_0} \Phi(\lambda_0) \right]_{\lambda_0 = \lambda_0^{m+1}} = \left[\phi(\lambda_0) \right]_{\lambda_0 = \lambda_0^{m+1}} + \left[\lambda_0 \frac{d}{d\lambda_0} \phi(\lambda_0) \right]_{\lambda_0 = \lambda_0^{m+1}} \quad (71)$$

$$\left[\frac{d}{d\lambda_0} \Phi(\lambda_0) \right]_{\lambda_0 = \lambda_0^{m+1}} = \left[\frac{\Phi(\lambda_0 + \Delta\lambda) - \Phi(\lambda_0)}{\Delta\lambda} \right]_{\lambda_0 = \lambda_0^{m+1}} \quad (72)$$

with $\Delta\lambda \leq \lambda_0 \times 10^{-6}$ and the central pass wavelength of the F.P. filter $\lambda_0 = 135$ nm.

From Fig. 10 it follows that the F.P. filter centered at $\lambda_0 = 135$ nm should have $T_{\max} \geq 30\%$ and $(\Delta\lambda)_h \leq 10$ nm for $\text{H} = \text{BaF}_2$ and $p = 6$. The design of the F.P. filter becomes

$$\text{air}[(\text{LH})^6 \text{L}(\text{HL})^6] \text{substrate}, \quad (73)$$

where the substrate is bulk MgF_2 .

The experimentally obtained and theoretically calculated spectral performance of such a filter is shown in Fig. 13. The theoretical curve is not corrected for loss due to MgF_2 substrate absorption and back side reflection (23% at $\lambda_0 = 135$ nm). The experimentally obtained bandwidth is smaller than the one predicted in Fig. 10. This can be explained by much higher values of the extinction coefficient of BaF_2 for wavelengths below 131 nm than for $\lambda_0 \geq 135$ nm.

To improve the transmittance at central wavelength $\lambda_0 = 135$ nm, a F.P. filter with two spacing layers may be designed such as

$$\text{air}[(\text{LH})^2 \text{L}(\text{HL})^2 \text{H} \text{L}(\text{HL})^2] \text{substrate}, \quad (74)$$

where H and L represent the quarterwave optical thicknesses of BaF_2 and MgF_2 respectively, and the substrate is bulk MgF_2 . The calculated and experimentally obtained transmittances of this filter are shown in Fig. 14. The effects of the MgF_2 substrate absorption and back side reflection are not taken into account in the theoretical curve. The bandwidth of the filter is again smaller than that calculated using a

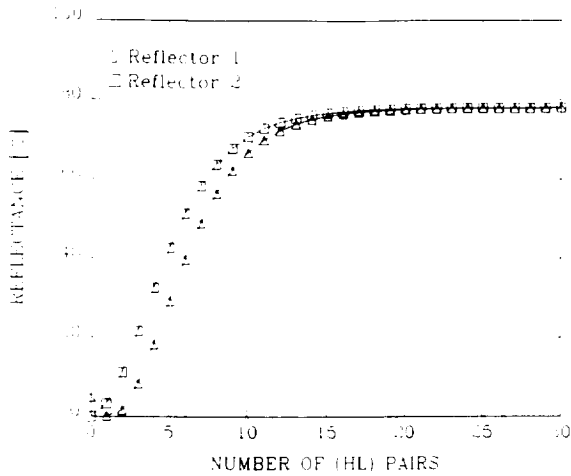


Fig. 7. Reflectances of the partial reflectors of the Fabry-Perot type filter as functions of the number of (HL) pairs: H = barium fluoride and L = magnesium fluoride.

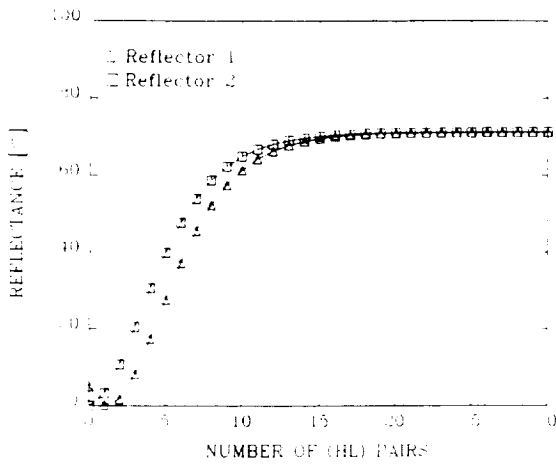


Fig. 8. Reflectances of the partial reflectors of the Fabry-Perot type filter as functions of the number of (HL) pairs: H = lanthanum fluoride and L = magnesium fluoride.

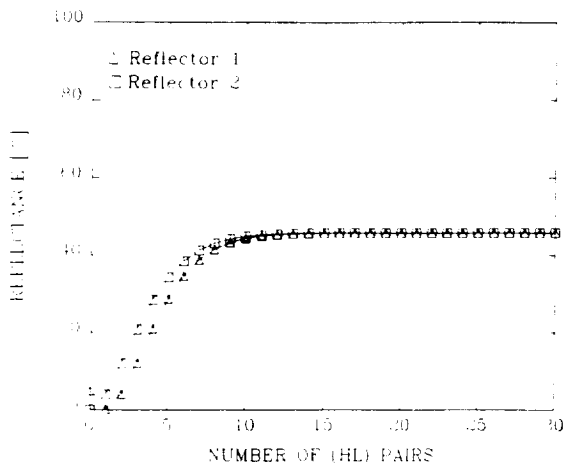


Fig. 9. Reflectances of the partial reflectors of the Fabry-Perot type filter as functions of the number of (HL) pairs: H = silicon dioxide and L = magnesium fluoride.

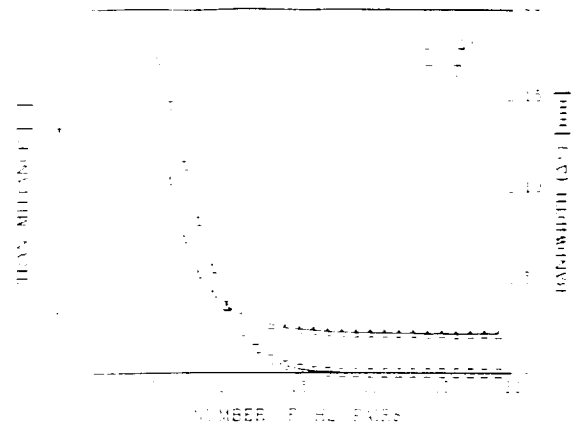


Fig. 10. Maximum transmittance and bandwidth of the Fabry-Perot type filter calculated using Eqs. (62) and (67), respectively: H = barium fluoride and L = magnesium fluoride.

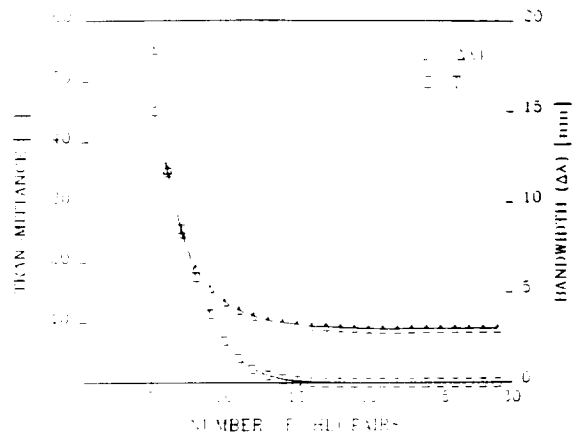


Fig. 11. Maximum transmittance and bandwidth of the Fabry-Perot type filter calculated using Eqs. (62) and (67), respectively: H = lanthanum fluoride and L = magnesium fluoride.

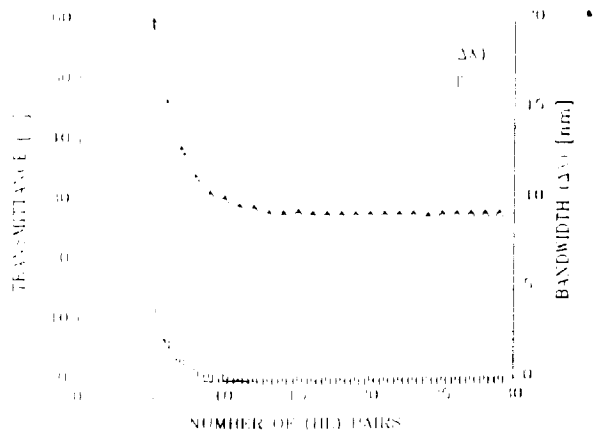


Fig. 12. Maximum transmittance and bandwidth of the Fabry-Perot type filter calculated using Eqs. (62) and (67), respectively: H = silicon dioxide and L = magnesium fluoride.

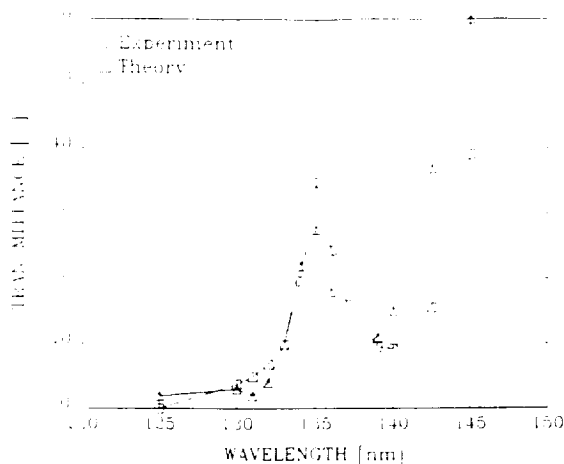


Fig. 13. Twenty-five-layer Fabry-Perot type filter: H = barium fluoride and L = magnesium fluoride.

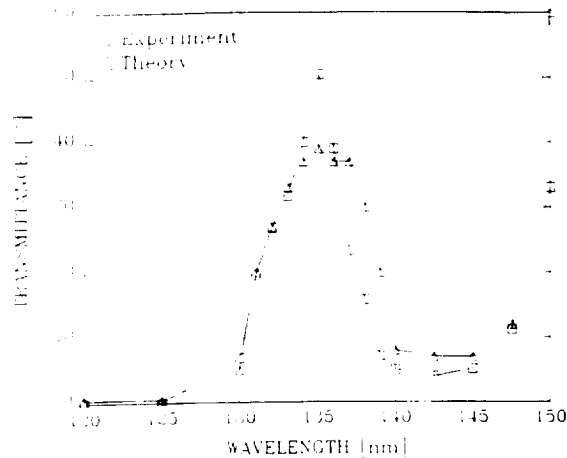


Fig. 15. Twenty-five-layer QW tuned filter with the high reflection zone centered at 140 nm: H = barium fluoride and L = magnesium fluoride.

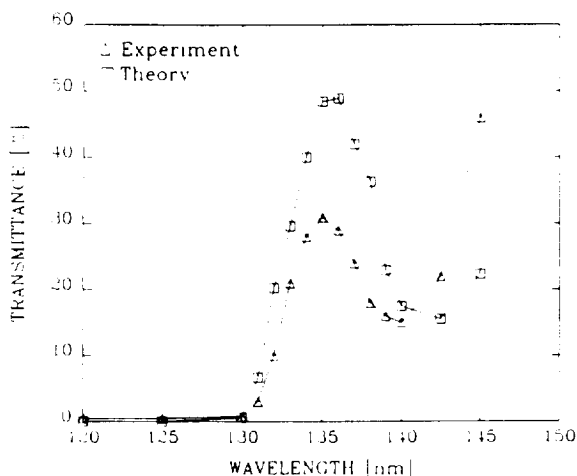


Fig. 14. Twenty-nine-layer Fabry-Perot filter with two spacing layers: H = barium fluoride and L = magnesium fluoride.

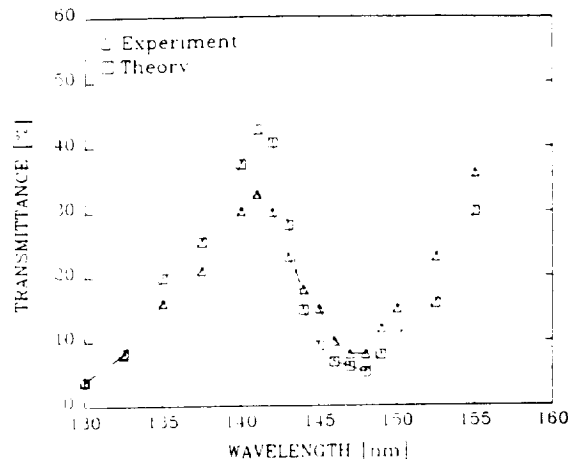


Fig. 16. Twenty-five-layer TW tuned filter with the high reflection zone centered at 147.5 nm: H = silicon dioxide and L = magnesium fluoride.

formula similar to Eq. (67) for the bandwidth of the F.P. filter with two spacing layers.⁹ This can also be attributed to the much higher k values of BaF_2 films for shorter wavelengths; $k = 0.1$ at $\lambda = 130$ nm compared with $k = 0.026$ at $\lambda = 135$ nm.

2. Tuned Stack

The fact that the extinction coefficient of a BaF_2 film is almost four times larger at 130 nm than at 135 nm can be used for the design of a narrowband filter centered at 135 nm. The design of such a filter is a simple QW tuned stack with the high reflection zone centered at 140 nm. The theoretical and experimental spectral curves of the twenty-five-layer QW tuned filter are shown in Fig. 15. The interference effects are predominant in the wavelength region above 135 nm, while the absorption of BaF_2 dominates for wavelengths shorter than 135 nm. The peak value of the transmittance is $T_{\text{max}} = 39\%$ at $\lambda_0 = 135$ nm. The theoretical curve in Fig. 15 is not corrected for loss due

to MgF_2 substrate absorption and back side reflection.

The filter shown in Fig. 15, which combines absorption effects of the film material (BaF_2) to reject shorter wavelengths and interference effects to reject longer wavelengths relative to the central wavelength $\lambda_0 = 135$ nm, has a higher peak transmittance and at the same time provides better rejection of the longer wavelengths. Another possible design of such a filter centered at 141 nm with a twenty-five-layer TW tuned multilayer is shown in Fig. 16. The rapidly changing extinction coefficient k of SiO_2 film within $135 \text{ nm} \leq \lambda \leq 145 \text{ nm}$ is utilized.

All these filters suffer from pass windows at longer wavelengths. An edge filter is needed which will reject longer wavelengths. When the edge filter is combined with the narrowband transmission filter, the combination should provide useful transmittance at λ_0 . For the filters centered at 135 nm, the edge filter might be required (for some applications) to reject longer wavelengths up to at least 170 nm to better than 95%, and at

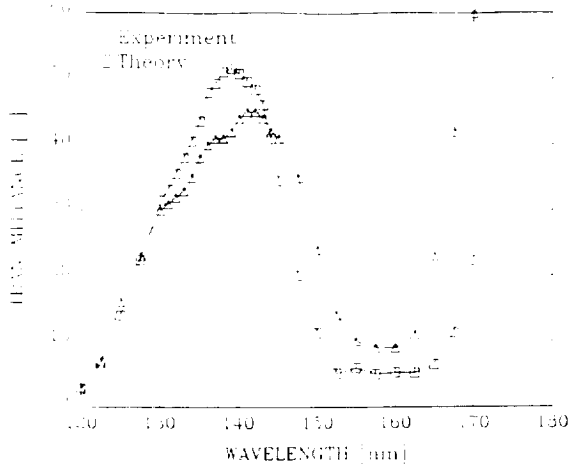


Fig. 17. Twenty-five-layer QW tuned filter with the high reflection zone centered at 160 nm: H = lanthanum fluoride and L = magnesium fluoride.

the same time provide $T \geq 50\%$ at $\lambda_0 = 135$ nm. The basic design of such a filter is again a tuned multilayer with either QW or TW optical thicknesses. The QW stacks generally have a wider high reflection zone than TW stacks. The width of the high reflection zone of a QW multilayer with nonabsorbing film materials is given by⁸

$$(\Delta\lambda)_{H.R.} = \frac{4\lambda_0}{\pi} \sin^{-1} \left(\frac{n_H - n_L}{n_H + n_L} \right), \quad (75)$$

where n_H and n_L are the refractive indices of the high and low index materials, respectively. If the presence of absorption in the films affects only the maximum value of the reflectance but not the width of the high reflection zone, $(\Delta\lambda)_{H.R.} = 21.6$ nm for H = LaF₃ and L = MgF₂ at $\lambda_0 = 160$ nm. Because of the transmission requirements at 135 nm, the idea of coupling QW or TW multilayers centered at several wavelengths within the wavelength interval from 140 to 170 nm cannot be used. Hence, the edge filter which would provide the required transmission at 135-nm wavelength and at the same time reject longer wavelengths up to 170 nm cannot be designed with the dielectrics known to us. The twenty-five layer QW stack shown in Fig. 17 justifies calculations done using Eq. (75); the high reflection zone of the measured spectral curve $(\Delta\lambda)_{H.R.} \leq 15$ nm.

B. Reflection Filters

Designs of the dielectric cut-on filters which would have a useful range of transmittance ($T \geq 50\%$) for wavelengths below 145 nm and at the same time reject the longer wavelengths up to 230 nm better than 95% do not seem to be feasible at the moment. Another possibility in solving this problem is to try to design a reflection filter at an incident angle of, say, 45°, which would reject a narrow spectral band with a reflectance of 50% or more at the desired wavelength. If this type of filter is then combined with one of the previously

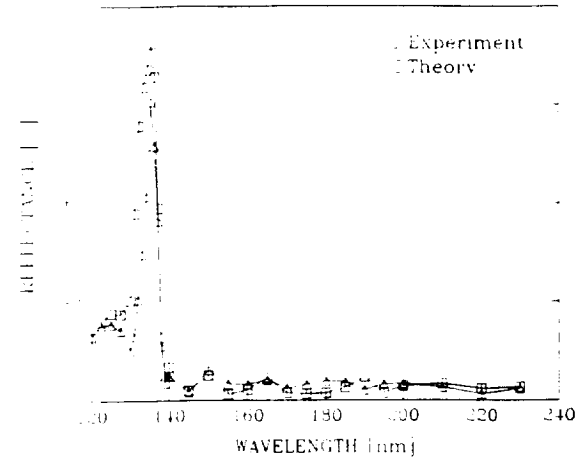


Fig. 18. Twenty-five-layer second-order QW tuned filter with the high reflection zone centered at 135 nm. The angle of incidence is 45°: H = lanthanum fluoride and L = magnesium fluoride.

presented transmission filters, the combination could provide excellent rejection for the shorter wavelengths, high peak transmittance, and reasonably good blocking of the longer wavelengths.

The design of the reflection filter is once again a QE or TW multilayer with the optical thicknesses of the films corrected for oblique incidence. A first-order QW stack generally has a wider high reflection zone and suffers from high side reflection ripples. The ripples can be reduced by introducing films with optical thicknesses $H'/2$ or $L'/2$ (primes denote correction of the quarterwave optical thickness for the oblique incidence) at the first and last positions in the stack. The width of the high reflection zone decreases if the order of the QW multilayer is increased. The increase of the order by 1 means a change in the optical thickness of one of the film materials from $\lambda_0/4$ to $3\lambda_0/4$. Obviously, in the VUV range MgF₂ is a material whose optical thickness can be increased from L' to $3L'$ without affecting the maximum value of reflectance possible with a first-order QW stack.

The experimental and theoretical spectral curves of the second-order QW stack at an angle of incidence $\theta_0 = 45^\circ$ are shown in Fig. 18. The design of the filter is given by

$$\text{air} \left[\frac{3L'}{2} (H'3L')^{11} H' \frac{3L'}{2} \right]_{\text{substrate}}, \quad (76)$$

where $H' = \text{BaF}_2$, $L' = \text{MgF}_2$, $\lambda_0 = 135$ nm, and primes denote the correction for oblique incidence. The width of the high reflection zone $(\Delta\lambda)_{H.R.} \leq 5$ nm and the reflectance at the central wavelength is 60%.

The measured overall transmittance of the filter presented in Fig. 15 combined with the reflection filter (Fig. 18) is shown in Fig. 19. The central wavelength of this filter is $\lambda_0 = 135$ nm, the peak value of the transmittance is $T_{\max} = 24\%$, and the bandwidth $(\Delta\lambda)_b = 4$ nm. The average transmittance for the longer wavelengths is $<3\%$, while for wavelengths shorter than 130 nm the transmittance is $<0.1\%$. A cone angle

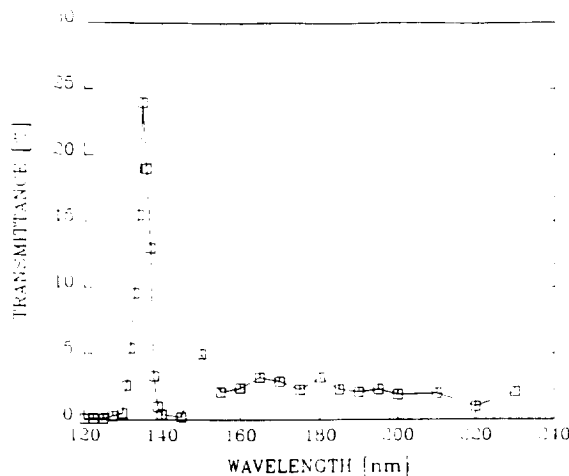


Fig. 19. Measured transmittance of the filters shown in Figs. 15 and 18 combined.

of incident light of $\pm 5^\circ$ causes the bandwidth to increase up to 7 nm.

The overall transmittance of the filter shown in Fig. 16 combined with the QW multilayer reflector centered at 141 nm is shown in Fig. 20. The bandwidth of the filter is 3.5 nm and peak transmittance is 25%. The film materials used for the reflection filter are LaF_3 and MgF_2 .

V. Summary

The idea of utilizing the natural absorption of one of the film materials to limit the transmission at shorter wavelengths and a combination of this filter with a reflection filter to control the transmission at the long wavelength end of the bandpass constitutes the basis of our design of narrowband filters. The two filters that we designed and evaluated to demonstrate the approach have bandwidths smaller than 5 nm and peak transmittances higher than 25% for collimated incident light. The average transmittance in the region of longer wavelengths is $< 3\%$ while the transmittance in the region of shorter wavelength is $< 0.1\%$.

The values of the extinction coefficients of BaF_2 and LaF_3 films are much smaller at longer wavelengths than at 135 nm, which makes the design of a narrowband high reflector much easier. Other film materials such as Al_2O_3 and HfO_2 or suitable bulk materials (substrates) such as BaF_2 , fused silica, and Al_2O_3 can be used to reject different shorter wavelength ranges. When such materials are combined with reflection multilayers, narrowband filters with bandwidths smaller than 5 nm and overall transmittances higher than 25% can be made for the whole VUV region from 120 to 230 nm.

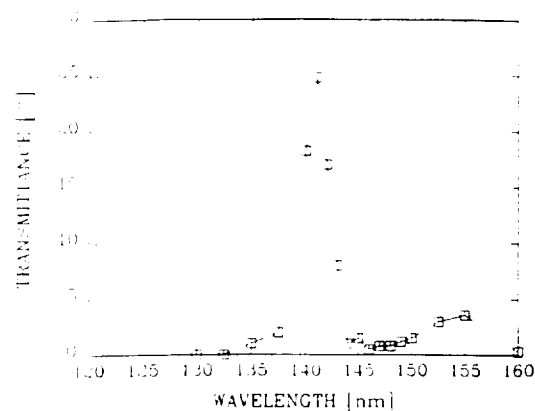


Fig. 20. Combined filter centered at 141 nm.

The discrepancies between theory and experiment may be partially explained by the random errors which occur in the film thickness monitoring during deposition. There are certainly some other effects to consider such as scattering, film thickness nonuniformities, and possible film inhomogeneities. Since the discrepancy between theory and experiment varied for different designs, it seems that these effects do not affect each of them equally.

The first author would like to thank the Physics Department of the University of Alabama in Huntsville (UAH) for the graduate student assistantship received during this study, and the ZRAK Optics Co. in Sarajevo, Yugoslavia, for additional financial support.

This work was supported by NASA contracts NAS8-37586 and NAS8-37576 and NASA grants NAG8-639 and NAG8-086.

References

1. D. F. Heath and P. A. Sacher, "Effects of a Simulated High-Energy Space Environment on the Ultraviolet Transmittance of Optical Materials Between 1050 Å and 3000 Å," *Appl. Opt.* **5**, 937-943 (1966).
2. M. Zukic, D. G. Torr, J. F. Spann, and M. R. Torr, "Vacuum Ultraviolet Thin Films. 1: Optical Constants of BaF_2 , CaF_2 , LaF_3 , MgF_2 , Al_2O_3 , HfO_2 , and SiO_2 Thin Films," *Appl. Opt.* **29**, 0000-0000 (1990), same issue.
3. M. Born and E. Wolf, *Principles of Optics* (Pergamon, New York, 1980), p. 60.
4. Ref. 3, p. 616.
5. Z. Knittl, *Optics of Thin Films* (Wiley, New York, 1976), Chaps. 5 and 6.
6. H. A. Macleod, *Thin-Film Optical Filters* (Adam Hilger, Bristol, 1969), Chaps. 2 and 7.
7. Ref. 3, p. 347.
8. Ref. 6, p. 98.

ORIGINAL PAGE IS
OF POOR QUALITY

APPENDIX D

Auroral Modeling of the 3371 Å Emission Rate: Dependence on Characteristic Electron Energy

P. G. RICHARDS

*Computer Science Department and Center for Space Plasma and Aeronomic Research
University of Alabama in Huntsville*

D. G. TORR

*Physics Department and Center for Space Plasma and Aeronomic Research
University of Alabama in Huntsville*

We have developed an efficient two-stream auroral electron model to study the deposition of auroral energy and the dependence of auroral emission rates on characteristic energy. This model incorporates the concept of average energy loss to reduce the computation time. Our simple two-stream model produces integrated emission rates that are in excellent agreement with the much more complex multistream model of Strickland et al. (1983) but disagrees with a recent study by Rees and Lummerzheim (1989) that indicates that the N₂ second positive emission rate is a strongly decreasing function of the characteristic energy of the precipitating flux. Our calculations reveal that a 10 keV electron will undergo approximately 160 ionizing collisions with an average energy loss per collision of 62 eV before thermalizing. The secondary electrons are created with an average energy of 42 eV. When all processes including the backscattered escape fluxes are taken into account, the average energy loss per electron-ion pair is 35 eV in good agreement with laboratory results.

1. INTRODUCTION

There is currently renewed interest in the use of auroral optical emission rates to deduce the characteristics of the precipitating particle fluxes, and ultimately, the global auroral energy input to the Earth's upper atmosphere. Images from the Dynamics Explorer satellite have been used by Rees et al. [1988] to calculate the energetic electron flux and its characteristic energy. Imaging instruments planned for the ISTP mission will monitor key UV emissions on a global scale for the express purpose of determining the global energy input.

Early work in determining auroral particle characteristics from emissions concentrated on the use of the ratios of atomic oxygen emission rates (6300 Å, 5577 Å) to molecular nitrogen ion emission rates (3914 Å, 4278 Å) to deduce the incident auroral spectrum [Rees and Luckey, 1974; Vallance Jones, 1975; Shepherd et al., 1980; Strickland et al., 1983]. The higher energy auroral electrons penetrate deeper into the thermosphere where the relative proportion of atomic oxygen is smaller. Thus the ratio of atomic to molecular emission rates decreases with increasing electron energy. Unfortunately, chemical processes play an important role in the atomic oxygen emissions and it is difficult to separate the effects caused by the characteristics of the auroral energy flux from the effects caused by changes in the atmospheric composition. Therefore, it would be useful to find an emission rate ratio that is sensitive to the auroral characteristics but which is not complicated by chemical factors.

Recently, Rees and Lummerzheim [1989] suggested that the ratio of the second positive to first negative emission rates could be used to determine the characteristic energy of the auroral electron flux. Using an auroral electron model developed by Lummerzheim et al. [1989], Rees and Lummerzheim [1989] found that the N₂ second positive (3371 Å) emission rate decreases substantially with increasing characteristic energy of the auroral electrons while the N₂⁺ emission rates are almost constant. This ratio would be an attractive alternative to those used previously because it would be independent of atmospheric composition and both emissions are prompt, thus eliminating chemical effects. Unfortunately, the calculations of Rees and Lummerzheim [1989] are in conflict with the earlier calculations by Daniell and Strickland [1986] who found that the 3371 Å emission rate was nearly independent of the characteristic energy.

The experimental evidence also seems to be in conflict. Rees and Lummerzheim [1989] present data from high flying aircraft that support their theoretical calculations. On the other hand, Solomon [1989] presented data from the visible airglow instrument on the Atmosphere Explorer C satellite showing that the ratio of the N₂ 3371 Å to N₂⁺ 4278 Å emission rates has only a small dependence on the characteristic energy, which can be accounted for by contamination of the 3371 Å second positive emission by the Vegard-Kaplan (0-9) band. The VAE data support the earlier calculations of Daniell and Strickland [1986] and Strickland et al. [1983]. Solomon was able to reproduce the observed ratios using his own two-stream auroral electron deposition code. We note that the experimental data presented by Solomon [1989] for the ratio of N₂ 3371 Å to N₂⁺ 4278 Å is in excellent agreement with the ratio of N₂ 3371 Å to N₂⁺ 3914 Å that was measured on a 1974 rocket flight by Sharp et al. [1979].

The source of the discrepancy between the models is difficult to understand. Both *Rees and Lummerzheim* [1989] and *Strickland et al.* [1983] use relatively complete multi-stream models. The model used by *Solomon* [1989] is a simpler two-stream model and his calculations are in agreement with the calculations of *Strickland et al.* [1983] and *Daniell and Strickland* [1986] which show little variation in the 3371 Å to 3914 Å emission rate ratio as a function of characteristic energy. In this paper we present calculations of a number of important emission rates obtained from a two-stream auroral electron model that we have developed. The calculated emission rates for the 3371 Å emission rate and a number of other emission rates are in accord with the earlier calculations of *Strickland et al.* [1983] and *Daniell and Strickland* [1986] for the dependence on characteristic energy of the precipitating flux. However, mainly due to the use of a revised cross section, our atomic oxygen 1356 Å emission rate is a factor of 2.5 lower than that calculated by *Strickland et al.* [1983].

2. MODEL

2.1. General Principles

The model that we have developed is based on the two-stream photoelectron flux model of *Nagy and Banks* [1970] that was subsequently extended to 500 eV and combined with a continuous energy loss model to calculate auroral electron fluxes by *Banks et al.* [1974]. Although both our model and the model of *Solomon et al.* [1988] have origins in the *Nagy and Banks* [1970] two-stream model, they have evolved substantially along entirely separate paths. Our model owes much to our earlier work with the ionospheric photoelectron flux [*Richards and Torr*, 1984; 1985a].

By incorporating a variable energy grid developed by *Swartz* [1985] and a variable altitude grid we have been able to extend the two-stream model up to energies greater than 20 keV. This has eliminated problems encountered by *Banks et al.* [1974] in matching the continuous slowing down approach that they used above 500 eV with the two-stream approach they used below 500 eV. The continuously variable altitude grid allows altitude steps of less than a kilometer below 90 km up to 50 km at 500 km with a manageable number of grid points.

Further economy in computer time is achieved by introducing the concept of an average energy loss for an excitation or an ionization event. This concept allows the use of only the total excitation and ionization cross sections instead of treating each partial excitation or ionization process separately. That is, the excitation (or ionization) is treated as arising from a single average state for each thermospheric species. The average energy loss depends on the species and also on the energy of the primary electron. The calculation of the emission rates then becomes a two stage process with just the total cross sections being needed to calculate the electron flux as a function of energy and altitude in the first stage. In the second stage, the partial cross sections are folded with the electron fluxes to produce the excitation rates.

For each of the 3 main neutral atmospheric components (O, O₂, N₂) the total cross sections are made up of partial cross sections from the numerous electronic states of each species each corresponding to a different energy state of the atom or molecule. In addition, each electronic state of a molecule can be created in any one of a large number of vibrational energy states. A complete evaluation of the electron flux would require the separate accounting of all these energy losses which we have replaced with a single, energy dependent average energy loss for the excitation and ionization of each of the three main thermospheric species O, O₂, and N₂.

The treatment of excitation processes is relatively straightforward; the average energy loss is specified and the electrons deposited in the correct lower energy bin. However, ionizing collisions are more complex because of the production of secondary electrons which may be produced with energies ranging from 0 up to $E_p - I_i$ where E_p is the energy of the primary electron and I_i is the ionization potential of the state i being produced. We follow the approach of *Banks et al.* [1974] and designate the higher energy electron as the degraded primary and the lower energy electron as the secondary. This means that the maximum secondary energy is then $(E_p - I_i)/2$ as is the minimum energy of the degraded primary. We treat ionization as arising from a single state with an average ionization potential I and we use the measured secondary electron distributions of *Opal et al.* [1971] to determine the average energy E_s of the secondary electrons produced by an electron of energy E_p (we note that the measured secondary electron distributions are in fact a sum of the contributions from all the ionization states). The average energy of the degraded primaries is then $E_p - I - E_s$. A separate ionization potential could be used for each species but a further improvement in computational efficiency can be made by observing that the ionization potentials and secondary electron distributions are similar enough that a single ionization potential and secondary electron distribution for all 3 major species will suffice. Since N₂ is the most important species in aurora, we adopt the N₂ ionization characteristics. At each electron energy, the total number of secondary electrons from O, O₂, and N₂ is calculated and then they are distributed according to the measured secondary electron distributions of *Opal et al.* [1971]. The model has been found to conserve energy to better than 5% for characteristic energies in the range .1 to 20 keV.

2.2. Average Ionization Potentials

The calculation of the average ionization potential follows from the knowledge of the ionization potentials and the partial cross sections for the various ionization states of each of the thermospheric species. For example, N₂ ionization results in the formation of the X, A, and B states of N₂⁺ and also N⁺ which arises from several higher lying states that dissociate. The ionization potentials for the X, A, and B states are 15.6, 16.8, and 18.8 eV respectively while the bulk of the N⁺ probably arises from a state with a threshold near 37 eV [*Erdman and Zipf*, 1986]. The actual energy lost by the primary electrons may be greater than threshold due

to the ions being vibrationally excited and because, in the case of dissociative ionization, the atomic fragments are observed to carry substantial kinetic energy [Liliana and Stordale, 1975]. To complete the calculation of the average ionization energy for N_2 we also need the ratios of the partial cross sections. We examine the high energy case first where the proportions of the various partial cross sections are practically constant and the calculation is straightforward. Above approximately 100 eV, dissociation accounts for $\sim 20\%$ [Rapp et al., 1965] and the B state $\sim 10\%$ [Borst and Zipf, 1970] of the total cross section. According to Cartwright et al. [1975], the X and A state cross sections are approximately equal (that is, $\sim 35\%$). Using these percentages for the partial cross sections and ionization potentials given above, the average ionization potential is ~ 20 eV for high energy electron impact ionization of N_2 . We now examine the low energy average energy loss per collision. The average ionization potential begins at 15.6 eV at threshold when the X state is produced but increases to ~ 16 eV above 17 eV when the A state threshold is reached. There is only a marginal increase when the B state threshold is reached at 18.8 eV because it accounts for less than 10% of the total cross section at these energies and the energy loss of 18.8 eV is only marginally larger than 16.8 eV. After about 30 eV dissociative ionization becomes important. The ionization potential then rises steadily to approximately 19 eV at 50 eV before leveling off toward 20 eV at high energies.

A similar calculation yields an average ionization potential of approximately 18 eV for both O and O_2 , at high energies. Because N_2 is the dominant constituent and all three ionization potentials are similar, we use the average N_2 ionization potential for all three species. This simplifies the calculation and reduces the computation time without introducing significant errors. The adopted ionization and excitation energy losses as a function of primary electron energy are shown in Figure 1. This figure also shows the average energy of the secondary electrons as a function of the primary energy. Below 25 eV the ionization potential is assumed to be 16 eV while above 25 eV it is represented by $10(1 + (1 - 15/E)^{1/2})$ eV.

2.3. Average Secondary Electron Energy

To obtain the secondary electron distribution we adopt the Banks et al. [1974] parameterization of the Opal et al. [1971] measured distributions. The probability of a secondary electron of energy E , is given by

$$P_s(E_s) = \frac{A}{1 + (E_s/\bar{E})^2} \quad (1)$$

where $A = [(\bar{E} \arctan(E_m/\bar{E}))^{-1}]$ is a normalization factor that ensures a total probability of unity when integrated over all secondary energies from 0 to $E_m = (E_p - I)/2$ and $\bar{E} = 14$ is an empirical normalization factor. The product of E_s and Equation 1 integrated over energy yields the average secondary electron energy for a primary energy E_p as

$$E_{s,av} = 0.5 A \bar{E}^2 \ln \left(1 + (E_p/\bar{E})^2 \right) \quad (2)$$

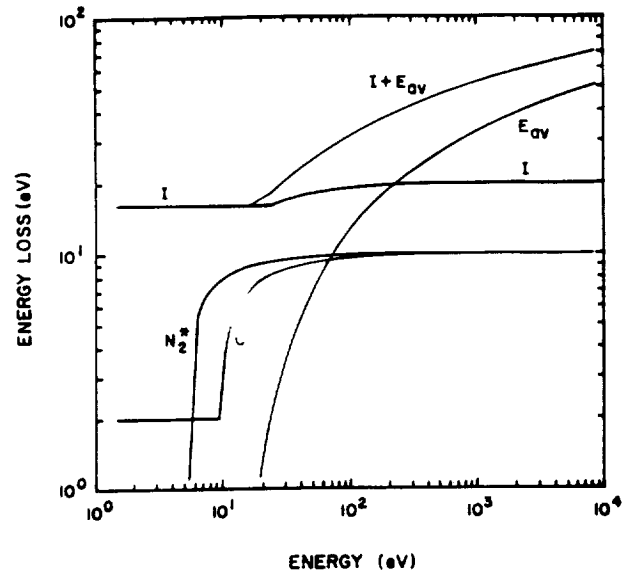


Fig. 1. Average energy losses per collision and average secondary electron energies ($E_{s,av}$) as a function of primary electron energy. The average ionization potential is labelled I and the total energy loss per ionization is labelled $I + E_{s,av}$. The average excitation potentials are indicated by an asterisk and the O_2 excitation potential is set equal to that of N_2 . Note that below 5 eV, the N_2 excitation potential is set at 1 eV.

The dependence of the average secondary energy on the primary energy is shown in Figure 1 along with the average total energy loss of the primary ($I + E_{s,av}$). The average energy of the secondaries increases steadily from 0 near threshold to 52 eV for 10 keV primary electrons. The total energy loss per ionizing collision for 10 keV electrons is 72 eV, when the 20 eV ionization potential is included. The average energy of the secondaries is approximately equal to the ionization energy for 200 eV primary electrons.

A quantity of interest, in relation to energy degradation of high energy electrons, is the average energy required to produce each electron-ion pair. The average energy required to produce each electron-ion pair is a quantity that is independent of electron energy and is also remarkably independent of the species being ionized. The experimental value for the energy lost per electron-ion pair for high energy electron is 35 eV [Valentine and Curran, 1958]. This energy loss per electron-ion pair was used in early auroral electron deposition codes [Rees, 1963; Rees et al. 1969; Rees and Jones, 1973].

An approximate value for the energy loss per electron-ion pair can be deduced by using the average energy losses depicted in Figure 1, assuming that for electron energies above approximately 100 eV the energy lost to excitation collisions is small and can be neglected. With this assumption, it requires about 160 ionizing collisions to thermalize a single 10 keV electron. Thus, on the average, 62 eV is lost in the creation of each of the 160 electron-ion pairs. Since the ionization energy is 20 eV for electron energies above 100 eV, the average energy of the secondaries is ~ 42 eV. This means that

the 160 secondary electrons are sufficiently energetic to create one more electron-ion pair each. If all secondaries created an additional electron-ion pair, the total number of pairs would be 320 and the average energy per electron-ion pair would decrease from 62 to 31 eV. In reality this does not happen because, below 100 eV, excitation processes begin to compete effectively with the ionization processes for the available electron energy and the number of additional electron-ion pairs produced by the secondary electrons would be less than 160. In fact, for a 42 eV electron the total ionization and excitation cross sections are approximately equal and only half the secondaries could be expected to produce an additional electron-ion pair. This agrees with our previous calculations that show that a third rather than a half, of the total ionization is created by degraded primaries and secondaries with energies below 100 eV [Richards and Torr, 1985b]. Thus the original 10 keV electron would ultimately produce about 240 electron ion pairs and yield an average energy loss per electron-ion pair of 42 eV. This is only an estimate of the energy lost per electron-ion pair and a more detailed calculation including transport is required to determine the actual value. It was pointed out by Banks *et al.* [1971] that escaping backscattered electrons will be lost to the system and act to increase the energy loss per electron-ion pair.

We have summed the total ion production rate in our full auroral calculation, and we obtain an average energy loss per electron-ion pair of 35 eV, which is smaller than our estimate but in agreement with the laboratory measured value. A slightly higher value of 37 eV was obtained by Fox and Victor [1988] using their discrete local energy loss method. The reason that the energy lost per electron-ion pair is not a strong function of electron energy has to do with the relationship between the average secondary electron energy and the primary electron energy. Electrons with higher initial energies suffer a greater energy loss per collision as they degrade but they produce higher energy secondaries which are more likely to generate secondary ionization. For example, a 1 keV electron will undergo only 22 ionizing collisions with an average energy loss of 45 eV before it thermalizes. Thus, the secondary electrons have an average energy of only 25 eV compared to the 42 eV for the 10 keV electrons and are much less likely to produce additional ions.

2.4. Cross Sections

In a number of previous studies of the ionospheric photoelectron flux we have chosen measured total excitation cross sections that produce good agreement between theory and the photoelectron spectrometer measurements from the AE-E satellite [Lee *et al.*, 1980]. At low altitudes where N_2 is the dominant species, the total cross section obtained from electron mobility studies by Pitchford and Phelps [1982] was found to be compatible with the PES measurements. At high altitudes where atomic oxygen is the dominant species, the emission cross sections measured by Zipf and co-workers produced good agreement between theory and PES measurements. These total cross sections for energies be-

low 100 eV have been published by Richards and Torr [1988]. Basically the same cross sections have been used in this study but they have been reparameterized to extend them to higher energies.

Above 100 eV, the excitation cross sections decay rapidly with increasing energy and are much less important than the ionization cross sections both because they are smaller and because the energy loss per collision is smaller. The total ionization cross sections are better established than the total excitation cross sections although there are some differences [Kieffer and Dunn, 1966]. We have adopted the N_2 and O_2 total ionization cross sections of Rapp and Englander-Golden [1965] which have also been used by most other modelers. The total ionization cross section for O is from Brook *et al.* [1978]. The elastic cross sections are very important because of their role in inhibiting transport. We have used the elastic cross sections of Solomon *et al.* [1988] and also their elastic backscatter coefficients. The total cross sections used in our auroral model are shown in Figure 2. Our N_2 total excitation cross section is comparable to that of Solomon *et al.* [1988] below 25 eV but is smaller at higher energies. The differences at high energies have little effect on the calculated fluxes because the excitation cross section is smaller than the ionization cross section. However, differences in cross sections below 30 eV produce comparable differences in fluxes. The N_2 total excitation cross section of Strickland *et al.* [1983] is almost a factor of two larger than ours at all energies and their fluxes would be a factor of two lower below 30 eV, at least below 200 km where N_2 is the dominant species. The cross sections of Solomon *et al.* [1988] and Strickland *et al.* [1983] were obtained by summing the partial cross sections and there is the possibility of double counting some cross sections; for example, those that lead to dissociation. Moreover, Strickland *et al.* [1983] included large

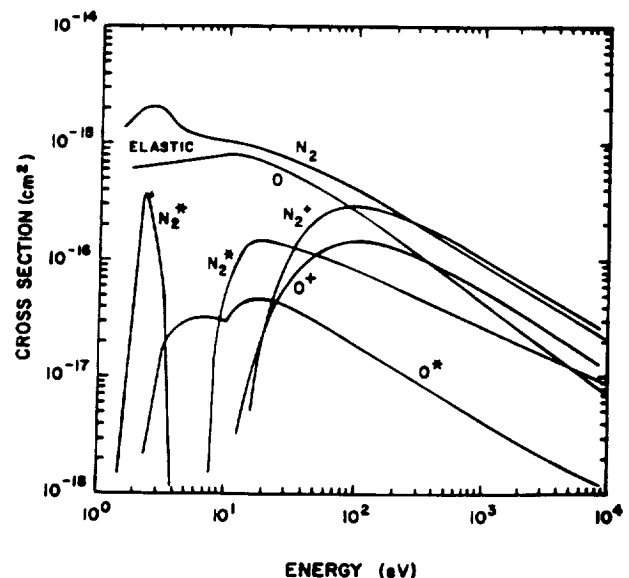


Fig. 2. Total elastic, excitation, and ionization cross sections employed in the model. The ionization cross sections are indicated by a plus while the excitation cross sections are indicated by an asterisk.

Rydberg cross sections from *Green and Stolarski* [1972] which have been revised sharply downward by *Porter et al.* [1976]. There is now good agreement between the total cross section of *Pitchford and Phelps* [1982] and the sum of the partial excitation cross sections of *Cartwright et al.* [1977a,b] as revised by *Trajmar et al.* [1983], below 20 eV. Above 20 eV, the ionization cross section becomes an increasingly important component of the total inelastic cross section and it is not easy to compare the two cross sections.

The total atomic oxygen excitation cross section employed by *Solomon et al.* [1988] is a factor of 2 larger than ours above 15 eV and will produce a similar difference in flux above 250 km where O is the dominant species but the atomic oxygen cross section has little effect on the integrated emission rates. Our atomic oxygen excitation cross section was obtained by summing the measured emission cross sections for 1304, 1356, and 1027 Å [*Zipf and Erdman*, 1985], the 989 cross section from *Gulcicek and Doering* [1988], and the theoretical 1D and 1S from *Henry et al.* [1969]. Implicit in this procedure is the assumption that the higher lying triplet and quintet states are included in the 1304 and 1356 emission cross sections via cascade. We have left out some theoretical Rydberg cross sections proposed by *Jackman et al.* [1977] and some minor states that radiate directly to the ground state but for which there is no experimental data. Thus, our cross section must be regarded as a lower limit.

Figure 3 shows the excitation cross sections for the second positive ($C^3\pi_u$) and Lyman-Birge-Hopfield ($a^1\pi_g$) systems of N_2 . Also shown is the cross section used for calculation of the $O(^5S)$ 1356 Å emission rate. We obtained this cross section by reducing the measured cross section of *Stone and Zipf* [1974] by the factor 3.1 which is the same factor that the 1304 Å emission cross section of *Stone and Zipf* [1974] was reduced by *Zipf and Erdman* [1985]. The ($C^3\pi_u$) cross section was obtained

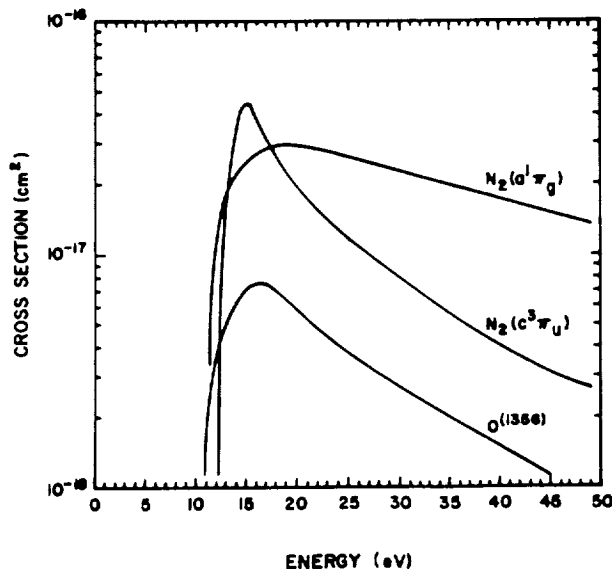


Fig. 3. Cross sections for the three excited states giving rise to the emissions studied in this paper.

by multiplying the 3371 Å cross section of *Imami and Borst* [1974] by 4 and the ($a^1\pi_g$) cross section is from *Ajello and Shemansky* [1985].

We have examined the sensitivity of the emission rate ratios to cross sections and this will be discussed later. In all these calculations we have used the $1 \text{ erg cm}^{-2} \text{ s}^{-1}$ Gaussian incident flux distribution, and the neutral atmosphere employed by *Strickland et al.* [1983].

3. RESULTS

3.1. Comparison With Previous Work

We have calculated the N_2 3371 Å, N_2^+ 3914 Å, N_2^+ 4278 Å, O 1356 Å, and several N_2 LBH band emission rates as a function of energy and these are shown in Figure 4. This figure shows that both the 3371 Å and 3914 Å emission rates are independent of the characteristic energy of the precipitating flux for energies above 2 keV in agreement with the results of *Strickland et al.* [1983] and *Daniell and Strickland* [1986]. Not only is the shape in good agreement but, except for the 1356 Å emission rates, the magnitudes are also in good agreement. Although the shape of the 1356 Å curve is in good agreement with that of *Strickland et al.* [1983], the magnitude is a factor of 2.5 lower owing to the use of the revised cross section of *Zipf and Erdman* [1985].

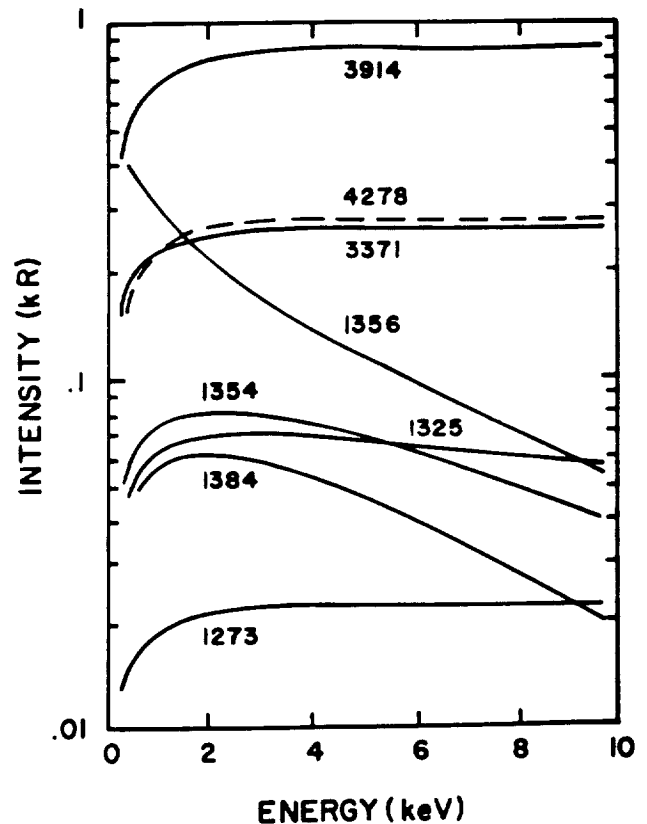


Fig. 4. Calculated emission rates as a function of the characteristic energy for a Gaussian energy distribution with a total incident energy flux of $1 \text{ erg cm}^{-2} \text{ s}^{-1}$. When differences in cross sections are taken into account, there is excellent agreement with the calculations in Figure 8 of *Strickland et al.* (1983) and Figure 11 of *Daniell and Strickland* (1986).

We have included O_2 Schuman-Runge absorption which affects both the 1356 Å and the 1200-1600 Å LBH bands when the characteristic energies are high and the electrons penetrate to lower altitudes [Strickland *et al.*, 1983]. The ratios of the LBH bands are taken from Ajello and Shemansky [1985].

Our calculated second positive to first negative emission rate ratios are within 20% of the measured values for the N_2 emissions. At 10 keV, our 3371 Å to 3914 Å ratio is 0.3 compared to 0.25 from Sharp *et al.* [1979] and our 3371 Å to 4278 Å ratio is 0.98 compared to 0.8 from Solomon [1989]. Solomon obtained better agreement between his model ratios and the measured ratios but there is sufficient uncertainty in the input parameters to account for the differences.

3.2. Sensitivity of Ratios

We have performed some parameter studies to characterize the sensitivity of the ratio of the second positive to first negative integrated emission rates to possible errors in the model inputs. Obviously, a reduction of 20% in the 3371 Å emission rate cross section would bring the calculated and measured values into excellent agreement but a 30% increase in the N_2 total excitation cross section has a similar effect by decreasing the low energy electron flux which is responsible for most of the 3371 Å emission. Likewise, a 30% increase in the N_2 total ionization cross section above 100 eV reduces the ratio from 0.3 to 0.25 by increasing the 3914 Å production rate. The integrated ratio is not sensitive to changes of up to a factor of two in most other parameters including: the atomic and molecular oxygen inelastic cross sections, the O, O_2 , and N_2 elastic cross sections and backscatter coefficients, and the relative concentrations of the species. We estimate a possible error of 10% in our computed average excitation and ionization potentials but this has negligible effect on our computed ratios.

3.3. Energy Budget

The incident electron energy flux is initially partitioned into a large number of excitation and ionization processes before it finally emerges as heat for the thermosphere or is radiated into space. Figure 5 shows the gross energy partition amongst ionizations, excitations, thermal electron heating and backscattered escape flux as a function of characteristic energy. N_2 ions capture the greatest share of the available energy (35%). Excitation of N_2 is next with (20%) while only 15% is lost through the escaping backscattered flux. This escape flux is much smaller than the 45% obtained by Banks *et al.* [1974], possibly as a result of the use of different cross sections and backscatter coefficients. Below 1 keV, ionization and excitation of atomic oxygen absorption are important energy sinks for the electron energy, but they become small for high energy incident fluxes. Absorption in molecular oxygen shows the opposite trend, becoming more important with the deeper penetration of the higher energy fluxes. Thermal electrons capture a greater proportion of the available energy, the lower the characteristic energy.

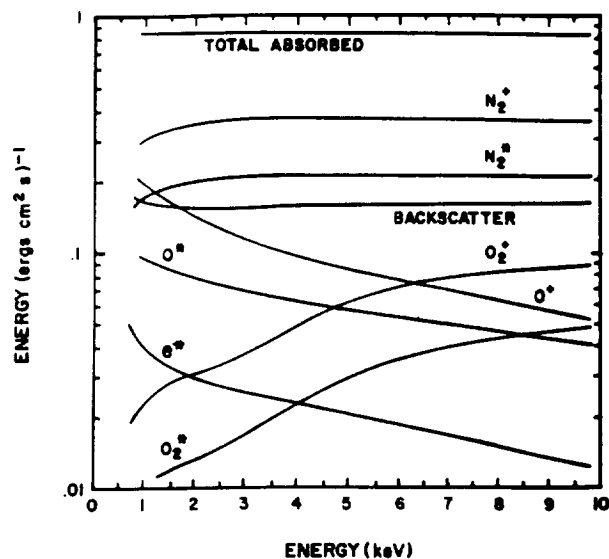


Fig. 5. The initial partitioning of the incident $1 \text{ erg cm}^{-2} \text{ s}^{-1}$ energy flux between ionization, excitation, thermal electron heating, and backscatter as a function of characteristic energy. The largest proportion of the energy ($\sim 35\%$) goes initially into the ionization potential of the N_2^+ while ($\sim 20\%$) goes into N_2 excitation. Only ($\sim 16\%$) is backscattered out of the thermosphere. O is an important absorber of energy at the lowest energies while O_2 becomes increasingly important as the characteristic energy increases.

3.4. Electron Flux Spectra

Downward moving fluxes at 120, 174, 223, and 326 km are shown in Figure 6 for a 5 keV incident Gaussian flux with an energy flux of $1 \text{ erg cm}^{-2} \text{ s}^{-1}$. The incident flux can be seen centered at 5 keV in Figure 6. At the two highest altitudes, there is very little degradation of this initial flux but the degradation is noticeable at 174 km and pronounced at 120 km. Because there is so

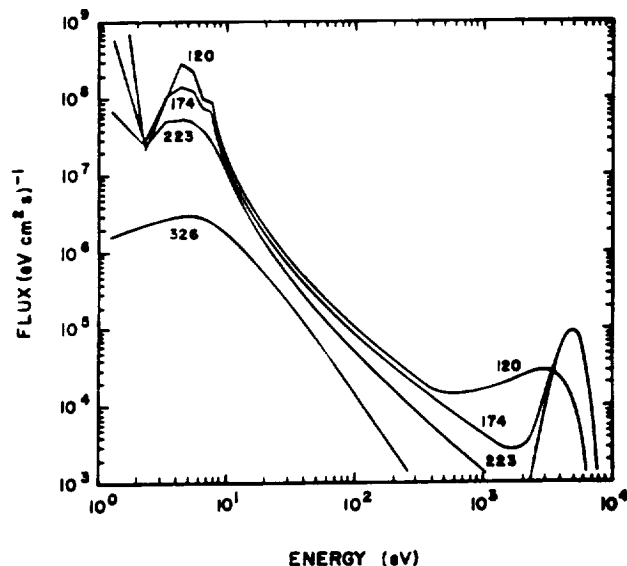


Fig. 6. Downward moving electron flux spectra at several altitudes for a 5 keV Gaussian incident flux. The incident energy flux is $1 \text{ erg cm}^{-2} \text{ s}^{-1}$.

little interaction with the thermosphere for high energy electrons at the high altitudes, there are few degraded primaries to fill in the region between 300 eV and 5 keV. However, at the lowest altitudes this intermediate energy range is filled in. Comparison of the downward fluxes in Figure 6 with the upward fluxes in Figure 7 reveals that, below 225 km, where transport is inhibited, the electron flux is isotropic for energies less than 300 eV. At 326 km, the upward (escape) flux is a factor of 2 larger than the downward flux at low energies and orders of magnitude larger at intermediate energies.

4. CONCLUSIONS

We have developed an efficient two-stream auroral electron model that incorporates the concept of average energy loss. This model produces integrated emission rates that are in excellent agreement with the more sophisticated multi-stream model of Strickland *et al.* [1983] but is in disagreement with the model of Rees and Lummerzheim [1989] with regards to the energy dependence of the N₂ 3371 Å second positive emission rate. Our calculations give a value of 35 eV for the average energy lost per electron-ion pair produced independent of primary electron energy and we have explained this behavior in terms of the variation in the energy of the secondary electrons. We find that more than 30% of the initial energy flux is stored initially as ionization energy of N₂⁺ while about 20% goes into excited states of N₂ while only 15% is backscattered out of the thermosphere. All other processes are minor except at low incident energies where 20% of the energy is stored in atomic oxygen ions.

Acknowledgments. This work was supported by NSF grants ATM-8713693, ATM-8716036, ATM-8907808, and ATM-8714461; and NASA grants NAGW-922, and NAGW-996 at The University of Alabama in Huntsville.

The Editor thanks R. E. Daniell and M. H. Rees for their assistance in evaluating this paper.

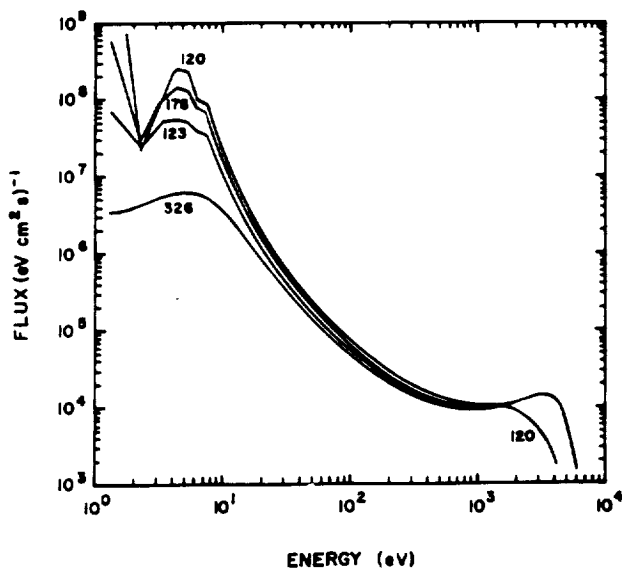


Fig. 7. Upward moving electron flux spectra for the 5 keV Gaussian incident flux shown in Figure 6.

REFERENCES

- Ajello, J. M., and D. E. Shemansky, A reexamination of important N₂ cross sections by electron impact with application to the dayglow: The Lyman-Birge-Hopfield band system and N I (119.99 nm), *J. Geophys. Res.*, *90*, (A10), 1985.
- Banks, P. M. and C. R. Chappell, and A. F. Nagy, A new model for the interaction of auroral electrons with the atmosphere: spectral degradation, backscatter, optical emission, and ionization, *J. Geophys. Res.*, *79*, 1459, 1974.
- Borst, W. L., and E. C. Zipf, Cross section for electron-impact excitation of the (0,0) first negative band of N₂⁺ from threshold to 3 keV, *Phys. Rev. A*, *1*, 834, 1970.
- Brook, E., M. F. A. Harrison, and A. C. H. Smith, Measurements of the electron impact ionisation cross sections of He, C, O and N atoms, *J. Phys. B*, *11*, 3115, 1978.
- Cartwright, D. C., W. R. Pendleton, and L. D. Weaver, Auroral emission of the N₂⁺ Meinel bands, *J. Geophys. Res.*, *80*, 651, 1975.
- Cartwright, D. C., A. Chutjian, S. Trajmar, and W. Williams, Electron impact excitation of the electronic states of N₂, I, Differential cross sections at incident energies from 10 to 50 eV, *Phys. Rev. A*, *16*, 1013, 1977a.
- Cartwright, D. C., S. Trajmar, A. Chutjian, and W. Williams, Electron impact excitation of the electronic states of N₂, II, Integral cross sections at incident energies from 10 to 50 eV, *Phys. Rev. A*, *16*, 1041, 1977b.
- Daniell, R. E., and D. J. Strickland, Dependence of the auroral middle UV emissions on the incident electron spectrum and neutral atmosphere, *J. Geophys. Res.*, *91*, 321, 1986.
- Erdman, P. W., and E. C. Zipf, Dissociative excitation of the NI(⁵S) state by electron impact on N₂: Excitation function and quenching, *J. Geophys. Res.*, *91*, 1986.
- Fox, J. L., and G. A. Victor, Electron energy deposition in N₂ gas, *Planet. Space Sci.*, *36*, 326, 1988.
- Garstang, R. H., Multiplet intensities for lines ⁴S-²D of SII, OII and NI, *Astrophys. J.*, *115*, 506, 1952.
- Green, A. E. S. and R. S. Stolarski, Analytic models of electron impact excitation cross sections, *J. Atmos. Terr. Phys.*, *34*, 1703, 1972.
- Gulcicek, E. E., and J. P. Doering, Absolute differential and integral electron excitation cross sections of the atomic oxygen ³P and ⁵P states at 30 eV, *J. Geophys. Res.*, *92*(A4), 3445-3448, 1988.
- Henry, R. J. W., P. G. Burke and A. L. Sinfailam, Scattering of electrons by C, N, O, N⁺, O⁺ and O⁺⁺, *Phys. Rev.*, *178* 218, 1969.
- Jackman, C. H., R. M. Garvey, and A. E. S. Green, Electron impact on atmospheric gases, I. Updated cross sections, *J. Geophys. Res.*, *82*, 5081-5090, 1977.

- Kieffer, L. J., and G. H. Dunn, Electron impact ionization cross section data for atoms, atomic ions and diatomic molecules: I. experimental data, *Rev. Mod. Phys.*, *38*, 1, 1966.
- Lee, J. S., J. P. Doering, T. A. Potemra, and L. H. Brace, Measurements of the ambient photoelectron spectrum from Atmosphere Explorer, I, AE-E measurements below 300 km during solar minimum conditions, *Planet. Space Sci.*, *28*, 947, 1980.
- Liliana, D., and J. A. D. Stockdale, Dissociative ionization of molecules by electron impact, II, Kinetic energy and angular distributions of N^+ and N^{++} ions from N_2^+ , *J. Chem. Phys.*, *63*, 3898-3906, 1975.
- Lummerzheim, D., M. H. Rees, and H. R. Anderson, Angular dependent transport of auroral electrons in the upper atmosphere, *Planet. Space Sci.*, *37*, 109, 1989.
- Mahmood, I., and Walter L. Borst, Electron excitation of the (0,0) second positive band of nitrogen from threshold to 1000 eV⁻, *J. Chem. Phys.*, *61*, 1115, 1974.
- Nagy, A. F., and P. M. Banks, Photoelectron fluxes in the ionosphere, *J. Geophys. Res.*, *75*, 6260, 1970.
- Opal, C. B., W. K. Peterson, and E. C. Beaty, Measurements of secondary-electron spectra produced by electron impact ionization of a number of simple gases, *J. Chem. Phys.*, *55*, 4100, 1971.
- Pitchford, L. C., and A. V. Phelps, Comparative calculations of electron swarm properties in N_2 at moderate E/N values, *Phys. Rev. A* *25*, 540, 1982.
- Porter, H. S., C. H. Jackman, and A. E. S. Green, Efficiencies for production of atomic nitrogen and oxygen by relativistic proton impact in air, *J. Chem. Phys.*, *65*, 154-167, 1976.
- Rapp, D., and P. Englander-Golden, Total cross sections for ionization and attachment in gases by electron impact I, Positive ionization. *J. Chem. Phys.*, *43*, 1464, 1965.
- Rees, M. H., Auroral ionization and excitation by incident energetic electrons, *Planet. Space Sci.*, *11*, 1209, 1963.
- Rees, M. H. and R. A. Jones, Time dependent studies of the aurora, II, Spectroscopic morphology, *Planet. Space Sci.*, *21*, 1213, 1973.
- Rees, M. H., and D. Luckey, Auroral electron energy derived from the ratio of spectroscopic emissions, 1, Model computations, *J. Geophys. Res.*, *79*, 5181, 1974.
- Rees, M. H., and D. Lummerzheim, Characteristics of auroral electron precipitation derived from optical spectroscopy, *J. Geophys. Res.*, *94*, 6799, 1989.
- Rees, M. H., D. Lummerzheim, R. G. Roble, J. D. Winningham, J. D. Craven, and L. A. Frank, Auroral Energy deposition rate, characteristic electron energy and ionospheric parameters derived from Dynamics Explorer 1 images, *J. Geophys. Res.*, *93*, 12841, 1988.
- Rees, M. H., A. I. Stewart, and J. C. G. Walker, Secondary electrons in aurora, *Planet. Space Sci.*, *17*, 1997, 1969.
- Richards, P. G., and D. G. Torr, An investigation of the consistency of the ionospheric measurements of the photoelectron flux and solar EUV flux, *J. Geophys. Res.*, *89*, 5625, 1984.
- Richards, P. G., and D. G. Torr, The altitude variation of the ionospheric photoelectron flux: a comparison of theory and measurement, *J. Geophys. Res.*, *90*, 2877, 1985a.
- Richards, P. G. and D. G. Torr, On the production of N^+ by energetic electrons, *J. Geophys. Res.* *90*, 9917, 1985b.
- Richards, P. G., and D. G. Torr, Ratio of photoelectron to EUV ionization rates for aeronomic studies *J. Geophys. Res.*, *93*, 4060, 1988.
- Sharp, W. E., M. H. Rees, and A. I. Stewart, Coordinated rocket and satellite measurements of an auroral event, 2, The rocket observations and analysis, *J. Geophys. Res.*, *84*, 1977, 1979.
- Shepherd, G. G., J. D. Winningham, F. E. Bunn, and F. W. Thirkettle, An empirical determination of the production efficiency for auroral 6300-Å emission by energetic electrons, *J. Geophys. Res.*, *85*, 715, 1980.
- Solomon, S. C., Auroral excitation of the N_2 2P(0,0) and VK(0,9) bands, *J. Geophys. Res.*, *94*, 17215, 1989.
- Solomon, S. C., P. B. Hays, and V. J. Abreu, The auroral 6300 Å emission: Observations and modeling, *J. Geophys. Res.*, *93*(A9), 9867, 1988.
- Stone, E.J., and E.C. Zipf, Electron-impact excitation of the $^3S^o$ and $^5S^o$ states of atomic oxygen, *J. Chem. Phys.*, *60*, 4237, 1974.
- Strickland, D. J., J. R. Jasperse, and J. A. Whalen, Dependence of auroral FUV emissions on the incident electron spectrum and neutral atmosphere, *J. Geophys. Res.*, *88*, 8051, 1983.
- Swartz, W. E., Optimization of energetic electron energy degradation calculations, *J. Geophys. Res.*, *90*, 6587, 1985.
- Trajmar, S., D. F. Register, and A. Chutjian, Electron scattering by molecules, II, Experimental methods and data, *Phys. Rep.*, *97*, 219, 1983.
- Vallance Jones, A., A model for the excitation of electron aurora and some applications, *Can. J. Phys.*, *53*, 2276, 1975.
- Zipf, E. C., and P. W. Erdman, Electron impact excitation of atomic oxygen: Revised cross sections, *J. Geophys. Res.*, *90*, 11087, 1985.

P. G. Richards and D. G. Torr, University of Alabama, Research Institute C-10, Huntsville, AL 35899.

(Received October 18, 1989;
accepted November 28, 1989.)

The Dependence of Modeled OI 1356 and N₂ Lyman Birge Hopfield Auroral Emissions on the Neutral Atmosphere

G. A. GERMANY AND M. R. TORR

Space Science Laboratory, NASA Marshall Space Flight Center, Huntsville, Alabama

P. G. RICHARDS AND D. G. TORR

University of Alabama in Huntsville, Huntsville, Alabama

Images of the entire auroral oval at carefully selected wavelengths contain information on the global energy influx due to energetic particles and some information on the characteristic energy of the precipitating particles. In this paper we investigate the sensitivity of selected auroral emissions to changes in the neutral atmosphere. In particular, we examine the behavior of OI 1356 Å and two Lyman Birge Hopfield (LBH) bands and their ratios to each other with changing atmospheric composition. The two LBH bands are selected so that one lies in the region of strong O₂ absorption (1464 Å) and one lies at a wavelength where O₂ absorption is effectively negligible (1838 Å). We find that for anticipated average uncertainties in the neutral atmosphere (factor of 2 at auroral altitudes), the resultant change in the modeled intensities is comparable to or less than the uncertainty in the neutral atmosphere. The smallest variations, for example, are for I 1838 (approximately 10 to 20%) while the largest variation is seen in the OI 1356 Å emission which is linear with [O] to within 20%. We have also investigated the dependence of these intensities, and their ratios, to much larger changes in the composition (i.e., [O]/[N₂]) such as might be encountered in large magnetic storms, or over seasonal or solar cycle extremes. We find that the variation in the I 1356/I 1838 ratio over the equivalent of a solar cycle is less than 50%. The summer-to-winter changes are approximately a factor of 2. The I 1356/I 1838 ratio is a very sensitive indicator of the characteristic energy, showing a change of 13 over the energy range 200 eV to 10 keV. The corresponding change in the LBH long-to-short wavelength ratio is much less (about a factor of 3). However, the latter is insensitive to changes in the neutral atmosphere (<20% changes in LBH emission ratio for large changes in N₂). The three emissions therefore potentially provide a most valuable diagnostic of particle characteristic energy and energy flux.

1. INTRODUCTION

While in situ observations of energetic particles provide accurate information on the particle characteristics at the point of measurement, imaging from space of the entire auroral oval holds the potential for providing details on total auroral energy influx, estimates of the characteristic energy of the auroral particles, and the capability to map and relate the footprint of this derived information back along the magnetic field lines to various regions of the magnetosphere. Auroral imaging in the vacuum ultraviolet permits observations of the regions of interest under both day and night conditions. Work by *Rees and Luckey* [1974] on the ratios of visible emissions, UV emission intensity calculations by *Strickland et al.* [1983], and analysis of UV auroral spectra by *Ishimoto et al.* [1988] all indicate the potential value of using ratios of emission intensities to study auroral processes. A major focus of work in this area at the present time is to establish the quantitative footing on which such determinations can be placed.

With the exception of H I Ly α , the OI multiplets at 1304 Å and 1356 Å and the N₂ Lyman Birge Hopfield (LBH) bands are the most prominent vacuum ultraviolet auroral emissions. The OI 1304 Å emission has a high efficiency for multiple scattering. As a result, it has limited use for actual auroral imaging, although it does have potential value as an indicator of the O concentration. While the 1356 Å emission does undergo multiple scattering, the efficiency is relatively small [*Strickland and Anderson*, 1983] and we ignore multiple scattering for I 1356 for this study. Similar

considerations allow us to also ignore multiple scattering for the N₂ LBH emissions that are also considered in this study. The OI 1356 Å emission is absorbed increasingly by O₂ with decreasing altitude. Thus its intensity varies strongly (inversely) with increasing depth of penetration of the incident auroral electrons and hence with increasing energy. The N₂ LBH transitions are electric dipole forbidden and the only prominent excitation mechanism is electron impact. The LBH emission may therefore serve as a direct measure of the total energy flux of charged particles into the atmosphere. The longer wavelength LBH bands, which lie outside the region of substantial O₂ absorption, are useful indicators of the total energy influx, while the long-to-short wavelength LBH intensity ratio provides information on the O₂, and thus also some information on energy. These are the emissions (OI 1356, long and short wavelength LBH) on which we shall concentrate in this study.

The purpose of this paper is to examine the sensitivity of these emissions to both likely uncertainties and anticipated changes in the neutral atmosphere. This is just one step in the process of making quantitative interpretations of auroral images, but an important one. We will consider other aspects (energy spectral characteristics and wavelength spectral extraction) elsewhere. In this paper we conduct a series of sensitivity studies using an auroral emission code that has been developed by our group [*Richards and Torr*, 1990]. The results are discussed below.

2. DESCRIPTION OF AURORAL CODE

The behavior of auroral OI 1356 and N₂ LBH emissions has been studied with the use of an auroral computer model. The model is a two-stream auroral electron energy loss code that determines the energy degradation of the primary spectrum as a func-

tion of energy and altitude and determines the production rates of prominent auroral emissions. A more complete description of the program, the selected cross sections, and comparison with other auroral models is given by *Richards and Torr* [1990]. The N_2 ($a^1\pi_g$) cross section, as well as the ratios of the individual LBH bands are taken from *Ajello and Suemansky* [1985]. Attenuation due to molecular oxygen absorption is explicitly computed with O_2 absorption cross sections taken from *Ogawa and Ogawa* [1975] and *Hudson* [1971]. The model currently assumes that O_2 absorption at wavelengths beyond 1750 Å can be ignored.

The model is optimized by incorporating variable energy bins [*Torr et al.*, 1974; *Swartz*, 1985] for the energy grid. To prevent numerical instabilities and violation of energy conservation, the altitude grid is variable to allow small grid steps (less than 1 km) at low altitudes. As a result, energy is typically conserved to within 10%. The code utilizes either the MSIS-86 neutral atmosphere [*Hedin*, 1987] or a user-supplied atmosphere. Either monoenergetic fluxes or a specified energy spectrum may be used. The incident energy spectrum may be modeled as a Gaussian or Maxwellian distribution, after *Strickland et al.* [1983] (hereafter *SJW*), or a user-supplied distribution may be used. All simulations reported below employed a $1 \text{ erg cm}^{-2} \text{ s}^{-1}$ Gaussian incident flux distribution. The Gaussian scale parameter, labeled W in *SJW*, has been set equal to $0.25 E_{\text{char}}$ which yields a full width at half maximum of $0.5 [\ln 2]^{1/2} E_{\text{char}}$, where E_{char} is the characteristic energy.

3. SENSITIVITY STUDIES

The emission studies reported here involved modeling auroral emissions at local midnight at 60 degrees north latitude. Table 1 lists the MSIS parameters used in this study as well as detailing the range of solar activity investigated in the latter part of the study.

TABLE 1. MSIS Model Parameters

	Solar Activity		
	Minimum	Moderate	Maximum
$F_{10.7}$ cm Flux Index	75	110	200
Average $F_{10.7}$ cm Index	75	110	200
A_p Magnetic Activity Index	4	20	100

Geographic latitude, 60 degrees; geographic longitude, 0 degrees; solar apparent time, 0.0 hours; days 173, 356

Three emission ratios were studied. The first ratio was $OI\ 1356/LBH_{\text{long}}$, where LBH_{long} designates an N_2 LBH emission not strongly dominated by O_2 absorption. Specifically, the (2,8) band at 1838 Å was chosen for this purpose. Second, the ratio $OI\ 1356/LBH_{\text{short}}$ was also modeled to investigate the relative influence of absorption by molecular oxygen. Here, LBH_{short} is represented by the (1,1) band at 1464 Å. By analogy with the previous definition LBH_{short} is an LBH emission which is strongly absorbed by O_2 . The final ratio studied was $LBH_{\text{long}}/LBH_{\text{short}}$. The volume emission rates integrated over altitude give the surface brightness or column intensity of the emission which we shall designate $I\ 1356$, $I\ 1464$, and $I\ 1838$. These are the intensities that would be seen by a nadir viewing instrument from above the emission layer.

3.1. Sensitivity to the Uncertainty of a Single Constituent

The first question we chose to investigate was the dependence of the selected emissions and emission ratios on the uncertainties at any given time in our knowledge of the neutral atmosphere. We have assumed for this purpose that if we base our calculations on the MSIS-86 model atmosphere, the concentrations of O , O_2 , or N_2 at auroral altitudes may on the average be uncertain by as much

as a factor of 2. There will be occasions on which the uncertainty will exceed a factor of 2, but typically it will be less. This is similar to studies performed in *SJW*, but extends the investigation to study the dependence of auroral emissions to each of the major atmospheric constituents. In addition, in section 3.2 below, we further extend the study to include larger compositional variations due to seasonal and solar cyclic variations.

The unperturbed, or reference, atmosphere is an MSIS model for high solar activity at summer solstice. Figure 1. Figure 2

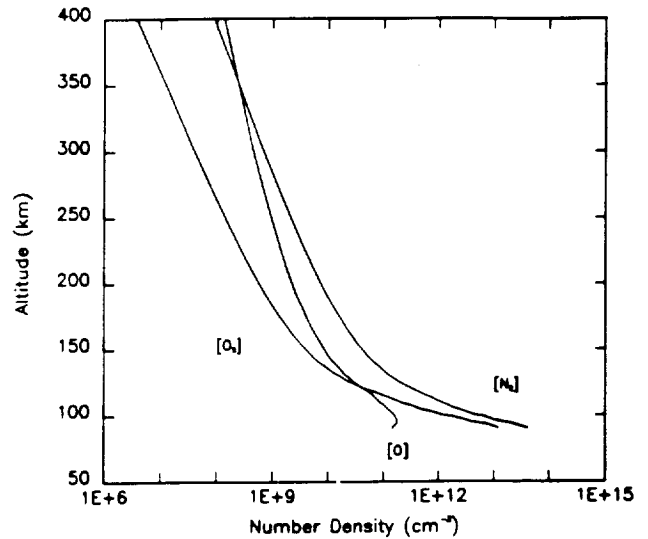


Fig. 1. MSIS-86 reference atmosphere used as the standard case in this study (Day = 173, $F_{10.7} = 200$, $A_p = 100$).

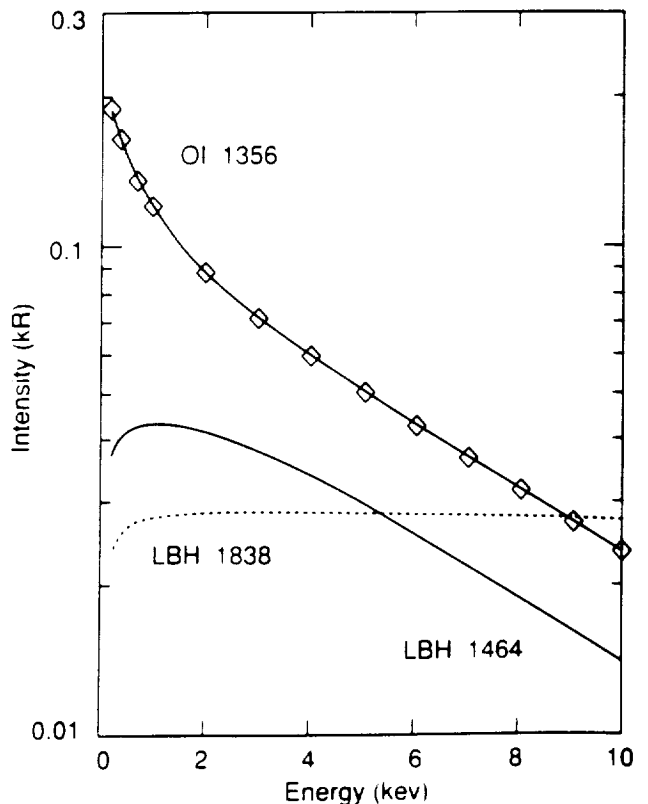


Fig. 2. Nadir viewing column brightnesses ($I\ 1356$, $I\ 1464$, and $I\ 1838$) calculated using the reference atmosphere shown in Figure 1. The diamonds here and in the remainder of the figures show the selected Gaussian characteristic energies for the incident electron energy distribution.

shows the computed I 1356, I 1464, and I 1838 intensities for this model atmosphere as a function of energy over the range 200 eV to 10 keV as determined by our auroral code. In what follows we shall compare these results with those obtained when each of the atmospheric constituents (O, O₂, N₂) is, in turn, individually multiplied by 2 at all altitudes, while the other two are held constant.

Before examining the results of these atmospheric changes, let us consider the possible impact of the changes. Doubling the concentration of a constituent might at first be expected to double the effect of that specie on the column brightness of the monitored auroral emissions. In reality, however, there are a number of possible options in the interaction of the penetrating electrons and the atmospheric gases that render the situation more complex. An electron of a given initial energy will undergo a fixed number of collisions in a particular gas before thermalizing. Thus in the very simple case of a single constituent atmosphere, changing the concentration simply raises or lowers the altitude of the peak energy loss (and peak emission). This example (single-constituent atmosphere) is representative of those altitudes in which the concentration of one atmospheric constituent dominates. From Figure 1 it can be seen that (for the conditions chosen) O tends to dominate above 400 km and N₂ tends to dominate below 300 km. In a mixture of gases, increasing the concentration of one specie relative to the others may also have the effect of raising the penetration depth. However, the gases will compete for incoming electrons in proportion to their mixing ratios and collision cross sections, and the ratio of the resulting emissions changes accordingly.

Figure 3 shows the volume emission rate profiles for OI 1356 Å photons for the reference atmosphere case for selected energies. Only the very soft electrons (<200 eV) lose their energy in the altitude region where O is the major species. All other energies lie in altitude regions where the various gases can compete for collisions with the precipitating electrons. Thus, for example, increasing the concentration of N₂ will result in a decrease in the production of OI 1356 Å photons, because electrons that would have collided with O atoms now have an increased probability of colliding with N₂ molecules. The results of changing the O, O₂, and N₂ concentrations individually by a factor of 2 are shown in Figures 4 and 5.

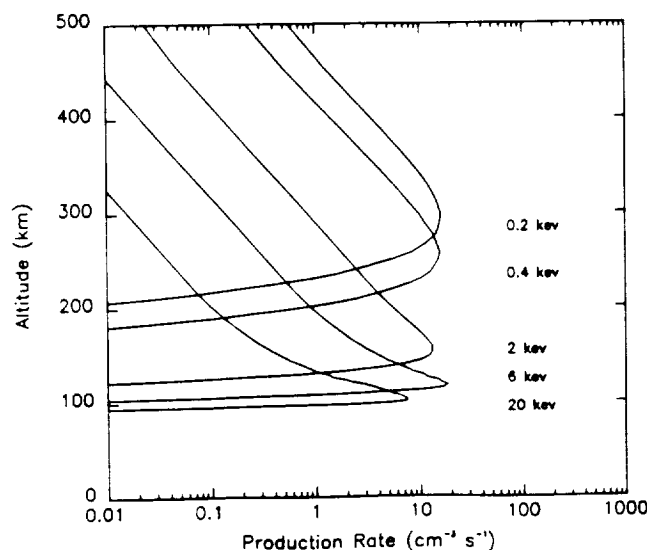


Fig. 3. Volume emission rate profiles for OI 1356 Å for the reference atmosphere shown in Figure 1.

Figures 4a and 5a show the impact on the computed OI 1356 Å and LBH surface brightness of the doubling of [N₂]. The 1356 Å intensity at 2 keV drops to 65% of the reference model, and then rises back to 86% of the reference model by 10 keV. The I 1356 is reduced at all modeled energies due to the fact that there are now more collisions with N₂, with a corresponding decrease in the production of O emissions. The decrease is not a full factor of 2 because of the abundance of atomic oxygen at the higher altitudes. For the very lowest energies (highest altitudes), where [N₂] is much less than [O], the I 1356 should tend to an intensity level unchanged from the standard case, as the emission is simply raised in altitude. The modeled emissions do not include initial energies less than 200 eV which would lose their energy above 400 km, but the lowest energy emissions do show this trend. At the higher energies, the emission is produced primarily at altitudes where N₂ is the major constituent and increased N₂ does not result in a significant change in the competition between O and N₂.

For the LBH 1464 Å emission, doubling the N₂ reduces the relative concentration of the dominant absorber, O₂. Thus for the higher energies which penetrate to greater depths, the emission from the increased N₂ overwhelms the O₂ absorption. Absorption by O₂ is not significant for the LBH 1838 Å emission; there is thus little dependence on the energy of the incident electrons.

Doubling the O₂ density (Figures 4b and 5b) increases the absorption of I 1356 and I 1464 at the higher energies (lower altitudes) resulting in reduced column brightnesses. The LBH 1838 Å emission is relatively unaffected by O₂ absorption and is influenced only by increased competition for collisions of the energetic particles with O₂ molecules. However, since [N₂] remains the major specie relative to [O₂], I 1838 shows only small changes.

The effect of doubling the [O] is shown for I 1356 in Figure 4c and for the LBH emissions in Figure 5c. For I 1356 the effect is close to a factor of 2 increase in the emission at all energies, while for the LBH emissions there is almost no effect at all energies. For the very low energies (not modeled) where O is the major constituent, the effect of doubling the O is simply to raise the altitude of the 1356 Å emission. The trend to an unchanged emission can be seen at the lower energies. For the LBH emissions, the effect of doubling the O concentration is only seen at the very low energies (high altitudes) where the competition with N₂ is further increased. In the altitude regimes where N₂ is a larger component, the O does not play a significant role.

From the results shown in Figures 4 and 5 it can be seen that uncertainties of a factor of 2 in any of the principal neutral atmospheric species translate into uncertainties of less than 20% for I 1838. The LBH 1464 Å emission shows variations up to 70% for factor of 2 uncertainties in [N₂] and less than 40% variation due to other constituents. OI 1356 is weakly sensitive to changes in O₂ and N₂, but varies almost in direct proportion to changes in O.

3.2. Sensitivity to Larger Compositional Changes

The neutral atmosphere exhibits relatively large compositional changes in the course of the seasonal, solar cyclic and magnetic storm variations. In this section we report the results of our assessment of the dependence on the computed emissions chosen for this study to changes of this magnitude. In order to simulate changes we have varied the input parameters (F_{10.7}, Ap, day of year) to the MSIS-86 model atmosphere, yielding neutral atmospheres at summer and winter solstice for conditions corresponding to low, moderate, and high solar activity (Table 1). The relative

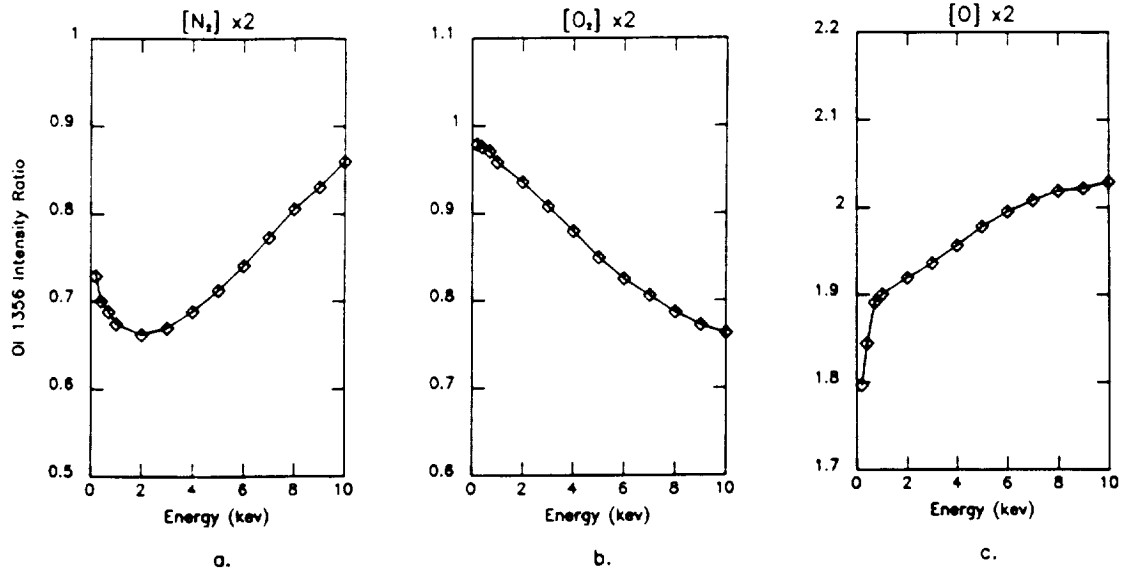


Fig. 4. OI 1356 dependence on [O], [O₂], and [N₂]. Each curve shows I 1356 for the doubled constituent case divided by I 1356 from the standard (unchanged) case.

compositional changes produced by these cases are illustrated in Figure 6.

The variations in the emission ratio of OI 1356 Å to LBH 1838 Å due to such composition changes are illustrated in Figure 7. This particular ratio is very sensitive to incident energy. For any given atmospheric conditions, the ratio varies by a factor of 13 over the energy range shown in the figure. What is interesting to note in Figure 8 is that the variation due to the compositional changes produced by solar activity variations (low, moderate, and high F_{10.7} cm flux) are small (≤30%), while the variations resulting from compositional changes of the type produced by seasonal variations are much larger (about a factor of 2). In Figure 8 we show the energy dependence for these various composition cases for the individual I 1356 and I 1838 intensities. The LBH intensity

is relatively insensitive to the changing atmospheric conditions, while the OI 1356 is found to be primarily responsible for the variations shown in Figure 7.

The reason for this can be seen in Figure 9 which shows the ratio of the individual concentration changes relative to the standard case. Figure 9a shows that the atomic oxygen concentration (for altitudes below 300 km, which correspond to the initial energies modeled here) is significantly higher for the winter cases than the summer cases.

Figure 10 shows the modeled volume emission rate altitude profiles for the solar minimum and solar maximum summer cases. As the atmosphere expands under the influence of increased solar activity, the production rate for a given energy peaks at higher altitudes. Note is the fact that the behavior of the production

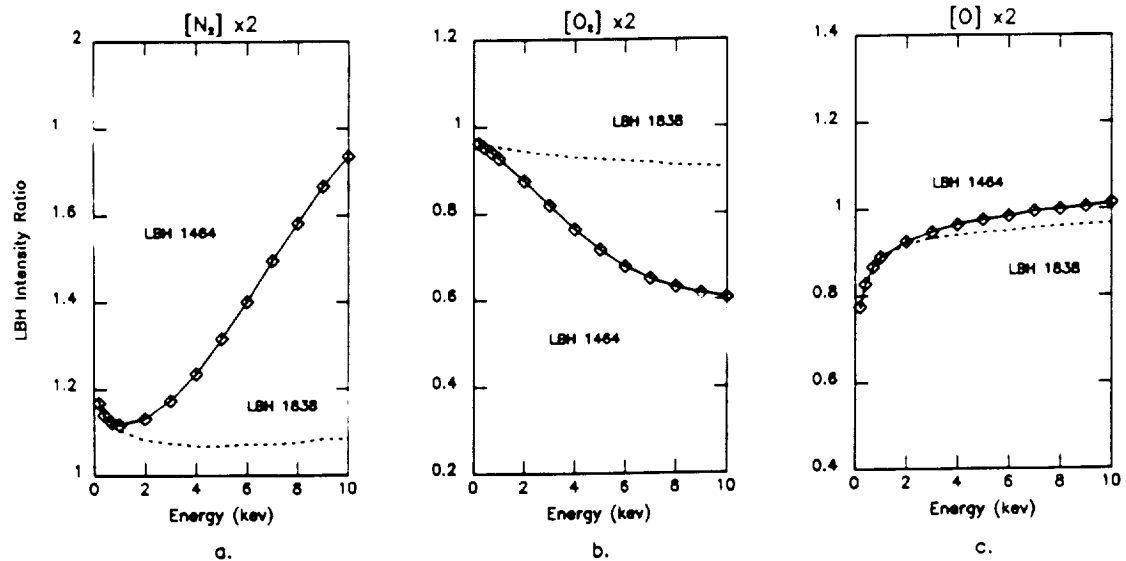


Fig. 5. LBH dependence on [O], [O₂], and [N₂]. Each curve shows the LBH intensity for the doubled constituent case divided by the LBH intensity from the standard (unchanged) case.

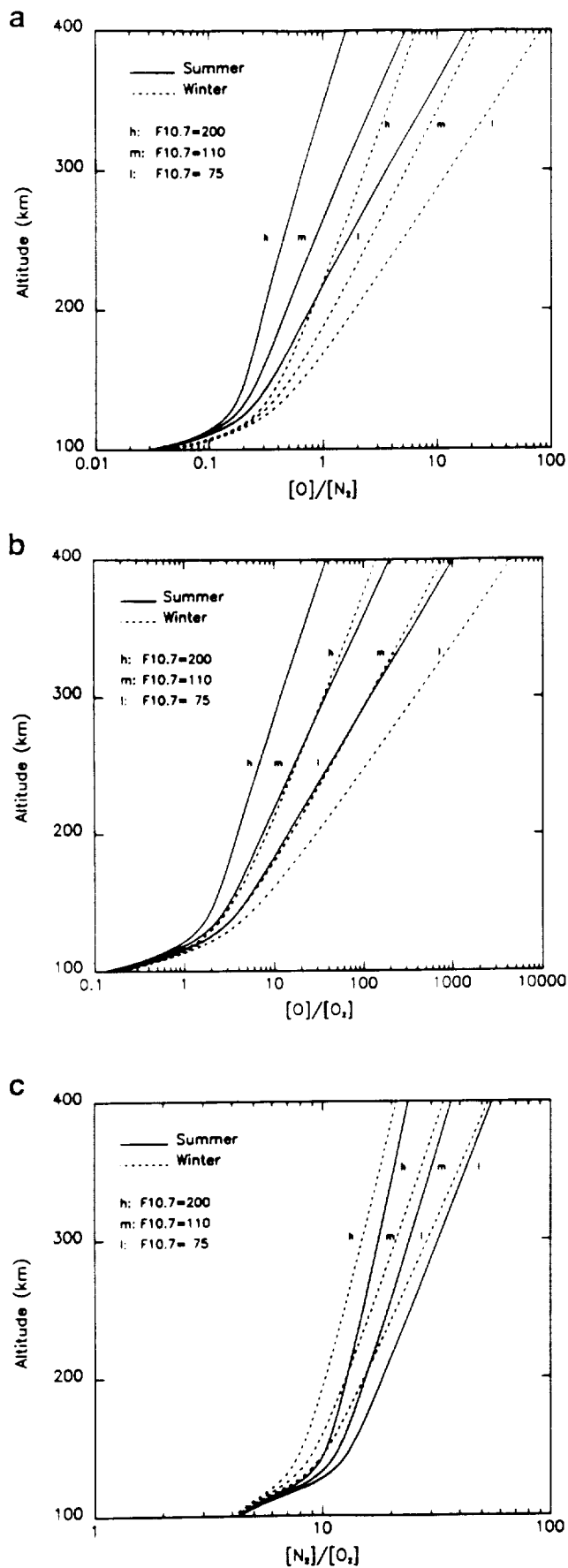


Fig. 6. Relative altitude density profile variations as a function of solar activity and seasonal variation.

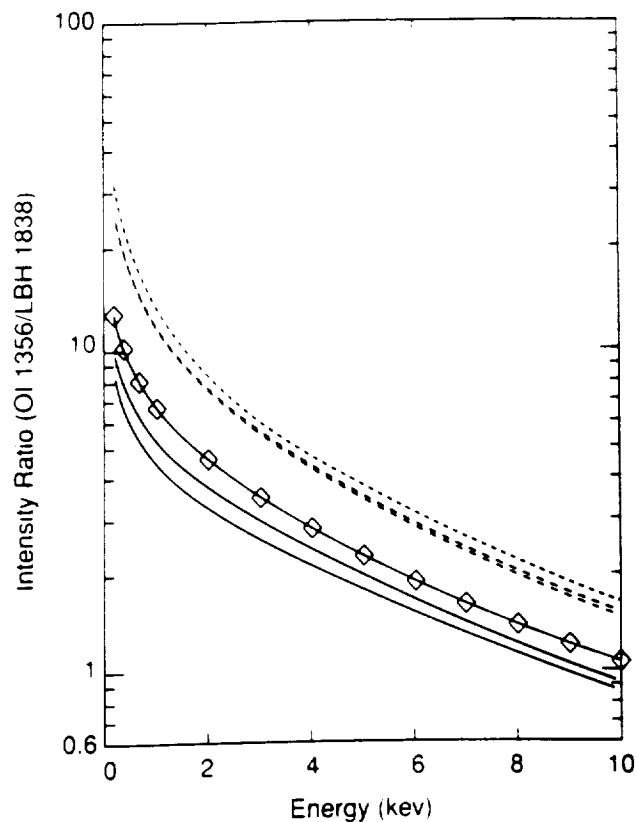


Fig. 7. Sensitivity of the OI 1356/LBH 1838 intensity ratio to solar activity and seasonal variation. Solid lines indicate summer conditions; dashed lines are for winter. Within each seasonal set of curves, the largest intensity ratios are obtained at solar minimum activity; the smallest ratios occur at solar maximum.

rate profiles for electron energies below 2 keV is markedly different from that above 2 keV. The altitude at which this energy loss peaks is approximately 140 km. This is the altitude below which O_2 becomes a competitive constituent (see Figure 1).

Figure 11 illustrates the effect of local O_2 absorption. As would be expected, for emissions lying outside the region of O_2 absorption (LBH 1838), the production rates are unchanged by local O_2 absorption. For emissions within the Schumann-Runge absorption continuum, however, the shape of the emission rate profiles is changed significantly due to local O_2 absorption.

The final ratio modeled was LBH_{long}/LBH_{short} (Figure 12). The ratio of LBH 1838 to LBH 1464 shows a dependence on the incident electron energy that varies only slightly with solar activity. As above, this variation can be explained by the relative densities of N_2 and O_2 . The observed variability from solar minimum to solar maximum is due to changes in the O_2 column density and hence in the O_2 absorption.

4. DISCUSSION

We have shown the intensity ratio $OI\ 1356/LBH_{long}$ to be a useful diagnostic for determining the characteristic energy of the auroral particles using LBH_{long} to be LBH 1838. The $I\ 1356/I\ 1838$ ratio is a very sensitive indicator of characteristic energy, changing by a factor of 13 or more over the range 200 eV to 10 keV, but this ratio can vary by up to factors of 2 with changes in the neutral atmosphere. Almost all the change is due to variations in $I\ 1356$. In addition, the $I\ 1838/I\ 1464$ ratio shown in Figure 12

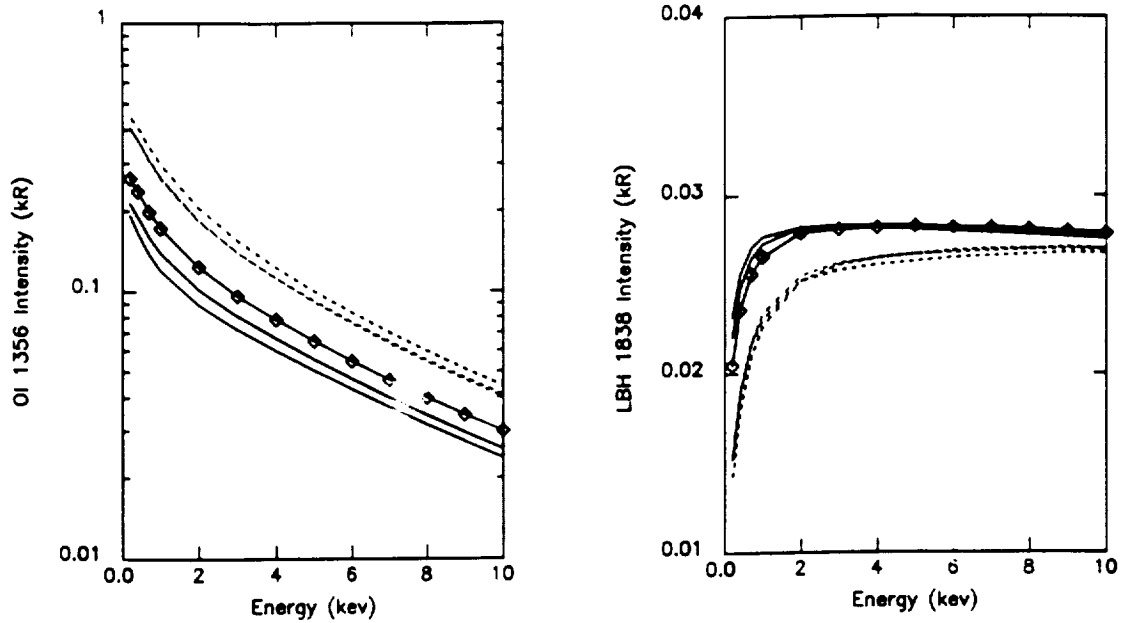


Fig. 8. Dependence of LBH 1838 and OI 1356 on solar activity and seasonal variation. The curves have the same interpretation as in Figure 7.

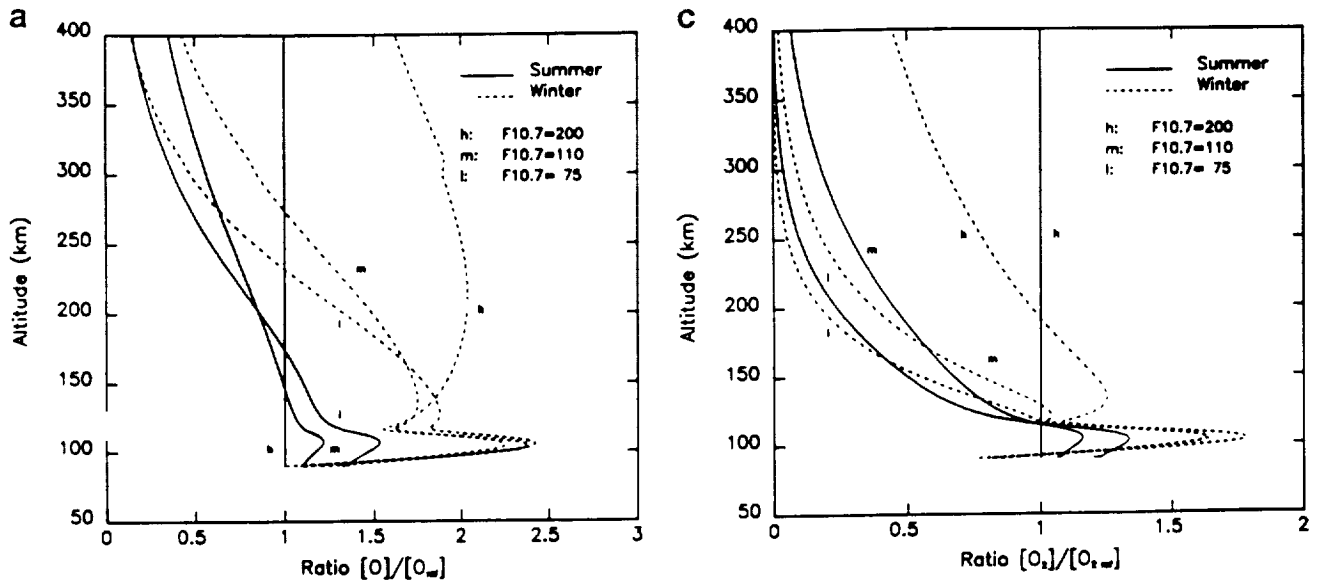


Fig. 9. Variation of altitude density profiles as a function of solar cyclic and seasonal variations. The profiles have been normalized to the standard case (summer, $F_{10.7} = 200$).

is found to be another potentially useful determinant of characteristic energy. The N_2 LBH long-to-short wavelength ratio varies by about a factor of 3 between 0.2 and 10 keV but, unlike the OI 1356 emission, is almost insensitive to changing atmospheric composition. The longer wavelength LBH bands are also useful indicators of the total energy influx, while the long-to-short wavelength LBH intensity ratio provides information on the O_2 .

Other workers have also attempted to use optical emissions to characterize the auroral electron precipitation. For example, *Ishimoto et al.* [1988] studied a similar ratio (OI 1356/LBH 1928) using a recent version of the Strickland model. Their modeled emission ratio shows a sensitivity of 9 between 1 and 10 keV, in good agreement with our results. In their description of the auroral code used in this study, *Richards and Torr* [1990] conduct a comparison between the two-stream model used here and the

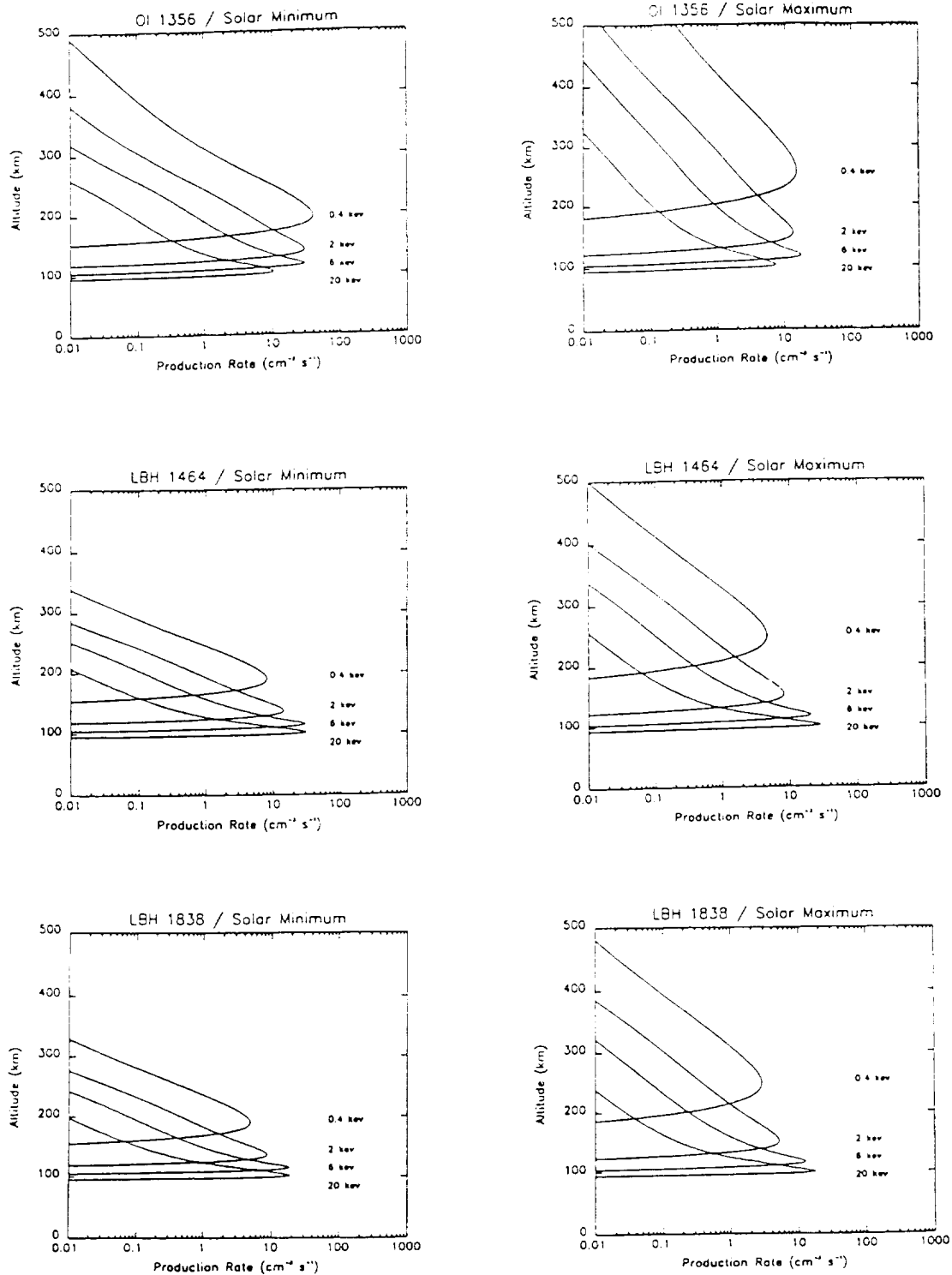


Fig. 10. Emission production rate altitude profiles for OI 1356 and LBH

more sophisticated multi-stream model of *SJW* and find good agreement in the shape of the OI 1356 emission curve. (Differences in magnitude are due to the use of revised OI cross sections in our model.) In addition to these studies, *Rees and Lummerzheim* [1989] have suggested the N_2 3371/ N_2^+ 4278 emission ratio as a determinant of the incident auroral energy. Their results, however, disagree with calculations by *SJW* and with our model, which shows the 3371 emission to be independent of characteristic energy above 0.5 keV [*Richards and Torr*, 1990].

We have investigated the sensitivity of OI 1356 Å, LBH 1464 Å, and LBH 1838 Å auroral emissions to changes in the neutral atmosphere. Our studies show that OI 1356 varies linearly with [O] to within 20% and shows much less variation with other atmospheric constituents. The LBH 1838 Å intensity is relatively insensitive to typical uncertainties in the neutral atmosphere (factor of 2 at auroral altitudes). LBH 1464 shows larger variations because of its additional interaction with O_2 . Our results are in good agreement with similar sensitivity studies performed by *SJW*

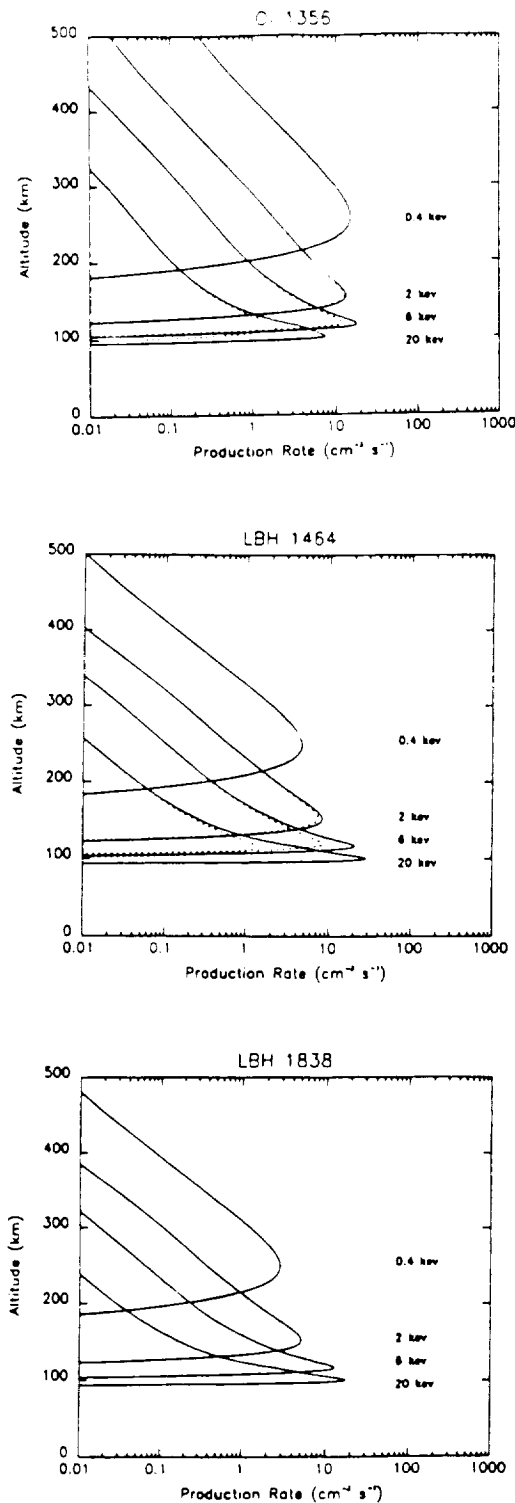


Fig. 11. Same as Figure 10 (solar maximum), but illustrating the effects of local O_2 absorption. The dashed curves are with local O_2 absorption.

who used a Jacchia model atmosphere [Jacchia, 1977] to model OI 1356 dependence on [O]. The dependence of these intensities on much larger changes in the composition such as might be encountered over seasonal or solar cycle extremes has also been investigated. It is found that the OI 1356 Å intensity is sensitive to compositional changes while the N_2 LBH long wavelength emission is relatively insensitive to such changes.

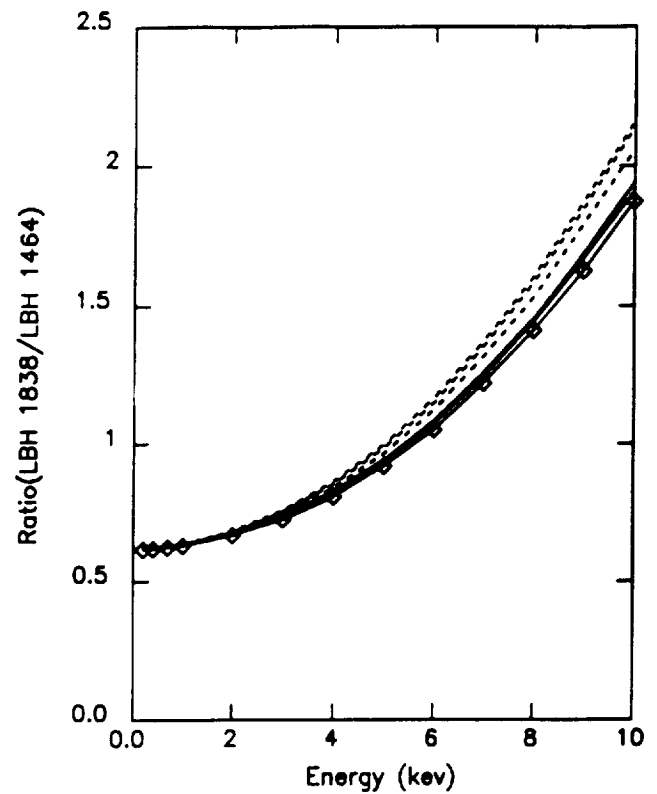


Fig. 12. Sensitivity of LBH_{long}/LBH_{short} intensity ratio to solar activity and seasonal variation. The curves have the same interpretation as in Figure 7.

Acknowledgments. This work was supported by NASA contracts NAS8-36955 and NAS8-37586, NASA grant NAGW-996, and NSF grant ATM 8713693 to the University of Alabama in Huntsville. This work was done while one of the authors (GAG) held a National Research Council-NASA Research Associateship.

The Editor thanks Manfred Rees and Donald Shemansky for their assistance in evaluating this paper.

REFERENCES

- Ajello, J. M. and D. E. Shemansky, A reexamination of important N_2 cross sections by electron impact with application to the dayglow: The Lyman-Birge-Hopfield band system and NI (119.99 nm), *J. Geophys. Res.*, **90**, 9845, 1985.
- Hedin, A. H., MSIS-86 thermospheric model, *J. Geophys. Res.*, **92**, 4649, 1987.
- Hudson, R. D., Critical review of ultraviolet photoabsorption cross sections for molecules of astrophysical and aeronomic interest, *Rev. Geophys.*, **9**, 305, 1971.
- Ishimoto, M., C.-I. Meng, G. J. Romick, and R. E. Huffman, Auroral electron energy and flux from molecular nitrogen ultraviolet emissions observed by the S3-4 satellite, *J. Geophys. Res.*, **93**, 9854, 1988.
- Jacchia, L. G., Thermospheric temperature, density, and composition: New models, *Spec. Rep. 375*, Smithsonian Astrophys. Observ., Cambridge, Mass., 1977.
- Meier, R. R., D. J. Strickland, P. D. Feldman, and E. P. Gentieu, The ultraviolet dayglow. 1. Far UV emissions of N and N_2 , *J. Geophys. Res.*, **85**, 2177, 1980.
- Ogawa, S., and M. Ogawa, Absorption cross sections of $O_2(a^1\Delta_g)$ and $O_2(X^1\Sigma_g^-)$ in the region from 1087 to 1700 Å, *Can. J. Phys.*, **53**, 1845, 1975.
- Rees, M. H., and D. Luckey, Auroral electron energy derived from ratio of spectroscopic emissions. I. Model computations, *J. Geophys. Res.*, **79**, 5181, 1974.
- Rees, M. H., and D. Lummerzheim, Characteristics of auroral electron precipitation derived from optical spectroscopy, *J. Geophys. Res.*, **94**, 6799, 1989.

- Richards, P. G., and D. G. Torr, Theoretical modeling of the dependence of the N₂ second positive 3371 Å auroral emission on characteristic energy, *J. Geophys. Res.*, in press, 1990.
- Strickland, D. J., and D. E. Anderson, Jr., Radiation transport effects on the OI 1356 Å limb intensity profile in the dayglow, *J. Geophys. Res.*, 88, 9260, 1983.
- Strickland, D. J., J. R. Jasperse, and J. A. Whalen, Dependence of auroral EUV emissions on the incident electron spectrum and neutral atmosphere, *J. Geophys. Res.*, 88, 8051, 1983.
- Swartz, W. E., Optimization of energetic electron energy degradation calculations, *J. Geophys. Res.*, 90, 6587, 1985.
- Torr, M. R., J. C. G. Walker, and D. G. Torr, Escape of fast oxygen from

the atmosphere during geomagnetic storms, *J. Geophys. Res.*, 79, 5267, 1974.

G. A. Germany and M. R. Torr, Space Sciences Laboratory, NASA Marshall Space Flight Center, Huntsville, AL 35812.
P. G. Richards and D. G. Torr, The University of Alabama in Huntsville, Huntsville, AL 35899.

(Received October 6, 1989;
revised December 13, 1989;
accepted December 14, 1989.)

ORIGINAL PAGE IS
OF POOR QUALITY

Mid- and Low-Latitude Model of Thermospheric Emissions

1. $O^+(^2P)$ 7320 Å and $N_2(2P)$ 3371 Å

MARSHA R. TORR

Space Science Laboratory, NASA Marshall Space Flight Center, Huntsville, Alabama

D. G. TORR AND P. G. RICHARDS

University of Alabama in Huntsville

S. P. YUNG

Boeing Corporation, Huntsville, Alabama

ORIGINAL PAGE IS
OF POOR QUALITY

The capability has been developed to model thermospheric airglow emissions on a semiglobal scale ($L < 5$). This model produces volume emission rates as a function of altitude, latitude, longitude, and local time for any selected date, and solar and magnetic conditions. The model can thus be used to provide three-dimensional maps of the selected emission for comparison with data obtained from orbiting vehicles. As such it becomes an essential tool in the planning and interpretation of airglow observations. A unique feature of the model is that it incorporates full interhemispheric coupling by solving all the appropriate coupled equations along the magnetic flux tubes from the mesosphere in one hemisphere to the mesosphere in the other hemisphere. As a result the effects of conjugate photoelectrons (and heat fluxes) can be fully explored. In this paper we select two thermospheric emissions with which to demonstrate the capability. The first is the 7320-Å emission from the metastable $O^+(^2P)$. The second is the permitted emission at 3371 Å from the N_2 second positive 0-0 band. These two emissions, for which the photochemistry is relatively well understood, are used to show the seasonal, diurnal and solar cyclic variations on a scale that covers mid- and low-latitudes, and the effects of interhemispheric coupling (conjugate photoelectrons).

INTRODUCTION

Airglow emissions are important indicators of atmospheric composition and the mechanisms responsible for the production and loss of the particular excited state from which the airglow is radiated. For example, the 0-0 band of the N_2 second positive system, which radiates at 3371 Å, is excited in the airglow by photoelectron impact, and is lost only by radiation. As a result, this emission is an excellent indicator of the photoelectron excitation rate [Kopp *et al.*, 1977]. The $O^+(^2P)$ metastable state, which radiates at 7320 Å, is excited both by photoelectrons and by extreme ultraviolet photons. However, because it is a long-lived state, it is lost by quenching by O, N_2 , and electrons in addition to radiation. Thus at high altitudes, where radiation is the dominant loss mechanism, the 7320-Å emission can be used to infer either the atomic oxygen concentration or the solar ultraviolet flux if the other is known [Mernvether *et al.*, 1978; Rusch *et al.*, 1976].

In the past, a number of detailed studies of these emissions have been made using measurements of the surface brightness altitude profiles obtained from orbiting spacecraft (see, for example, Walker *et al.* [1975] and Rusch *et al.* [1977]). In this study we have globally modeled these two emissions for a variety of conditions.

The model we have used here is one that we have steadily developed over the years. We solve the coupled time dependent energy, momentum, continuity, and photoelectron transport equations from 80 km in one hemisphere, along a field line to 80 km in the other hemisphere (Figure 1) [Young *et al.*, 1980a,b;

Richards and Torr, 1985a, 1988]. The equations that are solved are summarized below:

1. Ion continuity equation for major ions is given by

$$\frac{\partial N_i}{\partial t} = Q_i - L_i N_i - \nabla \cdot \phi_i \quad (1)$$

where N_i is the concentration of the i th major ion, Q_i and L_i are its production and loss frequency, respectively, and ϕ_i is the ion flux defined below. The electron density is assumed to be equal to the sum of the ion densities.

2. Momentum equation is given by

$$\phi_i = N_i U_i \quad (2)$$

where

$$U_i = \left(\frac{v_{ij}}{\Sigma(v)} \right) U_j - D_i \left(\frac{1}{N_i} \nabla N_i - \frac{m_i G}{k T_i} + \frac{1}{T_i} \nabla T_i + \frac{T_i \nabla T_i}{n_e} \nabla N_e + \frac{1}{T_i} \nabla T_e + \frac{N_j}{N_i + N_j} \left(\frac{\alpha_{ij}}{T_i} \nabla T_i - \frac{\alpha_{ij}^*}{T_j} \nabla T_j \right) \right) + \left(\frac{v_{in}}{\Sigma(v)} \right) U_n \quad (3)$$

where U_n is the neutral wind velocity and where the subscripts i and j are applied first to O^+ and H^+ respectively, and then to H^+ and He^+ respectively. O^+ , H^+ , and He^+ are coupled through collisions and the polarization electric fields. Since the influence of O^+ and He^+ on H^+ becomes significant in different altitude regimes and since the effect of He^+ and O^+ is small due to their mass ratio, this decoupling of a system of three major ions into 2 pairs of major ions considerably simplifies the numerical calculation of the major ion densities. Here α_{ij} and α_{ij}^* are thermal diffusion coefficients and D_i is the ordinary ion diffusion coefficient of species i , as in the work by St. Maurice and Schunk [1977].

3. The thermal electron energy equation is

$$\frac{3}{2} N_e k \frac{\partial T_e}{\partial t} = -N_e k T_e \nabla \cdot U_e - \frac{3}{2} N_e k U_e \cdot \nabla T_e - \nabla \cdot q_e + \Sigma Q_e - \Sigma L_e \quad (4)$$

4. The ion energy equation is

$$\frac{3}{2} N_i k \frac{\partial T_i}{\partial t} = -N_i k T_i \nabla \cdot U_i - \frac{3}{2} N_i k U_i \cdot \nabla T_i - \nabla \cdot q_i + \Sigma Q_i - \Sigma L_i \quad (5)$$

5. The ion heat flow equation is

$$q_i = \frac{1}{1-\xi} \left(-\lambda_i \nabla T_i - \frac{N_i m_i v_i'}{N_i \rho_i v_i'} \lambda_i \nabla T_i \right) \quad (6)$$

6. The electron heat flow equation is

$$q_e = -\lambda_e \nabla T_e \quad (7)$$

The thermal conductivity coefficients λ_i and λ_e , and the term

$$\xi = \nu_{ij}' \nu_{ji}' / (\nu_i' \nu_j')$$

where ν_{ij}' , ν_{ji}' , ν_i' , and ν_j' are the effective collision frequencies, are given by *St. Maurice and Schunk* [1977]. The ion-neutral collision frequencies ν_{in} are from *Schunk and Nagy* [1980].

7. The photoelectron Liouville equation is given by

$$B \frac{d}{ds} \frac{\Phi^+}{B} = -T_2 \Phi^+ + T_1 \Phi^- + \frac{q}{2 \langle \cos \theta \rangle} + \frac{q^+}{\langle \cos \theta \rangle} \quad (8)$$

$$-B \frac{d}{ds} \frac{\Phi^-}{B} = -T_2 \Phi^- + T_1 \Phi^+ + \frac{q}{2 \langle \cos \theta \rangle} + \frac{q^-}{\langle \cos \theta \rangle} \quad (9)$$

where

- $\Phi^+(E, s)$ photoelectron flux outward along s ;
- $\Phi^-(E, s)$ photoelectron flux inward along s ;
- $q(E, s)$ photoelectron production rate in the range E to $E + dE$ due to direct ionization processes;
- q^\pm photoelectron production in the range E to $E + dE$ due to cascading from higher energy photoelectrons undergoing inelastic collisions;
- $\langle \cos \theta \rangle$ average cosine of pitch angle;
- B magnetic field strength;
- $T_1 = \sum_k n_k p_e^k \sigma_e^k$;
- $T_2 = \sum_k n_k (\sigma_e^k + p_e^k \sigma_e^k)$;

and

- n_k k th species number density;
- p_e^k photoelectron backscatter probability for elastic conditions with the k th species;
- σ_e^k photoelectron total scattering cross section for elastic conditions with the k th species;
- σ_e^{ik} inelastic cross section for excitation of the k th particle species.

The model includes an option to increase the $O^- - O$ collision frequency as recommended by *Burnside et al.* [1987]. The use of the *Schunk and Nagy* [1980] values here does not significantly influence the results of this paper.

The above formulation corresponds to conditions where the differences between species temperatures and flow velocities are assumed to be small, i.e., stress and nonlinear acceleration terms are neglected. In addition, density and temperature gradients normal to the geomagnetic field lines are neglected and we assume that the electron and ion temperature distributions are isotropic.

The continuity equation is solved using a rather unique approach. We can rewrite (1) in terms of a function F :

$$dF = \frac{\partial N_i}{\partial t} + \nabla \cdot (N_i U_i) - Q_i + L_i N_i \quad (10)$$

Then, using a Newton iterative procedure to find the minimum of F , we solve for the density at the grid point, j . Figure 2 shows how the field line is divided into elements about the actual grid point j . The lower limit of the element (ℓ) is placed midway between the grid points j and $j-1$, and the upper limit (u) is placed midway between j and $j+1$. The lower limit of one element is the upper limit of the preceding element. We then integrate (10) between u and ℓ , and obtain the densities by solving

$$F = \int_{\ell}^u \frac{1}{B} \left(\frac{\partial N_i}{\partial t} - Q + L \right) ds + \left(\frac{N_i u U_{iu}}{B_u} - \frac{N_i \ell U_{i\ell}}{B_{\ell}} \right) = 0 \quad (11)$$

where B is the amplitude of the magnetic field. The values of $\partial N_i / \partial t$, Q , and L are obtained at the limits of integration, u and ℓ , by interpolation between the actual grid points.

In the past, many models have encountered numerical problems above about 3000 km, due to the large diffusion coefficient in this region which results in small density changes producing large changes in velocity. At lower altitudes, both ion-ion and ion-neutral collisions are important, while at greater altitudes, collisions become less important and the plasma can be accurately

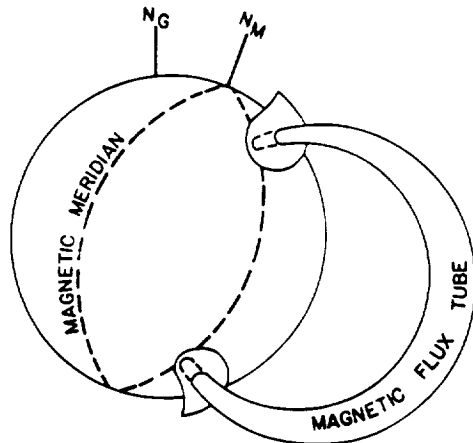


Fig. 1. Illustration of the interhemispheric nature of the code in which the coupled and time dependent equations are solved from 80 km in one hemisphere, along a field line, to 80 km in the conjugate hemisphere.

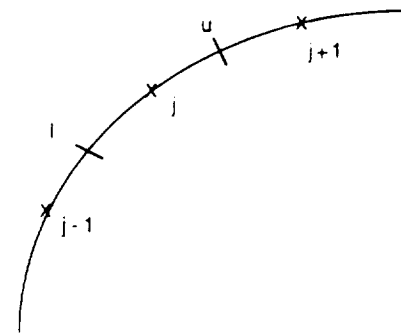


Fig. 2. The numerical grid scheme used for the solution of the continuity equation.

described using a diffusive equilibrium approach. The solution of (11) distinguishes this model from previous methods which evaluate the terms of the integral at only one point. As can be seen from (11) and Figure 2, the flux at the upper limit of one element becomes the flux at the lower limit of the next element. These fluxes must be identical and hence this method has been called the "flux preserving scheme." Furthermore, the flux at any grid point is closely tied to the flux at neighboring grid points, allowing stable solutions even for regions where large changes would give rise to unstable solutions with other numerical methods.

The model starts at noon with "best guess" initial values. It is allowed to run for 12 hours (in local time) before results are used in order to reduce dependence on initial conditions. It has been found that the ionospheric densities over a midnight to midnight diurnal cycle typically repeat with only small differences due, for example, to plasmaspheric refilling. The plasmaspheric H^+ and He^+ contents are initially low, and the flux tubes are allowed to fill continuously. The transport equations for the three major ions, He^+ , H^+ , and O^+ , are carried out in two steps. As mentioned above, the coupled O^+ and H^+ equations are solved first, followed by the He^+ and H^+ equations, where the latter use the O^+ - H^+ results. Thus the equations for the three major ions are essentially solved in a simultaneous manner. Below approximately 180 km, NO^+ and O_2^+ become major ions, but are obtained from photochemical equilibrium calculations.

The numerical solution of these equations, boundary conditions and other details are further discussed by Young *et al.* [1980a,b].

The full interhemispheric coupling is difficult to handle, but once incorporated it imposes no artificial upper boundary conditions for both thermal and photoelectron fluxes. This is most important for thermal coupling and the proper treatment of conjugate photoelectrons [Richards and Torr, 1985b] which can be significant in the calculation of airglow emissions. Typically, attenuation of the conjugate photoelectron flux by Coulomb collisions results in approximately 5% energy loss. The model includes the option to specify loss due to pitch angle scattering which we assumed to be zero for this paper. A tilted dipole approximation is used for the Earth's magnetic field [Richards and Torr, 1986a].

The concentrations of the major neutral species are provided by the MSIS-86 [Hedin, 1987] to the model which then computes the concentrations of minor and excited state species and major ions [Torr, 1985; Richards *et al.*, 1982a, 1986b]. In this paper a simple model giving daytime poleward winds and equatorward neutral winds was employed. This behavior is consistent with the results obtained using the method of Richards and Torr [1986b] and Miller *et al.* [1986]. The model includes the option to use model winds of Hedin *et al.* [1988], Killeen *et al.* [1987] and Killeen (private communication 1989). Note, if the Hedin *et al.* [1988] model is used, the O^+ - O collision frequency of Burnside *et al.* [1987] should be used in order to produce the observed $h_m F_2$ at night.

The chemistry of all significant emitting species is incorporated in detail, including the excitation of the metastable states [M. R. Torr and Torr, 1982] and vibrational states [Richards *et al.*, 1986a; Richards and Torr, 1986c], and the odd nitrogen chemistry [Richards *et al.*, 1981, 1982b; Richards, 1986]. The vibrational population distributions of N_2 are determined, an important factor in calculating the ionospheric O^+ and N_2 concentrations. The model also includes calculation of the vibrational populations of N_2^+ , but this does not significantly affect the results reported here. The photochemistry is that described by

Torr [1985] as updated and shown here in Table 1 and illustrated in Figure 3. At equatorial latitudes, where electric fields play an important role, the electron concentrations are obtained from the fully analytical ionospheric model of Anderson *et al.* [1989]. Elsewhere, the electron densities are computed self-consistently by this model. The transition occurs between $L = 1.5$ and 1.8 with interpolation between these L shells. The major elements of the code are shown in Figures 4a and 4b. The solar EUV flux is obtained in the following way. For solar minimum ($F10.7 = 71$) the model utilizes the F74113 reference spectrum from Torr *et al.* [1979], with the fluxes below 250 Å doubled as recommended by Richards and Torr [1984] and supported by Ogawa and Judge [1986]. For other levels of solar activity, each of the 37 wavelength intervals is scaled linearly as a function of $F10.7$ using the solar maximum measured flux at $F10.7 = 206$ given by Torr and Torr [1985]. For further details, see Richards and Torr [1988], which also provides the cross sections used.

The main outputs of the model include ion densities (O^+ , $O^+(^4S)$, $O^+(^2D)$, $O^+(^2P)$, H^+ , He^+ , N^+ , NO^+ , N_2^+ , N_2^{+*} , N_2^{+*s}), neutral densities ($N(^4S)$, $N(^2D)$, $N(^2P)$, NO , $O(^1D)$, $O(^3S)$, $N_2(A^1\Sigma_u^+)$, N_2^*), electron and ion temperatures and flow velocities, the photoelectron flux, and a large number of emissions (see Figure 4a).

During the Atmosphere Explorer C, D, and E program, numerous studies were conducted which compared the photochemistry of the code with in situ measurements of species concentrations. The photochemistry yields results consistent with the data base taken over the lifetime of the AE satellites. Generally, very good agreement with measurements has been obtained with regard to all parameters with the exception of high altitude electron temperatures in the plasmasphere and ionosphere [Newberry *et al.*, 1989]. The model has been extensively tested against comprehensive satellite and incoherent scatter radar data bases [Young *et al.*, 1980a,b; Chandler *et al.*, 1983; Richards and Torr, 1988; Newberry *et al.*, 1989; Horwitz *et al.*, 1990; Richards *et al.*, 1989]. Apart from the input parameters (such as data and location) the only free parameter in the code is the pitch angle scattering of photoelectrons in the plasmasphere. In its present form, the model is ideally suited for studies of the airglow emissions.

The code is run on the Marshall Space Flight Center CRAY XMP computer. Values of output parameters are provided on a global grid of points, providing results in a latitude, longitude, altitude, and local time mesh for any selected date, or solar or magnetic conditions. For the cases discussed in this paper, we have run the model for 144 flux tubes, which corresponds to 144 northern and 144 southern hemisphere locations. Figure 5 shows the locations of the field lines along which the equations are solved. These are constrained to $L \leq 5$.

We have chosen the $O^+(^2P)$ emission at 7320 Å and the N_2 second positive 0-0 band emission at 3371 Å for the initial global modeling. The calculations have been made for November 28, 1983 for which the $F10.7$ cm flux was 89, and the A_p index was 23. Thus the November 1983 calculations correspond to a period of relatively low solar activity. An earlier example of the results for the 7320 Å case has been shown by Torr *et al.* [1990]. The results shown here represent a significant improvement over the Torr *et al.* [1990] case, in that we have added approximately 50 more flux tubes at low latitudes (144 versus 96). In addition we have used much smaller time steps through the twilight conditions (5 minutes versus 20 minutes). For comparison, we have also run the calculations for the same day of year, but for conditions

TABLE 1. Summary of Photochemistry Used in the Interhemispheric Model

Reaction Number	Reaction	Rate Coefficient (cm ³ s ⁻¹) or Rate (s ⁻¹)	Reference
1.	$O^+ + e^- \rightarrow O + h\nu$	$\sim 4 \times 10^{-12} (T_e/300)^{0.7}$	Torr [1985]
2.	$O_2^+ + e^- \rightarrow O + O$	$1.6 \times 10^{-7} (300/T_e)^{0.55}$ for $T_e \geq 1200$ K $2 \times 10^{-7} (300/T_e)^{0.7}$ for $T_e < 1200$ K	Torr and Torr (1981); Mehr and Biondi [1969]
3.	$O^+ + O_2 \rightarrow O_2^+ + O$	$2.1 \times 10^{-11} (T_e + 2 T_e/3 \times 300)^{-0.763}$	Chen et al. [1978] ^a
4.	$O^+ + N_2 \rightarrow NO^+ + N$	$1.533 \times 10^{-12} - 5.92 \times 10^{-13} (T_{eff}/300)$ $+ 8.60 \times 10^{-14} (T_{eff}/300)^2$ for $300 \leq T_{eff} \leq 1700$ K $2.73 \times 10^{-12} - 1.155 \times 10^{-12} (T_{eff}/300)$ $+ 1.483 \times 10^{-13} (T_{eff}/300)^2$ for $1700 < T_{eff} < 6000$ K	St. Maurice and Torr [1978]; Albritton [1978]; Chen et al. [1978]
5.	$NO^+ + e^- \rightarrow N + O$	$4.3 \times 10^{-7} (T_e/300)^{-1}$	Torr and Torr [1979]
6.	$N_2^+ + O \rightarrow NO^+ + N$	$1.4 \times 10^{-10} (T_e/300)^{-0.44}$ for $T_e < 1500$ K	McFarland et al. [1974]; Torr [1979]
7.	$N_2^+ + e^- \rightarrow N + N$	2.7×10^{-7}	Abdou et al. [1984]
8.	$N_2^+ + O \rightarrow O^+ + N_2$	$0.07 k_6 (T_e/300)^{0.21}$	McFarland et al. [1974]
9.	$N_2^+ + O_2 \rightarrow O_2^+ + N_2$	$9.1 \times 10^{-11} \exp(-0.002 T_{eff})$	Lindinger et al. [1974]
10.	$N^+ + O_2 \rightarrow O_2^+ + N$	4×10^{-10}	Huntress and Anicich [1976]
11.	$N^+ + O_2 \rightarrow NO^+ + O$	2×10^{-10}	Huntress and Anicich [1976]
12.	$N^+ + O_2 \rightarrow NO^+ + O(^1D)$	$\beta = 0.7$	Langford et al. [1985]
13.	$O_2^+ + N \rightarrow NO^+ + O$	1.2×10^{-10}	Fehsenfeld [1977]
14.	$O_2^+ + NO \rightarrow NO^+ + O_2$	4.4×10^{-10}	Lindinger et al. [1974]
15.	$O^+(^2D) + N_2 \rightarrow N_2^+ + O$	8×10^{-10}	Rowe et al. [1980]; Johnsen and Biondi [1980]
16.	$O^+(^2D) + O \rightarrow O^+(^4S) + O$	5×10^{-12}	Abdou et al. [1984]
17.	$O^+(^2D) + O_2 \rightarrow O_2^+ + O$	7×10^{-10}	Johnsen and Biondi [1980]
18.	$O^+(^2D) + e^- \rightarrow O^+(^4S) + e^-$	$6.6 \times 10^{-8} (300/T_e)^5$	Henry et al. [1969]
19.	$O^+(^2P) \rightarrow O^+(^2D) + h\nu$	0.173 s^{-1}	Seaton and Osterbrock [1957]
20.	$O^+(^2P) \rightarrow O^+(^4S) + h\nu$	0.047 s^{-1}	Seaton and Osterbrock [1957]
21.	$O^+(^2P) + e^- \rightarrow O^+(^2D) + e^-$	$1.5 \times 10^{-7} (300/T_e)^5$	Henry et al. [1969]
22.	$O^+(^2P) + e^- \rightarrow O^+(^2D) + e^-$	$4.7 \times 10^{-8} \cdot (300/T_e)^5$	Henry et al. [1969]
23.	$O^+(^2P) + N_2 \rightarrow \text{products}$	4.8×10^{-10}	Rusch et al. [1977]
24.	$O^+(^2P) + O \rightarrow \text{products}$	5.2×10^{-11}	Rusch et al. [1977]
25.	$He + h\nu \rightarrow He^+ + e^-$	$4.0 \times 10^{-8} - 1.2 \times 10^7 \text{ (c)}$	Torr and Torr [1985]
26.	$He^+ + N_2 \rightarrow N_2^+ + N + He$	1×10^{-9}	Adams and Smith [1976]
27.	$He^+ + N_2 \rightarrow N_2^+ + He$	6.5×10^{-10}	Adams and Smith [1976]
28.	$O^+ + H \rightarrow H^+ + O$	$2.2 \times 10^{-11} \cdot (T_e)^5$	derived from Banks and Kockarts [1973]
29.	$H^+ + O \rightarrow O^+ + H$	$2.5 \times 10^{-11} \cdot (T_e)^5$	derived from Banks and Kockarts [1973]
30.	$O^+ + N(^2D) \rightarrow N^+ + O$	5×10^{-11}	Torr et al. [1979]
31.	$NO^+ + e^- \rightarrow N(^2D) + O$	$\beta \cdot k_5$ where $\beta = 0.76$	Klev et al. [1977]
32.	$N_2^+ + e^- \rightarrow N(^2D) + N$	$\beta \cdot k_7$ where $\beta = 1.9$	Queffelec et al. [1985]
33.	$N_2^+ + O \rightarrow N(^2D) + NO^+$	$\beta \cdot k_8$ where $\beta = 1.0$	Frederick and Rusch [1977]
34.	$N^+ + O_2 \rightarrow N(^2D) + O_2^+$	$\beta \cdot k_{10}$ where $\beta = 1.0$	assumed
35.	$N(^2D) + O \rightarrow N(^4S) + O$	$\sim 7 \times 10^{-13}$	Richards et al. [1981]
36.	$N(^2D) + O_2 \rightarrow NO + O$	6×10^{-12}	Lin and Kaufman [1971]
37.	$N(^2D) + e^- \rightarrow N(^4S) + e^-$	$5 \times 10^{-10} (T_e/300)^5$	Frederick and Rusch [1977]
38.	$N(^2D) + O_2^+ \rightarrow NO^+ + O$	1×10^{-11}	Dalgarno [1970]
39.	$N(^4S) + O_2 \rightarrow NO + O$	$4.4 \times 10^{-12} \exp(-3220/T)$	Becker et al. [1969]
40.	$N + NO \rightarrow N_2 + O$	3.4×10^{-11}	Lee et al. [1978]
41.	$O_2 + h\nu \rightarrow O(^1D) + O$	$\beta = 1; J_{\infty}(O_2)_{SR} = (1.5 - 2.8) \times 10^{-8}$	Torr et al. [1980]
42.	$O_2^+ + e^- \rightarrow O(^1D) + O$	βk_2 where $\beta = 1.2$	Abreu et al. [1986]
43.	$O(^1D) + N_2 \rightarrow O(^3P) + N_2$	$2.0 \times 10^{-11} \exp(107.8 T_e)$	Sireit et al. [1976]
44.	$O(^1D) + O_2 \rightarrow O(^3P) + O_2$	$2.9 \times 10^{-11} \exp(67.5/T_e)$	Sireit et al. [1976]
45.	$O(^1D) \rightarrow O(^3P) + h\nu$	0.00934	Fischer and Saha [1983]
46.	$N(^2D) + O_2 \rightarrow O(^1D) + NO$	$\sim 5 \times 10^{-12}$	Rusch et al. [1978]; D. G. Torr et al. [1981]
47.	$O_2^+ + e^- \rightarrow O(^1S) + O$	βk_2 where $\beta = 0.08$	Bates and Zipf [1981]; Abreu et al. [1986]
48.	$O_2^+ + N \rightarrow O(^1S) + NO^+$	$\sim 2 \times 10^{-11}$	Frederick et al. [1976]
49.	$O(^1S) + O(^3P) \rightarrow O + O$	2×10^{-14}	Slanger and Black [1981]
50.	$O(^1D) + O \rightarrow O + O$	8×10^{-12}	Abreu et al. [1986]

TABLE 1. (continued)

Reaction Number	Reaction	Rate Coefficient (cm ³ s ⁻¹) or Rate (s ⁻¹)	Reference
51.	$O(^1S) \rightarrow O(^1D) + h\nu$	1.07	<i>Kernahan and Pang</i> [1975]
	$\rightarrow O(^1P) + h\nu$	0.0444	
52.	$N(^2D) + NO \rightarrow N_2 + O$	7×10^{-11}	<i>Lin and Kaufman</i> [1971]
53.	$O(^1S) + O_2 \rightarrow O(^1P) + O_2$	$4.9 \times 10^{-12} \exp(-1730/RT)$	<i>Zipf</i> [1979]
54.	$N_2(A^3\Sigma_u^+) + O \rightarrow \text{products}$	2×10^{-11}	<i>Piper</i> (1982)
55.	$N_2(A^3\Sigma_u^+) + O \rightarrow O(^1S) + N_2$	$\beta \cdot k_{54}$ where $\beta = 0.37$	<i>Piper</i> (1982)
56.	$N_2^{+*} + O \rightarrow O^+ + N_2$	$\sim 2 \times 10^{-10\beta}$	<i>Abdou et al.</i> [1984]; <i>Torr</i> (1985)
	$N_2 + h\nu \rightarrow N^+ + N + e$	$(1.78 - 5.14) \times 10^{-18}$	
57.	$\rightarrow N_2^+ + e$	$(3.06 - 8.82) \times 10^{-7}$	<i>Torr and Torr</i> (1985) ^c
	$O + h\nu \rightarrow O^+(^4S) + e$	$(0.98 - 2.81) \times 10^{-7}$	
	$\rightarrow O^+(^2D) + e$	$(0.79 - 2.34) \times 10^{-7}$	
	$\rightarrow O^+(^2P) + e$	$(0.45 - 1.38) \times 10^{-7}$	
	$\rightarrow O^+(^4P) + e$	$(1.04 - 3.43) \times 10^{-8}$	
	$\rightarrow O^+(^2P^o) + e$	$(0.46 - 1.42) \times 10^{-8}$	

^aSince the results of *Chen et al.* [1978] stop at 700°K, we normalize the converted drift tube data parameterized by *St. Maurice and Torr* [1978] at this temperature.

^bThe model computes this rate coefficient as a function of N₂⁺ vibrational temperature (T_v). The value reduces to that given by equation (6) when T_v = T_g. Inclusion of this process is an option available [see *Abdou et al.*, 1984].

^cThe ranges given for the ionization frequencies indicate the variation over a solar cycle.

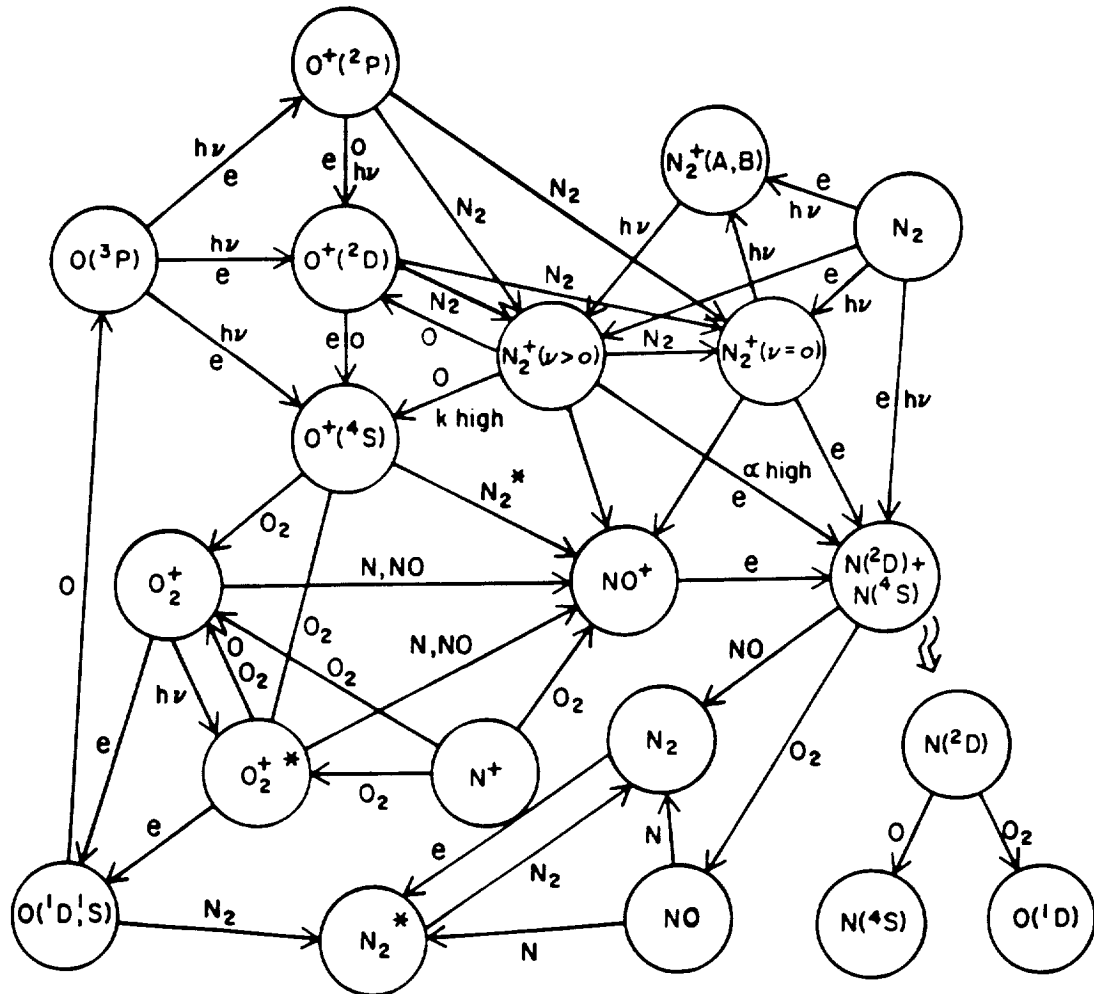


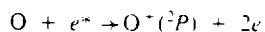
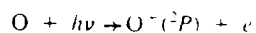
Fig. 3. Schematic of the thermospheric and ionospheric chemistry that is incorporated in the model.

corresponding to solar maximum ($F10.7 = 194$, $A_p = 23$). This study deals only with the airglow, and we do not show results for latitudes higher than $L = 5$.

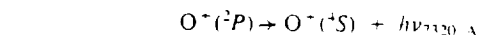
Details of the results are given in the following section.

MODELING OF THE 7320-Å AIRGLOW EMISSION

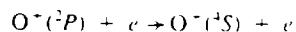
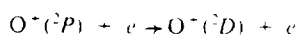
The 7320-Å emission arises from the $O^+(^2P)$ state, which is produced in the thermosphere by two mechanisms: photoionization and photoelectron ionization:



where the photoelectrons may be those produced locally, or those produced in the conjugate hemisphere and transported along the magnetic field lines. The $O^+(^2P)$ is lost by several mechanisms:



collisional deactivation



This photochemistry has been reviewed by *Torr and Torr* [1982]. It should be noted that since publication of the aeronomically derived values of the rate coefficients by *Rusch et al.* [1977], the solar EUV flux below $\approx 250 \text{ \AA}$ was doubled. We estimate that when quenching dominates, the reported intensities may be about 30% too high.

Plate 1 shows the 7320-Å volume emission rate at the peak of the layer as a function of latitude, local time (longitude) and altitude. The upper plot shows the peak volume emission rate as a function of latitude and local time. Because the model has longitudinal variability resulting from both the MSIS [Hedin 1987] model atmosphere, and the interhemispheric coupling, this particular plot is shown for 00 UT. This UT is equivalent to placing midnight at 0° longitude, the Greenwich meridian, and noon at 180° longitude, i.e. over the Pacific Ocean. Where the volume emission rate becomes so small as to be effectively zero, the values are not plotted. These regions can be seen near midnight for equatorial latitudes, and represent no production at these times. The graphics tend to smear the northern and southern latitude boundaries by a few degrees to the north and south, respectively. The solutions are only valid, however, within the $L \leq 5$ region illustrated in Figure 5.

The basic features shown in Plate 1 have been discussed by *Torr et al.* [1990] but we will review them here briefly as this plate will be used for the comparison with other cases. Summer is

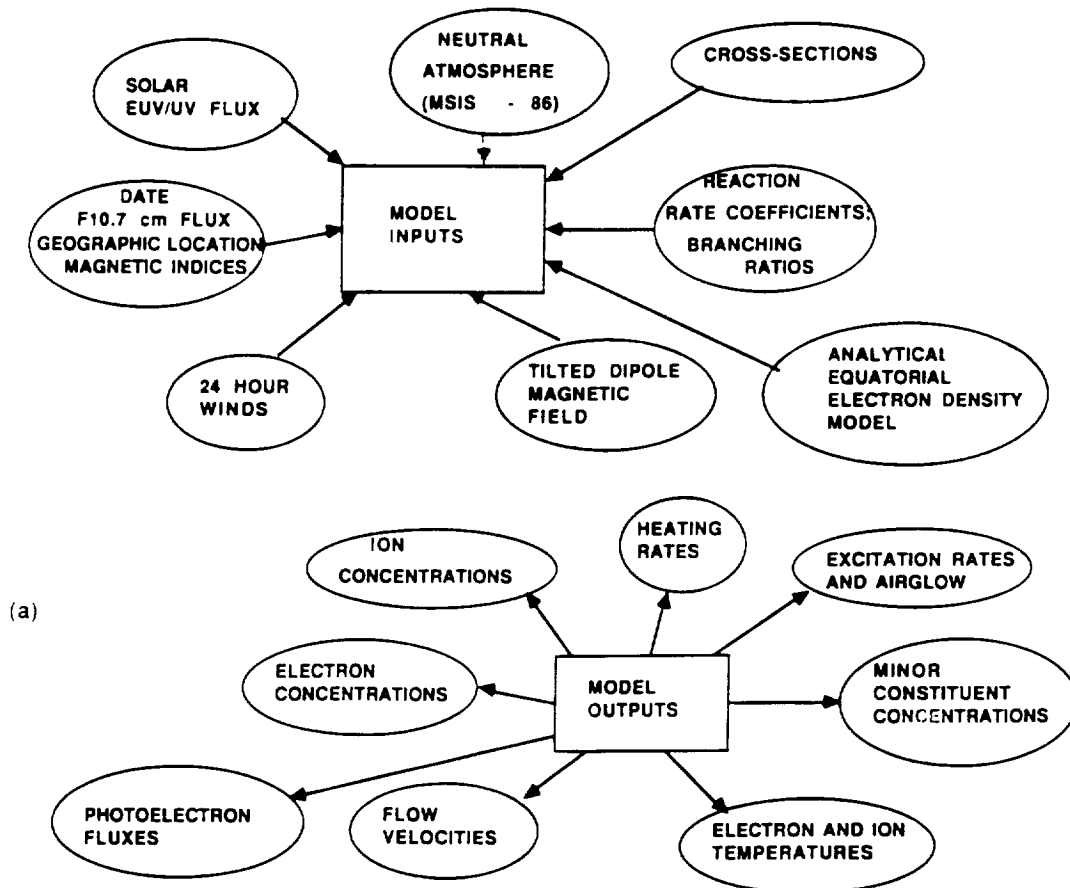


Fig. 4(a). Schematic illustration of the major input and output elements of the field line interhemispheric plasma (FLIP) code; (b) illustration of the flow of the solutions.

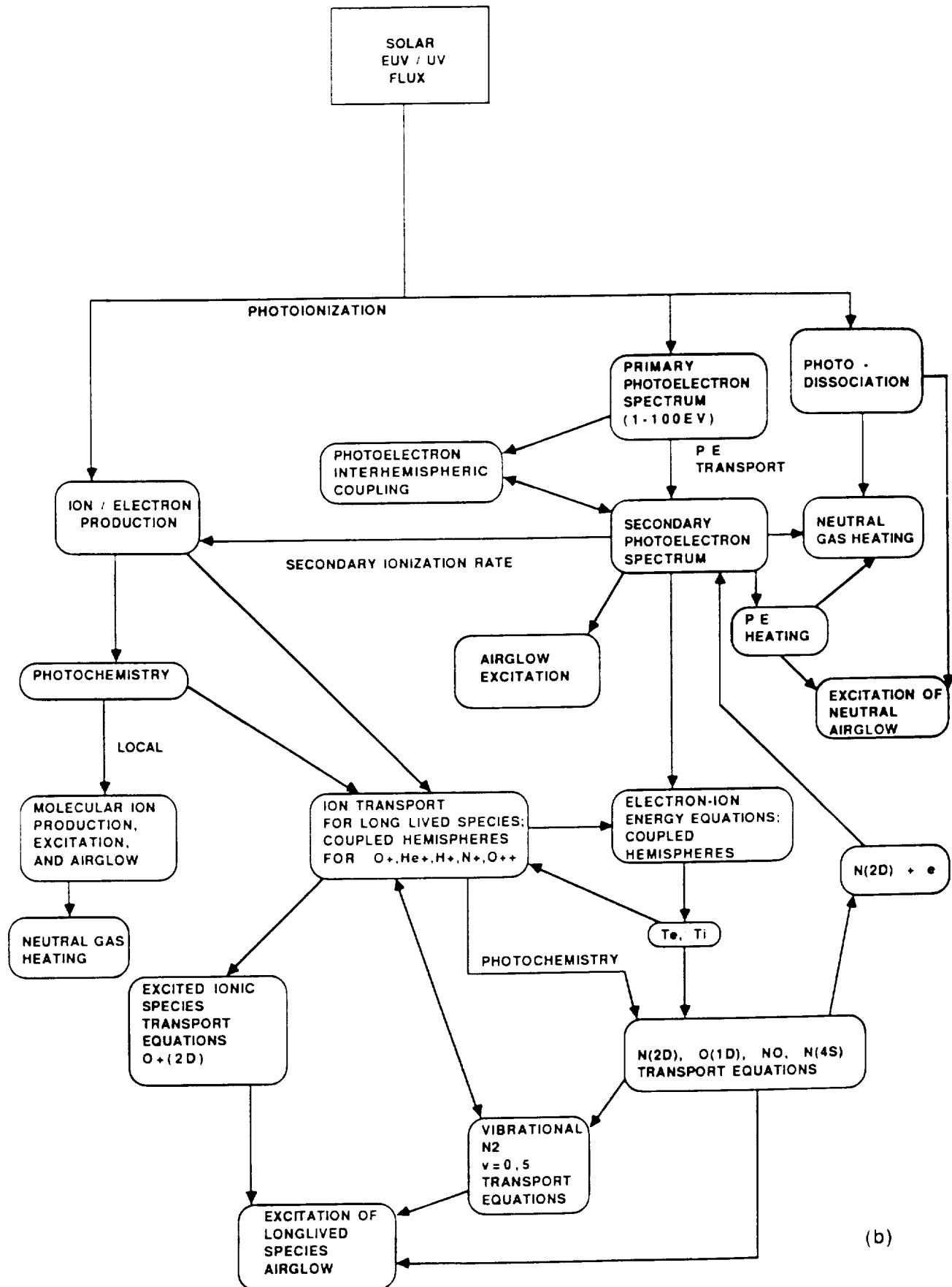


Fig. 4. (continued)

in the southern hemisphere as is immediately seen by the longer duration of the midday peak volume emission rates. Figure 6 shows the production and loss rates at northern and southern mid-latitudes near noon. In both cases the major production mechanism is photoionization with photoelectron impact contributing

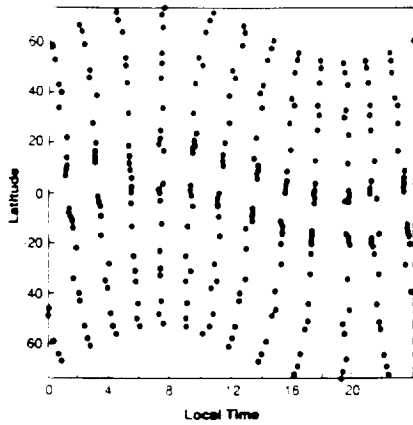


Fig. 5. Locations of grid points in which diurnal altitude solutions were obtained.

about 25%. The major high altitude loss mechanism is radiation, while quenching by N_2 dominates at lower altitudes. It is interesting to note in Plate 1 that the midday peak volume emission rates in the winter (northern) hemisphere are somewhat larger than in the summer hemisphere. The reason for this can be seen in Figure 6. While the N_2 peak quenching rate is almost identical in both hemispheres, the N_2 quenching falls off with altitude with a smaller scale height in the winter hemisphere, so that radiation dominates to a lower altitude with the resulting higher emission rate.

At and beyond the terminators (for solar zenith angles larger than 90°) sunlight illuminates increasingly higher altitudes, and the peak altitude rises while the volume emission rate falls sharply. In Figure 7 we show the production and loss rates for a solar zenith angle of 105° in the evening southern hemisphere. The peak UV photoionization has risen to above 600 km. A second peak is formed near 300 km. The latter is a result of photoelectrons which are produced in the ionization process that caused the upper peak. The photoelectrons are transported downward and lose their energy near 300 km in the impact ionization of atomic oxygen. Plate 2 shows the same information as was given in Plate 1, but versus solar zenith angle instead of local time. This plate shows the extent to which seasonal hemispheric asymmetries are reduced when the data are plotted in this format.

ORIGINAL PAGE IS
OF POOR QUALITY.

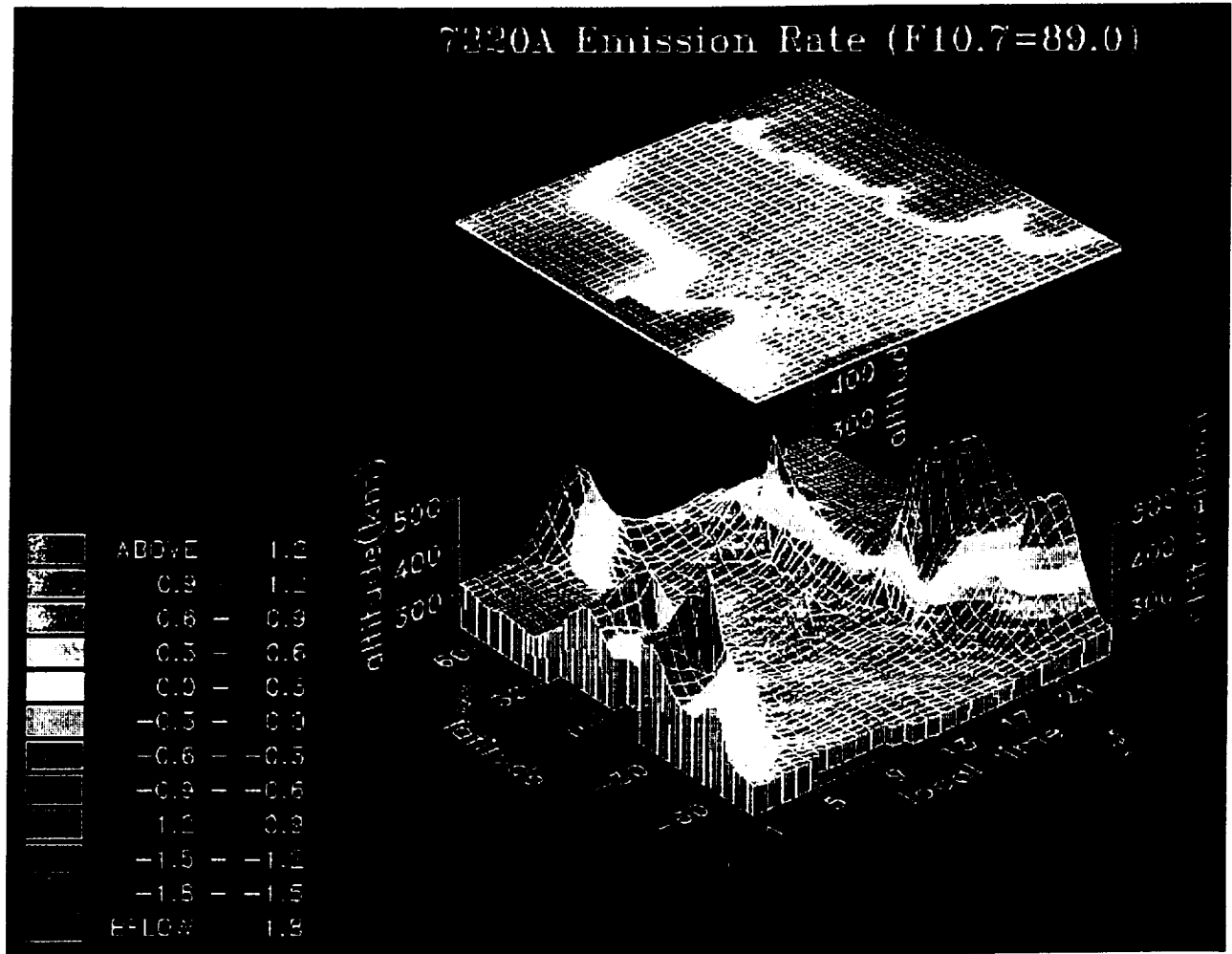


Plate 1. The 7320-A volume emission rate (photons $cm^{-3} s^{-1}$) at the peak of the layer as a function of altitude, latitude, and local time (longitude) for 00 UT. The upper plot shows the peak volume emission rate only as a function of latitude and local time. The volume emission rate is on a log scale. The results are only valid within the $L \leq 5$ boundaries shown in Figure 5.

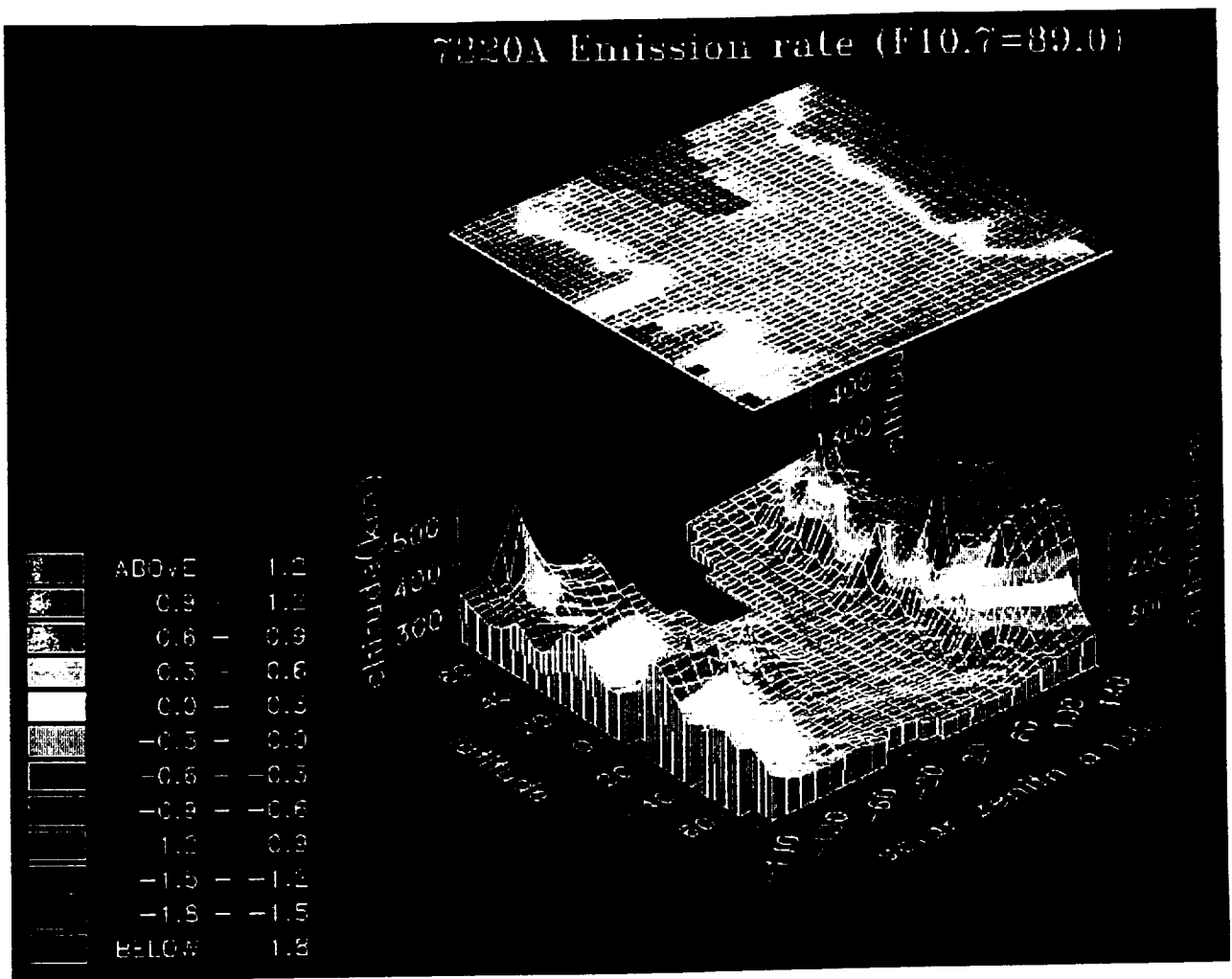


Plate 2. The 7320-A volume emission rate (photons $\text{cm}^{-3} \text{s}^{-1}$) at the peak of the layer as a function of altitude, latitude, and solar zenith angle. The volume emission rate is on a log scale.

ORIGINAL PAGE IS
OF, POOR QUALITY

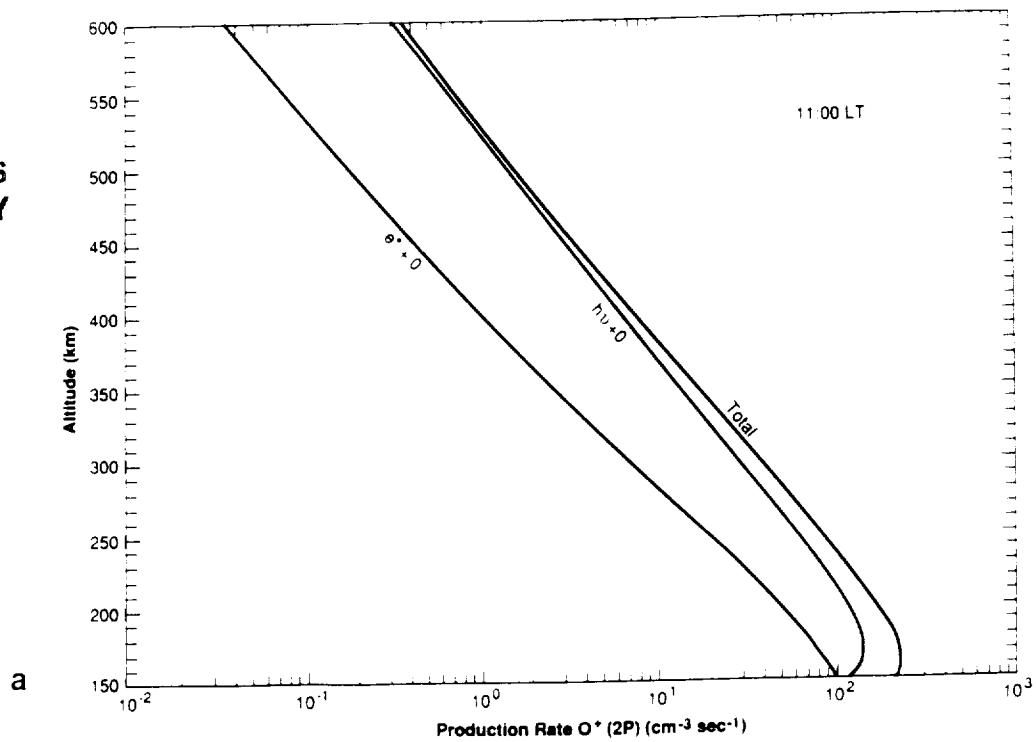


Fig. 6. Midday, mid-latitude production and loss rates for $\text{O}^+(2P)$: (a) and (b) southern hemisphere for 48°S , 11 LT, $\chi = 28^\circ$; (c) and (d) northern hemisphere for 40°N , 12 LT, $\chi = 60^\circ$.

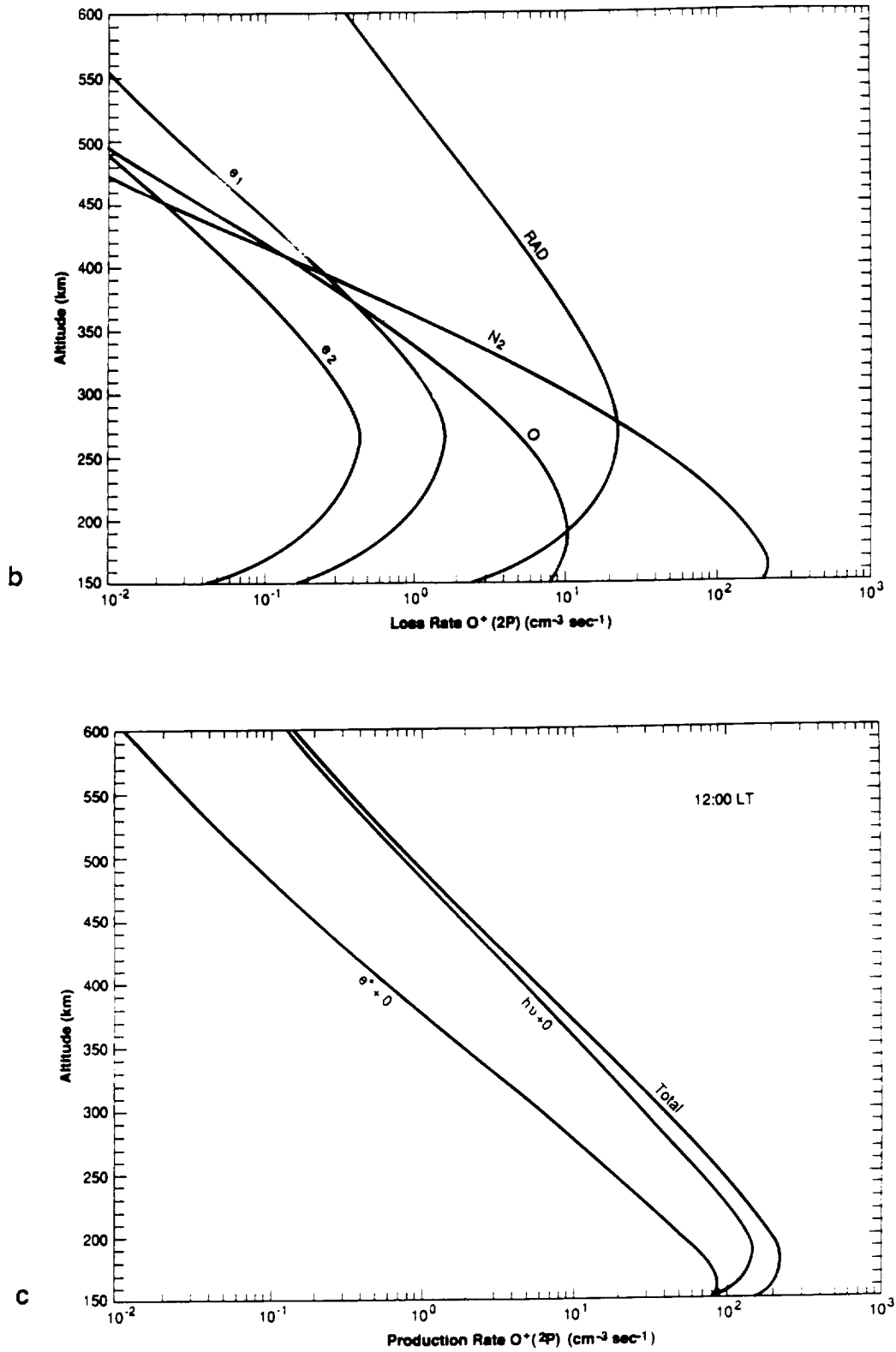


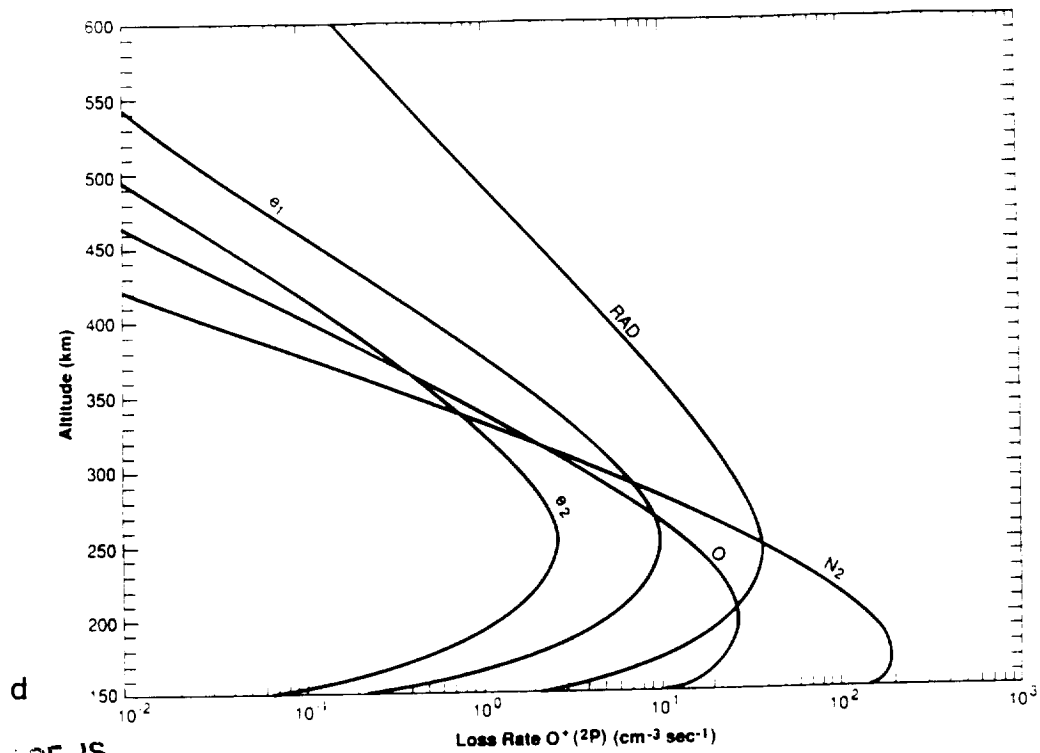
Fig. 6. (continued)

ORIGINAL PAGE IS
OF POOR QUALITY.

An interesting feature of Plate 1 is the fact that there is significant production ($\approx 0.2 \text{ cm}^{-3} \text{ s}^{-1}$) at high altitudes at midnight in the winter hemisphere. This is due entirely to photoelectrons transported from the summer hemisphere. This conjugate electron production rate together with the loss processes are shown in

Figure 8. Without the interhemispheric capability this production source would not be modeled.

Because of the longitudinal asymmetries of the Earth's magnetic field, the conjugate photoelectron production rate varies for different maps generated for different universal times. Plate 3



ORIGINAL PAGE IS
OF POOR QUALITY.

Fig. 6 (continued)

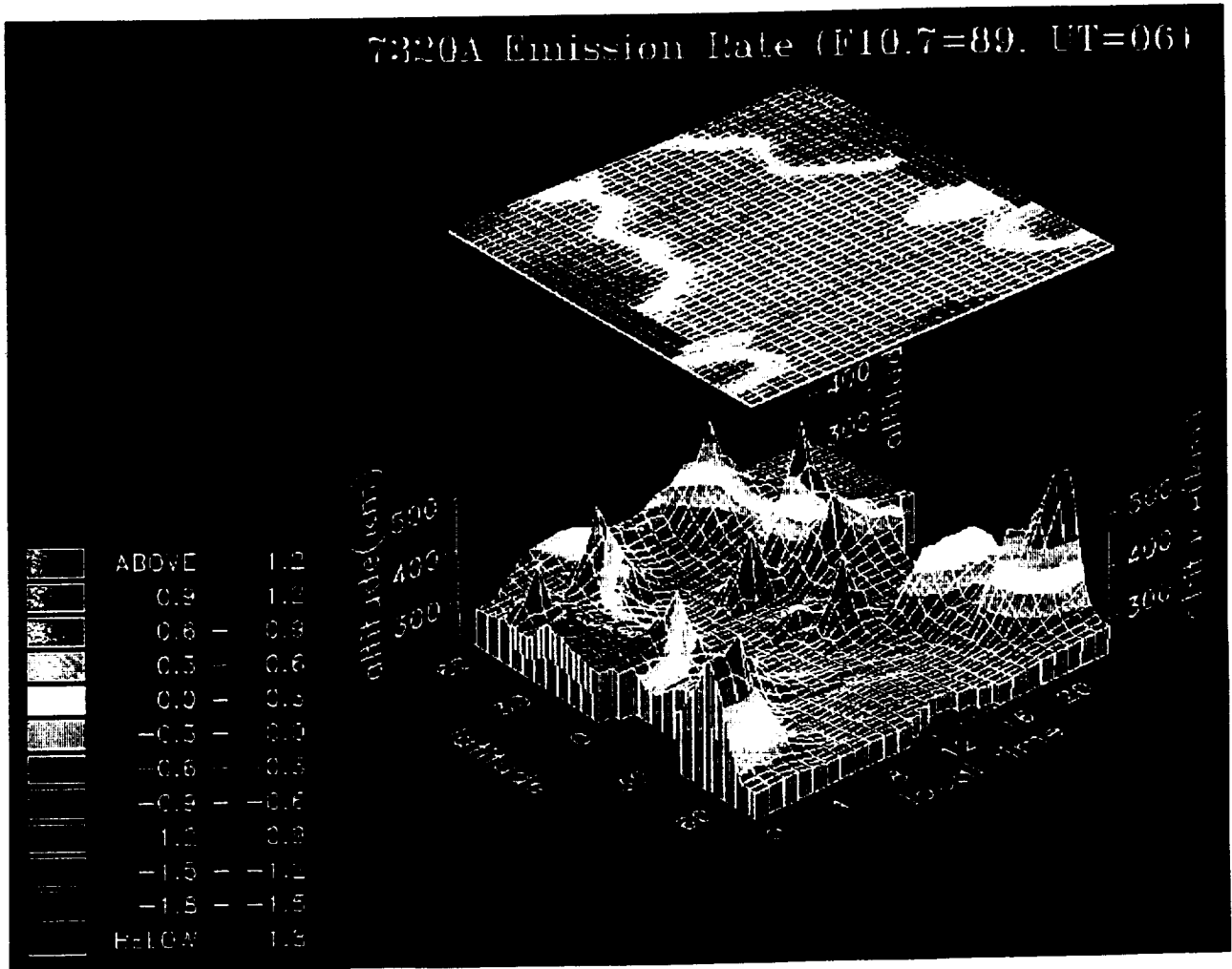


Plate 3. The 7320-A volume emission rate (photons $cm^{-3} s^{-1}$) at the peak of the layer as a function of altitude, latitude, and local time for 06 UT. The volume emission rate is on a log scale. The missing areas near the equator at midnight are where the emission rate has effectively gone to zero.

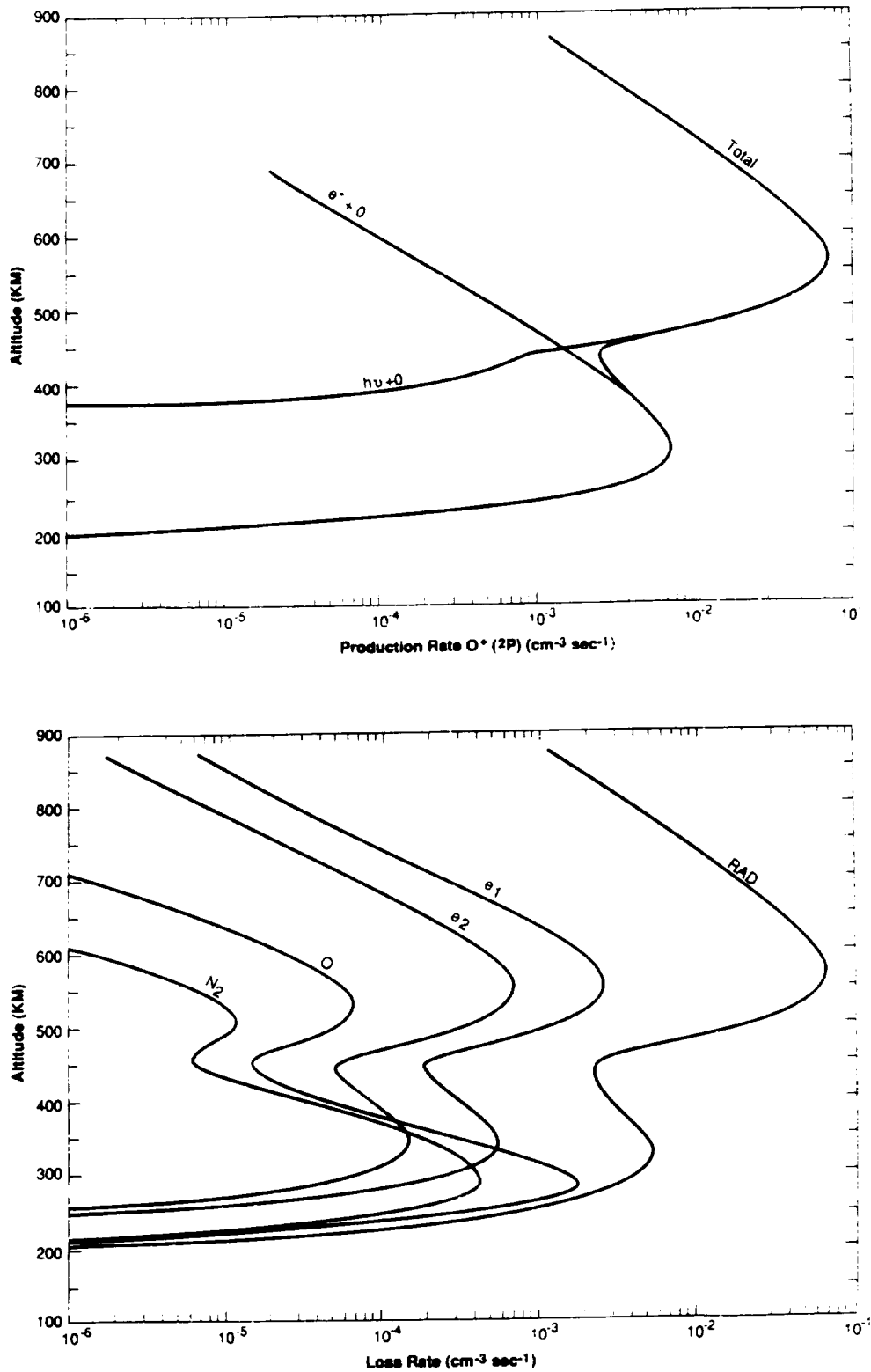


Fig. 7. Production and loss rates for 54°S for a solar zenith angle of 105° (LT = 00).

shows the global plot for the same conditions as Plate 1, but for UT = 0600. This is equivalent to placing midnight at 90°W, over the eastern United States. In this longitudinal sector, higher southern latitudes (solar illuminated) map to lower northern latitudes. Above 50°S the Sun does not set and conjugate electrons

are present all through the night near 50°N. Thus the conjugate source is seen to be significantly more pronounced than for 00 UT. Plate 4 shows the integrated volume emission rate, or surface brightness (in rayleighs), with and without the conjugate photoelectron source. The scale has been adjusted to enhance the winter

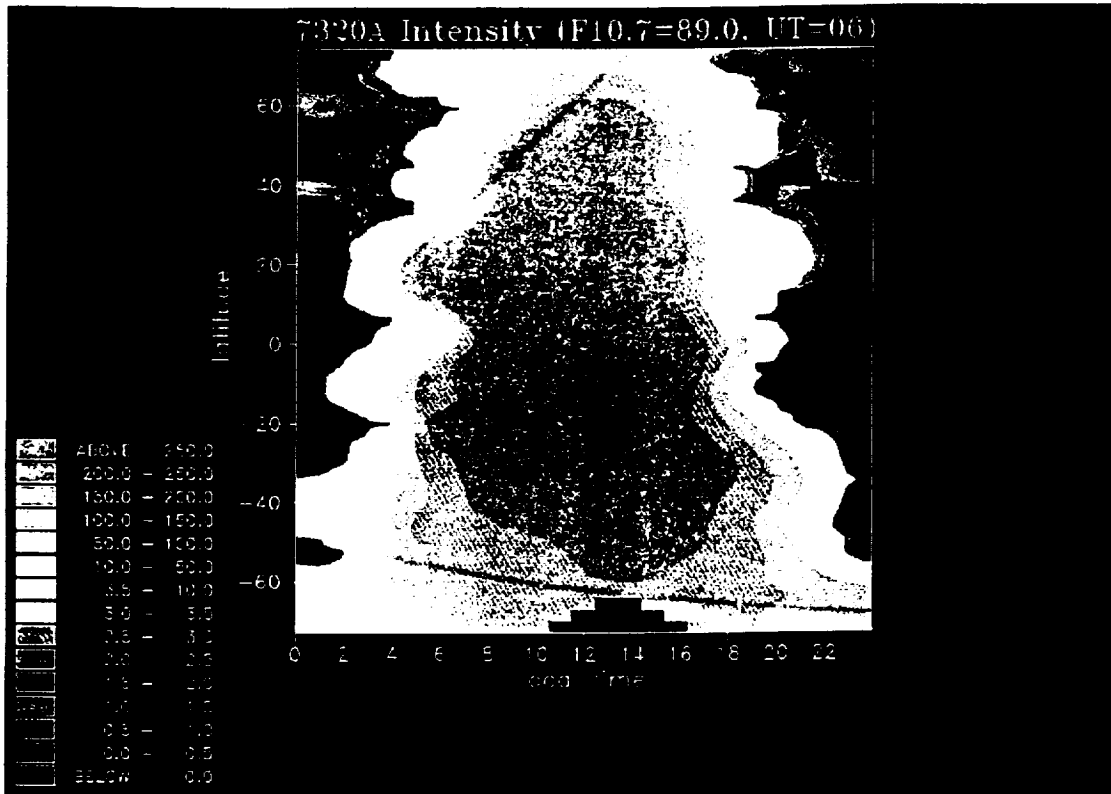


Plate 4a With conjugate photoelectron production.

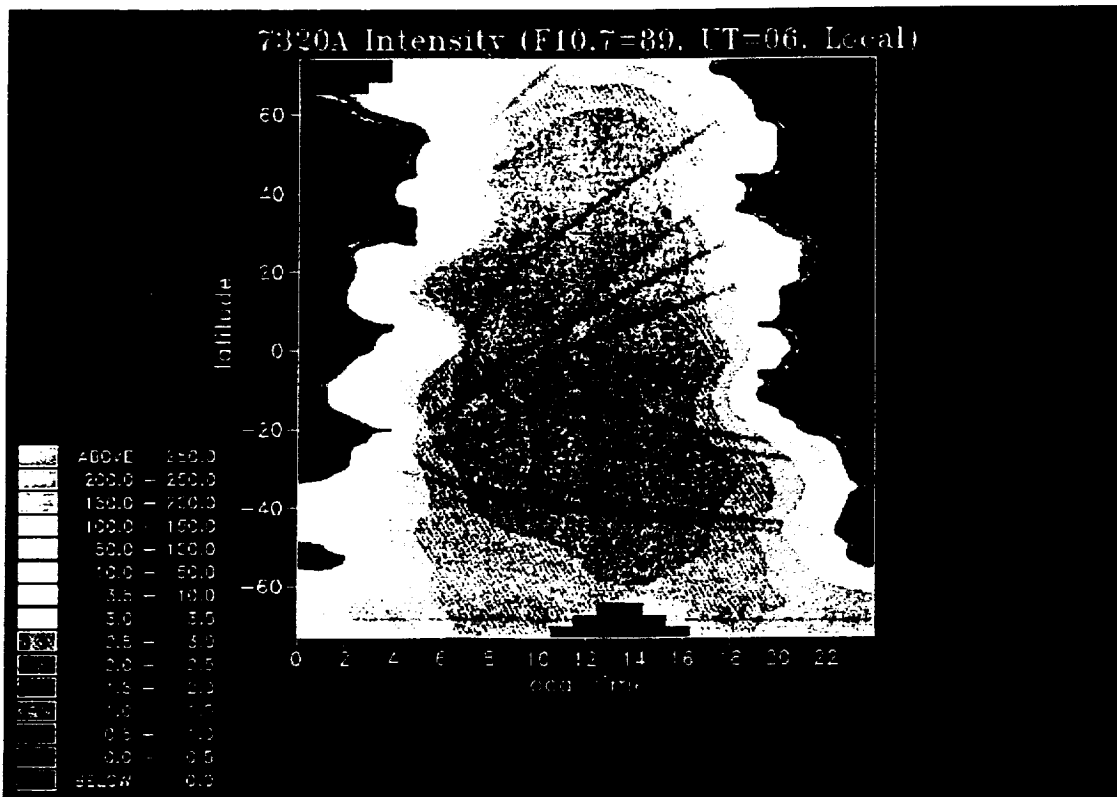


Plate 4b Without conjugate photoelectron production.

**ORIGINAL PAGE IS
OF POOR QUALITY**

Plate 4 Vertical 7320-A intensity (rayleighs) for solar minimum at UT = 06. The solution is only valid within the $L = 5$ boundaries shown in Figure 5.

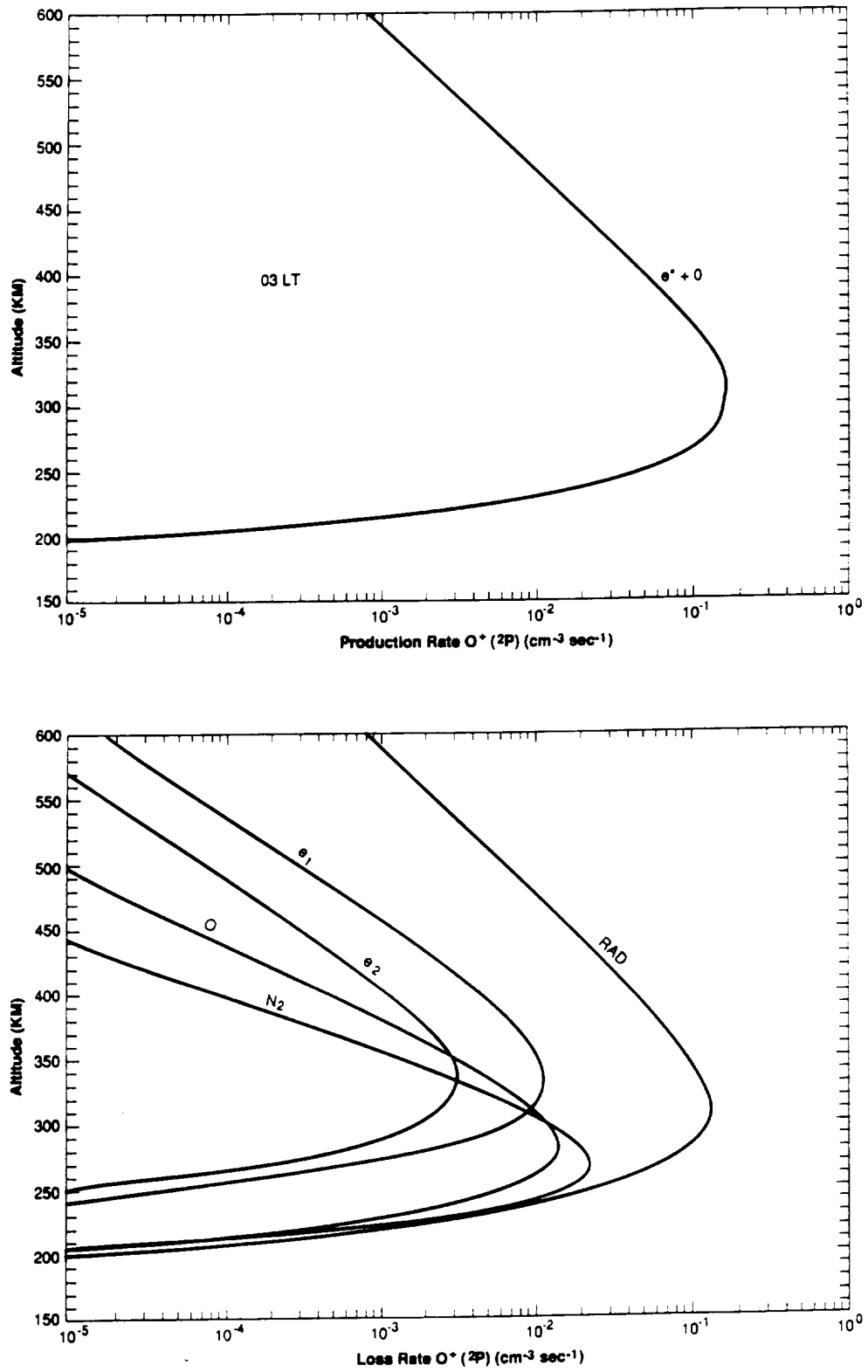


Fig. 8. Conjugate photoelectron production of $\text{O}^+(2P)$ at night in the winter hemisphere (49°N , $\chi = 137^\circ$). The corresponding loss rates are also shown.

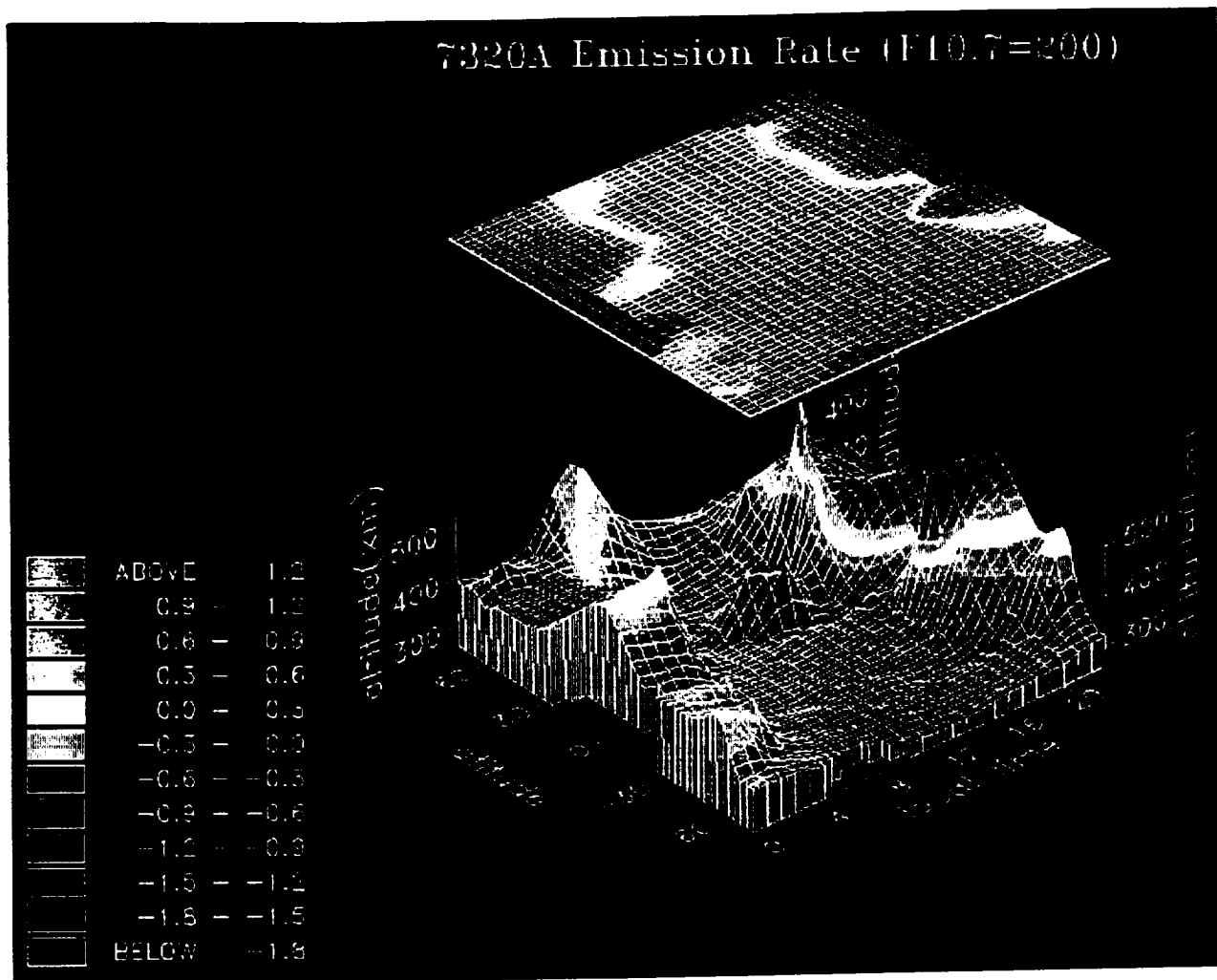


Plate 5. The 7320-A volume emission rate (photons $\text{cm}^{-3} \text{s}^{-1}$) at the peak of the layer as a function of altitude, latitude, and local time for 00 UT. The results are for the same day as Plate 1 (November 28) but for solar maximum conditions. The volume emission rate is shown on a log scale.

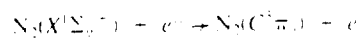
nighttime conjugate production. This interhemispheric source results in 2 to 3 R of 7320-A airglow.

Plate 5 shows the same day of year as Plate 1, but for conditions representing solar maximum. The principal differences between these two are in the overall increase in emission rate and the overall increase in altitude of the emission peak. Both of these effects are to be expected on the basis of the solar flux and neutral atmosphere changes.

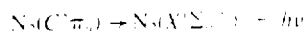
Plate 6 shows the results of integrating the volume emission rates of the solar minimum and maximum cases (Plates 1 and 5) over altitude to obtain the vertical surface brightness. These intensities (in rayleighs) are what an orbiting instrument would see looking vertically downward on the atmosphere.

MODELING OF THE N_2 3371-A AIRGLOW

The production mechanism for the excitation of the N_2 second positive system in the dayglow is photoelectron impact:



The 3371-A emission arises from the 0-0 band of the second positive system:



Since the transition is permitted, radiation is the only loss process. The excitation cross sections for the 0-0 band are those of *Imami and Borst* [1974] which are 25% of the total cross section.

Plate 7 shows the results of the semiglobal solution of the 3371-A volume emission rates. The production rates for noon at mid-latitudes are shown in Figure 9. The results shown in Plate 7 follow the behavior anticipated from a simple photoelectron source and radiative loss. The behavior changes after sunset in that the peak production rises in altitude and falls in magnitude. Again, the high latitude conjugate photoelectron source can be seen during the night in the winter hemisphere. While we do not show the 06 UT case here, the conjugate source again becomes more pronounced for the different magnetic field orientation, as it did for the 7320-A case, because of the more favorable alignment of the magnetic field lines for this purpose.

Plate 8 shows the global model of the peak 3371-A volume emission rate for solar maximum. What is interesting to note in this case is that, apart from an overall increase in the altitude of the emission peak, the peak emission rate distribution is very similar at solar maximum and solar minimum. However, the difference in the vertical intensity is significant. This is seen in Plate 9 which shows the integrated column surface brightness for solar minimum and maximum. The difference is largely due to the differing scale heights, as can be seen in Figure 9.

ORIGINAL PAGE IS
OF POOR QUALITY

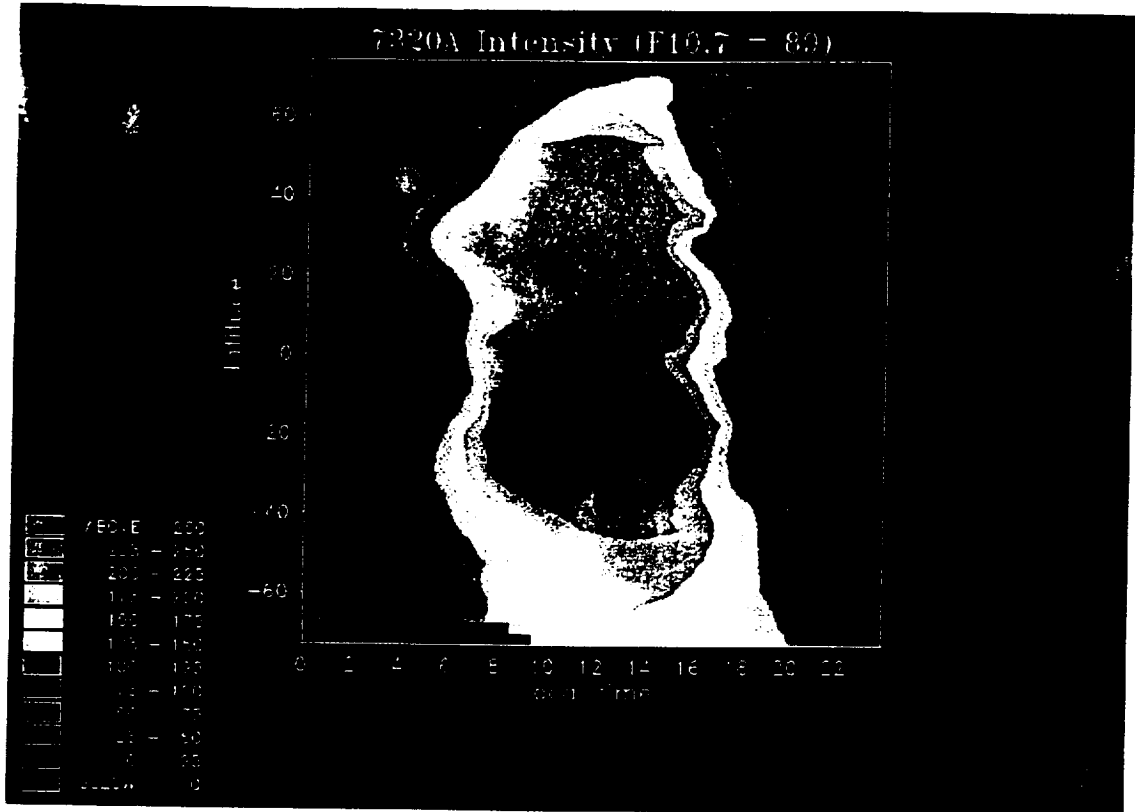


Plate 6a. Solar minimum case shown in Plate 1.

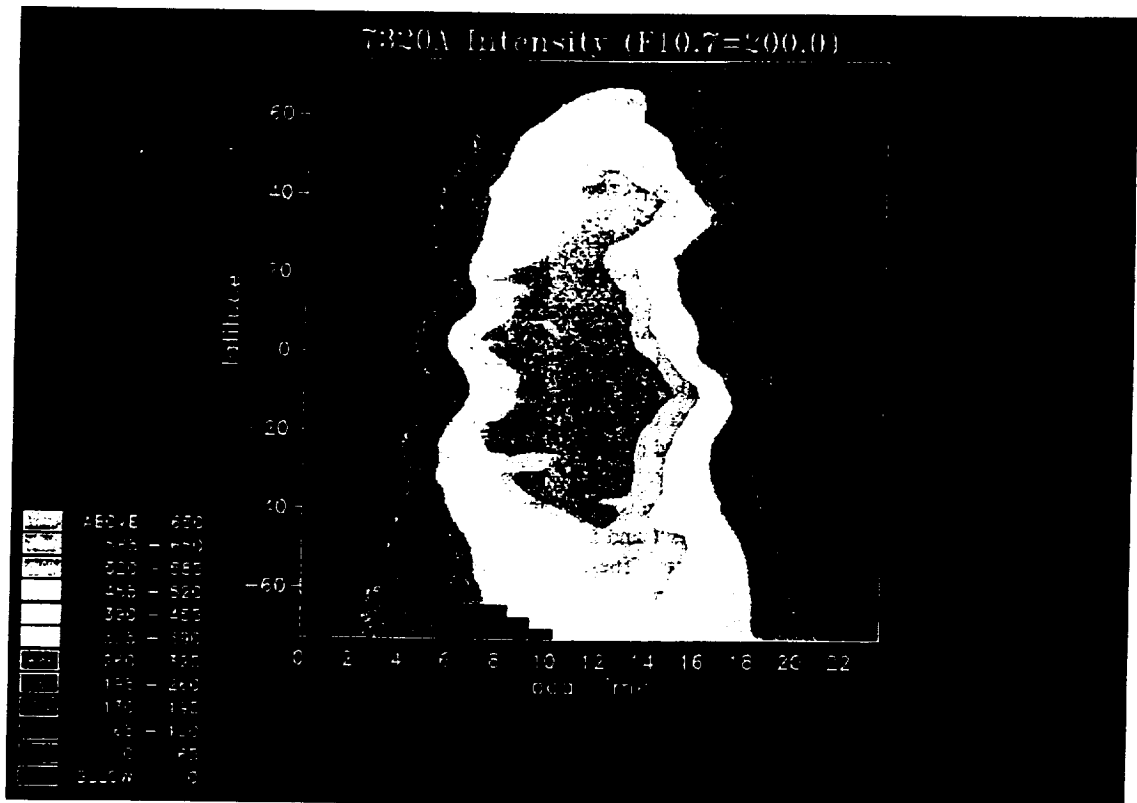


Plate 6b. Solar maximum case shown in Plate 5.

Plate 6. Vertical column integrated surface brightness (in rayleighs). The results are only valid within the $L \approx 5$ boundaries shown in Figure 5.

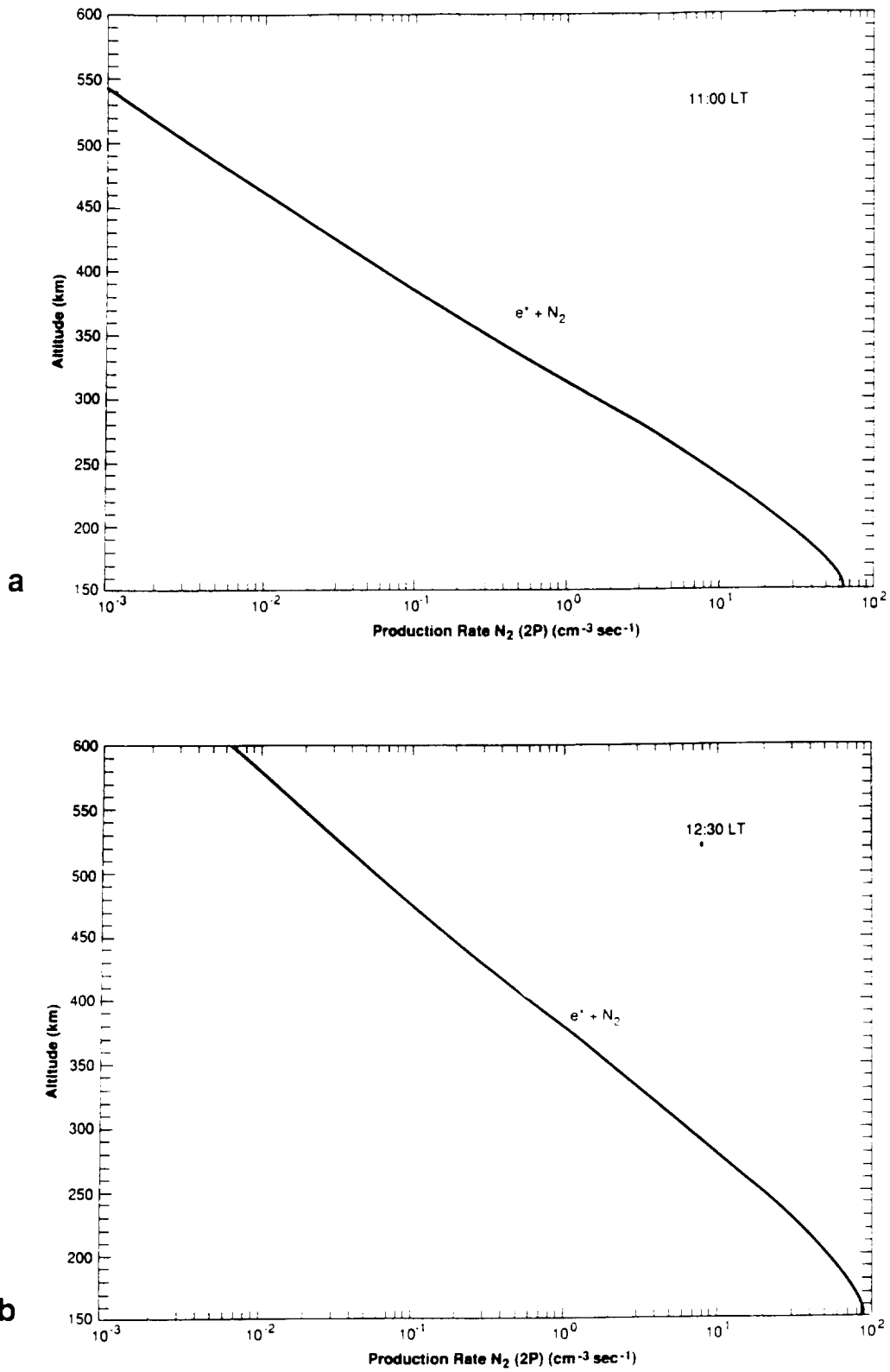


Fig. 9. Production rates for the $N_2(2P)$ state for 00 UT (a) for solar minimum ($48^\circ S$) and (b) for solar maximum ($53^\circ S$).

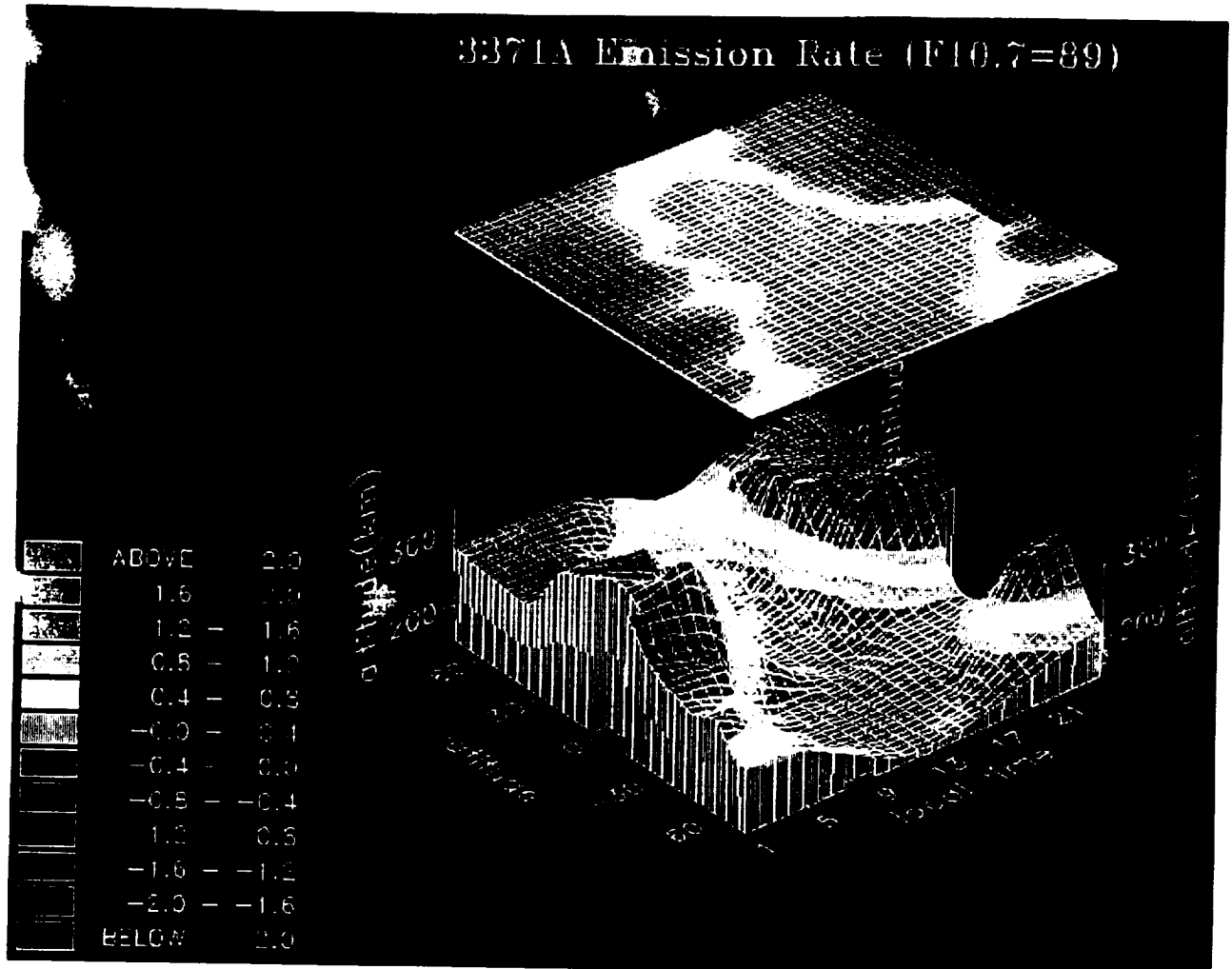


Plate 7. Volume emission rate (photons $\text{cm}^{-3}\text{s}^{-1}$) at the peak of the 3371-A layer versus altitude, latitude, and local time (longitude) for near solar minimum conditions. The volume emission rate is plotted on a log scale. The results are only valid within the $L = 5$ boundaries shown in Figure 5.

SUMMARY

In this paper we have presented the first interhemispherically coupled models of the $\text{O}^+(\text{}^2P)$ and $\text{N}_2^+(\text{}^2C)$ airglow emission at 7320 Å and 3371 Å, respectively, covering mid and low latitudes. These are two emissions for which the mechanisms are relatively well understood, allowing us to examine here the morphology. The semiglobal graphical maps clearly illustrate the diurnal, seasonal and solar cyclic variability of these emissions. In both cases, conjugate photoelectrons result in excitation at mid to high nighttime latitudes in the winter hemisphere. The interhemispheric coupling capability of the model allows us to examine the

extent and the longitudinal variability of the conjugate photoelectron effects.

This model provides a capability which will greatly enhance the ability to interpret airglow observations made from spacecraft. Any line of sight geometry can now be projected through the three-dimensional model solution, and by integrating along the projected line of sight, surface brightness (vertical or slant path) can be obtained for comparison with the observations. Furthermore, because of the complex variability exhibited by these emissions over the $L = 5$ range, this model also provides a valuable tool for planning of such observations.

Plate 9. Vertical intensity of the 3371-A airglow (in rayleighs) for solar minimum and solar maximum conditions. The solar maximum plot is shown on two scales: one to show the intensity variation and one to allow comparison with the solar minimum plot shown in Plate 9a. The results are only valid within the $L = 5$ boundaries shown in Figure 5.

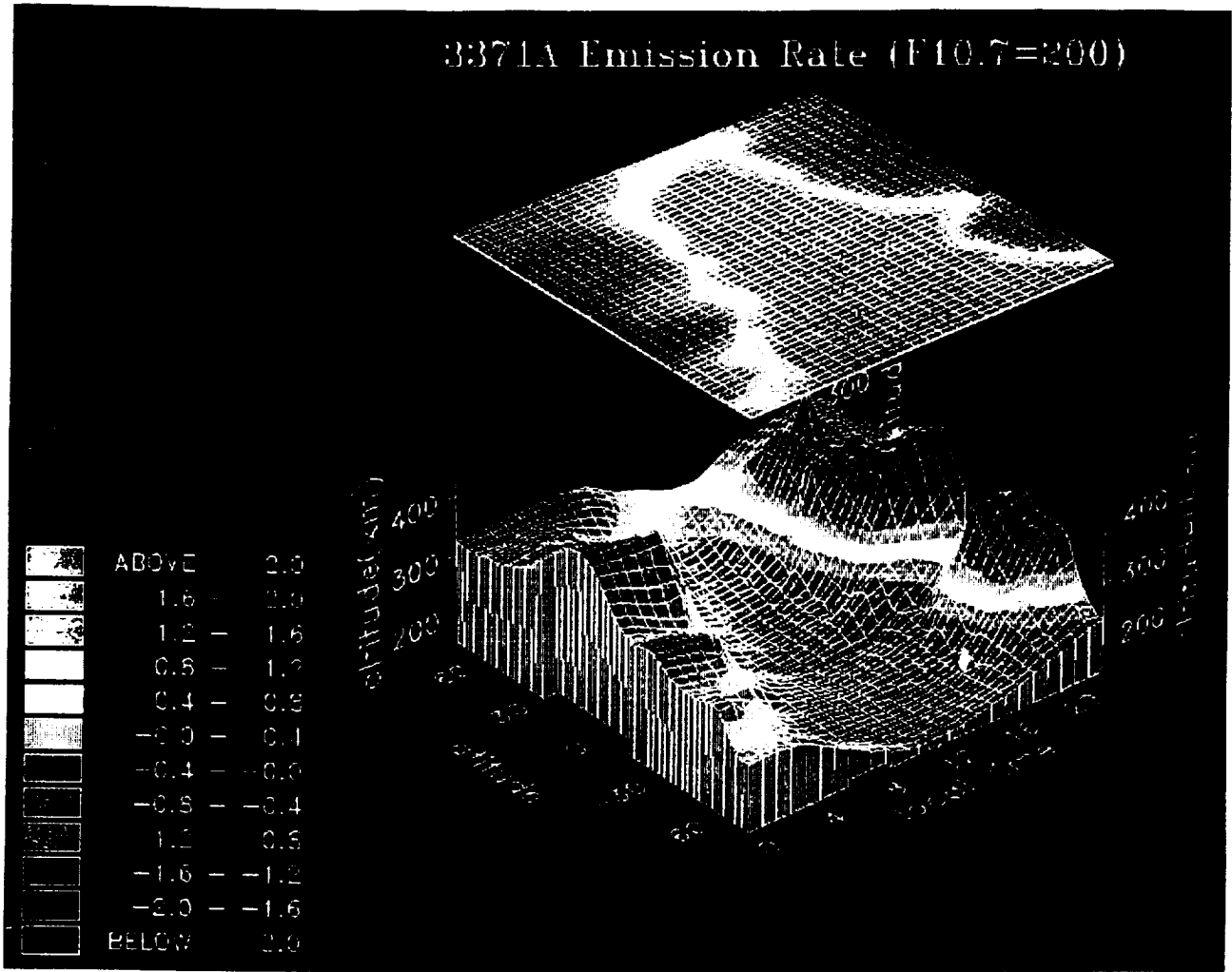


Plate 8. Volume emission rate (photons $\text{cm}^{-2} \text{s}^{-1}$) at the peak of the 3371-Å layer for solar maximum conditions. The volume emission rate is plotted on a log scale.

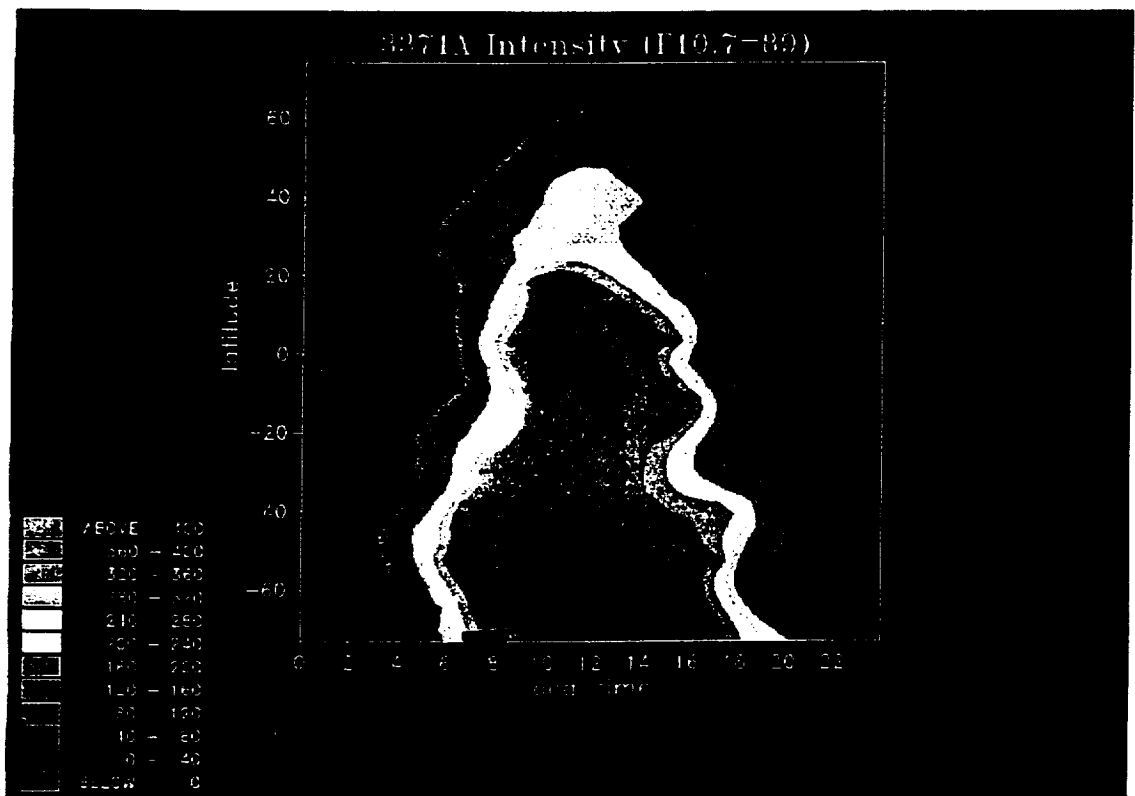


Plate 9a
Solar minimum

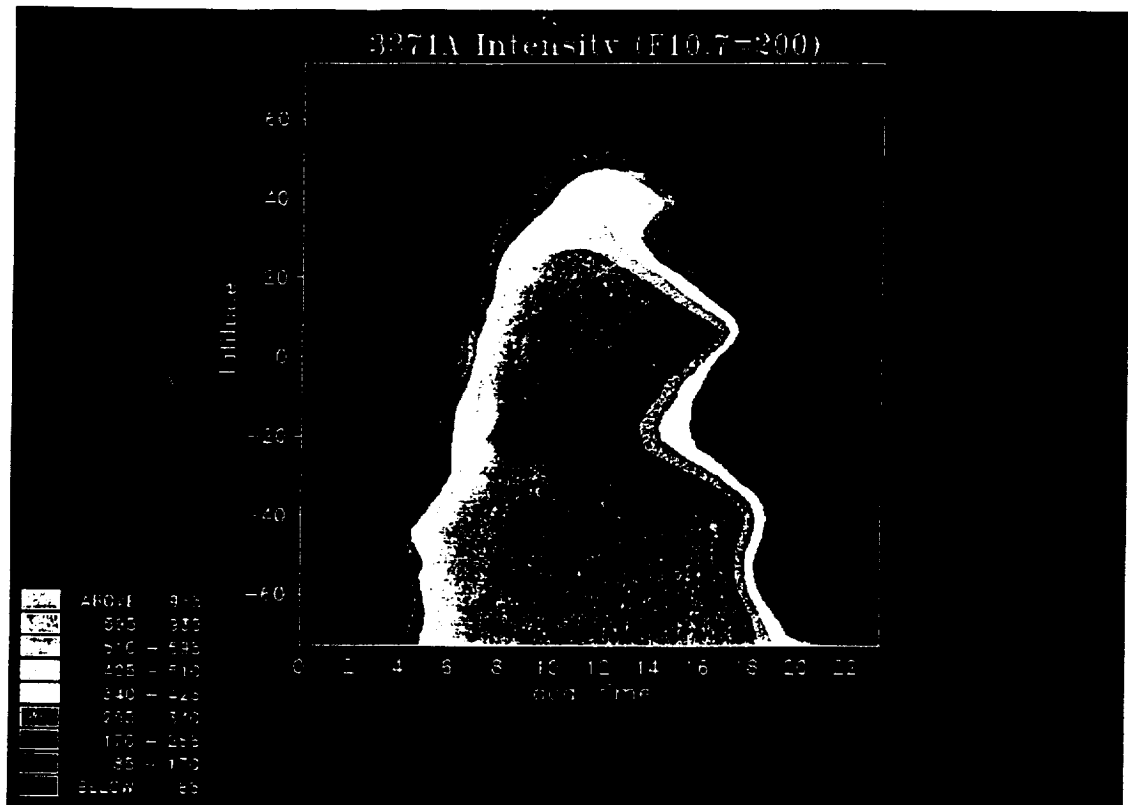


Plate 9b. Solar maximum, scaled to brightest intensities.

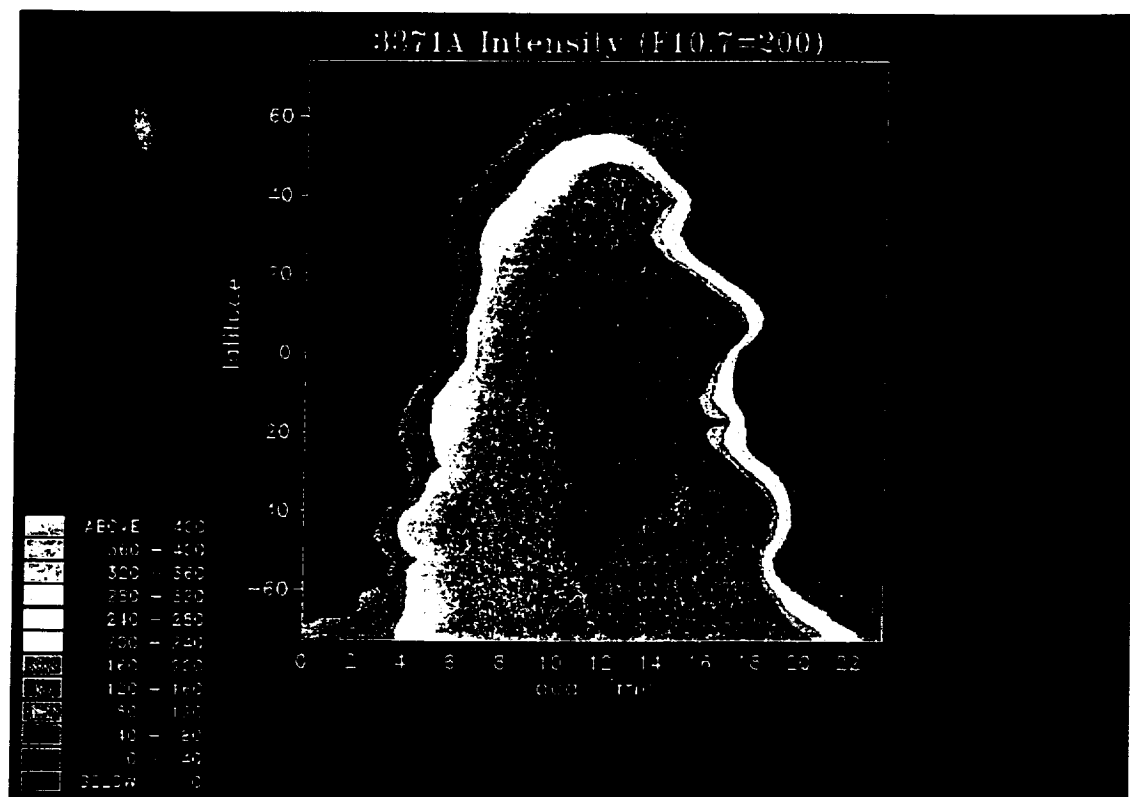


Plate 9c. Solar maximum, same scale as solar minimum.

Acknowledgments. This work was supported at the University of Alabama in Huntsville by NASA contract NAS8-37106 and grant NAGW 996, and National Science Foundation grants ATM-8713693, ATM 8907808, ATM-8915898, and ATM-8716036.

The editor thanks S. C. Solomon and another referee for their assistance in evaluating this paper.

REFERENCES

- Abdou, W. A., D. G. Torr, P. G. Richards, M. R. Torr, and E. L. Breg. Results of a comprehensive study of the photochemistry of N_2^+ in the ionosphere. *J. Geophys. Res.*, **89**, 9060, 1984.
- Abreu, V. J., J. H. Yee, S. C. Solomon, and A. Dalgarno. The quenching rate of $O(^1D)$ by $O(^3P)$. *Planet. Space Sci.*, **11**, 1143, 1986.
- Adams, N. G., and D. Smith. Production distributions for some ion-molecule reactions. *J. Phys.*, **B9**, 1439, 1976.
- Albritton, D. L. Ion-neutral reaction-rate constants measured in flow reactors through 1977. *Atomic Data and Nuclear Data Tables*, **22**, 1, 1978.
- Anderson, D. N., J. M. Forbes, and M. Codrescu. A fully analytic, low- and middle-latitude ionospheric model. *J. Geophys. Res.*, **94**, 1520, 1989.
- Banks, P. M., and G. Kockarts. *Aeronomy*, Part A, p. 225. Academic, San Diego, Calif., 1973.
- Bates, D. R., and E. C. Zipf. The $O(^1S)$ quantum yield from O_2^+ dissociation recombination. *Planet. Space Sci.*, **28**, 1081, 1981.
- Becker, K. H., W. Groth, and D. Z. Kley. The rate constant for the aeronomic reaction $N + O_2$. *Naturforsch.*, **24a**, 1280, 1969.
- Burnside, R. G., C. A. Tepley, and V. B. Wickwar. The $O^- - O$ collision cross section: Can it be inferred from aeronomic measurements? *Annales Geophysicae*, **5A**, 343, 1987.
- Chandler, M. O., R. A. Behnke, A. F. Nagy, E. G. Fontheim, P. G. Richards, and D. G. Torr. Comparison of measured and calculated low-latitude ionospheric properties. *J. Geophys. Res.*, **88**, 9187, 1983.
- Chen, A., R. Johnson, and M. A. Biondi. Measurements of the $O^- + N_2$ and $O^- + O_2$ reaction rates from 300 to 900 K. *J. Chem. Phys.*, **69**, 2688, 1978.
- Dalgarno, A. Metastable species in the ionosphere. *Ann Geophys.*, **26**, 601, 1970.
- Fehsenfeld, F. C. The reaction of O_2^+ with atomic nitrogen and NO^+ , H_2O , and NO_2^+ with atomic oxygen. *Planet. Space Sci.*, **25**, 195, 1977.
- Fischer, C. F., and H. P. Saha. Multiconfiguration Hartree-Fock results with Breit-Pauli corrections for forbidden transitions in the $2P^2$ configuration. *Phys. Rev. A*, **28**, 3169, 1983.
- Frederick, J. E., and D. W. Rusch. On the chemistry of metastable atomic nitrogen in the F region deduced from simultaneous satellite measurement of the 5200 Å airglow and atmospheric composition. *J. Geophys. Res.*, **82**, 3509, 1977.
- Frederick, J. E., D. W. Rusch, G. A. Victor, W. E. Sharp, P. B. Hays, and H. C. Brinton. The O I (8446 Å) airglow: Observations and excitation mechanisms. *J. Geophys. Res.*, **81**, 3923, 1976.
- Hedin, A. H. MSIS-86 thermospheric model. *J. Geophys. Res.*, **92**, 4649, 1987.
- Hedin, A. E., N. W. Spencer, and T. Killeen. Empirical global model of upper thermosphere winds based on Atmosphere and Dynamics Explorer satellite data. *J. Geophys. Res.*, **93**, 99959, 1988.
- Henry, R. J. W., P. G. Burke, and A. L. Sinfailam. Scattering of electrons by C , N , O , N^+ , O^+ , and O^{++} . *Phys. Rev.*, **178**, 218, 1969.
- Horwitz, J. I., R. H. Compton, P. G. Richards, M. O. Chandler, C. R. Chappell, P. Anderson, W. B. Hanson, and L. H. Brace. Plasma-sphere-ionosphere coupling. 2. Ion composition measurements at plasma-sphere and ionospheric altitudes and comparison with modeling results. *J. Geophys. Res.*, **95**, 7949, 1990.
- Huntress, W. T., and P. G. Anicich. On the reaction of N^+ ions with O_2 . *Geophys. Res. Lett.*, **3**, 317, 1976.
- Imami, M., and W. L. Borst. Electron excitation of the (0,0) second positive band of nitrogen from threshold to 1000 eV*. *J. Chem. Phys.*, **61**, 1115, 1974.
- Johnsen, R., and M. A. Biondi. Laboratory measurements of the $O^-(^2D) + N_2$ and $O^-(^2D) + O_2$ reaction rate coefficients and their ionospheric implications. *Geophys. Res. Lett.*, **7**, 401, 1980.
- Kernahan, J. H., and H. L. Pang. Experimental determination absolute A coefficients for "forbidden" atomic oxygen lines. *Can. J. Phys.*, **53**, 455, 1975.
- Killeen, T. L., R. G. Roble, and N. W. Spencer. A computer model of global thermospheric winds and temperatures. *Adv. Space Res.*, **7**, 207, 1987.
- Kley, D., G. M. Lawrence, and E. T. Stone. The yield of $N(^2D)$ atoms in the dissociative recombination of NO^+ . *J. Chem. Phys.*, **66**, 4157, 1977.
- Kopp, J. P., D. W. Rusch, R. G. Roble, G. A. Victor, and P. B. Hays. Photoemission in the second positive system of molecular nitrogen in the Earth's dayglow. *J. Geophys. Res.*, **82**, 555, 1977.
- Langford, A. O., V. M. Bierbaum, and S. R. Leone. Auroral implications of recent measurement on $O(^1S)$ and $O(^1D)$ formation on the reaction of N^+ with O_2 . *Planet. Space Sci.*, **33**, 1225, 1985.
- Lee, J. H., J. V. Michael, W. A. Payne, and L. J. Stief. Absolute rate of the reaction of $N(^2S)$ with NO from 196–400 K with DF-RF and FP-RF techniques. *J. Chem. Phys.*, **69**, 3069, 1978.
- Lin, C. L., and F. Kautman. Reactions of metastable nitrogen atoms. *J. Chem. Phys.*, **55**, 3760, 1971.
- Lindinger, W., F. C. Fehsenfeld, A. L. Schmeltekopf, and E. E. Ferguson. Temperature dependence of some ionospheric ion-neutral reactions from 300° to 900°K. *J. Geophys. Res.*, **79**, 4753, 1974.
- McFarland, M., D. L. Albritton, F. C. Fehsenfeld, E. E. Ferguson, and A. L. Schmeltekopf. Energy dependence and branching ratio of the $N_2^+ + O$ reaction. *J. Geophys. Res.*, **79**, 2925, 1974.
- Mehr, F. J., and M. A. Biondi. Electron temperature dependence of O_2^+ and N_2^+ ions with electrons. *Phys. Rev.*, **181**, 264, 1969.
- Menwether, J. W., D. G. Torr, J. C. G. Walker, and A. O. Nier. The $O^-(^2P)$ emission at 7320 Å in twilight. *J. Geophys. Res.*, **83**, 3311, 1978.
- Miller, K. L., D. G. Torr, and P. G. Richards. Meridional winds in the thermosphere derived from measurements of F_2 layer height. *J. Geophys. Res.*, **91**, 4531, 1986.
- Newberry, I. T., R. H. Compton, P. G. Richards, and C. R. Chappell. Thermal He^+ in the plasmasphere: Comparison of observations with numerical calculations. *J. Geophys. Res.*, **94**, 15,265, 1989.
- Ogawa, H. S., and D. L. Judge. Absolute solar flux measurement shortward of 575 Å. *J. Geophys. Res.*, **91**, 7089, 1986.
- Piper, L. G. The excitation of $O(^1S)$ in the reaction between $N_2(A^1\Sigma_u^+)$ and $O(^3P)$. *J. Chem. Phys.*, **77**, 2373, 1982.
- Queffelec, J. L., B. R. Rowe, M. Morlais, J. C. Gomet, and F. Vallee. The dissociative recombination of $N_2^+(v=0,1)$ as a source of metastable atoms in planetary atmospheres. *Planet. Space Sci.*, **33**, 263, 1985.
- Richards, P. G. Thermal electron quenching of $N(^2D)$: Consequences for the ionospheric photoelectron flux and the thermal electron temperature. *Planet. Space Sci.*, **34**, 689, 1986.
- Richards, P. G., and D. G. Torr. An investigation of the consistency of the ionospheric measurements of the photoelectron flux and solar EUV flux. *J. Geophys. Res.*, **89**, 5625, 1984.
- Richards, P. G., and D. G. Torr. Seasonal, diurnal, and solar cyclical variations of the limiting H^+ flux in the Earth's topside ionosphere. *J. Geophys. Res.*, **90**, 5261, 1985a.
- Richards, P. G., and D. G. Torr. The altitude variation of the ionospheric photoelectron flux: A comparison of theory and measurements. *J. Geophys. Res.*, **90**, 2877, 1985b.
- Richards, P. G., and D. G. Torr. Thermal coupling of conjugate ionospheres and the tilt of the Earth's magnetic field. *J. Geophys. Res.*, **91**, 9017, 1986a.
- Richards, P. G., and D. G. Torr. A method of extracting meridional winds from ionosonde measurements by using ionospheric models. in *Proceedings of the Thermospheric Dynamics Workshop II*, edited by H. G. Mayr and N. J. Miller. NASA Conf. Pub. 2398, p. 369, 1986b.
- Richards, P. G., and D. G. Torr. A factor of 2 reduction in the theoretical F2 peak electron density due to enhanced vibrational excitation of N_2 in summer at solar maximum. *J. Geophys. Res.*, **91**, 11331, 1986c.
- Richards, P. G., and D. G. Torr. Ratios of photoelectron to EUV ionization rates for aeronomic studies. *J. Geophys. Res.*, **93**, 4060, 1988.
- Richards, P. G., D. G. Torr, and M. R. Torr. Photodissociation of N_2 : A significant source of thermospheric atomic nitrogen. *J. Geophys. Res.*, **86**, 1495, 1981.
- Richards, P. G., D. G. Torr, and P. J. Espy. Determination of photoionization branching ratios and total photoionization cross sections at 304 Å from experimental ionospheric photoelectron fluxes. *J. Geophys. Res.*, **87**, 3599, 1982a.
- Richards, P. G., M. R. Torr, and D. G. Torr. The seasonal effect of nitric oxide cooling in the thermospheric UV heat budget. *Planet. Space Sci.*, **30**, 515, 1982b.
- Richards, P. G., D. G. Torr, and W. A. Abdou. Effects of vibrational

- enhancement of N_2^+ on the cooling rate of ionospheric thermal electrons, *J. Geophys. Res.*, **91**, 304, 1986a.
- Richards, P. G., D. G. Torr, J. L. Horwitz, and M. R. Torr, Models of the plasmaspheric thermal plasma distribution, *Adv. Space Res.*, **6**, 141, 1986b.
- Richards, P. G., D. G. Torr, M. J. Buonsanto, and K. L. Miller, The behavior of the electron density and temperature at Millstone Hill during the equinox transition study, September 1984, *J. Geophys. Res.*, **94**, 16,969, 1989.
- Rowe, B. R., D. W. Fahey, F. C. Fehsenfeld, and D. L. Albritton, Rate constants for the reactions of metastable O^+ ions with N_2 and O_2 at collision energies 0.04 to 0.2 eV and the mobilities of these ions at 300 K, *J. Chem. Phys.*, **73**, 194, 1980.
- Rusch, D. W., D. G. Torr, P. B. Hays, M. R. Torr, and A. O. Nier, Determination of the $O^+(^2P)$ ionization frequency using satellite airglow and particle data and its implications on the EUV solar flux, *Geophys. Res. Lett.*, **3**, 537, 1976.
- Rusch, D. W., D. G. Torr, P. B. Hays, and J. C. G. Walker, The O II (19–7330 Å) dayglow, *J. Geophys. Res.*, **82**, 719, 1977.
- Rusch, D. W., J. C. Gérard, and W. E. Sharp, The reaction of $N(^4D)$ with O_2 as a source of $O(^1D)$ atoms in auroras, *Geophys. Res. Lett.*, **5**, 1043, 1978.
- Schunk, R. W., and A. F. Nagy, Ionospheres of the terrestrial planets, *Rev. Geophys.*, **18**, 813, 1980.
- Seaton, M. J., and D. E. Osterbrock, Relative O II intensities in gaseous nebulae, *Astrophys. J.*, **125**, 66, 1957.
- Slinger, F. G., and G. Black, Quenching of $O(^1S)$ by $O_2(a^1\Delta_g)$, *Geophys. Res. Lett.*, **8**, 535, 1981.
- St. Maurice, J. P., and R. W. Schunk, Diffusion and heat flow equations for the mid-latitude topside ionosphere, *Planet. Space Sci.*, **25**, 907, 1977.
- St. Maurice, J. P., and D. G. Torr, Nonthermal rate coefficients in the ionosphere: The reaction of O^+ with N_2 , O_2 , and NO , *J. Geophys. Res.*, **83**, 969, 1978.
- Streit, G. E., C. J. Howard, O. L. Schmeliokopf, J. A. Davidson, and H. I. Schittl, Temperature Dependence of $O(^1D)$ rate constants for reactions with O_2 , N_2 , CO_2 , O_3 , and H_2O , *J. Chem. Phys.*, **65**, 4761, 1976.
- Torr, D. G., Refinement of aeronomically determined rate coefficient for the reaction of N_2^+ with O , *J. Geophys. Res.*, **84**, 1939, 1979.
- Torr, D. G., The photochemistry of the upper atmosphere, in *The Photochemistry of Atmospheres*, edited by J. S. Levine, pp. 165–278, Academic, San Diego, Calif., 1985.
- Torr, D. G., P. G. Richards, M. R. Torr, and V. J. Abreu, Further quantification of the sources and sinks of thermospheric $O(^1D)$ atoms, *Planet. Space Sci.*, **29**, 595, 1981.
- Torr, M. R., and D. G. Torr, Recombination of NO^+ in the mid-latitude trough and the polar ionization hole, *J. Geophys. Res.*, **84**, 4316, 1979.
- Torr, M. R., and D. G. Torr, The dissociative recombination of O_2^+ in the ionosphere, *Planet. Space Sci.*, **29**, 999, 1981.
- Torr, M. R., and D. G. Torr, The role of metastable species in the thermosphere, *Rev. Geophys.*, **20**, 91, 1982.
- Torr, M. R., and D. G. Torr, Ionization frequencies for solar cycle 21: Revised, *J. Geophys. Res.*, **90**, 6675, 1985.
- Torr, M. R., D. G. Torr, R. A. Ong, and H. E. Hinteregger, Ionization frequencies for major thermospheric constituents as a function of solar cycle 21, *Geophys. Res. Lett.*, **6**, 771, 1979.
- Torr, M. R., D. G. Torr, and H. E. Hinteregger, Solar flux variability in the Schumann-Runge continuum as a function of solar cycle 21, *J. Geophys. Res.*, **85**, 6063, 1980.
- Torr, M. R., D. G. Torr, and P. G. Richards, A mid-latitude interhemispheric model of the $O^+(^2P)$ airglow emission at 7320 Å, *Geophys. Res. Lett.*, **17**, 65, 1990.
- Walker, J. C. G., D. G. Torr, P. B. Hays, D. W. Rusch, K. Döcken, G. Victor, and M. Oppenheimer, Metastable 2P oxygen ions in the daytime thermosphere, *J. Geophys. Res.*, **80**, 1026, 1975.
- Young, E. R., P. G. Richards, and D. G. Torr, A flux preserving method of coupling first and second order equations to simulate the flow of plasma between the protonosphere and ionosphere, *J. Comput. Phys.*, **38**, 141, 1980a.
- Young, E. R., D. G. Torr, P. G. Richards, and A. F. Nagy, A computer simulation of the mid-latitude plasmasphere and ionosphere, *Planet. Space Sci.*, **28**, 881, 1980b.
- Zipl, E. C., The $O(^1S)$ state: Its quenching by O_2 and formation by dissociative recombination of vibrationally excited O_2^+ ions, *Geophys. Res. Lett.*, **6**, 881, 1979.
- P. G. Richards and D. G. Torr, University of Alabama in Huntsville, Huntsville, AL 35899.
- Marsha R. Torr, Space Sciences Laboratory, NASA Marshall Space Flight Center, Huntsville, AL 35812.
- S. P. Yung, Boeing Corporation, Huntsville, AL 35899.

(Received October 13, 1989;
revised March 19, 1990;
accepted April 10, 1990)

ORIGINAL PAGE IS
OF POOR QUALITY

A MIDLATITUDE INTERHEMISPHERIC MODEL OF THE $O^+(\text{}^2P)$ AIRGLOW EMISSION AT 7320 Å

Marsha R. Torr

Space Science Laboratory, Marshall Space Flight Center, Huntsville, Alabama

D. G. Torr and P. G. Richards

Center for Space Plasma and Aeronomy, The University of Alabama in Huntsville

Abstract. The results are reported of the first interhemispheric model of the 7320 Å airglow covering mid- and low latitudes, at all longitudes. A comprehensive model of the ionosphere and thermosphere is used to compute volume emission rates as a function of altitude, latitude, longitude, and local time. Selected results are shown here to illustrate the computational capability. In particular we discuss the diurnal and seasonal variability and interhemispheric coupling of conjugate photoelectrons. The model is particularly well suited for airglow studies, and provides a valuable tool for the comparison, interpretation, and planning of spectroscopic observations made from orbiting platforms for all significant thermospheric emissions.

Introduction

The $O^+(\text{}^2P)$ airglow emission at 7320 Å provides a means of determining the $O^+(\text{}^2P)$ concentration. Measurements of this emission can be used to determine the atomic oxygen concentration or the solar UV ionization frequency [Meriwether et al., 1978; Rusch et al., 1976]. The photochemistry of this species has been established largely on the basis of the comparison of steady-state altitude profile calculations with surface brightness measurements made from satellites [Walker et al., 1975; Rusch et al., 1977]. Observations of limb brightness are inverted to yield altitude profiles of volume emission rates. The principal sources and sinks of $O^+(\text{}^2P)$ have been discussed in detail by Torr and Torr [1982].

Over the years, we have developed a comprehensive model of the ionosphere, thermosphere, and plasmasphere. This model solves the coupled time-dependent energy, momentum, continuity, and photoelectron transport equations from 80 km in one hemisphere, along the field line, to 80 km in the conjugate hemisphere [Young et al., 1980]. The full interhemispheric capability allows for the proper treatment of thermal coupling [Richards and Torr, 1986] and conjugate photoelectrons [Richards and Torr, 1985], which is important in the calculation of airglow emissions. The concentrations of the major neutral species are provided as input from MSIS-86 [Hedin, 1987] to the model which then provides the minor and excited state species and ions [Torr, 1985]. The chemistry of all the emitting species is comprehensively included [Torr, 1985]. Ab initio calculations of the excitation and loss rates are performed for the metastable species [Torr and Torr, 1982] and the vibrational states of molecules and ions [Richards et al., 1986]. The concentrations of odd nitrogen species are also computed together with those of other minor constituents [Torr et al., 1980]. The photochemistry currently used in the model is that defined by Torr [1985] (Tables A-8 through A-12 and A-19 through A-21) with the updates, corrections, and additions summarized in Table 1.

The three-dimensional capability is achieved by running the code for approximately 100 magnetic flux tubes. Because the model is interhemispheric, solutions are obtained simultaneously for the conjugate hemisphere. This yields a total of approximately 200 grid points. The flux tubes are selected along various L-shells for $L \leq 5$ and the grid on which the code is run is shown in Figure 1 in geo-

graphic space. Because of the large computational requirements, the MSFC CRAY II computer is used. Results are output on a four-dimensional global grid, comprising latitude, longitude, altitude, and local time. Input parameters are date and solar and magnetic indices.

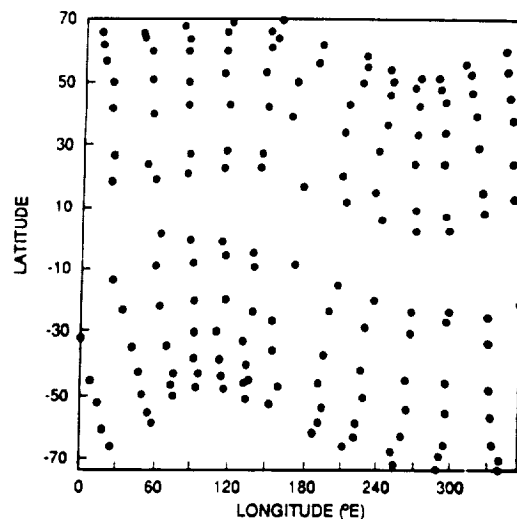


Fig. 1. Location of the conjugate points along $L = 1.08$ to $L = 5$ which mark the field lines along which the computations were made.

In this paper we have selected the 7320 Å emission to illustrate the global airglow modeling capability. The calculations have been made for conditions corresponding to November 28, 1983, for which the F10.7 cm flux was 89 and the Ap index was 23. Thus these calculations correspond to a period of relatively low solar activity.

Results

Figure 2 shows the results of the global solution of the 7320 Å emission. The volume emission rate at the peak of the layer is plotted as a function of altitude, latitude, and local time (longitude). This particular plot is shown for 00 UT, which is equivalent to placing midnight at 0° longitude, and noon at 180° longitude.

Several interesting features appear in the results shown in Figure 2. Summer is in the southern hemisphere and the more extensive solar illumination in this hemisphere is immediately evident in the longer duration of the daytime peak values (volume emission rates of the order of $10 \text{ photons} \cdot \text{cm}^{-3} \cdot \text{s}^{-1}$). The model results are valid for the latitudinal regime indicated by the envelope of the points shown in Figure 1. The interpolation routine tends to smear the high latitude boundary in Figure 2 by about 3°. Figure 3 shows the production and loss rate profiles for noon at southern midlatitudes. The peak production of $O^+(\text{}^2P)$ occurs near 170 km with photoionization the major source. The dominant loss mechanism above 280 km is radiation, and below 280 km it is collisional deactivation by N_2 . The combination of these processes results in the emission peak being formed at approximately 260 km.

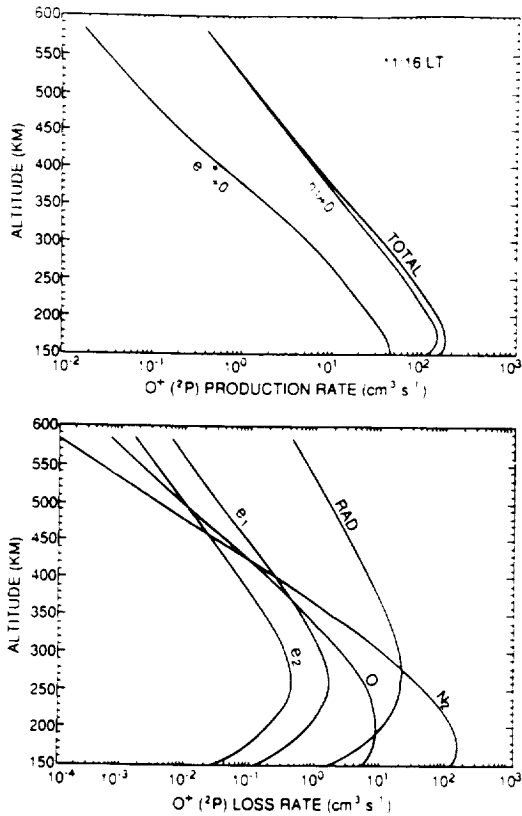


Fig. 3. Sources (a) and sinks (b) of $O^+(^2P)$ for the location corresponding to $48^\circ S$ at 11:16 LT in Figure 2. Sources are photoionization and photoelectron impact ionization. Sinks are radiation and quenching by O , N_2 , and electrons.

At twilight the situation changes rapidly. The photoionization peak rises rapidly in altitude and the production rate falls sharply. Figure 4 shows the production rates for $48^\circ S$ at 22:23 LT. At this time the solar zenith angle is 107° , so that the high altitudes are illuminated. There is a second peak at about 300 km due to transported local photoelectrons which are produced during the ionization process which created the upper peak. Radiative loss dominates most of the profile. At low latitudes at midnight, the peak production rate tends to zero at very high altitudes. When the production rate effectively drops to zero these values are omitted in Figure 2, so as not to obscure the main results.

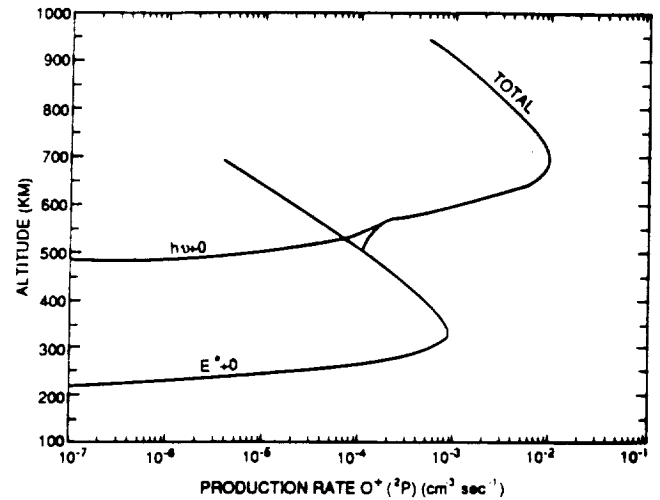


Fig. 4. Sources (a) and sinks (b) of $O^+(^2P)$ for the location corresponding to $48^\circ S$ at 22:23 LT in Figure 2.

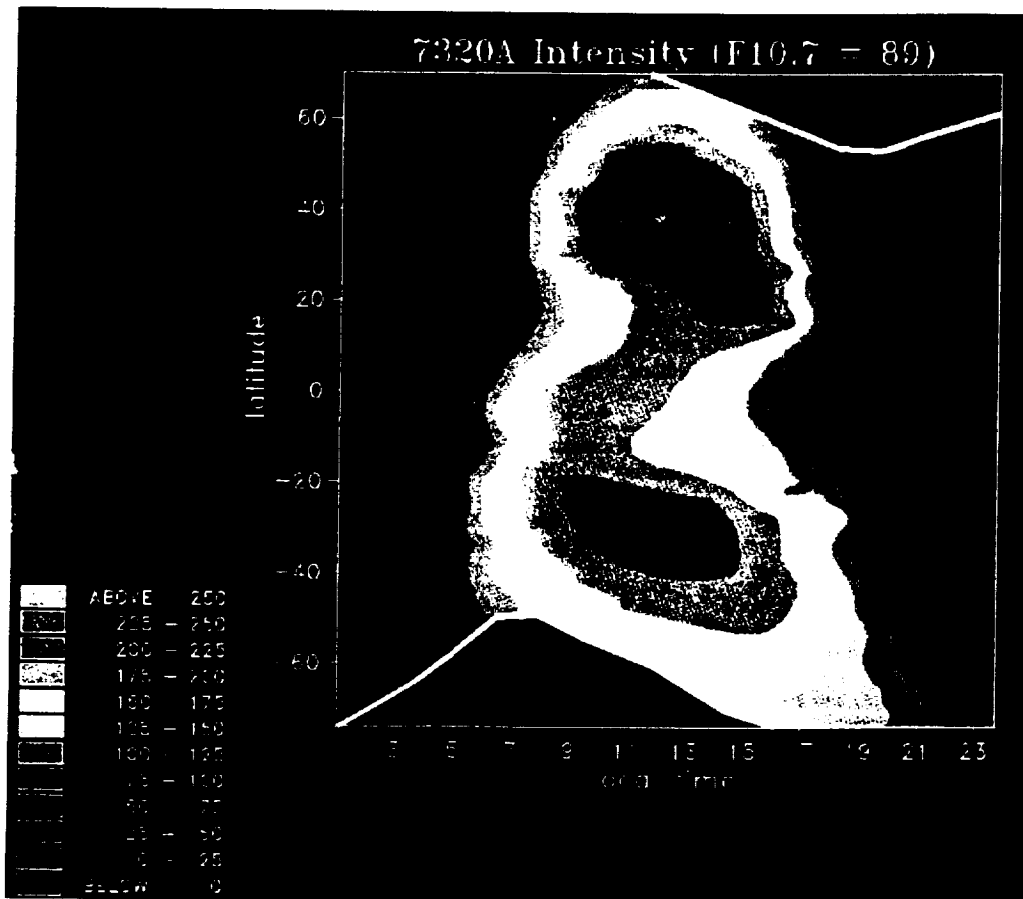


Fig. 5. Vertical column integrated surface brightness (in Rayleighs) for the same case shown in Figure 2.

In the winter (northern) hemisphere the twilights draw closer together but the photochemistry of the daytime and twilight 7320 Å emission is essentially the same as that described above. What is interesting to note here is that there is some production of $O^+(^2P)$ at high latitudes even at midnight. The source is impact ionization by photoelectrons from the sunlit conjugate hemisphere. The conjugate photoelectron source produces a column integrated surface brightness of 2 to 3 R of 7320 Å emission.

Figure 5 shows the global map of the 7320 Å intensity for the same case as Figure 2. This is what would be seen by an instrument looking straight down at the Earth for a fixed UT. The midday intensities in the winter hemisphere are slightly larger than those in the summer hemisphere. This is because the winter hemisphere is somewhat colder, and radiative loss dominates to a lower altitude.

Summary

We have reported the first results of a midlatitude interhemispheric-coupled model of the 7320 Å airglow. These results show the diurnal and seasonal variation for conditions representative of near solar minimum. The magnitude and extent of the conjugate photoelectron source is quantified, together with the sources and sinks at selected times. In another paper (Torr et al., 1989) we show further details of the longitudinal and solar cycle variations. This model allows three-dimensional maps of any airglow emission to be generated. Any line of sight geometry can be projected through these maps and the volume emission rate integrated along the viewing direction to enable comparisons with observation. A three-dimensional perspective of airglow emission rates or brightnesses is of relevance to the interpretation of measurements taken from an orbiting vehicle. A satellite flying in a circular orbit through the topology represented in Figure 2 would observe large variations in emission through the structured regions. Semi-global maps of the type produced here provide rapid insight into the sources of the variability.

Acknowledgments. This work was supported by NASA contract NAS8-37106 and NSF grants ATM-8713693 and ATM-8714461 to The University of Alabama in Huntsville. We thank So Po Yung for her assistance in running the code and generating the graphical displays.

References

- Abdou, W. A., D. G. Torr, P. G. Richards, M. R. Torr, and E. L. Breig, Results of a comprehensive study of the photochemistry of N_2^+ in the ionosphere, *J. Geophys. Res.*, **89**, 9069, 1984.
- Abreu, V. J., J. H. Yee, S. C. Solomon, and A. Dalgarno, The quenching rate of $O(^1D)$ by $O(^1P)$, *Planet. Space Sci.*, **11**, 1143, 1986.
- Banks, P. M., and G. Kockarts, *Aeronomy*, Academic Press, Inc., New York, 1973.
- Chen, A., R. Johnsen, and M. A. Biondi, Measurements of the $O^+ + N_2$ and $O^+ + O_2$ reaction rates from 300 to 900 K, *J. Chem. Phys.*, **69**, 2688, 1978.
- Fischer, C. F. and H. P. Saha, Multiconfiguration Hartree-Fock results with Briet-Pauli corrections for forbidden transitions in the $2P^+$ configuration, *Phys. Rev. A*, **28**, 3169, 1983.
- Hedin, A. H., MSIS-86 thermospheric model, *J. Geophys. Res.*, **92**, 4649, 1987.
- Kernahan, J. H., and H. L. Pang, Experimental determination of absolute A coefficients for "forbidden" atomic oxygen lines, *Can. J. Phys.*, **53**, 455, 1975.
- Lin, C. L., and F. Kaufman, Reactions of metastable nitrogen atoms, *J. Chem. Phys.*, **55**, 3760, 1971.
- Lindinger, W., F. C. Fehsenfeld, A. L. Schmeltekopf, and E. E. Ferguson, Temperature dependence of some ionospheric ion-neutral reactions from 300° to 900° K, *J. Geophys. Res.*, **79**, 4753, 1974.
- Meriwether, J. W., D. G. Torr, J. C. G. Walker, and A. O. Nier, The $O^+(^2P)$ emission at 7320 Å in twilight, *J. Geophys. Res.*, **83**, 3311, 1978.
- Piper, L. G., The excitation of $O(^1S)$ in the reaction between $N_2(A^3\Sigma_g^-)$ and $O(^1P)$, *J. Chem. Phys.*, **77**, 2373, 1982.
- Piper, L. G., G. E. Caledonia, and J. P. Kennealy, Rate constants for deactivation of $N_2(A)^v = 0,1$ by O_2 , *J. Chem. Phys.*, **74**, 2888, 1981.
- Queffelec, J. L., B. R. Rowe, M. Morlais, J. C. Gomet, and F. Vallee, The dissociative recombination of $N^+(^2P, v = 0,1)$ as a source of metastable atoms in planetary atmospheres, *Planet. Space Sci.*, **33**, 263, 1985.
- Richards, P. G., and D. G. Torr, The altitude variation of the ionospheric photoelectron flux: A comparison of theory and measurement, *J. Geophys. Res.*, **90**, 2877, 1985.
- Richards, P. G., and D. G. Torr, Thermal coupling of conjugate ionospheres and the tilt of the Earth's magnetic field, *J. Geophys. Res.*, **91**, 9017, 1986.
- Richards, P. G., D. G. Torr, and W. A. Abdou, Effects of vibrational enhancement of N_2 on the cooling rate of ionospheric thermal electrons, *J. Geophys. Res.*, **91**, 304, 1986.
- Rusch, D. W., D. G. Torr, P. B. Hays, M. R. Torr, and A. O. Nier, Determination of the $O^+(^2P)$ ionization frequency using satellite airglow and particle data and its implications on the EUV solar flux, *Geophys. Res. Lett.*, **3**, 537, 1976.
- Rusch, D. W., D. G. Torr, P. B. Hays, and J. C. G. Walker, The OII (7310–7330 Å) dayglow, *J. Geophys. Res.*, **82**, 719, 1977.
- Streit, G. E., C. J. Howard, O. L. Schmeltekopf, J. A. Davidson, and H. I. Schiff, Temperature dependence of $O(^1D)$ rate constants for reactions with O_2 , N_2 , CO_2 , O_3 , and H_2O , *J. Chem. Phys.*, **65**, 4761, 1976.
- Torr, D. G., The photochemistry of the upper atmosphere, in *The Photochemistry of Atmospheres*, ed., J. S. Levine, Academic Press, Inc., New York, pp. 165–278, 1985.
- Torr, D. G., M. R. Torr, W. B. Hanson, and J. H. Hoffman, Determination of the sources and sinks of N^+ ions in the thermosphere, *Geophys. Res. Lett.*, **6**, 573, 1979.
- Torr, Marsha R., and D. G. Torr, The role of metastable species in the thermosphere, *Rev. Geophys.*, **20**, 91, 1982.
- Torr, M. R., P. G. Richards, and D. G. Torr, A new determination of the ultraviolet heating efficiency of the thermosphere, *J. Geophys. Res.*, **85**, 6819, 1980.
- Torr, Marsha R., D. G. Torr, P. G. Richards, and S. P. Yung, Mid and low latitude model of thermospheric emissions: 1. $O^+(^2P)$ 7320 Å and $N_2(^2P)$ 3371 Å, *J. Geophys. Res.*, submitted, 1989.
- Walker, J. C. G., D. G. Torr, P. B. Hays, D. W. Rusch, K. Docken, G. Victor, and M. Oppenheimer, Metastable 2P oxygen ions in the daytime thermosphere, *J. Geophys. Res.*, **80**, 1026, 1975.
- Young, E. R., P. G. Richards, and D. G. Torr, A flux preserving method of coupling first and second order equations to simulate the flow of plasma between the protonosphere and the ionosphere, *J. Comp. Phys.*, **38**, 141, 1980.

P. G. Richards and D. G. Torr, Center for Space Plasma and Aeronomy, The University of Alabama in Huntsville, Huntsville, AL 35899.

M. R. Torr, Space Science Laboratory, Marshall Space Flight Center, Huntsville, AL 35812.

(Received June 27, 1989;
revised September 20, 1989;
accepted October 25, 1989)

APPENDIX E

PRELIMINARY INTERPRETATION OF THE VACUUM ULTRAVIOLET GLOW
OBSERVED ON SPACELAB 1 AND THE S3-4 SPACECRAFT

D. G. Torr^{1,2,5}, M. R. Torr³, J. W. Eun^{4,5},
P. G. Richards^{2,6} and T. D. Gordon⁷

1. Science and Engineering Associates, Inc.
500 Wynn Drive, Suite 304-D
Huntsville, Alabama 35816
2. Center for Space Plasma and Aeronomic Research
The University of Alabama in Huntsville
Huntsville, Alabama 35899
3. George C. Marshall Space Flight Center
Huntsville, Alabama 35812
4. Electronics and Telecommunications Research Institute
Daejeon, Korea
5. Physics Department
The University of Alabama in Huntsville
Huntsville, Alabama 35899
6. Computer Science Department
The University of Alabama in Huntsville
Huntsville, Alabama 35899
7. Science and Engineering Associates, Inc.
6535 S. Dayton Street, Suite 2100
Englewood, Colorado 80111

Submitted to Journal Geophysical Research
February 1990

ABSTRACT

Emissions in the vacuum ultraviolet of the Lyman-Birge-Hopfield (LBH) bands of N_2 have been observed at night from the S3-4 spacecraft and on Spacelab 1. Conway et al. have reported that the intensity of the LBH emission observed on S3-4 in the nadir varied approximately as $[N_2]^3$ with altitude, indicating a vehicle-atmosphere interaction. Observations were made at right angles to and into the velocity vector (ram) on Spacelab 1. The LBH intensity in the ram direction shows a factor of 3 to 4 decrease with respect to the 90° case which were taken two days earlier. The latter observations also suggest that the N_2 Vegard Kaplan bands occur simultaneously with the LBH. The Shuttle LBH intensities are brighter than those observed on S3-4 by several orders of magnitude. The following model is proposed to account for the above observations.

N_2 striking the vehicle surface is excited to vibrational levels near $v = 13$, allowing the exothermic surface reaction $N_2(X)^* + O \rightarrow NO + N$ to proceed rapidly, thereby producing N in abundance on the surface. Surface recombination of the atomic nitrogen leads to the formation of vibrationally excited and electronic states of N_2 including $N_2(A^3\Sigma^+_u)$ $v = 9$ to 13 (7.6 to 8.2 eV) which we shall designate $N_2(A)^*$. After thermal accommodation on the surface, the $N_2(A)^*$ desorbs into the local Shuttle environment. The long-lived metastable $N_2(A)^*$ component is then collisionally excited to the $a^1\Pi_g$ state which radiates in the LBH bands. In the ram direction there is a large enhancement in gas

concentration which results in attenuation of inflowing ambient N_2 and O and possible collisional deactivation of the $N_2(A)^*$ reducing the LBH intensity. For collisional excitation of $N_2(A)^*$ by ambient N_2 the net altitude dependence is $\sim [N_2]^3$ above 200 km altitude, changing to $\sim [N_2]^2[O]$ at lower altitudes in agreement with this behavior seen in the S3-4 data. The S3-4 spacecraft intensities are smaller than the shuttle intensities because of the smaller spacecraft size, and because of increased attenuation at the lower altitudes, and possibly due to different reaction rates for different surface materials.

1. INTRODUCTION

Conway et al. (1987) have reported observations of vehicle induced emission in the Lyman-Birge-Hopfield (LBH) bands of N_2 on the S3-4 spacecraft. The $N_2(a^1\Pi_g)$ state, from which the LBH bands arise, requires 8.6 eV for excitation of the $v = 0$ level and up to 9.75 eV for excitation of the higher lying levels below the dissociation threshold. There is no identified source for these bands in the non-auroral nightglow. Figure 1 reproduces the results of Conway et al. for the altitude variation of the integrated band intensities between 1400 and 1700 Å for nadir viewing. They report that the intensity varies with altitude as $[N_2]^3$ (or $[N_2]^2[O]$). They demonstrated that if the source mechanism is a three-stage excitation process involving the surface, then the expected LBH intensity would be ~16 orders of magnitude short of explaining the observed intensities.

Observations of vacuum ultraviolet (VUV) emissions were also made by Torr et al. (1985) on the Shuttle with the Imaging Spectrometric Observatory (ISO). Observations were made in the nadir and at 90° to the velocity vector at night, the ram at twilight, and the wake in daylight. For the nadir and 90° observations, the Shuttle was flying in an upside down airplane mode, i.e. with the nose (x axis) pointing into the velocity vector and the bay (-z axis) pointing in the nadir. Under these conditions the ISO views out along the -z axis when the scan mirrors are stowed out of the field of view. (The open mirrors are stowed $\geq 180^\circ$ to the closed position). The 90° to ram data were made looking under the -y wing using the scan mirrors

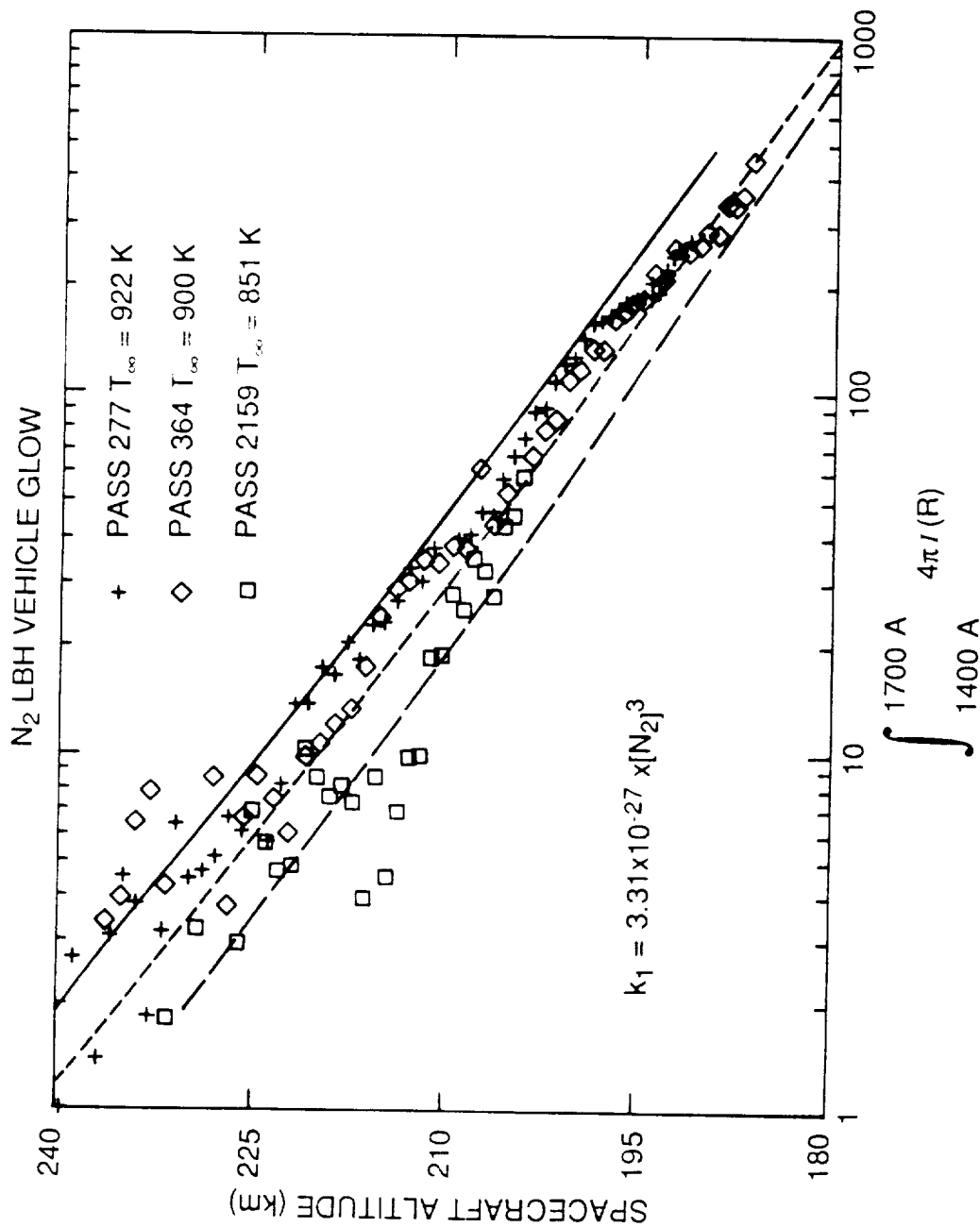


Figure 1: Observations of the N₂ LBH glow reported by Conway et al. (1987) for the S3-4 spacecraft.

to point the field-of-view of the instrument between 90 and 250 km tangent ray height. The ram data were taken with the scan mirrors stowed and the line-of-sight of the instrument pointing directly into ram, i.e. with the $-z$ axis of the Shuttle into ram.

Intensities were observed to be brightest at 90° to ram, decreasing in the ram and wake directions.

Figure 2 shows an example from Torr et al (1985) of the vacuum ultraviolet spectrum observed on Spacelab 1 at 250 km at night on December 5, 1983 at 90° to ram. Curve a shows the synthesized LBH band system for comparison. The maximum allowable intensities are constrained by the lower values observed at the shorter wavelength side. Thus, it is apparent that the VUV glow observed on Spacelab 1 cannot be attributed entirely to the LBH bands. Curve b shows the effect of including the Vegard Kaplan bands of N_2 , where the maximum allowable intensities are constrained by the lower values at both the short and long wavelength sides of the measured spectrum.

Torr et al. (1985) also identified the presence of strong NO γ bands at night at wavelengths longward of those shown in Figure 2. Figure 3 shows the effect of including the NO ϵ and δ bands which have transition characteristics which allow the system intensities to peak near 1650 Å. Thus it is evident that a plausible synthetic spectral fit can be achieved with a composite system of bands comprising N_2 LBH, VK and NO ϵ and δ bands.

It is clear that the spectral identification of the shuttle VUV emissions may not be unique, because there is no one-to-one match with

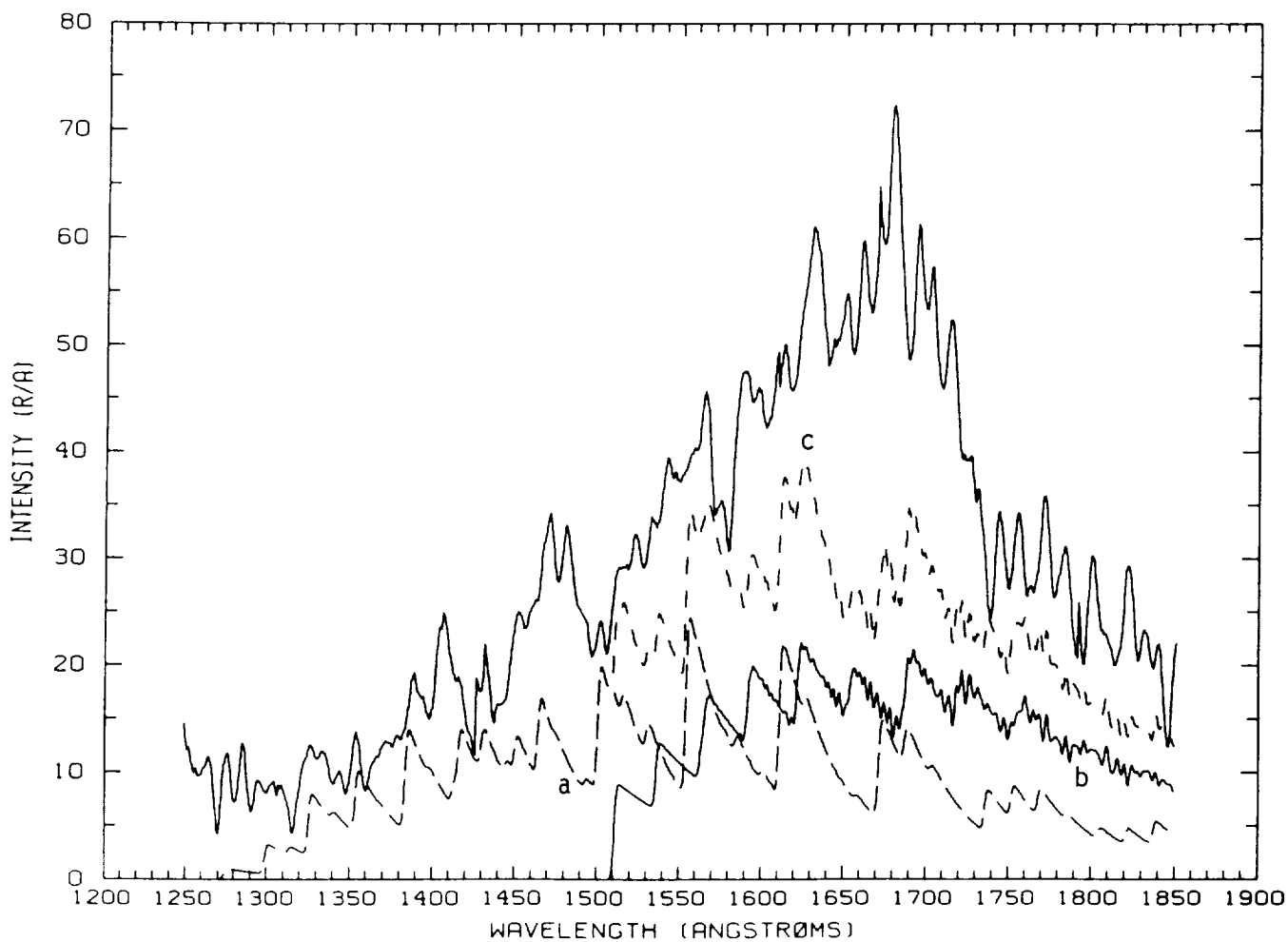


Figure 2: An example of the vacuum ultraviolet spectrum observed on Spacelab 1 at 250 km on December 5, 1983 at $\sim 130^\circ$ W, at 21 hours local time, solar zenith angle = 107° , at mid-latitudes. A mirror was used to view the 90° direction across the -Y wing of the Shuttle. Curves a and b are synthetic spectra of the N_2 Lyman-Birge-Hopfield and Vegard Kaplan band systems respectively. Curve c shows a composite spectrum of these two systems.

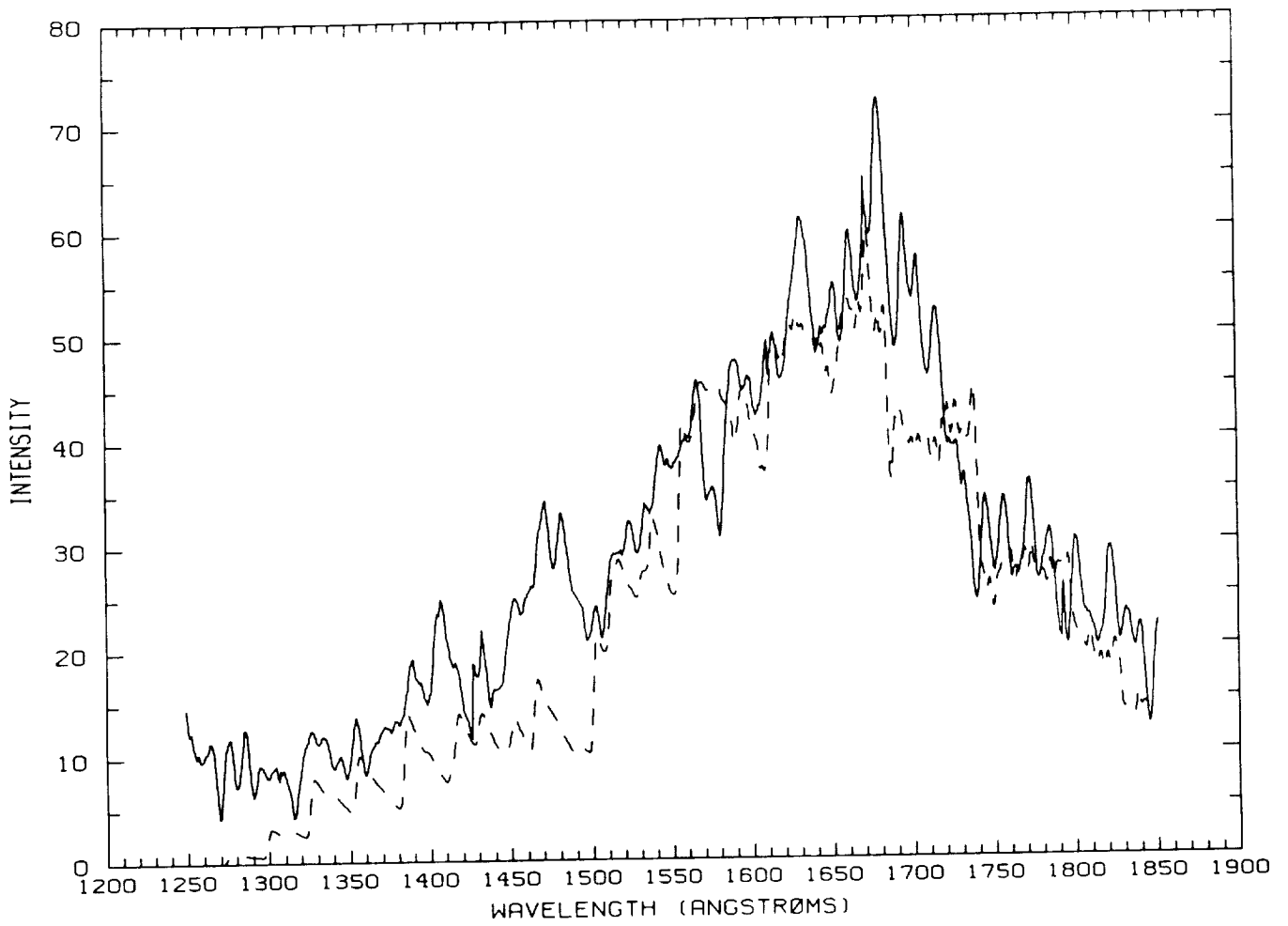


Figure 3: A comparison of the observations shown in Figure 2 with a composite synthetic spectrum comprising the N_2 LBH, VK and NO ϵ and δ bands.

discrete spectral features, but only with the general envelope of the observed VUV pseudo continuum glow. Thus the identification of the VK emission is not definitive. Detailed fitting may not be possible because it requires several grating steps to cover the full VUV range, and temporal variations which are severe may distort the relative emission ratios. Given the $[N_2]^3$ dependence of the glow indicated by the S3-4 data it is evident that relatively small changes in the N_2 concentration due to gravity waves for example, could cause significant changes in the VUV emission because of the strong non-linear dependence.

If the presence of the VK bands is accepted, one is led to the conclusion that there could be a significant far-field component to the glow. This conclusion is based on the fact that the ISO field of view was directed away from shuttle surfaces, and for the viewing geometry in question the instrument itself was shielded from direct interactions with the ram flux by the Spacelab 1 module and the aft bulkhead. Slanger (1986) has presented evidence which strongly suggests that shadowing of surfaces from exposure to ram significantly reduces visible surface glow brightness.

For comparison, Figure 4 shows the VUV emission observed in the ram direction at 250 km on December 7, 1983. The most striking feature of these data in comparison with that shown in Figures 2 and 3 is a reduction in intensity of the N_2 and NO bands by of a factor of 3 to 4.

Given the fact that the inferred intensities for the VK system

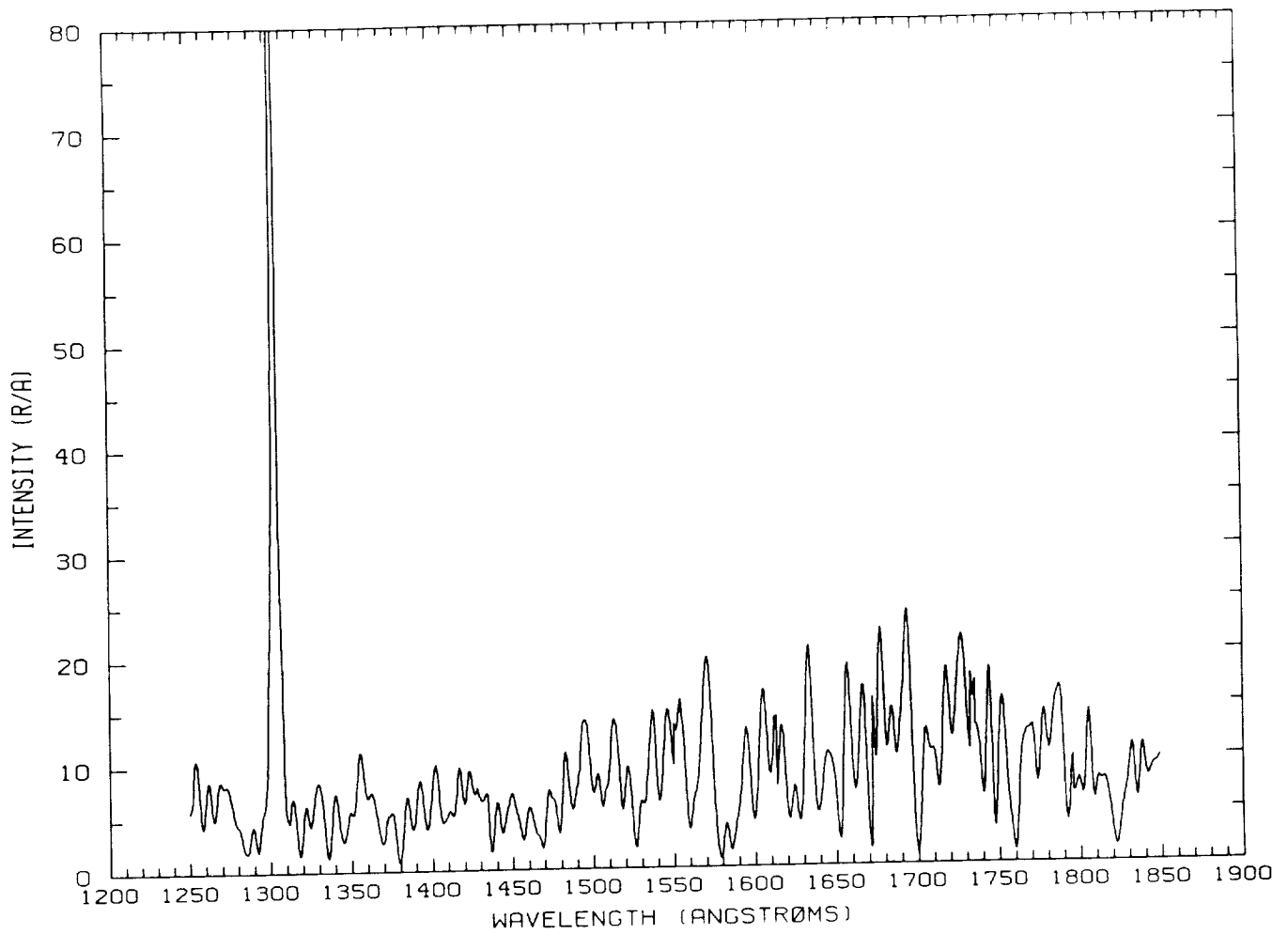
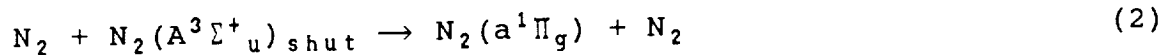
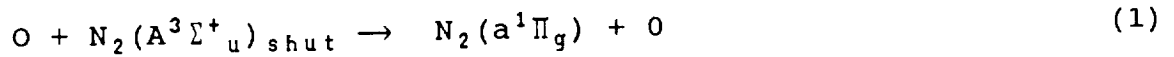


Figure 4: The ram VUV spectrum observed on Spacelab 1 on December 7. The spectra were taken under similar geophysical conditions to those shown in Figure 3, except that the local time was ~ 04 hours which corresponds to twilight conditions.

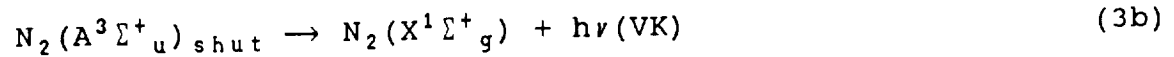
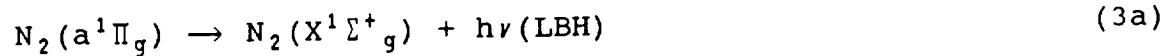
(~3kR) can be used to roughly obtain the column abundance of $N_2(A)^*$, which we find to be large ($\sim 6 \times 10^9 \text{ cm}^{-2}$), we investigate the plausibility of collisional excitation of desorbed $N_2(A)^*$ by the influx of ambient O and N_2 as a source of the LBH emission. We show that the apparent decrease in N_2 LBH (and VK) emission in the ram direction, may be due to the attenuation of the incident ambient flux of N_2 and O and quenching of $N_2(A)^*$ by O and N_2 re-emitted by the surface. The concentration of O and N_2 is believed to be significantly enhanced on the ram side of the Shuttle (Rantanen and Gordon (1987)). We consider only excitation of N_2 emissions in this paper, and will deal with the source of NO excitation in a future paper.

2. THE MODEL

We investigate the production of LBH emission via the reactions



followed by:



where $N_2(A^3\Sigma^+_u)_{\text{shut}}$ refers to metastable N_2 desorbed from the vehicle surface and the usual notation (O, N_2) refers to the ambient gases.

3. THE PROPOSED LBH GLOW MECHANISM

The desorbed vibrationally excited $N_2(A)^*$ internal energy peaks between 7.6 and 8.2 eV. Both S3-4 and Spacelab 1 observations indicate LBH emissions arising from $v' = 0$ to 6, that is from vibrational levels lying between about 8.6 and 9.7 eV. The mean relative energy in the center-of-mass system available for processes (1) and (2) is $\sim 3.9 \pm 1$ and $\sim 4.6 \pm 1$ eV respectively. Thus, both processes are energetically capable of exciting N_2 states above the $a^1\Pi_g$ state.

The volume emission rate for the LBH system, η , at a distance s from the surface is given by

$$\eta(s) = \sum \sigma_{jE} F_j(s) [N_2(A)^*]_s \quad (4)$$

where $F_j(s)$ represents the total incident flux of ambient neutral species j , σ_{jE} represents an excitation cross-section for collisions with the j^{th} particle species where $j = 0$ and 1 designates O and N_2 respectively, and $[N_2(A)^*]_s$ is the concentration of desorbed vibrationally excited $N_2(A)^*$ at a distance $s-s_0$ from the vehicle/instrument surface at s_0 . The total LBH irradiance is given by

$$I_{LBH} = \int_{s_0}^{\infty} \eta(s) ds = \int_{s_0}^{\infty} \{F(N_2)_s \sigma_{1E} + F(O)_s \sigma_{0E}\} [N_2(A)^*]_s ds \quad (5)$$

where σ_{1E} and σ_{0E} are cross-sections for collisional excitation of $N_2(A)^*$ to $N_2(a)$ by N_2 and O respectively. The flux $F(x)_s$ is given by

$$F(x)_s = F(x)_\infty e^{-\tau_{ax}} \quad \text{or} \quad F_j = F_{j\infty} e^{-\tau_{aj}} \quad (6)$$

where F_∞ refers to the unattenuated flux, x refers to O ($j = 0$) or N_2 ($j = 1$), and τ_{aj} represents the attenuation depth at a point along a given line-of-sight s defined by

$$\tau_{aj} = \int_s^\infty \sum_i \sigma_{ji} n_i(s) ds' \quad (7)$$

where s' is in a direction antiparallel to the velocity vector, σ_{ji} is the collision cross-section for species j and i and $n_i(s)$ is the induced gas concentration of the i^{th} constituent in the environment of the vehicle at distance s from the surface. Equation (6) is formulated under the assumption that after one collision, incident O and N_2 will no longer be capable of exciting $N_2(A)^*$ to the $a^1\Pi_g$ state. To evaluate the viability of the proposed excitation mechanism we first consider the case where the attenuation of the incident flux by the gases comprising the vehicle environment is negligible, i.e., where $\tau_{aj} \ll 1$. Under these conditions, (5) simplifies to

$$I_{LBH} = \sum_j F_{j\infty} \sigma_{jE} \int_{s_0}^{\infty} [N_2(A)^*] ds \quad (8)$$

$$= \sum F_{j\infty} \sigma_{jE} [N_2(A)^*]_{c01} \quad (9)$$

where $[N_2(A)^*]_{c01}$ is the column concentration of vibrationally excited $N_2(A)$, and subscript $j\infty$ refers to the unattenuated flux of the j^{th} species.

We use the Spacelab 1 measurements of the VUV VK band systems to evaluate $[N_2(A)^*]_{c01}$. Given that the LBH and VK nadir intensities are ~ 3.5 kR and 3 kR respectively and using the relationship

$$I = \sum A_i [X_i] \quad (10)$$

where I is the total intensity of a band system, A_i is the Einstein coefficient for all transitions from the i^{th} vibrational level of the emitting electronic state X , and $[X_i]$ is the concentration of the i^{th} vibrational level, we evaluate the total column abundance of $N_2(A)^*$ from the intensities for the VK system, assuming an average lifetime of 2 seconds based on the results of Shemansky et al. (1971) for low-lying vibrational levels. Thus, we find that

$$[N_2(A)^*]_{c01} \approx 6 \times 10^9 \text{ cm}^{-2} \quad (11)$$

We use (9) and (11) to estimate the collision excitation cross-section needed to account for the observed LBH emission.

$$\bar{\sigma}_E \geq \frac{I_{LBH}}{F_\infty [N_2(A)]_{col}} \quad (12)$$

Where $\bar{\sigma}_E$ is an intensity weighted cross-section, and F_∞ is the total ambient neutral flux. Using the MSIS model atmosphere (Hedin, 1987) for the Spacelab 1 conditions, i.e. November/December 1983 at 250 km, $\sum_j F_{j\infty} = 1.3 \times 10^{15} \text{ cm}^{-2} \text{ s}^{-1}$.

Thus,

$$\bar{\sigma}_E \geq \frac{5 \times 10^9}{1.3 \times 10^{15} \times 6 \times 10^9} = 4.5 \times 10^{-16} \text{ cm}^2$$

which does not appear to be unreasonable.

The obvious questions that arise are the following: 1) What is the source of the $N_2(A)$ molecules? 2) Why are the LBH and VK intensities weaker in the ram direction? 3) How does the $[N_2]^3$ (or $[N_2]^2[O]$) altitude dependence arise?

4. SOURCE OF THE $N_2(A)$ GLOW

In principle, there are several possible ways of generating electronically excited $N_2(A)$. However, all but the surface recombination of atomic nitrogen can be effectively eliminated by energy arguments (Kofsky, 1988). Surface catalyzed inverse predissociation of N_2 appears to be the only process capable of accounting for the highly efficient excitation of $N_2(A)$ in high vibrational levels. Reduction of available energy in the center of mass system of the reactants, and the fact that a significant fraction

of the kinetic energy must be shared with the surface eliminates the direct excitation of N_2 investigated by Conway et al. (1987) or impact dissociation of N_2 (suggested by Green, 1984) as sources of electronically excited N_2 or of atomic nitrogen. The available flux of ambient thermospheric nitrogen would require unrealistic efficiencies for N-N recombination.

Meyerott and Swenson (1990) have noted the importance of being able to account for the observed anomalous vibrational distribution of the LBH emission. They point out that direct recombination of N into the $a^1\Pi_g$ state via the $A^5\Sigma^+_g$ surface should result in predominant population of vibrational levels near $v = 5$ where the crossing of these states occur.

In order to provide a comparison with our model we briefly describe their approach. To explain the far-field vehicle glow they propose resonance fluorescence scattering of EUV photons which will give rise to $a^1\Pi_g$ by cascade from higher lying singlet Rydberg states of N_2 . To initially populate these singlet states they invoke a Rideal surface recombination mechanism in which one N is attached to the surface and the second is ambient atomic nitrogen. The relative kinetic energy of the latter provides the energy source needed to access the singlet Rydberg states. It is presumed that the transition probabilities from these states will be consistent with dominant cascade to the $v = 0$ and 1 levels of the $a^1\Pi_g$ state. Recombination can occur via either one or both of the $A^5\Sigma^+_g$ or $^7\Sigma^+_g$

surfaces.

Swenson and Meyerott (1988) have also proposed the gas phase reaction

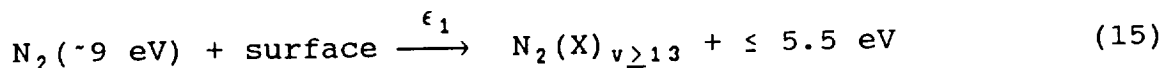


as the main source of surface N, and their calculations suggest that (13) could provide a sufficient source of N to account for the LBH glow observed on Spacelab 1 and the S3-4 satellite. Because the branching ratio from the singlet states to the ground state of N_2 is about 30 to 100 times larger than to the $a^1\Pi_g$, strong EUV emission is predicted together with the Herman Gaydon near UV bands associated with the cascade process.

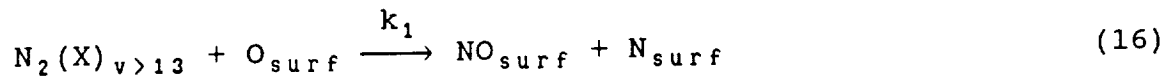
It should also be noted that the $^5\Sigma_g^+$ and $^7\Sigma_g^+$ paths require one more step than the $A^3\Sigma_u^+$ in the recombination process. In the case of direct recombination into $\text{N}_2(A)$, one would expect high lying vibrational levels to be populated, with possible partial surface induced vibrational relaxation. According to Green (1984) some fraction of the molecules will leave the surface in the $\text{N}_2(A)$ state. Currently it is believed that recombination should be preferred through the $^3\Sigma_u^+$ channel, because this state correlates directly with the ground state atoms, and it is thought that laboratory observations of emissions from singlet states are due to quenching of high lying vibrational levels of the $A^3\Sigma_u^+$ state (B. D. Green private communication, 1989).

As mentioned above, the $N_2(A)$ vibrational distribution observed on Spacelab 1 is constrained rather well by the envelope of the pseudo VUV continuum. The distribution required to fit the data shown in Figure 2 is given in Figure 5. These values show that the $N_2(A)$ must be populated predominantly in $v = 7$ to 13. Also measurements of $N_2(A)$ emissions from $v' = 0$ in the near UV preclude low lying vibrational levels as a possible precursor. Although collisional excitation of $N_2(A)$ ($v'' \gg 0$) to $a^1\Pi_g$ ($v' \gg 0$) is preferred from the Franck-Condon perspective, transitions which violate the Franck-Condon principal are not precluded for heavy particle collisions. Thus collisional excitation from high lying vibrational levels of $N_2(A)$ could populate low lying vibrational levels of $N_2(a)$.

As stated earlier, the only mechanism capable of producing $N_2(A)^*$ is surface catalyzed recombination of N. Thus, the next step is to identify a source of N that will yield the correct altitude dependence of the LBH emission. We consider the surface reaction of O and N_2^* where the following sources of O and N_2^* are proposed.



followed by the exothermic surface reactions



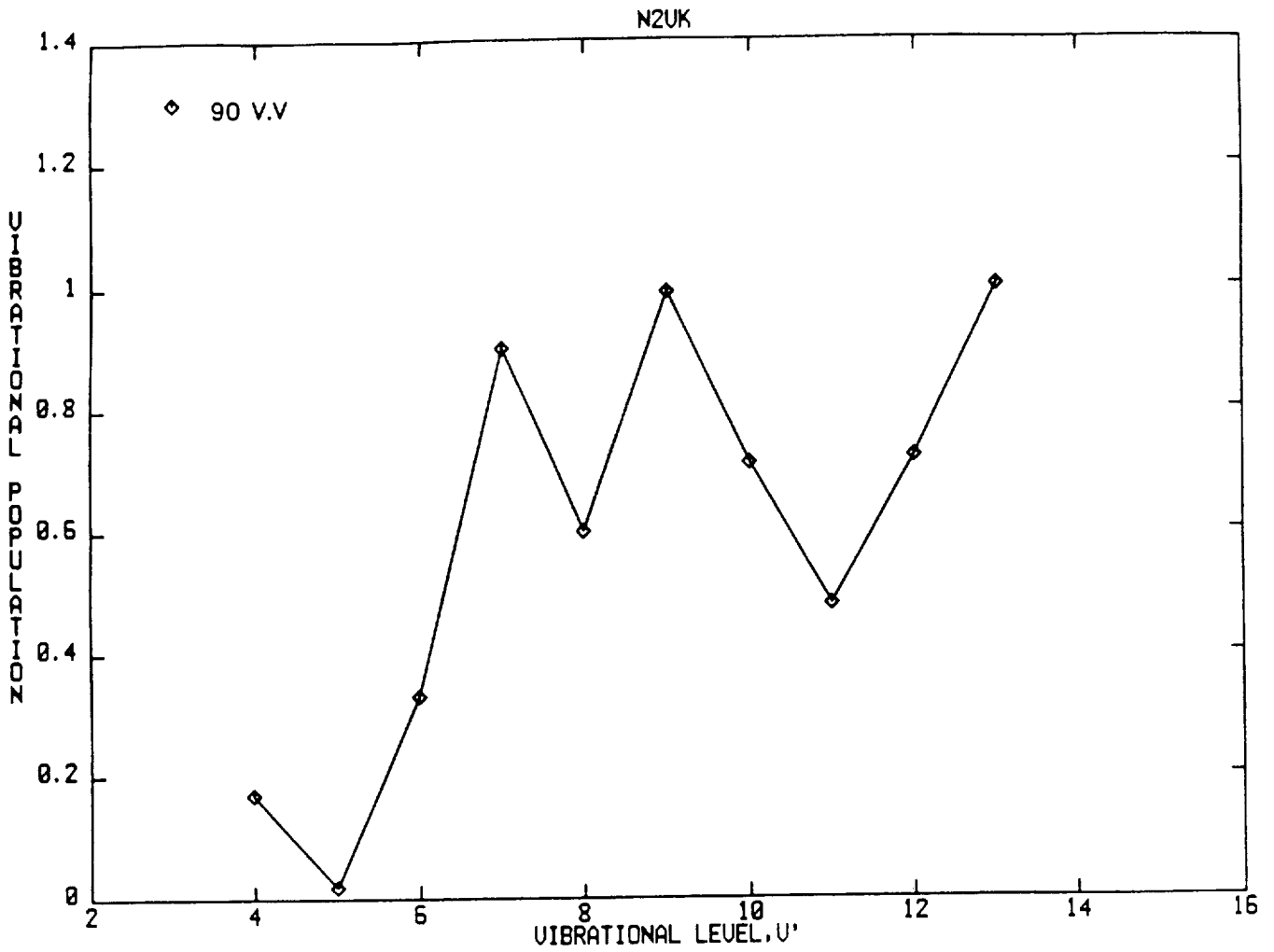
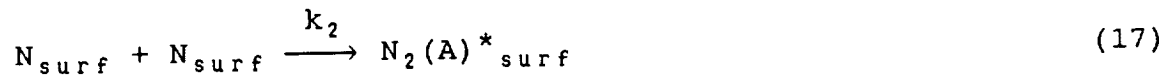


Figure 5: The $N_2(A^3\Sigma_u^+)$ vibrational distribution required to produce the synthetic spectral fit shown in Figure 2. The results are normalized to unity at the peak value.



followed by desorption of the $N_2(A)^*$ and Reactions (1) and (2). The species is probably long lived with a radiative lifetime of the order of a second.

In this model, the $N_2(A)^*$ could be formed on the surfaces of the shuttle wings. Then the desorbed $N_2(A)^*$ could flow through the field of view of the instrument when viewing over the wing in a direction 90° to ram.

Alternatively, it is possible that direct impact of surface O and N_2 by the flux of ambient O and N_2 could also result in the production of N and NO, however, this will result in a different scale height for the observed LBH and VK emissions.

Processes (15) and (16) need to be highly efficient in order to result in significant production of N. The ram flux of O will be the major source of surface O needed in (16). As pointed out by Kofsky (1988), the probability for N recombination ranges between 1 and 10^{-6} depending on surface material (Evenson and Burch, 1966; Halpern and Rosner, 1978, 1982).

The production of N, $Q(N)$ is given by

$$Q(N) = k_1 [N_2(X)^*_{surf}][O_{surf}] \quad (18)$$

It will become evident that the processes which control the

concentration of $N_2(X)^*_{surf}$ and O_{surf} will determine the dependence of the LBH glow on altitude. In Section 5 we demonstrate that an $[N_2]^3$ dependence requires that $[N_2(X)^*_{surf}]$ scale linearly with ambient $[N_2]$ and that $[O_{surf}]$ scale as $[O]^{1/2}$. Here we show that these dependences can be provided in terms of likely processes. If we consider the steady state production of $N_2(X)_{surf}$ by ambient inflow and loss by (16) and desorption, then we can write:

$$\epsilon_1 F(N_2) = (k_1 [O_{surf}] + J_1) [N_2(X)^*_{surf}] \quad (19)$$

where J_1 represents a desorption coefficient (units: s^{-1})

$$\text{If } J_1 \gg k_1 [O_{surf}],$$

(which is possible because of the internal excitation energy of $N_2(X)^*$ which may be available to overcome the surface bonding energy)

$$[N_2(X)^*_{surf}] = \frac{\epsilon_1 F(N_2)}{J_1} \quad (20)$$

which satisfies the required dependence. This condition implies that Reaction (16) is a major source of N but a minor loss for $N_2(X)^*$.

If we assume that the primary loss mechanism for surface O is recombination (at least for Shuttle surfaces), either directly or catalytically such that the net effective process can be represented by



and if the source of O_{surf} , $Q(O)$, is the flux of ambient O , $F(O)$, then,

$$[O_{surf}] = \left(\frac{\epsilon_0 F(O)}{k_3} \right)^{1/2} \quad (22)$$

The assumption that surface recombination of O is a major loss process for O is supported by the well known fact that satellite borne closed source mass spectrometer measurements of O yield both O and O_2 signatures when O is the dominant ambient species present. Thus the atomic nitrogen production rate (18) can be written as

$$Q(N) = k_1 \frac{\epsilon_1 F(N_2)}{J_1} \left(\frac{\epsilon_0 F(O)}{k_3} \right)^{1/2} = \alpha [N_2][O]^{1/2} \quad (23)$$

where

$$\alpha = \epsilon_1 \sqrt{\epsilon_0} k_1 v^{3/2} / (J_1 \sqrt{k_3}) e^{-(\tau_1 + \tau_0/2)} \quad (24)$$

$$\text{where } \tau_j = \int_s^\infty \sum_i \sigma_{ji} n_i ds' \quad (25)$$

from (7), and s' is always anti-parallel to the velocity vector. Subscript j refers to the incident particle and i to the attenuating constituents.

If Reaction (16) is sufficiently exothermic desorption of N may be the dominant loss process and assuming state steady state

conditions apply,

$$Q(N) = J_2[N]$$

Then

$$[N] = \frac{Q[N]}{J_2} \quad (26)$$

and the production rate of desorbed $N_2(A)$ from (17) is given by

$$F(N_2A)_{s_0} = \epsilon_2 k_2 \left(\frac{Q(N)}{J_2} \right)^2 = \gamma [N_2]^2 [O] e^{-(2\tau_1 + \tau_0)} \quad (27)$$

where, using (24)

$$\gamma = \epsilon_2 k_2 \left(\frac{\alpha}{J_2} \right)^2 = \frac{\epsilon_0 \epsilon_1^2 \epsilon_2 k_1^2 k_2 v^3}{J_1^2 J_2^2 k_3} \quad (28)$$

ϵ_2 is the yield of desorbed $N_2(A)^*$.

Once the $N_2(A)^*$ desorbs from the surface it may be quenched by constituents of the gas cloud. If quenching of $N_2(A)^*$ is negligible then the concentration of $N_2(A)^*$ close to the surface is given by:

$$[N_2(A)^*] \propto [N_2]^2 [O] e^{-(2\tau_1 + \tau_0)} \quad (29)$$

It is known from laboratory and aeronautical data that $N_2(A)_{v>0}$ is quenched by O, and O_2 (see Torr and Torr, 1982; Piper et al. 1981; Sharp and Torr, 1979). Quenching of $N_2(A)^*$ by NO is also rapid ($6 \times 10^{-11} \text{ cm}^3 \text{ s}^{-1}$). Thus, it is reasonable to assume that $N_2(A)_{v \geq 7}$ will be quenched both vibrationally and electronically. It is likely that

all major constituents of the vehicle gas cloud could quench the $N_2(A)^*$. The fraction of the $N_2(A)^*$ flux that is quenched will be determined by the relative magnitudes of the transport and chemical (or quenching) lifetimes.

Having computed the desorbed flux of $N_2(A)^*$ it remains only to include both the effects of transport and quenching on the distribution. To evaluate the effects of both transport and quenching on $N_2(A)^*$ we solve the continuity equation (and dropping the superscript *)

$$\frac{\partial(N_2A)}{\partial t} = q - \beta[N_2A] - \frac{1}{G} \nabla(\phi G) \quad (30)$$

where q = gas phase production rate of $N_2(A) = 0$

β = $N_2(A)$ loss frequency = $\sum k_i n_i + A_{vk}$

k_i = quenching rate coefficient for species $i = \sigma_i v_i$

A_{vk} = Einstein coefficient for the VK system

n_i = concentration of the i^{th} constituent of the vehicle gas "cloud"

ϕ = $v_T [N_2A] = N_2(A)$ flux at point s

v_T = is the bulk velocity of desorbed species which is characterized by the temperature of the surface at which desorption occurs

G = geometrical function which characterizes the effects of the radial outflow of gas

t = time

For purposes of deriving analytical solutions to (30) to facilitate discussion, we assume steady state conditions,

$$\beta[N_2A] = -\frac{1}{G}(G\nabla\phi + \phi\nabla G) \quad (31a)$$

or

$$-\beta/v_T = \frac{\nabla[N_2A]}{[N_2A]} + \frac{\nabla G}{G} \quad (31b)$$

If $\nabla = d/ds$ for a given viewing direction and

$$\beta = \sum_i k_i n_i + A_{VK} = v_T \sum_i \sigma_{qi} n_i + A_{VK} \equiv \bar{\sigma}_q n v_T + A_{VK} \quad (32)$$

where $\bar{\sigma}_q$ is a density weighted quenching cross-section

$$n = \sum_i n_i$$

Upon integrating (31) and adding attenuation of the incident flux to β we obtain

$$[N_2A]_s = \frac{[N_2A]_{s_0} G_0 e^{-(\tau_q + 2\tau_1 + \tau_0)}}{G_s} \quad (33)$$

$$\text{where } \tau_q = \int_{s_0}^s (\bar{\sigma}_q n + A_{VK}/v_T) ds \quad (34)$$

and τ_1 and τ_0 are the attenuation depths for the incident N_2 and 0 respectively.

5. THE ANGULAR DEPENDENCE OF THE SHUTTLE VUV GLOW

Using (34) in (4) the LBH volume emission rate is given by

$$\eta_{LBH}(s) = \frac{\sum_j \sigma_j E F_{j\infty} [N_2 A]_{s_0} G_0 e^{-\tau_j(s)}}{G_s} \quad (35)$$

which can be written as

$$\tau_j(s) = \int_s^\infty \sum_i \sigma_{ji} n_i ds' + \int_{s_0}^s \bar{\sigma}_q n ds + 2 \int_{s_0}^\infty \sum_i \sigma_{1i} n_i ds' + \int_{s_0}^\infty \sum_i \sigma_{0i} n_i ds' \quad (36)$$

$$\eta_{LBH}(s) = \frac{\sum_j \eta_j(s_0) G_0 e^{-\tau_j(s)}}{G_s} \quad (37)$$

The LBH integrated emission rate can be readily evaluated

$$I_{LBH} = \sum_j \eta_{0j}(s_0) G_0 \left(\frac{e^{-\tau_j(s)}}{G_s} \right)_{s_0}^\infty ds \quad (38)$$

where, as mentioned previously, s is along the line of sight, and s' is antiparallel to ram. The attenuation terms represent the following in order of appearance:

- 1) Attenuation of the incident ambient flux of O or N_2 ($j = 0$ or 1 respectively) between ∞ and point s

- 2) Quenching of $N_2(A)^*$ between the surface and s
- 3) Attenuation of the ambient N_2 flux to the surface which produces N_2 (vib.)
- 4) Attenuation of the ambient O flux to the surface which produces surface O.

In practice, (38) is evaluated numerically for any given viewing direction. However, since it is relatively straight forward to evaluate the case analytically for the line of sight directed into ram, and since this case is the most relevant for our discussion, we will utilize this case as a point of departure for further discussion.

First we define

$$\bar{\sigma}_j n = \sum_i \sigma_{ji} n_i \quad (39)$$

For ram viewing (36) then becomes:

$$\bar{\tau}_j(\text{ram}) = \bar{\sigma}_j \int_s^\infty n ds + \bar{\sigma}_q \int_{s_0}^s n ds + (2\bar{\sigma}_1 + \bar{\sigma}_0) \int_{s_0}^\infty n ds \quad (40)$$

i.e.

$$\bar{\tau}_j(\text{ram}) = \bar{\tau}_{aj}(s) + \bar{\tau}_a(s) + 2\bar{\tau}_1 + \bar{\tau}_0 \quad (41)$$

where $\int_{s_0}^\infty n ds = N$, the total ram column density of the vehicle gas cloud (42)

Thus (38) becomes

$$I_{LBH}(\text{ram}) = \sum_j \eta_{0j} G_0 \int_{s_0}^{\infty} \frac{e^{-\bar{\tau}_j(\text{ram})}}{G_s} ds \quad (43)$$

$$\text{where } \eta_{0j} = \eta_{0j}(s_0) = F_{j\infty} \sigma_{jE} [N_2 A]_{s_0} \quad (44)$$

$$\text{If } G_s = s^2 \text{ and } \bar{\sigma}_j \approx \bar{\sigma}_q \quad (45)$$

$$I_{LBH}(\text{ram}) = \sum_j \eta_{0j} s_0 e^{-\bar{\tau}_j(\text{ram})} \quad (46)$$

where s_0 is of the order of the vehicle dimensions (L), and

$$\bar{\tau}_j = \bar{\tau}_2 + \bar{\tau}_0 + 2\bar{\tau}_1 \text{ where } \bar{\tau}_2 = \bar{\tau}_{aj} + \bar{\tau}_q = \bar{\sigma}_{aj} \int_{s_0}^{\infty} nds \quad (47)$$

The attenuation depths for the incident O and N_2 fluxes depend critically on the surfaces underlying the line-of-sight of the instrument. For example, if the line-of-sight runs parallel and close to a large surface such as the Shuttle wing, the flux of desorbed $N_2(A)^*$ will be largest if the wing surface is normal to ram. However, this will also result in large values for all the attenuation depths, yielding a large value for $\bar{\tau}_j$. On the other hand, if the wing edge is directed into ram, as in the airplane mode, the flux of desorbed $N_2(A)^*$ and the attenuation factors $\bar{\tau}_{aj}$, $\bar{\tau}_0$ and $\bar{\tau}_1$ will be reduced roughly in proportion to the area exposed directly to ram. The attenuation of incident ambients will decrease as $\exp[-(\bar{\tau}_{aj} + \bar{\tau}_0 + 2\bar{\tau}_1)]$, that is

exponentially with respect to the decrease in the flux of $N_2(A)^*$. Similarly, when the line of sight is directed into ram, there is a large buildup of quenching/attenuating constituents which may cause the attenuation and quenching terms to overwhelm the enhancement in $N_2(A)^*$.

In what follows we report the results of a preliminary assessment of the magnitude of these effects for the databases discussed in the introduction.

From (38) we see that the angular dependence of the emission will depend on the attenuation depth $\bar{\tau}_j(\theta)$ which varies as the column concentration N of desorbed species (see (40) for example) which can be obtained via detailed modeling of the vehicle "gas cloud" dynamics, which is currently underway and will be reported at a later time.

In order to estimate values of $\bar{\tau}_j(\theta)$ for $\theta = 0$ and 90° we use the calculations of Rantanen and Gordon (1987). Their results typically indicate a decrease in column density from ram to 90° (for the vehicles studied) of about an order of magnitude.

If $\bar{\sigma}_{a0} = \bar{\sigma}_{a1} = \bar{\sigma}_0 = \bar{\sigma}_1 = \bar{\sigma}_q \approx 2.5 \times 10^{-15} \text{ cm}^2$ for example, the $N_2(A)$ quenching rate coefficient by N_2 is given by $k_{N_2} \approx v_T \bar{\sigma}_A \approx 4 \times 10^4 \times 2.5 \times 10^{-15} = 1 \times 10^{-10} \text{ cm}^3 \text{ s}^{-1}$ which may not be unreasonable for high lying vibrational levels.

Thus $\bar{\tau}_{j(\text{ram})} \approx 10^{-14} N = 1.2$ and the column density of the gas cloud needed to account for the attenuation of the ram flux is $1.2 \times 10^{14} \text{ cm}^{-2}$. If $L \approx 30\text{m}$, (see(46)) the near surface gas density is $4 \times 10^{10} \text{ cm}^{-3}$ which is reasonable and corresponds to a ram enhancement of a

factor of 27.

(Note the Rantanen and Gordon (1987) ISEM model predicts a non-linear increase in gas density with a few meters scale length near the surface, which can severely affect the attenuation of molecules en route to the surface.)

Table 1 provides a summary list of approximate numerical values required for relevant parameters if the proposed model is to be viable.

6. ALTITUDE DEPENDENCE OF THE S3-4 GLOW

ANALYTICAL FORMULATION

Differentiating (46) with respect to altitude h , for a single species and simplifying notation, we obtain

$$\frac{dI}{dh} = \frac{dI_0}{dh} e^{-\tau} - I_0 e^{-\tau} \frac{d\tau}{dh} \quad (48)$$

where $I_0 = \eta_0 L$, the unattenuated LBH intensity from which we deduce the scale height H for the LBH emissions, namely,

$$\frac{-1}{H} = \frac{1}{I} \frac{dI}{dh} = \frac{1}{I_0} \frac{dI_0}{dh} - \frac{d\tau}{dh} \quad (49)$$

i.e.

$$\frac{1}{H} = \frac{1}{H_0} + \frac{1}{H_\tau} \quad (50)$$

where H_0 is the scale height associated with η_0 defined by (51)

TABLE 1

SPACELAB 1 PARAMETERS

90° DATA

$$\left. \begin{array}{l} F(N_2) = 4.5 \times 10^{14} \text{ cm}^{-2}\text{s}^{-1} \\ F(O) = 8.5 \times 10^{14} \text{ cm}^{-2}\text{s}^{-1} \end{array} \right\} \begin{array}{l} \text{MSIS 1986} \\ \text{AT} \\ \text{250 km} \end{array}$$

$$[N_2A]_{c01}^* = 6 \times 10^9 \text{ cm}^{-2} \text{ (measured)}$$

$$F(N_2A) = 8.7 \times 10^{10} \text{ cm}^{-2}\text{s}^{-1}$$

$$N_2(A)/N_2 = 1.9 \times 10^{-4}$$

$$N_2(X) \nu \geq 13/N_2 = 0.08 \text{ ASSUMED}$$

$$N/N_2^* = 0.1 \text{ ASSUMED}$$

$$N_2(A)/N \text{ RECOMB.} = 0.02$$

$$N_2(a)/N_2(A) = 0.04$$

$$\text{LBH PHOTONS}/N_2 = 7.6 \times 10^{-6}$$

$$\text{VK PHOTONS}/N_2 = 6.6 \times 10^{-6}$$

From (35) and (29)

$$\eta_0 \propto [N_2]^2 [O] n_j \quad (n_j = [O] \text{ or } [N_2]) \quad (51)$$

Thus

$$\frac{1}{H_0} = \frac{3}{H_{N_2}} + \frac{1}{H_{Ox}} \quad \text{for } n_j = [N_2] \quad (52a)$$

and

$$\frac{1}{H_0} = \frac{2}{H_{N_2}} + \frac{2}{H_{Ox}} \quad \text{for } n_j = [O] \quad (52b)$$

where H_{N_2} and H_{Ox} are the scale heights of atmospheric N_2 and O respectively. We now evaluate H_T .

From (40) and (41) we approximate τ_j by

$$\tau = \bar{\sigma} \int_{S_0}^{\infty} n ds = \bar{\sigma} n_0 L \quad (53)$$

and

$$\frac{d\tau}{dh} = \frac{\sigma L dn_0}{dh} \quad (54)$$

where

$$n_0 = \frac{f n_r T_r e^{-z_n}}{T} \quad (55)$$

$$z_n = \int_{h_r}^h \frac{dh}{H_n} \quad (56)$$

TABLE 2

Height Dependence for N₂ Collisions (Reaction 2)

Ht (km)	$[O]$ (cm ⁻³)	$[N_2]$ (cm ⁻³)	α_0	$\frac{n}{1-\alpha_0}$	α_1	$\frac{m}{3-\alpha_1}$	LBH
							ALT DEPENDENCE $[N_2]^m [O]^n$
180	5.50x10 ⁹	5.60x10 ⁹	1.10	-0.10	1.12	1.9	$[N_2]^{1.9} [O]^{-0.1}$
190	4.34x10 ⁹	3.70x10 ⁹	0.87	0.13	0.74	2.3	$[N_2]^{2.3} [O]^{0.1}$
200	3.40x10 ⁹	2.50x10 ⁹	0.68	0.32	0.50	2.5	$[N_2]^{2.5} [O]^{0.3}$
220	2.20x10 ⁹	1.20x10 ⁹	0.44	0.56	0.24	2.8	$[N_2]^{2.8} [O]^{0.6}$
240	1.50x10 ⁹	6.00x10 ⁸	0.30	0.70	0.12	2.9	$[N_2]^{2.9} [O]^{0.7}$

Height Dependence for O Collisions (Reaction 1)

Ht	$[N_2]^m [O]^n$
180	$[N_2]^{0.9} [O]^{0.9}$
190	$[N_2]^{1.3} [O]^{1.1}$
200	$[N_2]^{1.5} [O]^{1.3}$
220	$[N_2]^{1.8} [O]^{1.6}$
240	$[N_2]^{1.9} [O]^{1.7}$

n_r = the total ambient density at reference height h_r

H_n = the mean density weighted scale height of the ambient gas

T = atmospheric temperature

f = ram density enhancement factor at s_0

We assume that the atmosphere is isothermal (i.e. $T = T_r$) and obtain

$$\frac{1}{H_r} = \frac{d\tau}{dh} = \frac{-f\bar{\sigma}Ln_0 dz_r}{dh} \quad (57)$$

$$= \frac{-f\bar{\sigma}Ln_0}{H_n} \quad (58)$$

From Rantanen and Gordon (1987) for $L \approx 6\text{m}$ (assumed for the S3-4 spacecraft), $f \approx 30$.

$$\text{Recall } \bar{\sigma} = \sum_i \sigma_i \approx 10^{-14} \text{ cm}^2 \quad (59)$$

Thus $f\bar{\sigma}L \approx 2 \times 10^{-10} \text{ cm}^3$ for the S3-4 spacecraft.

Table 2 gives average concentrations for O and N_2 from MSIS 86 as a function of altitude for the S3-4 spacecraft.

Equation (57) can be written in terms of the individual number densities of O and N_2 , i.e.

$$\frac{1}{H_r} = -f\bar{\sigma}L \left(\frac{[O]}{H_{Ox}} + \frac{[N_2]}{H_{n2}} \right) \quad (60)$$

$$= - \frac{\alpha_0}{H_{Ox}} - \frac{\alpha_1}{H_{N_2}} \quad (61)$$

Using (61) with (52) in (50)

$$\frac{1}{H} = \frac{(3 - \alpha_1)}{H_{N_2}} + \frac{(1 - \alpha_0)}{H_{Ox}} \quad (62)$$

where $\alpha_0 = f\bar{\sigma}L[O]$

$\alpha_1 = f\bar{\sigma}L[N_2]$

Equation (62) allows the altitude dependence of the LBH glow to be expressed in the form

$$I_{LBH} [N_2]^m [O]^n$$

where

$$m = 3 - \alpha_1 \text{ and } n = 1 - \alpha_0$$

Table 2 also lists values for α_0 , α_1 , m and n as a function of height for the S3-4 spacecraft. Figure 6 shows a comparison of the intensity of the computed LBH emission compared with the S3-4 observations. Here the intensities have been scaled to the measurements at ~200 km, in order to evaluate the altitude dependence predicted by the model, which is reasonably good. If the quantity $f\bar{\sigma}L$ has been overestimated, i.e. α_0 and α_1 are too large, then the calculated scale height will approach the high altitude limit of $[N_2]^3[O]$ more rapidly than observed. If on the other hand α_0 and α_1 have been underestimated, then there would be indications of a more

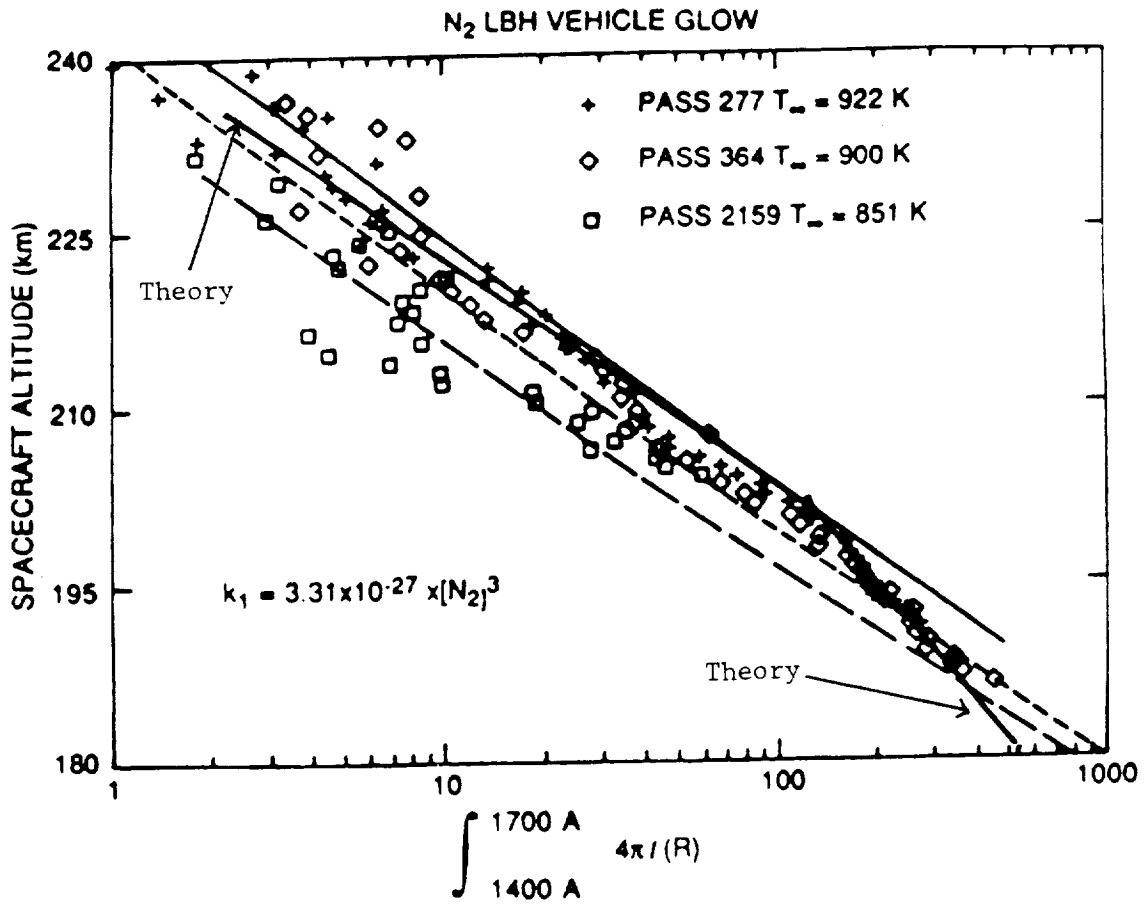


Figure 6: Comparison of estimated theoretical intensities based on the model results with the S3-4 observations of LBH glow as a function of altitude.

rapid increase in scale height below ~200 km, which would ultimately lead to the formation of a peak in glow brightness, because of the effects of increased attenuation.

It should be noted that these calculations do not take into account possible surface saturation effects. This will be done during the next phase of the work when the emission will be comprehensively numerically modeled.

7. SURFACE GENERATED LBH GLOW

Equation (17), namely



also allows for the direct production of $N_2(a^1\Pi_g)$ on the surface. The radiative lifetime for the $a^1\Pi_g$ state is ~100 μs which yields an e folding distance of 4.4 cm, which would not be observable by the ISO, but could be the mechanism responsible for the S3-4 glow. The scale height dependence of the glow is then given by (27) as modified for $N_2(a)$, namely

$$F(N_2 a)_{s_0} = \epsilon_3 k_2 (Q(N)/J_2)^2 = \gamma_a [N_2]^2 [O] e^{-(2\tau_1 + \tau_0)} \quad (64)$$

where

$$\gamma_a = \frac{\gamma \epsilon_3}{\epsilon_2} \quad (65)$$

ϵ_3 = efficiency for the production of $N_2(a^1\Pi_g)$ by (17)

and

$$\eta_{LBH} = \frac{\gamma_a [N_2]^2 [O] e^{-(2\tau_1 + \tau_0)}}{V_T} \quad (66)$$

Thus, the LBH glow will vary as $[N_2]^2 [O]$ at heights when attenuation of the incident O and N_2 ambient flux is negligible, changing to a larger scale height when attenuation becomes significant at lower altitudes, which is also qualitatively consistent with the S3-4 observations shown in Figure 1. It is possible that surface materials on S3-4 result in negligible production of $N_2(A)$ and with a small production of $N_2(a)$ accounting for the lower intensities than those observed on Spacelab 1.

CONCLUSIONS

Observations of vacuum ultraviolet emissions (VUV) made by the Imaging Spectrometric Observatory (ISO) on Spacelab 1 in 1983 and the S3-4 spacecraft are interpreted in the light of the following proposed model. Key features of the observations include a decrease in VUV emissions in the ram direction on Spacelab 1 compared to 90° to ram, and an $[N_2]^3$ altitude dependence on S3-4.

It is argued that since the ISO optical surfaces were shielded from the direct ambient neutral flux, the observed emissions must be of far-field origin. The Spacelab 1 observations could be synthetically fitted with the following bands: N_2 LBH and Vegard Kaplan, $NO \epsilon$ and δ . Because the LBH radiative lifetime is short ($\sim 100 \mu s$) and because of energy considerations, it appears that collisional excitation by the inflowing ambient N_2 or O of a long lived

excited state of N_2 to the $a^1\Pi_g$ state is needed to account for the LBH component of the glow. The metastable $N_2(A^3\Sigma^+_u)$ species not only meets this need, but it also accounts for the presence of the inferred VK bands. Interpretation of the NO emissions is deferred for a later paper. Based on the measured LBH and VK intensities, the cross-section for excitation of $N_2(A)$ to $N_2(a)$ is estimated to be $\sim 4.5 \times 10^{-16} \text{ cm}^2$.

A mechanism is proposed for the surface production of $N_2(A)$ by inverse predissociation of surface N. To provide an adequate source of N which yields the correct altitude dependence observed on S3-4 it is suggested that vibrationally excited N_2 recombines on the surface with O yielding NO and N as a product. The vibrational excitation which is needed to render the reaction of N_2 with O exothermic is generated by the impact of N_2 with the surface. The $N_2(A)$ formed on the surface then desorbs into the cloud surrounding the vehicle. The $N_2(A)$ flux is estimated to be $\sim 10^{11} \text{ cm}^{-2} \text{ s}^{-1}$ for the Spacelab 1 conditions.

To explain the angular dependence of the glow observed on Spacelab 1, it is argued that attenuation of the ambient flux of N_2 and O through the gas cloud plays a significant role. First, the N_2 and O that must reach the surface to produce surface N is attenuated, and the attenuation of each of these streams enters multiplicatively into the surface production of $N_2(A)$. Second, the $N_2(A)$ in the gas cloud may be quenched. Third, the incident N_2 and O impacting the $N_2(A)$ in the gas cloud is also attenuated. The net result is an accumulation of

several attenuating terms which become significant in determining the angular dependence of the glow. When the Shuttle flies with large surface areas such as the wings facing into the ram direction, there is a large buildup in the concentration of desorbed gases around the vehicle, which could result in significant attenuation. When the Shuttle flies in an airplane mode, there is an exponential reduction in attenuation (~an order of magnitude).

On Spacelab 1, the ISO instrument viewed directly out of the bay when the -z axis was directed into ram, and over the -y wing when the shuttle flew in the airplane mode. The larger intensities observed in the latter case are consistent with the exponential decrease in attenuation resulting in larger intensities at 90° than in the ram direction.

This model was also applied to an analysis of the S3-4 data which covered an altitude range from 180 to 240 km. It is demonstrated that at high altitudes, when attenuation is less significant, the altitude dependence of the LBH glow reduces to $[N_2]^3[O]$ or $N_2^2[O]^2$, and at low altitudes this changes to an $[N_2]$ or $[N_2][O]$ scale height depending on whether excitation of the $a^1\Pi_g$ state is by N_2 or O collisions respectively. A simple model calculation, with theoretical intensities normalized to the S3-4 observations at 200km, yields reasonably good agreement for the variation of the LBH glow with altitude.

ACKNOWLEDGEMENTS

This work was supported under NASA grant NAGW-922 to the

University of Alabama in Huntsville.

REFERENCES

- Conway, R. R., R. R. Meier, D. F. Strobel, and R. E. Huffman, The Far Ultraviolet Vehicle Glow of the S3-4 Satellite, Geophys. Res. Lett., in press, 1987.
- Evenson, K. M., and D. S. Burch, Atomic-nitrogen Recombination, J. Chem. Phys., 45, 2450-2457, 1966.
- Green, B. D., Atomic Recombination into Excited Molecular States - A Possible Mechanism for Shuttle Glow, Geophys. Res. Lett., 11, 576, 1984.
- Green, B. D., Private Communication, 1989.
- Halpern, B., and D. E. Rosner, Chemical Energy Accomodation at Catalyst Surfaces, J. Chem. Soc. Faraday Trans. I., 74, 1983-1903, 1978.
- Halpern, B., and D. E. Rosner, Incomplete Energy Accomodations in Surface-catalyzed Reactions, in Heterogeneous Atmospheric Chemistry - AGU Geophysical Monograph Series, 26, 167, 1982.
- Hedin, A. E., MSIS-86 Thermosphere Model, J. Geophys. Res., 92, 4649, 1987.
- Kofsky, I. L., Excitation of N₂ Lyman-Birge-Hopfield Bands Emission by Low Earth Orbiting Spacecraft, Geophys. Res. Lett., February 1988.
- Meyerott, R. E. and G. R. Swenson, A Surface Chemistry Model for the Production of N₂ LBH Spacecraft Glow, in press, Planet. Space Sci., 1990.
- Piper, L. G., G. E. Caledonia, and J. P. Kennealy, Rate Constants for Deactivation of N₂(A)v' = 0, 1 by O₂, J. Chem. Phys., 74, 2888, 1981.
- Rantanen, R. O. and T. D. Gordon, Contaminant Buildup on Ram-Facing Spacecraft Surfaces, SPIE, Paper 777-04, May 1987.
- Sharp, W. E. and D. G. Torr, Determination of the Auroral O(¹S) Production Sources from Coordinated Rocket and Satellite Measurements, J. Geophys. Res., 84, 5345, 1979.
- Shemansky, D. E., E. C. Zipf, and T. M. Donahue, Deactivation of N₂A³Σ_u⁺ Molecules in the Aurora, Planet. Space Sci., 19,

1669, 1971.

Slanger, T. G., Deductions from Space Shuttle Glow Photographs, Geophys. Res. Lett., 13, 431, 1986.

Swenson, G. R. and R. E. Meyerott, Spacecraft Ram Cloud Atom Exchange and N₂ LBH Glow, Geophys. Res. Lett., 15, 245, 1988.

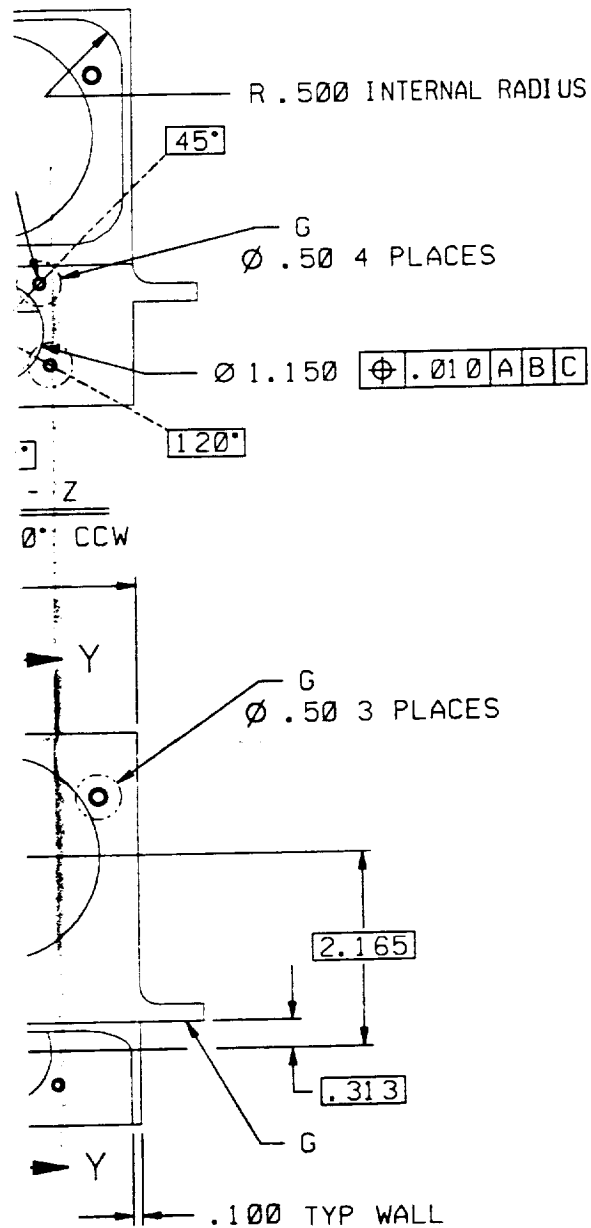
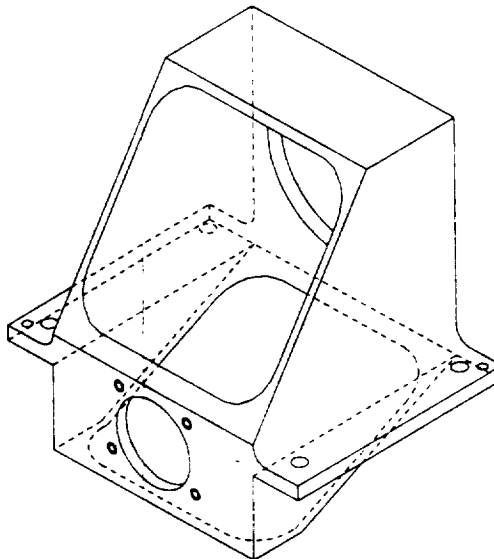
Torr, M. R. and D. G. Torr, The Role of Metastable Species in the Thermosphere, Rev. of Geophys., 20, 91, 1982.

Torr, M. R., D. G. Torr, and J. W. Eun, A Spectral Search for Lyman-Birge-Hopfield Band Nightglow from Spacelab 1, J. Geophys. Res., 90, 4427, 1985.

PREPARE HOLE AND INSTALL HELI-COIL INSERT
 #4-40 X 1.00 LONG) PER MS33537.
 A \varnothing 1.500 BC 4 PLACES AS SHOWN

DASHI ZONE I LTR		REVISIONS	DATE	APPROVED
		DESCRIPTION		

FOLDOUT FRAME



- 5.0 FINISH: CHEMICAL FILM PER MIL-C-5541 CLASS 3.
- 5.1 PAINT FLAT BLACK PER SR 679-1074 EXCEPT SURFACES MARKED G. OMIT PAINT FROM ALL HOLES.
- 4.0 STRESS RELIEVE PER SR0842.
 - 4.1 ROUGH MACHINE TO WITHIN .050 OF FINISHED SURFACE.
 - 4.2 STRESS RELIEVE PER SR0842 PAR 3.1.5B
 - 4.3 SEMI-FINAL MACHINE TO WITHIN .005 OF FINISHED SURFACE.
 - 4.4 TEMPERATURE CYCLE PER SR0842 PAR 3.1.5D.
 - 4.5 FINISH MACHINE.
3. ALL DIMENSIONS APPLY AT 68°F (20°C).
2. PIECEMARK PART NO., (TAG OR BAG), PER SG0211, METHOD 4.
1. WORKMANSHIP PER SG0075.

ALL HELI-COIL INSERT
 X 1.00 LONG) PER MS33537.
 SPACES EQUALLY SPACED

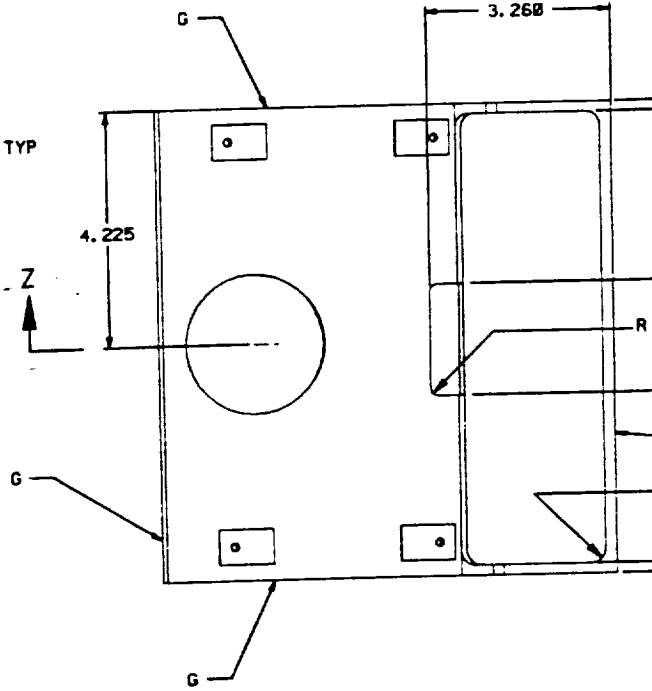
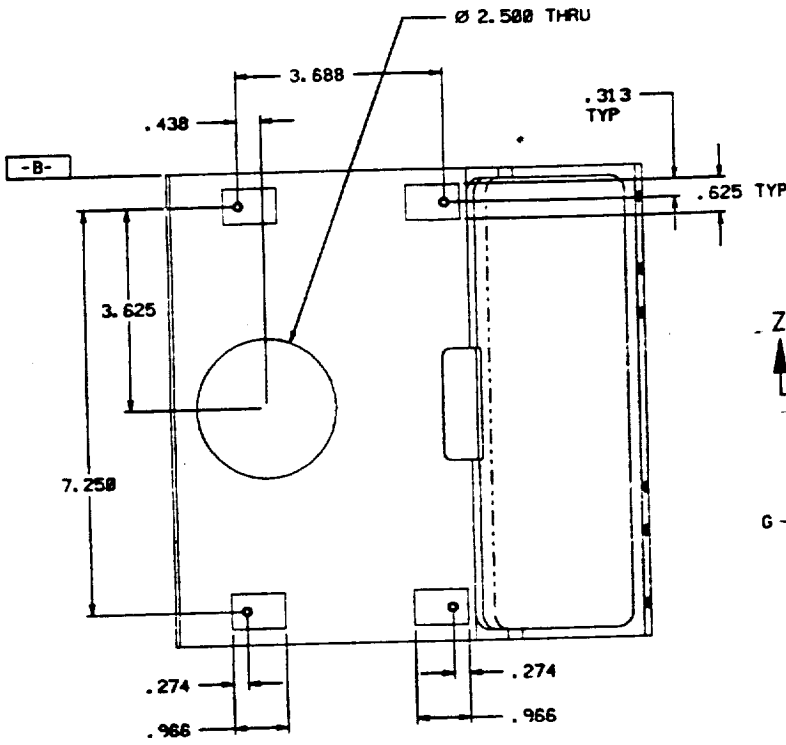
NOTICE			
ECOS BELOW FORM PART OF THIS DRAWING			

APPLICATION	QTY	USED ON	QTY
C13-10016	1		1
NEXT ASSY			

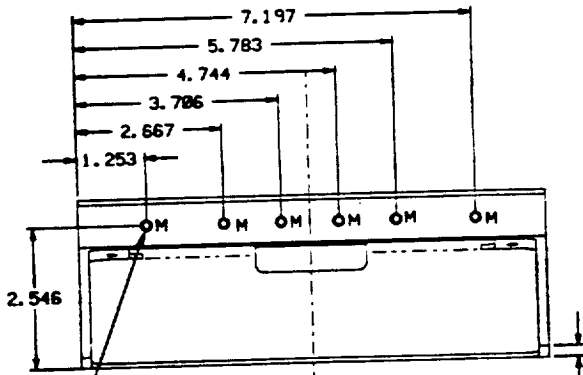
UNLESS OTHERWISE SPECIFIED DIMENSIONS ARE IN INCHES FRACTIONS DECIMALS ANGLES 1/8 1/16 1/32 1/64 3/16 1/4 5/16 3/8 7/16 1/2 5/8 3/4 7/8 1 1 1/8 1 1/4 1 1/2 1 3/4 2 2 1/4 2 1/2 3 3 1/4 3 1/2 4 4 1/4 4 1/2 5 5 1/4 5 1/2 6 6 1/4 6 1/2 7 7 1/4 7 1/2 8 8 1/4 8 1/2 9 9 1/4 9 1/2 10 10 1/4 10 1/2 11 11 1/4 11 1/2 12 12 1/4 12 1/2 13 13 1/4 13 1/2 14 14 1/4 14 1/2 15 15 1/4 15 1/2 16 16 1/4 16 1/2 17 17 1/4 17 1/2 18 18 1/4 18 1/2 19 19 1/4 19 1/2 20 20 1/4 20 1/2 21 21 1/4 21 1/2 22 22 1/4 22 1/2 23 23 1/4 23 1/2 24 24 1/4 24 1/2 25 25 1/4 25 1/2 26 26 1/4 26 1/2 27 27 1/4 27 1/2 28 28 1/4 28 1/2 29 29 1/4 29 1/2 30 30 1/4 30 1/2 31 31 1/4 31 1/2 32 32 1/4 32 1/2 33 33 1/4 33 1/2 34 34 1/4 34 1/2 35 35 1/4 35 1/2 36 36 1/4 36 1/2 37 37 1/4 37 1/2 38 38 1/4 38 1/2 39 39 1/4 39 1/2 40 40 1/4 40 1/2 41 41 1/4 41 1/2 42 42 1/4 42 1/2 43 43 1/4 43 1/2 44 44 1/4 44 1/2 45 45 1/4 45 1/2 46 46 1/4 46 1/2 47 47 1/4 47 1/2 48 48 1/4 48 1/2 49 49 1/4 49 1/2 50 50 1/4 50 1/2 51 51 1/4 51 1/2 52 52 1/4 52 1/2 53 53 1/4 53 1/2 54 54 1/4 54 1/2 55 55 1/4 55 1/2 56 56 1/4 56 1/2 57 57 1/4 57 1/2 58 58 1/4 58 1/2 59 59 1/4 59 1/2 60 60 1/4 60 1/2 61 61 1/4 61 1/2 62 62 1/4 62 1/2 63 63 1/4 63 1/2 64 64 1/4 64 1/2 65 65 1/4 65 1/2 66 66 1/4 66 1/2 67 67 1/4 67 1/2 68 68 1/4 68 1/2 69 69 1/4 69 1/2 70 70 1/4 70 1/2 71 71 1/4 71 1/2 72 72 1/4 72 1/2 73 73 1/4 73 1/2 74 74 1/4 74 1/2 75 75 1/4 75 1/2 76 76 1/4 76 1/2 77 77 1/4 77 1/2 78 78 1/4 78 1/2 79 79 1/4 79 1/2 80 80 1/4 80 1/2 81 81 1/4 81 1/2 82 82 1/4 82 1/2 83 83 1/4 83 1/2 84 84 1/4 84 1/2 85 85 1/4 85 1/2 86 86 1/4 86 1/2 87 87 1/4 87 1/2 88 88 1/4 88 1/2 89 89 1/4 89 1/2 90 90 1/4 90 1/2 91 91 1/4 91 1/2 92 92 1/4 92 1/2 93 93 1/4 93 1/2 94 94 1/4 94 1/2 95 95 1/4 95 1/2 96 96 1/4 96 1/2 97 97 1/4 97 1/2 98 98 1/4 98 1/2 99 99 1/4 99 1/2 100 100 1/4 100 1/2	DRG DATE 10-2-89	PERKIN ELMER LTD.
MATERIAL ALUM #6061-T651	DRAWN BY T G HAYDEN	
FINISH SEE NOTE 5	CHECKER D W [Signature]	CONTRACT NO. 21 336-1 0000
	APPROVED	DESIGN ACTIVITY APPROVAL
	APPROVED	OTHER APPROVAL
	Q56: [64, 51UV] 02. S10	SCALE : 1 WT.
		SIZE CODE IDENT NO. D 46555 C13-1 0008-001
		SHEET 1 OF 1

CAD DRAWING
DO NOT REVISE MANUALLY

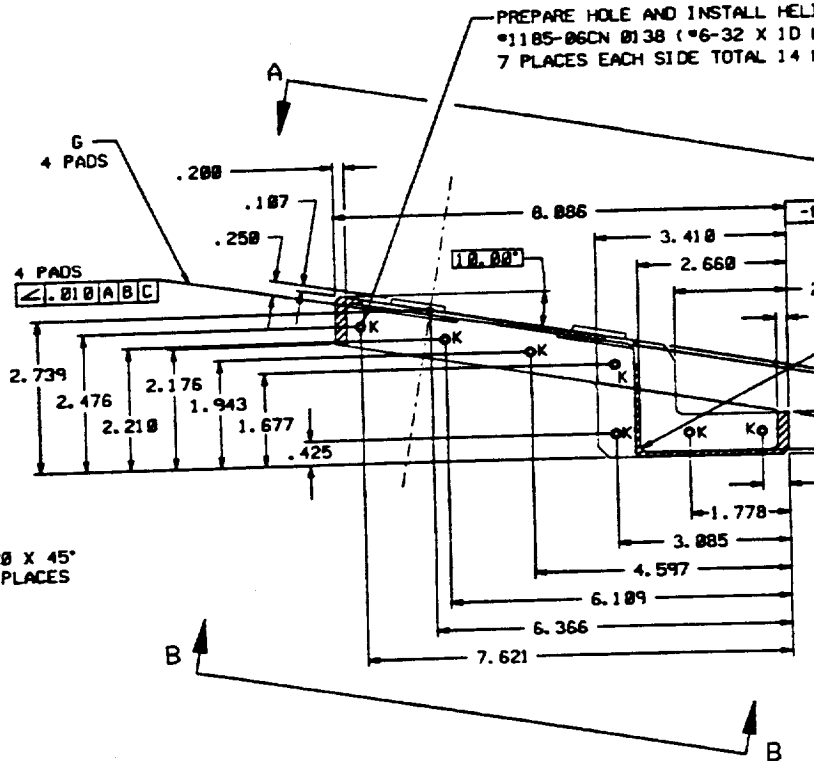
FOLDOUT FRAME



VIEW A - A
ROTATED 10° CCW



PREPARE HOLE AND INSTALL HELI-COIL INSERT
 #1185-2CN #164 (#8-32 X 1D LONG) PER MS33537.
 6 PLACES EACH SIDE TOTAL 12 MARKED M

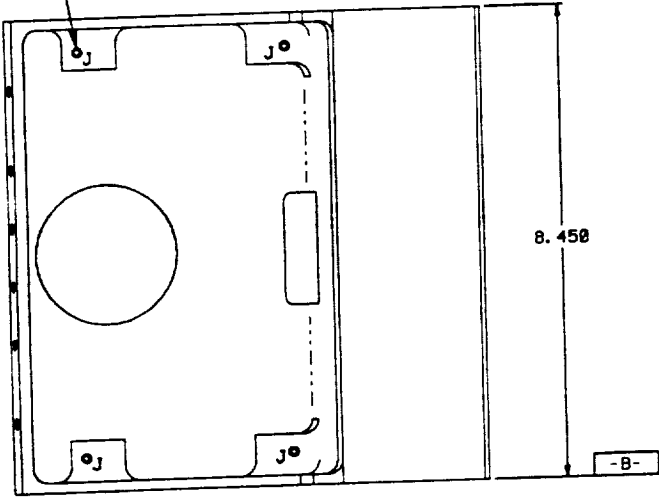


SECTION Z - Z

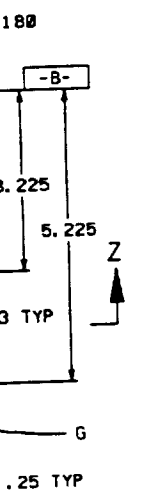
DATE	APPROVED

FOLDOUT FRAME 2

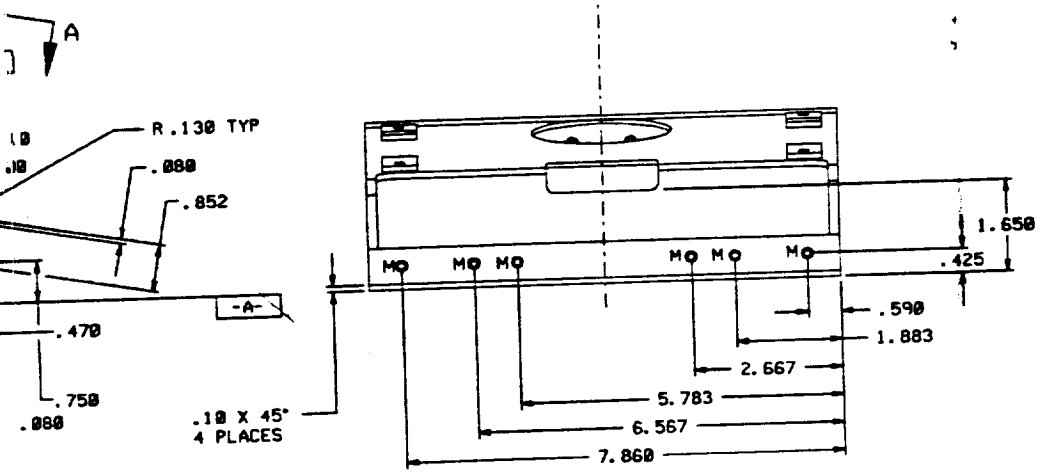
PREPARE HOLE AND INSTALL HELI-COIL INSERT
 *1185-06CN Ø138 (*6-32 X 1D LONG) PER MS33537.
 4 PLACES MARKED J



VIEW B - B
 ROTATED 18° CCW



OIL INSERT
 G) PER MS33537.
 MARKED K

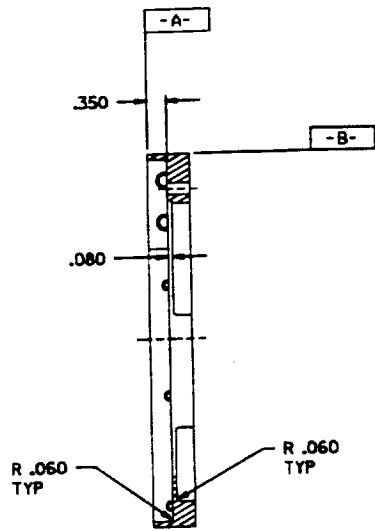


- 5.0 FINISH: CHEMICAL FILM PER MIL-C-5541 CLASS 3.
- 5.1 PAINT: FLAT BLACK PER SR 679-1074 EXCEPT SURFACES MARKED G. OMIT PAINT FROM ALL HOLES.
- 4.0 STRESS RELIEVE PER SR0842.
- 4.1 ROUGH MACHINE TO WITHIN .050 OF FINISHED SURFACE.
- 4.2 STRESS RELIEVE PER SR0842 PAR 3.1.50
- 4.3 SEMI-FINAL MACHINE TO WITHIN .005 OF FINISHED SURFACE.
- 4.4 TEMPERATURE CYCLE PER SR0842 PAR 3.1.50
- 4.5 FINISH MACHINE.
3. ALL DIMENSIONS APPLY AT 68°F (20°C).
2. PIECEMARK PART NO. (TAG OR BAG), PER S60211, METHOD 4.
1. WORKMANSHIP PER S60075.

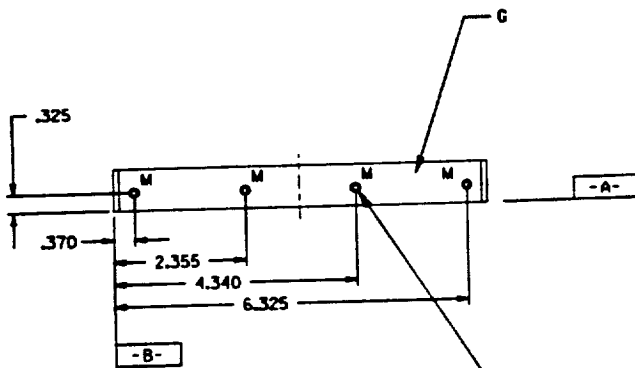
PERKIN ELMER SECONDARY SENSOR PANEL	PART NO. 21336-10000
	ALUM #6061-T651
SEE NOTE 5	PERKIN ELMER C13-10006-001

ORIGINAL PAGE IS
 OF POOR QUALITY

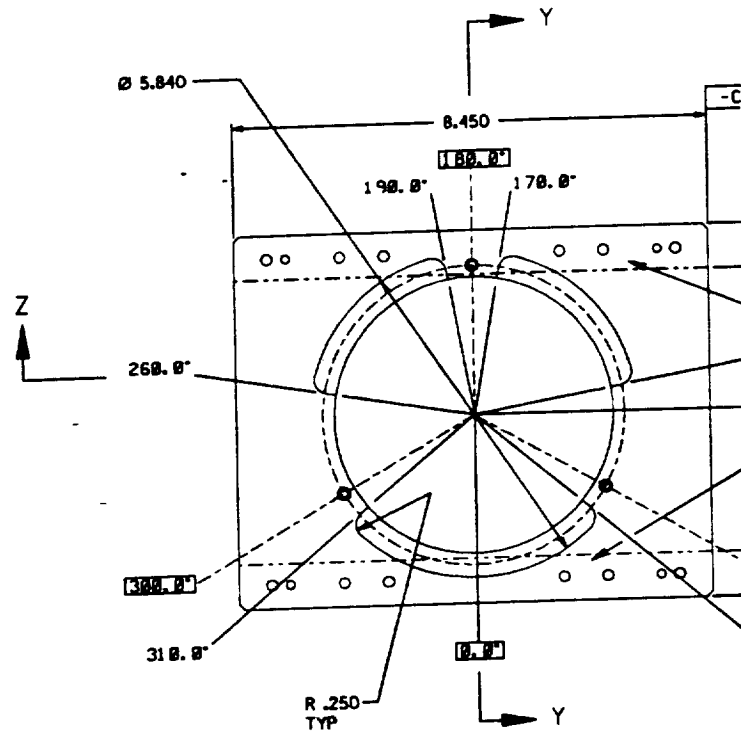
FOLDOUT FRAME



SECTION Y - Y



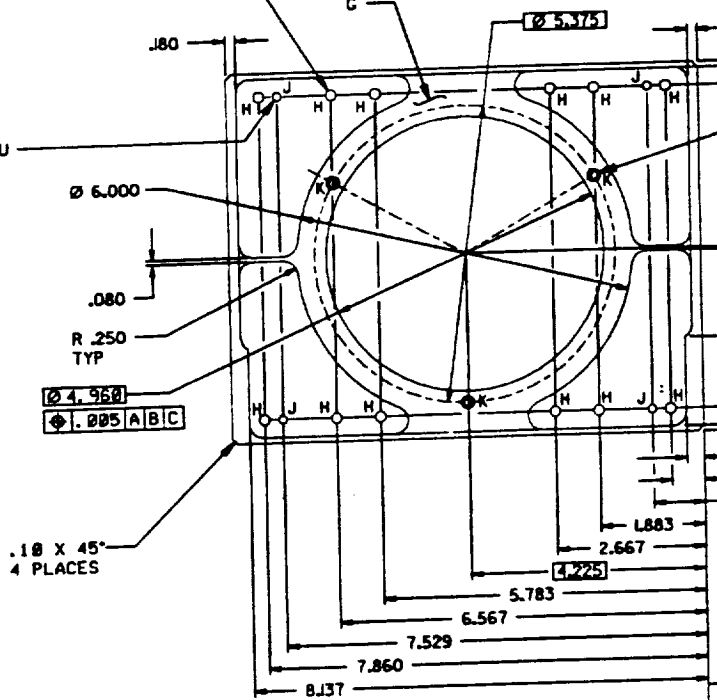
PREPARE HOLE AND INSTALL HELI-COIL INSERT
 #1185-B6CN Ø138 (*6-32 X 1D LONG) PER MS33537.
 TAP DRILL TO GO THRU ONE WALL
 4 PLACES MARKED M



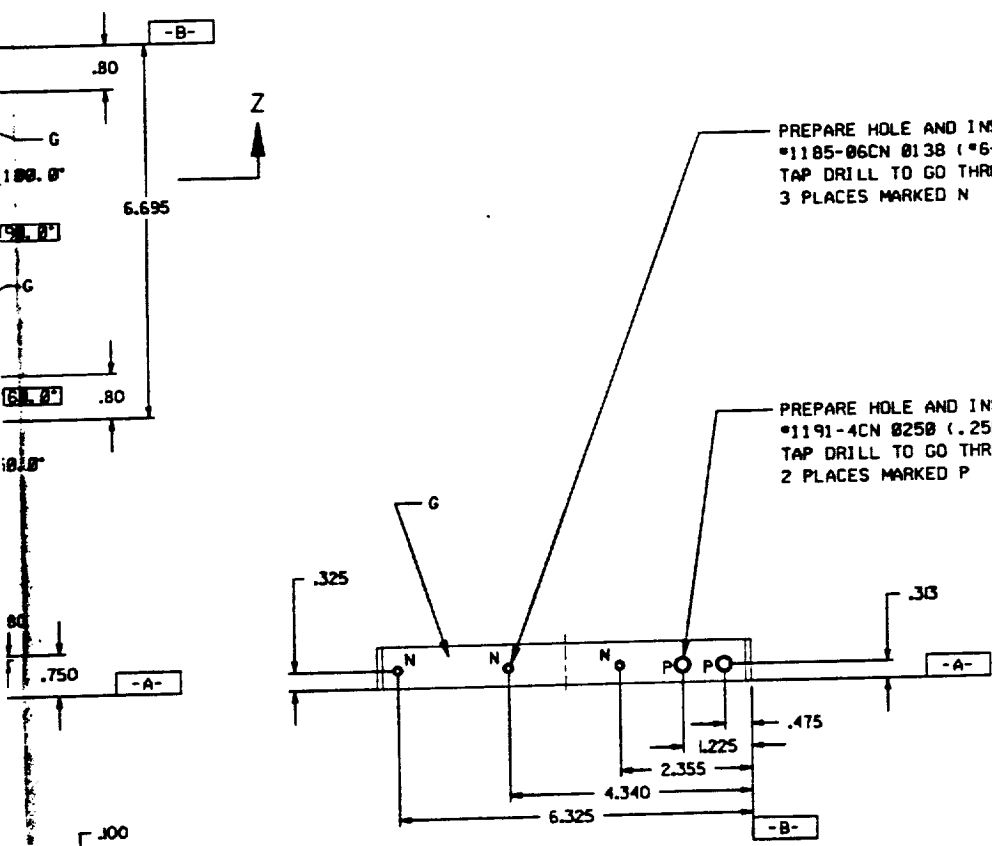
Ø .194 THRU
 12 HOLES
 MARKED H

SECTION Z - Z

Ø .141 THRU
 4 HOLES
 MARKED J



FOLDOUT FRAME 2



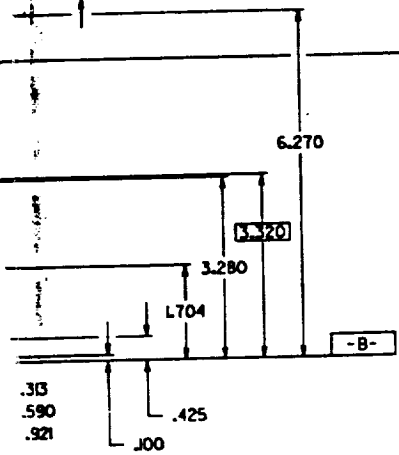
PREPARE HOLE AND INSTALL HELI-COIL INSERT
 *1185-06CN Ø138 (*6-32 X 10 LONG) PER MS33537.
 TAP DRILL TO GO THRU ONE WALL
 3 PLACES MARKED N

PREPARE HOLE AND INSTALL HELI-COIL INSERT
 *1191-4CN Ø25Ø (.25Ø-28 X 10 LONG) PER MS33537.
 TAP DRILL TO GO THRU ONE WALL
 2 PLACES MARKED P

PREPARE HOLE AND INSTALL HELI-COIL INSERT
 *1191-3CN Ø19Ø (*10-32 X 10 LONG) PER MS33537.
 TAP DRILL TO GO THRU
 3 PLACES EQUALLY SPACED ON BC SHOWN
 3 PLACES MARKED K
 ⌀.005 A B C

6. INSTALL HELI-COIL INSERTS AFTER FINAL FINISH.
5. FINISH: CHEMICAL FILM PER MIL-C-5541 CLASS 3.
- 5.1 PAINT FLAT BLACK PER SR 679-1074 EXCEPT SURFACES MARKED G. OMIT PAINT FROM ALL HOLES.
4. STRESS RELIEVE PER SR0842.
 - 4.1 ROUGH MACHINE TO WITHIN .050 OF FINISHED SURFACE.
 - 4.2 STRESS RELIEVE PER SR0842 PAR 3.1.5B
 - 4.3 SEMI-FINAL MACHINE TO WITHIN .005 OF FINISHED SURFACE.
 - 4.4 TEMPERATURE CYCLE PER SR0842 PAR 3.1.5D
 - 4.5 FINISH MACHINE.
3. ALL DIMENSIONS APPLY AT 68°F (20°C).
2. PIECEMARK PART NO. (TAG OR BAG) PER SG0211, METHOD 4.
1. WORKMANSHIP PER SG0075.

NOTES:



REV	DATE	BY	CHKD

CLASS	

ALUM *6061-T651	21 336-10000
SEE NOTE 5	

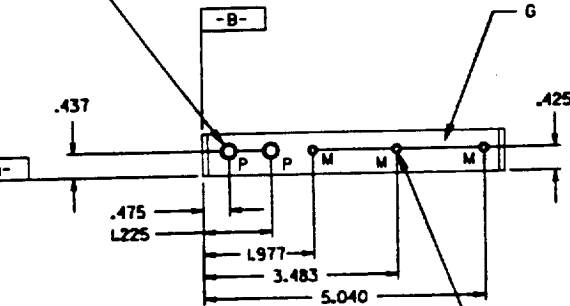
PERKIN ELMER	
TERTIARY MIRROR PANEL	
J 46325	C13-10012-001

FOLDOUT FRAME /

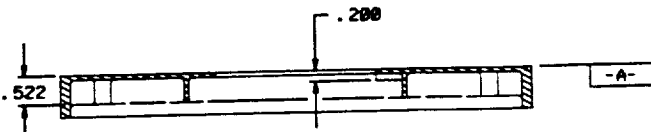
PREPARE HOLE AND INSTALL HELI-COIL INSERT
 *1185-04CN Ø112 (*4-40 X 1D LONG) PER MS33537.
 TAP DRILL TO GO THRU
 4 PLACES MARKED L

PREPARE HOLE AND INSTALL HELI-COIL INSERT
 *1185-06CN Ø138 (*6-32 X 1D LONG) PER MS33537.
 TAP DRILL TO GO THRU
 4 PLACES MARKED K

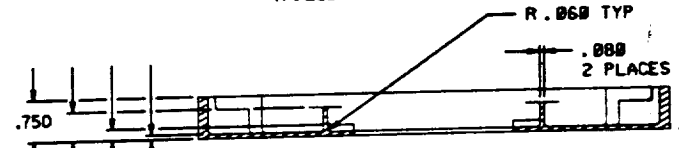
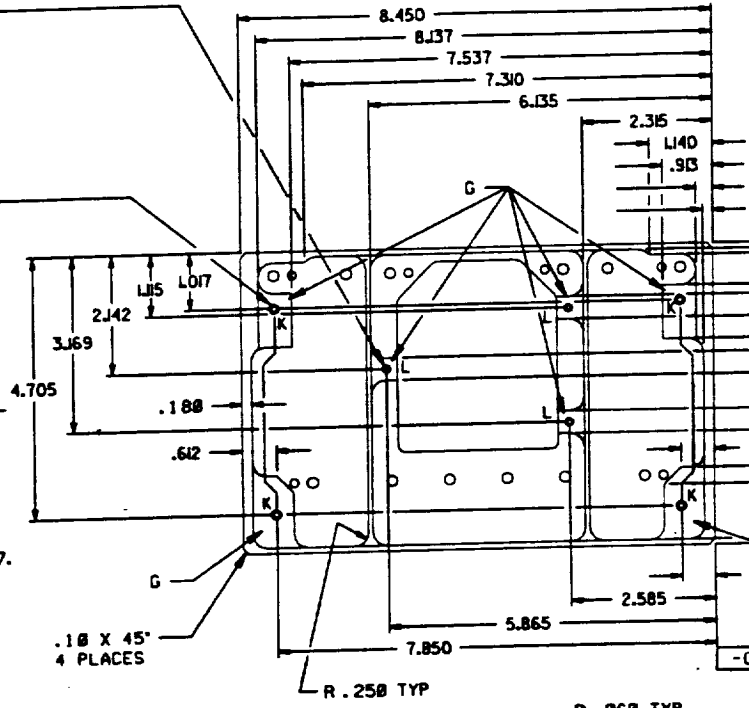
PREPARE HOLE AND INSTALL HELI-COIL INSERT
 *1191-4CN Ø375 (.250-28 X 1.5D LONG) PER MS33537.
 TAP DRILL TO GO THRU
 2 PLACES MARKED P



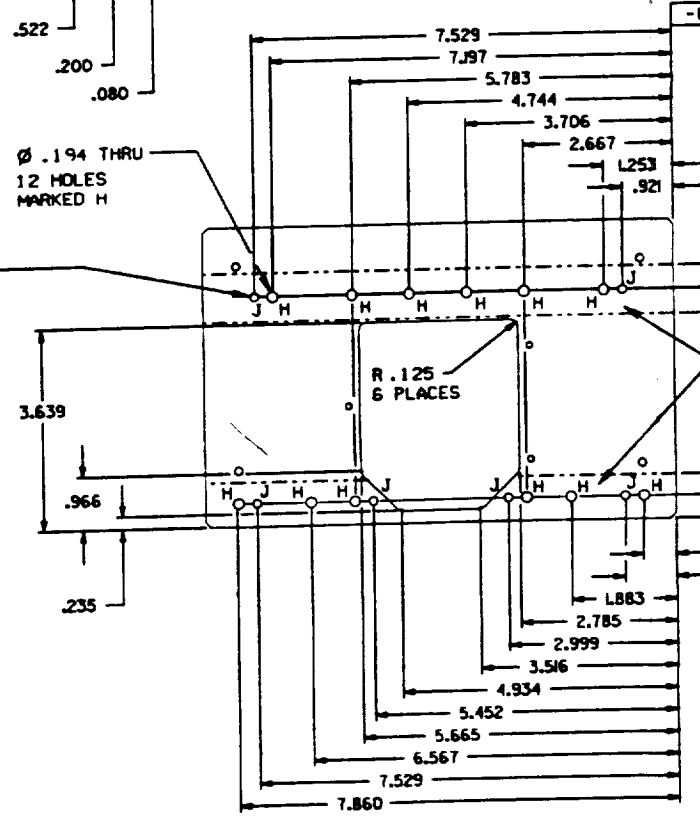
PREPARE HOLE AND INSTALL HELI-COIL INSERT
 *1185-06CN Ø138 (*6-32 X 1D LONG) PER MS33537.
 TAP DRILL TO GO THRU ONE WALL
 3 PLACES MARKED M



SECTION Y - Y

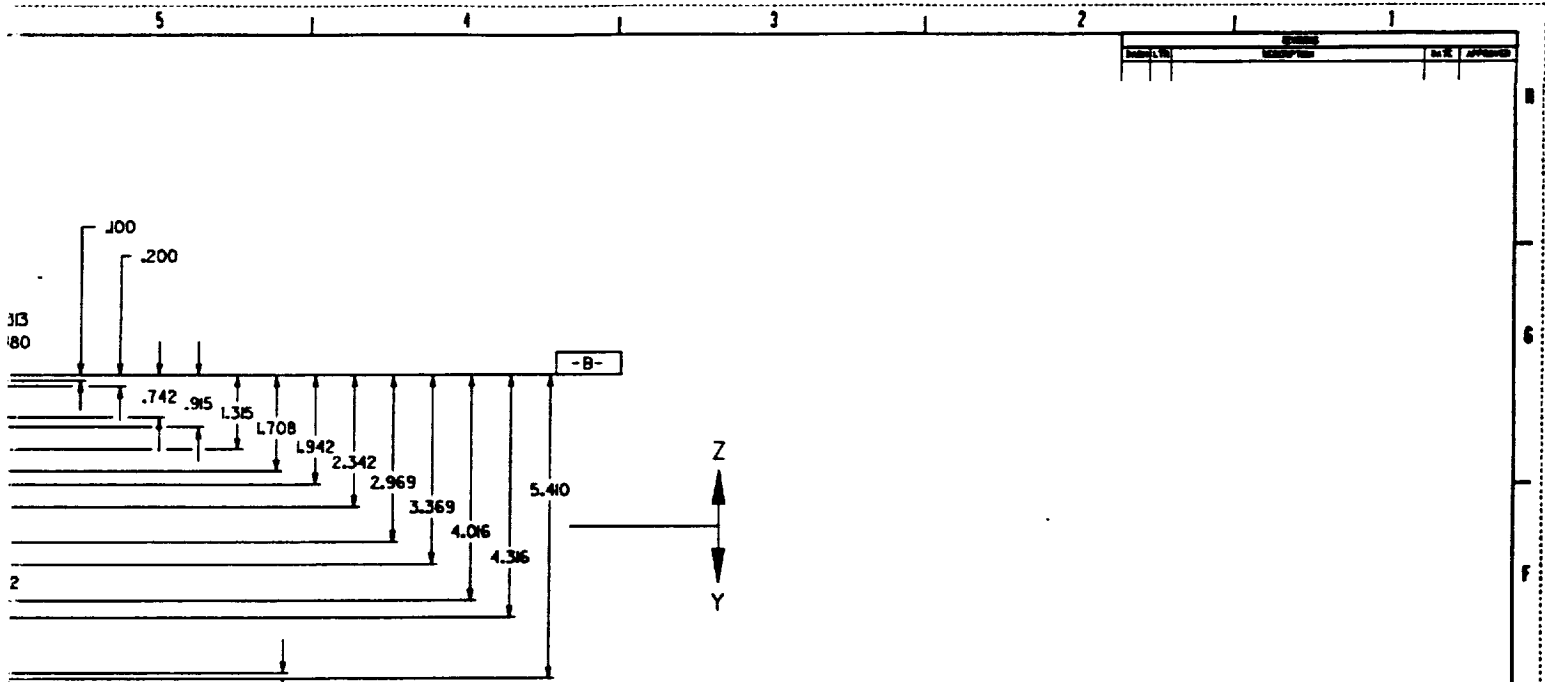


SECTION Z - Z

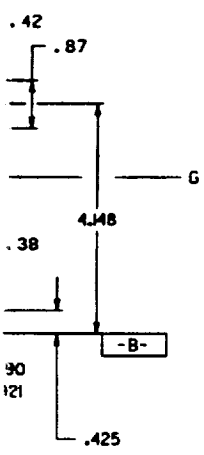
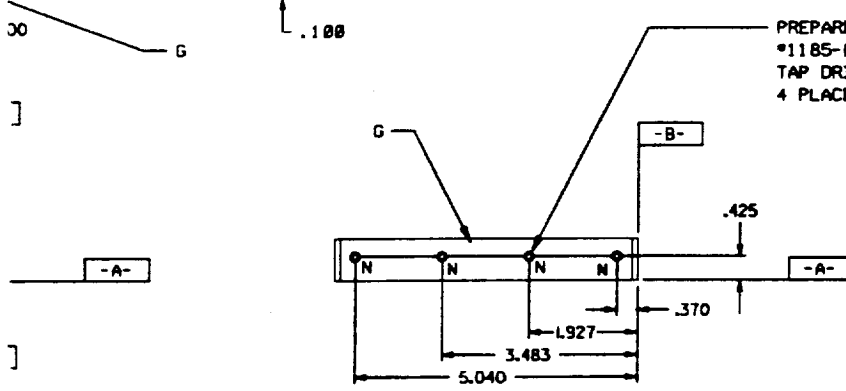


ORIGINAL PAGE IS
 OF POOR QUALITY

FOLDOUT FRAME



PREPARE HOLE AND INSTALL HELI-COIL INSERT
 *1185-06CN Ø138 (*6-32 X 1D LONG) PER MS33537.
 TAP DRILL TO GO THRU ONE WALL
 4 PLACES MARKED N



6. INSTALL HELI-COIL INSERTS AFTER FINAL FINISH.
- 5.0 FINISH: CHEMICAL FILM PER MIL-C-5541 CLASS 3.
- 5.1 PAINT FLAT BLACK PER SR 679-1074 EXCEPT SURFACES MARKED G. OMIT PAINT FROM ALL HOLES.
- 4.0 STRESS RELIEVE PER SR0042.
- 4.1 ROUGH MACHINE TO WITHIN .050 OF FINISHED SURFACE.
- 4.2 STRESS RELIEVE PER SR0042 PAR 3.1.5B
- 4.3 SEMI-FINAL MACHINE TO WITHIN .005 OF FINISHED SURFACE.
- 4.4 TEMPERATURE CYCLE PER SR0042 PAR 3.1.5D
- 4.5 FINISH MACHINE.
3. ALL DIMENSIONS APPLY AT 68°F (20°C).
2. PIECEMARK PART NO. (TAG OR BAG), PER SGB211, METHOD 4.
1. WORKMANSHIP PER SGB075.

NOTES:

REV	DATE	DESCRIPTION

CLASS	

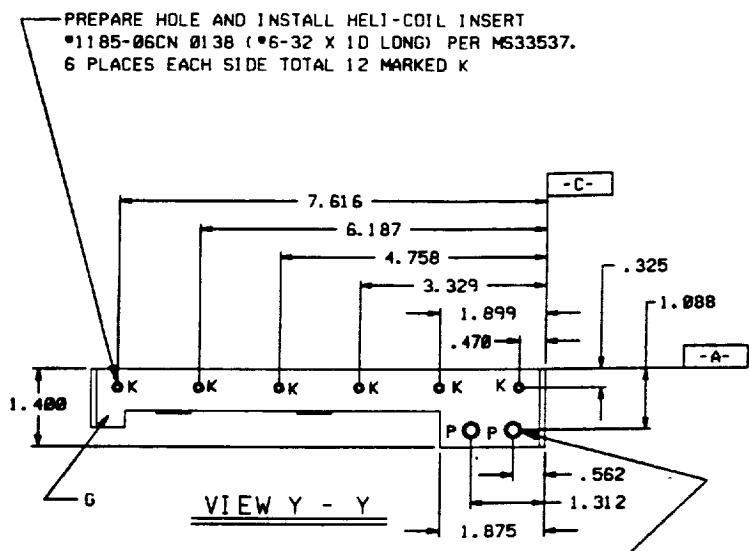
113-10011	

ALUM *6061-T651	
SEE NOTE 5	

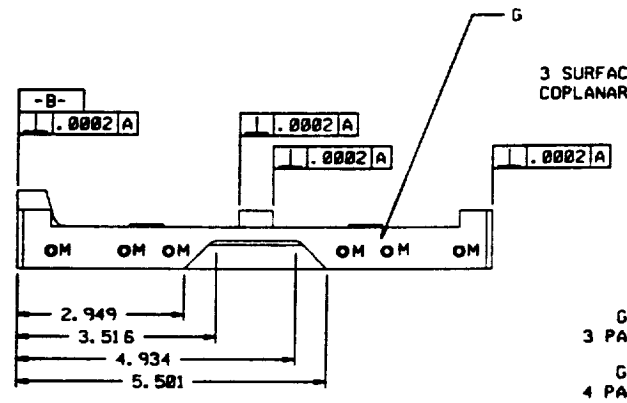
PERKIN ELMER	
PRIMARY SENSOR PANEL	
J 46555	C13-10011-001

ORIGINAL PAGE IS OF POOR QUALITY

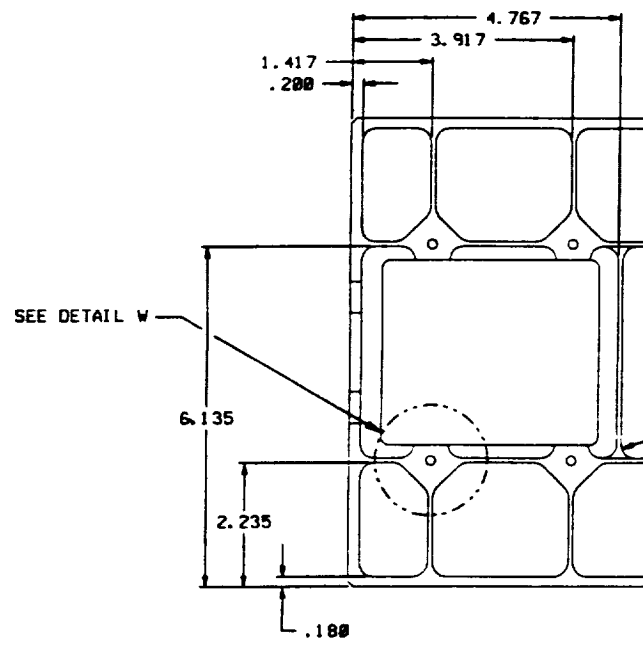
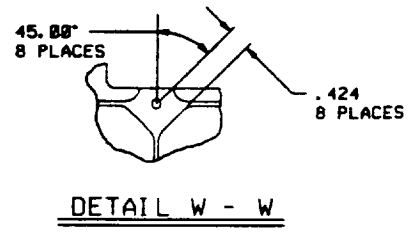
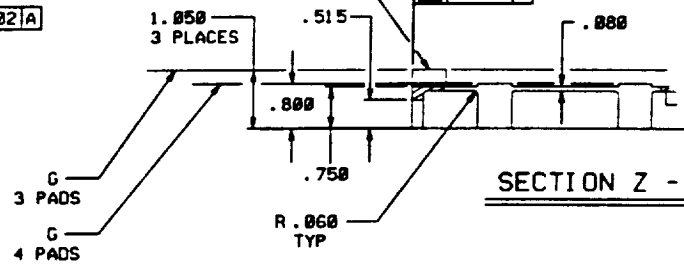
FOLDOUT FRAME



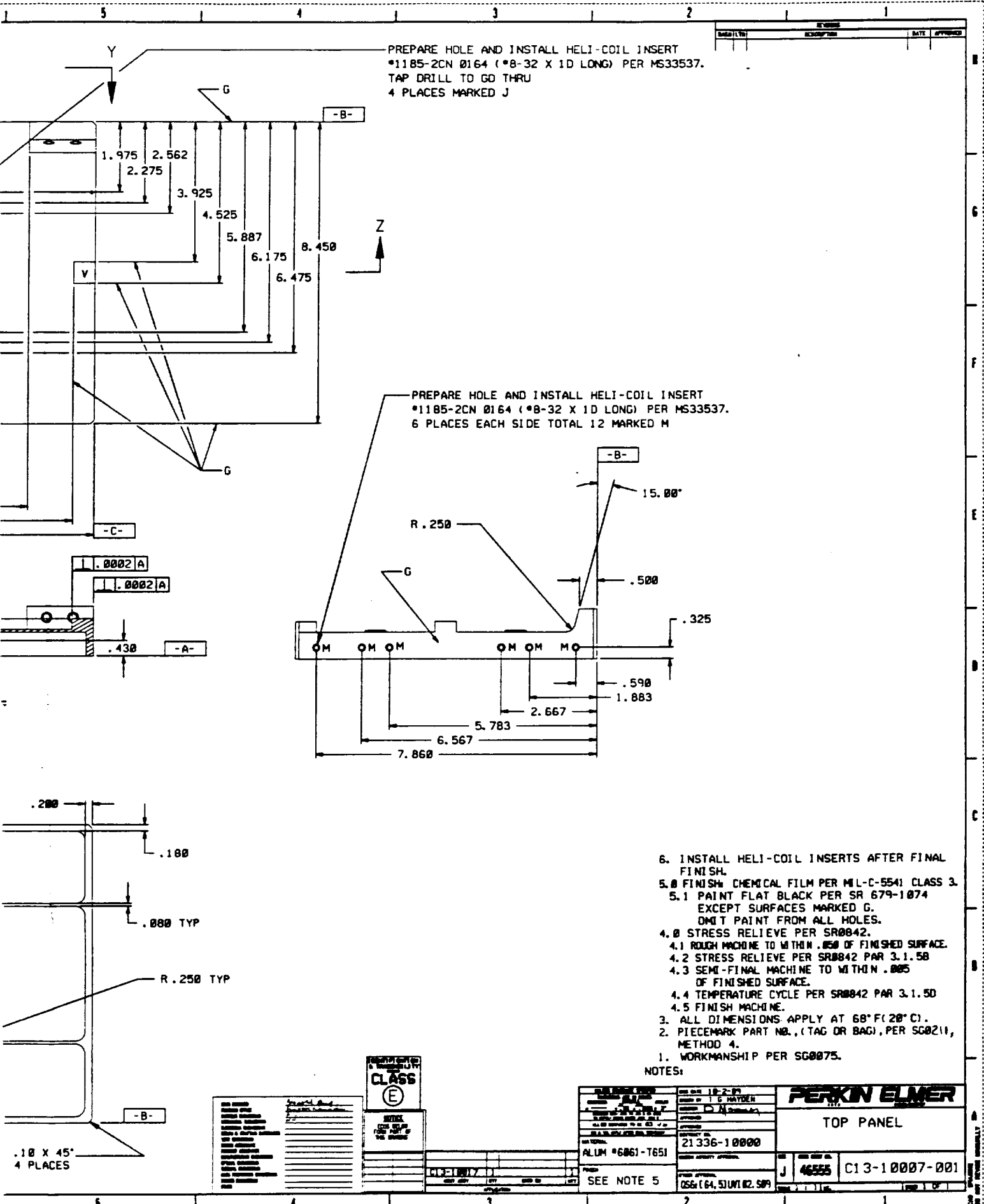
PREPARE HOLE AND INSTALL HELI-COIL INSERT
 *1191-4CN Ø375 (.250-28 X 1.50 LONG) PER MS33537.
 TAP DRILL TO GO THRU
 2 PLACES MARKED P



3 SURFACES MARKED V TO BE
 COPLANAR TO A WITHIN .0004



FOLDOUT FRAME



PREPARE HOLE AND INSTALL HELI-COIL INSERT
 *1185-2CN Ø164 (*8-32 X 1D LONG) PER MS33537.
 TAP DRILL TO GO THRU
 4 PLACES MARKED J

PREPARE HOLE AND INSTALL HELI-COIL INSERT
 *1185-2CN Ø164 (*8-32 X 1D LONG) PER MS33537.
 6 PLACES EACH SIDE TOTAL 12 MARKED M

6. INSTALL HELI-COIL INSERTS AFTER FINAL FINISH.
- 5.0 FINISH: CHEMICAL FILM PER MIL-C-5541 CLASS 3.
- 5.1 PAINT FLAT BLACK PER SR 679-1074 EXCEPT SURFACES MARKED G. OMIT PAINT FROM ALL HOLES.
- 4.0 STRESS RELIEVE PER SR0842.
- 4.1 ROUGH MACHINE TO WITHIN .050 OF FINISHED SURFACE.
- 4.2 STRESS RELIEVE PER SR0842 PAR 3.1.50
- 4.3 SEMI-FINAL MACHINE TO WITHIN .005 OF FINISHED SURFACE.
- 4.4 TEMPERATURE CYCLE PER SR0842 PAR 3.1.50
- 4.5 FINISH MACHINE.
3. ALL DIMENSIONS APPLY AT 68°F (20°C).
2. PIECEMARK PART NO., (TAG OR BAG), PER SG0211, METHOD 4.
1. WORKMANSHIP PER SG0075.

NOTES:

REV	DATE	DESCRIPTION

INSPECTED BY
CLASS
 (E)
 REVIEW
 DATE

ALUM #6061-T651	21336-10000
SEE NOTE 5	

PERKIN ELMER
 TOP PANEL
 J 46555 C13-10007-001

ORIGINAL PAGE IS
 OF POOR QUALITY